

Design, Modeling, Fabrication, and Testing of a Piezoelectric Microvalve for High Pressure, High Frequency Hydraulic Applications

by

David C. Roberts

S.B., Mechanical Engineering
Massachusetts Institute of Technology, 1995

S.M., Mechanical Engineering
Massachusetts Institute of Technology, 1998

SUBMITTED TO THE DEPARTMENT OF MECHANICAL ENGINEERING
IN PARTIAL FULFILLMENT OF THE DEGREE OF
DOCTORATE OF PHILOSOPHY

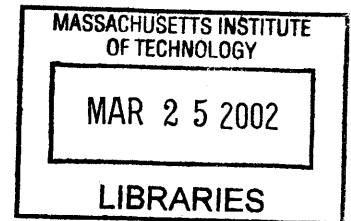
at the

MASSACHUSETTS INSTITUTE OF TECHNOLOGY

February 2002

© 2002 Massachusetts Institute of Technology
All rights reserved

BARKER



Signature of Author
Department of Mechanical Engineering
Certified by Doctoral Committee
January 10, 2002

.....
Nesbitt W. Hagood (Co-Chair), Associate
Professor of Aeronautics and Astronautics
.....
David L. Trumper (Co-Chair), Associate
Professor of Mechanical Engineering

.....
Martin A. Schmidt
Professor of Electrical Engineering
.....
S. Mark Spearing, Associate
Professor of Aeronautics and Astronautics

Accepted by
Professor Ain Sonin
Chairman, Department Graduate Committee

Design, Modeling, Fabrication, and Testing of a Piezoelectric Microvalve for High Pressure, High Frequency Hydraulic Applications

by

David C. Roberts

Submitted to the Department of Mechanical Engineering on January 10, 2002, in partial fulfillment of the requirements for the Degree of Doctor of Philosophy in Mechanical Engineering.

Abstract

A piezoelectrically-driven hydraulic amplification microvalve for use in high specific power hydraulic pumping applications was designed, fabricated, and experimentally characterized. High frequency, high force actuation capabilities were enabled through the incorporation of one or more bulk piezoelectric material elements beneath a micromachined annular tethered-piston structure. An hydraulic amplification mechanism was employed to amplify the limited stroke of this piezoelectrically-driven piston structure to a significantly larger motion (40-50x) of a micromachined valve membrane with attached valve cap. This valve cap was actuated through its stroke to open and close against a fluid orifice. These design features enabled the valve device to simultaneously meet a set of high frequency (1-10kHz), high pressure(0.1-1MPa), and large stroke (15-40 μ m) requirements that had not previously been satisfied by other microvalves presented in the literature.

This research was carried out through a series of modeling, design, fabrication, assembly, and experimental testing tasks. Linear and non-linear modeling tools characterizing the structural deformations of the active valve sub-systems were developed. These tools enabled accurate prediction of real-time stresses along the micromachined valve membrane structure during deflection into its non-linear large-deflection regime. A systematic design procedure was developed to generate an active valve geometry to satisfy membrane stress limitations and valve power consumption requirements set forth by external hydraulic system performance goals. Fabrication challenges, such as deep-reactive ion etching (DRIE) of the drive element and valve membrane structures, wafer-level silicon-to-silicon fusion bonding and silicon-to-glass anodic bonding operations, preparation and integration of piezoelectric material elements within the micromachined tethered piston structure, die-level assembly and bonding of silicon and glass dies, and filling of degassed fluid within the hydraulic amplification chamber were overcome.

The active valve structural behavior and flow regulation capabilities were evaluated over a range of applied piezoelectric voltages, actuation frequencies, and differential pressures across the valve. For applied piezoelectric voltages up to 500Vpp at 1kHz, the valve devices demonstrated amplification ratios of drive element deflection to valve cap deflection of 40-50x. These amplification ratios correlated within 5 – 10% of the model expectations. Flow regulation experiments proved that a peak average flow rate through the device of 0.21mL/s under a 1kHz sinusoidal drive voltage of 500Vpp, with valve opening of 17 μ m, against a differential pressure of 260kPa could be obtained. Tests revealed that fluid-structural interactions between the valve cap and membrane components and flow instabilities (due to transition between the laminar and turbulent flow regimes through the valve orifice) limited the valve performance capabilities.

Thesis Supervisor: Dr. Nesbitt W. Hagood

Title: Associate Professor of Aeronautics and Astronautics

Acknowledgements

This research work was sponsored by DARPA under Grant #DAAG55-98-1-0361
and by ONR under Grant #N00014-97-1-0880.

The research presented in this thesis could not have been accomplished without the generous support and hard work of a large group of individuals. First and foremost, I would like to thank my advisor, Dr. Nesbitt Hagood, for providing the programmatic resources and support for this research, as well as the numerous opportunities to present this work within the MIT community and at academic conferences. Additionally, his ability to always be one step ahead of the game kept me sharp and forced me to defend and clearly justify all of the decisions made along the path of my PhD work. I would also like to acknowledge my doctoral committee members, Dr. Martin Schmidt, Dr. Mark Spearing, and Dr. David Trumper, for their advice and direction during this work. These interactions have helped me to mature, both intellectually and personally. Additionally, I would like to acknowledge Dr. Kenneth Breuer, at Brown University, for his very helpful guidance on microscale fluid related issues.

I owe a great deal of thanks to Dr. Richard Mlcak, at Boston Microsystems, Inc, for his introduction to the world of MEMS, through initial piezoelectric material integration studies at the onset of the MHT research program four years ago and his continued support in the area of microscale fluid filling and sealing. Additionally, instrumental to the accomplishments embodied within this work were Dr. Laxman Saggere, for his advice on modeling assumptions within my active valve optimization code; Kevin Turner, for his contributions in the area of eutectic bonding; Blair Connelly, for her hard work in the development of testing apparatus for use with the laser vibrometer system used in this work; David Robertson, for his lab organization and debugging activities; Tim Glenn, for his generous support in providing exceptional renderings of MEMS devices for the MHT program; and Seward (Chip) Pulitzer, for his initial system modeling work at the beginning of the program.

Jorge Carretero and Onnik Yaglioglu have been sources of continual support in the development of fluid flow models and full system-level simulations for this active valve device and for MHT systems, in general. Dr. Yu-Hsuan Su was essential to the development of the finite-difference numerical modeling scheme, which serves as the backbone of the non-linear large deflection valve membrane code presented in Chapter 2 of this thesis. Dr. Hanqing Li deserves an unbelievable amount of recognition for his dedication in and out of the cleanroom, providing the MHT program with repeatable and robust fabrication processes for the creation of etched silicon wafers and silicon-glass bonded stacks. Lastly, from the programmatic side of things, I have to give a great deal of thanks to Lodewyk Steyn, who throughout his time on the MHT program, has performed duties above and beyond what were required of him in an effort to unselfishly move the program forward. Without his dedication, especially on the experimental testing side of the program, the validation of fluid-filled active valve devices would not have been accomplished in such an aggressive time frame.

Finally, I would like to thank my family. None of this work could have been accomplished without the positive support from my Mom, Dad, and brother Will. Most importantly, I have to thank my wife, Heather, for her unbelievable support and patience through four and half years of sometimes frustrating, sometimes exhilarating, and all the time stressful research work.

Contents

1	Introduction	25
1.1	Motivation	25
1.2	Overview of Previous Microvalve Technology	28
1.3	Concept	33
1.4	Challenges	35
1.4.1	Modeling and Design Challenges	36
1.4.2	Device Fabrication, Assembly, and Testing Challenges	37
1.5	Objectives	39
1.6	Approach	39
1.7	Thesis Executive Summary	41
2	Active Valve Linear Model	47
2.1	Valve Geometry and Modeling Procedure	47
2.2	Overview of Linear Plate Theory	48
2.2.1	Deflections Due to Bending	49
2.2.2	Deflections Due to Shearing	50
2.2.3	Combined Deflection Due to Bending and Shearing	51
2.2.4	Comparison of Bending/Shearing Deflections	51
2.3	Detailed Structural Modeling	52
2.3.1	Piezoelectric Material Behavior	52
2.3.2	Drive Element Piston and Tether Behavior	53
2.3.3	Bottom Structural Compliance	57
2.3.4	Fluid Compressibility	58
2.3.5	Top Structural Compliance	58
2.3.6	Valve Cap and Membrane Behavior	59
2.4	Full Active Valve Linear Model	61
2.5	Impact of Multiple Piezoelectric Cylinders	62
2.5.1	Finite-Element Analysis of Piston	62

2.5.2	Finite-Element Analysis of Bottom Plate	65
2.6	Further Modeling Issues	66
2.7	Conclusions	67
3	Non-Linear Deformation of the Valve Cap and Membrane	69
3.1	Introduction	69
3.2	Plate Geometry	70
3.3	Theory	70
3.3.1	Assumptions	70
3.3.2	Equilibrium Equations	71
3.3.3	Geometric Compatibilities	72
3.3.4	Constitutive Laws	73
3.3.5	Governing Equations	73
3.3.6	In-Plane Prestress	74
3.3.7	Non-Dimensionalized Governing Equations	76
3.3.8	Finite-Difference Implementation	78
3.3.9	Post-Processing Calculations	81
3.4	Results of Numerical Code	83
3.4.1	Loading: $P_1 = P_2 = 0, P_3 = 100kPa, N_o = 0$	84
3.4.2	Loading: $P_1 = 2.90MPa, P_2 = 0, P_3 = 1.30MPa, N_o = 0$	84
3.4.3	Loading: $P_1 = P_2 = 0$, Varying $P_3, N_o = 0$	85
3.4.4	Loading: $P_1 = P_2 = 0, P_{HAC} = 100kPa$, Varying N_o	86
3.5	Matlab Non-Linear Tools	87
3.6	Conclusions	89
4	Active Valve Non-Linear Model and Simulation	91
4.1	Quasi-Static Active Valve Model	91
4.2	Accuracy of Quasi-Static Model	93
4.2.1	Assumptions in Model	93
4.2.2	FEM Model Geometries and Correlation Procedure	94
4.2.3	Model Correlation Procedure	95
4.2.4	Valve Geometry	96
4.2.5	Model Correlation	97
4.3	Finite-Element Resonant Behavior	101
4.4	Dynamic Active Valve Simulation	102
4.4.1	Linear Matrix Relations	102
4.4.2	Non-Linear Look-Up Tables	103
4.4.3	Piston and Valve Cap Dynamics	104

4.5	Conclusions	106
5	Active Valve Design Procedure	109
5.1	Valve Requirements in Generic MHT System	110
5.2	Modeling of External Hydraulic System	111
5.2.1	MHT Chamber Stiffness	112
5.2.2	Valve Channel Inertial Effects	113
5.2.3	Valve Orifice Flow Relations	113
5.2.4	Chamber Filling Simulation Tool	116
5.3	Systematic Design Procedure	118
5.3.1	Overview	118
5.3.2	System Requirements	119
5.3.3	Step 1: Design of Valve Cap	119
5.3.4	Step 2: Design of Valve Membrane	121
5.3.5	Step 3: Design of Piezoelectric Drive Element	122
5.4	Design Freedoms Within Procedure	125
5.4.1	Design Freedom: $Z_{vc,stroke}$	125
5.4.2	Design Freedom: t_{vm}	126
5.5	Power Consumption in Active Valve	134
5.5.1	Overview of Energy/Power Consumption	134
5.5.2	Benefit of Multiple Valve Heads	135
5.6	Results of Systematic Design Procedure	138
5.7	Correlation With Dynamic Simulation	142
5.8	Conclusions	145
6	Device Fabrication and Preparation for Testing	147
6.1	Introduction	147
6.2	Fabrication Challenges and Procedures	148
6.2.1	Etching of Tethered Drive Element and Valve Membranes	149
6.2.2	Wafer-Level Bonding	151
6.2.3	Integration of Bulk Piezoelectric Elements	152
6.2.4	Die-Level Assembly and Bonding	157
6.2.5	Fluid Filling/Sealing of HAC	161
6.3	Sub-Component Testing Plan	165
6.3.1	Piezoelectric Drive Element	165
6.3.2	Valve Cap and Membrane	166
6.3.3	Full Active Valve	167
6.4	Testing Apparatus	167

6.4.1	Laser Vibrometer System	167
6.4.2	Fluids Test-Rig	168
6.5	Conclusions	168
7	Sub-Component Study: Piezoelectric Drive Element	173
7.1	Objectives	173
7.2	Device Test-Plan	174
7.2.1	1st Generation Devices	174
7.2.2	2nd Generation Device	176
7.3	Device Assembly	177
7.4	Testing Procedure	180
7.5	Experimental Results	180
7.5.1	1st Generation Devices	180
7.5.2	2nd Generation Device	196
7.6	Conclusions	200
8	Sub-Component Study: Valve Cap and Membrane	203
8.1	Objectives	203
8.2	Device Test-Plan	204
8.2.1	Geometry	204
8.2.2	Device Assembly	205
8.2.3	Testing Procedure	205
8.3	Theoretical Predictions	206
8.3.1	1st Modeling Procedure: Numerical Non-linear Deflection Code	206
8.3.2	2nd Modeling Procedure: Finite-element Code	207
8.4	Experimental Results	213
8.4.1	Fillet Radius Inspection	213
8.4.2	Pressure-Deflection Results	213
8.5	Conclusions	214
9	Active Valve Testing	217
9.1	Objectives	217
9.2	Device Test-Plan	218
9.2.1	Geometry	218
9.2.2	Plan of Study	218
9.3	Experimental Testing Section 1: Active Valve Structural Performance	220
9.3.1	Testing Section 1: Active Valve Structural Performance	220
9.3.2	Testing Section 2: Active Valve Fluid Flow Regulation	252

9.4	Conclusions	276
10	Conclusions and Recommendations	279
10.1	Summary and Conclusions	279
10.1.1	Thesis Summary	279
10.1.2	Thesis Contributions	284
10.2	Recommended Further Work and the Future of MHTs	285
10.2.1	Redesign for Enhanced Operational Frequency	286
10.2.2	Understanding of Flow Induced Structural Instabilities	287
10.2.3	Materials Characterization	290
10.2.4	Microfabrication Issues	291
10.2.5	Future of MHTs	292
A	Support Documentation for Active Valve Linear Model	295
A.1	ChapterExample.mws	296
A.2	FullActiveValve(LINEAR).mws [see Section 2.4]	299
B	Support Documentation for Non-Linear Valve Cap/Membrane	313
B.1	NLValveCapMembrane-CaseA.m [see Section 3.5]	314
B.2	NLValveCapMembrane-CaseB.m [see Section 3.5]	318
B.3	NLValveCapMembrane-CaseC.m [see Section 3.5]	322
C	Support Documentation for Full Non-Linear Active Valve Model	327
C.1	FullActiveValve(Non-Linear).mws [Section 4.1]	328
C.2	NLActiveValveMatlab.m [Section 4.1]	334

List of Figures

1.1	Upper bound on specific work vs. frequency for various actuation media	27
1.2	Generic block diagrams of Micro-Hydraulic Transducer systems	28
1.3	Selected thermal, electrostatic, and electromagnetic microvalves previously reported in the literature	29
1.4	Selected piezoelectrically-driven microvalves previously reported in the literature	31
1.5	3-D schematic of the piezoelectrically driven hydraulic amplification microvalve .	34
1.6	Schematic of the fabricated multi-layer active valve structure	36
1.7	Schematic of fabricated multi-layer MHT actuator device	37
1.8	Active valve sub-component fabrication and testing plan	41
1.9	Photograph of a 9-layer piezoelectrically-driven hydraulic amplification microvalve.	42
2.1	2-D schematic of the piezoelectrically-driven hydraulic amplification microvalve. .	48
2.2	Linear plate theory for a generic circular plate.	49
2.3	Bending and shearing contributions to plate deformation	52
2.4	Modeling of the piezoelectric material element	53
2.5	Modeling of the drive element tethered piston structure	54
2.6	Modeling of the bottom structural plate	58
2.7	Modeling of the top structural plate	59
2.8	Linear modeling of the valve cap and membrane structure	59
2.9	Simplified schematic of the valve membrane structure	60
2.10	Blow-up view of the modeled components in the microvalve	61
2.11	Finite-element schematics of the drive element piston	63
2.12	Compliance coefficients for the drive element piston with multiple piezoelectric cylinders	64
2.13	Finite-element schematics of the bottom plate structure	65
2.14	Compliance coefficients of the bottom plate structure with multiple piezoelectric cylinders	66
3.1	Simplified schematic of the valve membrane structure	70

3.2	Force and moment diagrams for a plate section	71
3.3	Schematic of a pretensioned annular plate	75
3.4	Coordinate transformation used within numerical code	79
3.5	Pressure loading terminology on an annular plate	83
3.6	Deflection of a thin annular plate under loading scenario 1	84
3.7	Deflection of a thin annular plate under loading scenario 2	86
3.8	Deflection of a thin annular plate under loading scenario 3	87
3.9	Deflection of a thin annular plate under loading scenario 4	88
3.10	Numerical code tools to be used throughout thesis	89
4.1	Quasi-static non-linear active valve model overview	92
4.2	Finite-element model of the active valve without fillet radii	94
4.3	Finite-element model of the active valve with fillet radii	95
4.4	Boundary conditions imposed in the active valve finite-element models	96
4.5	Monitored variables in the active valve models	97
4.6	Finite-element stresses predicted in the active valve device	100
4.7	Finite-element modal behavior of the active valve	102
4.8	Dynamic simulation architecture of the active valve	103
4.9	Look-up tables describing valve membrane large deflection behavior	104
4.10	Piston dynamics included in the simulation	105
4.11	Valve cap dynamics included in the simulation	105
5.1	Schematic of a generic MHT power harvesting device	110
5.2	Filling/evacuation of the harvesting chamber through the valves	112
5.3	Modeling of the valve orifice	113
5.4	Look-up tables for valve orifice coefficients	115
5.5	Simulation architecture for chamber filling through active valve	117
5.6	Simulation architecture for active valve orifice and channel	117
5.7	Flowchart for the quasi-static systematic active valve design procedure	118
5.8	Chamber filling as a function of valve cap radius	120
5.9	Design plots for the valve membrane	121
5.10	Modeling of the active valve structure in an impedance match condition	123
5.11	Drive element behavior design plots	124
5.12	Valve cap size vs. imposed valve cap stroke	126
5.13	Valve membrane size and thickness vs. imposed valve cap stroke: Case 1	127
5.14	Maximum valve membrane stress vs. membrane radius: Case 1	128
5.15	Example valve membrane deflection plots: Case 1	129
5.16	Valve membrane size and thickness vs. imposed valve cap stroke: Case 2	130

5.17	Maximum valve membrane stress vs. membrane radius: Case 2	131
5.18	Example valve membrane deflection plots: Case 2	133
5.19	Hysteretic energy loss in active valve	134
5.20	Full quasi-static design procedure results: Part 1	139
5.21	Full quasi-static design procedure results: Part 2	140
5.22	Full quasi-static design procedure results: Part 3	141
5.23	Simulation architecture for the filling/evacuation of the MHT system	143
5.24	System simulation plots using the designed active valve geometry	144
6.1	Schematic cross-section of a multi-layer MHT/active valve structure	148
6.2	DRIE etch characteristics of a drive element piston and tether	149
6.3	SEM etch images of a drive element piston and tether	150
6.4	Wafer-level silicon-silicon fusion and silicon-pyrex anodic bond steps	151
6.5	Piezoelectric material surface roughness scans	153
6.6	Piezoelectric thin-film eutectic alloy composition	154
6.7	Precision micrometer measurement of a piezoelectric element thickness	155
6.8	Piezoelectric element tolerancing within drive element structure	156
6.9	Die-level bonding procedure for active valve device	158
6.10	Die-level alignment and bonding jigs	160
6.11	Electrical contact to an active valve chip for anodic bonding	160
6.12	Fluid filling apparatus to fill active valve devices	161
6.13	Fluid filling schematic of component connections	162
6.14	Schematic of the high resistance fluid channel between the HAC and an external bias pressure	163
6.15	Model of the high resistance fluid channel between the HAC and an external bias pressure	164
6.16	Active valve sub-component fabrication and testing plan	165
6.17	Drive element sub-component test structures	166
6.18	Valve membrane sub-component study and full active valve study	167
6.19	Fluids test-rig for testing of the active valve and its sub-components	169
7.1	3-D schematic of a piezoelectric drive element device	174
7.2	Overview of the drive element sub-component test plan	175
7.3	Drive element geometries and piezoelectric element layout	176
7.4	Exploded view of drive element structure	177
7.5	Assembly of a piezoelectric drive element device	178
7.6	Photographs of fabricated 1st-generation drive element device	179
7.7	Photograph of an assembled 2nd-generation drive element device	179

7.8	Measurement points on drive element piston surface using scanning laser vibrometer	181
7.9	Inspection of fillet radii on 1st-generation devices	182
7.10	Piezoelectric material characterization of representative elements	183
7.11	Device 1 transfer functions of piston velocity versus frequency	185
7.12	Device 1 modal behavior	186
7.13	Vibrometer scan images of Device 1 low-frequency 15kHz displacement profile . .	186
7.14	Device 1 displacement time histories for a sinusoidal drive voltage of $500V \pm 500V$ at $f = 15kHz$	187
7.15	Device 1 displacement time histories for a sinusoidal drive voltage of $500V \pm 500V$ at $f = 7kHz$	187
7.16	Device 1 piston center displacement versus applied voltage at 100Hz	187
7.17	Device 2 transfer functions of piston velocity versus frequency	189
7.18	Device 2 modal behavior	190
7.19	Vibrometer scan images of Device 2 low-frequency 15kHz displacement profile . .	190
7.20	Device 2 displacement time histories for a sinusoidal drive voltage of $500V \pm 500V$ at $f = 15kHz$	191
7.21	Device 2 displacement time histories for a sinusoidal drive voltage of $500V \pm 500V$ at $f = 7kHz$	191
7.22	Device 2 piston center displacement versus applied voltage at 100Hz	191
7.23	Device 3 transfer functions of piston velocity versus frequency	193
7.24	Vibrometer scan images of selected Device 4 modal behavior	194
7.25	Device 3 ANSYS finite-element model prediction for 1st mode	194
7.26	Vibrometer scan images of Device 3 low-frequency 15kHz displacement profile . .	194
7.27	Device 3 displacement time histories for a sinusoidal drive voltage of $500V \pm 500V$ at $f = 15kHz$	195
7.28	Device 3 displacement time histories for a sinusoidal drive voltage of $500V \pm 500V$ at $f = 7kHz$	195
7.29	Device 3 piston center displacement versus applied voltage at 100Hz	195
7.30	Device 4 transfer functions of piston velocity versus frequency	197
7.31	Vibrometer scan images of selected Device 4 modal behavior	198
7.32	Vibrometer scan images of Device 4 low-frequency 15kHz displacement profile . .	198
7.33	Device 4 displacement time histories for a sinusoidal drive voltage $500V \pm 500V$ at $f = 15kHz$	199
7.34	Device 4 piston center displacement versus applied voltage at 100Hz	199
8.1	2-D schematic of a valve cap and membrane structure	204
8.2	Dimensions of the fabricated valve cap and membrane structures	204

8.3	Valve cap and membrane sub-component structure	205
8.4	Baseline valve cap and membrane design dimensions	209
8.5	Sensitivity of baseline valve cap and membrane design to variations in valve membrane thickness	210
8.6	Finite-element mesh of valve cap and membrane structure	211
8.7	Finite-element stress contours resulting from applied differential pressure loading	211
8.8	Sensitivity of baseline valve cap and membrane design to variations in fillet radius size	212
8.9	Valve cap and membrane experimental pressure-deflection results	214
9.1	Dimensions of active valve devices AV1 and AV2	219
9.2	Device AV1 low-voltage valve cap frequency response from 500Hz to 100kHz, with and without oil present above the valve structure.	223
9.3	Device AV1 low-voltage piston and valve cap frequency responses from 500Hz to 100kHz, with oil present above the valve structure.	224
9.4	Device AV1 low-voltage valve cap frequency responses from 500Hz to 100kHz, for varying P_{bias}	225
9.5	Device AV1 low-voltage valve cap frequency responses from 500Hz to 100kHz, for varying differential pressure applied to valve cap and membrane structure.	226
9.6	Device AV1 valve cap frequency responses from 500Hz to 3kHz, for $P_{bias} =$ $500kPa$ and increasing high voltage drive levels.	227
9.7	Device AV1 high-voltage piston and valve cap frequency responses from 500Hz to 3kHz, for $P_{bias} = 500kPa$	228
9.8	Device AV1 valve cap and piston deflection time histories for 1kHz sinusoidal drive voltage levels.	230
9.9	Device AV1 valve cap peak-peak motion, piston peak-peak motion, and device amplification ratio as a function of 1kHz sinusoidal drive voltage levels.	231
9.10	Device AV1 valve cap peak-peak motion, piston peak-peak motion, and device amplification ratio as a function of 1kHz sinusoidal drive voltage levels, with $P_{vc,vm} = 50kPa$	232
9.11	Experimental verification of the high-frequency channel in device AV1.	233
9.12	Device AV2 low-voltage valve cap frequency response from 500Hz to 100kHz, with and without oil present above the valve structure.	236
9.13	Device AV2 low-voltage valve cap frequency responses from 500Hz to 100kHz, for varying P_{bias}	237
9.14	Device AV2 valve cap frequency responses from 500Hz to 3kHz, for $P_{bias} =$ $500kPa$ and increasing high voltage drive levels.	238

9.15	Device AV2 high-voltage piston and valve cap frequency responses from 500Hz to 3kHz, for $P_{bias} = 500kPa$.	239
9.16	Device AV2 valve cap and piston deflection time histories for 1kHz sinusoidal drive voltage levels.	240
9.17	Device AV2 valve cap peak-peak motion, piston peak-peak motion, and device amplification ratio as a function of 1kHz sinusoidal drive voltage levels.	241
9.18	Device AV1 and device AV2 quasi-static 1kHz model correlation for fluid bulk modulus $K_f = 2.0GPa$.	244
9.19	Device AV1 and device AV2 quasi-static 1kHz model correlation for varying fluid bulk modulus K_f .	245
9.20	Finite-element active valve modal frequency sensitivity studies	248
9.21	Finite-element modal frequency sensitivity to valve cap added mass	251
9.22	Model correlation to device AV1 quasi-static fluid flow rate versus valve opening behavior for differing imposed differential pressures	253
9.23	Schematic of valve cap and membrane orifice structure.	257
9.24	Representative displacement signals corresponding to stable and unstable valve cap behavior during quasi-static opening.	258
9.25	Representative plots for valve cap behavior, differential pressure, and flow rate during quasi-static opening for $P_1 - P_2 = 80kPa$.	259
9.26	Valve cap Instability Values during quasi-static opening for $P_1 - P_2 = 80kPa$, $P_1 - P_2 = 130kPa$, and $P_1 - P_2 = 160kPa$.	260
9.27	Valve cap Instability Values during quasi-static opening for $P_1 - P_2 = 200kPa$, $P_1 - P_2 = 230kPa$, and $P_1 - P_2 = 240kPa$.	261
9.28	Valve cap Instability Values during quasi-static opening for $P_1 - P_2 = 305kPa$ and $P_1 - P_2 = 360kPa$.	262
9.29	Complete grouping of all valve cap Instability Values plotted as $P_1 - P_2$ vs. $Z_{vc,opening}$.	263
9.30	Estimated boundaries for smooth, rough, and oscillatory regions plotted as $P_1 - P_2$ vs. $Z_{vc,opening}$.	264
9.31	Estimated boundaries for unstable and stable regions plotted as $P_1 - P_2$ vs. $Z_{vc,opening}$.	265
9.32	Estimated constant Reynolds number curves plotted as $P_1 - P_2$ vs. $Z_{vc,opening}$.	266
9.33	Constant Reynolds number curves (experimental vs. model predictions) plotted as $P_1 - P_2$ vs. $Z_{vc,opening}$.	267
9.34	Plot of flow resistance coefficient versus Reynolds number for a generic flow orifice contraction structure.	268

9.35	Device AV1 estimated laminar, transition, and turbulent flow regimes based on experimental data.	269
9.36	Schematic of vorticity formation in contraction and expansion fluid flow sections.	270
9.37	Laminar, transition, and turbulent representative flow behavior	271
9.38	Device AV1 valve cap time histories under varying duty cycle voltage waveforms to piezoelectric drive element.	273
9.39	Device AV1 model correlation to experimental flow rate results for varying duty cycles.	274
9.40	Device AV1 dynamic flow regulation model correlation at 1kHz for varying differential pressures.	275

Nomenclature

A_c	high frequency channel cross-sectional area
A_p	piezoelectric material area
A_{pis}	drive element piston area
A_{vc}	valve cap area
A_{vm}	valve membrane area
dP_{HAC}	hydraulic amplification chamber pressurization
dV_{EHC}	fluid volume change within external energy harvesting chamber
dV_{fluid}	hydraulic amplification chamber fluid volume change
dV_{pis}	drive element piston swept volume
dV_{te}	drive element tether swept volume
dV_{de}	drive element total swept volume
dV_{top}	top structural plate volume change
dV_{vm}	valve cap and membrane swept volume
d_{33}	piezoelectric material coefficient
E_p	piezoelectric material Young's modulus
E_{si}	silicon Young's modulus
E_{pyrex}	Pyrex Young's modulus
fR	fillet radius
F_{vc}	force on valve cap structure
F_{vm}	valve membrane force on top structural plate
G_{si}	silicon shear modulus
H_{HAC}	hydraulic amplification chamber height
K_{EHC}	generalized external energy harvesting chamber stiffness
K_f	fluid bulk modulus
L_c	high frequency channel length
L_p	piezoelectric material length
N_{vh}	number of valve heads used in parallel within active valve
P_{bias}	hydraulic amplification chamber bias pressure
P_{EHC}	external energy harvesting chamber pressure
P_{EHC}^*	pressure within inlet valve orifice channel
P_{EHC}^{**}	pressure within outlet valve orifice channel

P_{HAC}	hydraulic amplification chamber pressure
P_{HPR}	high pressure reservoir pressure
P_{LPR}	low pressure reservoir pressure
P_{pis}	applied pressure beneath drive element piston
P_1	generalized pressure above valve cap
P_2	generalized pressure above valve membrane
Q_{in}	flow rate through inlet valve
Q_{out}	flow rate through outlet valve
R_{bot}, D_{bot}	bottom structural plate radius, diameter
R_{cp}	piezoelectric material spacing radius from drive element center
$R_{orifice}, D_{orifice}$	valve fluid orifice radius, diameter
R_p, D_p	piezoelectric material radius, diameter
R_{pis}, D_{pis}	drive element piston radius, diameter
R_{te}, D_{te}	drive element tethers outer radius, diameter
R_{top}, D_{top}	top structural plate radius, diameter
R_{vc}, D_{vc}	valve cap radius, diameter
R_{vm}, D_{vm}	valve membrane radius, diameter
RE	generalized Reynolds number
$RE_{Dorifice}$	Reynolds number through valve orifice
t_{bot}	bottom structural plate thickness
t_{pis}	drive element piston thickness
t_{tetop}	top drive element tether thickness
t_{tebot}	bottom drive element tether thickness
t_{top}	top structural plate thickness
t_{vc}	valve cap thickness
t_{vm}	valve membrane thickness
T_p	piezoelectric material stress
V_p	piezoelectric material voltage
V_{HAC}	hydraulic amplification chamber volume
W_{hys}	hysteretic energy consumption of active valve
Z_{bot}	bottom structural plate deflection
Z_{de}	drive element total deflection
Z_p	piezoelectric material deflection
Z_{pis}	drive element piston deflection

Z_{te}	top drive element tether deflection
Z_{top}	top structural plate deflection
Z_{vc}	valve cap deflection (absolute)
$Z_{vc,opening}$	valve cap opening distance from orifice
$Z_{vc,stroke}$	valve cap peak-peak stroke
α_{si}	silicon shear correction factor
ϵ_p	piezoelectric material strain
ν_p	piezoelectric material Poisson ratio
ν_{Pyrex}	Pyrex Poisson ratio
ν_{si}	silicon Poisson ratio
ρ_{fluid}	fluid density
σ_{vm}	valve membrane radial stress
$\sigma_{vm,max}$	maximum valve membrane radial stress
$\zeta_{orifice}$	valve orifice loss coefficient
$\Xi_{Zpis}^P, \Xi_{Zpis}^T, \Xi_{dVpis}^P, \Xi_{dVpis}^T$	drive element piston compliance coefficients
$\Xi_{Ztetop}^F, \Xi_{Ztetop}^P, \Xi_{dVtetop}^F, \Xi_{dVtetop}^P$	top drive element tether compliance coefficients
$\Xi_{Ztebot}^F, \Xi_{Ztebot}^P$	bottom drive element tether compliance coefficients
Ξ_{Zbot}^T	bottom structural plate compliance coefficient
$\Xi_{Ztop}^F, \Xi_{Ztop}^P, \Xi_{dVtop}^F, \Xi_{dVtop}^P$	top structural plate compliance coefficients
$\Xi_{Zvc}^F, \Xi_{Zvc}^P, \Xi_{dVvm}^F, \Xi_{dVvm}^P$	valve cap and membrane compliance coefficients (linear deformation theory)

Chapter 1

Introduction

1.1 Motivation

The development of a fluidic microvalve, capable of high frequency control of high pressure liquid fluid flows, is a key task in the realization of high specific power ($\frac{W}{kg}$) micropumping technology. Currently, many research efforts around the world are underway to develop compact liquid micropumping systems, the term “micro” referring to devices which are created with fabrication procedures capable of μm -size tolerances and which produce overall micropump dimensions on the order of a few millimeters to a few centimeters. However, the vast majority of these systems are designed for low pressure and low flow rate applications [1] [2] [3] [4] [5] such as drug dispensing and microdosing [6] [7] [8]. The higher performing of these systems are capable of pumping liquids with flow rates on the order of $1000-3000 \frac{\mu L}{min}$ ($0.017-0.050 \frac{mL}{s}$) against differential pressures of between 10kPa and 50kPa. With a typical device mass on the order of ~ 1 gram, these performance values correlate to device-level specific powers below $2.5 \frac{W}{kg}$.

In an effort to develop high specific power micropumping technology (with specific powers $\sim 100-1000 \frac{W}{kg}$) for both actuation and power generation applications, a novel class of Micro-Hydraulic Transducer (MHT) devices has been introduced [1] [10] [11] [12] [13]. These devices combine bulk piezoelectric materials with stiff micromachined structural elements and are designed to enable high frequency pumping of fluid (10-20kHz) against pressure differentials on the order of $\sim 1-2$ MPa, creating flow rates near or in excess of $1 \frac{mL}{s}$.

Piezoelectric materials are well-suited for transducer applications because of their inherently high peak specific powers. Figure 1.1 provides a comparison of the single stroke specific energy ($\frac{J}{kg}$), bandwidth (kHz), and theoretical peak specific power ($\frac{W}{kg}$) for a variety of transducer materials [14] [15] [16]. The product of a material’s single stroke specific energy and its bandwidth provides a value for the material’s specific power ($\frac{W}{kg}$). Shape-memory alloy materials (denoted SMA), for example, possess a relatively large single stroke specific work ($\sim 5000 \frac{J}{kg}$) in com-

parison to that of standard polycrystalline piezoelectric materials such as PZT-5H ($\sim 10 \frac{J}{kg}$). The maximum operational frequency, or bandwidth ($\sim 10\text{Hz}$), of SMA materials, however, is significantly less than that of standard piezoelectrics ($\sim 100\text{kHz}$). SMA materials and standard piezoelectrics both possess specific powers near $100 \frac{W}{kg}$, however, their optimal implementation as actuation mechanisms is far different. In an application where low frequency, large stroke actuation is desired (such as an on-off microvalve), the use of an SMA material might be preferred over a standard piezoelectric material. Conversely, for an application whereby high frequency, low stroke actuation is required, a piezoelectric material may be preferred. In fact, for this reason, the vast majority of high frequency micropumping systems use piezoelectric materials as their actuation mechanism in conjunction with fast-acting valves. The recent development of single-crystal ferroelectric materials (e.g. PZN-PT), characterized by specific powers approaching $10 \frac{kW}{kg}$ ($\sim 100\times$ greater than those of standard polycrystalline PZT materials) [17], offers further advantages in strain capability over the standard piezoelectrics. These high performing materials, however, have yet to be integrated within high frequency micropumping systems.

The piezoelectric micropumping devices and systems that have been presented in the literature up until this time typically utilize one of two actuation methods as a means to pump fluid: either (1) a deposited thin-film, thick disk, or bimorph of piezoelectric material [2] [3] [6] in contact with a compliant membrane, or (2) a direct-drive stack actuator in contact with a moveable silicon diaphragm. The thin-film, thick-film, and bimorph structural designs presented are not conducive to both high force and high-frequency operation. The direct-drive stack actuation designs [18] [19] [20] are capable of achieving higher frequency operation than the thin-film, thick-film, and bimorph designs, however the presented micropump devices using these designs are limited in their flow rate, pressurization, and frequency capabilities due to inadequacies of the accompanying one-way passive valves used to regulate the fluid flow. Additionally, these previously presented direct-drive stack designs require a significant length of piezoelectric actuation material to create the deflection and fluid pumping volume required for reasonable fluid flow rates. Due to this significant actuator size, an epoxy bonding agent and a relatively compliant silicon diaphragm are required to tolerance the piezoelectric material within the structures. The key design feature which differentiates Micro-Hydraulic Transducer devices from these previous piezoelectric micropumps is the incorporation of a stiff micromachined structural “piston-like” actuation element not only within the pumping chamber of the device, but also within accompanying flow regulation active valves. The annularly-tethered micromachined “piston” structure, driven by miniature bulk piezoelectric elements (almost an order of magnitude smaller than those used in [18] [19] [20]) attached using a thin-film eutectic alloy bond, can achieve structural frequencies well above 10kHz and can actuate against fluid pressurizations near 1MPa . The implementation of such a stiff structure within fluidic systems can enable significantly higher frequency and pressurization capabilities than the previously

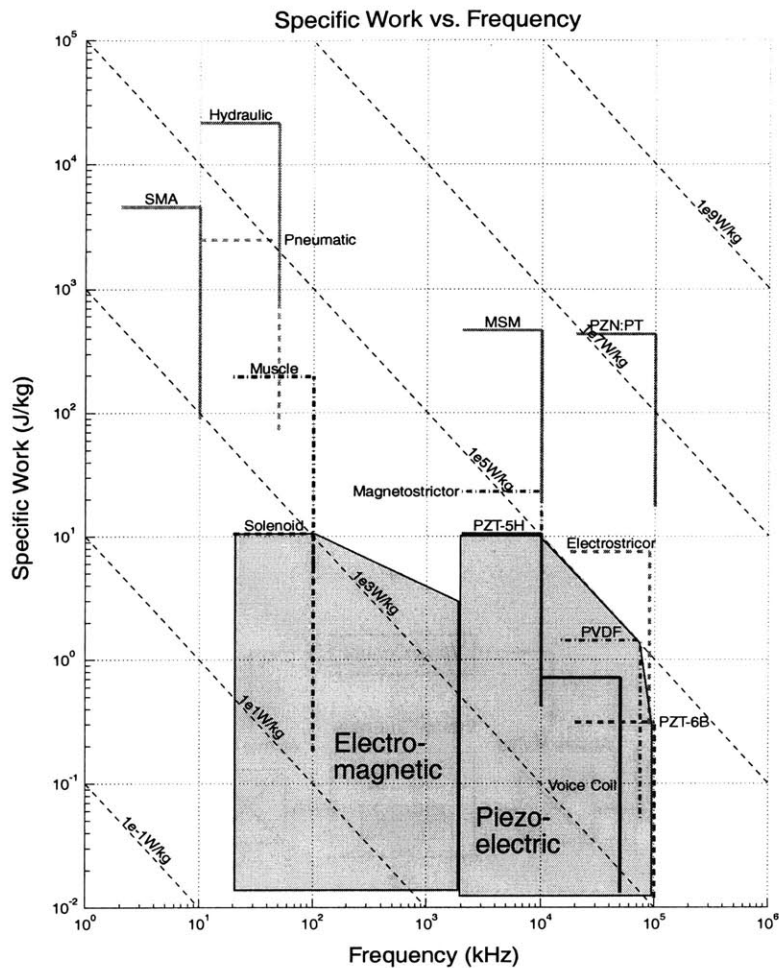


Figure 1.1: Upper bound on specific work vs. frequency for various actuation media. SMA is shape-memory alloy; PZN-PT is single-crystal piezoelectric; MSM is magnetic shape memory materials.

presented piezoelectric micropumps.

As shown in Figure 1.2, a Micro-Hydraulic Transducer system consists of a piezoelectric pump chamber, two actively controlled valves, and a low and high pressure fluid reservoir. In the MHT actuator, electrical energy supplied to the piezoelectric pump chamber results in a pumping of fluid through the valves from the low to high pressure reservoir. In the MHT power harvester, sequenced operation of the valves results in fluid flow from the high to low pressure reservoir, producing a “pinging” of the piezoelectric element within the pump chamber. This cyclic strain on the element induces electrical charge, which can be rectified and stored. The specific power of these transducer devices scales linearly with the frequency of operation and the pressure drop across which the device can operate. Since structural frequencies scale inversely with the geometric size of the device, it is advantageous to build these systems as small as

possible, hence the need for MEMS fabrication and process technologies. The performance of these MHT systems is directly governed by the capabilities of the active valves, which regulate flow into and out of the pump chamber. As a result, to achieve high specific power Micro-Hydraulic Transducer devices, a compact high frequency, high pressure active valve is required. The development of such an active valve is the subject of this thesis.

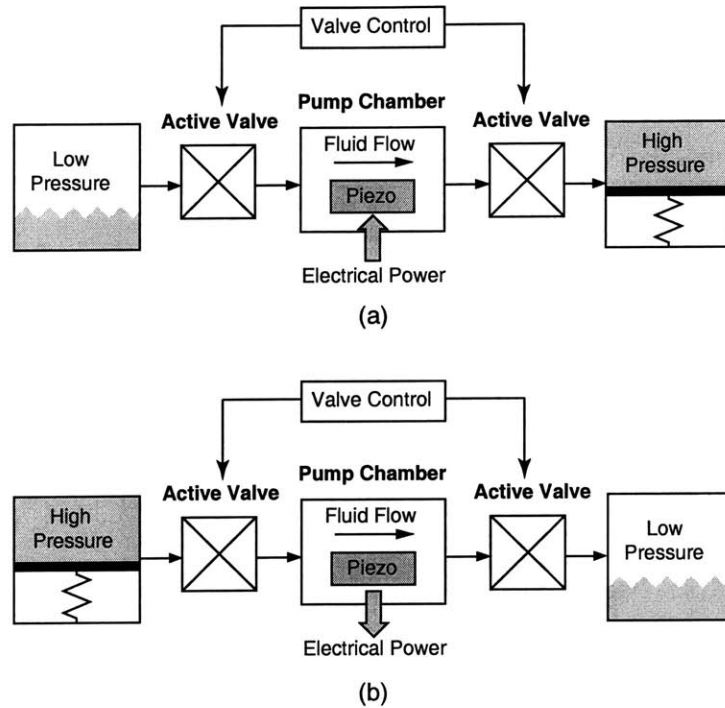


Figure 1.2: Schematics of Micro-Hydraulic Transducer systems: (a) MHT actuator system, (b) MHT power harvesting system. High specific power is achieved through the integration of piezoelectric material with structural stiff small-scale hydraulic systems.

1.2 Overview of Previous Microvalve Technology

Although a significant amount of literature is available describing the development of active valve devices and technology, few if any have been designed for high frequency control of high pressure liquid fluid flows. Novel microvalve designs using thermopneumatic actuation [21] [22], thermal bimetallic actuation [24], SMA actuation [23], electrostatic actuation [25] [26], electromagnetic actuation [27] [28], piezoelectric bender-type actuation (both thin-film and thick film) [29] [30] [31], and piezoelectric stack-type actuation [18] [19] [20] have been presented. A sampling of previously reported microvalves is shown in Figure 1.3 and Figure 1.4.

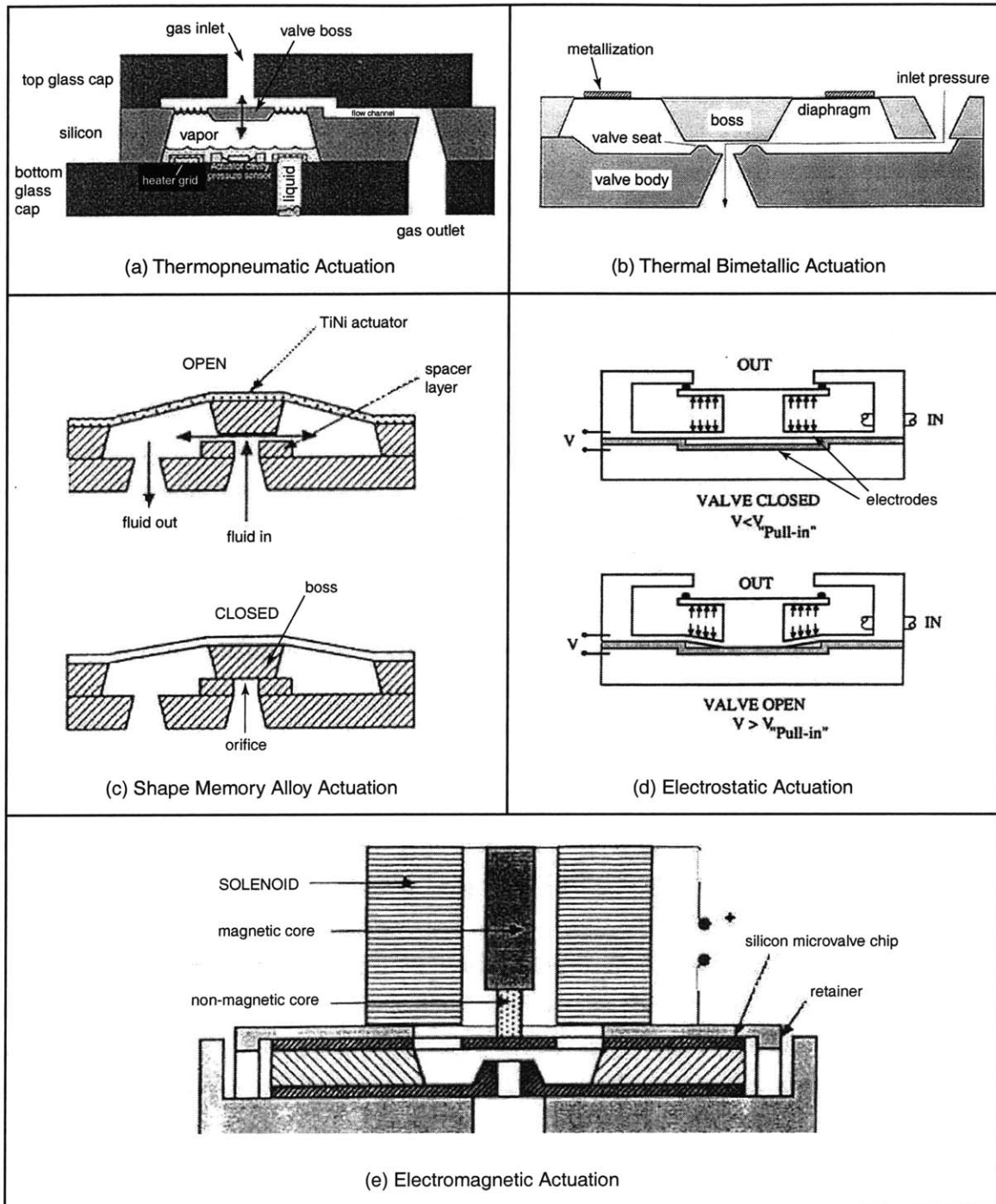


Figure 1.3: Previously reported microvalves: (a) thermopneumatic actuation, Rich [22], (b) thermal bimetallic actuation, Jerman [24], (c) shape memory alloy actuation, Huff [23], (d) electrostatic actuation, Huff [25], and (e) electromagnetic actuation, Pourahmadi [27].

Figure 1.3(a) shows a thermopneumatic microvalve [22] for control of gas flows. A valve central boss is supported by a corrugated silicon membrane. The deflection of the boss is controlled by the vapor pressure of the heated working fluid (parylene) within the contained chamber. A micromachined heater grid exists within the chamber to increase the fluid temperature. For typical operation, a temperature of 80°C (and a corresponding power dissipation of 300mW) is required to move the valve boss through a stroke of $9\mu\text{m}$ in a time of approximately 15 seconds. Maximum pressure rise within the fluid chamber was reported to be 100kPa.

Figure 1.3(b) illustrates a thermal bimetallic valve [24] for use in pneumatic closed-loop pressure or flow control applications. The valve consists of a diaphragm actuator with a central boss which mates to an etched silicon valve body. The actuator includes a circular silicon diaphragm with integrated diffused resistors and an annular region of deposited aluminum. As current is passed through the resistors, the diaphragm increases in temperature. The thermal expansion mismatch between the silicon and aluminum results in a controlled displacement of the central boss. An operational boss deflection of $15\mu\text{m}$ was obtained in response to a temperature increase of 100°C (and a reported corresponding power dissipation of 1W). Regulation of 200kPa differential pressure gas flows in an on-off fashion was demonstrated, resulting in gas flow rates of up to 2mL/s. No actuation response time was reported.

Figure 1.3(c) displays a shape-memory alloy (titanium nickel) actuated microvalve [23] for precise regulation of liquid fluid flow in micro-chemical analysis and drug delivery applications. The shape-memory effect is an athermal phase transformation between the austenitic (high temperature rigid) and martensitic (low temperature ductile) phases. In this valve, a TiNi diaphragm with attached silicon boss is actuated to open and close against a micromachined orifice. The valve was tested in an on-off fashion and it was reported to enable a liquid (DI water) flow rate of 0.1mL/s for an applied differential pressure of 5kPa. Maximum stroke of the valve boss was not reported.

Figure 1.3(d) displays an electrostatic microvalve [25] with a pressure-balancing structural feature that allows it to control fluids at pressures significantly larger than the necessary actuation pressure. The fluid provides a balancing force on the moving part of the structure thereby reducing the force required to open the valve. The moving part of the valve is a plunger which is actuated vertically, and consists of a center-bossed circular base and cap. Electrostatic actuation is enabled through a small gap between the underside of the membrane and the top surface of a bottom support structure. This on-off valve was able to control 220kPa differential gas flows with an actuation voltage of 210V, resulting in a peak flow rate of 2.5mL/s. Due to significant ohmic heating in the device (because of a poor oxide layer), power dissipation was reported to be greater than 10W.

Figure 1.3(e) illustrates an electromagnetic microvalve [27] designed for applications requiring large stroke and large on-off gas flow rates. The microvalve consists of a solenoid housing

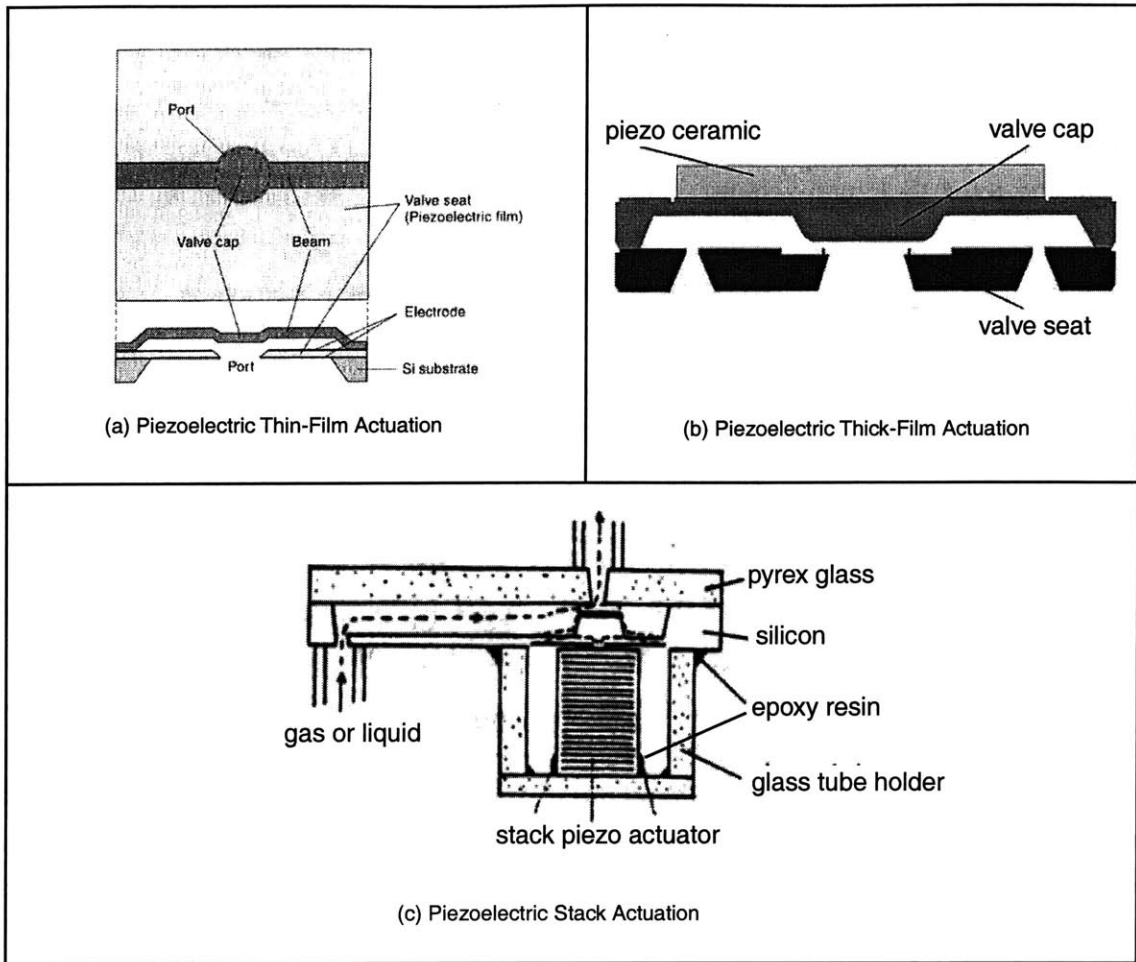


Figure 1.4: Previously reported piezoelectric microvalves: (a) piezoelectric thin-film actuation, Watanabe [30], (b) piezoelectric thick-film actuation, Kluge [31], and (c) piezoelectric stack actuation, Esashi [19].

and a plunger which is rigidly attached to a diaphragm structure. Current applied to the solenoid results in a motion of the plunger against a micromachined orifice. Dimensions of the solenoid attachment are unknown, however the author states that the application for this valve does not require the device to fit within a compact volume. For on-off operation, this direct drive is reported to achieve a maximum valve cap displacement of $100\mu\text{m}$ against a differential pressure of 90kPa , resulting in peak flow rates near 5mL/s . Power dissipation was reported to be greater than 1W .

Figure 1.4(a) displays a portion of a piezoelectrically-driven microvalve matrix [30] for controlling precise levels of gas flow. The valve is constructed of a thin beam with a round valve cap at the center and a valve seat of piezoelectric thin-film bifurcated in the normal direction.

The valve is normally closed due to a residual stress in the beam. For voltage applied to the valve seat, the piezoelectric film shrinks and the inner edge moves radially outward thereby increasing the flow area between the valve cap and this inner edge. The outer diameter of the piezoelectric thin-film is $600\mu\text{m}$ and its thickness is $1\mu\text{m}$. In response to a voltage of 1V, the valve was reported to actuate against a differential pressure of 0.1kPa, resulting in a gas flow rate of 2mL/s.

Figure 1.4(b) illustrates a thick-film piezoelectrically-actuated microvalve [31] for use in high gas flow applications. The valve consists of a micromachined valve cap and membrane structure with an attached (via epoxy) piezoceramic disk to actuate the valve cap against a micromachined valve seat orifice. The valve seat diameter is 2.25mm and the achievable stroke of the valve cap is $30\mu\text{m}$ for an applied voltage of up to 3000V. For on-off operation, the valve was reported to regulate gas flow at 11.6Hz against a differential pressure of 400kPa. The thickness of the piezoceramic disk structure was not detailed.

Figure 1.4(c) displays a piezoelectrically-driven microvalve [19] using a direct drive piezoelectric stack as the actuation mechanism. This valve was designed for use in a liquid micropumping system. The microvalve consists of one silicon and two glass layers anodically bonded together. The silicon contains a inlet through hole, a flow channel, and a moveable diaphragm with a central boss structure. A piezoelectric stack 9mm in length is attached to the underside of the boss using epoxy. In response to a voltage of 90V at a frequency of 30Hz, an estimated liquid pressurization of 8kPa in the pumping chamber of the micropump and a corresponding flow rate of 0.00025mL/s was reported.

The previously described microvalves were selected to illustrate the wide variety of actuation concepts previously reported in the literature. All of these microvalves share a common operational geometry (except for Watanabe [30]) in that a valve boss is affixed to a diaphragm or membrane structure which carries the boss through a predetermined stroke, in response to some form of actuation principle. The majority of these valves were designed for gas flows, and as such estimating their capabilities in handling liquids is difficult to do, although typically flow rates of liquids for a given differential pressure can be expected to be 100-1000x smaller than gas flow rates under the same differential pressures. In general, based on their reported capabilities, it can be concluded that none of these valves is capable of simultaneously satisfying the set of high frequency (1-10kHz), high pressure (0.1-1MPa), and large stroke ($15\text{-}40\mu\text{m}$) requirements needed within full MHT liquid micropumping systems.

The thermal actuation designs (based on thermopneumatic, thermal bimetallic, and shape memory alloy principles) potentially can achieve large stroke and reasonable actuation force. However, these thermally-based devices exhibit excessive power consumption and poor response times on the order of seconds. High-frequency actuation in the kHz range is therefore unachievable. The electrostatic devices are limited in their deflection and pressure generation capabili-

ties, since the electrostatic force generated between two parallel plates scales inversely with their spacing and since electrical breakdown across the gap must be avoided. The electromagnetic concept is impeded by the overall size of external solenoid and housing structures needed to actuate the valve structure. Piezoelectric thin-film and thick-film bender-type designs are limited in their ability to generate both high force and large deflection output. Shoji and Esashi's work aimed at solving this problem through the use of a stack-type piezoelectric actuator material to directly drive the valve membrane. In doing so, however, the piezoelectric stack material was required to be long ($\sim 9\text{mm}$), resulting in a large actuator mass and size. The operational frequency of this device was reported only up to 30Hz.

A promising method for achieving high frequency operation in conjunction with large force and high stroke capability would be to design a microvalve with a means to amplify the stroke of a piezoelectric bulk-type material (for example 1mm in thickness - almost an order of magnitude smaller in length than Shoji and Esashi's stack) into a larger valve membrane stroke. This could be done using a stiff hydraulic fluid within an enclosed chamber to couple the piezoelectric material motion to the valve cap motion using an area ratio amplification concept. This type of structure would thereby achieve high frequency, high pressure, and large valve cap stroke actuation with minimal device power consumption (a further advantage of piezoelectric materials). Numerous macroscale piezoelectric hydraulic amplification mechanisms have been presented in the literature. In an application for active vibration control, a piezoelectric actuator uses the volume change of a piezoelectric ring to create a large deflection of a smaller area contact surface [32]. In an application for vibration control of a rotary dynamic system, the deflection of a stack-type piezoelectric actuator is coupled through a hydraulic line to a smaller size piston, which helps to control the motion of a rotating shaft [33]. These and other [34] piezoelectric hydraulic amplification mechanisms are novel in design, yet do not face the difficult fabrication, assembly, and tolerancing challenges inherent in the development of high frequency MEMS-scale devices.

1.3 Concept

This thesis focuses on the design, modeling, fabrication, and experimental testing of a piezoelectrically driven hydraulic amplification microvalve for high pressure, high frequency applications. The proposed microvalve is shown in Figure 1.5. This device is desired to achieve large valve cap stroke (up to $\sim 40\mu\text{m}$) against high pressure loads ($\sim 0.1\text{-}1\text{MPa}$) through a novel hydraulic amplification mechanism that converts the small displacement ($\sim 1\mu\text{m}$) of a piezoelectric material element into a significantly larger valve cap stroke. The inherent stiffness of the piezoelectric material and the hydraulic fluid chamber enable both high-frequency and high-force actuation capabilities.

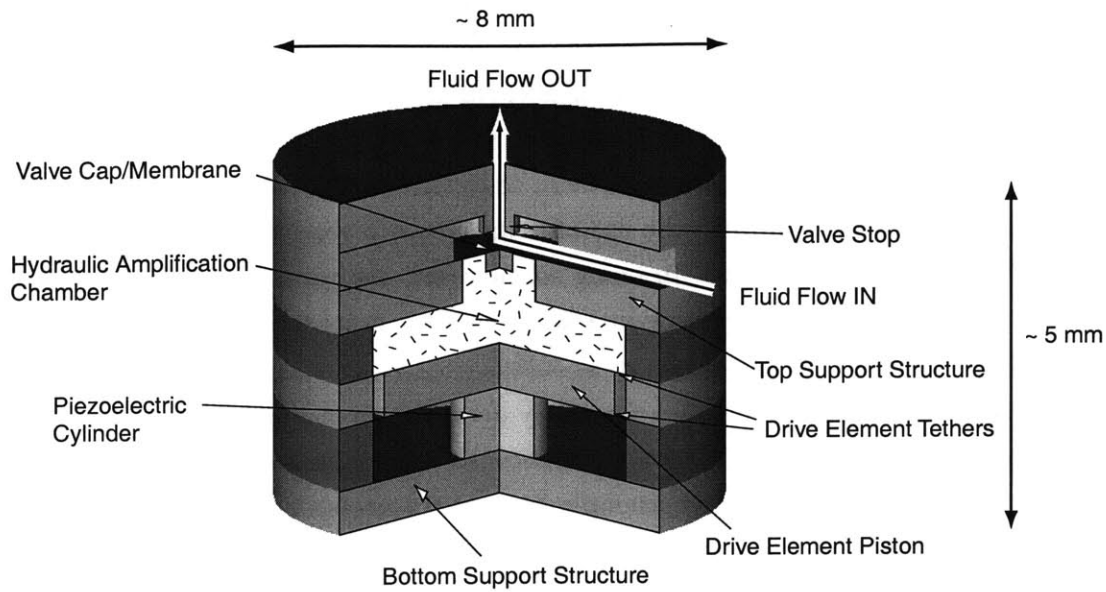


Figure 1.5: Schematic of a piezoelectrically-driven hydraulic amplification microvalve. The primary structural components are designated with arrows. External hydraulic system pressure loading is applied on the top surface of the valve cap and membrane.

The active valve consists of three primary components: a piezoelectric drive element, an enclosed fluid amplification chamber, and a membrane with attached valve cap. The drive element incorporates a circular piston structure supported from beneath by one or more small bulk piezoelectric cylinders and is suspended circumferentially from a surrounding support structure by thin annular micromachined tethers. This novel compact “piston-type” design enables high frequency actuation against a large external pressurization due to the high stiffness of the piston structure and integration of miniature bulk piezoelectric elements beneath the piston using a thin-film bond layer. The lateral dimensions of the tethers are designed to make the tethers compliant enough to allow for rigid piston motion up and down, yet stiff enough to resist bowing under pressurization caused by the hydraulic fluid above the tether during actuation. The tethers provide a seal between the hydraulic fluid above the piston and the piezoelectric chamber below the piston, and also provide a path for electrical contact to the top surface of the piezoelectric cylinders. The fluid chamber resides between the top surface of the drive element piston and the bottom surface of a thin, smaller diameter silicon micromachined valve cap membrane. These design features enable the valve device to simultaneously meet a set of high frequency, high pressure, and large stroke requirements that have not previously been satisfied by other microvalves presented in the literature.

In response to applied piezoelectric voltage, the piezoelectric material strains. The resulting deflection of the drive element piston generates a pressure within the hydraulic amplification chamber which in turn deflects the valve cap and membrane against a fluid orifice, thereby regulating fluid flow through the external hydraulic system. The pressure loadings on the valve cap and membrane during device operation depend on the external microfluidic system application. The piezoelectric material capabilities, the ratio of the piston diameter to the valve membrane diameter, the compliances of the fluid and structural elements in the chamber, the severity to which the valve cap membrane experiences nonlinear behavior, and the nature of the external loading all contribute to the performance of this microvalve device.

The proposed fabrication process for this microvalve involves the assembly of five silicon layers and four glass layers. A 2-D schematic of the microvalve device, illustrating individual silicon and glass layers, is shown in Figure 1.6. The middle glass layer (Layer 3) forms the drive element support structure and the top (Layer 9) and bottom (Layer 1) glass layers provide structural support. The bottom silicon layer (Layer 2) and drive piston silicon layers (Layers 4,5) provide a path for electrical contact to the piezoelectric cylinders. The top four silicon layers (Layers 4,5,7,8) and glass layer (Layer 6) house the hydraulic amplification chamber, valve cap and membrane structure, and fluid inlet and outlet channels. All silicon-silicon wafer interfaces are bonded with high-temperature ($\sim 1300^{\circ}\text{C}$) fusion bonds, and all silicon-glass layer interfaces are bonded using low temperature ($\sim 300^{\circ}\text{C}$) anodic bonds. Attachment of the top and bottom piezoelectric cylinder surfaces to the adjoining silicon is achieved with a low temperature ($\sim 300^{\circ}\text{C}$) AuSn eutectic bond.

Shown in Figure 1.7 is a 3-D schematic of a fabricated silicon and glass multi-layer Micro-Hydraulic Transducer actuator system. This system consists of an inlet and outlet piezoelectrically driven active valve and a centrally-located piezoelectric pump chamber. The pump chamber is comprised essentially of the same drive element structure contained within each active valve component. All of the fabrication and assembly challenges (see Section 1.4.2) inherent in the realization of the active valve component structures are shared by the full MHT device, and as a result the efforts documented within this thesis to successfully fabricate a workable valve device at the same time demonstrate the ability to realize complete MHT systems.

1.4 Challenges

A significant number of challenges had to be overcome to realize a functional piezoelectrically driven hydraulic amplification microvalve. These challenges can be organized into two major groupings: (1) modeling and design challenges and (2) fabrication, assembly, and testing challenges. These challenges are highlighted in the following sections.

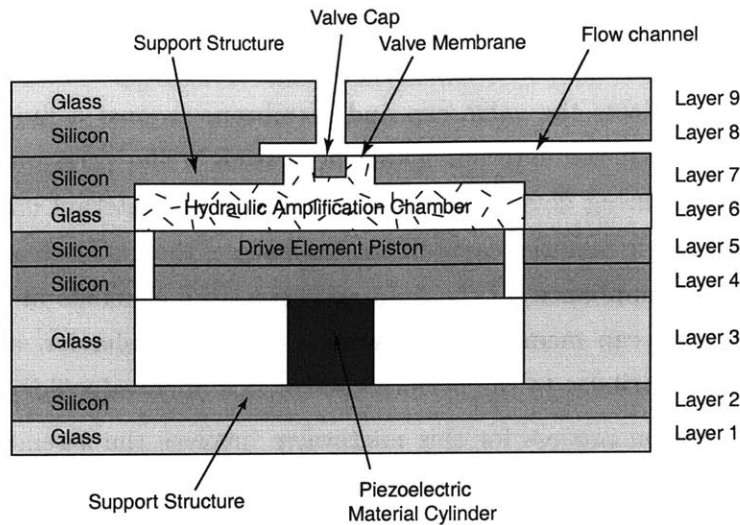


Figure 1.6: 2-D schematic of a microvalve multi-layer silicon and glass structure. Five silicon layers, four glass layers, and one or more piezoelectric material cylinders are joined together to form the microvalve. Enclosed fluid within the hydraulic amplification chamber couples the drive element piston deflection to the valve cap motion.

1.4.1 Modeling and Design Challenges

Structural Modeling of Active Valve

The development of a comprehensive structural model for the active valve requires detailed modeling of the piezoelectric material behavior, the bottom support plate structural compliance, the drive element piston and tether compliances, the hydraulic chamber fluid stiffness, the top support plate structural compliance, and the valve membrane deflection behavior. Stresses within the piezoelectric material, the drive piston tethers, and the valve membrane must be calculated to ensure structural integrity of the device under worst-case system loading conditions. Linear plate deformation theory is adequate for calculating the deflections and stresses associated with the drive piston tether and chamber compliances since these structural deflections are small in comparison to the respective structural thicknesses. However, modeling of the valve membrane requires more advanced non-linear deformation theory.

Non-linear Modeling of Valve Membrane

To achieve a high stroke actuation capability within the active valve device, the valve membrane/plate structure is designed to experience peak deflection magnitudes which exceed the plate structural thickness. This type of large-deflection deformation behavior is characterized by an elongation or stretching of the plate structure and a subsequent generation of a non-zero in-plane tensile stress along the neutral axis. As the plate is deformed significantly into the

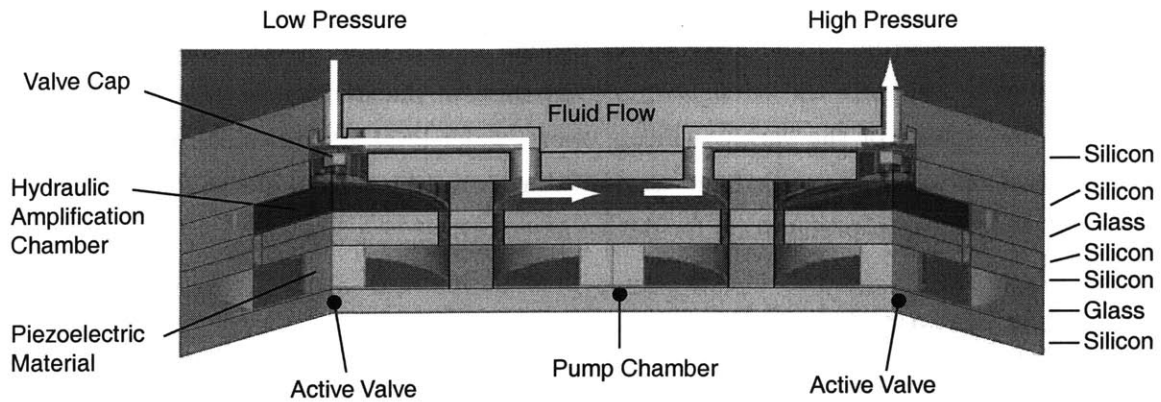


Figure 1.7: 3-D schematic of a Micro-Hydraulic Transducer multi-layer silicon and glass structure. Since a complete MHT system relies on identical fabrication and assembly procedures to those of the component valve, successful testing of the piezoelectrically driven active valve device validates the capability to realize the full MHT system.

large deflection regime, the in-plane tensile stress begins to exceed the bending stresses and the plate stiffness increases. Linear plate theory is inadequate to capture these stiffening effects, and as a result, tools have been developed to accurately model the non-linear large deflection behavior of the valve membrane/plate structure.

Development of Systematic Active Valve Design Procedure

The design and formulation of an active valve geometry which can satisfy performance requirements imposed by an external hydraulic system is an important step in the development of MHT systems. Accurate modeling of the fluid flow behavior through the hydraulic system and interaction of the valve structure with this external system must be developed. Additionally, design parameter variations, such as valve membrane thickness, valve cap stroke, and the number of valve membranes working together in parallel within the active valve device must be properly investigated so as to create an active valve whose membrane structures experience stresses below fracture limits and, as a whole, that consumes as little power as possible during operation.

1.4.2 Device Fabrication, Assembly, and Testing Challenges

Micromachining and Wafer-Bonding

Micromachining of the valve membrane and drive element tether structures within the active valve device is a critical step in the fabrication process. To achieve precise dimensional control of these thin-membrane structures, silicon-on-insulator (SOI) wafers containing a buried oxide

etch-stop layer are used. In performing deep etches in these wafers, the surface roughness of the etch and the tailoring of the fillet radius profiles at the base of the etch must be well-controlled so as to maintain the strength and robustness of the structures. Additionally, upon completing the etching of the various silicon layers, wafer-level silicon-silicon fusion bonding and wafer-level silicon-glass anodic bonding procedures must be carried out to form multi-layer wafer stack structures, in preparation for device assembly.

Piezoelectric Material Integration

Integration of bulk piezoelectric material within the thin-tethered drive element structures is the most critical step in the active valve assembly. Preparation of the material, including polishing, thin-film deposition, and core-drilling, is performed to provide an optimal surface finish of the material in preparation for eutectic bonding to the adjoining silicon layers within the device. Additionally, accurate measurement of the individual piezoelectric element dimensional thicknesses, prior to integration, is required to ensure optimal static and operational deflections of the piston structure which result in minimal stresses in the etched piston tethers. Incorporation of multiple smaller area piezoelectric materials spread out beneath the piston membrane is desired over placement of a single larger area piezoelectric material at the piston center, so as to reduce system compliances and increase actuation efficiency. However, tolerance issues become even more important when dealing with the requirements of multiple bonded elements.

Fluid Filling and Sealing

Encapsulation of a working fluid in the device is a significant challenge at the microscale because surface-to-volume ratios are typically quite large, with surface energies playing a dominant role. Any gas bubbles present in the sealed operational device can create enormous system compliances, potentially rendering the device useless. The elimination of trapped gases during filling of the device and during encapsulation of the fluid port used for filling is critical for high-level performance. The development of a systematic fluid degassing and filling procedure is required for successful realization of a working active valve device.

Device Testing

Experimental testing of a complex microfabricated device can be an extremely challenging activity, due primarily to the lack of physical access to the structures within the device. To thoroughly characterize the performance of the active valve device presented in this thesis, drive element piston and valve cap deflections in response to applied voltages must be measured real-time. Additionally, dynamic pressures (between 0 and 2 MPa) upstream and downstream of the valve orifice and real-time fluid flow rates (as low as $10 \frac{\mu L}{min}$ and as high as $1 \frac{ml}{s}$) must

be monitored. Development of a test-rig apparatus for carrying out these measurements is a critical task for proper evaluation of the device behavior.

1.5 Objectives

The primary objective of this thesis is to develop a piezoelectrically driven hydraulic amplification microactuator structure, which can be operate as a microvalve for high frequency control of high pressure fluid flows. This research is carried out through a series of modeling, design, fabrication, assembly, and experimental testing tasks. This work will demonstrate the microactuator and valve concepts and evaluate their experimental performance in comparison to behavior predicted by the models developed in the thesis.

A secondary goal of this thesis is to provide a framework of linear and non-linear structural modeling tools and design procedures that can be implemented in the development of high frequency piezoelectric micropumping and microvalving systems. Additionally, a further goal of this thesis is to present a method for small-scale bulk piezoelectric material integration within silicon micromachined thin-tethered structures, a procedure which can enable the realization of compact high-frequency high-stiffness hydraulic actuator structures.

1.6 Approach

The overall scope of this thesis includes each of the challenges presented in Section 1.4, and consequently the thesis is divided into two major parts. The first part (Chapters 2 through 5) focuses on active valve modeling and design. The second part (Chapters 6 through 9) concentrates on active valve fabrication, assembly, and testing. Use of the modeling tools developed in the first part of the thesis enables model-experiment correlation in the later sections.

Chapter 2 introduces the concept of the active valve device and details the procedures used to model the structural valve component compliances. Linear plate theory, with bending and shearing deformation effects included, is implemented. Additionally, the benefits of multiple piezoelectric elements spread out beneath the drive element piston rather than a single centrally-located element are presented through a series of finite-element studies.

Chapter 3 presents the development of a numerical code to model the large deflection behavior of a thin annular plate structure with rigid central cap under pressure loading. This theory has been specifically developed to capture the non-linear stiffening effects present in the valve membrane structure of the active valve, effects which are unaccounted for in the basic linear plate theory presented in Chapter 2. The finite-differencing scheme presented in this chapter is based upon the work of Su [1].

Chapter 4 combines the linear and non-linear modeling tools presented in Chapters 2 and 3 to create a quasi-static structural model of the active valve. In addition, the chapter introduces a dynamic simulation architecture for the valve, which includes inertia and damping associated with the drive element piston and valve cap structural elements. Calculation of the coupled fluid-structure resonant valve frequency, based on finite-element analyses, is also presented.

Chapter 5 uses the modeling tools and simulations developed in the first three chapters to formulate a systematic quasi-static design procedure that can be used to design an active valve geometry based on external hydraulic system performance requirements. This design procedure incorporates the governing fluid flow relations linking the valve cap motion to the external hydraulic system pressures and enables variation of key parameters within the active valve geometry to minimize power consumption. As a check, full system dynamic simulations are run to validate the quality of the valve geometry created using the quasi-static procedure.

Chapter 6 presents an overview of the fabrication challenges encountered and the solutions implemented in the development of the active valve device. A detailed sub-component testing plan for the active valve is presented as well. This systematic plan, as shown in Figure 1.8, breaks the complete active valve structure into manageable sub-component structures according to the primary challenges already detailed. The piezoelectric drive element sub-component study proves the ability to micromachine the tethered piston structure and integrate bulk piezoelectric material beneath the piston. The valve cap and membrane sub-component study validates the non-linear large deflection behavior of the valve membrane structure. Following successful completion of these sub-component studies, a complete active valve device can be fabricated and tested.

Chapter 7 details the piezoelectric drive element sub-component study. Devices are fabricated that incorporate both standard polycrystalline PZT-5H piezoelectric material elements as well as higher-strain single-crystal PZN-PT piezoelectric material. Additionally, devices with three piezoelectric elements spread out beneath the drive piston are compared to single element devices to demonstrate the stiffening benefit of incorporating multiple piezoelectric elements within the drive element structure. These devices are quasi-statically and dynamically characterized to frequencies in excess of 100 kHz.

Chapter 8 details the valve cap and membrane sub-component study. Valve membrane structures are fabricated and inspected to ensure adequate fillet radius control at the base of the etched features. Pressure-deflection experiments are carried out to characterize the degree of non-linearity present in these structures. Experimental results are compared to analytical and finite-element model results in which key parameters have been varied (membrane thickness and fillet radius size) in an effort to determine the sensitivity of the membrane behavior to these parameters.

Schematic Cross-Sections of Test Articles in the Test Plan

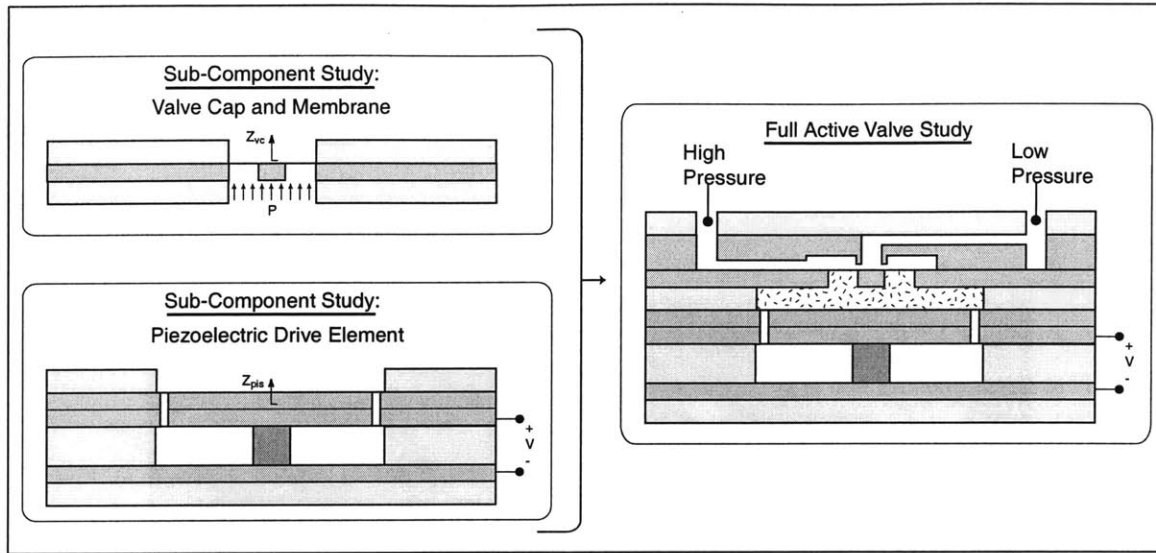


Figure 1.8: Active valve sub-component testing plan. Realization of the full active valve requires performance validation of piezoelectric drive element sub-component, valve cap and membrane sub-component, and hydraulic amplification chamber sub-component.

Chapter 9 presents the experimental testing of the full active valve device, with a focus on voltage-valve cap deformation frequency-dependent behavior, as well as differential pressure-flow characterization of the valve. Correlation to quasi-static and dynamic models is presented.

Lastly, **Chapter 10** concludes the thesis with a summary of accomplishments. Conclusions are drawn and recommendations are made for future work. Appendices are also included, which detail many of the structural models and dynamic simulations presented throughout the thesis.

1.7 Thesis Executive Summary

This thesis demonstrates, through a series of modeling, design, fabrication, assembly, and experimental testing tasks, successful operation of a piezoelectrically-driven hydraulic amplification microvalve for use in Micro-Hydraulic Transducer systems. Linear and non-linear modeling tools characterizing the structural deformations of the active valve sub-systems were developed. These tools enabled accurate prediction of real-time stresses along the micromachined valve membrane structure as it was deflected into its non-linear large-deflection regime. A systematic design procedure was developed to generate an active valve geometry to satisfy membrane stress limitations and valve power consumption requirements set forth by external hydraulic system performance goals. Fabrication challenges, such as deep-reactive ion etching (DRIE) of the drive element and valve membrane structures, wafer-level silicon-to-silicon

fusion bonding and silicon-to-glass anodic bonding operations, preparation and integration of piezoelectric material elements within the micromachined tethered piston structure, die-level assembly and bonding of silicon and glass dies, and filling of degassed fluid within the hydraulic amplification chamber were overcome. A photograph of the completed 9-layer microfabricated valve is shown in Figure 1.9.

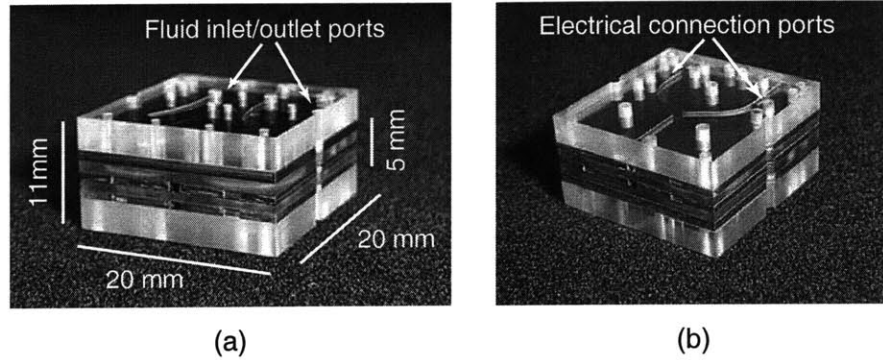


Figure 1.9: Photograph of a 9-layer silicon and glass piezoelectrically-driven hydraulic amplification microvalve, as part of a full MHT system. Dimensions of the valve structure within the full MHT chip are 8mm x 8mm x 5mm.

The active valve structural behavior and flow regulation capabilities were evaluated over a range of applied piezoelectric voltages, actuation frequencies, and differential pressures across the valve. For applied piezoelectric voltages up to 500V_{pp} at 1kHz, the valve devices demonstrated amplification ratios of drive element deflection to valve cap deflection of 40-50x. These amplification ratios correlate within 5 – 10% of the model expectations. Flow regulation experiments proved that a peak average flow rate through the device of 0.21mL/s under a sinusoidal drive voltage of 500V_{pp}, with valve opening of 17 μ m, against a differential pressure of 260kPa could be obtained. Tests revealed that fluid-structural interactions between the valve cap and membrane components and flow instabilities (due to transition between the laminar and turbulent flow regimes through the valve orifice) limited the valve performance capabilities.

Bibliography

- [1] H. Van Lintel, F. van de Pol, and A. Bouwstra, "Piezoelectric micropump based on micro-machining of silicon", *Sensors and Actuators*, 15, pp. 153-167, 1988.
- [2] M. Stehr, S. Messner, H. Sandmaier, and R. Zengerle, "The VAMP - a new device for handling liquids or gases," *Sensors and Actuators A*, 57, pp. 153-157, 1996.
- [3] V. Gass, B. van der Schoot, S. Jeanneret, and N. de Rooij, "Integrated flow-regulated silicon micropump," *Sensors and Actuators A*, 43, pp. 335-338, 1994.
- [4] S. Shoji and M. Esashi, "Microflow devices and systems," *Journal of Micromechanics and Microengineering*, 4, pp. 157-171, 1994.
- [5] K. Ikuta, T. Hasewaga, and T. Adachi, "The Optimized SMA Micro Pump Chip Applicable to Liquids and Gases," *Proceedings of the 2001 International Conference on Solid-State Sensors and Actuators (Transducers '01)*, 2001.
- [6] M. Koch, N. Harris, R. Maas, A. Evans, N. White, and A. Brunnschweiler, "Novel micropump design with thick-film piezoelectric actuation," *Measurement Science and Technology*, v.8 n.1, pp. 49-57, Jan 1997.
- [7] P. Watler and M. Sefton, "A Piezoelectric Driven Controlled Release Micropump for Insulin Delivery," *Trans Am Soc Artif Intern Organs*, Vol. XXXVI, pp. 70-77, 1990.
- [8] B. Wagner, H. Quenzer, S. Hoerschmann, T. Lisec, and M. Jueress, "Micromachined bistable valves for implantable drug delivery systems," *Proceedings of the 18th Annual International Conference of the IEEE Engineering in Medicine and Biology Society*, pp. 254-255, 1997.
- [9] N.W. Hagood, D.C. Roberts, L. Saggere, K.S. Breuer, K.-S. Chen, J.A. Carretero, H.Q. Li, R. Mlcak, S. Pulitzer, M.A. Schmidt, S.M. Spearing, and Y.-H. Su, "Micro Hydraulic Transducer Technology for Actuation and Power Generation," *Proceedings of SPIE: SPIE's 7th Annual International Symposium on Smart Structures and Materials*, Vol. 3985, pp. 680-688, 2000.

- [10] H.Q. Li, D.C. Roberts, J.L. Steyn, K.T. Turner, J.A. Carretero, O. Yaglioglu, Y.-H. Su, L. Saggere, N.W. Hagood, S.M. Spearing, M.A. Schmidt, R. Mlcak, and K.S. Breuer, "A High Frequency High Flow Rate Piezoelectrically Driven MEMS Micropump," Proceedings of the IEEE Solid-State Sensor and Actuator Workshop, Hilton Head, SC. pp. 69-72, 2000.
- [11] D.C. Roberts, J.L. Steyn, H.Q. Li, K.T. Turner, R. Mlcak, L. Saggere, S.M. Spearing, M.A. Schmidt, and N.W. Hagood, "A High-Frequency, High-Stiffness Piezoelectric Micro-Actuator For Hydraulic Applications," Proceedings of the 2001 International Conference on Solid-State Sensors and Actuators (Transducers '01), 2001.
- [12] D.C. Roberts, N.W. Hagood, Y.-H. Su, H.Q. Li, and J.A. Carretero, "Design of a Piezoelectrically-Driven Hydraulic Amplification Microvalve for High Pressure, High Frequency Applications," Proceedings of SPIE's 7th International Symposium on Smart Structures and Materials, Vol. 3985, pp. 616-628, 2000.
- [13] D.C. Roberts, O. Yaglioglu, J. Carretero, Y.-H. Su, L. Saggere, and N.W. Hagood, "Modeling, Design, and Simulation of a Piezoelectric Microvalve for High Pressure, High Frequency Applications," Proceedings of SPIE's 8th International Symposium on Smart Structures and Materials, Vol. 4327, 2001.
- [14] J.M. Hollerbach, I.W. Hunter, J. Ballantyne, "A comparative analysis of actuator technologies for robotics," *Robotics Review* 2, Eds. Khatib and Oussama, MIT Press, pp. 299-342.
- [15] J.E. Huber, N.A. Fleck, and M.F. Ashby, "The selection of mechanical actuators based on performance indices," Proceedings of the Royal Society of London, Series A, Vol. 453, No. 1965, p. 2185.
- [16] S.W. Pulitzer III, "Feasability Assessment and Design of Micro Hydraulic Solid-State Transducers," MIT Master's Thesis. June 1998.
- [17] S. Park and T. Shrout, "Characteristics of Relaxor-Based Piezoelectric Single Crystals for Ultrasonic Transducers," *IEEE Transactions on Ultrasonics, Ferroelectrics, and Frequency Control*, Vol. 44, No. 5, pp. 1140-1147, 1997.
- [18] M. Esashi, S. Shoji, and A. Nakano, "Normally Closed Microvalve and Micropump Fabricated on a Silicon Wafer," *Sensors and Actuators* 20, pp. 163-169, 1989.
- [19] M. Esashi, "Integrated Micro Flow Control Systems," *Sensors and Actuators*, A21-A23, pp. 161-167, 1990.
- [20] S. Shoji, B. Van der Schoot, N. de Rooij, and M. Esashi, "Smallest Dead Volume Microvalves for Integrated Chemical Analyzing Systems," Proceedings of the 1991 Interna-

- tional Conference on Solid-State Sensors and Actuators (Transducers '91), pp. 1052-1055, 1991.
- [21] K. Henning, "Liquid and gas-liquid phase behavior in thermopneumatically actuated microvalves," Proceedings of SPIE- The International Society for Optical Engineering v3515, pp. 53-63, 1998.
- [22] C. Rich and K. Wise, "A Thermopneumatically-Actuated Microvalve With Improved Thermal Efficiency and Integrated State Sensing," Proceedings of the IEEE Solid-State Sensor and Actuator Workshop, Hilton Head, SC, pp. 234-237, 2000.
- [23] M.A. Huff and W.L. Benard, "Thin film titanium-nickel shape memory alloy microfluidic devices," Proceedings of the Third International Symposium on Microstructures and Microfabricated Systems, pp. 26-38, 1997.
- [24] H. Jerman, "Electrically-Activated, Micromachined Diaphragm Valves," Proceedings of the 1991 International Conference on Solid-State Sensors and Actuators (Transducers '91), pp. 1045-1048, 1991.
- [25] M.A. Huff, "Silicon Micromachined Wafer-Bonded Valves," Ph.D. Thesis, Massachusetts Institute of Technology, 1993.
- [26] M. Shikida, K. Sato, S. Tanaka, Y. Kawamura, and Y. Fujisaki, "Electrostatically driven gas valve with high conductance," Journal of Microelectromechanical Systems, 3(2), pp.76-80, June 1994.
- [27] F. Pourahmadi, L. Christel, K. Petersen, J. Mallon, and J. Bryzek, "Variable-Flow Micro-Valve Structure Fabricated with Silicon Fusion Bonding," Proceedings of the IEEE Solid-State Sensor and Actuator Workshop, Hilton Head, SC, pp. 78-81, 1990.
- [28] A. Meckes, J. Behrens, and W. Benecke, "Electromagnetically Driven Microvalve Fabricated in Silicon," Proceedings of the 1997 International Conference on Solid-State Sensors and Actuators (Transducers '97), pp. 821-824, 1997.
- [29] J.G. Smits, "Piezoelectric Micropump with Microvalves", Proc Eighth Bienn Univ Gov Ind Microelectron Symp. (IEEE n 89CH2769-8), Piscataway, NJ, USA. p 92-94
- [30] T. Watanabe and H. Kuwano, "A microvalve matrix using piezoelectric actuators," Microsystem Technologies, pp. 107-111, 1997.
- [31] S. Kluge, G. Neumayer, U. Schaber, and M. Wackerle, "Pneumatic Silicon Microvalves with Piezoelectric Actuation," Proceedings of the 2001 International Conference on Solid-State Sensors and Actuators (Transducers '01), 2001.

- [32] J. Garcia-Bonito, M.J. Brennan, S.J. Elliot, A. David, and R.J. Pinnington, "A novel high-displacement piezoelectric actuator for active vibration control," *Smart Mater. Struct.* 7, pp. 31-42, 1998.
- [33] P. Tang, A. Palazzolo, A. Kascak, G. Montague, and W. Li, "Combined Piezoelectric-Hydraulic Actuator Based Active Vibration Control for Rotordynamic System," *Journal of Vibration and Acoustics* 117, pp. 285-293, 1995.
- [34] Tsukamoto, "Piezo-Actuator's Displacement Magnifying Mechanism," US Patent 5,233,834. 1993.
- [35] Y.H. Su, K.S. Chen, D.C. Roberts, and S.M. Spearing, "Large Deflection Analysis of a Pre-Stressed Annular Plate With a Rigid Boss Under Axisymmetric Loading", *Journal of Micromech. Microeng.* 11 (2001) pp. 645-653.

Chapter 2

Active Valve Linear Model

This chapter presents the analytical modeling structure of the active valve, focusing on the linear deformation behavior of the various structural components. This chapter begins with an overview of each of the components of the active valve, detailing the corresponding structural geometries and associated assumptions used to model them. This first-level active valve model assumes a single cylindrical piezo material under the drive element piston for ease of modeling. Toward the conclusion of the chapter, the effects of incorporating multiple piezoelectric cylinders are discussed and the corresponding benefits to structural stiffnesses of the piston and the bottom structural plate are presented. The chapter concludes with an identification of the valve components that require further development of non-linear theory.

2.1 Valve Geometry and Modeling Procedure

The proposed piezoelectrically driven hydraulic amplification microvalve is schematically shown in Figure 2.1. The axisymmetric valve is comprised of three primary sub-structures: a piezoelectric drive element, a closed hydraulic amplification chamber, and a membrane with attached valve cap. The drive element sub-structure consists of one or more bulk piezoelectric material cylinders located at the center of the device, each bonded on its top surface to a silicon micromachined piston and on its bottom surface to a silicon support structure. The drive element piston is attached along its outer circumference to a silicon support structure with two thin silicon tethers. The fluid chamber resides between the top surface of the drive element piston and the bottom surface of a smaller diameter silicon micromachined valve cap membrane. In response to an applied piezoelectric voltage, a small deflection of the drive element piston translates into a much larger deflection of the valve cap membrane. The ratio of the piston diameter to the valve membrane diameter, the compliances of the fluid and structural chamber, the severity to which the valve cap membrane experiences nonlinear behavior, and the piezoelectric material performance determine the potential valve stroke for a given applied piezoelectric voltage.

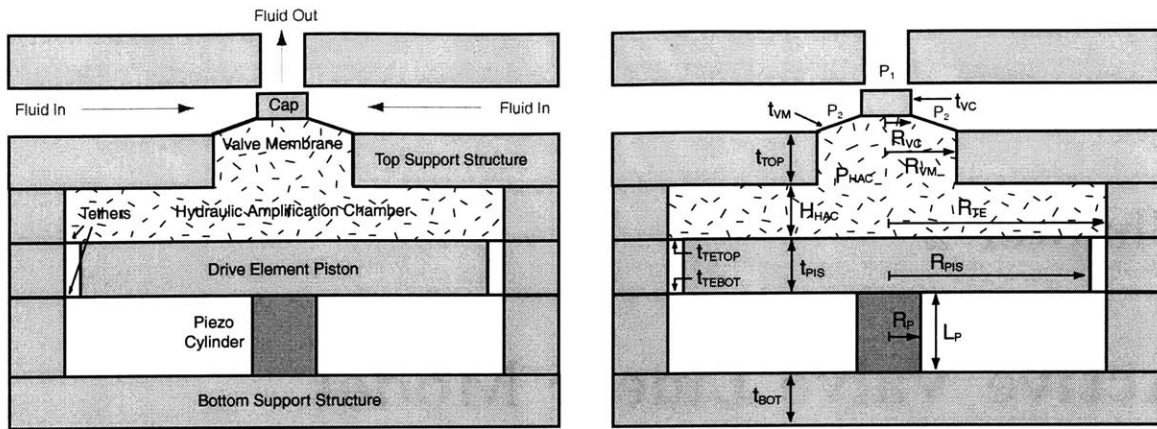


Figure 2.1: 2-D schematic of the piezoelectrically-driven hydraulic amplification microvalve. The nomenclature and key dimensions are detailed.

In developing a comprehensive analytical model for the active valve, the following aspects need to be accurately represented: (1) piezoelectric material behavior, (2) drive element piston and tether deflection behavior, (3) fluid compressibility, (4) hydraulic amplification chamber structural compliance, (5) valve cap and membrane deflection behavior, and (6) bottom structural plate behavior beneath piezoelectric material. The efficiency of the valve drive is a function of how much volume is created due to the various system compliances. The ideal design would call for a very stiff hydraulic fluid and a completely rigid drive element piston and chamber structure. In this case, all of the volume change created by the drive element deflection would exhibit itself in the volume change associated with the valve membrane deflection. Modeling of aspects (2), (4), (5), and (6) require a detailed understanding of linear plate theory. Each of these aspects will be modeled as a plate with applied loading and boundary conditions to determine the deflections and swept volumes due to bending and shearing effects. Non-linear issues such as in-plane stretching will be discussed at the close of the chapter.

2.2 Overview of Linear Plate Theory

In general, a symmetrically loaded circular plate will experience deflections due to bending and shearing. If the plate thickness is small compared to the plate outer radius, the deflection due to bending will be significantly larger than that due to shearing. If the plate thickness is of the same order of magnitude as the plate outer radius, however, the deflection contribution due to shearing effects will no longer be negligible. In these cases, it is advisable to obtain the total deflection as a sum of these two contributing effects. As detailed above, the top chamber structure, the drive element piston, the drive element tethers, the bottom chamber structure, and the valve cap/membrane can be modeled using linear plate theory. The degree to which

each of these structural components may experience non-linear deflection behavior is discussed at the conclusion of this chapter. This section presents the methodology used to model these plate behaviors (in a linear fashion) by way of a simple example. The following sections then detail each of the modeled valve compliances.

An example of a symmetrically loaded circular plate is shown in Figure 2.2. This plate is clamped at its outer radius ($r=a$), guided at its inner radius ($r=b$), and subjected to a pressure loading P over its bottom surface. The plate will experience deflections due to bending and shearing effects.

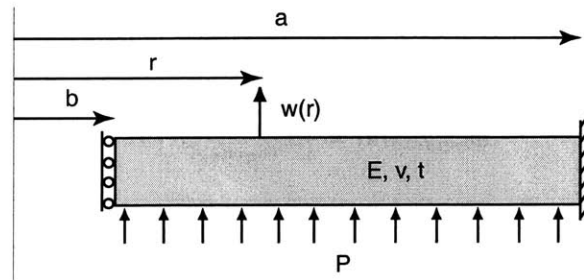


Figure 2.2: Circular plate under axisymmetric pressure loading, with a guided boundary condition at inner radius b and a clamped boundary condition at outer radius a .

2.2.1 Deflections Due to Bending

The governing differential equation for the symmetrical bending of a circular plate can be written as:

$$\frac{d}{dr} \frac{d}{dr} r \left(\frac{d}{dr} w(r) \right) = \frac{Q(r)}{D} \quad (2.1)$$

where $D = \frac{Et^3}{12(1-\nu^2)}$ is the flexural rigidity of the plate and $Q(r)$ is the shear force per unit length as a function of r . $Q(r)$ depends on the nature of the plate loading. In this example case, the shear force is:

$$Q(r) = \frac{P(r^2 - b^2)}{2r} \quad (2.2)$$

The boundary conditions in this example case are:

$$BC1 : w(r = a) = 0 \quad (2.3)$$

$$BC2 : \frac{dw}{dr}(r = a) = 0 \quad (2.4)$$

$$BC3 : \frac{dw}{dr}(r = b) = 0 \quad (2.5)$$

By integrating the governing differential equation and applying the imposed boundary conditions, the deflection of the plate $w(r)$ can be determined. In addition, the swept volume associated with the deflection can then be calculated as follows:

$$dV = \int 2\pi r w(r) \partial r. \quad (2.6)$$

For this example plate bending case, the plate deflection at the inner radius ($r=b$) and the swept volume are found to be:

$$w_{bending}(b) = \left[\Xi_{w_{bending}(b)}^P \right] P \quad (2.7)$$

$$dV_{bending} = \left[\Xi_{dV_{bending}}^P \right] P \quad (2.8)$$

where $\Xi_{w_{bending}(b)}^P$ and $\Xi_{dV_{bending}}^P$ are the plate bending compliances,

$$\Xi_{w_{bending}(b)}^P = \left(\frac{1}{64D(b^2 - a^2)} \right) \left(3b^6 + a^2b^4 \left(-7 + 4 \ln \left[\frac{b}{a} \right] - 16 \ln \left[\frac{b}{a} \right]^2 \right) + a^4b^2 \left(5 - 4 \ln \left[\frac{b}{a} \right] \right) - a^6 \right) \quad (2.9)$$

$$\Xi_{dV_{bending}}^P = \left(\frac{-\pi}{192D(b^2 - a^2)} \right) \left(a^8 - 10a^6b^2 + 24a^4b^4 \left(1 - \ln \left[\frac{b}{a} \right] \right) + a^2b^6 \left(-22 + 24 \ln \left[\frac{b}{a} \right] \right) + 7b^8 \right) \quad (2.10)$$

These compliance coefficients are derived in detail in Appendix A.1.

2.2.2 Deflections Due to Shearing

In cases where the plate thickness is not small compared to the plate outer radius, shearing effects may contribute significantly to the overall deflection. The following analysis structure will allow for estimations of this deflection due to shear.

In general, shearing stresses vary across the thickness of a plate according to the same principle as for beams of narrow rectangular cross-sectional area [3]. The corresponding shearing strain can be written as:

$$\frac{dw}{dr} = \frac{-\alpha Q(r)}{Gt} \quad (2.11)$$

where $G = \frac{E}{2(1-\nu)}$ is the modulus of elasticity in shear of a plate, t is the plate thickness, and $Q(r)$ is, again, the shear force per unit length as a function of r . The coefficient α is the shear correction factor. The boundary condition in this example case is:

$$BC4: w(r = a) = 0 \quad (2.12)$$

By integrating the differential equation and applying the imposed boundary condition, the deflection of the plate $w(r)$ can be determined. The swept volume associated with this deflection can be calculated according to Equation (2.6). For this example plate shearing case, the plate deflection at the inner radius ($r=b$) and the swept volume under the plate are found to be:

$$w_{shear}(b) = \left[\Xi_{w_{shear}(b)}^P \right] P \quad (2.13)$$

$$dV_{shear} = \left[\Xi_{dV_{shear}}^P \right] P \quad (2.14)$$

where $\Xi_{w_{shear}(b)}^P$ and $\Xi_{dV_{shear}}^P$ are the plate shear compliances,

$$\Xi_{w_{shear}(b)}^P = \left(\frac{\alpha}{4Gh} \right) \left(a^2 + b^2 \left(-1 + 2 \ln \left[\frac{b}{a} \right] \right) \right) \quad (2.15)$$

$$\Xi_{dV_{shear}}^P = \left(\frac{\pi\alpha}{8Gh} \right) \left(a^4 - 4a^2b^2 + b^4 \left(3 - 4 \ln \left[\frac{b}{a} \right] \right) \right) \quad (2.16)$$

These compliance coefficients are derived in detail in Appendix A.1.

2.2.3 Combined Deflection Due to Bending and Shearing

The total deflection at ($r=b$) and swept volume of the plate are sums of those contributions due to pure bending effects and shearing effects. In this example case, the plate deflection and swept volume can therefore be written, respectively, as:

$$w(b) = \left[\Xi_{w_{bending}(b)}^P + \Xi_{w_{shear}(b)}^P \right] P = \left[\Xi_{w(b)}^P \right] P \quad (2.17)$$

$$dV = \left[\Xi_{dV_{bending}}^P + \Xi_{dV_{shear}}^P \right] P = \left[\Xi_{dV}^P \right] P \quad (2.18)$$

It is clear from this example that the plate deflection at a desired location and the swept volume can be expressed as linear functions of the loading parameters.

2.2.4 Comparison of Bending/Shearing Deflections

To illustrate the importance of the bending and shearing contributions to the example symmetric annular plate discussed thus far, the overall radial dimensions of the plate and the applied pressure loading are held constant and the plate thickness is varied from a value that is small compared to the plate radial dimensions to a value that is of the same order of magnitude as the radial dimensions. In doing this, one would expect to observe an increasing importance of

the shearing contribution as the plate thickness increases. The following dimensions, material constants, and loading parameters are assigned to the example case, and are typical of those found in the proposed active valve:

$$a = 3\text{mm}, b = 0.5\text{mm}, E = 165\text{GPa}, \nu = 0.22, \alpha = 1.5, P = 1\text{MPa}. \quad (2.19)$$

Deflections (at $r=b$) due to bending and shearing are calculated as the plate thickness is varied from $t = 20\mu\text{m}$ to $t = 2\text{mm}$. The results are shown in Figure 2.3.

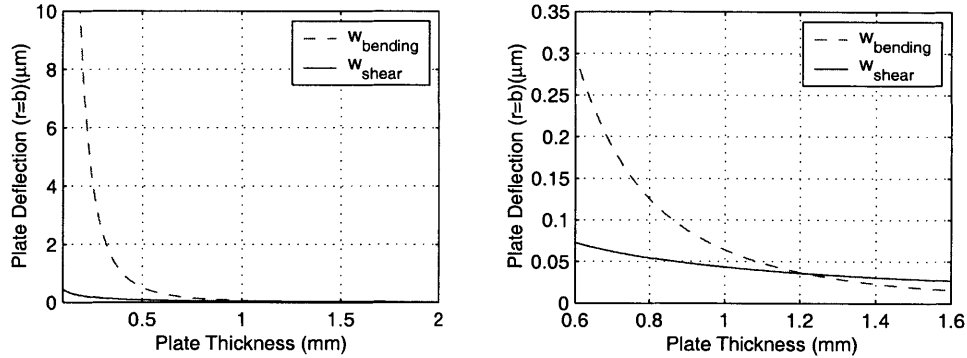


Figure 2.3: Bending and shearing contributions to plate deflection at inner radius ($r=b$). The plot on the right is a close-up view. As the ratio of plate thickness to plate outer radius approaches 1, the deflection due to shearing becomes important. For ratios $\ll 1$, shearing effects are inconsequential compared to bending effects.

These results illustrate the importance of shearing effects as the ratio of plate thickness to plate outer radius approaches 1. For ratios significantly less than 1, deflections due to bending far exceed those due to shearing. In this case, neglecting the shear contributions would have little effect on the calculated deformation. On the other hand, for ratios near and greater than 1, shear contributions are important and therefore, neglecting them would result in overall deformations smaller than those expected in reality. For each of the compliant plate structures within the active valve, except for the valve membrane (where its thickness \ll radial dimensions), both bending and shear effects are included in the deformation analyses.

2.3 Detailed Structural Modeling

2.3.1 Piezoelectric Material Behavior

The piezoelectric material cylinder within the valve drive element strains when a voltage is applied to it. Often, the loading on the material may increase during this actuation step. In the drive element structure, this actuation compressive loading is a combination of the hydraulic

amplification chamber pressure acting over the piston top surface and the tensile drive element tether force acting along the piston outer circumference. In general, for a bulk cylindrical piezoelectric element, as shown in Figure 2.4, subject to an applied voltage V_p and an actuation compressive axial stress ΔT_p , the material axial strain is:

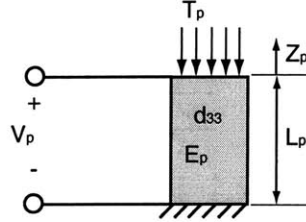


Figure 2.4: Cylindrical piezoelectric element with applied voltage and stress loading.

$$\varepsilon_p = \frac{\Delta Z_p}{L_p} = \frac{d_{33} V_p}{L_p} - \frac{\Delta T_p}{E_p} \quad (2.20)$$

The parameter d_{33} is the piezoelectric material coefficient and E_p is the modulus of elasticity. Under the case of zero actuation loading, $\Delta T_p = 0$, the material experiences a maximum strain in response to a voltage V_p . This is termed the free strain condition, $\varepsilon_{p,free} = \frac{d_{33} V_p}{L_p}$. At a sufficiently large external load, the material experiences no net strain in response to a voltage. This is termed the blocked force condition, $\Delta T_{p,blocked} = \frac{d_{33} V_p E_p}{L_p}$.

Equation 2.20 assumes perfect 33-direction actuation. In reality, this is not achieved due to transverse clamping of the piezoelectric element at its top and bottom. However, the incorporation of multiple, smaller diameter piezoelectric elements rather than a single large diameter element helps to reduce this clamping effect and supports the assumption. The implementation of multiple, smaller diameter piezoelectric elements is discussed in Section 2.5. For the purposes of the active valve model development in this section, however, a single piezoelectric material cylinder placed at the center of the drive element chamber is assumed.

2.3.2 Drive Element Piston and Tether Behavior

The drive element substructure provides a volume change, which is transferred to the valve cap/membrane through the use of hydraulic fluid. In an ideal case, the drive piston would be a rigid structure and the drive element tethers would be stiff enough to resist significant volume deformation due to the hydraulic amplification chamber pressure, yet compliant enough to allow for adequate piston deflection and to ensure tether stresses below critical levels. The drive element piston and tether structure can be broken into two linked sub-models, as shown in Figure 2.5. The first sub-model captures the behavior of the drive piston and the second sub-model captures the behavior of the drive element tethers.

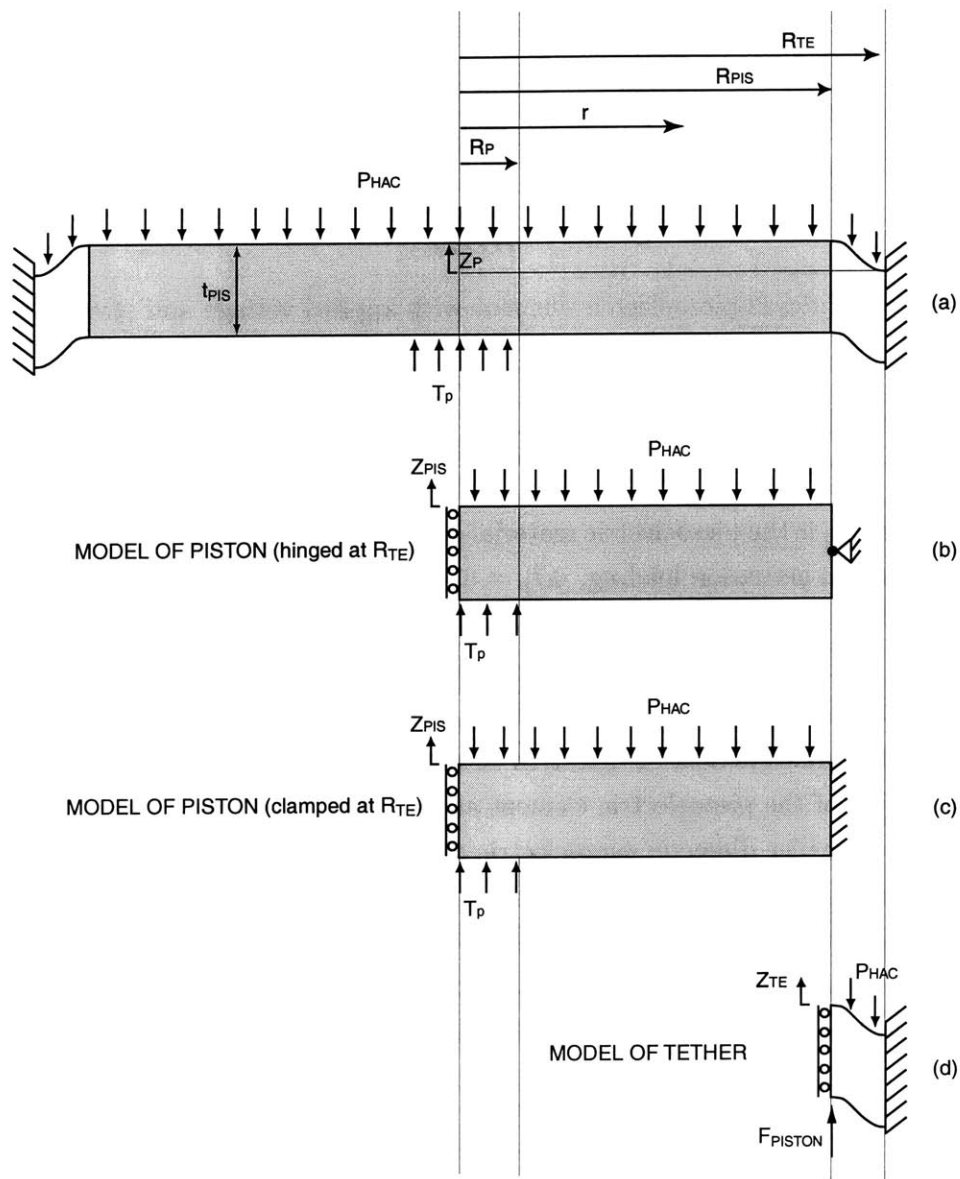


Figure 2.5: Simplification of pressure and stress loading on the drive element piston for use in the linear deflection analysis of the drive element tethers.

Drive Element Piston

Figures 2.5(b) and 2.5(c) present two potential ways to model the deformation of the drive element piston. Both scenarios model the piston as a circular plate with outer radius R_{pis} and thickness t_{pis} and assume the plate to experience a guided boundary condition at its center. Finite-element models have shown this to be a more appropriate (and conservative) boundary condition than enforcing a guided boundary condition at the edge of piezo material, R_p . The piezoelectric material is not infinitely rigid, and therefore does allow for plate bending over the region where the material contacts the piston. The primary difference in the two scenarios is the boundary condition assumptions at the outer piston radius R_{pis} . If the drive element tethers possessed negligible stiffness, one could assume that they exert an insignificant bending moment on the drive piston, resulting in an appropriate hinged boundary condition at R_{pis} , as shown in Figure 2.5(b). On the other hand, if the tethers possessed an infinite stiffness, one could assume them to create a rigid boundary on the piston at this location, as shown in Figure 2.5(c). Finite-element studies have shown that for the typical range of design space for the tethers and piston in this active valve device, the actual structural behavior is approximately halfway between these two limiting scenarios. Therefore, the drive element piston compliances are taken as the average of these limiting scenarios. The hydraulic amplification chamber pressure P_{HAC} acts over the entire top surface of the plate from $r = 0$ to $r = R_{pis}$ and the piezoelectric material stress T_p acts over the bottom surface of the plate from $r = 0$ to $r = R_p$. The piston center deflection Z_{pis} and piston swept volume dV_{pis} (referenced to the hinged outer radius) can therefore be represented by the following relations,

$$Z_{pis} = \left[\Xi_{Z_{pis}}^T \right] T_P - \left[\Xi_{Z_{pis}}^P \right] P_{HAC} \quad (2.21)$$

$$dV_{pis} = \left[\Xi_{dV_{pis}}^T \right] T_P - \left[\Xi_{dV_{pis}}^P \right] P_{HAC} \quad (2.22)$$

where $\Xi_{Z_{pis}}^T$, $\Xi_{Z_{pis}}^P$, $\Xi_{dV_{pis}}^T$, and $\Xi_{dV_{pis}}^P$ are the compliance coefficients defined explicitly in Appendix A.2.

Drive Element Tethers

In Figure 2.5(c), each drive element tether is modeled as a circular plate with inner radius R_{pis} and outer radius R_{ch} . In order to allow for flexibility in design, the top and bottom tethers are defined to have different thicknesses (t_{tetop} or t_{tebot}). Again, assuming that the piston slope at R_{pis} is zero, the boundary condition on each tether at this location is that of a guided interface. At R_{ch} , each plate is rigidly clamped to the valve support structure. The top tether experiences a concentrated force F_{tetop} at $r = R_{pis}$ and a pressure loading P_{HAC} from $r = R_{pis}$ to $r = R_{ch}$

while the bottom tether experiences only a concentrated force F_{tebot} at $r = R_{pis}$. The deflection (at $r = R_{pis}$) and swept volume of the top tether alone can be written as,

$$Z_{tetop} = \left[\Xi_{Z_{tetop}}^F \right] F_{tetop} - \left[\Xi_{Z_{tetop}}^P \right] P_{HAC} \quad (2.23)$$

$$dV_{tetop} = \left[\Xi_{dV_{tetop}}^F \right] F_{tetop} - \left[\Xi_{dV_{tetop}}^P \right] P_{HAC} + A_{pis} Z_{tetop} \quad (2.24)$$

where $\Xi_{Z_{tetop}}^F$, $\Xi_{Z_{tetop}}^P$, $\Xi_{dV_{tetop}}^F$, and $\Xi_{dV_{tetop}}^P$ are coefficients defined explicitly in Appendix A.2.

The deflection (at $r = R_{pis}$) and swept volume of the bottom tether alone can be written as,

$$Z_{tebot} = \left[\Xi_{Z_{tebot}}^F \right] F_{tebot} \quad (2.25)$$

$$dV_{tebot} = \left[\Xi_{dV_{tebot}}^F \right] F_{tebot} + A_{pis} Z_{tebot} \quad (2.26)$$

where $\Xi_{Z_{tebot}}^F$ and $\Xi_{dV_{tebot}}^F$ are coefficients defined explicitly in Appendix A.2.

Although the equations for the behavior of each tether alone are straightforward, the behavior resulting from both tethers together is more complex. In a two-tether system, both tethers share the same deflection at $r = R_{pis}$; that is, $Z_{te} = Z_{tetop} = Z_{tebot}$. Additionally, the sum of the piston forces on the tethers must be equal to the total force on the piston itself,

$$F_{tetop} + F_{tebot} = F_{piston} = A_p T_p - A_{pis} P_{HAC}. \quad (2.27)$$

The distribution of this force on the tethers is determined by the relative stiffnesses of the tethers, and therefore, the force taken by the top tether can be written as,

$$F_{tetop} = \left[\frac{\Xi_{Z_{tebot}}^F}{\Xi_{Z_{tebot}}^F + \Xi_{Z_{tetop}}^F} \right] F_{piston} \quad (2.28)$$

One can observe from this relation that if the bottom tether has a thickness much less than that of the top tether (ie: $\Xi_{Z_{tebot}}^F \gg \Xi_{Z_{tetop}}^F$), then all of the piston load is taken by the top tether, $F_{tetop} \approx F_{piston}$. Likewise, if the tethers have the same thickness, then each tether carries half of the piston force. Following these arguments, the tether deflection (at $r = R_{pis}$) and the tether swept volume can be expressed as,

$$Z_{te} = Z_{tetop} = \left[\frac{\Xi_{Z_{tetop}}^F \Xi_{Z_{tebot}}^F}{\Xi_{Z_{tebot}}^F + \Xi_{Z_{tetop}}^F} \right] (A_p T_p - A_{pis} P_{HAC}) - \left[\frac{\Xi_{Z_{tetop}}^P \Xi_{Z_{tebot}}^P}{\Xi_{Z_{tebot}}^P + \Xi_{Z_{tetop}}^P} \right] P_{HAC} \quad (2.29)$$

$$dV_{te} = dV_{tetop} = \left[\frac{\Xi_{dV_{tetop}}^F \Xi_{Z_{tebot}}^F}{\Xi_{Z_{tebot}}^F + \Xi_{Z_{tetop}}^F} \right] (A_p T_p - A_{pis} P_{HAC}) - \left[\frac{\Xi_{dV_{tetop}}^P \Xi_{Z_{tebot}}^P}{\Xi_{Z_{tebot}}^P + \Xi_{Z_{tetop}}^P} \right] P_{HAC} + A_{pis} Z_{te} \quad (2.30)$$

In this manner, the deflection of the drive element piston outer radius and the swept volume of the piston and top tether is determined.

Combined Piston and Tether Behavior

Having modeled the piston and tethers individually, it is now possible to express the complete piston/tether deflection and swept volume. The drive element piston center deflection with respect to the active valve structural support is the sum of the piston deflection in the first sub-model and the tether deflection in the second sub-model,

$$Z_{de} = Z_{pis} + Z_{te}. \quad (2.31)$$

Likewise, the total drive element volume change is the sum of the piston swept volume in the first sub-model and the top tether swept volume in the second sub-model,

$$dV_{de} = dV_{pis} + dV_{te}. \quad (2.32)$$

These relations, therefore, fully describe the drive element center deflection and swept volume as a function of the piston and tether stiffness coefficients and the loading, T_p and P_{HAC} .

2.3.3 Bottom Structural Compliance

A rigid valve structure beneath the piezoelectric material cylinder would ensure that all of the piezoelectric strain during actuation goes into the drive element volume change needed for valve cap motion. In reality, this structure is not rigid and as a result this bottom structure deformation serves only to reduce the effective volume change that can be produced by the drive element.

As shown in Figure 2.6, this structure can be modeled as a circular plate with thickness t_{bot} , guided at its center, and clamped at outer radius R_{ch} . Again, as for the drive element piston, the assumption that the piezo in no way helps to stiffen the plate is taken as a conservative estimate. The only loading applied to the plate is the piezoelectric material stress T_p from $r = 0$ to $r = R_p$. The bottom plate center deflection Z_{bot} can therefore be represented by the following relation,

$$Z_{bot} = - \left[\Xi_{Z_{bot}}^T \right] T_p \quad (2.33)$$

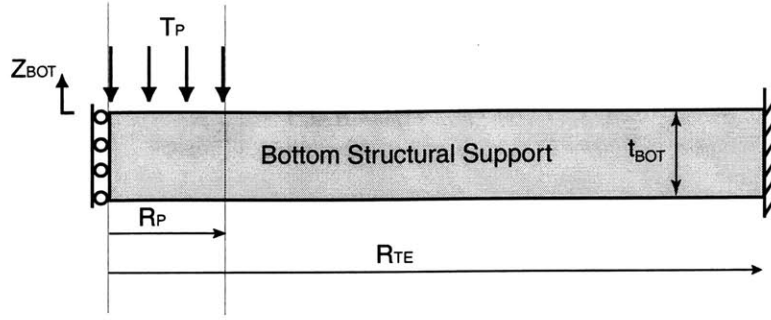


Figure 2.6: Compliance of bottom structure beneath piezoelectric material.

where $\Xi_{Z_{bot}}^T$ is defined explicitly in Appendix A.2.

2.3.4 Fluid Compressibility

During valve actuation, increased pressure within the hydraulic amplification chamber results in compression of the contained fluid. A portion of the drive element volume change will be lost in this undesired volume change of the fluid. The relationship between the fluid volume change dV_{HAC} and the fluid pressure change dP_{HAC} is:

$$dV_{HAC} = - \left(\frac{V_{HAC}}{K_f} \right) dP_{HAC} \quad (2.34)$$

where K_f is the fluid bulk modulus and V_{HAC} is the total fluid volume of the hydraulic amplification chamber.

2.3.5 Top Structural Compliance

For efficient hydraulic amplification within the active valve, the top structural compliance should be small so that minimal drive element actuation volume is lost in this chamber deformation. As shown in Figure 2.7, the top chamber structure can be modeled as an annular plate with inner radius R_{vm} , outer radius R_{ch} , and thickness t_{top} . At R_{vm} , the plate is free and experiences a concentrated force F_{vm} , corresponding to the sum of all the forces acting on the valve cap and membrane,

$$F_{vm} = P_{HAC} A_{vm} - P_1 A_{vc} - P_2 (A_{vm} - A_{vc}). \quad (2.35)$$

The plate is rigidly clamped at R_{te} . The plate experiences a pressure loading P_{HAC} on its underside.

The top plate inner radius deflection Z_{top} and swept volume dV_{top} can therefore be represented by the following relation,

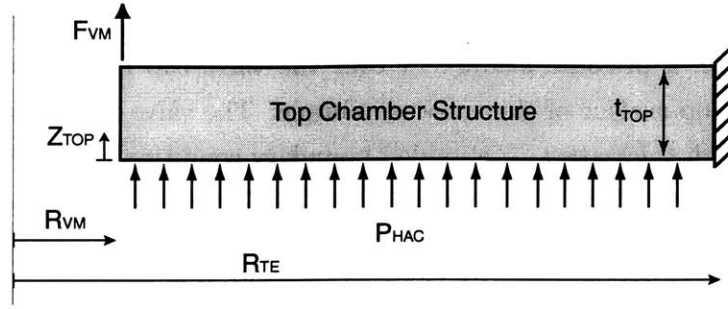


Figure 2.7: Hydraulic amplification chamber structural deformation under P_{HAC} and F_{vm} loading.

$$Z_{top} = [\Xi_{Z_{top}}^P] P_{HAC} + [\Xi_{Z_{top}}^F] F_{vm} \quad (2.36)$$

$$dV_{top} = [\Xi_{dV_{top}}^P] P_{HAC} + [\Xi_{dV_{top}}^F] F_{vm} + A_{vm} Z_{top} \quad (2.37)$$

where $\Xi_{Z_{top}}^P$, $\Xi_{Z_{top}}^F$, $\Xi_{dV_{top}}^P$, and $\Xi_{dV_{top}}^F$ are defined explicitly in Appendix A.2. In reality, the region above the annular chamber structure will not be completely unsupported. As a result, this model provides a worst-case value for the structural chamber volume change.

2.3.6 Valve Cap and Membrane Behavior

For the fluid flow directionality shown in Figure 2.1, a pressure drop occurs as the fluid flows radially inward over the valve membrane, through the contraction over the valve cap, and finally through the expansion into the exit channel. In the structural modeling of the valve cap and membrane, the pressure P_2 is assumed constant over the valve membrane area and the pressure P_1 is assumed constant over the valve cap area (see Chapter 5 for further discussion of these fluid modeling assumptions).

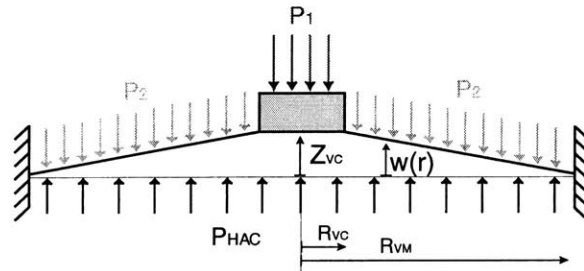


Figure 2.8: Valve membrane and cap, deflected upward from their equilibrium position, under pressure loadings P_{HAC} , P_1 , and P_2 .

As shown in Figure 2.8, the valve membrane experiences a pressure loading P_{HAC} over its entire bottom surface, a pressure loading P_1 over the valve cap top surface, and a pressure loading P_2 over the top surface of the valve membrane. The valve membrane can be modeled as a circular plate with thickness t_{vm} , a guided boundary condition at $r = R_{vc}$, and a clamped boundary condition at $r = R_{vm}$, with a pressure loading $P_{vm} = (P_{HAC} - P_2)$ on the underside of the membrane and a concentrated force $F_{vc} = A_{vc}(P_{HAC} - P_1)$ acting in the upward direction at $r = R_{vc}$ (see Figure 2.9). Bending of the valve cap is neglected in this model. For typical valve cap and membrane dimensions within the active valve structure, finite-element studies have shown that this rigid cap assumption is valid.

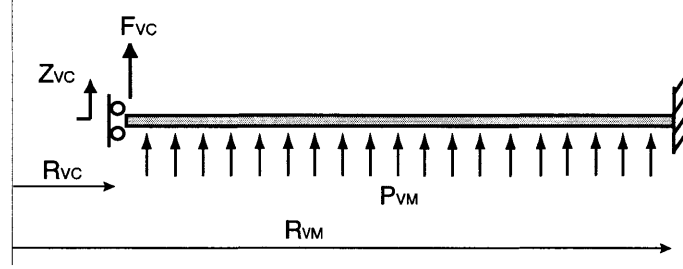


Figure 2.9: Simplified model of the valve cap and membrane with imposed boundary conditions and applied loading.

For linear theory, the inner radius deflection Z_{vc} and the swept volume dV_{vm} can be represented by the following relations,

$$Z_{vc} = \left[\Xi_{Z_{vc}}^P \right] P_{vm} + \left[\Xi_{Z_{vc}}^F \right] F_{vc} \quad (2.38)$$

$$dV_{VM} = \left[\Xi_{dV_{vm}}^P \right] P_{vm} + \left[\Xi_{dV_{vm}}^F \right] F_{vc} + A_{vc} Z_{vc} \quad (2.39)$$

where $\Xi_{Z_{vc}}^P$, $\Xi_{Z_{vc}}^F$, $\Xi_{dV_{vm}}^P$, and $\Xi_{dV_{vm}}^F$ are defined explicitly in Appendix A.2.

2.4 Full Active Valve Linear Model

The complete quasi-static active valve model consists of Equations 6.2, 6.3, 6.4, 2.29, 2.30, 2.33, 2.34, 2.35, 2.36, 2.37, 2.38, and 2.39, combined with the following two equations for displacement matching and volume conservation,

$$Z_p + Z_{bot} = Z_{te} + Z_{pis} \quad (2.40)$$

$$dV_{te} + dV_{pis} + dV_{fluid} - dV_{top} - dV_{vm} = 0. \quad (2.41)$$

Figure 2.10 summarizes the modeling components of the active valve. All equations are represented in a Maple code that solves for T_p and all of the structural component displacements and swept volumes, given the voltage input V_p and the external valve cap and membrane pressure loadings P_1 and P_2 . This model is included in Appendix A.2 for reference.

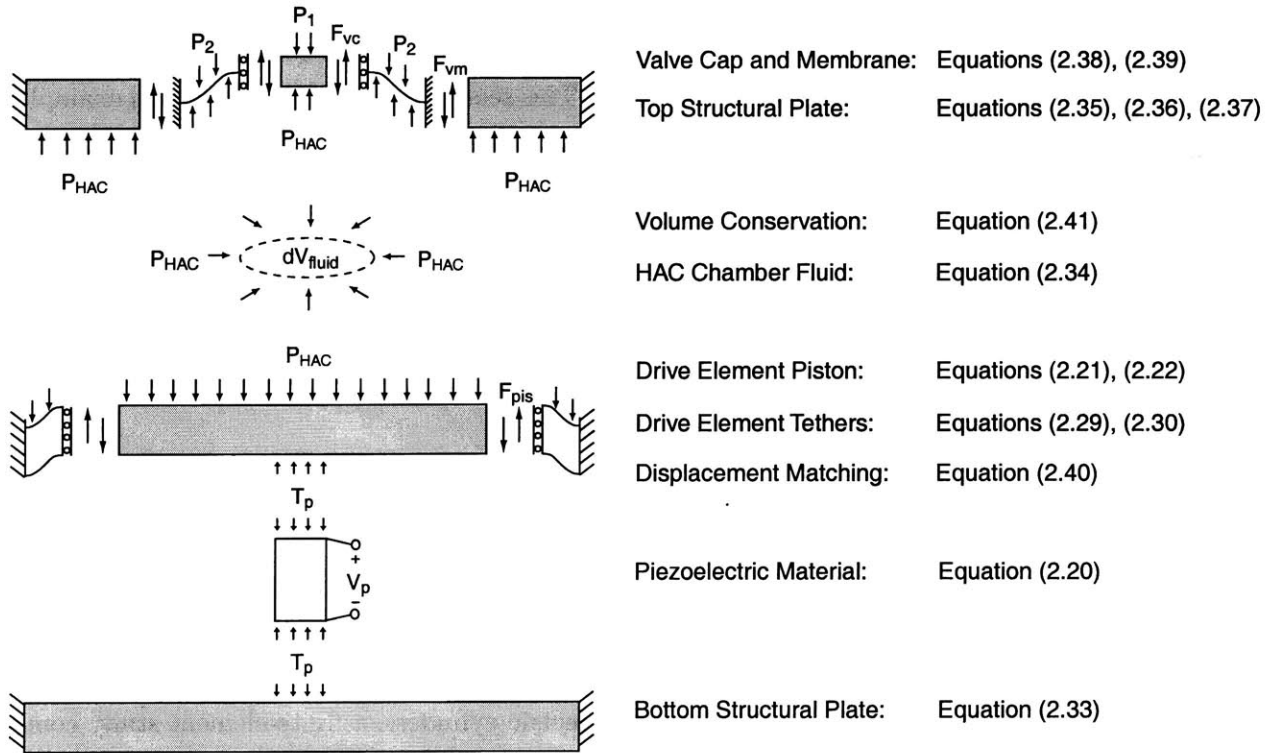


Figure 2.10: Complete linear quasi-static active valve structural model.

2.5 Impact of Multiple Piezoelectric Cylinders

The previous development of analytical theory for the active valve has assumed the piezoelectric actuation material to be a single cylinder located at the center of the drive element piston. To stiffen the drive element actuator structure, it would be desirable to incorporate a matrix of small diameter piezoelectric rods under the piston rather than a single centrally-located large-size cylinder (as long as the rods are sized properly to avoid buckling). Although incorporation of a matrix of rod structures is beyond the scope of this thesis, the use of three smaller diameter piezoelectric cylinders spread out beneath the piston is realizable (Chapter 8 experimentally evaluates this concept). This modeling section investigates the benefits of using three smaller diameter piezoelectric cylinders rather than a single centrally-located one in order to effectively “stiffen” the drive element piston and bottom plate structures.

Since the analytical relations developed thus far have assumed plate theory with boundary conditions corresponding to a single centrally-located piezoelectric cylinder, and since derivation of 3-dimensional plate behavior for multiple cylinder geometries is complex, finite-element models of the structural components are required. This section demonstrates, through example cases, how finite-element models of the drive element piston structure and bottom plate structure can be used to determine the $\Xi_{Z_p}^T$, $\Xi_{Z_p}^P$, $\Xi_{dV_{pis}}^T$, $\Xi_{dV_{pis}}^P$, and $\Xi_{Z_{bot}}^T$ compliance coefficients for three-piezoelectric cylinder geometries. Once determined, these coefficients can simply be substituted into the corresponding structural equations developed for the single-cylinder geometry presented in Sections 2.3.2 and 2.3.3.

2.5.1 Finite-Element Analysis of Piston

As presented in Section 2.3.2, the Ξ compliance coefficients for the piston structure are taken as the average of the hinged and clamped boundary condition scenarios at R_p . For clarity, this section will analyze the effects of three piezoelectric cylinders on a drive piston in the hinged boundary condition scenario. A similar procedure can be carried out for the clamped scenario, but is not documented in the section.

To illustrate the benefits of using three piezoelectric cylinders, a finite-element study comparing a single piezoelectric cylinder piston geometry to geometries with three piezoelectric cylinders is presented. In this study, representative piston geometry and material properties are taken to be: $R_{pis} = 3mm$, $t_{pis} = 800\mu m$, $E_{Si} = 165GPa$, and $\nu_{Si} = 0.22$. For the single piezoelectric cylinder geometry, the cylinder radius is $R_p = 1mm$. For the three piezoelectric cylinder geometry, the radius of each cylinder is sized ($R_p = 0.577mm$) such that the total area of all three is identical to the area of the cylinder in the single piezoelectric cylinder case. The distance R_{cp} of each cylinder from the piston center is varied in this study to illustrate the effect of cylinder placement on the piston compliance. Schematics of the single cylinder and

three cylinder finite-element model geometries are shown in Figure 2.11. The piston structure is guided at its center ($r = 0$) and hinged at its outer radius ($r = R_{pis}$).

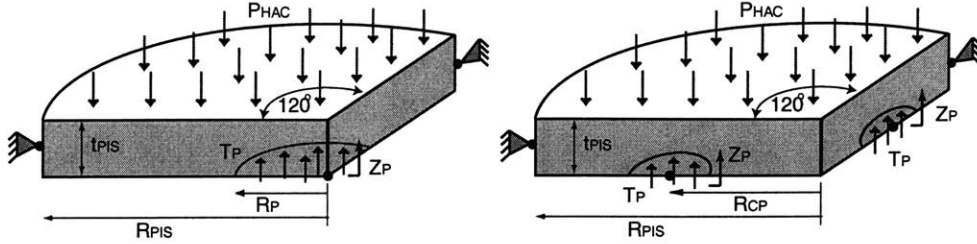


Figure 2.11: Finite-element (ANSYS) models of (a) a single centrally located piezoelectric cylinder beneath the drive element piston, and (b) a three piezoelectric cylinder design with the cylinders spread out beneath the drive element piston.

To determine the compliance coefficients $\Xi_{Z_p}^T$ and $\Xi_{dV_{pis}}^T$ for the drive piston structure, a stress T is applied on the underside of the piston where the cylinder(s) make contact. The resulting displacement at the center of the cylinder(s), Z_p , and the resulting swept volume of the piston structure, dV_{pis} are recorded. Similarly, to determine the compliance coefficients $\Xi_{Z_p}^P$ and $\Xi_{dV_{pis}}^P$, a pressure P is applied on the entire top surface of the piston. The resulting displacement at the center of the cylinder(s), Z_P , and the resulting swept volume of the piston structure, dV_{pis} are recorded. From these responses, the compliance coefficients are calculated.

Single Piezoelectric Cylinder Geometry

In performing finite-element analyses for this single cylinder geometry, the resulting piston compliance coefficients were found to be:

Loading	Z_p Compliance	dV_{de} Compliance
Stress	$\Xi_{Z_p}^T = 2.09e^{-13} \frac{m}{Pa}$	$\Xi_{dV_{pis}}^T = 2.42e^{-18} \frac{m^3}{Pa}$
Pressure	$\Xi_{Z_p}^P = 8.20e^{-13} \frac{m}{Pa}$	$\Xi_{dV_{pis}}^P = 1.08e^{-17} \frac{m^3}{Pa}$

Three Piezoelectric Cylinder Geometries

Finite-element analyses for the three cylinder geometry were performed, with R_{cp} varying from 1 mm to 2.25 mm. Figure 2.12 plots the compliance coefficients of the three-cylinder geometries as a function of R_{cp} . Taking as an example case, $R_{cp} = 2.25mm$, the compliance coefficients were found to be:

Loading	Z_p Compliance	dV_{de} Compliance
Stress	$\Xi_{Z_p}^T = 0.36e^{-13} \frac{m}{Pa}$	$\Xi_{dV_{pis}}^T = 0.94e^{-18} \frac{m^3}{Pa}$
Pressure	$\Xi_{Z_p}^P = 3.12e^{-13} \frac{m}{Pa}$	$\Xi_{dV_{pis}}^P = 1.08e^{-17} \frac{m^3}{Pa}$

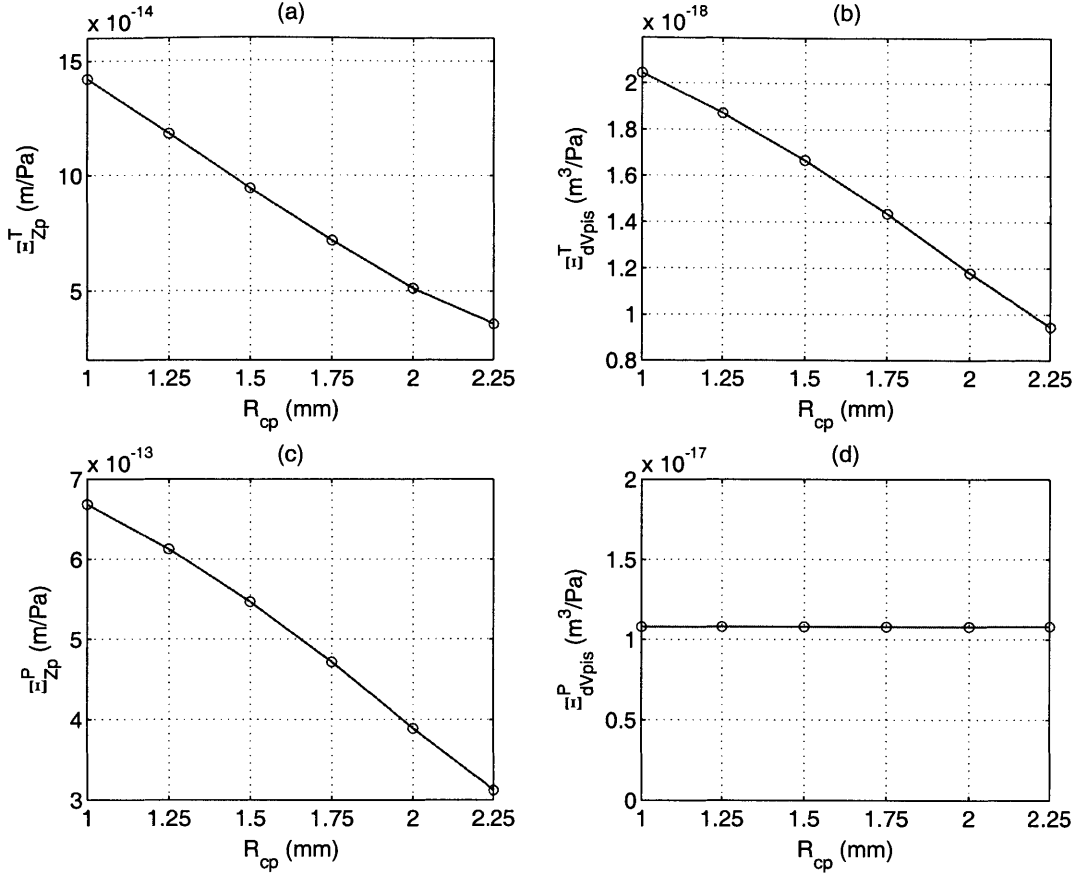


Figure 2.12: Compliance coefficients of the three cylinder piston geometry for varying R_{cp} : (a) $\Xi_{Z_p}^T$, (b) $\Xi_{dV_{pis}}^T$, (c) $\Xi_{Z_p}^P$, and (d) $\Xi_{dV_{pis}}^P$.

In comparing these results (for $R_{cp}=2.25$ mm) to those of the single cylinder geometry, it is observed that $\Xi_{Z_p}^T$ is reduced by 5.8x, $\Xi_{dV_{pis}}^T$ is reduced by 2.6x, and $\Xi_{Z_p}^P$ is reduced by 2.6x. Clearly, the use of three cylinders spread out beneath the piston is beneficial in reducing these coefficients, and therefore stiffening the structure. $\Xi_{dV_{pis}}^P$, however, remains the same. This is expected since the swept volume of the piston structure (with no cylinders present below) in response to an applied pressure on the piston top surface should be identical for the single and three cylinder geometries. These results demonstrate the stiffening benefits of incorporating three piezoelectric cylinders beneath the drive element piston rather than a single centrally-located one. With these types of finite-element models, one can obtain compliance coefficients for a particular three cylinder drive piston geometry and use these coefficients in the analytical equations developed in Section 2.3.2 to accurately model the valve structural behavior.

2.5.2 Finite-Element Analysis of Bottom Plate

To illustrate the stiffening benefit of using three piezoelectric cylinders above the bottom plate, a finite-element study comparing a single piezoelectric cylinder bottom plate geometry to geometries with three piezoelectric cylinders is presented. In this study, the chamber bottom plate geometry and material properties are assumed to be: $R_{te} = 3.2mm$, $t_{pis} = 1000\mu m$, $E_{Si} = 165GPa$, and $\nu_{Si} = 0.22$. For the single piezoelectric cylinder geometry, the cylinder radius is $R_p = 1mm$. For the three piezoelectric cylinder geometry, the radius of each cylinder is sized ($R_p = 0.577mm$) such that the total area of all three is identical to the area of the cylinder in the single piezoelectric cylinder case. Schematics of the single cylinder and three cylinder finite-element model geometries are shown in Figure 2.13. The piston structure is guided at its center ($r = 0$) and clamped at its outer radius ($r = R_{te}$).

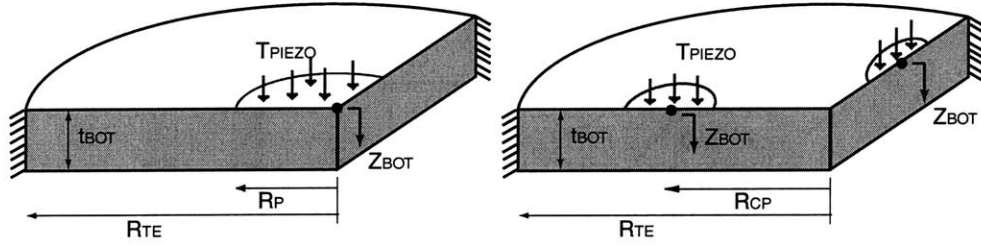


Figure 2.13: Finite-element (ANSYS) models of bottom plate structure with (a) a single centrally located cylinder above the bottom plate, and (b) a three cylinder design, with the cylinders spread out above the bottom plate.

To determine the compliance coefficient for the bottom plate structure $\Xi_{Z_{bot}}^T$, a pressure (stress) T is applied to the top surface of the plate where the cylinder(s) make contact. The resulting displacement at the center of the cylinder(s), Z_{bot} is recorded. From this response, the compliance coefficient is calculated.

Single Piezoelectric Cylinder Geometry

In performing the finite-element analysis for this single cylinder geometry, the resulting piston compliance coefficient was found to be:

Loading	Z_{bot} Compliance
Stress	$\Xi_{Z_{bot}}^T = 4.79e^{-14} \frac{m}{Pa}$

Three Piezoelectric Cylinder Geometries

Finite-element analyses for the three cylinder geometry were performed, with R_{cp} varying from 1 mm to 2.25 mm. Figure 2.14 plots the compliance coefficient $\Xi_{Z_{bot}}^T$ of the three-cylinder

geometry as a function of this varying R_{cp} . Taking as an example case, $R_{cp} = 2.25\text{mm}$, the compliance coefficient was found to be:

Loading	Z_{bot} Compliance
Stress	$\Xi_{Z_{bot}}^T = 0.98e^{-14} \frac{m}{Pa}$

In comparing this result (for $R_{cp}=2.25\text{ mm}$) to that of the single cylinder geometry, it is observed that $\Xi_{Z_p}^T$ is reduced by 4.9x. Clearly, the use of three cylinders spread out above the bottom plate is beneficial in reducing the amount by which the centers of the cylinders move downward into the plate. These results demonstrate the stiffening benefits of incorporating three piezoelectric cylinders above the bottom plate structure rather than a single centrally-located one. With this type of finite-element model, one can obtain the compliance coefficient for a particular three cylinder bottom plate geometry and use this coefficient in the analytical equations developed in Section 2.3.3 to accurately model the valve structural behavior.

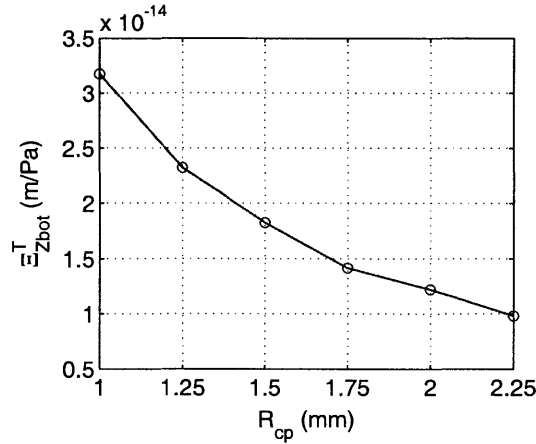


Figure 2.14: Compliance coefficient $\Xi_{Z_{bot}}^T$ of the three cylinder bottom plate geometry for varying R_{cp} .

2.6 Further Modeling Issues

The structural component that requires additional modeling focus is that of the valve cap and membrane. For the typical design space in the proposed active valve, this plate/membrane structure is designed to have a thickness of approximately $10\ \mu\text{m}$, yet experience deflections on this order or larger. In this deflection regime, the plate will begin to stretch, resulting in the generation of in-plane tensile stresses that are unaccounted for in the linear plate theory presented in this chapter. The drive element tethers also possess thicknesses near $10\ \mu\text{m}$, however, because the piston deflection during device operation is expected to be only 1-2 μm , these tethers can be accurately modeled by the linear relations detailed thus far.

2.7 Conclusions

This chapter has developed a linear, quasi-static structural model of the proposed active valve device, including piezoelectric material behavior, deformation of the drive element tethers and the valve cap/membrane structure, and the compliances associated with the drive element piston, bottom structural plate, top structural plate, and hydraulic fluid. In addition, the chapter has demonstrated, through the use of representative finite-element models, the benefits of incorporating multiple piezoelectric cylinders spread out beneath the drive element piston rather than a single centrally-located one. The following chapter will detail the development of numerical non-linear modeling tools for understanding the large deflection deformation behavior of the valve cap and membrane structure.

Bibliography

- [1] S. Timoshenko. *Theory of Plates and Shells*. McGraw-Hill Book Company, Inc., New York and London, 1940.

Chapter 3

Non-Linear Deformation of the Valve Cap and Membrane

This chapter presents the development of a numerical code for the non-linear large-deflection modeling of a thin annular plate structure with rigid central cap under pressure loading. This theory has been specifically developed to model the valve cap and membrane behavior in the proposed active valve device. The chapter begins within an introduction to the valve cap geometry under investigation and the associated nature of the geometric non-linearity. The theory behind this non-linear deformation is then presented, with detailed derivation of the governing equations used in the numerical integration. Representative loading plots for a given valve geometry are then presented to illustrate the numerical code's capability to capture in-plane tensile stresses and boundary layer phenomena. Lastly, three MatlabTM codes are presented that serve as non-linear modeling tools for use in Chapters 4, 5, and 8 of this thesis. The finite-differencing scheme presented in this chapter is based upon the work of Su [1].

3.1 Introduction

In general, the deflection of a structural plate can be represented using linear deformation theory only if the deflection of the plate is less than about half the thickness of the plate. In this small deflection regime, it can be assumed that the plate's neutral axis is unchanged in length as it deforms, ie: it experiences no tensile stress. The only stresses that exist in this plate are the compressive and tensile bending stresses above and below this neutral axis. In a plate experiencing large deflections (that is, deflections greater than half the thickness of the plate), however, the plate begins to stretch and the assumption of zero in-plane tensile stress at the neutral axis is no longer valid. As the plate is deformed more and more into the large deflection regime, the in-plane tensile stress begins to dominate the bending stresses, thereby

increasing the plate stiffness. This marks the onset of membrane behavior, characterized by the inability to withstand bending moments. For plates that experience loads that create this large deflection behavior, it is critical that this in-plane stress be modeled and that the plate stiffening effects be captured.

3.2 Plate Geometry

The plate geometry under consideration in this chapter is shown in Figure 3.1. The plate has outer radius, r_a , inner radius r_b , thickness t , a Young's Modulus E , and a poisson ratio ν . The plate is clamped at its outer radius and guided at its inner radius. The assumption of a guided boundary condition at r_b is a reasonable one since bending of the valve cap is negligible. The plate experiences a pressure loading p underneath the plate from r_b to r_a and a concentrated circumferential force f at r_b .

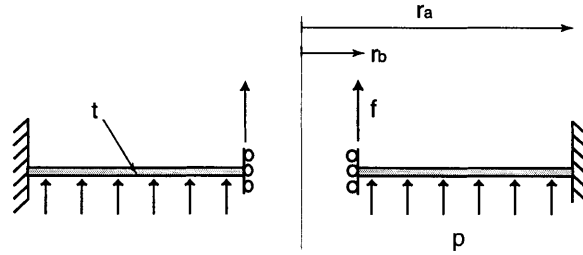


Figure 3.1: Schematic of an annular plate with a rigid central boss under pressure loading.

3.3 Theory

The work presented in this chapter is an extension of Sheplak and Dugundji's work on the large deflection behavior of clamped circular plates (without rigid central caps) [2]. Additionally, the finite-difference implementation contained within this chapter is the result of work done by Su [1].

3.3.1 Assumptions

This chapter follows von Karman plate theory, in which the vertical displacement of the plate w is assumed to be much larger than the lateral displacement u and v and the normals to the undeformed middle surface remain the normals to the deformed middle surface. As a result, the deformed shape of the thin plate can be fully described by the geometry of the neutral surface. In this analysis, only quadratic non-linear terms are retained.

3.3.2 Equilibrium Equations

The forces and moments experienced by a small section of the plate are shown in Figure 3.2, where M_r and M_θ are the radial and tangential moments respectively, N_r is the in-plane tension load per unit circumference, and Q_r is the shear force per unit circumference.

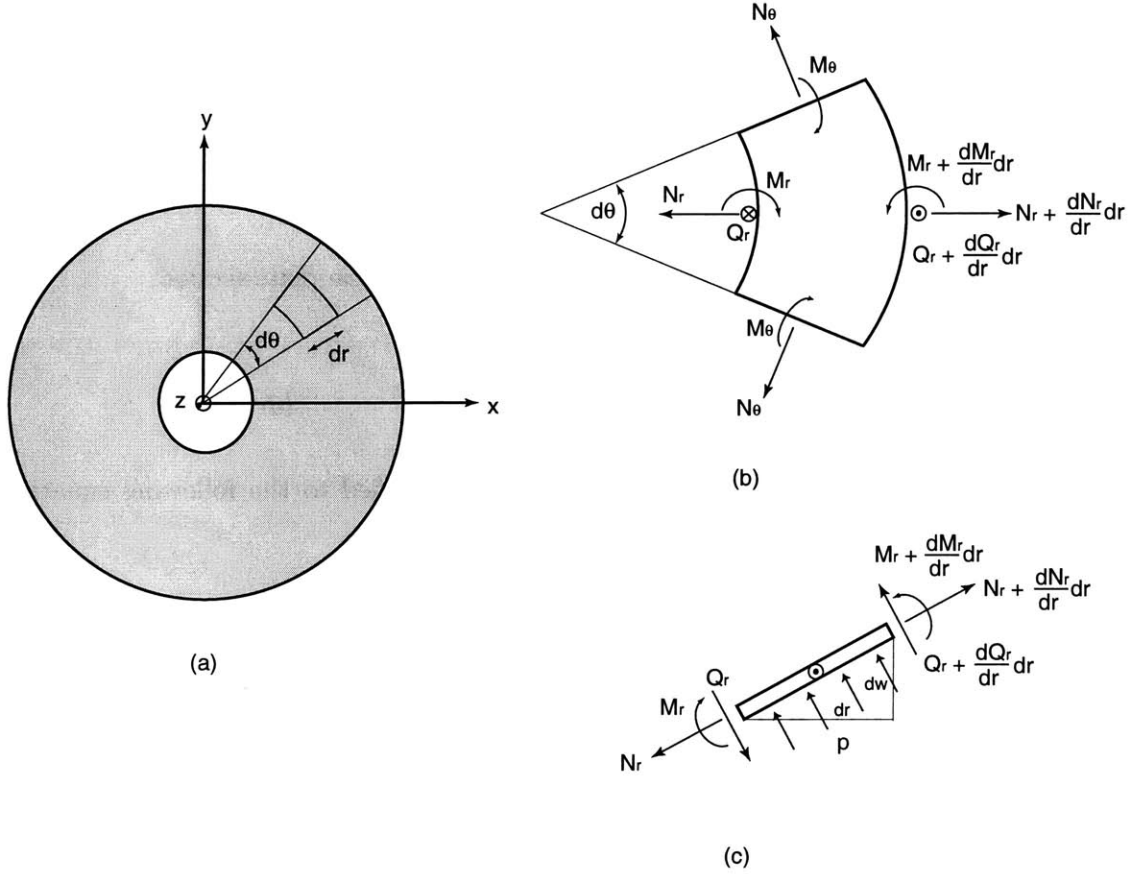


Figure 3.2: Force and moment free-body diagrams for an infinitesimal annular plate section: (a) top view of plate, (b) top view of plate section, (c) side-view of plate section.

To obtain the equilibrium equations for this plate, a radial force balance, a z-direction force balance, and a circumferential moment balance are performed.

The radial force balance produces the following initial relation,

$$\begin{aligned} \sum F_r \rightarrow & (N_r + \frac{dN_r}{dr} dr)(\cos \frac{dw}{dr})(r + dr)d\theta - N_r(\cos \frac{dw}{dr})rd\theta - 2N_\theta(\sin \frac{d\theta}{2})dr - \\ & (Q_r + \frac{dQ_r}{dr} dr)(\sin \frac{dw}{dr})(r + dr)d\theta + Q_r(\sin \frac{dw}{dr})rd\theta - p(\sin \frac{dw}{dr})rdrd\theta = 0. \end{aligned} \quad (3.1)$$

The z-direction force balance produces the following initial relation,

$$\begin{aligned} \sum F_z \rightarrow & (N_r + \frac{dN_r}{dr}dr)(\sin \frac{dw}{dr})(r + dr)d\theta - N_r(\sin \frac{dw}{dr})rd\theta + \\ & (Q_r + \frac{dQ_r}{dr}dr)(\cos \frac{dw}{dr})(r + dr)d\theta - Q_r(\cos \frac{dw}{dr})rd\theta + p(\cos \frac{dw}{dr})rdrd\theta = 0. \end{aligned} \quad (3.2)$$

The circumferential moment balance produces the following initial relation,

$$\sum M_r \rightarrow (M_r + \frac{dM_r}{dr}dr)(r + dr)d\theta - M_r r d\theta + (Q_r + \frac{dQ_r}{dr}dr)(r + dr)(r + dr)d\theta - Q_r r^2 d\theta = 0. \quad (3.3)$$

Using the following simplifying relations which hold true for the plate section,

$$\cos \frac{dw}{dr} \sim 1 \quad , \quad \sin \frac{dw}{dr} \sim \frac{dw}{dr} \quad , \quad \sin \frac{d\theta}{2} \sim \frac{d\theta}{2} \quad , \quad (dr)^2 \ll dr$$

the force and moment equilibrium balances can be simplified to the following equations respectively,

$$N_r - N_\theta + r \left(\frac{dN_r}{dr} \right) = 0, \quad (3.4)$$

$$\frac{d}{dr} \left(N_r r \frac{dw}{dr} \right) + \frac{d}{dr} (Q_r r) + pr = 0, \quad (3.5)$$

and

$$Q_r + \frac{dM_r}{dr} + \left(\frac{M_r - M_\theta}{r} \right) = 0. \quad (3.6)$$

3.3.3 Geometric Compatibilities

The radial elongation of the neutral axis during deformation can be represented by the following strain displacement relation [3],

$$\epsilon_r = \frac{du}{dr} + \frac{1}{2} \left[\left(\frac{du}{dr} \right)^2 + \left(\frac{dw}{dr} \right)^2 \right]. \quad (3.7)$$

Based on the assumption that $u \ll w$, it follows that the term $\left(\frac{du}{dr} \right)^2$ is negligible compared to the term $\left(\frac{dw}{dr} \right)^2$. Therefore, the radial strain displacement relation can be simplified to

$$\epsilon_r = \frac{du}{dr} + \frac{1}{2} \left(\frac{dw}{dr} \right)^2. \quad (3.8)$$

The circumferential strain-displacement relationship is

$$\epsilon_\theta = \frac{u}{r}. \quad (3.9)$$

The first and second principle curvatures for the plate are [3]

$$\kappa_r = -\frac{d^2w}{dr^2} \quad , \quad \kappa_\theta = -\frac{1}{r} \frac{dw}{dr}. \quad (3.10)$$

3.3.4 Constitutive Laws

Assuming that the plate experiences plane stress, ie: no variations in stress occur through the thickness of the plate, the material Hooke's Law can be written as

$$\epsilon_r = \frac{1}{E} \left(\frac{N_r}{t} - \nu \frac{N_\theta}{t} \right) \quad , \quad \epsilon_\theta = \frac{1}{E} \left(\frac{N_\theta}{t} - \nu \frac{N_r}{t} \right) \quad (3.11)$$

where E and ν are the material Young's Modulus and Poisson Ratio respectively. Moment equilibrium in the plate yields

$$M_r = -D(\kappa_r + \nu\kappa_\theta) \quad , \quad M_\theta = -D(\kappa_\theta + \nu\kappa_r) \quad (3.12)$$

where D is the plate flexural rigidity, defined by

$$D = \frac{Eh^3}{12(1 - \nu^2)}. \quad (3.13)$$

3.3.5 Governing Equations

Beginning with the three equilibrium equations (5.9), (5.10), and (3.6), the governing differential equations for the plate can be derived. Integrating (5.10) with respect to r from r_b to r yields

$$(Q_r r - Q_{r_b} r_b) + \left(N_r \frac{dw}{dr} - N_{r_b} \left(\frac{dw}{dr} \right)_{r_b} \right) + \frac{1}{2} p(r^2 - r_b^2) = 0 \quad (3.14)$$

Since the shear force at r_b is $Q_{r_b} = \frac{-f}{2\pi r_b}$ and since $(\frac{dw}{dr})_{r_b} = 0$, it follows that

$$Q_r + N_r \frac{dw}{dr} + \frac{f}{2\pi r} + \frac{p(r^2 - r_b^2)}{2r} = 0. \quad (3.15)$$

Substituting the moment-curvature relations (3.12) into (3.6) gives

$$Q_r + D \left(\frac{d^3w}{dr^3} + \frac{1}{r} \frac{d^2w}{dr^2} - \frac{1}{r^2} \frac{dw}{dr} \right) = 0. \quad (3.16)$$

Combining (3.16) with (3.15) produces

$$\frac{d^3w}{dr^3} + \frac{1}{r} \frac{d^2w}{dr^2} - \frac{1}{r^2} \frac{dw}{dr} - \frac{N_r}{D} \frac{dw}{dr} = \frac{f}{2\pi r D} + \frac{p(r^2 - r_b^2)}{2rD}. \quad (3.17)$$

Rewriting the strain-displacement relations (3.8) and (3.9) in the following manner,

$$r \frac{d\epsilon_r}{dr} + \epsilon_\theta - \epsilon_r + \frac{1}{2} \left(\frac{dw}{dr} \right)^2 = 0, \quad (3.18)$$

and substituting the material Hooke's Law relations (3.11) into (3.18) produces

$$\frac{dN_\theta}{dr} - \left(\frac{N_r - N_\theta}{r} \right) + \frac{Eh}{2r} \left(\frac{dw}{dr} \right)^2 = 0. \quad (3.19)$$

Equations (5.9), (3.17), and (3.19), therefore form a set of three non-linear differential equations in the three unknowns N_r , N_θ , and w . The boundary conditions corresponding to these equations can be written as follows:

$$\text{at } r = r_b : \quad u = r\epsilon_\theta = 0 \rightarrow N_\theta - \nu N_r = 0, \quad \frac{dw}{dr} = 0 \quad (3.20)$$

$$\text{at } r = r_a : \quad u = r\epsilon_\theta = 0 \rightarrow N_\theta - \nu N_r = 0, \quad \frac{dw}{dr} = 0 \quad (3.21)$$

It is interesting to note at this point that these equations are non-linear because of the term $\frac{N_r}{D} \frac{dw}{dr}$ in (3.17). If the plate were deforming only in the linear regime, the term $N_r = 0$, and therefore the three governing differential equations would condense into the following single linear equation,

$$\frac{d^3w}{dr^3} + \frac{1}{r} \frac{d^2w}{dr^2} - \frac{1}{r^2} \frac{dw}{dr} = \frac{f}{2\pi r D} + \frac{p(r^2 - r_b^2)}{2rD} \quad (3.22)$$

which could be integrated three times to obtain a solution for $w(r)$, as was detailed in Chapter 2 of this thesis.

3.3.6 In-Plane Prestress

As often is the case with micromachined thin plate structures, residual tensile stresses in the plate can exist prior to transverse loading. These initial in-plane loads serve to pretension the plate and can significantly affect the resulting deformation behavior. The complete loading parameters, N_r and N_θ , can therefore be decomposed into initial in-plane prestressing components N_{r0} and $N_{\theta0}$, and into components due to the transverse pressure loading \tilde{N}_r and \tilde{N}_θ , as

follows:

$$N_r = N_{r_o} + \tilde{N}_r \quad (3.23)$$

$$N_\theta = N_{\theta_o} + \tilde{N}_\theta. \quad (3.24)$$

These parameters, \tilde{N}_r and \tilde{N}_θ , can be thought of as incremental changes in N_r and N_θ due to the application of the transverse loading on top of the already prestressed plate.

Derivation of N_{r_o} and N_{θ_o}

It is desired to obtain expressions for the in-plane prestress that results from a uniform tension load $N_r = N_o$ applied at $r = r_a$ with zero displacement $u = 0$ at $r = r_b$. Since $p = 0$ and $w(r)$ and its derivatives with respect to r are zero, only (5.9) of the three governing equations remains. The strain-displacement relations (3.8) and (3.9) can be simplified to:

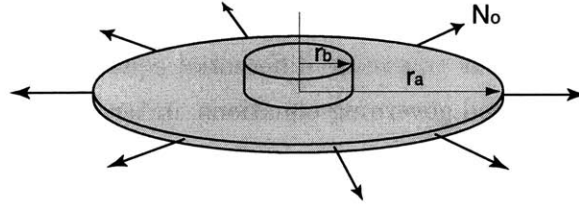


Figure 3.3: Schematic of an annular plate with a rigid central boss under pretension. Loading N_o is applied radially outward at $r = r_a$

$$\epsilon_r = \frac{du}{dr} \quad , \quad \epsilon_\theta = \frac{u}{r}. \quad (3.25)$$

Substituting (3.25) into (3.11) and rearranging for N_r and N_θ produces

$$N_r = \left(\frac{Et}{1-\nu^2} \right) \left(\frac{du}{dr} + \frac{\nu u}{r} \right) \quad , \quad N_\theta = \left(\frac{Et}{1-\nu^2} \right) \left(\nu \frac{du}{dr} + \frac{u}{r} \right). \quad (3.26)$$

Inserting (3.26) into (5.9) results in a solution for $u(r)$:

$$u(r) = \frac{N_o}{\left(\frac{Et}{1-\nu^2} \right) \left[(1+\nu) + \left(\frac{r_b}{r_a} \right)^2 (1-\nu) \right]} \left[r - \frac{r_b^2}{r} \right]. \quad (3.27)$$

Inserting this relation for $u(r)$ back into (3.26) yields the following expressions for the initial in-plane tensile loads:

$$N_{ro} = \left(\frac{N_o}{1 + \beta^2} \right) \left[1 + \beta^2 \left(\frac{r_a}{r} \right)^2 \right] \quad (3.28)$$

and

$$N_{\theta o} = \left(\frac{N_o}{1 + \beta^2} \right) \left[1 - \beta^2 \left(\frac{r_a}{r} \right)^2 \right] \quad (3.29)$$

where

$$\beta = \left(\frac{r_b}{r_a} \right) \sqrt{\frac{1 - \nu}{1 + \nu}}. \quad (3.30)$$

It is interesting to observe here that these in-plane tensile loads vary with r , unlike the in-plane tensile loads for a circular plate with no rigid central boss, which do not vary with r ,

$$N_{ro} = N_{\theta o} = \frac{N_o(1 - \nu)^2}{Et}. \quad (3.31)$$

Governing Equations for Complete Loading

Having found expressions for the initial prestressing in-plane loads, (5.2) and (3.29) can be substituted into the three previous governing differential equations (5.9), (3.17), and 3.19) to produce the following three refined governing equations, in terms of \tilde{N}_r , \tilde{N}_θ , and N_o ,

$$\frac{d\tilde{N}_r}{dr} + \frac{\tilde{N}_r - \tilde{N}_\theta}{r} = 0, \quad (3.32)$$

$$\frac{d^3 w}{dr^3} + \frac{1}{r} \frac{d^2 w}{dr^2} - \left(\frac{\beta^2 r_a^2 N_o}{D(1 + \beta^2)} + 1 \right) \frac{dw}{dr} - \left(\frac{\tilde{N}_r}{D} + \frac{N_o}{D(1 + \beta^2)} \right) \frac{dw}{dr} = \frac{f}{2\pi r D} + \frac{p(r^2 - r_b^2)}{2r D}, \quad (3.33)$$

and

$$\frac{d\tilde{N}_r}{dr} - \left(\frac{\tilde{N}_r - \tilde{N}_\theta}{r} \right) + \frac{Et}{2r} \left(\frac{dw}{dr} \right)^2 = 0. \quad (3.34)$$

3.3.7 Non-Dimensionalized Governing Equations

In order to generalize these equations for ease of use, the non-dimensionalization procedure of Sheplak and Dugundji is followed, with the subsequent non-dimensional parameters being defined,

$$\begin{aligned} \xi &= \frac{r}{r_a} & (') &= \frac{d}{d\xi} & W &= \frac{w}{t} & U &= \frac{u}{h} \\ \theta &= \frac{dW}{d\xi} = \frac{r_a}{t} \frac{dw}{dr} & \Psi &= \frac{d\theta}{d\xi} = \frac{r_a^2}{t} \frac{d^2 w}{dr^2} \end{aligned}$$

$$S_r = \frac{\tilde{N}_r r_a^2}{Et^3} \quad S_\theta = \frac{\tilde{N}_\theta r_a^2}{Et^3}. \quad (3.35)$$

The governing equations (3.32), (3.33), and (3.34) can therefore be reexpressed in non-dimensional form as

$$S_r' + \frac{S_r - S_\theta}{\xi} = 0, \quad (3.36)$$

$$\theta'' + \frac{\theta'}{\xi} - \left(k^2 + \frac{s^2 + 1}{\xi^2} \right) \theta - 12(1 - \nu^2) S_r \theta = 6(1 - \nu^2) \left(P\xi - \frac{P}{\xi} \left(\frac{r_b}{r_a} \right)^2 + \frac{F}{\xi} \right), \quad (3.37)$$

and

$$S_\theta' - \left(\frac{S_r - S_\theta}{\xi} \right) = -\frac{1}{2\xi} \theta^2 \quad (3.38)$$

where

$$k = \left(\frac{r_a}{t} \right) \sqrt{\frac{12(1 - \nu^2) N_o}{Et(1 + \beta^2)}} \quad , \quad s = \beta k \quad , \quad P = \frac{pr_a^4}{Et^4}, \quad F = \frac{fr_a^2}{\pi Et^4}. \quad (3.39)$$

The parameters k and s are dimensionless pretension parameters and P is a dimensionless transverse loading parameter. The boundary conditions can be written as

$$\text{at } \xi = \xi_b = \frac{r_b}{r_a} : \quad S_\theta - \nu S_r = 0 \quad , \quad \theta = 0 \quad (3.40)$$

$$\text{at } \xi = \xi_a = 1 : \quad S_\theta - \nu S_r = 0 \quad , \quad \theta = 0. \quad (3.41)$$

For use in the numerical finite-difference code to be discussed in the next section, (3.36), (3.37), and (3.38) can be simplified to two non-dimensional governing equations in the variables S_r and θ by substituting (3.36) into (3.38) to eliminate S_θ . Therefore, the following set of equations is ready for finite-difference implementation:

$$\xi^2 S_r'' + 3\xi S_r' = -\frac{\theta^2}{2} \quad (3.42)$$

$$\xi^2 \theta'' + \xi \theta' - [(s^2 + 1) + \xi^2(k^2 + 12(1 - \nu^2) S_r)] \theta = 6(1 - \nu^2) \left(P\xi^3 - P\xi \left(\frac{r_b}{r_a} \right)^2 + F\xi \right) \quad (3.43)$$

where

$$k = \left(\frac{r_a}{t}\right) \sqrt{\frac{12(1-\nu^2)N_o}{Et(1+\beta^2)}} \quad s = \beta k \quad P = \frac{pr_a^4}{Et^4} \quad F = \frac{fr_a^2}{\pi Et^4} \quad (3.44)$$

Boundary Conditions:

$$\text{at } \xi = \xi_b : \quad \xi S'_r + (1-\nu)S_r = 0 \quad , \quad \theta = 0 \quad (3.45)$$

$$\text{at } \xi = \xi_a : \quad \xi S'_r + (1-\nu)S_r = 0 \quad , \quad \theta = 0 \quad (3.46)$$

Post-Equation:

$$S_\theta = \xi S'_r + S_r. \quad (3.47)$$

3.3.8 Finite-Difference Implementation

The non-linear dimensionless governing differential equations (3.42) and (3.43) can not be solved directly due to the presence of the non-linear term $S_r\theta$ in (3.43). As a result, they must be numerically solved. This section details the implementation of a finite-difference scheme to accomplish this goal. Sheplak and Dugundji's work on the non-linear deflection of clamped circular plates highlights the importance of a boundary layer region near the plate's clamped outer radius. For large deflections, it is within this region that a transition from membrane behavior to plate bending behavior occurs. To accurately model this region, Sheplak and Dugundji introduced a coordinate transformation that clusters a higher density of finite-difference grid points in this region than in the central regions of the plate.

In the case of an annular plate with clamped outer radius and guided inner radius (corresponding to a rigid central cap), a similar procedure can be carried out. However, in this situation, it is necessary to introduce a more detailed coordinate transformation that clusters grid points at both $r = r_a$ and $r = r_b$ so that the two corresponding boundary layer regions can be accurately resolved. Letting $\xi_c = \frac{1}{2}(\xi_b + \xi_a)$ and defining η to be a set of equally spaced grid points between 0 and 1, a proposed coordinate transformation is:

$$\text{for } 0 \leq \eta \leq 0.5 : \quad \xi = \xi_b + (\alpha - 1)(\xi_c - \xi_b) \left(\frac{\phi - \phi^{1-2\eta}}{1 + \phi^{1-2\eta}} \right) \quad (3.48)$$

$$\text{for } 0.5 < \eta \leq 1 : \quad \xi = \xi_a + (\alpha - 1)(\xi_c - \xi_a) \left(\frac{\phi - \phi^{2\eta-1}}{1 + \phi^{1-2\eta}} \right) \quad (3.49)$$

where α is a coordinate stretching parameter varying between 1 and ∞ and $\phi = \left[\frac{\alpha+1}{\alpha-1}\right]$.

The closer α is to 1, the higher the mesh density near $r = r_b$ and $r = r_a$ in the coordinate transformation.

An example of this coordinate transformation is illustrated in Figure 3.4, for the case of $\xi_b = 0.1$ and for 20 grid points existing between ξ_b and ξ_a . In Plot 3.4(a), a value of $\alpha = 10$ results in an evenly spaced finite-difference grid mesh between the inner and outer dimensionless boundary of the plate. As α approaches 1 in Plots 3.4(c) and 3.4(d), an increase in the mesh density begins to appear near the boundaries. For the numerical code implemented in this thesis, values of α between 1.01 and 1.05 and number of grid points between 100 and 200 were commonly employed.

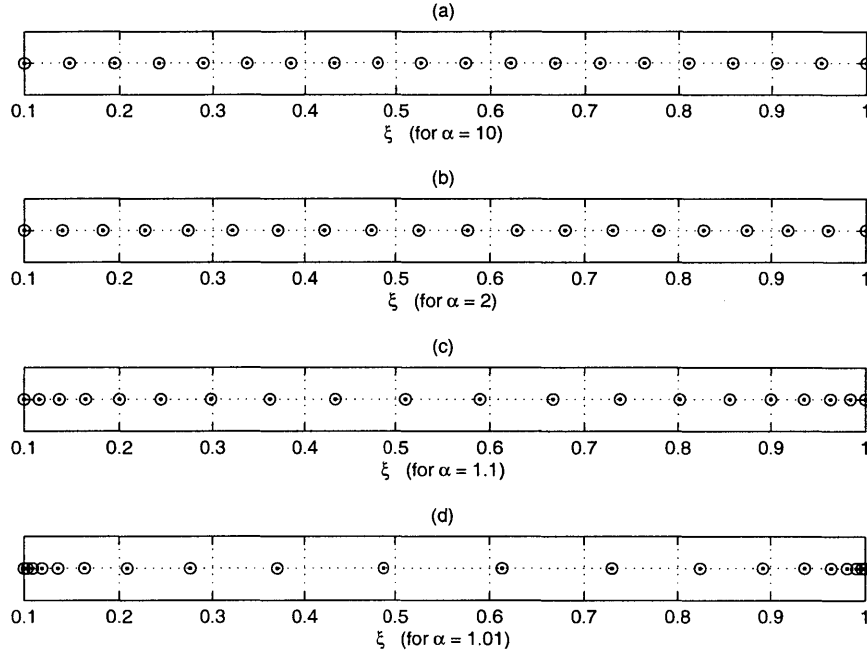


Figure 3.4: Coordinate transformation grid point locations for differing values of α .

Having defined these coordinate transformations, it is required to derive equations for η , $\frac{d\eta}{d\xi}$, and $\frac{d^2\eta}{d\xi^2}$ as functions of ξ for use in the final coordinate transformation governing differential equations to be presented on the following pages. Rearranging (3.48) and (3.49) and taking derivatives with respect to ξ produces the following relations:

For $\xi_b \leq \xi \leq \xi_c$:

$$\eta = \frac{1}{2} \left(1 - \left(\frac{1}{\ln \phi} \right) \ln \left(\frac{m\phi - (\xi - \xi_b)}{m + (\xi - \xi_b)} \right) \right) \quad (3.50)$$

$$\frac{d\eta}{d\xi} = \frac{1}{2 \ln \phi} \left(\frac{m(1 + \phi)}{(m\phi - (\xi - \xi_b))(m + (\xi - \xi_b))} \right) \quad (3.51)$$

$$\frac{d^2\eta}{d\xi^2} = \frac{-1}{2 \ln \phi} \left(\frac{m(1+\phi)(n-2\xi)}{[(m\phi - (\xi - \xi_b))(m + (\xi - \xi_b))]^2} \right) \quad (3.52)$$

$$\text{where} \quad m = (\alpha - 1)(\xi_c - \xi_b) \quad (3.53)$$

$$\text{where} \quad n = m\phi - m + 2\xi_b.$$

For $\xi_c \leq \xi \leq \xi_a$:

$$\eta = \frac{1}{2} \left(1 + \left(\frac{1}{\ln \phi} \right) \ln \left(\frac{m\phi - (\xi - \xi_a)}{m + (\xi - \xi_a)} \right) \right) \quad (3.54)$$

$$\frac{d\eta}{d\xi} = \frac{-1}{2 \ln \phi} \left(\frac{m(1+\phi)}{(m\phi - (\xi - \xi_a))(m + (\xi - \xi_a))} \right) \quad (3.55)$$

$$\frac{d^2\eta}{d\xi^2} = \frac{1}{2 \ln \phi} \left(\frac{m(1+\phi)(n-2\xi)}{[(m\phi - (\xi - \xi_a))(m + (\xi - \xi_a))]^2} \right) \quad (3.56)$$

$$\text{where} \quad m = (\alpha - 1)(\xi_c - \xi_a) \quad (3.57)$$

$$\text{where} \quad n = m\phi - m + 2\xi_a.$$

Incorporating these coordinate transformations into the set of Equations (3.42) - (3.47), the transformed set of equations can be written as

$$\xi^2(\eta) \left(\frac{d\eta}{d\xi} \right)^2 \frac{d^2 S_r(\eta)}{d\eta^2} + \left(\xi^2(\eta) \frac{d^2\eta}{d\xi^2} + 3\xi(\eta) \frac{d\eta}{d\xi} \right) \frac{dS_r(\eta)}{d\eta} = -\frac{\theta^2(\eta)}{2} \quad (3.58)$$

$$\begin{aligned} \xi^2(\eta) \left(\frac{d\eta}{d\xi} \right)^2 \frac{d^2\theta(\eta)}{d\eta^2} + \left(\xi^2(\eta) \frac{d^2\eta}{d\xi^2} + \xi(\eta) \frac{d\eta}{d\xi} \right) \frac{d\theta(\eta)}{d\eta} - [(s^2 + 1) + \xi^2(\eta)(k^2 + 12(1 - \nu^2)S_r(\eta))] \theta(\eta) \\ = 6(1 - \nu^2) \left(P\xi^3(\eta) - P\xi(\eta) \left(\frac{r_b}{r_a} \right)^2 + F\xi(\eta) \right) \end{aligned} \quad (3.59)$$

Boundary Conditions:

$$\text{at } \eta = 0 : \quad \xi \left(\frac{d\eta}{d\xi} \right) \left(\frac{dS_r}{d\eta} \right) + (1 - \nu)S_r(\eta) = 0 \quad , \quad \theta(\eta) = 0 \quad (3.60)$$

$$\text{at } \eta = 1 : \quad \xi \left(\frac{d\eta}{d\xi} \right) \left(\frac{dS_r}{d\eta} \right) + (1 - \nu)S_r(\eta) = 0 \quad , \quad \theta(\eta) = 0 \quad (3.61)$$

Post-Equation:

$$S_\theta(\eta) = \xi(\eta) \left(\frac{d\eta}{d\xi} \right) \frac{dS_r(\eta)}{d\eta} + S_r(\eta). \quad (3.62)$$

These equations are solved using a 2nd-order central finite difference scheme for the interior grid points, a 2nd-order forward difference scheme for the grid point corresponding to the boundary condition at the inner radius, and a 2nd-order backward difference scheme for the grid point corresponding to the boundary condition at the outer radius. These equations are cast into two matrix relations as follows:

$$[A]\theta = C \quad (3.63)$$

$$[B]S_r = -\frac{1}{2}\theta^2. \quad (3.64)$$

An initial guess for θ is taken based on the solution to the linear problem. Based on this θ , S_r is determined and the nonlinear term $12(1 - \nu^2)\xi^2(\eta)S_r$ is calculated. Having incorporated this nonlinear term into $[A]$, the new solution for θ is determined. The error between the previous θ and the newly obtained θ is calculated. If this error is sufficiently small, then the procedure is complete and the solution vector θ has been found. If the error is too large, an under relaxation technique is used to produce a new θ guess and the procedure is repeated. This iteration scheme continues until θ converges to a sufficiently accurate result.

3.3.9 Post-Processing Calculations

Once the non-linear solution procedure has been completed and S_r , S_θ , and θ have been found, it is desired to obtain the deflection w of the plate, the curvature $\frac{d^2w}{dr^2}$ of the plate, and the stresses σ_r and σ_θ within the plate. These calculations are described in the following sections.

Calculation of w

As detailed in (3.35), $\theta = \frac{dW}{d\xi} = \frac{r_a}{t} \frac{dw}{dr}$. To calculate w , finite differences are implemented to express θ in terms of W ,

$$\theta = [W_{matrix}]W. \quad (3.65)$$

Then, since the vector θ is known, this relation is rearranged to solve for W ,

$$W = [W_{matrix}]^{-1}\theta. \quad (3.66)$$

Finally, the dimensional vector w is calculated,

$$w = Wt. \quad (3.67)$$

Calculation of $\frac{d^2w}{dr^2}$

The non-dimensional plate curvature Ψ is calculated, according to (3.35), using 2nd-order finite difference schemes,

$$\Psi = \frac{d\theta}{d\xi}. \quad (3.68)$$

The dimensional plate curvature is then calculated,

$$\frac{d^2w}{dr^2} = \Psi \frac{t}{r_a^2}. \quad (3.69)$$

Calculation of σ_r and σ_θ

In general, the dimensional plate stresses can be expressed as

$$\sigma_r = \frac{Et^2}{r_a^2} (S_{r_o} + S_r + S_{r,bending}) \quad (3.70)$$

$$\sigma_\theta = \frac{Et^2}{r_a^2} (S_{\theta_o} + S_\theta + S_{\theta,bending}) \quad (3.71)$$

where S_{r_o} and S_{θ_o} are the dimensionless initial in-plane stresses prior to plate transverse loading, S_r and S_θ are the dimensionless in-plane stresses created during plate deflection, and $S_{r,bending}$ and $S_{\theta,bending}$ are the dimensionless bending stresses created during plate deflection. Each of these contributions is considered as follows.

S_{r_o} and S_{θ_o} Combining (5.2), (3.29), and (3.35), the dimensional initial in-plane stresses are found to be

$$S_{r_o} = S_{\theta_o} = \left(\frac{k^2}{12(1-\nu^2)} \right) \left[1 + \beta^2 \left(\frac{r_a}{r} \right)^2 \right]. \quad (3.72)$$

S_r and S_θ These are the results directly from the numerical code.

$S_{r,bending}$ and $S_{\theta,bending}$ For plate bending, the radial and tangential strains are functions of the distance from the neutral axis [3],

$$\epsilon_{r,bending} = -z \frac{d^2w}{dr^2} \quad , \quad \epsilon_{\theta,bending} = -\frac{z}{r} \frac{dw}{dr}. \quad (3.73)$$

According to (3.11),

$$\epsilon_r = \frac{1}{E}(\sigma_r - \nu\sigma_\theta) \quad , \quad \epsilon_\theta = \frac{1}{E}(\sigma_\theta - \nu\sigma_r). \quad (3.74)$$

Substituting (3.73) into (3.74) and rearranging in terms of σ_r and σ_θ , then incorporating (3.35) yields,

$$S_{r,bending} = S_{r,bending}(z) = \frac{-z}{(1-\nu^2)t} \left(\Psi + \frac{\nu\theta}{\xi} \right) \quad (3.75)$$

$$S_{\theta,bending} = S_{\theta,bending}(z) = \frac{-z}{(1-\nu^2)t} \left(\frac{\theta}{\xi} + \nu\Psi \right). \quad (3.76)$$

Therefore, the dimensional plate stresses σ_r and σ_θ can be assembled from these three stress contributions.

3.4 Results of Numerical Code

This section presents results to illustrate the capability of the numerical code to capture the non-linear large deflection behavior of a thin annular plate with a rigid central cap. As an example, consider a silicon plate with $r_b = 400\mu m$, $r_a = 800\mu m$, $t_{vm} = 7\mu m$, $E_{si} = 165GPa$, and $\nu = 0.22$. This structure is shown in Figure 3.5. The following subsections use this plate geometry under varying loads to show important non-linear phenomena. Sections 3.4.1 and 3.4.2 highlight the differences between linear and non-linear deflection theory for two distinct loading scenarios. Section 3.4.3 focuses on the presence of thin boundary layer regions near the clamped boundaries and the change in these regions as the plate is deflected more and more into the large deflection regime. And Section 3.4.4 discusses the effect that initial in-plane tension can have on the plate deflection behavior.

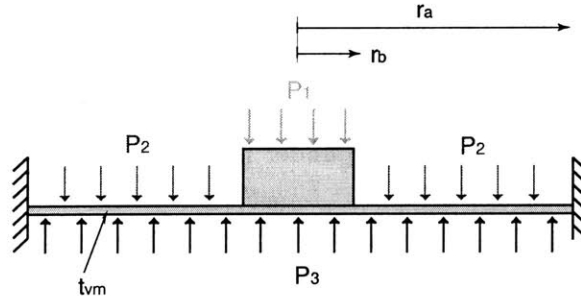


Figure 3.5: Schematic of an annular plate with a rigid central boss under pressure loading P_1 , P_2 , and P_3 .

3.4.1 Loading: $P_1 = P_2 = 0$, $P_3 = 100kPa$, $N_o = 0$

Figure 3.6 displays the linear and non-linear plate behavior for loading of $P_1 = P_2 = 0kPa$ and $P_3 = 100kPa$ and zero initial in-plane tension. From plot(a), it is clear that the deflection ($= 11.5\mu m$) calculated using the numerical code is significantly less than that ($= 31.5\mu m$) predicted by linear theory. Thin plate structures, such as the one under consideration, experience significant in-plane stresses as the deflections grow larger than the plate thickness. It is evident that this non-linear code captures this behavior. Shown in plots (b) and (c) are the dimensional linear and non-linear plate slopes ($\frac{dw}{dr}$) and curvatures ($\frac{d^2w}{dr^2}$). Note the boundary condition enforcement of zero slope at r_b and r_a . Plot (d) illustrates the stress σ_r at the top and bottom plate surfaces predicted by the non-linear code. In this case, the peak tensile stress in the plate is $0.45GPa$ and occurs on the underside of the plate at r_a .

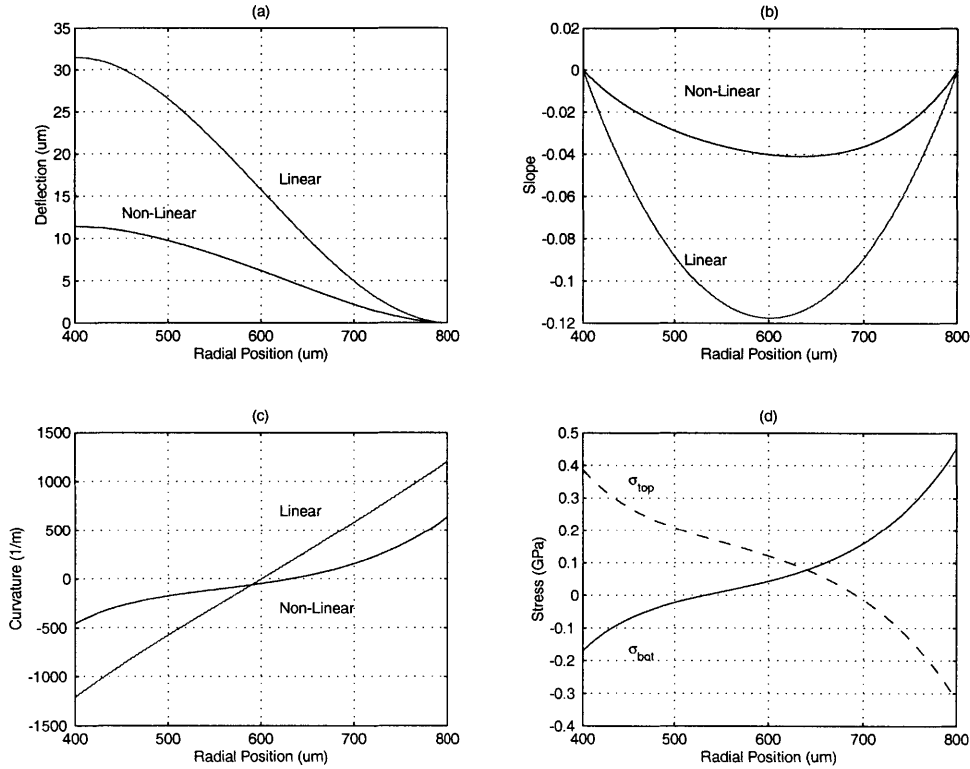


Figure 3.6: Deflection of thin annular plate under loading $P_1 = P_2 = 0$, $P_3 = 100kPa$. Plate dimensions and properties: $r_b = 400\mu m$, $r_a = 800\mu m$, $t = 7\mu m$, $E_{si} = 165GPa$, and $\nu = 0.22$.

3.4.2 Loading: $P_1 = 2.90MPa$, $P_2 = 0$, $P_3 = 1.30MPa$, $N_o = 0$

Figure 3.7 displays the linear and non-linear plate behavior for loading of $P_1 = 2.90MPa$, $P_2 = 0MPa$ and $P_3 = 1.30MPa$, and zero initial in-plane tension loading. These pressure

loadings were chosen to illustrate the difference between linear and non-linear theory even when the valve cap deflection predicted in both cases is identical. From plot(a), it is clear that the inner radius deflection predicted by both the linear and non-linear code is identical ($= 0.7\mu m$). However, the deflection behavior of the interior sections of the plate are quite different, due to the stiffening effect of the plate, which is accurately captured by the non-linear code. Linear theory predicts a peak plate deflection near $18\mu m$ whereas non-linear theory predicts a plate deflection near $9\mu m$. Shown in plots (b) and (c) are the dimensional linear and non-linear plate slopes ($\frac{dw}{dr}$) and curvatures ($\frac{d^2w}{dr^2}$). Again, note the boundary condition enforcement of zero slope at r_b and r_a . Also, note the presence of near constant curvature toward the central portions of the plate for the non-linear theory. This is due to the fact that the structure is behaving more like a membrane than a plate in these sections. At values of r closer to the boundaries at r_b and r_a , the curvature changes significantly. It is in these boundary layer regions that the bending stresses become greater than the in-plane tensile stresses, and the structure transitions back to plate behavior. Plot (d) further illustrates this point. The total stress σ_r at the top and bottom plate surfaces remain almost constant in these central membrane sections, however they increase sharply toward the boundaries. It is here that the bending stresses dominate. In this case, the peak tensile stress in the plate is approximately $1.80GPa$ and occurs on the bottom of the plate at r_b . In this loading situation, although, the inner radius deflection is predicted to be the same by the linear and non-linear code, the deflection of the interior portions of the plate are quite different. When analyzing the active valve behavior, the volume swept under the membrane would be overestimated if linear theory were to be used.

3.4.3 Loading: $P_1 = P_2 = 0$, Varying P_3 , $N_o = 0$

To understand the concept of increasing plate stiffness and the presence of thin boundary layers regions near r_b and r_a as the plate is pushed further into the large deflection regime, the plate is subjected to varying pressure P_3 beneath the membrane and cap and no other loading. Figure 3.8(a) illustrates the cap deflection at $r = r_b$ for increasing applied pressure P_3 from 0 to 10 MPa. A non-linear pressure-deflection curve is evident. As the plate experiences larger deflections, higher pressure increase increments are required to produce the same deflection increments. The plate is becoming stiffer as its deflection increases. Figure 3.8(b) shows a magnification of part of this curve, from 0 to 0.06 MPa applied pressure. Notice that the pressure-deflection curve is linear up to deflections of approximately half the plate thickness, $t_{vm} = 3.5\mu m$. Linear deflection theory is accurate for this small deflection regime.

Figure 3.8(c) displays the normalized plate deflection shapes for P_3 loading of 0.01MPa, 0.1MPa, 1MPa, 10MPa, and 100MPa. When $P_3 = 0.01MPa$, the plate deflection is very small ($2.8\mu m$), and therefore the plate experiences only bending stresses. When $P_3 = 0.1MPa$, the plate deflection is $11\mu m$ and therefore the plate has entered the large deflection regime. From

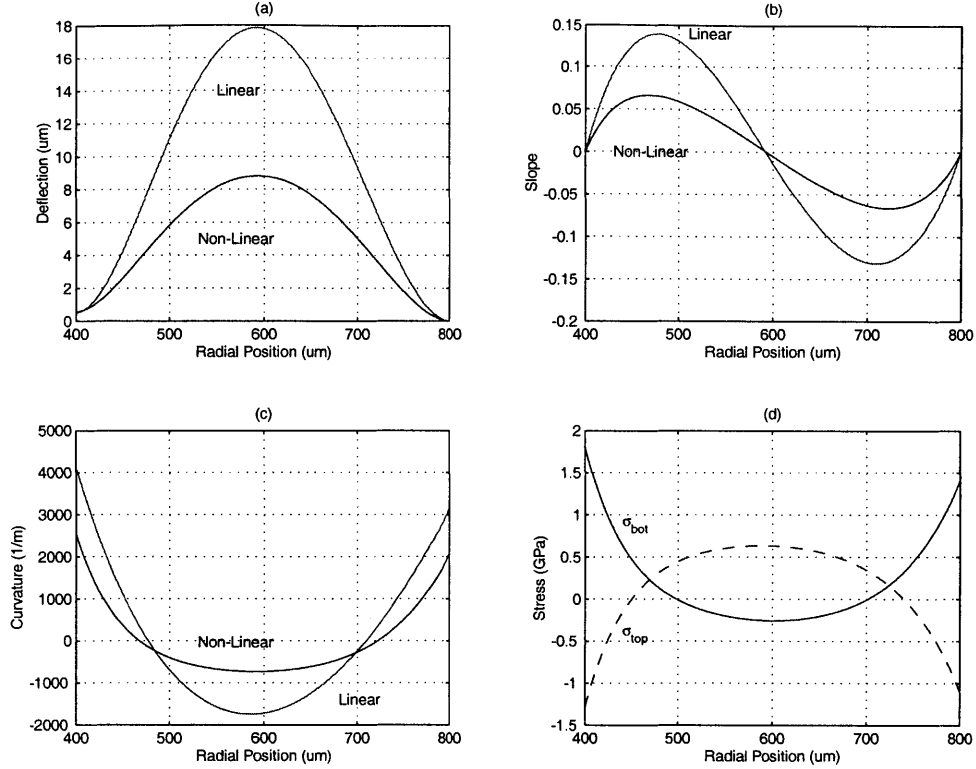


Figure 3.7: Deflection of thin annular plate under loading $P_1 = 2.9MPa$, $P_2 = 0$, $P_3 = 1.3MPa$. Plate dimensions and properties: $r_b = 400\mu m$, $r_a = 800\mu m$, $t = 7\mu m$, $E_{si} = 165GPa$, and $\nu = 0.22$.

Figure 3.8(d), one can observe a slight reduction in the size of boundary layer regions near r_b and r_a . When $P_3 = 10MPa$, the deflection is relatively large ($64\mu m$). The boundary layers have been decreased to very thin regions. In the central portions of the plate, the in-plane tensile stresses dominate the bending stresses and therefore the plate curvature is constant. However, near the boundaries, the bending stresses are not negligible and therefore the plate curvature changes significantly. This is the region of transition from membrane to plate behavior.

3.4.4 Loading: $P_1 = P_2 = 0$, $P_{HAC} = 100kPa$, Varying N_o

It is also interesting to note the effect of pretensioning on the plate deflection. Pretensioning the plate in the radial direction has the same effect as forcing the plate to experience large deflections, in that it increases the in-plane tensile stress within the plate. Figure 3.9 illustrates this phenomenon for the plate described above under pressure loading $P_1 = P_2 = 0$ and $P_3 = 100kPa$. As the plate pretension (in units of stress) is increased from zero to 750MPa, the plate deflection at r_b decreases from $11.5\mu m$ to $1.3\mu m$. It is therefore critical when micromachining thin plate structure to estimate the magnitude of residual in-plane stresses that could result from

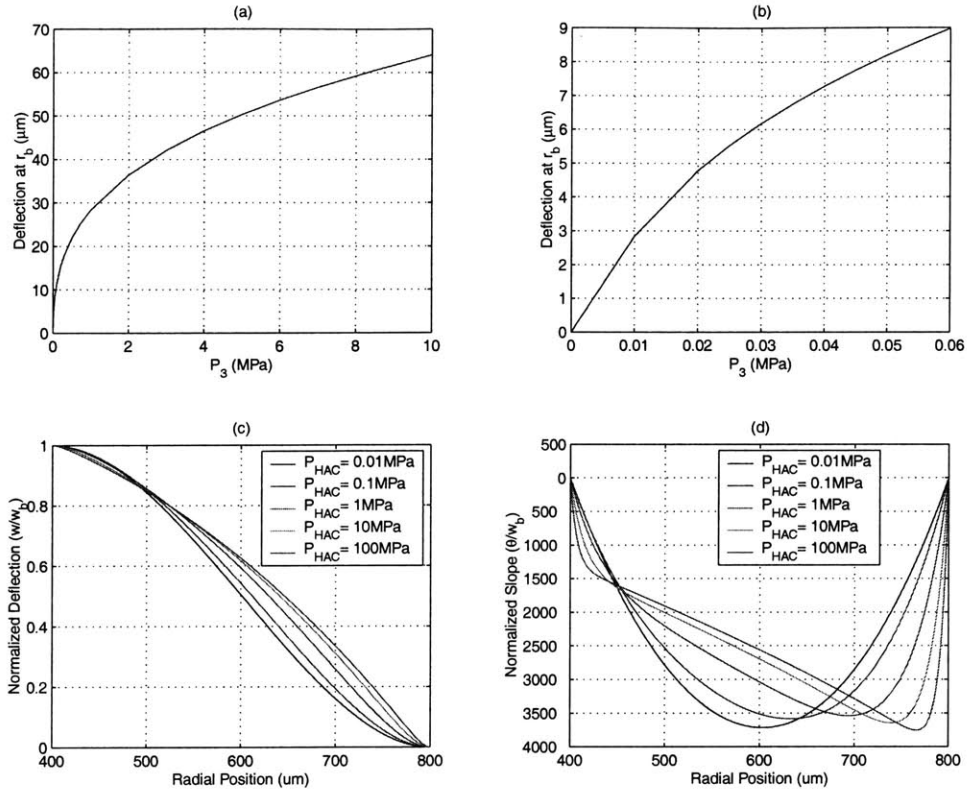


Figure 3.8: Deflection of thin annular plate under varying P_3 loading with $P_1 = P_2 = 0$ and $N_o = 0$. Plate dimensions and properties: $r_b = 400\mu\text{m}$, $r_a = 800\mu\text{m}$, $t = 7\mu\text{m}$, $E_{si} = 165\text{GPa}$, and $\nu = 0.22$.

wafer processing. The presence of any such stresses could substantially alter the performance from that predicted by theory.

3.5 Matlab Non-Linear Tools

The previous results have proven the capability of this numerical code to predict the non-linear deformation behavior of a thin plate structure with a rigid central cap. In the subsequent active valve design, modeling, and optimization chapters of the thesis, this large deflection numerical code is implemented in three distinct ways to allow for a variety of approaches to understanding the non-linear behavior of the valve cap and membrane. Each of these approaches is contained in a separate MatlabTM numerical code, and therefore act as a modeling tool for future use. These approaches are illustrated in Figure 3.10.

The first approach, detailed in Figure 3.10(a), calculates the valve cap deflection and associated plate behavior, given the pressure across the valve membrane P_{vm} and the effective force acting on the valve cap F_{vc} . For the loading terminology in this chapter, the effective

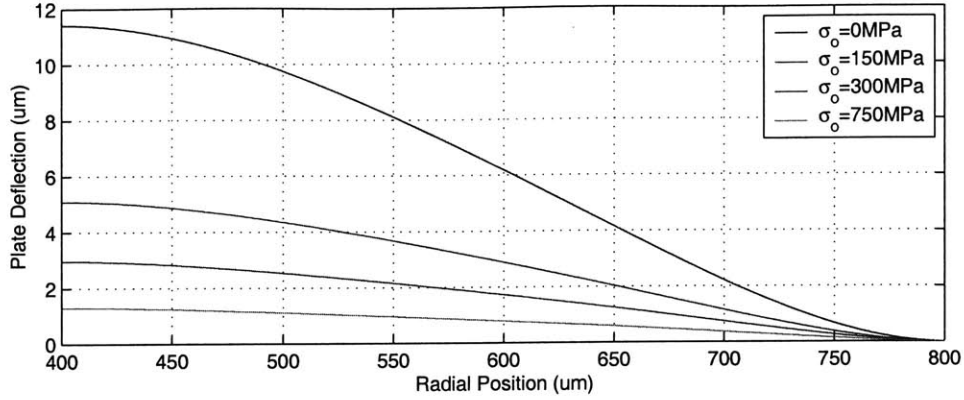


Figure 3.9: Deflection of a thin annular plate under loading $P_1 = P_2 = 0$, $P_{HAC} = 100kPa$, with varying N_o . Plate dimensions and properties: $r_b = 400\mu m$, $r_a = 800\mu m$, $t = 7\mu m$, $E_{si} = 165GPa$, and $\nu = 0.22$.

force on the valve cap would be $F_{vc} = A_{vc}(P_3 - P_1)$. The effective force could be the resultant of only pressures P_3 and P_1 (acting over the valve cap area) if the valve cap is unrestrained, or it could be the resultant of pressures P_3 , P_1 , and a reaction force imposed on the valve cap by an external structure if the cap is closed against a valve stop. This MatlabTM code, labeled NLValveCapMembrane-CaseA.m and included for reference in Appendix B.1, will be used in Chapter 3 as a part of the complete non-linear active valve quasi-static model.

The second approach, detailed in Figure 3.10(b), calculates the pressure across the valve membrane P_{vm} such that the valve deflection attains a certain value Z_{vc} , given a known value of F_{vc} . This MatlabTM code, labeled NLValveCapMembrane-CaseB.m and included for reference in Appendix B.2, will be important in Chapter 5 for determining the necessary $P_{HAC}(t)$ time history within the active valve in order to produce a desired $Z_{vc}(t)$ trajectory when the external loading time histories $P_1(t)$ and $P_2(t)$ are given.

The third approach, detailed in Figure 3.10(c), calculates the force on the valve cap F_{vc} required to produce a particular valve cap deflection Z_{vc} under a known loading P_{vm} . This MatlabTM code, labeled NLValveCapMembrane-CaseC.m and included for reference in Appendix B.3, will be used in Chapter 3 to determine the reaction force exerted by a valve stop structure on the valve cap when given all three pressure loadings P_1 , P_2 , P_3 , and an imposed valve cap deflection (ie: hitting a stop).

All three of these MatlabTM tools share the same non-linear theory and finite-difference implementation as presented in this chapter. They differ only in the organization of the system matrices and the procedure in which the various known and unknown quantities are handled. All are capable of outputting the entire plate spatial deflection vector, as well as the spatial slope and curvature vectors, and the plate top and bottom surface spatial stress vectors. The

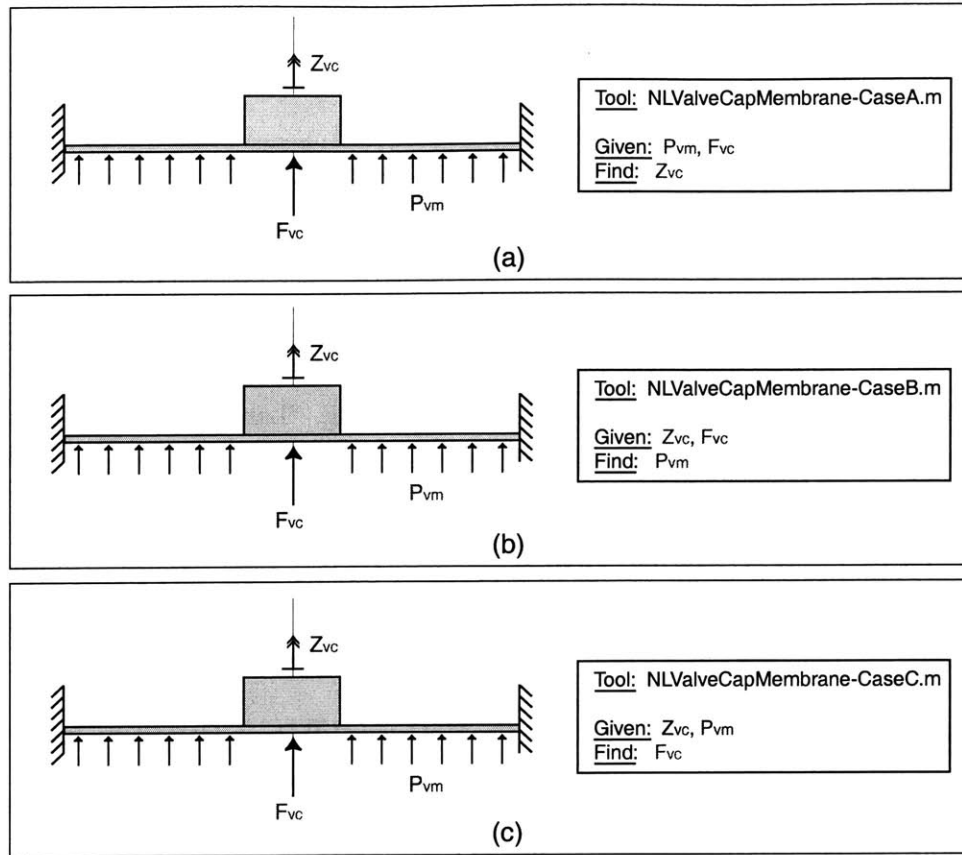


Figure 3.10: Matlab Tools for Use in Subsequent Chapters: (a) NLValveCapMembrane-CaseA.m, (b) NLValveCapMembrane-CaseB.m, and (c) NLValveCapMembrane-CaseC.m.

codes included in Appendix B are written as MatlabTM functions.

3.6 Conclusions

This chapter has presented the theory governing the non-linear deflection of a thin annular plate with a rigid central cap and has detailed the development of a numerical code to capture this behavior. The results of the code have been compared to linear theory and important phenomena such as in-plane pretension effects and plate/membrane boundary layer regions have been discussed. Since this theory is critical for the development of the active valve device proposed in this thesis, three distinct MatlabTM codes/tools have been written for use in the design, modeling, and valve optimization chapters that follow.

Bibliography

- [1] Y.H. Su, K.S. Chen, D.C. Roberts, and S.M. Spearing, “Large Deflection Analysis of a Pre-Stressed Annular Plate With a Rigid Boss Under Axisymmetric Loading”, *Journal of Micromech. Microeng.* 11 (2001) pp. 645-653.
- [2] M. Sheplak and J. Dugundji, “Large Deflections of Clamped Circular Plates Under Initial Tension and Transitions to Membrane Behavior”, *Journal of Applied Mechanics*, Vol. 65, pp.107-115, March 1998.
- [3] S. Timoshenko. *Theory of Plates and Shells*. McGraw-Hill Book Company, Inc., New York and London, 1940.

Chapter 4

Active Valve Non-Linear Model and Simulation

This chapter combines the linear and non-linear modeling tools presented in Chapters 2 and 3 to create a quasi-static structural model of the full piezoelectrically-driven active valve. In addition, the chapter introduces a dynamic simulation architecture for the valve, which includes the inertia and damping associated with the drive element piston and valve cap structural elements. Calculation of the coupled fluid-structure resonant valve frequency, based on finite-element models, is also presented.

4.1 Quasi-Static Active Valve Model

A quasi-static active valve model, incorporating only linear structural behavior, was presented in Chapter 2. By combining this model with the numerical code developed in Chapter 3 to model the large-deflection behavior of the valve membrane, a complete quasi-static non-linear active valve model can be formulated. This model consists of two primary solving steps, as shown in Figure 4.1. In the first step, a matrix A is generated which captures all linear relationships within the valve structure. In the second step, this matrix is used in combination with one of the previously described non-linear tools, `NLValveCapMembrane-CaseA.m`, to solve iteratively for the complete active valve behavior.

Since the valve membrane is the only structural component of the active valve for which non-linear modeling is required, the linear compliance matrix A can be defined by:

$$Y = [A]U. \quad (4.1)$$

where Y is a vector of active valve variables to be calculated using linear theory, and U is a vector of input variables required to calculate Y . This matrix relation can be rewritten in

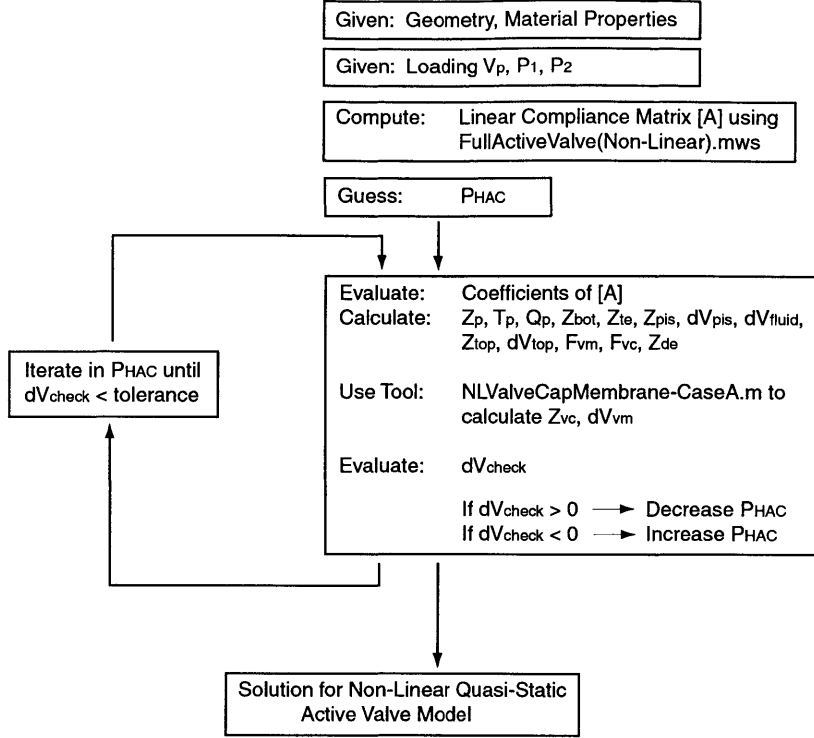


Figure 4.1: Calculation procedure for non-linear quasi-static active valve model.

more detail as:

$$\begin{bmatrix} Z_p \\ T_p \\ Q_p \\ Z_{bot} \\ Z_{te} \\ dV_{te} \\ Z_{pis} \\ dV_{pis} \\ dV_{fluid} \\ Z_{top} \\ dV_{top} \\ F_{vm} \\ F_{vc} \\ Z_{de} \end{bmatrix} = \begin{bmatrix} A_{1,1} & A_{1,2} & A_{1,3} & A_{1,4} \\ A_{2,1} & A_{2,2} & A_{2,3} & A_{2,4} \\ A_{3,1} & A_{3,2} & A_{3,3} & A_{3,4} \\ A_{4,1} & A_{4,2} & A_{4,3} & A_{4,4} \\ A_{5,1} & A_{5,2} & A_{5,3} & A_{5,4} \\ A_{6,1} & A_{6,2} & A_{6,3} & A_{6,4} \\ A_{7,1} & A_{7,2} & A_{7,3} & A_{7,4} \\ A_{8,1} & A_{8,2} & A_{8,3} & A_{8,4} \\ A_{9,1} & A_{9,2} & A_{9,3} & A_{9,4} \\ A_{10,1} & A_{10,2} & A_{10,3} & A_{10,4} \\ A_{11,1} & A_{11,2} & A_{11,3} & A_{11,4} \\ A_{12,1} & A_{12,2} & A_{12,3} & A_{12,4} \\ A_{13,1} & A_{13,2} & A_{13,3} & A_{13,4} \\ A_{14,1} & A_{14,2} & A_{14,3} & A_{14,4} \end{bmatrix} \begin{bmatrix} V_p \\ P_1 \\ P_2 \\ P_{HAC} \end{bmatrix}. \quad (4.2)$$

For a given active valve geometry, the coefficients of the linear compliance matrix A are calculated (see MapleTM code FullActiveValve(Non-Linear).mws in Appendix C.1). For a known set of loadings V_p , P_1 , and P_2 , an initial guess for the equilibrium pressure P_{HAC} is assumed,

and the variables contained in Y are calculated. With this value of P_{HAC} , the non-linear tool `NLValveCapMembrane-CaseA.m` is called to calculate Z_{vc} and dV_{vm} . A check is then made of the summation of swept volumes,

$$dV_{check} = dV_{vm} + dV_{top} - dV_{te} - dV_{pis} - dV_{fluid}. \quad (4.3)$$

If $dV_{check} > 0$, the initial guess for P_{HAC} was too large. Conversely, if $dV_{check} < 0$, the initial guess for P_{HAC} was too small. Depending on the result, a modified value of P_{HAC} is attempted. This iteration procedure is carried out until subsequent iteration values of dV_{check} are confined to within a specified tolerance. At this point, an equilibrium solution for the active valve under the specified loading conditions has been achieved.

4.2 Accuracy of Quasi-Static Model

The accuracy of this quasi-static active valve model can be verified by comparing its results under various loading conditions to those of a finite-element model. In making this comparison, the goodness of the assumptions used in this analytical model can be evaluated.

4.2.1 Assumptions in Model

The analytical active valve model uses linear and non-linear plate theory to model the compliances of the structural components. Boundary conditions for each of the components were chosen in an effort to accurately represent the geometries of a real device. However, it would be impossible to achieve 100% perfect correlation between the analytical model and a finite-element model, or a real device. Therefore, prior to comparing the analytical and finite-element models, the following thoughts concerning model correlation are put forth:

1. Both the valve membrane structure and the drive element piston tethers have been modeled with rigid boundary conditions along their respective inner and outer circumferences. In reality, because these interfaces are not in fact rigid, one might expect a “local” softening effect at these locations that would make these plate structures softer than predicted by theory.
2. Bending and shearing effects have been accounted for in the linear analytical equations governing the drive element piston, the top plate structure, and the bottom plate structure. Due to the fact that shearing coefficients are not well understood for these types of plate geometries, some non-correlation between analytical and finite-element results is expected. Additionally, because these plate geometries and associated boundary conditions are somewhat complex (ie: the presence of the piezoelectric cylinder beneath the piston and above the bottom plate), some degree of non-correlation is expected.

It is hoped, however, that even with all of these uncertain issues associated with material properties and geometric boundary conditions, the correlation between the analytical and finite-element model will be within $\sim 10\%$ for a range of loading parameters that covers the design space for the proposed active valve.

4.2.2 FEM Model Geometries and Correlation Procedure

Two finite-element models of the active valve have been developed to estimate the accuracy of the analytical quasi-static active valve model. The first model, illustrated in Figure 4.2, uses 8-node axisymmetric plane elements for all of the component structures, including the fluid. Material properties for silicon and pyrex are assigned appropriately, as are the bulk modulus properties for the contained hydraulic fluid. As shown in Figures 4.2(b) and 4.2(c), the valve membrane and drive element tethers structures do not include fillet radius features. Since the analytical model does not include the effect of fillet radii either, this allows for a level comparison. Estimates of maximum stress in these structures, however, will not be accurate.

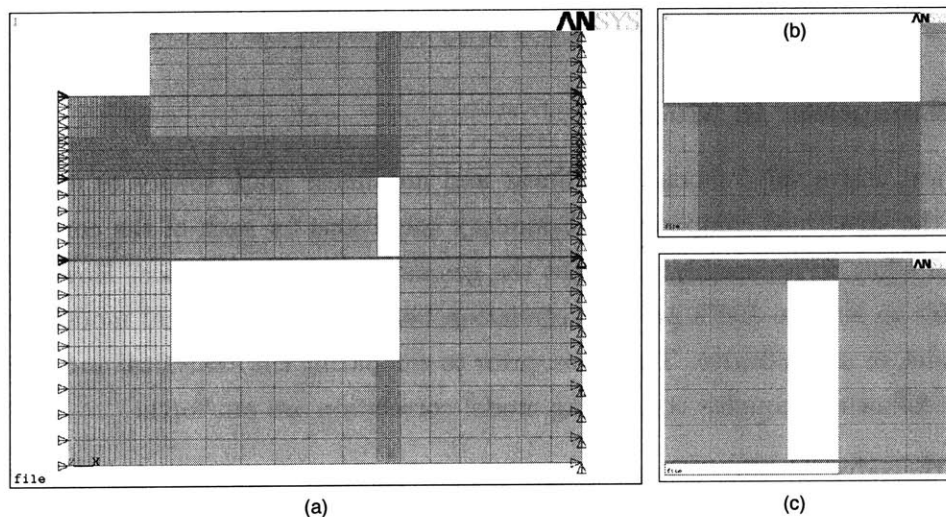


Figure 4.2: An ANSYSTM finite-element model of the full active valve without fillet radius features on the valve membrane and drive element tether structures : (a) entire device, (b) close-up view of valve cap and membrane, and (c) close-up view of drive element tethers.

The second model, illustrated in Figure 4.3, also used 8-node axisymmetric plane elements and the same material definitions. However, this model does include adjustable size fillet radius features on the valve membrane and the drive element tether structures. Figures 4.3(b) and 4.3(c) show close-ups of these regions. This enables a determination of the degree of stiffening that the fillets add to the structures and also allows for accurate estimation of stress concentrations in the structures. Both finite-element models have gone through a convergence

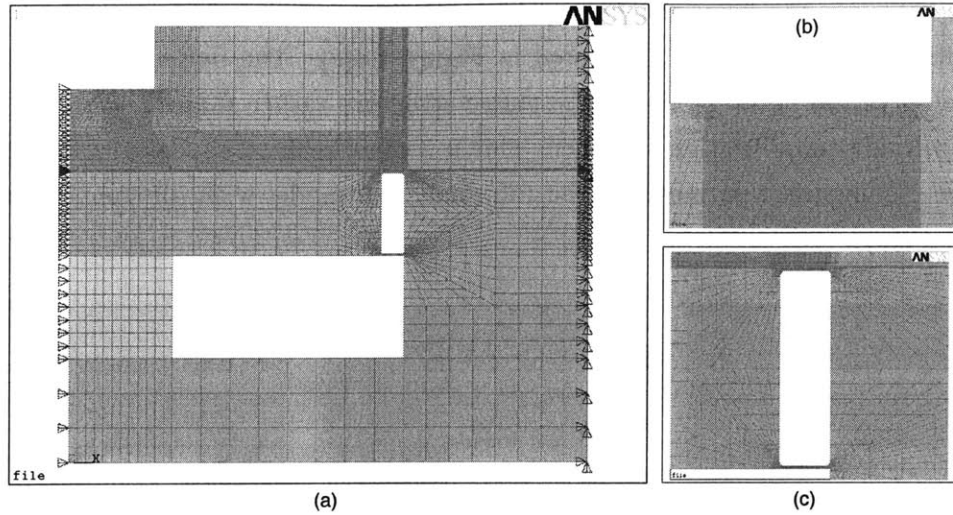


Figure 4.3: ANSYS finite-element model of full active valve with fillet radius features included: (a) entire device, (b) close-up view of valve cap and membrane, and (c) close-up view of drive element tethers.

study to ensure that the element mesh densities are fine enough to produce reliable results.

4.2.3 Model Correlation Procedure

The procedure for comparing the analytical quasi-static active valve model to the finite-element models is documented below. The procedure involves a systematic study of the correlation between these models for varying boundary condition and fillet radius assumptions.

1. To determine the modeling accuracy of the piezoelectric material, valve membrane, drive element tethers, and hydraulic fluid in the analytical model, all other structural components (valve cap, drive piston, top plate, and bottom plate) in the model are made rigid (ie: $\Xi_{Z_{bot}}^T = \Xi_{Z_{pis}}^T = \Xi_{dV_{pis}}^T = \Xi_{Z_{pis}}^P = \Xi_{dV_{pis}}^P = \Xi_{Z_{top}}^P = \Xi_{Z_{top}}^F = 0$). Behavior of the analytical valve is compared to the finite-element model (without fillets) with identical conditions on the component stiffnesses. Figure 4.4(a) illustrates the FEM model. Infinitely stiff regions are shaded dark.
2. To determine the modeling accuracy of the drive piston, top structural plate, and bottom structural plate, the analytical model is run with all compliances in their normal state. Behavior of the analytical model is compared to the finite-element model (without fillets) with infinitely stiff regions as shown in Figure 4.4(b). This comparison will validate the accuracy of the full analytical model with all compliances included.
3. To evaluate the effect of the fillet radius features and additional sidewall material on the

valve behavior, the finite-element model (with fillet radius = $25 \mu m$) with no regions of infinite stiffness is run, as illustrated in Figure 4.4(c). The boundary condition in this model is at the outer radius of the entire structure rather than at the outer radius of the hydraulic amplification chamber. This is a more realistic model of a fabricated valve device. Comparison is made to the full analytical model with all compliances in their normal state.

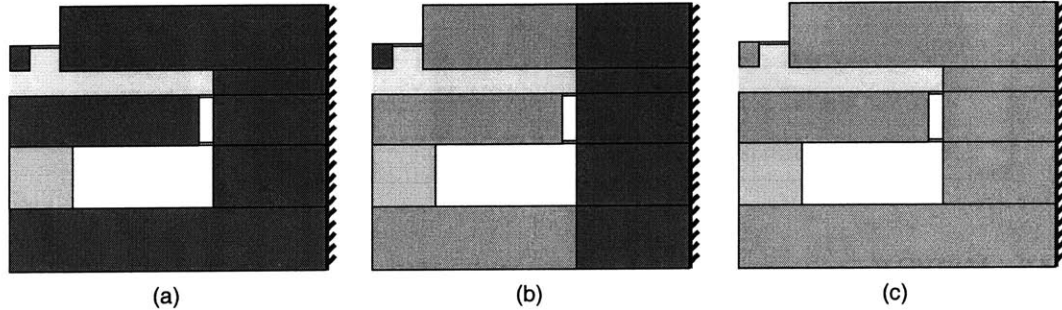


Figure 4.4: ANSYSTM finite-element comparison stages: (a) Top plate, bottom plate, piston, valve cap, and side structures are rigid, (b) Only valve cap and side structures are rigid, and (c) No structures rigid.

To cover the design space for the active valve geometry under consideration, the following three loading scenarios are applied:

1. $V_p=1000 \text{ V}$, $P_1=0$, $P_2 = 0$
2. $V_p=0$, $P_1=1 \text{ MPa}$, $P_2 = 1 \text{ MPa}$
3. $V_p=500 \text{ V}$, $P_1=0.5 \text{ MPa}$, $P_2 = 0$.

These loading scenarios are chosen to capture the valve behavior throughout a complete cycle of deflection. The first loading scenario produces a large positive valve cap deflection, the second loading scenario produces a large negative valve cap deflection, and the third scenario produces a small positive valve cap deflection. The comparison procedure detailed above is carried out for each of the loading scenarios to evaluate the accuracy of the analytical quasi-static active valve model.

4.2.4 Valve Geometry

The active valve geometry used in this comparison study is detailed in the following table. These dimensions are chosen to represent a typical active valve device.

Geometric Dimensions:

Component	Parameters			
Valve Cap	$R_{vc} = 310\mu m$	$R_{vm} = 800\mu m$	$t_{vm} = 10\mu m$	$t_{vc} = 400\mu m$
Top/Bottom Plate	$t_{top} = 1000\mu m$	$t_{bot} = 1000\mu m$		
HAC Chamber	$R_{te} = 3.225mm$	$H_{HAC} = 400\mu m$		
Piston/Tethers	$R_{pis} = 3mm$	$t_{pis} = 800\mu m$	$t_{tetop} = 10\mu m$	$t_{tebot} = 10\mu m$
Piezo	$L_p = 1mm$	$R_p = 1mm$		

Material Properties:

Material	Properties		
Silicon	$E_{Si} = 165GPa$	$\nu_{Si} = 0.22$	$\alpha_{Si} = 1.25$
Pyrex	$E_{pyrex} = 48GPa$	$\nu_{pyrex} = 0.20$	
Piezo	$d_{33} = 2000\frac{pC}{N}$	$E_{piezo} = 9.01GPa$	
Fluid	$K_{fluid} = 2.0GPa$		

The critical valve parameters chosen to serve as comparisons between the two models are the valve cap deflection Z_{vc} , the top plate structure deflection Z_{top} , the hydraulic amplification chamber pressure P_{HAC} , the drive piston center deflection Z_{pis} , the top tether deflection Z_{te} , and the bottom plate structure center deflection Z_{bot} . These parameters are reviewed in Figure 4.5. In addition, for the finite-element model with fillet radius features, the maximum membrane stress in the model is also monitored.

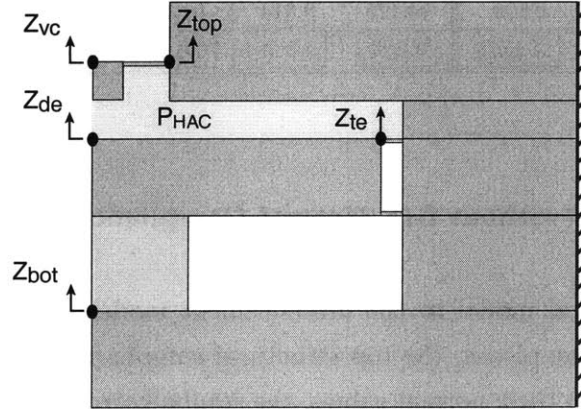


Figure 4.5: Variables monitored in analytic and FEM models.

4.2.5 Model Correlation

Finite-Element Model (without fR), Rigid Compliances

In comparing the analytical model to the finite-element model without fillet radius features for the case where the drive piston, the top structural compliance, the bottom structural compliance, and the valve cap are all designated to be rigid, the results correlate extremely well. Table

4.1 shown below compares these results for the three loading scenarios. For each of the three loading scenarios, the valve cap deflection correlates within 0.4%. All of the other parameters also correlate very well, within 1%. This correlation proves that the valve membrane non-linear relations, the drive element tether relations, the fluid compliance, and the piezoelectric material behavior are all modeled very accurately in the non-linear quasi-static analytical active valve model.

TABLE 4.1: Model Correlation (without fR), Rigid Compliances

Loading	Model	Variables to Monitor						
		Z_{vc} (μm)	Z_{de} (μm)	Z_{te} (μm)	Z_{top} (μm)	Z_{bot} (μm)	P_{HAC} (kPa)	σ_{max} (GPa)
Scenario 1 $V_p = 1000V$ $P_1 = 0, P_2 = 0$	Analytic	26.269	1.136	1.136	0	0	781	1.45
	FEM	26.218	1.143	1.143	0	0	775	n/a
	% Dif	0.2 %	0.6 %	0.6 %	0 %	0 %	0.8 %	n/a
Scenario 2 $V_p = 0V$ $P_1 = 1MPa, P_2 = 1MPa$	Analytic	-20.770	-0.597	-0.597	0	0	567	0.96
	FEM	-20.858	-0.591	-0.591	0	0	562	n/a
	% Dif	0.4 %	1.0 %	1.0 %	0 %	0 %	0.9 %	n/a
Scenario 3 $V_p = 500V$ $P_1 = 0.5MPa, P_2 = 0$	Analytic	14.207	0.612	0.612	0	0	349	0.66
	FEM	14.175	0.614	0.614	0	0	347	n/a
	% Dif	0.2 %	0.3 %	0.3 %	0 %	0 %	0.6 %	n/a

Finite-Element Model (without fR), Normal Compliances

In comparing the analytical model to the finite-element model without fillet radius features for the case where the drive piston, the top structural compliance, and the bottom structural compliance are returned to their normal values, the results correlate fairly well. The valve cap deflection for the first loading scenario correlates within 3.7%, for the second loading scenario within 0.4%, and for the third loading scenario within 7.5%. This larger value of 7.5% is not that bad since the valve cap deflection is relatively small. As loading is applied that forces the valve cap near zero deflection, one would expect the % error to increase even though the absolute difference between the model deflections is much smaller than $1\mu m$.

TABLE 4.2: Model Correlation (without fR), Normal Compliances

Loading	Model	Variables to Monitor						
		Z_{vc} (μm)	Z_{de} (μm)	Z_{te} (μm)	Z_{top} (μm)	Z_{bot} (μm)	P_{HAC} (kPa)	σ_{max} (GPa)
Scenario 1 $V_p = 1000V$ $P_1 = 0, P_2 = 0$	Analytic	21.787	1.213	0.792	0.087	-0.251	482	1.03
	FEM	22.629	1.267	0.837	0.094	-0.249	510	n/a
	% Dif	3.7 %	4.3 %	5.4 %	7.5 %	0.8 %	5.5 %	n/a
Scenario 2 $V_p = 0V$ $P_1 = 1MPa, P_2 = 1MPa$	Analytic	-24.107	-0.560	-0.846	0.031	-0.179	371	1.25
	FEM	-24.009	-0.532	0.834	0.039	-0.180	396	n/a
	% Dif	0.4 %	5.0 %	1.4 %	20.5 %	0.6 %	6.3 %	n/a
Scenario 3 $V_p = 500V$ $P_1 = 0.5MPa, P_2 = 0$	Analytic	9.654	0.595	0.378	0.042	-0.129	249	0.45
	FEM	10.436	0.628	0.409	0.044	-0.126	259	n/a
	% Dif	7.5 %	5.3 %	7.6 %	4.5 %	2.3 %	3.9 %	n/a

In looking at the other monitored variables, one notices that they all correlate within 7.5%, except for Z_{top} in Loading Scenario 1. Again, though, this deflection is extremely small, and therefore such a significant error has negligible effect on the rest of the system performance. In fact, from Loading Scenario 1, the following swept volumes are obtained from the analytical model: $dV_{pis} = 4.03e^{-12}m^3$, $dV_{te} = 2.38e^{-11}m^3$, $dV_{top} = 1.11e^{-12}m^3$, $dV_{fluid} = -3.32e^{-12}m^3$, and $dV_{vm} = 2.34e^{-11}m^3$. From these, it is calculated that the volume of fluid lost in the top structural plate compliance is approximately 4% of the swept volume of piston and tether together (the actuation swept volume). Overall, this 4% loss is important, but 20.5% of this 4% is not. In conclusion, the analytical valve model predicts the valve cap deflection very well.

Finite-Element Model (with fR), Normal Compliances

In order to evaluate the accuracy of the analytical valve model with respect to a finite-element model that is more characteristic of the real device, no rigidities are assumed in the finite-element model and fillet radius features are taken into consideration. The finite-element results for Loading Scenario 1 are illustrated graphically in Figure 4.6.

A major realistic effect that is considered in this model is the presence of the rigid boundary condition at the outer radius of the device rather than at R_{te} . This condition serves to soften the top and bottom plate compliances. From Table 4.3 below, it is clear that in all three loading scenarios, Z_{top} and Z_{bot} show very large correlation errors near 50%. This is a result of this softening. It is interesting, however, that even with these large deviations in Z_{top} and Z_{bot} , the overall valve cap deflection correlation is excellent (less than 4% for all loading scenarios). The principal reason for this, again, that the absolute swept volumes associated with these deflections are not very large.

TABLE 4.3: Model Correlation (with fR), Rigid Compliances

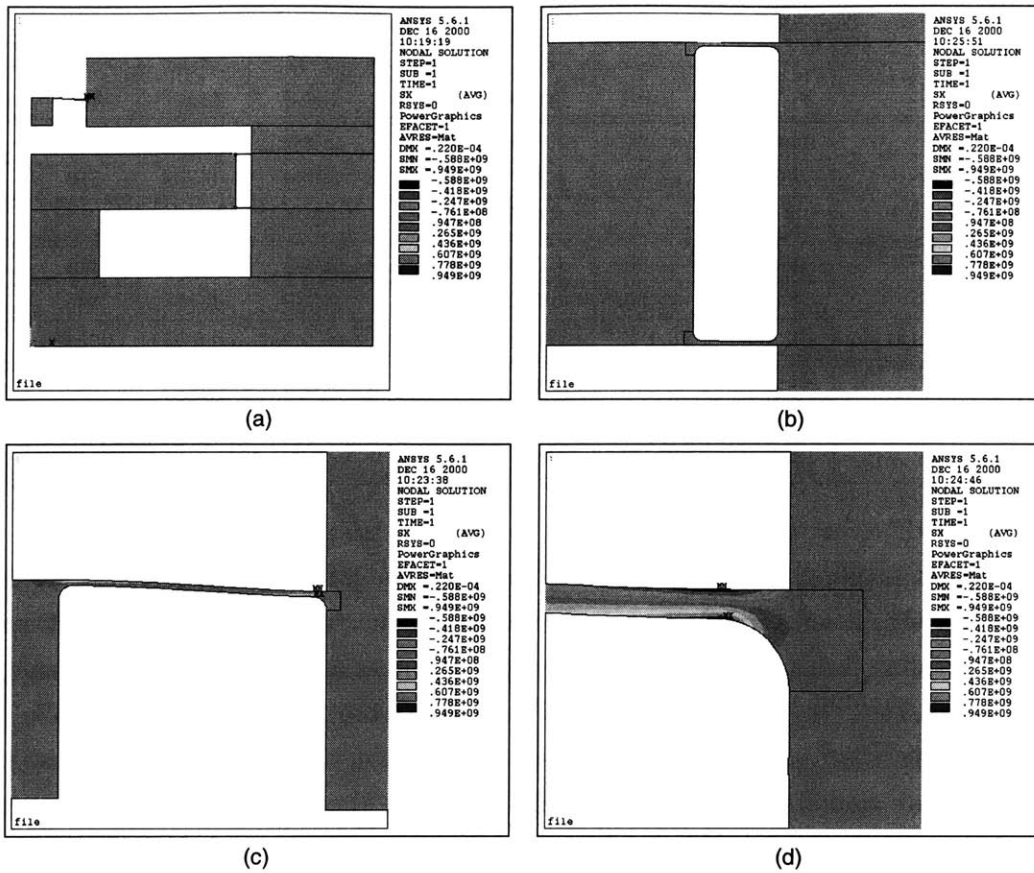


Figure 4.6: ANSYSTM FEM stress contour plots for Loading Scenario 1 on fillet radius model.

Loading	Model	Variables to Monitor						
		Z_{vc} (μm)	Z_{de} (μm)	Z_{te} (μm)	Z_{top} (μm)	Z_{bot} (μm)	P_{HAC} (kPa)	σ_{max} (GPa)
Scenario 1 $V_p = 1000V$ $P_1 = 0, P_2 = 0$	Analytic	21.787	1.213	0.792	0.087	-0.251	482	1.03
	FEM	22.002	1.225	0.809	0.157	-0.333	464	0.95
	% Dif	1.0 %	1.0 %	2.1 %	44.6 %	24.6 %	3.7 %	7.8 %
Scenario 2 $V_p = 0V$ $P_1 = 1MPa, P_2 = 1MPa$	Analytic	-24.107	-0.560	-0.846	0.031	-0.179	371	1.25
	FEM	-24.269	-0.552	-0.826	0.071	-0.237	365	1.05
	% Dif	0.7 %	1.4 %	2.4 %	56.3 %	24.5 %	1.6 %	16.0 %
Scenario 3 $V_p = 500V$ $P_1 = 0.5MPa, P_2 = 0$	Analytic	9.654	0.595	0.378	0.042	-0.129	249	0.45
	FEM	9.283	0.590	0.371	0.078	-0.176	246	0.41
	% Dif	3.8 %	0.8 %	1.9 %	46.2 %	26.7 %	1.2 %	8.9 %

Another reason, though, has to do with the behavior of the valve cap membrane. Thinking about the valve cap and membrane structure, because the valve cap is no longer rigid, the local behavior at the interface between the membrane and the cap may result in a softer structure. This appears to be the case since a 3.7% less P_{HAC} pressure deflects the valve cap 1.0% more

in the realistic finite-element model than in the analytical model. A counter-effect which most likely helps to minimize this softening of the valve cap and membrane is the presence of the fillet radii. Each fillet radius provides significantly more material at this interface and hence stiffens the structure.

To conclude this section on the analytical quasi-static active valve model, the comparisons between the analytical model and finite-element models have proven that the analytical model very accurately predicts the quasi-static active valve behavior of finite-element models with boundary conditions similar to those expected in fabricated devices. These quasi-static modeling techniques will now serve as the basis for dynamic models which will be able to capture higher-order dynamic effects within the active valve structure.

4.3 Finite-Element Resonant Behavior

To gain a rough idea of the frequency capabilities of this valve structure, a 2-D finite-element model without fillet radius features was evaluated using modal analyses in ANSYSTM. By definition, modal analyses are only valid for purely linear systems. Consequently, the resulting resonant frequencies are good predictions of active valve behavior only if the valve is operated such that valve cap and membrane deflections are within the small-deflection regime (ie: small applied voltage to the piezoelectric material). This model incorporates four-node plane elements for the silicon and glass structural parts of the valve and 4-node acoustic fluid elements for the liquid contained within the hydraulic amplification chamber. These acoustic elements enable fluid-structure interaction between the fluid and the surrounding structure of the HAC chamber. For the active valve geometry used in this chapter, the modal analysis results indicate a first modal frequency at $f_1 = 25.6kHz$ and a second modal frequency at $f_2 = 102.7kHz$, as shown in Figure 4.7.

Since, during real valve operation, the valve cap and membrane structure are required to experience deflections well into the non-linear regime, this first modal frequency can be taken as a lower limit to the actual resonant excitation. As a note to the reader, the active valve geometry considered in this chapter is slightly different from the valve devices built and tested in later parts of this thesis. The valve membrane is slightly thicker ($t_{vm} = 10\mu m$) than in the experimental devices ($t_{vm} = 6\mu m$) and the HAC chamber is slightly reduced in size ($R_{te} = 3.225mm$) than in the experimental devices ($R_{te} = 3.613mm$), differences which serve to make the experimental devices softer than the geometry evaluated in this chapter. As a result, a slightly reduced modal frequency can be expected in the experimental valve device, as detailed in Chapter 9. The modal finite-element models used through this thesis, however, are identical to the one presented in this chapter.

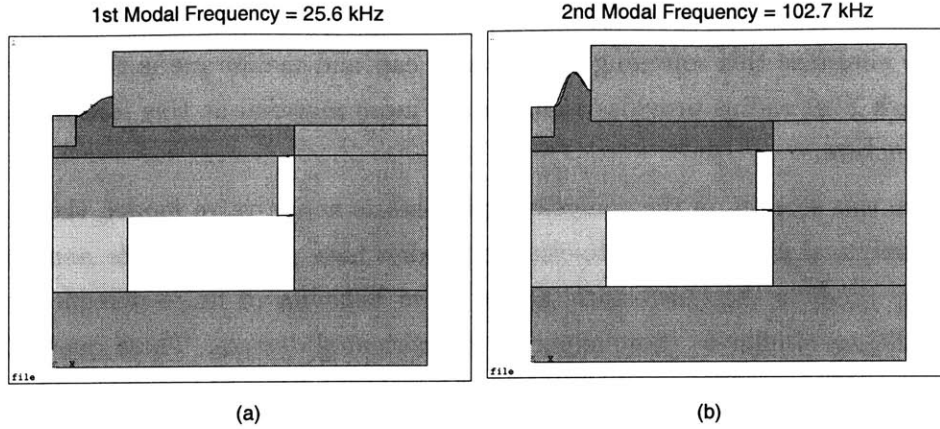


Figure 4.7: ANSYSTM FEM mode shapes: (a) 1st modal frequency = 25.601 kHz, (b) 2nd modal frequency = 102.67 kHz.

4.4 Dynamic Active Valve Simulation

To properly capture the non-linear effects of the valve membrane deformation at high frequency, and to include important dynamic effects, such as the drive element piston inertia and the valve cap inertia and damping, a SimulinkTM simulation architecture is presented in this section. The structural compliances within the active valve simulation are based exactly upon the linear and non-linear modeling tools presented in Chapters 2 and 3 of this thesis. The simulation architecture can be broken down into four major subsystems, as illustrated in Figure 4.8: a matrix of linear coefficients describing the bulk of the active valve behavior, a series of non-linear look-up tables that captures the large-deflection valve membrane deformation and stress, a valve cap dynamics block, and a drive piston dynamics block.

4.4.1 Linear Matrix Relations

As discussed in Chapter 2, all of the structural elements except the valve membrane operate in linear deformation regimes. Within the simulation, therefore, a matrix of compliance and parameter coefficients are included for these linear relations:

$$\begin{bmatrix} T_p \\ F_{te} \\ P_{HAC} \\ Z_{top} \\ Charge \end{bmatrix} = \begin{bmatrix} A_{1,1} & A_{1,2} & A_{1,3} & A_{1,4} & A_{1,5} \\ A_{2,1} & A_{2,2} & A_{2,3} & A_{2,4} & A_{2,5} \\ A_{3,1} & A_{3,2} & A_{3,3} & A_{3,4} & A_{3,5} \\ A_{4,1} & A_{4,2} & A_{4,3} & A_{4,4} & A_{4,5} \\ A_{5,1} & A_{5,2} & A_{5,3} & A_{5,4} & A_{5,5} \end{bmatrix} \begin{bmatrix} Z_{te} \\ F_{vc} \\ dV_{vm} \\ P_{HPR} \\ V_p \end{bmatrix} \quad (4.4)$$

Inputs to this matrix are the Z_p and Z_{vc} variables fed back from the piston and valve cap dynamic blocks respectively, dV_{vm} fed back from the non-linear valve membrane look-up table,

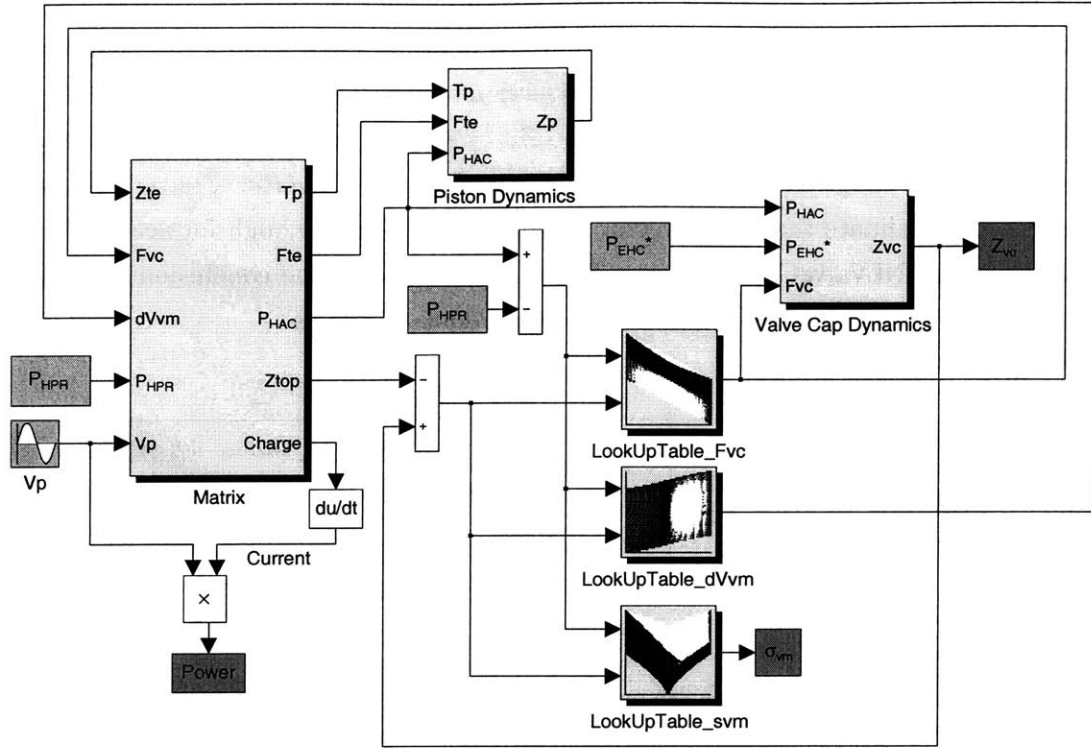


Figure 4.8: Complete SimulinkTM active valve system architecture, showing linear equation matrix, non-linear look-up tables, valve cap dynamics block, and drive element piston dynamics block. Architecture shown is for the inlet valve of a typical MHT system.

and the active valve loadings V_p and P_{HPR} . Outputs of this matrix are T_p , F_{te} , P_{HAC} , and Z_{top} . These outputs are fed to the other subsystems within the active valve model. These matrix coefficients are generated in an external MapleTM code, similar to that described in Section 4.1, and read into the SimulinkTM model.

4.4.2 Non-Linear Look-Up Tables

As detailed in Chapter 3, numerical modeling tools have been developed to calculate the non-linear large deflection behavior of the valve membrane. One possibility for capturing the non-linear behavior in the Simulink simulation would be to call the numerical code at each and every time step during a simulation run. However, the required computation for the simulation using this procedure is quite intensive. As a result, a method is implemented by which the numerical code is used to generate look-up tables for important non-linear behavioral variables, as shown in Figure 4.9. Taking as inputs the valve cap displacement Z_{vc} and the net pressure across the valve membrane $P_{vm} = P_{HAC} - P_{HPR}$, a lookup table is employed for each of the output

variables F_{vc} , dV_{vm} , and σ_{vm} . The size of the look-up tables is governed by the number of calculation points between the upper and lower limits of the inputs Z_{vc} and P_{vm} . For example, the look-up tables used in the simulations in this section take as inputs a Z_{vc} vector 100 elements in length, covering a range from $Z_{vc} = -50\mu m$ to $Z_{vc} = +50\mu m$, and a P_{vm} vector 100 elements in length, covering a range from $P_{vm} = -1.5MPa$ to $P_{vm} = +1.5MPa$. Convergence studies were performed to validate that these vector resolutions were fine enough for accurate results. The MatlabTM file, NLValveCapMembrane-CaseC.m, detailed at the conclusion of Chapter 3 and included in Appendix B.3, is used to create these look-up tables.

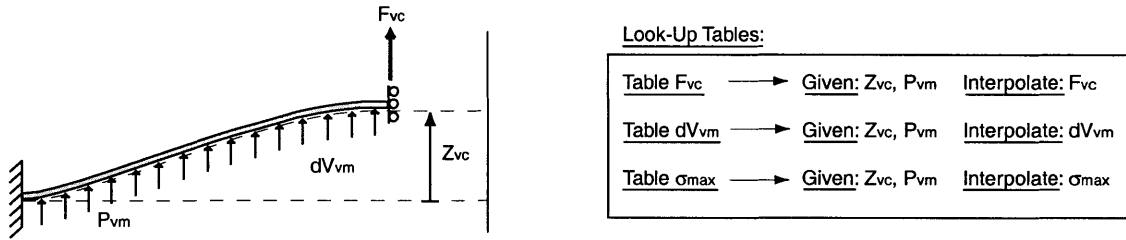


Figure 4.9: Numerical modeling tools are used to generate look-up tables for the non-linear large deflection behavior of the valve cap and membrane. Given a prescribed valve cap displacement Z_{vc} and pressure loading across the membrane P_{vm} , a look-up table for each of F_{vc} , dV_{vm} , and σ_{vm} is created.

4.4.3 Piston and Valve Cap Dynamics

The dynamic behavior of the drive piston structure is governed by the following relation:

$$M_{pis}\ddot{Z}_{pis} + C_{pis}\dot{Z}_{pis} = A_p T_p - A_{pis} P_{HAC} - F_{te} \quad (4.5)$$

The damping coefficient C_{pis} is a lumped parameter that is meant to include the effects of structural damping in the tethers and damping due to fluid interaction. Figure 4.10 displays a schematic of the valve cap mass and the corresponding Simulink block architecture included within the full active valve simulation.

In a similar fashion, the dynamic behavior of the valve cap is represented by the following relation:

$$M_{vc}\ddot{Z}_{vc} + C_{vc}\dot{Z}_{vc} = A_{vc}(P_{HAC} - P_1) - F_{vc} \quad (4.6)$$

The damping coefficient C_{vc} is a lumped parameter that includes the effects of structural damping in the membrane, squeeze film damping due to the valve cap motion when closing the valve, and damping due to fluid-structure interaction. Figure 4.11 displays a schematic of

the valve cap mass and the corresponding Simulink block architecture included within the full active valve simulation.

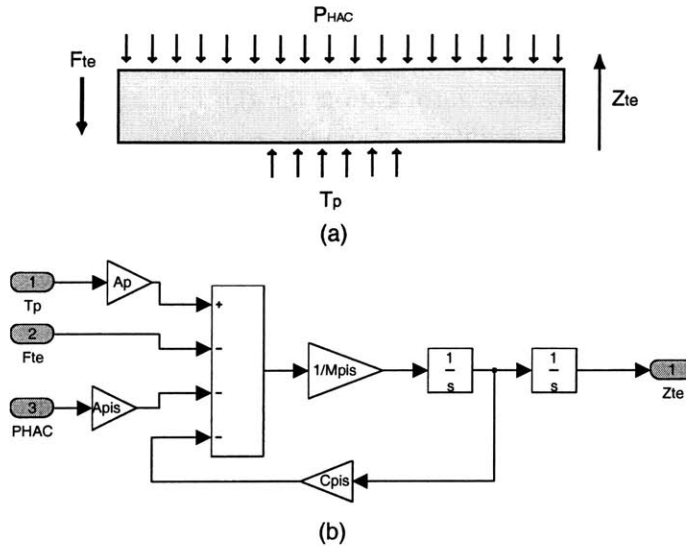


Figure 4.10: Piston Dynamics: (a) free-body diagram of piston structure, and (b) Simulink block architecture.

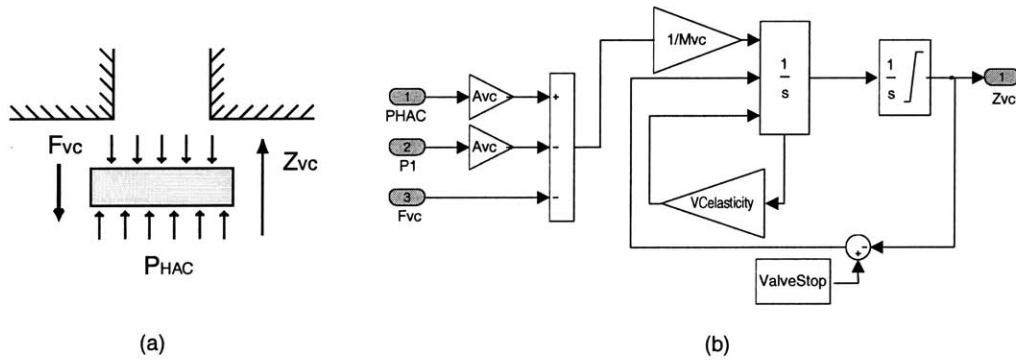


Figure 4.11: Valve cap dynamics: (a) free-body diagram of valve cap structure, and (b) Simulink block architecture.

Exact values of C_{pis} and C_{vc} are difficult to estimate accurately. Values are therefore chosen that result in dynamic responses that are relatively free of high-order oscillations (see results in Figure 5.24), yet still exhibit inertia and phase lag effects. Estimates for the damping ratios of the piston and valve cap (ζ_{pis} and ζ_{vc}) are calculated from these C_{pis} and C_{vc} values by observing the resonant frequency ω_n of each component in small deflection linear regimes, according to the relations $\zeta_{pis} = \frac{C_{pis}}{2\omega_{pis}}$ and $\zeta_{vc} = \frac{C_{vc}}{2\omega_{vc}}$ respectively.

The Simulink block which captures this valve cap dynamic behavior also includes the effect

of the valve cap as it comes into contact with valve stops, either above and/or below the valve cap. This hitting behavior is modeled as an inelastic collision between the cap and the stop. The assumption here is that if the cap impacts the stop with a velocity V_1 , it will bounce back with a lesser velocity V_2 , according to the relation $V_2 = \sqrt{r}V_1$, where $r < 1$ is called the coefficient of restitution. The above formulation for the hitting can be implemented in Simulink by setting V_2 as the initial condition for the valve velocity at the subsequent time step immediately following impact. For further details on active valve and full MHT system simulation results, see Yaglioglu's MIT Master's thesis [8].

4.5 Conclusions

This chapter has presented a complete quasi-static analytical active valve model and a full dynamic active valve simulation architecture for use in predicting structural behavior of a given active valve geometry to a variety of loading conditions. Both models integrate the linear and non-linear tools presented in Chapters 2 and 3, respectively. Overall, the quasi-static analytical active valve model correlates very well with representative finite-element models, thereby justifying many of the boundary condition assumptions in the analytical model. The dynamic simulation architecture enables further investigation of higher-order dynamic effects in the drive element piston and valve cap structures.

Bibliography

- [1] O. Yaglioglu. Master's Thesis, Massachusetts Institute of Technology, 2002.

Chapter 5

Active Valve Design Procedure

So far, this thesis has presented detailed linear and non-linear structural modeling tools that can be used to predict the performance of a given active valve geometry, in response to an applied voltage on the piezoelectric material elements and against known external pressure loadings on the valve cap and membrane structure. Although it is quite important to be able to predict the performance of a predetermined active valve geometry, it is also critical to be able to design a structural geometry that can meet the specifications of and therefore be used within a complete MHT system. In order to accomplish this, relations governing the fluid flow behavior through the MHT system and the interaction of the valve structure with this external hydraulic system must be developed. The goals of this chapter, therefore, are (1) to present modeling tools that capture the interaction between the valve structure and the external hydraulic system, (2) to develop a systematic design procedure that can be used to formulate of an active valve geometry which will satisfy the pressure-flow requirements set by an overall MHT system, and (3) to present higher-order design benefits of incorporating multiple valve cap and membrane structures within the active valve so as to minimize power consumption of the valve.

Section 5.1 revisits a generic MHT system and discusses the performance requirements that this system demands from its active valves. Section 5.2 presents the tools for modeling the pressure-flow relationships in the hydraulic system external to the active valve and develops a related simulation tool for use in the the subsequent design procedure. Section 5.3 details the systematic procedure used to design a single valve cap and membrane active valve geometry. This procedure demonstrates the fundamental steps involved in the design of the active valve, but does not include design options for multiple valve heads. Section 5.4 highlights some important issues associated with free design variables within the procedure. Section 5.5 presents the theory behind valve power consumption and the benefit of incorporating multiple valve caps and membranes within the active valve structure. Section 5.6 presents results of the updated systematic design procedure, which allows for inclusion of multiple valve caps and membranes in the design process. Finally, Section 5.7 validates the capability of the quasi-static design

procedure by comparing the performance of a generated active valve geometry to that of a full dynamic simulation.

5.1 Valve Requirements in Generic MHT System

A schematic of an MHT power harvesting device is shown in Figure 5.1. Out of phase operation of two active valves results in a pulsing flow of fluid from a high pressure reservoir (P_{HPR}) to a low pressure reservoir (P_{LPR}) through a central piezoelectric harvesting chamber [1]. With each cycle of device operation, the increasing and decreasing fluid pressure P_{EHC} in the harvesting chamber (as the chamber fills and evacuates) results in a stressing of the piezoelectric material element(s) and a subsequent generation of charge. For a given harvesting chamber geometry, the system operational frequency f_{sys} and peak-peak pressure P_{EHC} fluctuation in the chamber directly determine the achievable power generation levels. The required cyclic flow rates into and out of the chamber, Q_{in} and Q_{out} , are functions of this pressure fluctuation and the structural chamber volumetric stiffness. Therefore, assuming that a harvesting chamber structural geometry is known, and that f_{sys} , P_{HPR} , P_{LPR} , and a desired P_{EHC} pressure fluctuation are also required, then an inlet and outlet active valve can be designed to permit this overall MHT system performance.

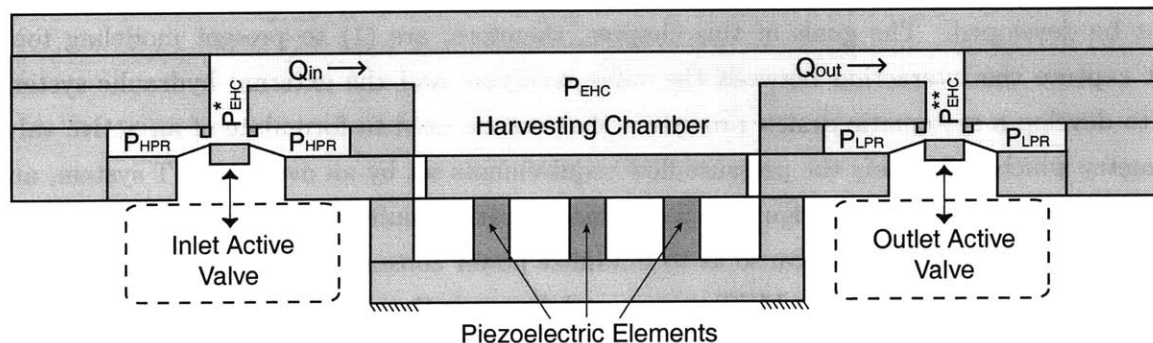


Figure 5.1: Schematic of an MHT power harvesting device. Two active valves regulate flow at high frequency from a high pressure P_{HPR} to a low pressure P_{LPR} . Cyclic pressure change in the harvesting chamber P_{EHC} creates a stressing of the piezoelectric material and a subsequent generation of charge.

In the example MHT power harvesting system shown in Figure 5.1, the top surface of the inlet valve membrane is in contact with the high pressure reservoir and therefore experiences a constant P_{HPR} . The valve cap, on the other hand, sees a changing pressure P_{EHC}^* as the chamber fills and evacuates. Likewise, the top surface of the outlet valve membrane is in contact with the low pressure reservoir and therefore experiences a constant P_{LPR} while the valve cap

sees a changing pressure P_{EHC}^{**} as the chamber fills and evacuates. The assumptions for the areas over which these system pressures act is further detailed in Section 5.2.3. The amounts by which P_{EHC}^* and P_{EHC}^{**} differ from P_{EHC} are functions of the fluid inertial effects in the inlet and outlet flow channels (see Section 5.2.2). With the ability to model these pressure-flow relations through the MHT system, a design procedure can be developed and implemented to design the active valve geometries for the system.

The systematic active valve design procedure that is developed in this chapter is based on quasi-static valve structural behavior. In other words, dynamic effects within the active valve such as those associated with the valve cap mass, the drive element piston mass, and any damping effects are not included. In this way, the basic process of the design procedure can be well understood and estimates for valve geometries to satisfy the MHT system requirements can be generated. Once an active valve geometry is designed in this way, full dynamic simulations of the structure can be run in order to evaluate the goodness of the quasi-static valve design and to enable tweaking of the valve geometries to achieve higher performance. Although this quasi-static design procedure is generic to both the MHT actuator and power harvesting applications, for purposes of clarity, the discussions in this thesis will center on the design of active valves to be used in the previously described MHT power harvesting system. Furthermore, without any loss of generality, the focus of this chapter will be solely on the design of the inlet active valve for the harvesting system.

To regulate flow into the MHT harvesting chamber so as to meet the overall system requirements, the inlet valve membrane and cap structure must be sized properly to ensure adequate stroke of the valve cap and to allow sufficient fluid flow through the orifice to fill the chamber in the allotted time. In addition, under these external pressure loadings, stresses within the valve cap and membrane structure must be kept below the fracture strength of the membrane material. The piezoelectric drive portion of the valve must be designed so as to minimize the overall volume of the device, yet still provide adequate actuation for pressurizing and producing volume change to the hydraulic amplification chamber. Further design issues, such as valve power consumption and the incorporation of multiple valve heads within a single active valve structure, will be covered in detail in this chapter.

5.2 Modeling of External Hydraulic System

Before presenting the quasi-static active valve design procedure, the modeling of the fluid-flow relations in the MHT system external to the active valve structure must be discussed. The inlet active valve within the example MHT power harvesting device regulates flow from the high pressure reservoir to the harvesting chamber. As fluid passes over the valve membrane and cap, it exerts pressures on these structures. These pressures and flow rates are a function

of the opening and closing action of the valve cap against its stop, the geometry of the fluid channel that carries fluid from the valve to the chamber, and the effective hydraulic stiffness of the harvesting chamber being filled. This section details the techniques used to model the pressure-flow relations for each of these system features. In the following discussions, it is assumed that that inlet and outlet valves operate each with a 50% duty cycle, ie: the inlet valve is open exactly for the first half of the MHT system period $T_{sys} = \frac{2\pi}{f_{sys}}$ while the outlet valve is open for exactly the second half of the system period.

5.2.1 MHT Chamber Stiffness

During the first half of a complete device cycle, the inlet valve is open and the outlet valve is closed. As fluid passes through the valve into the harvesting chamber, the chamber pressure increases. The relationship between the amount of fluid entering the chamber and the pressure rise within the chamber is determined by the effective hydraulic chamber stiffness, K_{EHC} . Figure 5.2(a) shows a simplified schematic of this filling process.

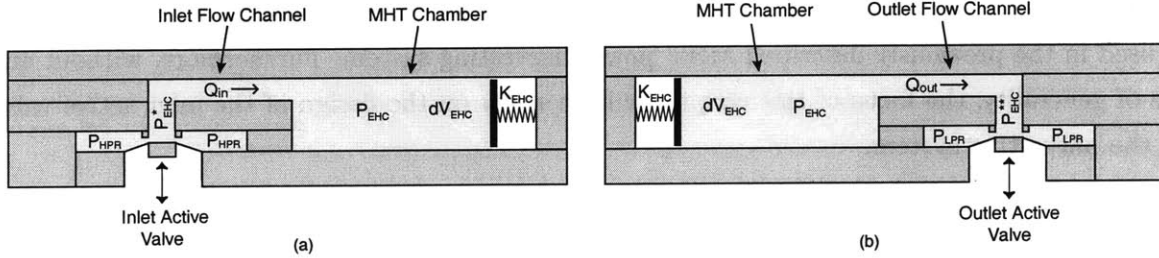


Figure 5.2: Filling and evacuation models for an MHT system: (a) During inlet valve opening and closing, fluid fills the harvesting chamber. (b) During outlet valve opening and closing, fluid evacuates the harvesting chamber. The associated chamber pressure time history $P_{EHC}(t)$ during filling and evacuation is a function of the amount of fluid entering/evacuating the chamber and the chamber volumetric stiffness K_{EHC} .

K_{EHC} is a function of the chamber geometry, material properties, and fluid initial volume. A large K_{EHC} means that a small amount of fluid $dV_{EHC} = \int Q_{in}(t)dt$ flowing into the chamber will result in a large increase in chamber pressure P_{EHC} , whereas a small K_{EHC} means that even a large amount of fluid flow into the chamber will result in only a small chamber pressure increase. The chamber pressure increase as a function of time can be written as

$$\frac{dP_{EHC}}{dt} = K_{EHC}Q_{in}(t). \quad (5.1)$$

A similar model can be used to evaluate the evacuation of fluid through the outlet valve, resulting in a chamber pressure decrease as fluid flows to a low pressure P_{LPR} (see Figure

5.2(b)). For the purposes of this thesis, however, only the inlet valve and corresponding filling of the harvesting chamber are considered.

5.2.2 Valve Channel Inertial Effects

Fluid inertial effects within the flow channel connecting the valve to the harvesting chamber can play a significant role in determining the difference between $P_{EHC}^*(t)$ and $P_{EHC}(t)$ during device operation. This pressure-flow relation can be written as

$$P_{EHC}^*(t) - P_{EHC}(t) = \left(\frac{\rho L_c}{A_c} \right) \dot{Q}_{in} \quad (5.2)$$

where ρ is the fluid density, L_c is the channel length, and A_c is the channel area. For a long channel with small cross-section area, one can expect fluid inertial effects to play a significant role as the pressure P_{EHC}^* builds up to accelerate the fluid slug into the chamber. Conversely, for short channels with large areas, the inertial effects are negligible and the pressure $P_{EHC}^*(t)$ and $P_{EHC}(t)$ will not differ at all. It is important to be aware of these inertial effects when designing and modeling any sort of hydraulic system that contains small channels.

5.2.3 Valve Orifice Flow Relations

Work by previous researchers [3] [4] [5] has shown that for small openings, poppet valves (such as the valve cap in this proposed active valve device) behave as long orifices in which the effects of flow separation and subsequent reattachment dominate the valve flow dynamics.

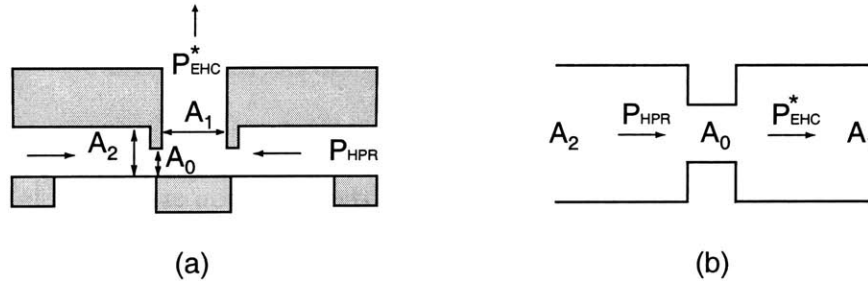


Figure 5.3: Valve orifice representation: (a) valve cap geometry and fluid flow areas, (b) representation of flow through valve as a flow contraction followed by a flow expansion.

Qualitatively, the valve flow can be approximated by a simplified order-of-magnitude valve model. The valve orifice may be characterized as a flow contraction followed by a flow expansion as shown in Figure 5.3(a) and (b). An integral analysis gives a relationship for the combined effect of the flow expansion and contraction. The loss coefficient $\zeta_{orifice}$ is defined as the total

pressure drop $\Delta P = P_{HPR} - P_{EHC}^*$ over the dynamic pressure based on the orifice local mean velocity ($\bar{u} = \frac{Q}{A_o}$)

$$\zeta_{orifice} = \frac{\Delta P}{\frac{1}{2}\rho\bar{u}^2} = \left[\frac{1}{2} \left(1 - \frac{A_0}{A_1}\right)^{\frac{3}{4}} + \left(1 - \frac{A_0}{A_2}\right)^2 \right] \quad (5.3)$$

where the upstream flow area can be approximated as $A_2 = 2\pi R_{vc} H_{upstream}$, the throat area can be approximated by $A_0 = 2\pi R_{vc} Z_{stroke}$, and the downstream flow area can be approximated as $A_1 = \pi R_{vc}^2 \cdot H_{upstream}$. $H_{upstream}$ is the height of the radial flow channel above the valve membrane to the cap and Z_{stroke} is the valve cap opening distance from the valve stop structure.

This approximation, however, is independent of the Reynolds number and therefore holds only for $Re > 10,000$, where fully turbulent flow regimes exist. In microfluidic systems, such as the MHT power harvesting device, Reynolds numbers are expected to fluctuate between approximately 10 and 20,000 as the valve opens and closes [2]. For this reason, correction factors (obtained from experimental results) need to be employed to obtain better estimates of the loss coefficients for these low turbulence and laminar flow regimes [2]. A loss coefficient for each of the contraction and expansion geometries ($\zeta_{contraction}$ and $\zeta_{expansion}$, respectively) is used to approximate the total loss coefficient through the valve, as detailed in the following relation

$$\zeta_{orifice}^* = \zeta_{contraction}(Re, \frac{A_0}{A_2}) + \zeta_{expansion}(Re, \frac{A_0}{A_1}) \quad (5.4)$$

where the Reynolds number is defined as

$$Re = \frac{1}{\pi} \frac{Q}{R_{vc}\nu}. \quad (5.5)$$

Figure 5.4(a) plots $\zeta_{contraction}$ as a function of Re and the contraction area ratio $\frac{A_0}{A_2}$ and Figure 5.4(b) plots $\zeta_{expansion}$ as a function of Re and the expansion area ratio $\frac{A_0}{A_1}$. As a result, the pressure-flow relation for the full valve orifice geometry can be written as

$$\Delta P = P_{HPR} - P_{EHC}^* = \frac{1}{2}\rho\zeta_{orifice}^* \left(\frac{Q^2}{A_0^2}\right). \quad (5.6)$$

All subsequent fluid models discussed in this thesis incorporate these higher-order correction factors to obtain an accurate estimation of the flow behavior. These flow models are based on steady flow phenomenon and do not capture frequency dependent losses. The following assumptions are made to define the valve cap and membrane areas over which the upstream pressure P_{HPR} and the downstream pressure P_{EHC}^* act. Since the valve cap stroke during

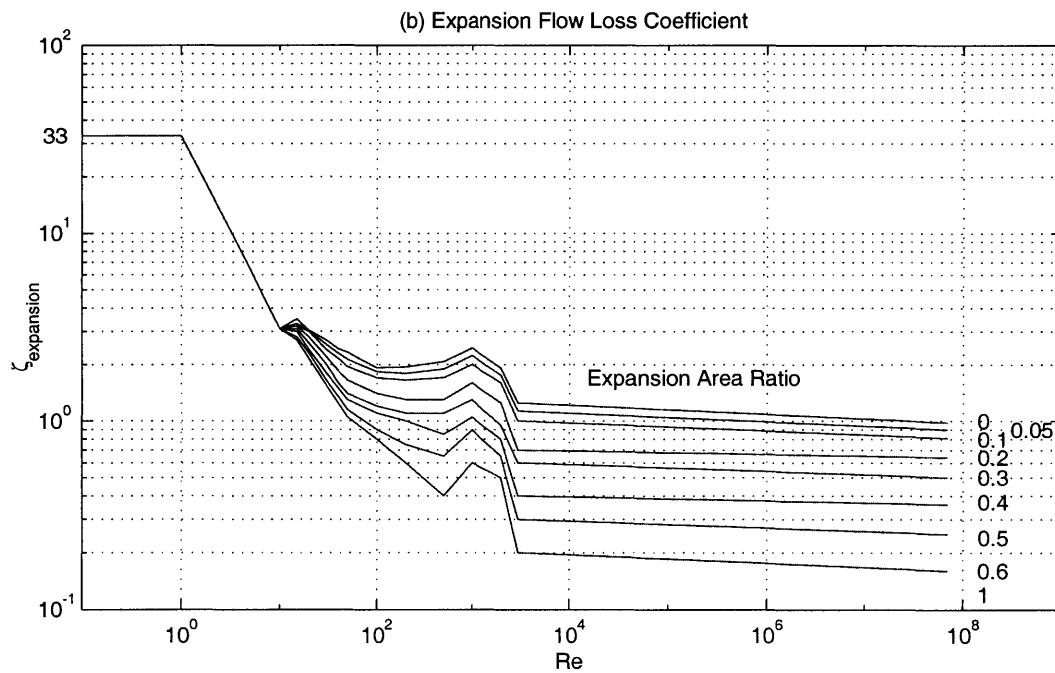
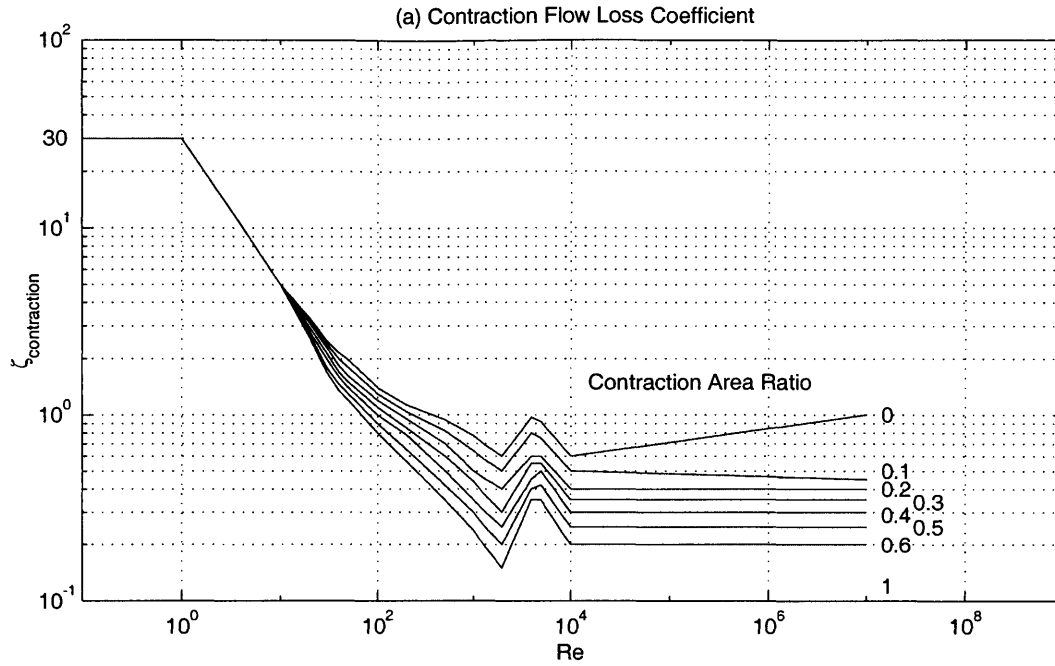


Figure 5.4: Look-Up Tables for flow loss contraction and expansion coefficients. For further details, see [2].

operation is significantly less than $H_{upstream}$, R_{vm} , and R_{vc} , the majority of pressure drop through the valve structures occurs across the contraction and expansion at the valve cap circumference. As a result, at any given instant of time, the pressure acting over the valve membrane area can be approximated as the reservoir pressure P_{HPR} and the pressure acting over the valve cap area can be approximated as P_{EHC}^* . For a specific value of valve cap opening at a given time during the cycle, a relationship therefore exists for the instantaneous fluid flow through the valve as a function of the pressure drop across the valve.

5.2.4 Chamber Filling Simulation Tool

The previously described pressure-flow relations for the harvesting chamber stiffness, valve orifice, and flow channel connecting the valve and chamber can be recast in SimulinkTM to create a simulation tool for fluid filling of the harvesting chamber. For known dimensions of the valve cap, the surrounding structure forming the upstream and downstream flow areas, the valve channel dimensions, the harvesting chamber dimensions and material properties, P_{HPR} , and the desired minimum pressure in the harvesting chamber $P_{EHC,min}$ (the pressure immediately when the outlet valve has closed), and for an assumed valve cap opening profile $Z_{vc,opening}$, the filling behavior of the system through the inlet valve orifice can be simulated. Figure 5.5 illustrates the high-level SimulinkTM model, and Figure 5.6 shows the fluid orifice and valve channel block diagram structure.

A major assumption underlying this simulation is that the accompanying outlet valve of the MHT system has been designed properly to ensure that the harvesting chamber pressure P_{EHC} has decreased to a value of $P_{EHC,min}$ at the instant the outlet valve fully closes. Furthermore, the variable $Z_{vc,opening}$ is the distance between the valve stop and the surface of the valve cap. For example, if the valve being modeled is forced to experience a sinusoidal absolute deflection history from $Z_{vc} = -20\mu m$ (fully open) to $Z_{vc} = +20\mu m$ (fully closed), the corresponding $Z_{vc,opening}$ values are $Z_{vc,opening} = +40\mu m$ (fully open) to $Z_{vc,opening} = 0\mu m$ (fully closed).

This filling simulation will be an important part of the systematic active valve design procedure detailed in the following sections. It will allow for the determination of a valve cap size and imposed valve opening so as to achieve the required P_{EHC} pressure excursion during MHT system filling.

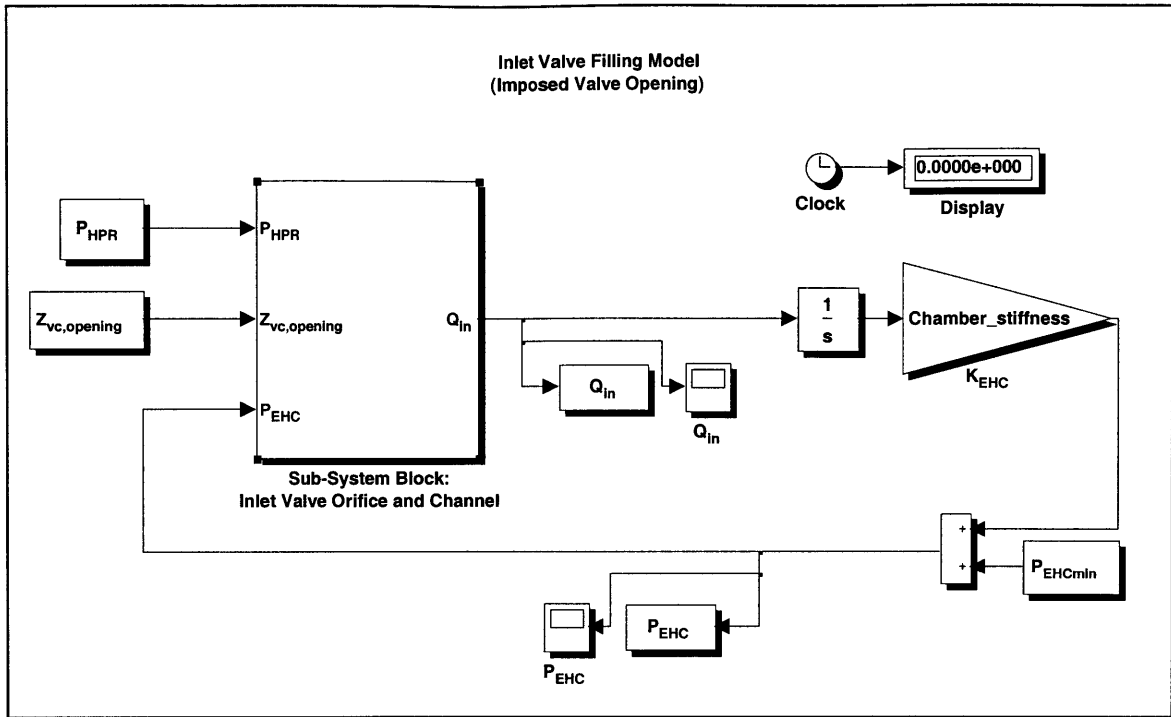


Figure 5.5: SimulinkTM high-level simulation overview for filling of the MHT system through the inlet active valve.

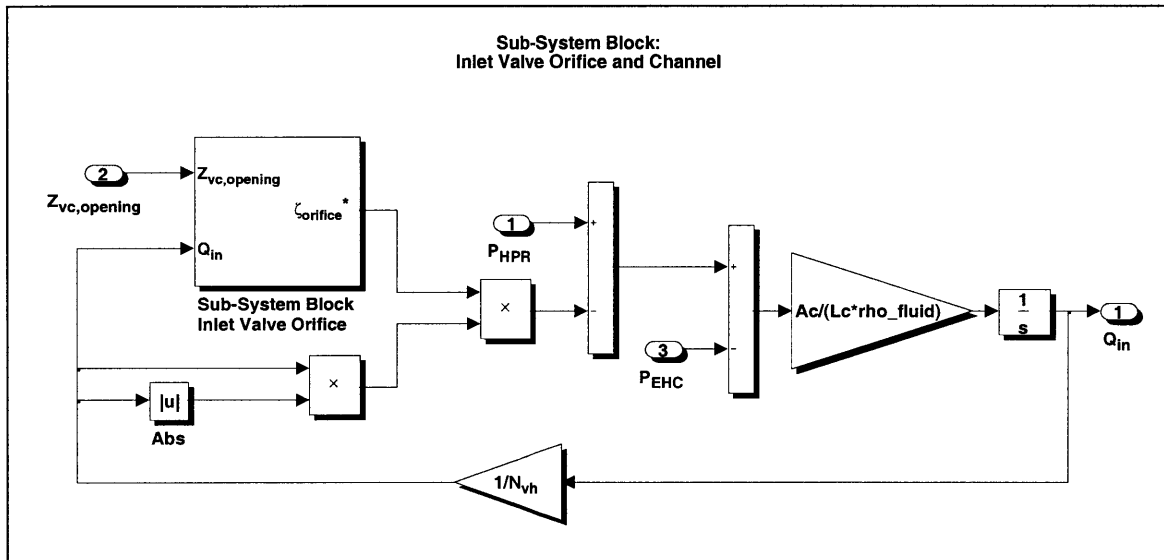


Figure 5.6: SimulinkTM valve orifice and channel sub-system block for filling of the MHT system through the inlet active valve.

5.3 Systematic Design Procedure

This section introduces a systematic design procedure that can be implemented to calculate dimensions of the valve cap, valve membrane, hydraulic amplification chamber, and drive element portion of the inlet active valve to satisfy requirements set forth by the external hydraulic system. This design procedure is based upon quasi-static valve piston and valve cap behavior (ie: $\ddot{Z}_{vc} = \dot{Z}_{vc} = \ddot{Z}_{pis} = \dot{Z}_{pis} = 0$). Depending upon the frequency of operation, this assumption may or may not be a valid one, since system dynamic effects could come into play. It is therefore the purpose of this quasi-static design procedure to generate a valve design, from which a full dynamic simulation can be run to evaluate the goodness of the design and be used as a tool for fine-tuning the valve geometry.

5.3.1 Overview

Figure 5.7 presents a generalized flowchart for this quasi-static design process. Given external system requirements, such as the chamber stiffness K_{EHC} , the P_{EHC} pressure fluctuation from a $P_{EHC,min}$ to a $P_{EHC,max}$ during filling, the reservoir pressure P_{HPR} , and the overall desired system frequency f_{sys} , the following steps are carried out:

1. The valve cap radius R_{vc} (for a chosen valve stroke Z_{stroke}) is calculated to allow for adequate filling of the harvesting chamber.
2. The valve membrane outer radius R_{vm} and required $P_{HAC}(t)$ time history (for a given membrane thickness t_{vm}) are calculated to allow for motion of the cap along its desired trajectory against the known external loads while at the same time ensuring membrane stresses below critical levels.
3. The drive element piston area A_{pis} and piezo area A_p are calculated to provide a stiffness match between the drive piston structure and the load that it encounters and to ensure adequate actuation capabilities.

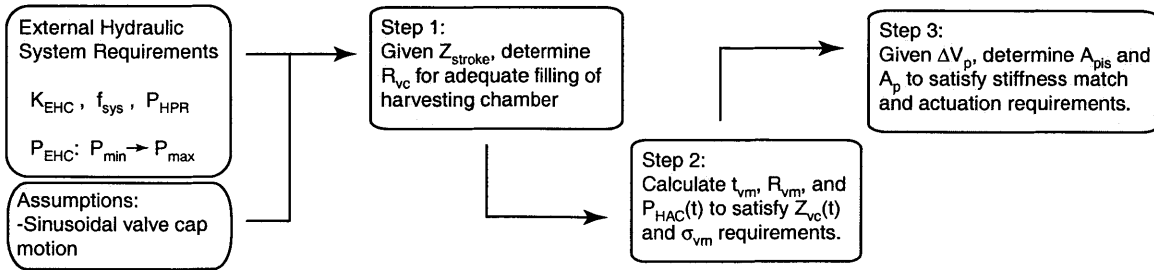


Figure 5.7: Flowchart illustrating the design procedure for the inlet active valve.

The full active valve design procedure, which will be discussed in Section 5.6, includes the ability to consider single valve cap and membrane designs as well as multiple valve cap and membrane designs (from now on N_{vh} is designated as the number of valve heads in the design), varying valve cap strokes $Z_{vc,stroke}$, and varying valve membrane thicknesses t_{vm} . There are important and interesting design issues associated with each of these design freedoms. Sections 5.4.1, 5.4.2, and 5.5 detail these issues. However, in this section, in order to present clearly the physical intuition behind the main steps in the design procedure, the following assumptions are made. First, this section focuses on generation of a single valve cap and membrane valve design. Second, in Step 1 when calculating the valve cap radius for adequate filling of the harvesting chamber, a value for $Z_{vc,stroke}$ is assumed. Third, in Step 2, the valve membrane radius R_{vm} and required $P_{HAC}(t)$ are calculated for an assumed valve membrane thickness t_{vm} .

5.3.2 System Requirements

To facilitate the understanding of the basic steps in the design procedure detailed in the following subsections, numerical system requirements characteristic of a typical MHT are presented here. For $P_{HPR} = 1.2MPa$, the inlet valve opens in a sinusoidal manner to fill a harvesting chamber with $K_{EHC} = 1.5e^{16} \frac{Pa}{m^3}$. The system frequency is chosen to be $f_{sys} = 10kHz$ and it is desired that during this filling process, P_{EHC} should rise from a minimum pressure $P_{min} = 0.2MPa$ to a maximum pressure $P_{max} = 1.0MPa$. It is assumed that the outlet valve is designed properly to allow evacuation from $P_{max} = 1.0MPa$ to $P_{min} = 0.2MPa$ during the time that the inlet valve is closed. In addition, for this example system, the channel dimensions L_c and A_c are chosen to ensure that fluid inertial effects in the channel are negligible (ie: $P_{EHC} = P_{EHC}^*$ at all times).

5.3.3 Step 1: Design of Valve Cap

In the first step of the design procedure, the valve cap radius R_{vc} is calculated so as to allow for exact filling of the harvesting chamber. With the imposed valve cap motion $Z_{vc}(t)$ and the external hydraulic system modeling tools described in Section 5.2, R_{vc} is determined such that the pressure rise in the harvesting chamber increases from its initial minimum of P_{min} to the desired maximum pressure P_{max} at the time the valve completely closes again. In this example procedure, the valve cap stroke is taken to be $Z_{stroke} = 40\mu m$. Equations 5.1, 5.2, 5.3, 5.6 are solved in the previously described Simulink simulation for this purpose. Insufficient filling will result if R_{vc} is not large enough. Conversely, if R_{vc} is too large, the chamber will be filled in excess. Figure 5.8 illustrates adequate and inadequate filling scenarios.

For the example MHT system, a value of $R_{vc} = 241\mu m$ is determined, through iteration, that results in a harvesting chamber pressure rise from $P_{EHC} = 0.2MPa$ to $P_{EHC} = 1.0MPa$

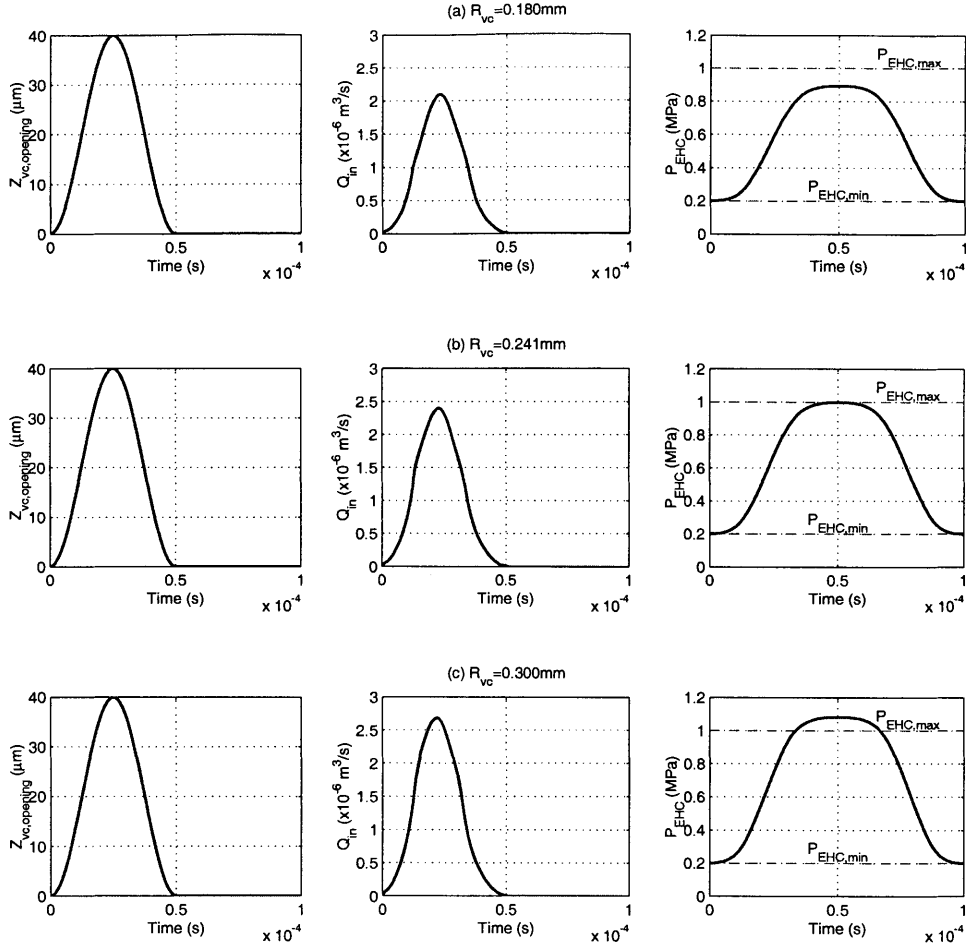


Figure 5.8: Chamber filling plots corresponding to $Z_{stroke} = 40\mu m$ and differing values of R_{vc} : (a) if $R_{vc} = 180\mu m$, the chamber can not fill adequately, (b) if $R_{vc} = 241\mu m$, the chamber fills the desired amount, and (c) if $R_{vc} = 300\mu m$, the chamber fills in excess of the desired amount.

during the time that the inlet valve is open. Figure 5.8(b) displays the imposed valve cap deflection, the corresponding flow rate Q_{in} through the valve, and the resulting $P_{EHC}(t)$ time history for this case. The valve is completely closed when $Z_{vc,opening} = 0\mu m$ and is fully open when $Z_{vc,opening} = +40\mu m$. Note that the chamber fills properly since the pressure at the instant of valve closing is 1.0 MPa. Since a complete $P_{EHC}(t)$ time history is needed for further steps in the design procedure, it is assumed that an outlet valve for the system has been sufficiently designed to evacuate the fluid during the second half of the device cycle. Figure 5.8(a) shows the corresponding results for the case where the valve cap radius is too small, $R_{vc} = 180\mu m$. Here, the chamber pressure is only able to rise to $P_{EHC} = 0.9MPa$ at the instant the inlet valve closes. Figure 5.8(c) shows the corresponding results for the case where the valve cap radius is too large, $R_{vc} = 300\mu m$. Here, the chamber pressure rises in excess of

the desired value to $P_{EHC} = 1.08MPa$ at the instant the inlet valve closes.

5.3.4 Step 2: Design of Valve Membrane

In the second step of the design procedure, for a given valve membrane thickness t_{vm} , the outer membrane radius R_{vm} and required $P_{HAC}(t)$ time history are calculated such that the valve cap properly follows its imposed trajectory $Z_{vc}(t)$ and experiences a maximum tensile membrane stress during this motion of $\sigma_{vm} = \sigma_{limit}$. The code calculates the entire stress field along the membrane, however it records only the maximum tensile value for each time instant during the cycle and calls it σ_{vm} . A limiting value for $\sigma_{limit} = 1.0GPa$ is taken from [6] [5]. Since a small value of t_{vm} is desired to minimize actuation requirements, an initial value of $t_{vm} = 7\mu m$ is employed. For the given value of t_{vm} , a guess for R_{vm} is taken. Under the constant P_{HPR} loading on the valve membrane and the time-varying loading $P_{EHC}^*(t)$ on the valve cap calculated in Step 1, the required $P_{HAC}(t)$ time history is calculated to force the valve membrane and cap to follow its imposed trajectory $Z_{vc}(t)$. During this time cycle, σ_{vm} is monitored. This procedure becomes an iterative process in R_{vm} until a value of R_{vm} is determined such that at some time during the complete cycle, a peak tensile stress of σ_{limit} is reached. As will be discussed in Section 5.4.2, it might be the case that it is impossible to arrive at a membrane design for this particular value of t_{vm} due to high stresses in the membrane, at which point it will be necessary to increase the membrane thickness. However, this issue is held off until Section 5.4.2.

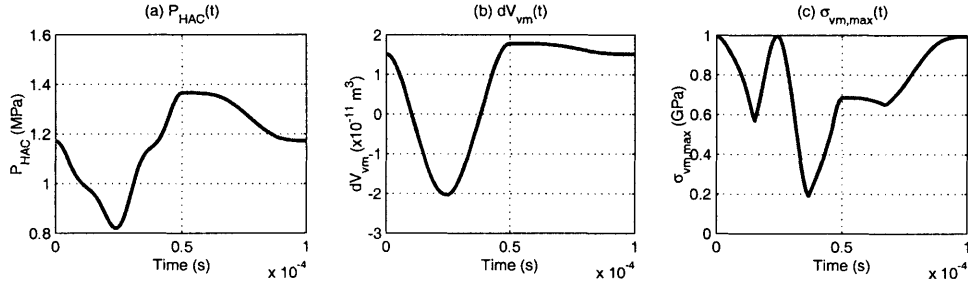


Figure 5.9: Valve membrane behavior corresponding to $Z_{stroke} = 40\mu m$, $R_{vc} = 241\mu m$, $t_{vm} = 7\mu m$, and $R_{vm} = 757\mu m$: (a) required hydraulic amplification chamber $P_{HAC}(t)$, (b) corresponding valve cap and membrane swept volume $dV_{vm}(t)$, and (c) peak stress in valve membrane $\sigma_{vm}(t)$.

For the example MHT system, a value of $R_{vm} = 757\mu m$ is determined for $t_{vm} = 7\mu m$. The required $P_{HAC}(t)$ time history, swept volume time history under the membrane and cap $dV_{vm}(t)$, and the associated membrane stress time history $\sigma_{vm}(t)$ are shown in Figures 5.9(a), (b), and (c) respectively. In Figure 5.9(c), notice that the maximum stress in the membrane during the cycle occurs when the cap is deflected to its minimum value of $Z_{vc} = -20\mu m$. The

membrane again experiences a stress of $1.0GPa$ when the cap is at its maximum deflection of $Z_{vc} = +20\mu m$. This reconfirms the design choice to force the membrane into symmetric upward and downward motion so as to maximize total valve cap stroke when restricted to limited membrane stress levels.

5.3.5 Step 3: Design of Piezoelectric Drive Element

In the third step of the design procedure, the piezoelectric material area and drive element piston area are determined so as to create a quasi-static stiffness match with the loading seen by this structure. The goal in doing this is to maximize the energy transfer from the piezoelectric material to the load. As shown in Figure 5.10, the valve cap/membrane and external hydraulic system appear to the drive structure as a stiffness K_{vm} in series with a fluid stiffness K_{HAC} of the hydraulic amplification chamber. A linearization of the actuation curve associated with the motion of the valve cap (described by the time histories $P_{HAC}(t)$ and $dV_{vm}(t)$ calculated in Step 2 of the design procedure and plotted against one another in Figure 5.10(a)) provides an approximation for this K_{vm} stiffness. Combining K_{vm} and K_{HAC} together produces an overall load K_{load} seen by the piezoelectric element. This model neglects the stiffness of the drive piston tethers. Studies have shown that the stiffnesses of these tethers in relation to the K_{vm} and K_{HAC} are small for typical active valve designs. The requirement of a stiffness match between K_{piezo} and K_{load} therefore results in the following equality,

$$K_{piezo} = K_{load} \quad \rightarrow \quad \frac{E_p A_p}{L_p} = \frac{A_{pis}^2}{\left(\frac{\Delta V_{vm}}{\Delta P_{HAC}}\right) + \left(\frac{A_{pis} H_{HAC}}{K_{fluid}}\right)}. \quad (5.7)$$

Substituting this requirement into the following piezoelectric material actuator equation, one obtains a relationship between Z_p and V_p ,

$$Z_p = d_{33} V_p - \frac{F_p}{K_p} = d_{33} V_p - \left(\frac{K_{load}}{K_{piezo}}\right) Z_p \quad \rightarrow \quad Z_p = \frac{1}{2} d_{33} V_p. \quad (5.8)$$

In addition to this impedance match requirement on Z_p , Z_p must also satisfy the volume conservation relation within the active valve structure,

$$Z_p = \frac{\Delta V_{de}}{A_{pis}} = \frac{\Delta V_{vm} + \Delta V_{fluid}}{A_{pis}} = \left(\frac{1}{A_{pis}}\right) \left[\Delta V_{vm} + \left(\frac{A_{pis} H_{HAC}}{K_{fluid}}\right) \Delta P_{HAC}\right]. \quad (5.9)$$

Eliminating Z_p in Equations 5.8 and 5.9 results in the following equality,

$$\frac{1}{2} d_{33} V_p = \left(\frac{1}{A_{pis}}\right) \left[\Delta V_{vm} + \left(\frac{A_{pis} H_{HAC}}{K_{fluid}}\right) \Delta P_{HAC}\right]. \quad (5.10)$$

Therefore, equations 5.7 and 5.10 form a set of two equations with three unknowns A_{pis} , A_p , and V_p . Equation 5.7 sets the relationship between A_{pis} and A_p for a stiffness match between piezo and load to be achieved while equation 5.10 defines the condition under which valve performance is met, relating the input piezo voltage V_p to the A_{pis} . In observing these equations, it is clear that the smaller the voltage V_p , the larger the values of A_{pis} and A_p need to be. Since one of the goals in the design of this active valve is make its total volume as small as possible, this implies that the valve should work at as large a voltage as possible. In real devices, a limitation of electrical breakdown across the air gap between drive element piston and the bottom structural plate exists, and therefore a maximum allowable V_p for the given piezo length L_p is set. As a result, in the design of this valve, voltage now becomes an imposed quantity. The set of two equations can be solved for the two remaining geometric free design variables A_{pis} and A_p to create a quasi-static stiffness match condition between the piezo and load and to ensure adequate valve performance to satisfy the actuation requirements passed down from the membrane and cap design steps.

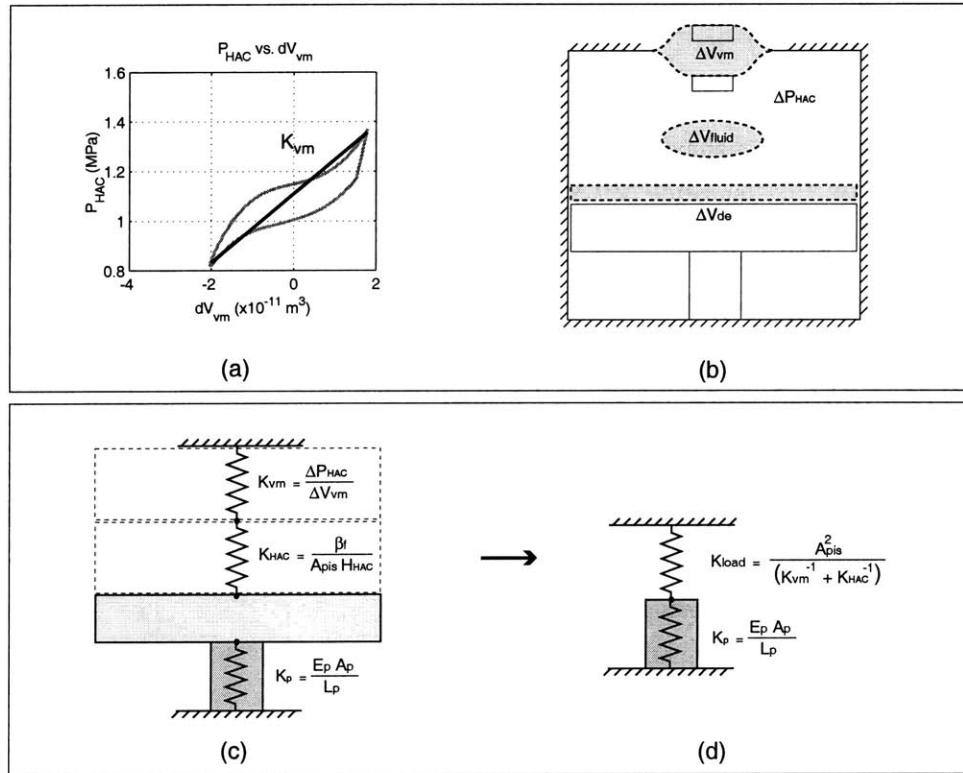


Figure 5.10: Simplification of the active valve device in a quasi-static stiffness match analogy: (a) determination of linearized K_{vm} stiffness load, (b) important actuation volume change and pressure variables, (c) valve membrane volumetric stiffness in series with fluid hydraulic stiffness acting through piston area against piezo displacement stiffness, and (d) lumped linear load spring acting against piezo material.

For the example MHT system, the piezoelectric material thickness is assumed to be $L_p = 1mm$ and the applied peak-peak voltage is assumed to be $V_p = 1000V$. Under these assumptions, a drive piston area and piezo area are calculated to correspond to $R_{pis} = 3.59mm$ and $R_p = 0.88mm$. Figures 5.11(a), (b), and (c) show the required piezoelectric voltage time history V_p to force the valve cap to follow the desired trajectory $Z_{vc}(t)$, the drive element P_{HAC} vs. dV_{de} actuation curve, and the resulting piezoelectric material stress time history T_p , respectively. In comparing Figure 5.11(b) to Figure 5.10(a), notice the increased volume change between dV_{de} and dV_{vm} . This difference is exactly equal to the fluid compressibility volume change dV_{HAC} under the pressure loading $P_{HAC}(t)$. At this point, a design for the active valve has been achieved.

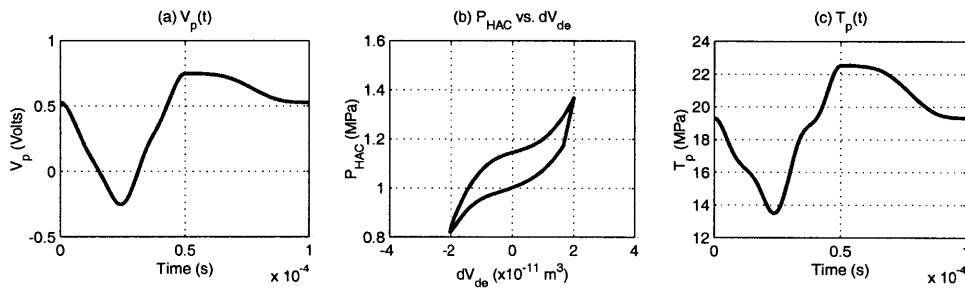


Figure 5.11: Drive element behavior corresponding to $R_{pis} = 3.59mm$ and $R_p = 0.88mm$: (a) required piezoelectric voltage $V_p(t)$, (b) corresponding drive element actuation curve, and (c) stress on piezoelectric material $T_p(t)$.

5.4 Design Freedoms Within Procedure

The basic design procedure for the active valve discussed in Section 5.3 was simplified in three ways in order to ease the explanation of the main steps. First, the valve design was carried out for a valve geometry with only a single valve cap and membrane above the hydraulic amplification chamber ($N_{vh} = 1$). Second, the design assumed a predetermined stroke $Z_{vc,stroke}$ of the valve cap. Third, the design assumed that a value of t_{vm} could be chosen that would result in the successful calculation of the valve membrane outer radius R_{vm} to guarantee stresses below a limiting value. In reality, when designing the active valve structure, one would like to relax all three of these design restrictions so that the design process creates an optimal valve geometry. It might therefore be the case that the optimal active valve design uses five valve caps and membranes in parallel above the hydraulic amplification chamber rather than a single valve cap and membrane, or that the stroke(s) of the valve cap(s) should be $20\mu m$ rather than $40\mu m$, or that $8\mu m$ is the minimal valve membrane thickness that can be used to create a strong enough valve membrane structure. This section will discuss two of these three design freedoms, $Z_{vc,stroke}$ and t_{vm} . The third design freedom, N_{vh} , will be discussed in Section 5.5. All three design freedoms will then be included in the final systematic design procedure presented in Section 5.6.

5.4.1 Design Freedom: $Z_{vc,stroke}$

In the example active valve design procedure presented in Section 5.3, the required valve cap size R_{vc} was calculated that would allow for adequate filling of the harvesting chamber, given that the valve cap was allowed to move through a stroke of $Z_{vc,stroke} = 40\mu m$. It would have also been possible to determine a value for R_{vc} if $Z_{vc,stroke} = 20\mu m$. To maintain fluid flow resistance through the valve structure, it makes sense that as the valve cap stroke is decreased, the radius of the valve cap itself must be increased. Figure 5.12 displays the calculated valve cap radius R_{vc} for a series of different valve cap strokes $Z_{vc,stroke}$ for the example MHT system described in the previous section. For an imposed $Z_{vc,stroke} = 40\mu m$, the design code simulation requires a value of $R_{vc} = 241\mu m$ to ensure proper filling of the harvesting chamber. Alternatively, for an imposed $Z_{vc,stroke} = 20\mu m$, the design code simulation requires a value of $R_{vc} = 688\mu m$ to ensure proper filling of the harvesting chamber. Therefore, different combinations of $Z_{vc,stroke}$ and R_{vc} can effectively fill the chamber, but as the full design procedure in Section 5.6 will illustrate, one combination may be better than others in designing the remaining structures of the valve.

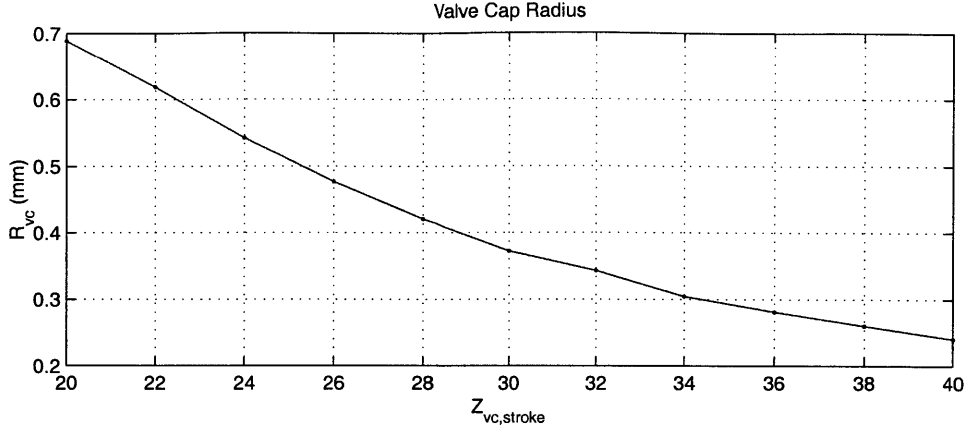


Figure 5.12: Design of valve cap, for $P_{HPR} = 1.2MPa$, $f_{sys} = 10kHz$, $P_{EHC,min} = 0.2MPa$, $P_{EHC,max} = 1.0MPa$, and varying $Z_{vc,stroke}$.

5.4.2 Design Freedom: t_{vm}

For a given size valve cap (value of R_{vc}), the next step in the design procedure is to design a membrane structure which can carry this valve cap through the imposed opening time history against the external pressure loadings, P_{HPR} and $P_{EHC}(t)$. During filling of the chamber, as was discussed in previous sections, P_{HPR} is constant with time over the valve membrane, however, P_{EHC} varies from a minimum to a maximum. The valve membrane radius R_{vm} and thickness t_{vm} must be determined to achieve the desired behavior.

Two example studies will be included in this section to illustrate some important issues concerning the design of the valve membrane structure. The first study will look at the design of the valve membranes for each of the valve cap sizes arrived at in Section 5.4.1, assuming that $P_{HPR} = P_{EHC} = 1.2MPa$ for all time during the opening and closing of the valve cap and membrane. This situation, where the pressures above the cap and membrane structure are constant with time, would never occur in reality. However, the purpose of this study is to illustrate an important point associated with the structural design of the membrane. The second study will then focus on the real case, where $P_{HPR} = 1.2MPa$ during opening and closing, but P_{EHC} does vary as calculated in the design code simulation. The overall conclusion from these comparative studies will be that this changing P_{EHC} pressure with time in certain circumstances does not allow for a valve design of a particular membrane thickness to be calculated that can satisfy the membrane stress limitations. In such cases, it will be necessary to iterate to larger membrane thicknesses to achieve a reasonable design.

Example Study: $P_{HPR} = 1.2MPa$ and $P_{EHC}(t) = 1.2MPa$

In this example study, for each of the valve cap designs presented in Figure 5.12, the design code calculates the valve membrane radius so that for the imposed valve cap displacements and under the constant external loading $P_{HPR} = P_{EHC} = 1.2MPa$, the membrane experiences a peak stress of $\sigma_{vm} = 1GPa$ during its opening/closing cycle. The valve membrane thickness is assumed to be $t_{vm} = 7\mu m$ for these calculations. This is really a lower limit for membrane thickness based on fabrication restrictions.

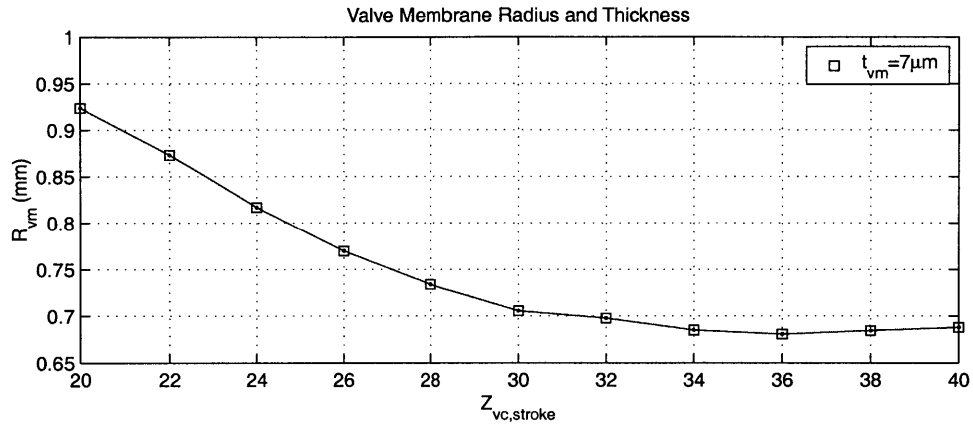


Figure 5.13: Design of valve membrane for the case where the external pressure loading on the valve cap and membrane are held constant during the time that the cap opens and closes, $P_{HPR} = P_{EHC} = 1.2MPa$ constant with time.

Figure 5.13 displays the calculated R_{vm} values for each of the imposed $Z_{vc,stroke}$ and previously calculated R_{vc} values. For an imposed $Z_{vc} = 40\mu m$ and therefore for the previously calculated $R_{vc} = 241\mu m$, the design code procedure calculates a membrane radius of $R_{vm} = 688\mu m$ to ensure stresses below the limit. For an imposed $Z_{vc} = 20\mu m$ and therefore for the previously calculated $R_{vc} = 688\mu m$, the design code procedure calculates a membrane radius of $R_{vm} = 924\mu m$ to ensure stresses below the limit. In all cases for the imposed valve cap stroke between $20\mu m$ and $40\mu m$, the membrane is able to designed with $t_{vm} = 7\mu m$.

To illustrate how the code determines R_{vm} , take the point design for an imposed $Z_{vc,stroke} = 20\mu m$. The valve cap radius has been previously calculated to be $R_{vc} = 688\mu m$. The code begins by guessing a value of R_{vm} , and then determines the required P_{HAC} pressure underneath the cap and membrane at each instant of time to satisfy the required cap displacement against the external pressure loadings. The membrane stress is recorded for all time instants during the complete opening/closing cycle of the valve cap. The code then iterates in R_{vm} until a value is determined that results in the desired peak stress occurring during the valve cap opening/closing cycle.

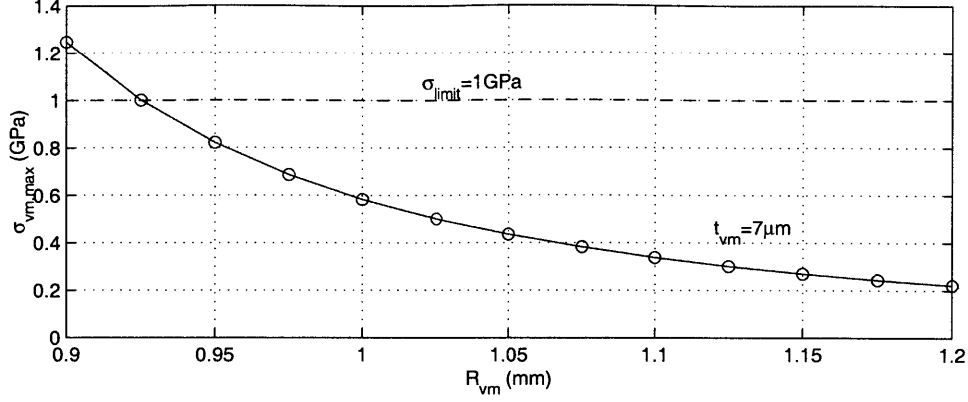


Figure 5.14: For $Z_{vc,stroke} = 20\mu m$, $R_{vc} = 688\mu m$, $P_{HPR} = P_{EHC} = 1.2MPa$ constant with time, and $t_{vm} = 7\mu m$, the membrane peak stress $\sigma_{vm,peak}$ during valve cap motion decreases as R_{vm} is decreased. An R_{vm} to meet the desired $\sigma_{vm,peak} = 1GPa$ can be determined.

Figure 5.14 plots the peak membrane stress during a complete valve membrane cycle for guesses of R_{vm} . Notice that the value of R_{vm} for which $\sigma_{vm,max} = 1.0$ is $924\mu m$. For a small value of $R_{vm} = 900\mu m$, the membrane stress reaches a peak stress of $\sigma_{vm} = 1.24GPa$ during the cycle, whereas for a large value of $R_{vm} = 1200\mu m$, the membrane stress reaches a peak stress of only $\sigma_{vm} = 0.22GPa$ during the cycle. For a value of $R_{vm} = 1010\mu m$ (chosen for demonstration purposes), a peak stress of $\sigma_{vm} = 0.52GPa$ during the cycle is determined. For all of these membrane designs, the peak stress occurs at the time during the cycle when the valve membrane is at peak positive displacement. Figure 5.15 illustrates the spatial displacement and stress distributions of the membrane for these three membrane designs. Notice in Figure 5.15(a), for $R_{vm} = 1200\mu m$, that the stress is low because of the minimal curvature in the membrane at the inner and outer boundaries. Also, there is only a slight shift in the mean stress on the top and bottom membrane surfaces (ie: the membrane is experiencing non-linear stretching of the neutral axis, but only slightly). In Figure 5.15(c), for $R_{vm} = 900\mu m$, the stress is high because of the significant curvature in the membrane at the inner and outer boundaries. In this case, there is a significant shift in the mean stress ($\sim 0.25GPa$) on the top and bottom membrane surfaces as the membrane experiences quite a bit of non-linear stretching. And in Figure 5.15(b), for $R_{vm} = 1010\mu m$, the membrane behavior is between the previous two cases.

The important conclusion from this example study with a constant P_{EHC} above the valve cap during the design of the valve membrane structure is that for the variety of valve cap strokes imposed, a valve membrane with thickness t_{vm} is able to be determined to satisfy the stress limitations. As will be shown in the following example study, as P_{EHC} is allowed to vary, as it would in a real system, different membrane thicknesses will have to be considered.

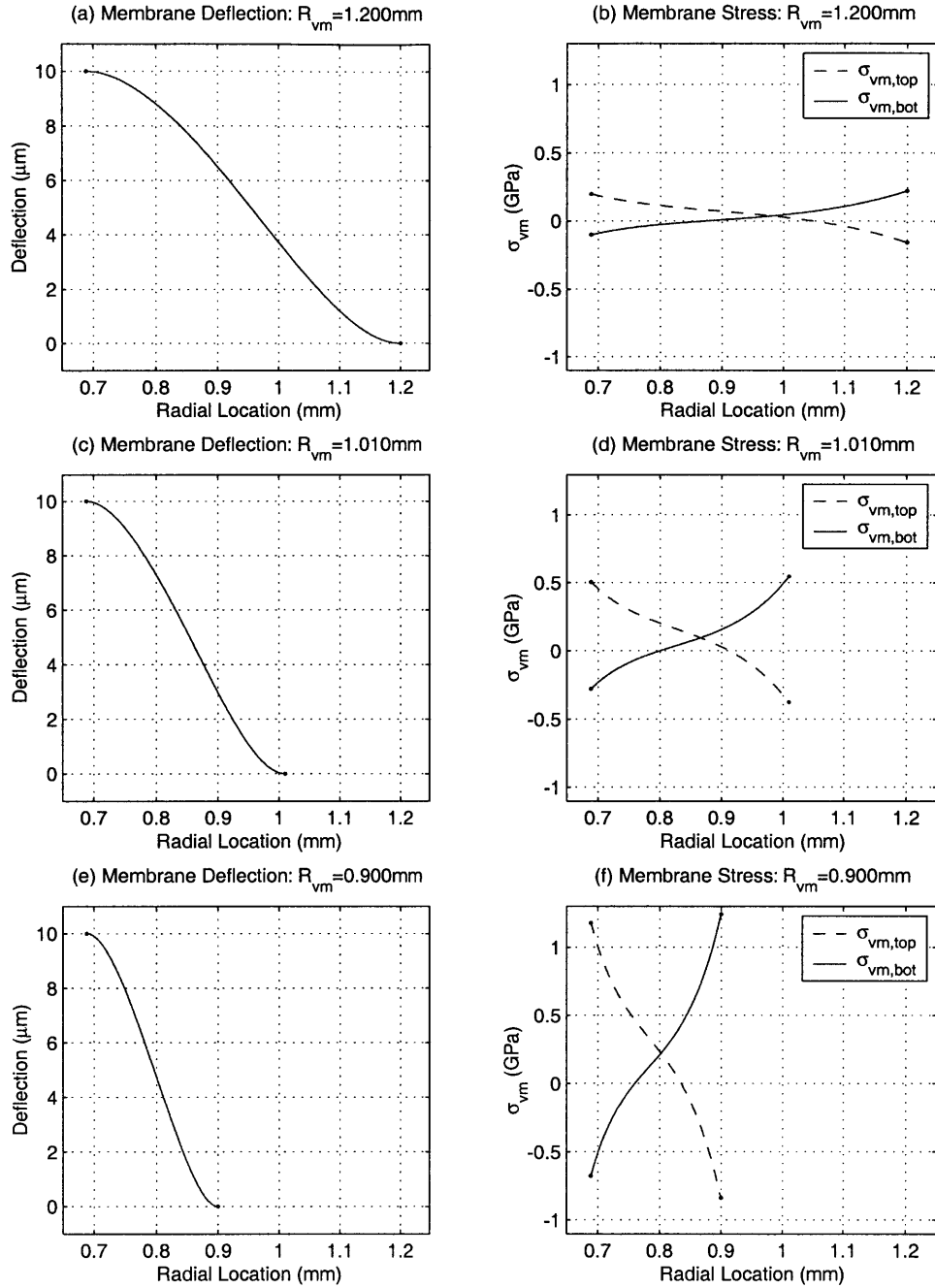


Figure 5.15: Example valve membrane deflection and stress plots for $Z_{vc,stroke} = 20\mu m$, $R_{vc} = 688\mu m$, $P_{HPR} = P_{EHC} = 1.2\text{MPa}$ constant with time, and $t_{vm} = 7\mu m$: (a) $R_{vm} = 1200\mu m$, (b) $R_{vm} = 1010\mu m$, and (c) $R_{vm} = 900\mu m$.

Example Study: $P_{HPR} = 1.2MPa$ and $P_{EHC}(t) = \text{varying}$

In this example study, for each of the valve cap designs presented in Figure 5.12, the design code calculates the valve membrane radius so that for the imposed valve cap displacements and under the external loading $P_{HPR} = 1.2MPa$ and $P_{EHC} = 0.2MPa \rightarrow 1.0MPa$, the membrane experiences a peak stress of $\sigma_{vm} = 1GPa$ during its opening/closing cycle. The valve membrane thickness is desired to be $t_{vm} = 7\mu m$ for these calculations, however, if a membrane design at a certain thickness can not be found, then the thickness is increased. Figure 5.16 displays the calculated R_{vm} values for each of the imposed $Z_{vc,stroke}$ and previously calculated R_{vc} values.

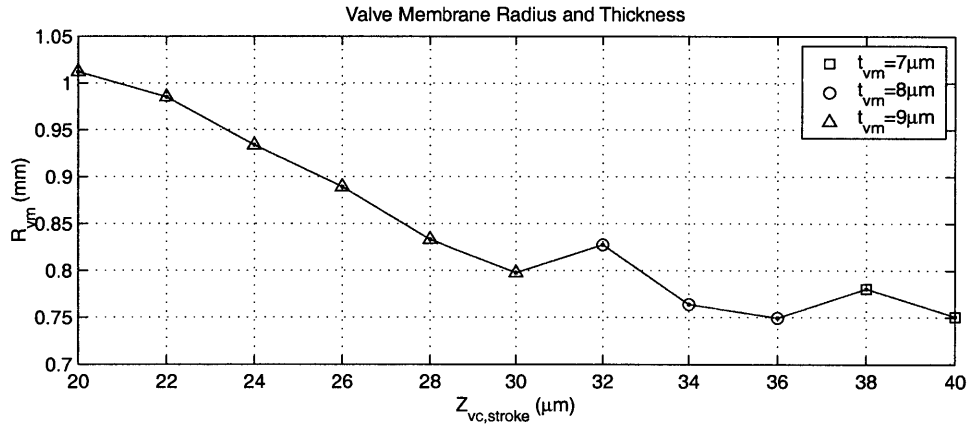


Figure 5.16: Design of the valve membrane for the case where $P_{HPR} = 1.2MPa$ and the external pressure loading on the valve cap P_{EHC} is allowed to vary with time, as it would in a real hydraulic system.

In comparison to the previous example study where a valve membrane with $t_{vm} = 7\mu m$ could be designed for each of the valve cap strokes, in this example study, as $Z_{vc,stroke}$ is reduced from $40\mu m$ to $20\mu m$, t_{vm} must be increased from $7\mu m$ so as to determine R_{vm} values that satisfy the stress requirements. This is a result of the changing P_{EHC} pressure over the valve cap as the cap moves through its cycle. For an imposed $Z_{vc,stroke} = 40\mu m$ and therefore for the previously calculated $R_{vc} = 241\mu m$, the design code procedure is able to determine a membrane radius of $R_{vm} = 751\mu m$ for $t_{vm} = 7\mu m$ to ensure stresses below the limit. For an imposed $Z_{vc,stroke} = 20\mu m$ and therefore for the previously calculated $R_{vc} = 688\mu m$, however, the design code procedure is not able to determine a satisfactory R_{vm} for either $t_{vm} = 7\mu m$ or $t_{vm} = 8\mu m$. Rather, it must increase the membrane thickness to $t_{vm} = 9\mu m$ in order to find a satisfactory membrane radius of $R_{vm} = 1010\mu m$ that ensures stresses below the limit.

Figure 5.17 plots the peak membrane stress during a complete valve membrane cycle for the case of imposed $Z_{vc,stroke} = 20\mu m$ for guesses of R_{vm} at the three thicknesses $t_{vm} = 7\mu m$, $t_{vm} = 8\mu m$, and $t_{vm} = 9\mu m$. For $t_{vm} = 7\mu m$, no value of R_{vm} can be chosen to bring

the stress below the critical limit of $\sigma_{limit} = 1GPa$. At this thickness, small values of R_{vm} and large values of R_{vm} both result in large stresses due to high membrane curvature at the membrane boundaries. In the case of small R_{vm} , the high curvature is a result of the membrane being so short in width, whereas for the case of large R_{vm} , the high curvature is a result of bowing of the membrane under the large negative pressure differential across the membrane (see later discussion). For $t_{vm} = 8\mu m$, again no value of R_{vm} can be determined, although the minimum of the curve is approaching σ_{limit} . Finally, for $t_{vm} = 9\mu m$, a valve membrane radius is achievable. In fact, there are two potential solutions, one at $R_{vm} = 1130\mu m$ and the other at $R_{vm} = 1015\mu m$. During the design procedure, the code picks the smaller of the two values, so as to minimize the valve size.

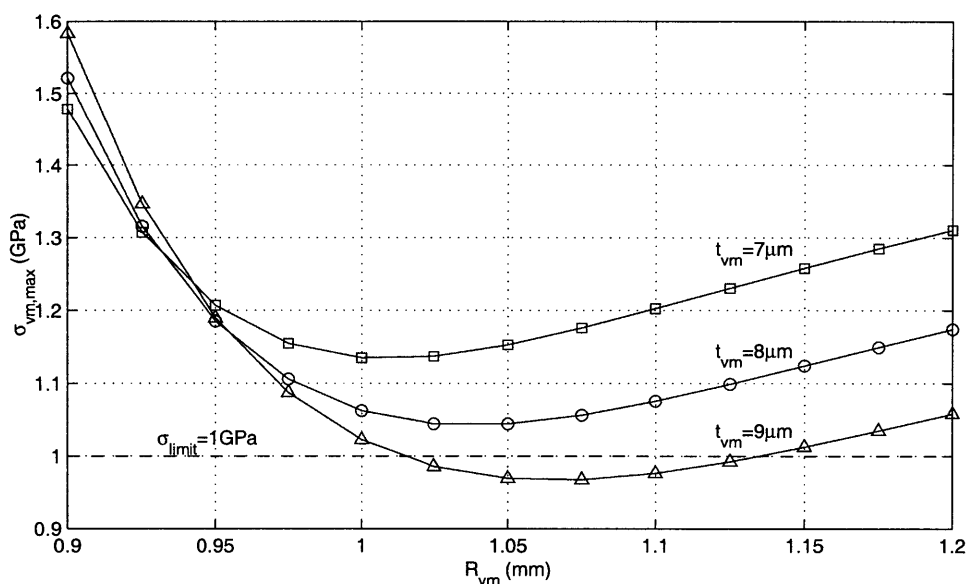


Figure 5.17: For $Z_{vc,stroke} = 20\mu m$, $R_{vc} = 688\mu m$, $P_{HPR} = 1.2MPa$, P_{EHC} varying with time, and for different t_{vm} , the membrane peak stress $\sigma_{vm,peak}$ during valve cap motion reaches a minimum at a particular R_{vm} . A satisfactory R_{vm} for $t_{vm} = 7\mu m$ and for $t_{vm} = 8\mu m$ can not be found, however an R_{vm} for $t_{vm} = 9\mu m$ can be determined to meet the desired $\sigma_{vm,peak} = 1GPa$.

Figure 5.15 illustrates the spatial displacement and stress distributions of the membrane for three values of membrane radius $R_{vm} = 1200\mu m$, $R_{vm} = 1010\mu m$, and $R_{vm} = 900\mu m$, all for $t_{vm} = 9\mu m$. Notice in Figure 5.18(a), for $R_{vm} = 1200\mu m$, that the stress is large because of the significant curvature in the membrane at the inner boundary due to the negative bowing of the membrane. This bowing develops because at the instant when the valve cap is at its maximum deflection upward, the pressure acting on the top surface of the valve cap is at its minimum $P_{EHC} = 0.2MPa$. Therefore, the required P_{HAC} within the valve hydraulic

amplification chamber at this time instant is low, resulting in a significant negative pressure across the valve membrane. In Figure 5.18(c), for $R_{vm} = 900\mu m$, the stress is high because of the significant curvature in the membrane at the inner and outer boundaries, due to the minimal width of the membrane. And in Figure 5.18(b), for $R_{vm} = 1010\mu m$, the peak membrane stress is $\sigma_{vm,peak} = 1.0GPa$ and occurs at the inner membrane boundary.

This study has shown that in designing to valve membranes to work under varying pressure time histories, depending on the magnitude of the external pressures and their behavior with time, it is sometimes impossible to determine a valve membrane radius for a given membrane thickness to achieve stresses below the critical limits. As a result of this, the final systematic active valve design procedure presented in Section 5.6 is capable of recognizing these restrictions and iterating on the membrane thickness until a satisfactory membrane design is achieved.

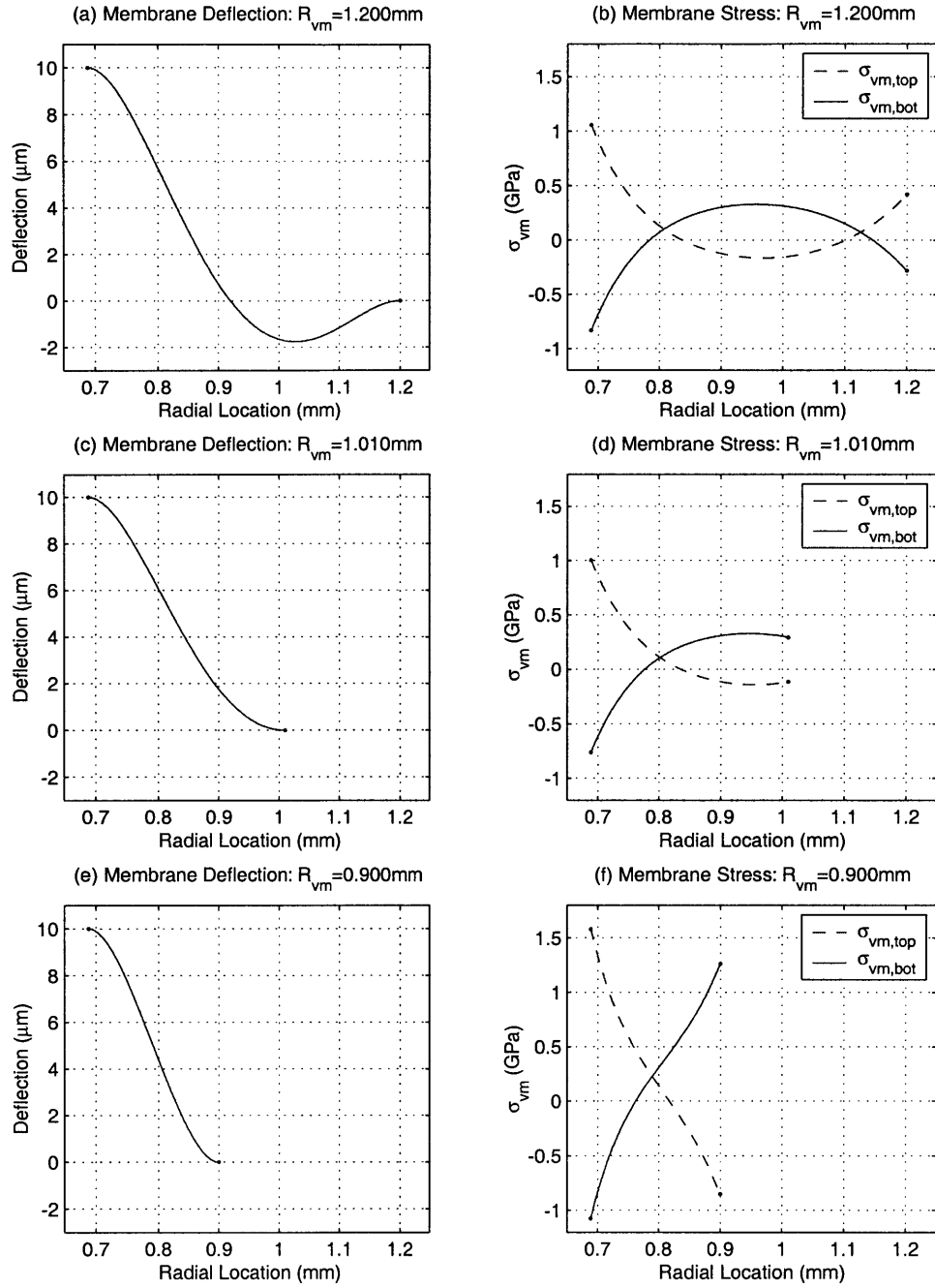


Figure 5.18: Example valve membrane deflection and stress plots for $Z_{vc,stroke} = 20\mu m$, $R_{vc} = 688\mu m$, $P_{HPR} = 1.2\text{MPa}$, P_{EHC} varying with time, and $t_{vm} = 9\mu m$: (a) $R_{vm} = 1200\mu m$, (b) $R_{vm} = 1010\mu m$, and (c) $R_{vm} = 900\mu m$.

5.5 Power Consumption in Active Valve

During each cycle of operation of the active valve, electrical energy flows into and out of the piezoelectric material. The amount of energy required is dependent on the strain of the material and the load that it actuates against. To create a simple method for evaluating these energies in a given active valve geometry, the drive element portion of the valve will be focused on. In the final step of the design procedure, the piezoelectric material diameter and drive element piston diameter were calculated to create a stiffness match condition with the loading that the drive element experienced (see details in Section 5.3.5). Figure 5.11(b) illustrated the drive element actuation curve for the example design in Section 5.3.2. This type of curve will be the basis for evaluating cyclic energy flow in the valve.

5.5.1 Overview of Energy/Power Consumption

Figure 5.19 displays representative drive element actuation plots for a typical active valve design. In Figure 5.19(a), as the piezoelectric material expands and creates a positive drive element volume change dV_{de} , the pressure within the hydraulic amplification chamber P_{HAC} increases, due to the stiffness of the valve membrane and the external pressure loading time histories P_{HPR} and $P_{EHC}(t)$. The piezoelectric material therefore does work W_1 on its environment. In Figure 5.19(b), the piezoelectric material deflection is decreasing, and the corresponding work done by the environment on the piezoelectric material (the drive element) is W_2 . Throughout a full cycle of the valve, a total hysteretic valve energy loss of $W_{hys} = W_1 - W_2$ results. This is due to the fact that during drive element motion upward, the average P_{HAC} pressure that the piston moves against is larger than that which exists to help move the piston downward in the second portion of the valve cycle. This hysteretic energy loss per valve cycle is being put into the external hydraulic system.

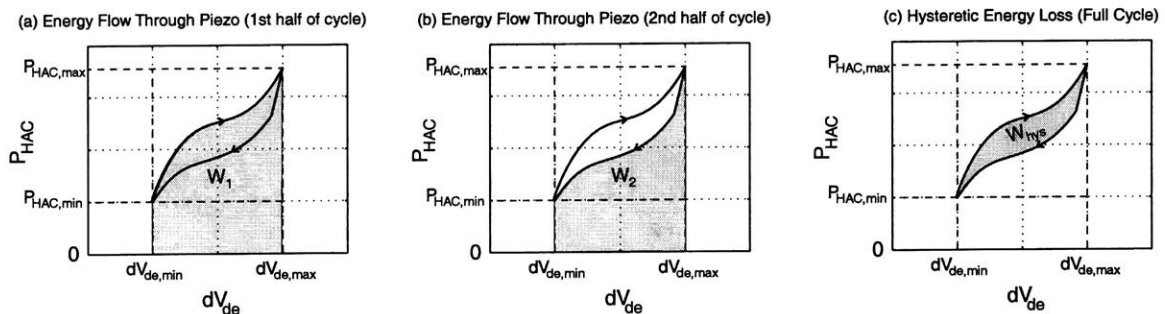


Figure 5.19: Schematic representation of energy flows and losses in active valve, based on drive element actuation behavior: (a) work done by piezo material on load during first half of valve cycle, (b) work done by load on piezo material during second half of valve cycle, and (c) hysteretic energy loss during a full valve cycle.

This hysteretic energy loss can be written in integral form as

$$W_{hys} = W_1 + W_2 = \int_1 P_{HAC} d(dV_{de}) + \int_2 P_{HAC} d(dV_{de}). \quad (5.11)$$

Note here that W_2 is a negative quantity since work is done by the environment on the drive element. If the piezoelectric material and attached circuitry were 100% efficient, then no other energy loss mechanisms would exist within the valve system. In reality, though, the piezoelectric material and the attached circuitry are not perfectly efficient. Assuming a lumped parameter γ_{loss} as the fraction of energy flowing through the piezoelectric material during a full valve cycle that is lost due to material and circuitry inefficiencies, the total amount of cyclic energy lost in these mechanisms is therefore

$$W_{loss} = \gamma_{loss} (W_1 + |W_2|). \quad (5.12)$$

In order to calculate the power consumption of the valve design, the frequency of operation of the valve f_{sys} is incorporated into the previous relations. The total valve power consumption is thus the product of the valve frequency of operation and the total energy lost by the valve during a single cycle of operation,

$$P_{consumption} = f_{sys} [W_{hys} + W_{loss}]. \quad (5.13)$$

These power consumption quantities P_{hys} , P_{loss} , and $P_{consumption}$ will be monitored in carrying out the full valve systematic design code in order to evaluate the benefits of a particular valve design over another one.

5.5.2 Benefit of Multiple Valve Heads

The incorporation of multiple smaller-sized valve heads (which are designed to achieve the same external system flow performance as a single larger valve head) has the potential to reduce hysteretic energy loss of the active valve device. This phenomenon will be presented from the point of view of the valve cap and membrane acting against the external pressure loadings, since this is the actual structural interface between the active valve and the rest of the MHT system. The hysteretic energy loss of the active valve per cycle is the same whether it is looked at from the point of view of the drive element or the point of view of the valve cap and membrane. This is true because no energy loss mechanisms exist within the valve between the drive piston and the valve cap and membrane. Certainly, structural compliances do exist, but these are energy storage elements, not loss mechanisms. Therefore, it is possible to calculate

the hysteretic energy loss by focusing on just the motion of the valve cap and membrane against the external pressure loadings encountered. Furthermore, since the valve membrane experiences a constant pressure P_{HPR} during the complete actuation cycle, no cyclic work is being done through the valve membrane interface. Therefore, the estimation of valve hysteretic energy loss can be made simply by looking at the valve cap itself, its motion against the time-varying external pressure loading $P_{EHC}(t)$ during a full actuation cycle.

This method of estimating valve hysteretic energy consumption will be used to explain the fundamental benefit of incorporating multiple valve heads within the active valve device rather than just a single valve head. For a given valve cap radius R_{vc} , imposed motion $Z_{vc}(t)$, and known external loading $P_{EHC}(t)$ on the valve cap, the hysteretic energy consumption of the valve during a full actuation cycle can be written as

$$W_{hys} = \int P_{EHC}(t)d(V_{vc}) = \int P_{EHC}(t)\pi(R_{vc})^2 dZ_{vc}. \quad (5.14)$$

where $dV_{vc}(t)$ is the swept volume of the valve cap. For simplicity in the following arguments, this relation can be simplified to the following proportionality,

$$W_{hys} \propto \Delta P_{EHC}^* \pi(R_{vc})^2 Z_{vc,stroke} \quad (5.15)$$

where ΔP_{EHC}^* is the difference between the average encountered pressure as the valve moves upward and the average encountered external pressure as the valve moves downward. Also for the given values of R_{vc} and $Z_{vc,stroke}$, the peak area through which fluid can flow during an actuation cycle is

$$A_{flow} = 2\pi R_{vc} Z_{vc,stroke}. \quad (5.16)$$

Therefore, for a given valve cap size, imposed stroke, and known external pressure loading time history on the valve cap, the hysteretic energy loss per cycle and the peak fluid flow area can be related by

$$\frac{W_{hys}}{A_{flow}} \propto R_{vc}. \quad (5.17)$$

This relation basically states that the ratio of the valve cap structural area (which is proportional to W_{hys}) to the valve cap circumference (which is proportional to fluid flow area) can be decreased by reducing the size of the valve cap radius R_{vc} . To reduce hysteretic energy consumption in the active valve, therefore, the goal should be to reduce this $\frac{W_{hys}}{A_{flow}}$ as much as

possible, while keeping A_{flow} constant. This can be achieved by making individual valve caps smaller and placing many in parallel with multiple valve orifices connecting the high pressure reservoir to the harvesting chamber. Updating Equations 5.15 and 5.16 above to include the freedom to choose a particular number of valve heads N_{vh} within the design leads to

$$W_{hys,N_{vh}} \propto N_{vh} \Delta P_{EHC}^* \pi R_{vc,N_{vh}}^2 Z_{vc,stroke,N_{vh}} \quad (5.18)$$

and

$$A_{flow,N_{vh}} = N_{vh} 2\pi R_{vc,N_{vh}} Z_{vc,stroke,N_{vh}}. \quad (5.19)$$

If the goal is to design a valve with $N_{vh} > 1$ that has the same total flow area as a valve with a single valve head, the following proportionality must be maintained (calculated by equating Equations 5.16 and 5.19),

$$\frac{R_{vc,N_{vh}}}{R_{vc}} \propto \frac{1}{N_{vh}} \frac{Z_{vc,stroke}}{Z_{vc,stroke,N_{vh}}}. \quad (5.20)$$

Inserting this proportionality into Equation 5.18 results in a relation for the hysteretic energy consumption as a function of the number of valve heads employed and the imposed valve cap stroke for the case of multiple valve heads versus the case of just a single valve head,

$$\frac{W_{hys,N_{vh}}}{W_{hys}} \propto \frac{1}{N_{vh}} \frac{Z_{vc,stroke}}{Z_{vc,stroke,N_{vh}}}. \quad (5.21)$$

Therefore, the potential exists to reduce significantly the hysteretic energy consumption in the active valve by incorporating multiple valve heads above the hydraulic amplification chamber rather than a single valve head. For example, by letting $N_{vh} = 10$ and requiring that each of the ten valve heads move through one-half the stroke of a single valve head design, the hysteretic energy consumption of the 10-valve design will be 20% of that of the single valve design. The updated systematic design code detailed in the following section, includes this ability to compare and contrast valve designs with varying N_{vh} and different imposed valve cap strokes $Z_{vc,stroke}$. An additional benefit of incorporating multiple valve heads (that each move a smaller stroke than a single large valve head) is that it becomes easier to structurally design the valve membranes (in that small valve membrane thicknesses are achievable) to support these valve caps within the required stress limitations. This will be illustrated in Section 5.6.

5.6 Results of Systematic Design Procedure

This section presents results of the full systematic active valve design procedure for the example valve requirements defined in Section 5.3.2. As detailed in previous sections, this quasi-static procedure will now incorporate the three design freedoms that were not included in the basic design procedure detailed in Section 5.3, namely the ability to design a valve structure for multiple valve heads ($N_{vh} > 1$), with varying valve cap strokes, and for differing valve membrane thicknesses. Specifically, the results presented in this section focus on a variety of chosen number of valve heads ($N_{vh} = 1, 2, 3, 5$), imposed valve cap strokes between $Z_{vc,stroke} = 8\mu m$ and $Z_{vc,stroke} = 40\mu m$, and available valve membrane thicknesses from $t_{vm} = 7\mu m$ and upward in increments of $1\mu m$. The results clearly demonstrate the potential benefits of multiple valve head geometries for reducing total valve power consumption.

Figure 5.20 plots the calculated valve cap radius, valve membrane thickness and radius, and drive element piston diameter for the variety of N_{vh} and $Z_{vc,stroke}$ values under question. Note that in Figure 5.20(b), for $N_{vh} \geq 2$, valve membranes with $t_{vm} = 7\mu m$ are achievable for all the imposed $Z_{vc,stroke}$ values. As more valve heads are allowed in parallel, each valve membrane gets smaller in size, resulting in reduced “bowing” of the membrane under the pressure loadings. This is the identical phenomenon to that discussed in Section 5.4.2. Also, notice in Figure 5.20(c) that as more valve heads are employed in the design, smaller drive piston dimensions are achieved, due to the fact that less swept volume is required by the valve membranes during actuation.

Figure 5.21 plots the calculated effective piezoelectric material diameter and the maximum compressive stress on the piezoelectric material during a full valve actuation cycle. Notice in Figure 5.21(a) that the required piezoelectric material diameter is generally increasing with increasing N_{vh} . This is due to the fact that the $P_{HAC}(t)$ actuation requirements are increased because of the increased stiffness of the valve membranes. It is important also to monitor the compressive stress seen by the piezoelectric material to ensure that it is below the compressive depolarization limits.

Figure 5.22 plots the estimated hysteretic power consumption, material and circuitry power loss, and total valve power consumption. As seen in Figure 5.22(a), the hysteretic power consumption can be significantly reduced by incorporating multiple valve heads working with moderate valve strokes. In addition, as shown in Figure 5.22(b) material and circuitry losses can also be reduced, since total energy flowing through the piezoelectric material is lessened. Finally, Figure 5.22(c) plots the combined power consumption for the various active valve designs. As indicated in this plot, the valve design that results in the minimum power consumption uses ten valve heads $N_{vh} = 5$, each traveling through a stroke of $Z_{vc,stroke} = 22\mu m$. These results demonstrate the capabilities of this systematic active valve design procedure in evaluating single

and multiple valve head designs under loading conditions put forth by a typical MHT system.

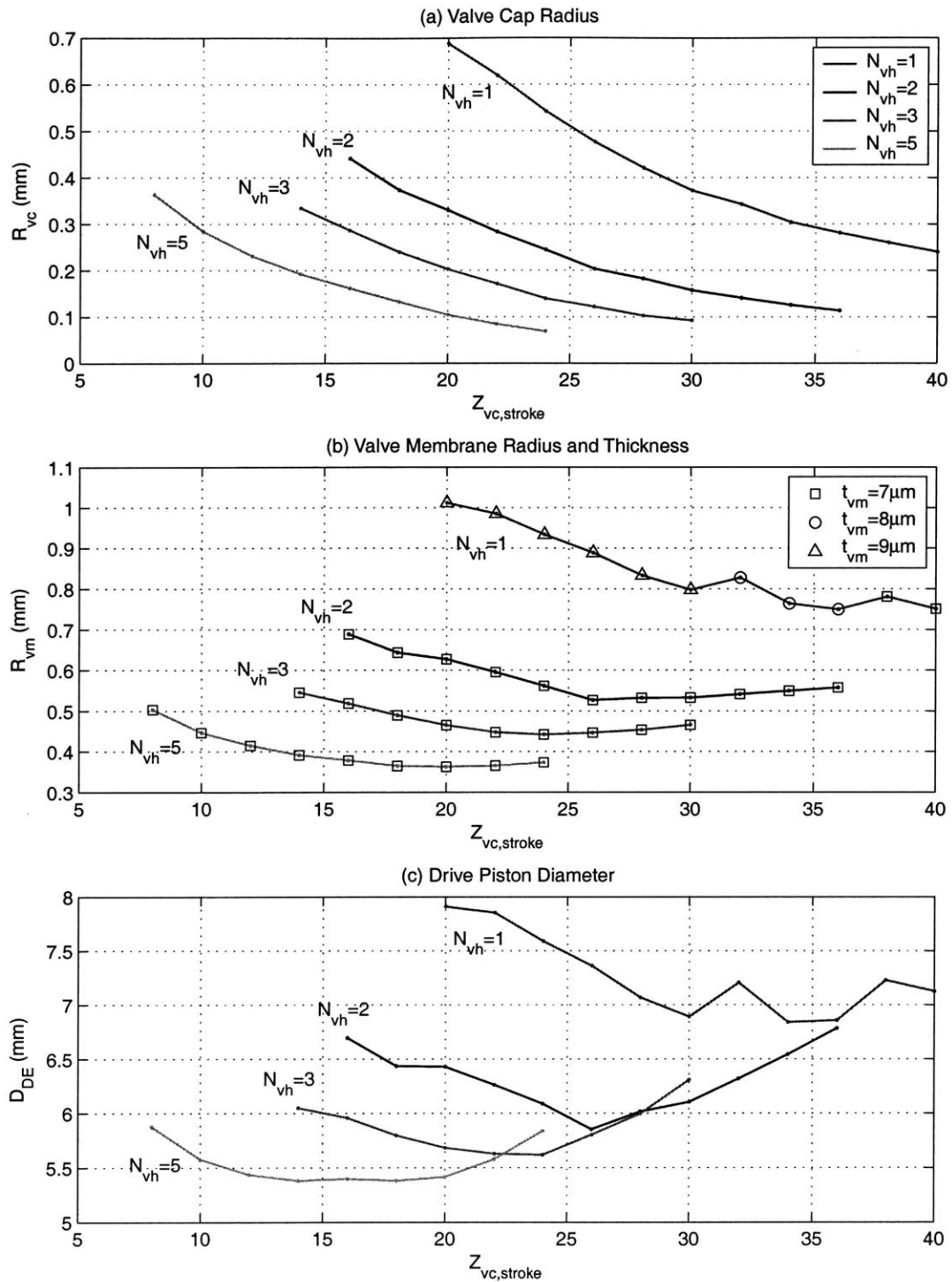


Figure 5.20: Multiple valve head comparison Plot 1

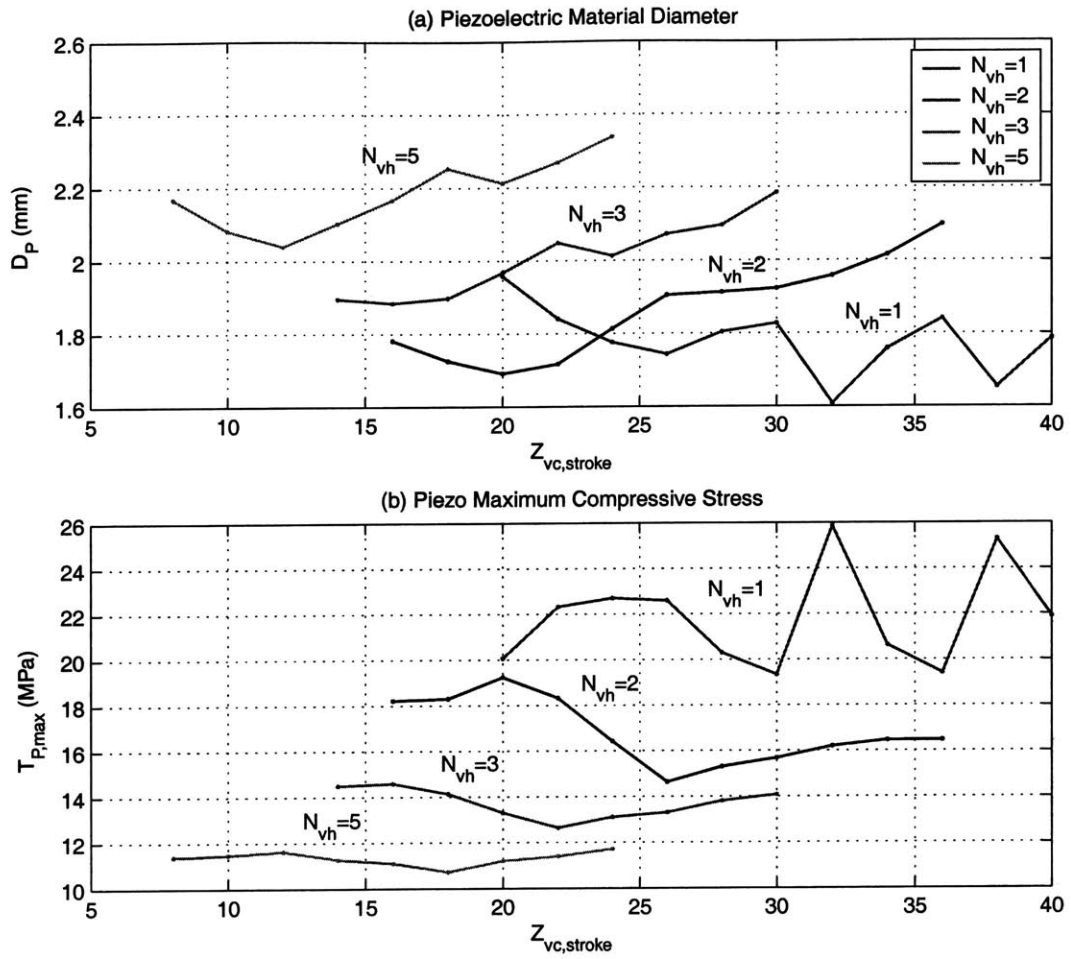


Figure 5.21: Multiple valve head comparison Plot 2

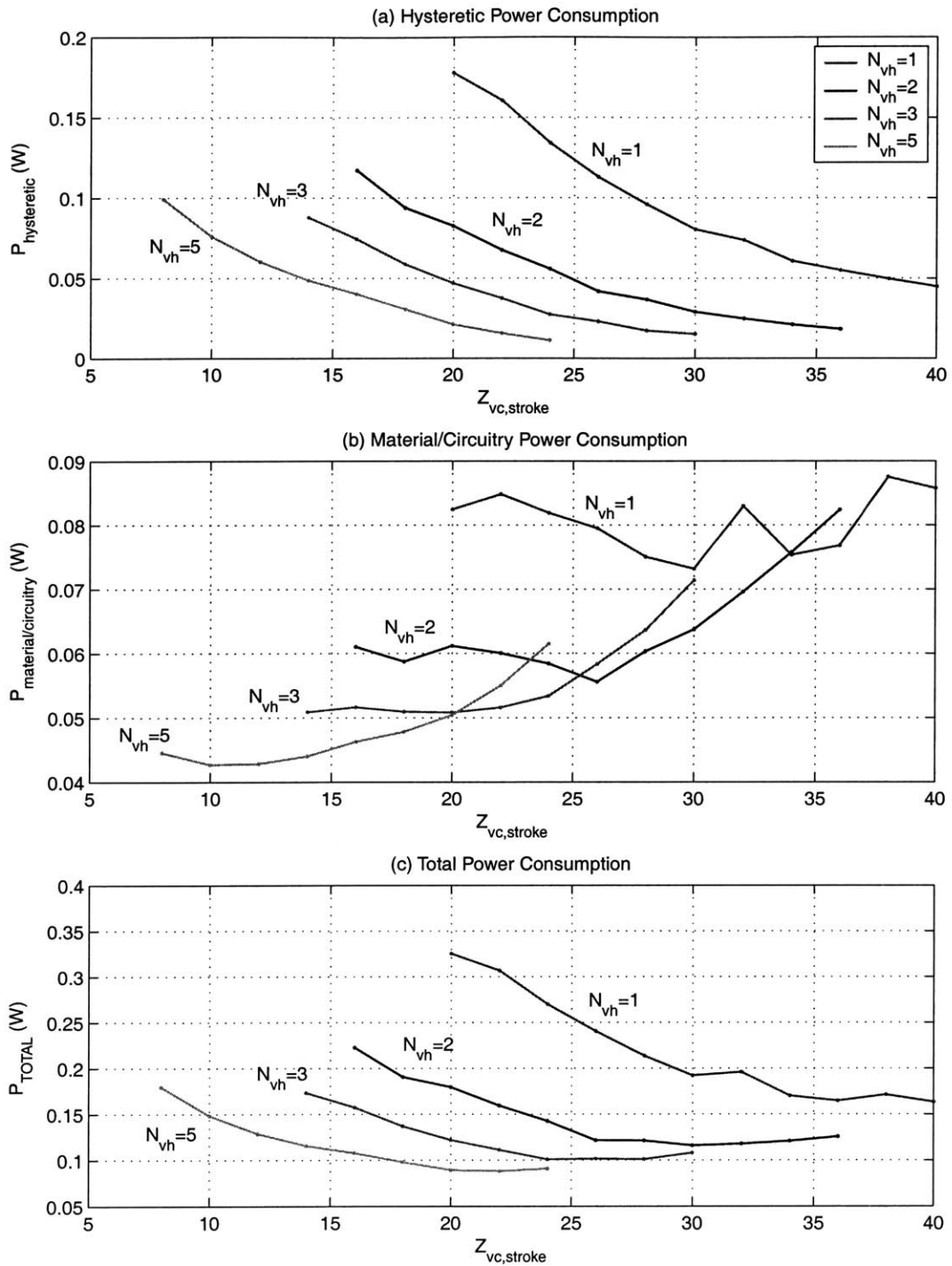


Figure 5.22: Multiple valve head comparison Plot 3

5.7 Correlation With Dynamic Simulation

The systematic design procedure presented in this chapter has been based on quasi-static structural behavior. In reality, dynamic effects within the active valve may result in performance of the valve that differs from quasi-static behavior. This section will take one of the active valve geometries formulated using the systematic design procedure in Section 5.6 and perform a full-scale dynamic simulation of this structure. The results will indicate that, indeed, the design formulated through the quasi-static procedure performs very close to expectations, thereby validating the use of the quasi-static procedure as a powerful tool for designing an active valve structure within a full hydraulic system.

The valve structure that was chosen for simulation is that corresponding to $N_{vh} = 1$ and $Z_{stroke} = 40\mu m$. Revisiting Figures 5.20, 5.21, and 5.22 in Section 5.6, the valve geometry is as follows: $R_{vc} = 241\mu m$, $t_{vm} = 7\mu m$, $R_{vm} = 757\mu m$, $R_{pis} = 3.59mm$, and $R_p = 0.88mm$. The peak-peak voltage applied to the piezoelectric material is 1000V at a frequency of $f = 10kHz$. Referring to Figures 5.8(b), 5.9, and 5.11, this active valve geometry is able to quasi-statically achieve the performance requirements set by the external hydraulic system, namely a pressure fluctuation in the harvesting chamber (with $K_{EHC} = 1.5e^{16} \frac{Pa}{m^3}$) from 0.2MPa to 1.0MPa, given reservoir pressures of $P_{HPR} = 1.2MPa$ and $P_{LPR} = 0$.

In order to evaluate this active valve geometry in a full dynamic simulation, a complete simulation architecture is implemented that includes the active valve simulation (presented in Chapter 4) and the external hydraulic system relations detailed in Section 5.2. Figure 5.23 shows this full simulation architecture. The additional external hydraulic system architecture (including the effects of the fluid orifice pressure-flow relations, the valve channel inertia, and the chamber stiffness) is coupled to this active valve system to simulate full filling and evacuation. In order to create full system pumping behavior, a chamber with both an inlet and outlet active valve is included in the simulation. In addition, critical valve variables, such as $\sigma_{vm}(t)$, $Z_{vc}(t)$, and $P_{HAC}(t)$ are monitored. In this simulation, a positive valve stop at a location of $Z_{vc} = 20\mu m$ is implemented. The results of this simulation for two different values of valve cap damping are shown in Figure 5.24. For further details on full MHT system simulations, refer to [8].

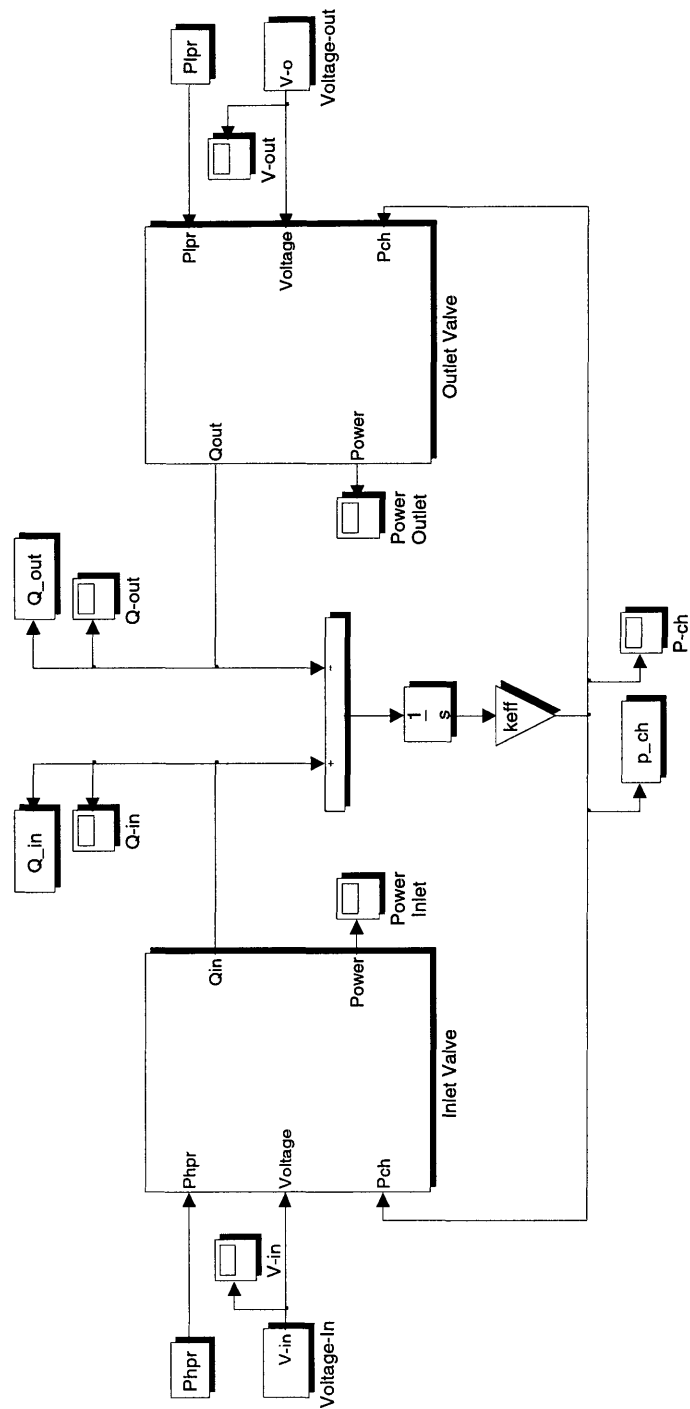


Figure 5.23: Complete Simulink MHT hydraulic system architecture, showing inlet and outlet active valves, fluid-orifice pressure-flow relations, valve channel inertia, and harvesting chamber stiffness.

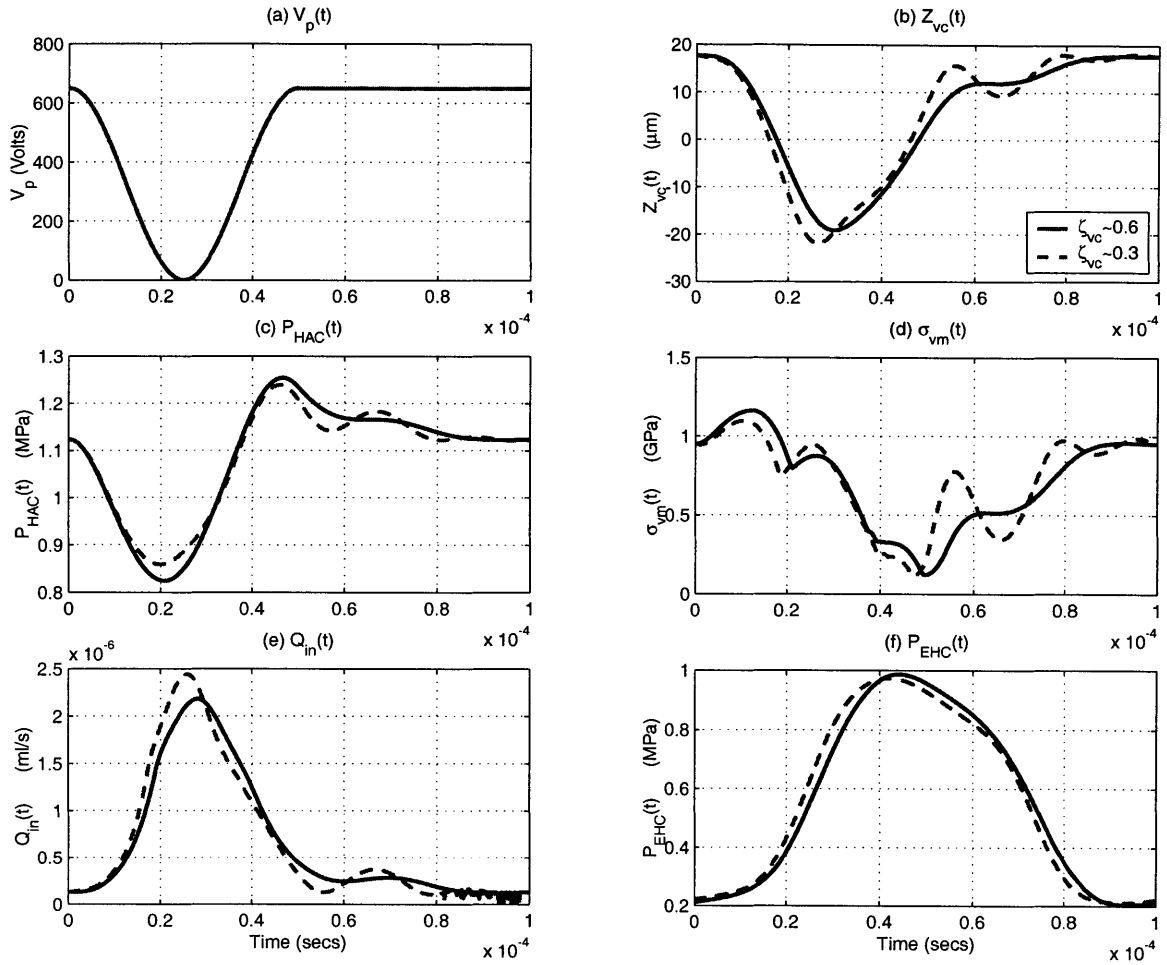


Figure 5.24: Full system simulations: (a) solid line represents case in which $\zeta_{pis} = 0.7$, $\zeta_{vc} = 0.6$, (b) dashed line represents case in which $\zeta_{pis} = 0.7$, $\zeta_{vc} = 0.3$. Note that in these cases, the valve cap does not hit the stop. In these plots, V_p is the applied piezoelectric voltage, $Z_{vc}(t)$ is the position of the valve cap, $P_{HAC}(t)$ is the hydraulic amplification chamber pressure, $\sigma_{vm}(t)$ is the maximum valve membrane stress, $Q_{in}(t)$ is the flow rate through the valve, and $P_{EHC}(t)$ is the external chamber pressure.

Due to dynamic effects in the active valve system, an applied peak-peak voltage of only 650V (compared to the quasi-static value of 1000V) is required to actuate the valve and to produce the proper filling behavior of the harvesting chamber. Notice that the valve cap $Z_{vc}(t)$, HAC pressure $P_{HAC}(t)$, inlet flow rate $Q_{in}(t)$, and resulting harvesting chamber pressure $P_{EHC}(t)$ time histories all correlate very closely to those predicted by the systematic quasi-static design procedure. One interesting note is that the valve membrane stress σ_{vm} time history differs slightly from the quasi-static prediction in the region when the valve cap is just beginning to open. Rather than immediately decreasing, as is predicted in the quasi-static procedure, σ_{vm} actually begins to increase to a peak value of $1.15GPa$ (for $\zeta_{vc} = 0.6$) and to a peak value of $1.05GPa$ (for $\zeta_{vc} = 0.3$) just after opening. This phenomenon is due to the dynamic effects on the valve membrane. Essentially, the P_{HAC} pressure below the membrane decreases substantially before the valve cap is able to move downward (due to the cap's inertia and the effect of damping), resulting in an enhanced membrane curvature at R_{vc} and therefore an increase in σ_{vm} .

These important observations on the membrane stress can be fed back to the quasi-static design procedure. Using a smaller value of limiting stress σ_{limit} , a slightly modified valve geometry can be generated so that dynamic membrane stresses do not exceed the desired bound. Overall, the dynamic performance of the active valve geometry formulated using the systematic quasi-static design procedure detailed in this chapter matches fairly well to desired requirements. This design procedure, therefore, can be very useful in developing valve geometries for use in full hydraulic systems.

5.8 Conclusions

This chapter has introduced the physical equations governing the fluid flow behavior within a generic MHT system, external to the valve cap and membrane structure of the active valve. With these relations, a comprehensive and systematic quasi-static design procedure has been presented that enables a designer to formulate an active valve geometry for use within an MHT system to satisfy certain pressure-flow requirements. This procedure formulates designs and evaluates valve power consumption for geometries with one or more valve heads acting in parallel above the hydraulic amplification chamber and for differing valve cap strokes. Additionally, valve membrane structures are designed to guarantee peak stress levels below a critical value during complete valve time histories. Active valve geometries produced by this design procedure have been analyzed using full dynamic system simulations, and results indicate that dynamic effects do not significantly affect the ability to meet the performance requirements. Overall, this design procedure enables the generation of active valve geometries for a potentially wide variety of hydraulic systems.

Bibliography

- [1] N.W. Hagood, D.C. Roberts, L. Saggere, K.S. Breuer, K-S. Chen, J.A. Carretero, H.Q. Li, R. Mlcak, S. Pulitzer, M.A. Schmidt, S.M. Spearing, and Y-H. Su, "Micro Hydraulic Transducer Technology for Actuation and Power Generation", Proceedings of SPIE, Vol. 3985 (2000), Newport Beach, CA, March 5-9, 2000, pp.680-688.
- [2] J. Carretero and K.S. Breuer, "Measurement and Modeling of the Flow Characteristics of Micro Disk Valves," Proceedings of the 1994 International Mechanical Engineering Conference and Exposition: Microfluidics Symposium, Orlando, FL, Nov. 2000.
- [3] E. Schrenk, "Disc valves, flow patterns, resistance and loading," BHRA T, 1957 (547). Translation from German.
- [4] A. Lichtarowicz, "Flow and Force Characteristics of Flapper Valves," Third International Symposium on Fluid Power, Turin, 1973, pp. B1-1.
- [5] D.N. Johnston, K.A. Edge, and N.D. Vaughan, "Experimental investigation of flow and force characteristics of hydraulic poppet and disc valves," Proceedings of the Institution of Mechanical Engineers, Part A: Power & Process Engineering, 1991 Vol 205, No 3, pp. 161-171.
- [6] S.M. Spearing and K.S. Chen, "Micro-gas turbine engine materials and structures," *Ceramic Engineering & Science Proceedings v.18n 4B*, p. 11-18, 1997.
- [7] K.T. Turner, An Evaluation of Critical Issues for Microhydraulic Transducers: Silicon Wafer Bonding, Strength of Silicon on Insulator Membranes and Gold-Tin Solder Bonding, Massachusetts Institute of Technology, Master's Thesis, 2001.
- [8] O. Yaglioglu. Master's Thesis, Massachusetts Institute of Technology, 2002.

Chapter 6

Device Fabrication and Preparation for Testing

6.1 Introduction

The proposed piezoelectrically-driven hydraulic-amplification microvalve is fabricated using a combination of microscale (silicon patterning and etching) and macroscale (piezoelectric material integration) procedures. As detailed in previous chapters of this thesis, the valve consists of multiple layers of silicon and glass (Pyrex 7740) with integrated piezoelectric elements, all bonded together to form the important structural features of the device. These features are the tethered-piston piezoelectric drive element, the enclosed hydraulic amplification chamber, the valve membrane and orifice structure, and the fluid channels to and from the valve. A cross-section of a full MHT system, with embedded multi-layered active valve structure, is shown in Figure 6.1. Successful fabrication and assembly of a complete MHT system involves overcoming the identical challenges associated with realizing a working active valve device, since the valve structure and full MHT system span the same layers. As a result, the fabrication and assembly processes presented in this chapter are not unique to the active valve, but rather provide a platform of procedures that can be implemented to create a wide variety of micro-hydraulic systems. For the purposes of this thesis, however, only the geometry of the active valve is referred to in the fabrication and assembly discussions.

Layers 1, 3, 6, and 9 of the active valve structure (shown in Figure 6.1) are each borosilicate glass (Pyrex 7740), the features of which are formed through wafer-level ultrasonic machining. Layers 2 and 8 are formed from standard silicon wafers and are etched using deep-reactive ion etching procedures. Layers 4, 5, and 7 are created from silicon-on-insulator (SOI) wafers. The drive element tethers supporting the piston structure in Layers 4 and 5 and the valve membrane and cap structure in Layer 7 are produced using deep-reactive etching, with the buried oxide

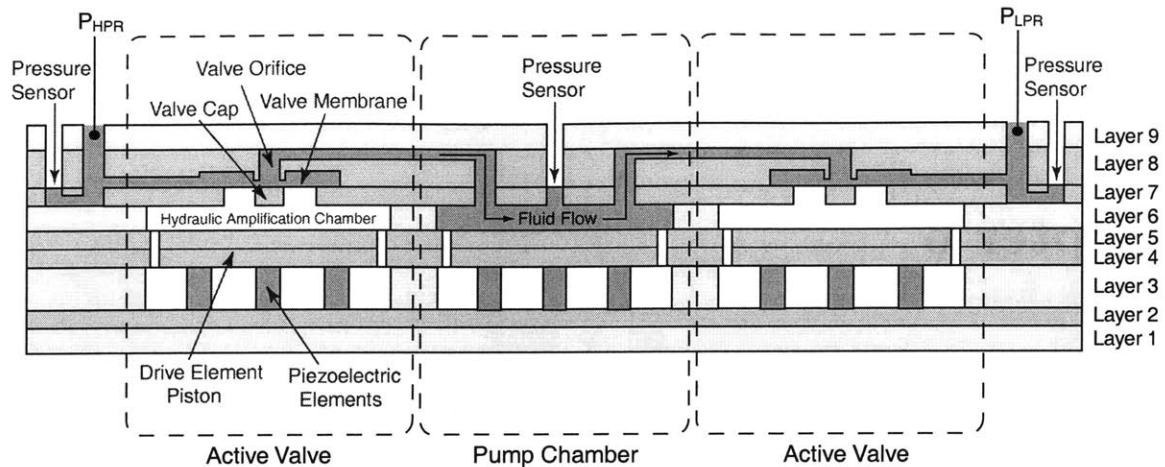


Figure 6.1: Cross-section schematic of a nine-layer multiple wafer MHT system with two embedded active valve structures. Realization of this active valve requires robust bonding of silicon-to-silicon and silicon-to-glass at the wafer-level and integration and bonding of piezoelectric material elements with silicon at the die-level, as will be discussed later in this chapter.

acting as an etch stop for precise control of tether and membrane thicknesses. Three primary bonding mechanisms are used to realize a complete valve device: silicon-silicon fusion bonding, silicon-glass anodic bonding, and silicon-piezoelectric material eutectic bonding.

This chapter first details the critical challenges associated with the fabrication and assembly of this multi-layer active valve device, namely (1) etching of the high-aspect ratio features in silicon-on-insulator wafers to form the tethered drive element piston and valve membrane structures, (2) wafer-level silicon-silicon fusion bonding and wafer-level silicon-glass anodic bonding, (3) preparation, integration, and bonding of the bulk piezoelectric material elements within the drive element structure, (4) die-level assembly of multiple silicon and glass layers, and (5) fluid filling and sealing of the hydraulic amplification chamber. Having laid out the details of these fabrication issues and the procedures used to overcome these obstacles, the chapter then presents a systematic fabrication and testing plan of important active valve sub-components, as a means to prove out the fabrication challenges. Details of each of the sub-component studies leading up to the full active valve are then documented in subsequent chapters of this thesis.

6.2 Fabrication Challenges and Procedures

This section attempts to follow the fabrication and assembly process in order of the steps and challenges involved. The first two challenges focus on the activities relating to wafer-level processing: etching of the drive element tether and valve membrane structures and silicon-silicon and silicon-glass wafer bonding procedures. The second two challenges are concerned

with die-level processing: preparation and integration of the piezoelectric elements within the device and the process flow associated with the die-level silicon-glass anodic bonding. The final challenge focuses on filling and sealing of fluid in the device once the active valve device has been successfully fabricated and assembled at the die-level.

6.2.1 Etching of Tethered Drive Element and Valve Membranes

The drive element tethers and valve membranes within the active valve device are designed to be quite thin (on the order of $7 - 10\mu m$). To achieve precise dimensional control of these features, SOI wafers containing a buried oxide layer a preset distance from one side of the wafer are used. In performing deep etches into the silicon wafer down to the buried oxide layer, it is critical that the surface roughness of the etch and the tailoring of fillet radii profiles at the base of the etched profiles be well-controlled so as to maintain strength and robustness of the thin-membrane structures. Figure 6.2 illustrates etch profiles at the SOI interface of a typical drive element piston that can result, depending on the process chosen and care given to performing the etch. Ideally, one would like to create a fillet radius between the thin tether and the much thicker ($\sim 400\mu m$) central piston structure to minimize stress concentrations, as shown in Figure 6.2(c). It is essential to avoid etch profiles such as the sharp corner shown in Figure 6.2(b) and the “footing” or “notching” profile shown in Figure 6.2(d). These serve to magnify stresses at these interface regions, thereby compromising the overall strength of the structure.

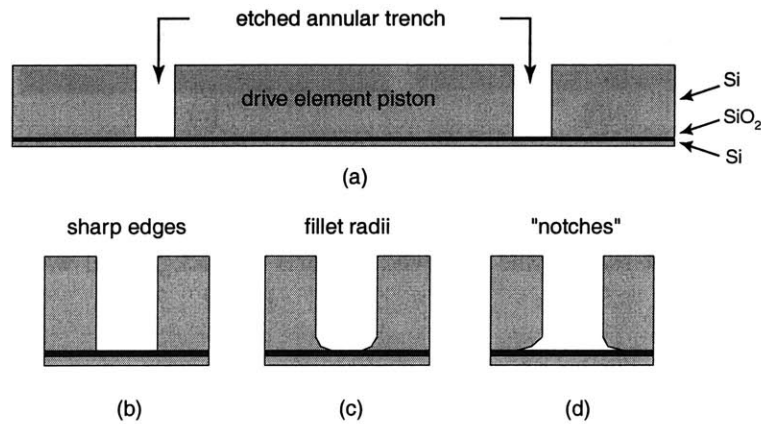


Figure 6.2: Etching of a typical drive element piston structure: (a) cross-section view of drive piston, (b) sharp corner etch features, (c) fillet radius features, and (d) “notching” or “footing” features.

Considerable research work has been done in developing and optimizing deep etching processes for single-crystal silicon materials [1] [2]. The Deep-Reactive Ion Etching (DRIE) process

used to create the structures and devices in this thesis is known as the Bosch Process [1]. This method involves repetitive cycles of plasma etching and passivation to create high aspect ratio deep trenches in silicon. Using photoresist as a masking agent, a timed plasma etch using SF_6 is carried out. Following this timed etch, a passivating film using C_4F_8 is deposited over all exposed surfaces of the wafer, including the etched trench bottom and sidewalls. During the next timed plasma etch, this passivating film is preferentially removed from the bottom of the trenches through ion bombardment, while the film on the sidewalls remains intact. This cyclic process is repeated until the buried-oxide etch stop layer is reached. At this juncture, carefully monitoring of the etch process is performed to ensure that fillet radii of a desired size (based on modeling specifications) are created. Figure 6.3 shows views of a successfully etched drive element piston structure with properly tailored fillet radii.

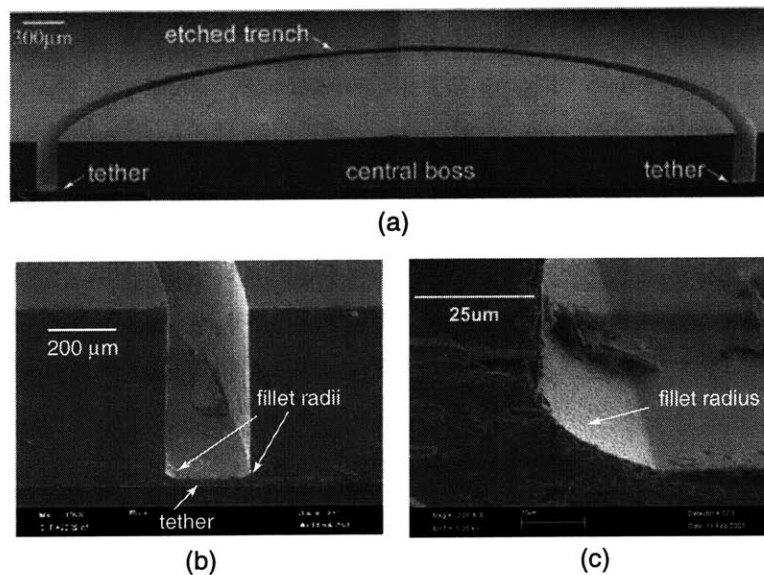


Figure 6.3: SEM images of an etched drive element piston: (a) cross-section view of SOI piston structure, (b) close-up of etched trench, and (c) further close-up of fillet radius feature. In this structure, a $20 - 25\mu m$ fillet radius was achieved. Debris in background was generated during die-saw procedures.

This final “fillet tailoring” step is tedious and difficult because once the silicon has been etched away such that portions of the oxide are visible, very little time is required for lateral etching of the remaining silicon above the oxide layer to be completely etched away, resulting in potential “footing” profiles at the interface. The rapid lateral etching has been studied and investigated by numerous individuals, and it is believed to result from plasma charging effects at the silicon/oxide interface [3] [4] [5]. Consistently controlling these fillet profiles is extremely hard to achieve, as etch parameters such as etch time, passivation time, SF_6 flow rate, electrode power during etching, electrode power during passivation, and C_4F_8 flow rate must be tuned

and optimized. The details of these DRIE process parameters are beyond the scope of this thesis. The purpose of this section, rather, has been to present the significant challenges and obstacles faced in the etching of thin-membrane structures with desired fillet radii profiles. A designer may specify a particular fillet size, but the cleanroom process of achieving that profile is often a time-consuming one.

6.2.2 Wafer-Level Bonding

For the multi-layer active valve structure presented in this thesis, various silicon-silicon and silicon-glass wafer-level bonds are performed. A silicon-silicon wafer-level fusion bonding process is used to bond Layers 4 and 5 together to form Stack 4-5 and Layers 7 and 8 together to form Stack 7-8. A silicon-glass wafer-level anodic bonding process is used to bond Layers 1 and 2 together to form Stack 1-2, Stack 4-5 and Layer 6 together to form Stack 4-5-6, and Stack 7-8 and Layer 9 together to form Stack 7-8-9. Following these wafer-level bonding steps, the stacks are die-sawed into individual dies and cleaned in preparation for die-level bonding and piezoelectric material integration. Further discussion of why certain bond steps are performed at the wafer-level and others at the die-level is covered in Section 6.2.4. Figure 6.4 illustrates the various wafer-level silicon-silicon and silicon-glass bonding steps.

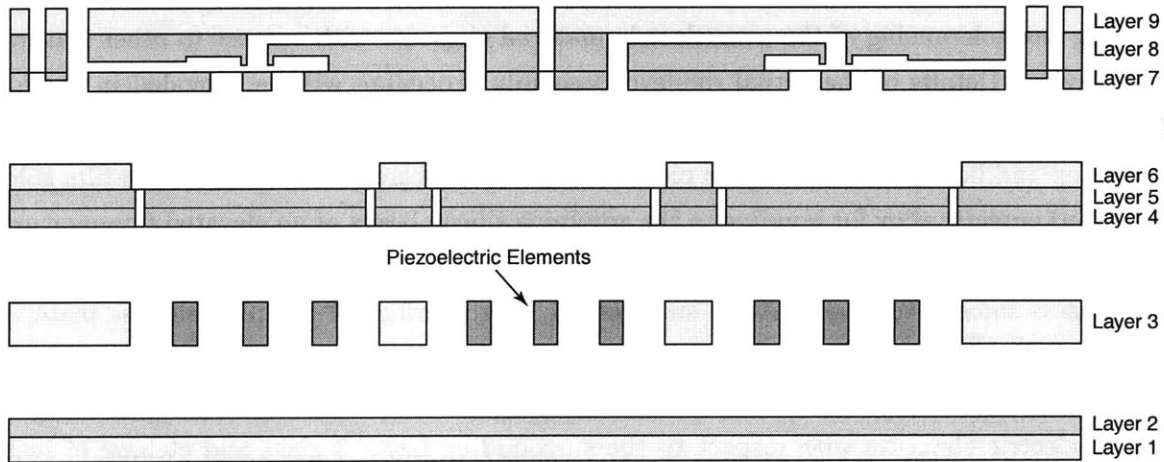


Figure 6.4: Wafer-level silicon-silicon fusion and silicon-glass anodic bonding steps are carried out prior to piezoelectric material integration.

The silicon-silicon fusion bonding process used to create wafer-level stacks for the active valve device is a well developed process and consists of three primary steps [6]: (1) preparation and treatment of the silicon wafer surface to produce a hydrophilic surface, (2) alignment and adhesion of two wafers together (weak van der Waals or hydrogen bonds maintain wafer-wafer adhesion) in a clean room-temperature environment, either in air, inert atmosphere, or vacuum, and (3) high temperature annealing of the wafer stack at 1000°C to promote strong covalent

bonding. The strength of this fusion bond is dependent on the annealing temperature and time [2]. Paramount in the bonding process is the cleanliness of the silicon wafers prior to bonding and of the alignment and bonding apparatus itself. Particulate matter present between the silicon wafers during adhesion can result in significant defect regions characterized by little or no bonding.

The silicon-glass anodic bonding process used to create wafer-level stacks also is a well-developed process. This process involves three primary steps: (1) preparation and cleaning of the silicon and glass surfaces using a piranha soak and an oxygen ashing step, (2) alignment and clamping of the two wafers together, and (3) application of a voltage (1000V) across the wafer interface at elevated temperature (300°). The negative electrode is applied to glass wafer surface not being bonded with the silicon wafer held at ground potential. As for the fusion bonding process, cleanliness of the wafers and the bonding apparatus is paramount for achieving high-quality and low-defect wafer-level bonds.

6.2.3 Integration of Bulk Piezoelectric Elements

Integration of the piezoelectric elements within the device constitutes a critical task in the assembly of the active valve device. This section discusses the important issues related to preparing and tolerancing of the piezoelectric material elements with respect to other features in the device. Details of the actual die-level assembly procedure will be provided in Section 6.2.4.

The top and bottom surfaces of the piezoelectric elements are covered with a thin-film gold-tin (Au-Sn) eutectic alloy for bonding to the adjoining silicon layers at an elevated temperature. In order to achieve good bonding over the complete interface area, the piezoelectric material must possess smooth top and bottom surfaces. A rough surface of the piezoelectric material (and therefore of the metallized layer), would result in only pinpoint contacts between the piezoelectric material and the silicon and therefore a weak bond. Prior to bonding, sizing of the piezoelectric elements with respect to the surrounding Layer 3 glass and etching of seats in the Layer 2 silicon to compensate for thickness mismatch between the piezoelectric material and glass is critical for ensuring a deflection of the drive element piston below levels of fracture stress in the tethers. Each of these piezoelectric material integration issues is covered in detail in the following sub-sections.

Piezoelectric Material Preparation

Virgin piezoelectric materials are obtained from vendors in the form of thin plates, each with a thickness of $\sim 1.1mm$ and diameter between 1 cm and 5 cm. As received, these plates possess a surface roughness as large as $5\mu m$. In order to achieve adequate eutectic bonding during

device assembly, a surface roughness near $0.5\mu m$ is required prior to metallization. To achieve this, the piezoelectric material plates are polished using coarse and fine grain diamond slurry polishing procedures. Figure 6.5 displays typical profilometer scans before and after material polishing for the two primary types of piezoelectric materials used in the valve, PZT-5H and PZN-PT.

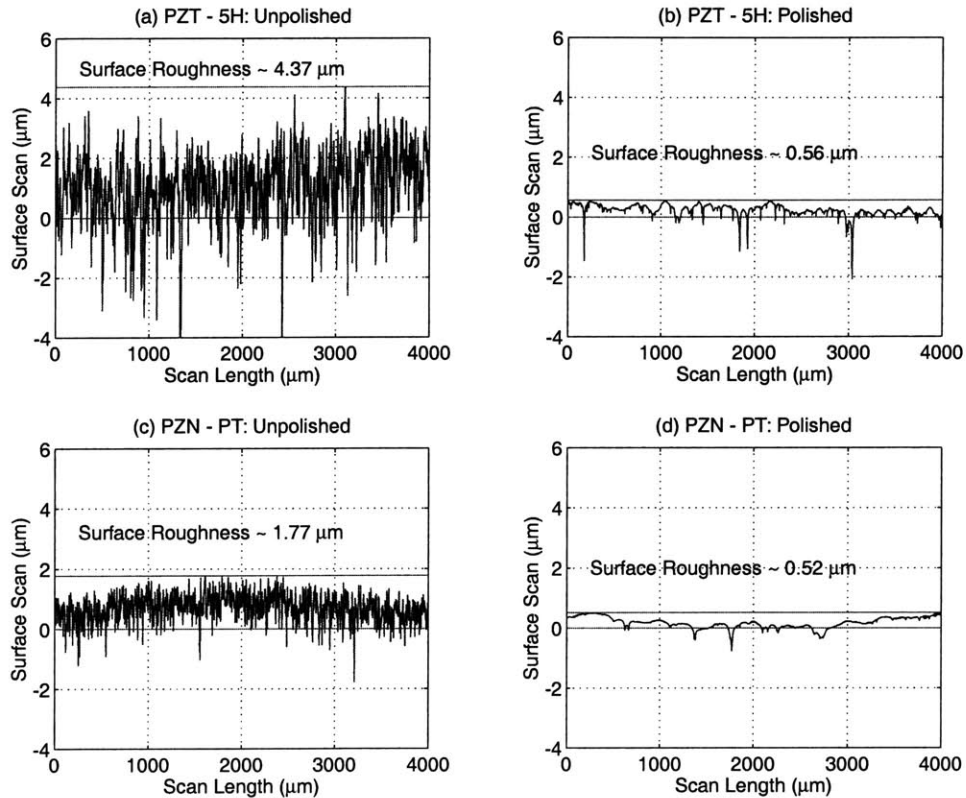


Figure 6.5: Profilometer surface roughness scans of PZT-5H and PZN-PT piezoelectric material plates before and after polishing steps: (a) unpolished PZT-5H material, (b) polished PZT-5H material, (c) unpolished PZN-PT material, (d) polished PZN-PT material. Note that thin deep trenches are not counted within the roughness estimate. However, thin tall “mountains” must be accounted for since these would serve to separate an adjoining layer of material.

During polishing, each plate is sized to yield a thickness of $1mm \pm 10\mu m$ with thickness variation across the plate of $\sim 2\mu m$. Prior to metallization, the material plates are solvent cleaned with a series of acetone, methanol, and isopropanol steps. Additionally, a further cleaning soak in a 20:1 water:nitric acid solution is carried out for 1 minute to remove particulate matter. At this point, the piezoelectric material plates are ready for metallization.

AuSn Eutectic Bonding

To bond mechanically and to connect electrically the piezoelectric material cylinders to the adjoining silicon layers in the active valve device, a reliable bonding mechanism must be employed. This bonding mechanism must allow for tight dimensional control over the bond layer thickness and allow for a bonding temperature and environment that is compatible with the rest of the die-level assembly process. Numerous bonding methods that could potentially work in this device, ranging from polyimides and epoxies to brazing and soldering to gold-based eutectic alloys, have been presented in the literature. A detailed discussion of these research efforts, with application toward the development of MHT technology, is found in [2]. The resulting conclusion of initial work by Mlcak [8] and the subsequent work by Turner [2] was to employ a thin-film AuSn eutectic alloy (composition: 80 wt. % Au and 20 wt. % Sn) as the bonding mechanism within MHT devices in general, and specifically within the active valve device presented in this thesis.

A four layer film structure on the piezoelectric material and a three layer film structure on each of the adjoining silicon layers is deposited in preparation for bonding, as shown in Figure 6.6. The four layer structure on the piezoelectric material consists of 50 nm Ti, 250 nm Pt, 4000 nm AuSn, and 50 nm Au. The Ti serves as an adhesion layer, the Pt as a diffusion barrier, and the final Au as a capping layer to prevent oxidation of Sn in the AuSn alloy. The AuSn layer, chosen to be thick enough ($4 \mu\text{m}$) to compensate for the piezoelectric material surface roughness ($\sim 0.5\mu\text{m}$), is sputtered from an alloy target with 80 wt. % Au and 20 wt. % Sn composition. Sputtering is chosen over evaporation because sputtering allows the stoichiometry of the target to be maintained in the deposited film [9]. The three layer Ti-Pt-Au structure on each of the adjoining silicon pieces enables the eutectic alloy to wet the silicon and is deposited on the die-level using e-beam evaporation procedures.

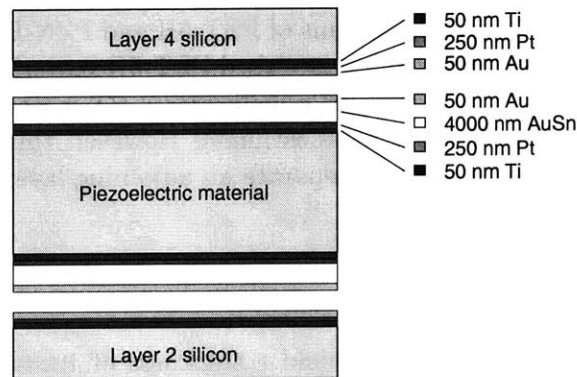


Figure 6.6: Eutectic alloy deposition on the piezoelectric material and adjoining silicon layers. The piezoelectric material contains a 4 layer film structure and each of the silicon layers contains a 3 layer film structure.

Dicing/Core-Drilling of Piezoelectric Elements

Following deposition of the eutectic alloy, the metallized piezoelectric material plates are core-drilled or diced to produce either cylindrical or square piezoelectric elements. As detailed in subsequent chapters of this thesis, devices integrating both cylindrical and square elements have been successfully fabricated and tested. The advantage of using square piezoelectric elements over cylindrical ones is that the process of dicing a piezoelectric material plate in a grid pattern results in the production of 2-3 times the number of elements than can be produced from core-drilling from a identical size plate. By sheer numbers and by the fact that closely located elements will possess almost identical thicknesses (relatively insensitive to variations in thickness across the material plates), the use of square elements increases the odds of being able to select multiple elements of identical thickness to insert into drive element structures. Once the material plate has been either core-drilled or diced, the resulting piezoelectric elements are individually measured for thickness using a hand-held precision micrometer, as shown in Figure 6.7. By calibrating the micrometer before each measurement with a precise thickness gauge block ($1\text{mm} \pm 0.01 \mu\text{m}$) and averaging repeated series of measurements of the same elements, these thickness measurements are estimated to be accurate within $\sim 0.5\mu\text{m}$. The elements are then organized and sorted according to the thickness.

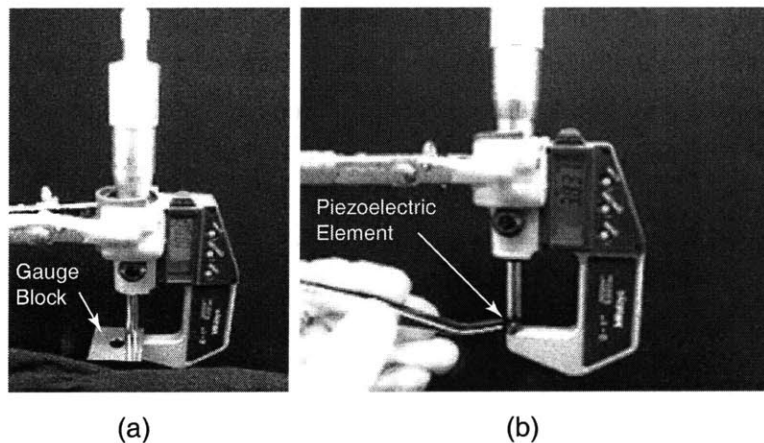


Figure 6.7: Precision micrometer used for thickness measurement of the piezoelectric elements and Layer 3 glass dies prior to device assembly: (a) calibration of micrometer with respect to a 1 mm gauge block, and (b) measurement of an individual piezoelectric element.

Etching of Piezoelectric Element Seats

One of the critical issues during integration of the piezoelectric material elements is guaranteeing an upward deflection of the drive element piston large enough to ensure a preload on the eutectic

alloy interface during bonding, yet small enough to ensure stresses in the piston tethers below the critical value of 1 GPa. Typically, in the drive element structures designed, fabricated, and tested in this thesis, the piston tethers will reach a tensile stress of 1 GPa for displacements near $\sim 9\mu m$. Therefore, at any time during the bonding, poling, and operation of a device, it is desired to maintain piston displacements no greater than a safe value of $\sim 6\mu m$. In terms of preload on the eutectic interface, it is desired to ensure a “piston push-up” of $\sim 2\mu m$. These requirements therefore dictate that at the instant of eutectic bonding, the piezoelectric element(s) beneath the drive element piston must be forcing the piston upward by $\sim 2\mu m$ and that for all time after that the piston must not be forced to displacements greater than $\sim 6\mu m$. Considering that this $4\mu m$ range is 0.4% of the total piezoelectric element thickness, this task represents quite a challenge.

In preparation for piezoelectric element integration, the Layer 3 glass wafer is diced into individual dies, and each of these dies is measured using the hand-held micrometer. As received from the vendor, each of the ultrasonically-machined Layer 3 glass wafers possesses a thickness between $967\mu m$ and $974\mu m$, with thickness variation across a given wafer less than $1\mu m$. At the time of integration, since the piezoelectric elements (with deposited eutectic alloy films) have thicknesses near $1000\mu m$ and the Layer 3 glass dies have thickness near $970\mu m$, it is necessary to have the capability to remove this thickness difference of $\sim 30\mu m$ between the piezoelectric material and the surrounding glass. Ideally, once integrated into the device, the piezoelectric elements’ top surfaces should be slightly above level with the Layer 3 glass top surface so as to produce predictable upward displacement of the drive element piston from its equilibrium position (“push-up”).

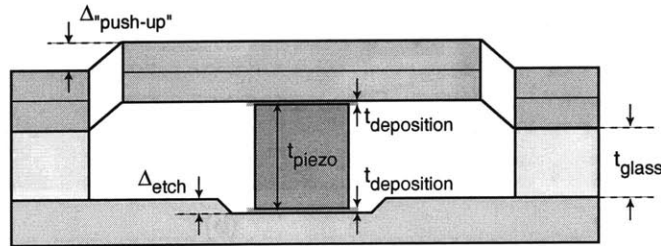


Figure 6.8: Compensation of the piezoelectric element - Layer 3 glass thickness mismatch by plasma etching shallow seats in the Layer 2 bottom silicon die. Precise control of the etch depth is necessary to achieve the desired “push-up” of the drive element piston.

This thickness matching is achieved by plasma etching shallow seats for all of the piezoelectric elements in the Layer 2 bottom silicon wafer, as shown in Figure 6.8. An iterative process of carefully timed etches followed by depth measurements using a scanning profilometer can result in etch depth control to within $\sim 0.5\mu m$. With this capability to compensate for thickness mismatch between the piezoelectric elements and the surrounding Layer 3 glass, proper

“push-up” of the drive element piston can be achieved during assembly and bonding. On the die-level, each Layer 2 silicon die is matched with a pre-measured (t_{piezo}) grouping of one or three piezoelectric elements (depending on whether a single or multiple piezoelectric valve is being fabricated) and with a pre-measured (t_{glass}) Layer 3 glass die. With knowledge of the three-layer film thickness $t_{deposition}$ (see Section 6.2.3) that will subsequently be deposited on the underside of the drive element piston in Layer 4 and on the top surface of the “to be etched” seats in Layer 2, and with the value of $\Delta_{“push-up”}$ desired after device assembly, the required etch depth (Δ_{etch}) in Layer 2 is determined, according to 6.1.

$$\Delta_{etch} = t_{piezo} + 2t_{deposition} - t_{glass} - \Delta_{“push-up”} \quad (6.1)$$

Following etching of the seats, the Layer 1-2 silicon dies are cleaned and combined with Stack 4-5-6 silicon dies for deposition of the three-layer Ti-Pt-Au film structure required for eutectic bonding. This deposition is performed using e-beam evaporation through specially-machined shadow masks to allow for selective coating of the dies. For the Stack 4-5-6 dies, the underside of the drive element piston is coated, and for Layer 2 dies the inside of each of the etch seats is coated.

6.2.4 Die-Level Assembly and Bonding

Assembly and Bonding Procedure

Final assembly of the active valve device is performed at the die-level. As shown in Figure 6.9(a), wafer-level etching and bonding procedures, followed by dicing of the stacks into individual dies have resulted in the creation of a Stack 7-8-9 die, a Stack 4-5-6 die, a Stack 1-2 die, and a Layer 3 die. Additionally, piezoelectric material preparations have created individual piezoelectric elements ready for insertion. It is desirable to perform these bonding steps at the die-level, rather than the wafer-level, so as to allow for individual measurements of the Layer 3 glass die thickness and to enable individual control of the seat etching in Layer 2. Additionally, die-level bonding significantly reduces the risk of losing an entire multi-layer wafer structure during wafer-level processing. The die-level assembly process consists of four main steps, as shown in Figure 6.9(b), (c), (d).

1. Die-level anodic bonding of Stack 4-5-6 to Stack 7-8-9 at a temperature of 300°C and an applied voltage of 1000V across the Layer 6 - Layer 7 interface. This bond is performed at atmospheric pressure. Time of bond = 20 minutes.
2. Die-level anodic bonding of Stack 1-2 to Layer 3 at a temperature of 300°C and an applied voltage of 1000V across the Layer 2 - Layer 3 interface. This bond is performed at atmospheric pressure. Time of bond = 45 minutes.

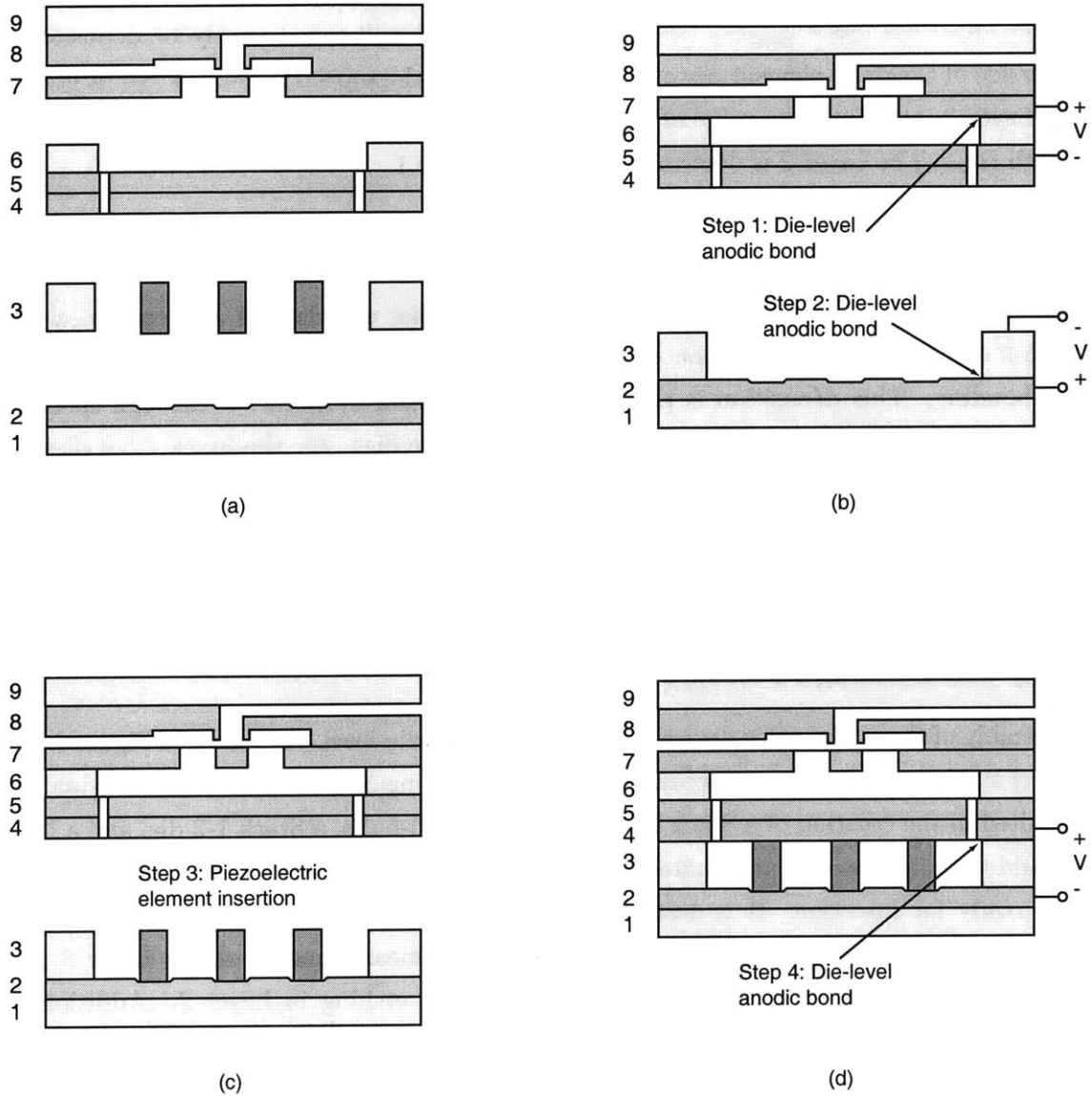


Figure 6.9: Die-level bonding procedure for active valve device: (a) beginning dies ready for assembly, (b) Step 1: anodic bonding of Stack 4-5-6 to Stack 7-8-9 ; Step 2: anodic bonding of Stack 1-2 to Layer 3, (c) Step 3: insertion of piezoelectric element(s), and (d) Step 4: anodic bonding of Stack 1-2-3 to Stack 4-5-6-7-8-9.

3. Alignment and placement of one or more piezoelectric material elements within the Stack 1-2-3 die.
4. Simultaneous die-level anodic bonding of Stack 1-2-3 to Stack 4-5-6-7-8-9 and eutectic bonding of piezoelectric element(s) to Layer 2 and Layer 4 silicon. This bond is performed in a reducing atmosphere of $Ar - 5\%H_2$ gas at pressure 10^{-2} torr and temperature $300^\circ C$. Additionally, a voltage of 1000V is applied across the Layer 3 - Layer 4 interface. Time of bond = 60 minutes.

A reducing atmosphere is chosen for the final simultaneous anodic/eutectic bond to ensure no oxidation of the Sn within the AuSn alloy and to achieve a void-free eutectic bond [2]. Additionally, following this bond, the device is cooled under vacuum to ensure removal of all trapped gases within the bond. Completion of these four die-level bonding steps produces an active valve structure that is ready for filling of the hydraulic amplification chamber.

Assembly Jigs

The die-level anodic bonding discussed above is performed using the specially machined alignment and bonding jigs shown in Figure 6.10. The 1st-generation jig, shown in Figure 6.10(a), provides a large central contact surface onto which a die can be placed and the bottom surface held at either positive or negative voltage. An outer ring with attached spring clamps for clamping of one die onto another is held at ground potential. Once inserted into an oven, electrical contact is made through attached feet on the underside of the jig. Alignment, placement, and clamping of a dies and insertion of piezoelectric elements is facilitated by a vacuum chuck with 3-axis motion capability and a range in each of these directions of 1 cm. The 2nd-generation jig, shown in Figure 6.10(b), is more compact than the 1st-generation jig. It likewise provides electrical contact through thin wire clamps, but additionally allows for edge alignment of dies to a central area with ceramic insulating locator pins. Figure 6.11 illustrates an active valve device in the final bonding step using the 2nd-generation anodic bonding jig.

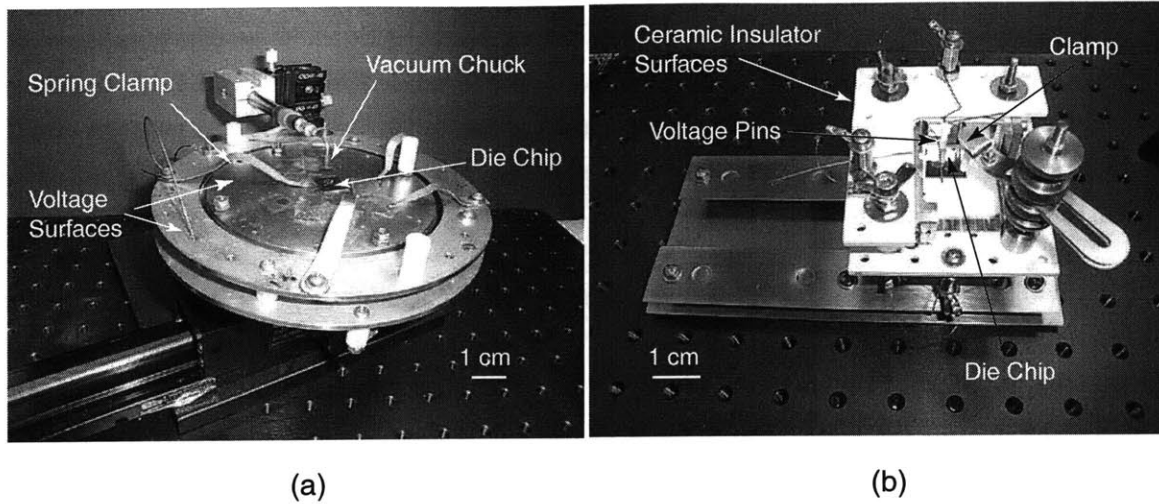


Figure 6.10: Die-level alignment and bonding jigs: (a) 1st-generation jig, (b) 2nd-generation jig.

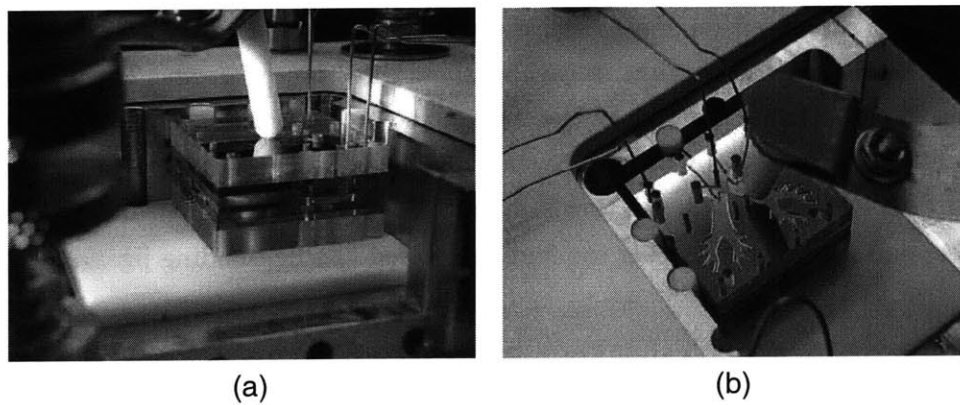


Figure 6.11: Electrical contact to an active valve chip for anodic bonding: (a) side view of chip in jig and (b) top view of chip in jig. Electrical cantilever pins contact various layers of the device for bonding procedures.

6.2.5 Fluid Filling/Sealing of HAC

Introducing fluid into the hydraulic amplification chamber of the active valve is a critical step in preparing the device for operation. Any bubbles or trapped residual gas within the amplification chamber will significantly increase its compliance, thereby eliminating efficient coupling between the drive element and valve membrane structure. This section briefly details the fluid filling procedure and issues associated with sealing.

Procedure for Filling

A fluid-filling apparatus and procedure developed by Richard Mlcak (Boston Microsystems, Inc) and updated by Lodewyk Steyn (MIT) was used to fill the active valve devices developed in this thesis. The apparatus, shown in Figure 6.12, consists of a filling chamber, a fluid reservoir chamber, a vacuum pump, and a series of valves connecting these components together. A schematic of the component connections is shown in Figure 6.13. A detailed explanation of the filling procedure and issues associated with the development of this procedure can be found in [10] and [11]. The major steps in the filling process are as follows:

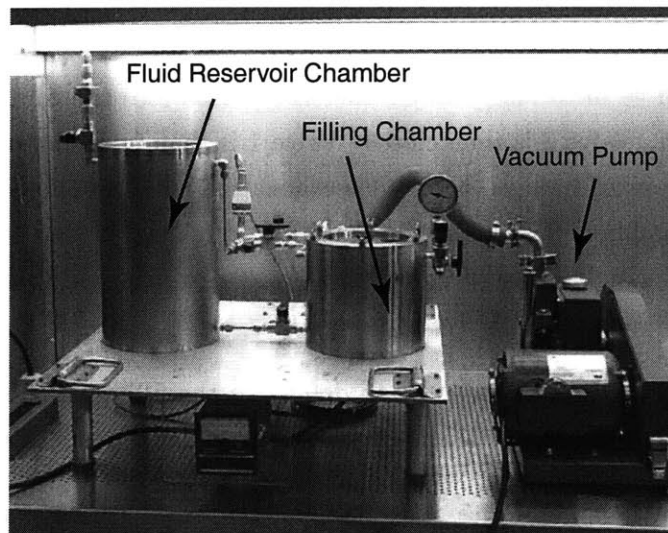


Figure 6.12: Fluid filling apparatus to fill active valve devices. System consists of a fluid reservoir chamber, a filling chamber, a vacuum pump, and series a valves connecting all components together.

1. The assembled, bonded, and poled active valve device is inserted into the filling chamber. The chamber is then closed, with no fluid present in this chamber. Valve 1, Valve 3, and Valve 5 are closed.

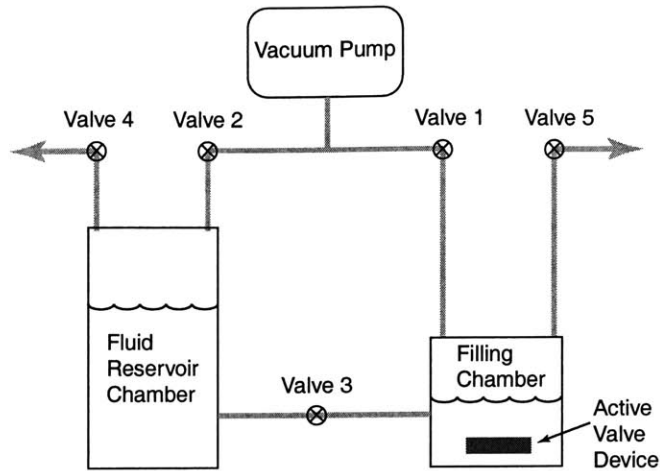


Figure 6.13: Fluid filling schematic of component connections.

2. With the fluid reservoir chamber full of fluid, Valve 4 is closed and Valve 2 is opened. The vacuum pump is initiated to outgas the fluid in the reservoir chamber. After a period of 1 hour, Valve 2 is closed. Valve 4 is then opened to bring the reservoir pressure back to atmospheric pressure.
3. Valve 3 is opened to introduce a small amount of fluid into the filling chamber from the reservoir chamber. Valve 3 is then closed. Valve 1 is then opened and the filling chamber is evacuated to approximately 1 torr. This evacuation acts to boil off the fluid introduced into the filling chamber. The hydraulic amplification chamber and other fluidic channels in the device are thereby filled with silicon oil vapor, which easily wets the walls of these structures. After 10 minutes, Valve 1 is closed.
4. Valve 3 is opened for a sufficient time to deliver to the filling chamber a volume of fluid that submerges the valve device and the jig within which it rests. Valve 3 is then closed.
5. Valve 5 is opened to pressurize the filling chamber to atmospheric pressure. This step, which lasts for approximately 1 hour, serves to “push” the fluid into the hydraulic amplification chamber. The device is then removed from the filling chamber and is ready for testing.

During this filling procedure, the active valve device is securely clamped within a test-jig apparatus. Prior to removal from the filling chamber, a valve located on the test jig that leads to the HAC chamber is closed. Once hooked up to the experimental testing apparatus, this valve is opened to an external pressure regulator (see next section).

Sealing Issues

In order to maintain a compressive stress on the piezoelectric elements at all times and to eliminate the potential for cavitation within the hydraulic amplification chamber during actuation, the fluid within the chamber is required to be held at a positive bias pressure (typically 0.5-2MPa). The value of this bias pressure P_{bias} is determined based on the P_{HAC} pressure fluctuations expected during active valve operation (determined using numerical simulation). P_{bias} should be chosen to ensure that P_{HAC} never passes below zero during actuation. Sealing of the HAC chamber at a desired bias pressure was not an option in this thesis because such a procedure had not been developed. Further discussion of sealing and encapsulation studies for these types of devices can be found in [11]. For the purposes of the active valve described in this thesis, therefore, it was required to develop a means to bias the P_{HAC} after the fluid filling operation was complete and without completely sealing the chamber.

To accomplish this objective, a small cross-sectional area fluid channel was etched into the underside of Layer 7 so to provide a connecting path between the hydraulic amplification chamber and an external pressure regulator. Figure 6.14 illustrates this concept. By incorporating a high resistance fluid channel in this location, static bias pressures dictated by the external regulator can be imposed on the chamber, however, high frequency pressure fluctuations created during actuation remain confined to the chamber. In essence, this channel acts as a low pass filter for transmission of pressure fluctuations into and out of the chamber. The channel length, width, and height were designed to be 1mm, $10\mu m$, and $10\mu m$ respectively. The channel was desired to be long and thin so as to create a large flow resistance during actuation. However, the channel width and height were designed large enough so as to be able to initially fill the device with fluid using the procedure detailed above in a reasonable amount of time (on the order of 20 minutes).

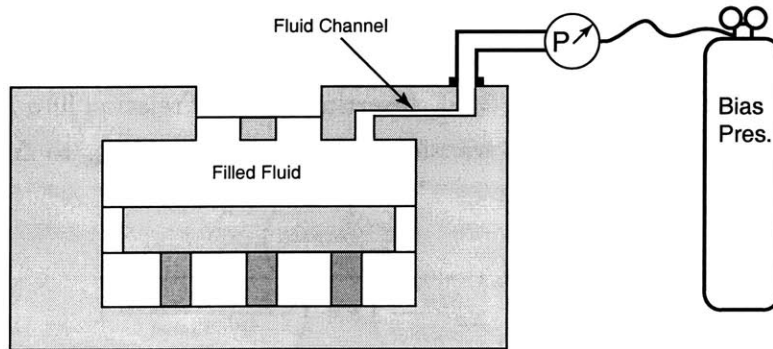


Figure 6.14: Schematic of the high resistance fluid channel between the HAC and an external bias pressure regulator. This channel was etched into the underside of Layer 7.

To design properly this high resistance flow channel for use in the active valve geometry

detailed in this thesis, a model was developed to capture the inertia and flow resistance associated with a fluid slug within the channel (see Figure 6.15). The assumptions in this model are: (1) the fluid slug occupies the entire length of the channel, (2) the fluid slug interacts with the volumetric stiffness of the hydraulic amplification chamber (designated as K_{HAC}), and (3) the fluid slug flow behavior is governed by Hagen-Poiseuille flow relations. The variable ΔV_{slug} is defined as the volume of fluid pushed into/pulled out of the HAC chamber during an actuation cycle of the active valve. The variable ΔP_{slug} is defined as the differential pressure seen across the fluid slug during this actuation cycle due to pressure fluctuations within the HAC chamber.

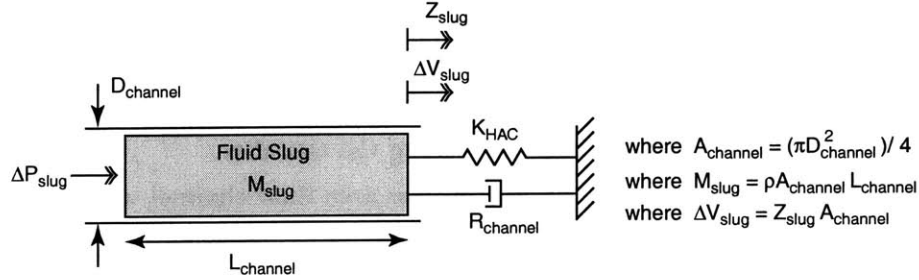


Figure 6.15: Model of the high resistance fluid channel between the HAC and an external bias pressure regulator. A fluid slug within the channel is modeled. This slug is acted upon by an external stiffness associated with the HAC chamber stiffness. Additionally, the flow resistance of this slug through the channel is modeled using laminar Hagen-Poiseuille flow relations.

Based on the model schematic in Figure 6.15, a differential equation for the slug behavior can be written,

$$\left(\frac{M_{slug}}{A_{channel}^2} \right) \Delta \ddot{V}_{slug} + R_{channel} \Delta \dot{V}_{slug} + K_{HAC} \Delta V_{slug} = \Delta P_{slug} \quad (6.2)$$

where $R_{channel} = \left(\frac{128\mu L_{channel}}{\pi D_{channel}^4} \right)$ is based on Hagen-Poiseuille flow in a circular channel [8]. In this relation, μ is the viscosity of the fluid. Inserting this flow relation into Equation 6.2 and rearranging in the frequency domain, a transfer function relating ΔV_{slug} to ΔP_{slug} is obtained

$$\frac{\Delta V_{slug}}{\Delta P_{slug}} = \frac{\left(\frac{\pi D_{channel}^2}{4\rho L_{channel}} \right)}{s^2 + \left(\frac{32\mu}{\rho D_{channel}^2} \right) s + \left(\frac{K_{HAC} \pi D_{channel}^2}{4\rho L_{channel}} \right)} \quad (6.3)$$

where ρ is the density of the fluid in the channel. The natural frequency (known as the Helmholtz frequency) of this fluid-structure interaction event can be written as

$$f_{Helmholtz} = \frac{1}{2\pi} \sqrt{\frac{K_{HAC} \pi D_{channel}^2}{4\rho L_{channel}}}. \quad (6.4)$$

In designing the channel dimensions, the following parameter values (which correlate with the active valve geometry fabricated in this thesis) were assumed: $L_{channel} = 1mm$, $D_{channel} = 11.3\mu m$, $K_{HAC} = 1.0e^{17} \frac{Pa}{m^3}$, $\rho = 760 \frac{kg}{m^3}$, and $\mu = 6.5e^{-4} \frac{kg}{ms}$. These values result in a frequency of 48Hz for which ΔV_{slug} is 1% of the drive element volume change. Additionally, a Helmholtz frequency of $f_{Helmholtz} = 578Hz$ results. However, Helmholtz resonant behavior of this slug is non-existent due to the dominant fluid viscous losses in the channel. Additionally, with these channel dimensions, it is estimated that during initial fluid filling, the HAC chamber should fill in approximately 5-10 minutes under atmospheric pressurization in Step 5 of the above fluid filling procedure. Chapter 9 includes experimental verification of the performance of this high fluid resistance channel within working high frequency active valve devices.

6.3 Sub-Component Testing Plan

To solve and to overcome the previously described fabrication challenges, a fabrication and experimental test plan was developed. This plan divides the full piezoelectrically-driven active valve device into simpler decoupled sub-components structures, which can be independently fabricated, assembled, and tested. The sub-component structures are the piezoelectric drive element and the valve cap and membrane structure. Figure 6.16 outlines this plan. This section provides a general overview of the sub-component geometries and the important questions that need to be answered in each of the sub-component studies. Subsequent chapters of this thesis go on to provide complete and detailed experimental validation of each of the sub-components.

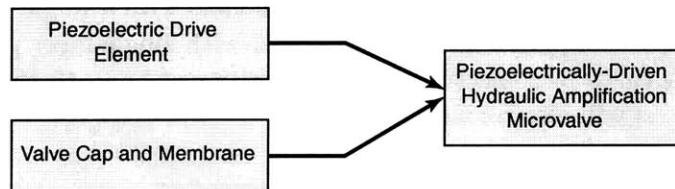


Figure 6.16: Sub-component fabrication and testing plan. Realization of a full piezoelectrically-driven hydraulic amplification microvalve depends on successful validation of the piezoelectric drive element and the valve cap and membrane deformation behavior. Fluid filling success is evaluated with the full active valve device.

6.3.1 Piezoelectric Drive Element

The piezoelectric drive element provides actuation volume change and pressurization to the hydraulic amplification chamber and therefore the valve cap and membrane as it opens and closes against a fluid orifice. This sub-component study proves that etching of the high-aspect ratio tethered piston structures and control of fillet radii at the base of these etches can be

performed in a repeatable fashion. Additionally, wafer-level silicon-silicon fusion bonding were validated to form Stack 4-5. As shown in Figure 6.17, devices were constructed with single-layer pistons as well as double-layer pistons for stiffness comparison. Piezoelectric material, both PZT-5H and PZN-PT, were processed to create individual piezoelectric elements for insertion into drive element structures. Sub-component devices with a single element placed centrally beneath the drive piston as well as devices with three piezoelectric elements spaced out uniformly beneath the drive piston were fabricated to validate enhanced stiffening benefits of drive element actuators with multiple piezoelectric elements (again see Figure 6.17). The drive element sub-component devices were experimentally tested to evaluate both quasi-static deformation behavior (frequencies ≤ 15 kHz) and dynamic modal behavior (up to 200 kHz) under a wide range of applied voltages. Completion of this sub-component study enables incorporation of the drive element actuator structure within complete active valve structures.

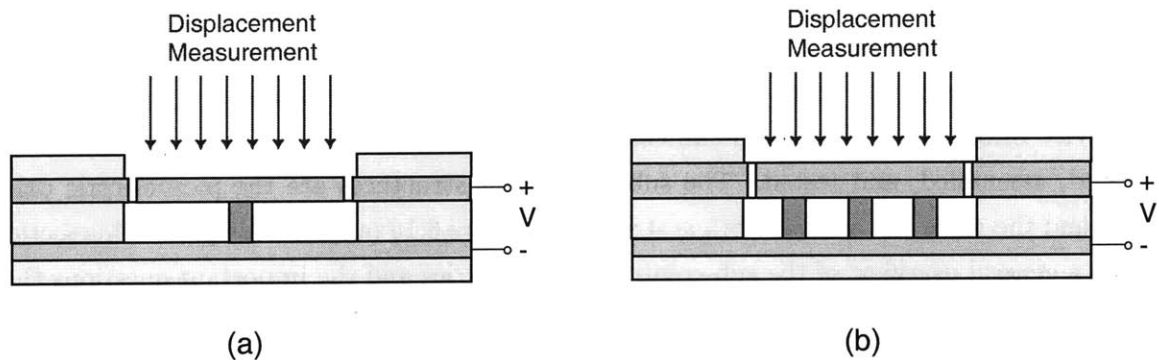


Figure 6.17: Drive element sub-component study: (a) devices with a single piezoelectric element centrally-located beneath the piston as well as devices with single-layer pistons will be fabricated, (b) devices with three piezoelectric elements positioned beneath the piston and devices with double-layer pistons will also be fabricated.

6.3.2 Valve Cap and Membrane

The valve cap and membrane structure reacts to differential pressures to open and close against a fluid orifice. This sub-component study validates the etching of the membrane and control of fillet radii at the oxide etch stop. Valve membrane structures were tested to verify non-linear pressure-deflection behavior, and results were compared to the non-linear numerical models presented in Chapter 3 of this thesis. The sub-component structure used for these tests is shown in Figure ??(a). Gas pressure was introduced into the amplification chamber to directly force the valve cap and membrane structure upward. Additionally, gas pressure was introduced above the membrane as well to deform the structure in the downward direction. Deflection of the valve cap was measured using a laser vibrometry system. Completion of this sub-component

study provides an understanding of the valve membrane stiffness in response to applied pressures and therefore enables subsequent fluid filling and testing of full active valve devices.

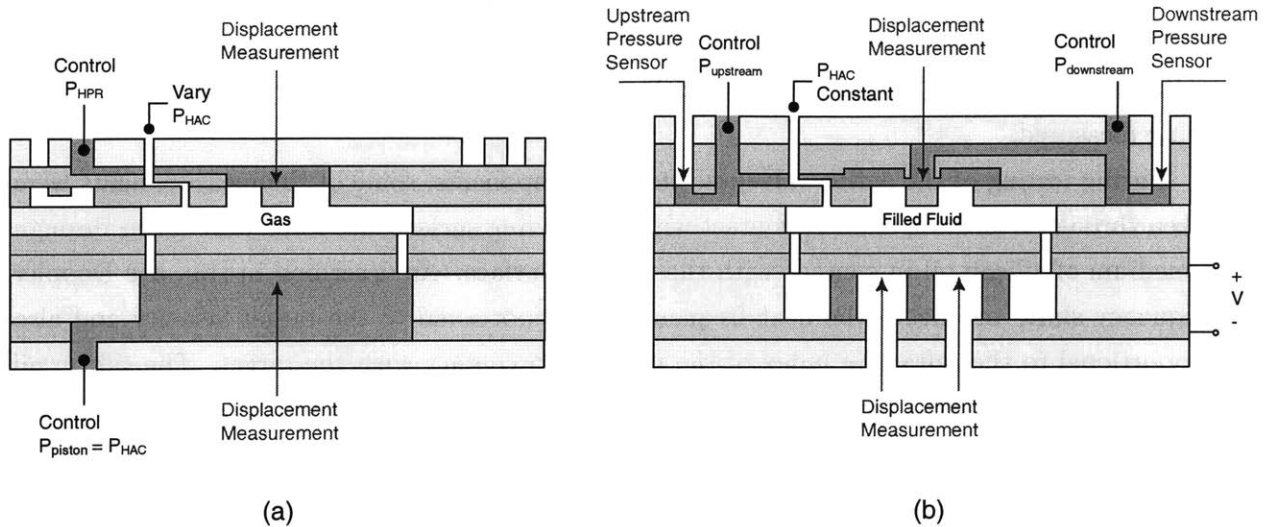


Figure 6.18: Valve membrane sub-component study and full active valve study: (a) valve cap and membrane within assembled chamber were deformed with gas pressure to determine structural stiffness, (b) the active valve device was fully characterized for pressure-flow behavior and limitations in dynamic performance. Note that the high resistance flow channel and the external fluid flow path above valve cap overlap in this schematic. In reality, these channels are offset spatially from one another.

6.3.3 Full Active Valve

Having successfully completed the two sub-component studies, a full active valve device was tested. The structure of this device is shown in Figure 6.18. Displacements of the valve cap in response to applied piezoelectric voltage were determined. In addition to evaluating the opening and closing capability of the valve in response to voltage, differential pressure - flow relations were established across the flow channel. Dynamic transfer functions of the full valve device were obtained and limitations in device performance were established.

6.4 Testing Apparatus

6.4.1 Laser Vibrometer System

A laser vibrometer system was used to measure the structural vibrations of the drive element piston and valve cap during the experimental testing of the full active valve and its sub-component structures. This system uses a technique known as laser doppler vibrometry to detect the ve-

locity of a moving surface. The wave used for this purpose is a laser, typically HeNe or of similar wavelength. When this wave strikes a moving surface and reflects back, a frequency shift is introduced. If the reflected wave is compared with the incident wave, the frequency shift results in a beating phenomenon, where the beat frequency is proportional to the velocity of the moving surface. Measuring this beat frequency therefore gives the velocity of the surface being measured.

During testing of the active valve and its sub-components, some of the measurements were taken through a medium of air in contact with the moving surface and some were taken through a medium of silicon oil in contact with the moving surface. As described in [13], the Doppler frequency shift, and hence the beat frequency, is proportional to the target velocity and also proportional to the refractive index of the medium in contact with the target. The silicon oil used in the valve (Dow Corning DC200 0.65 centistoke oil) has a refractive index of 1.375. Therefore, in taking measurements using this laser vibrometer system, any measurement values taken with this oil in contact with the moving surface were divided by 1.375 to obtain the proper values. All results incorporating oil in contact with the valve cap in subsequent chapters have been properly scaled by this value.

6.4.2 Fluids Test-Rig

The fluids testing rig used in the active valve and sub-component studies documented in this thesis was designed, built, and constructed by Lodewyk Steyn. Figure 6.19 illustrates a portion of this set-up. The explicit details of this test-rig are contained in [11]. In summary, this set-up enables the control of a wide range of pressure loadings on the drive element piston, within the HAC chamber, and on the valve cap and membrane upstream and downstream of the valve orifice flow channel for the active and sub-component studies. Fluid reservoirs contain degassed silicon oil for the purposes of creating fluid flow in testing the active valve device. A series of absolute and differential pressure sensors are located throughout the set-up to enable real-time measurements of the static and dynamic pressures at critical locations within the valve device. Further discussions of which pressures were measured for which experiments are included in the subsequent experimental chapters of this thesis.

6.5 Conclusions

This chapter has presented the fabrication and assembly challenges faced in realizing a working piezoelectrically driven hydraulic amplification microvalve. The wafer-level fabrication process, piezoelectric material preparation and integration issues, and die-level assembly and bonding procedures were discussed. Additionally, an overview of the active valve sub-component test plan was presented. The details of these sub-component studies are covered in subsequent

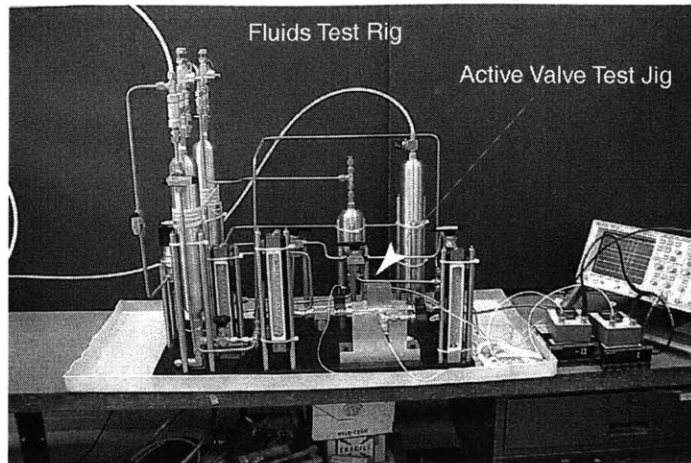


Figure 6.19: Fluids test-rig for testing of the active valve and its sub-components. This set-up contains fluid reservoirs, static and dynamic pressure sensors, flow sensors, and absolute and differential pressure sensors for evaluating device performance during testing.

chapters.

Bibliography

- [1] A.A. Ayon, K-S. Chen, K.A. Lohner, S.M. Spearing, H.H. Sawin, and M.A. Schmidt, "Deep Reactive Ion Etching of Silicon," *Materials Research Society Symposium Proceedings*. v. 546, pp.51-61, 1999.
- [2] K-S. Chen, A. Ayon, and S.M. Spearing, "Controlling and Testing the Fracture Strength of Silicon on the Mesoscale," *Journal of the American Ceramic Society*, 83 [6], pp.1476-84, 2000.
- [3] J.C. Arnold and H.H. Sawin, "Charging of pattern features during plasma etching," *J. Appl. Phys.*, vol. 70, no. 10, pp.5314-5317, 1991.
- [4] T. Kinoshita, M. Hane, and J.P. McVittie, "Notching as an example of charging in uniform high-density plasmas," *J. Vac. Sci. Technol. B, Microelectron. Process. Phenom.*, vol. B14, no. 1, pp.560-565, 1996.
- [5] T. Nowaza, T. Kinoshita, T. Nishizawa, A. Narai, T. Inoue, and A. Nakaue, "The electron charging effects of plasma on notch profile defects," *Jpn. J. Appl. Phys.*, vol. 34, pt. 1, no. 4B, pp.2107-2113, 1995.
- [6] U. Gosele and Q.-Y. Tong. Semiconductor wafer bonding. *Annual Review of Materials Science*, 28, pp. 215-241, 1998.
- [7] K.T. Turner, An Evaluation of Critical Issues for Microhydraulic Transducers: Silicon Wafer Bonding, Strength of Silicon on Insulator Membranes and Gold-Tin Solder Bonding. MIT Master's Thesis. June 2001.
- [8] R. Mlcak, Numerous presentations at MIT on the development of a bonding technology between piezoelectric material and silicon for use in MHT technology, 1997-2000.
- [9] M. Ohring. *The Materials Science of Thin Films*. Academic Press, New York, 1992.
- [10] R. Mlcak. *Wafer-scale Fluid Filling System: Standard Operating Procedure and Manual*. Document was provided to MIT from Boston Microsystems, Inc. in October 2000.

- [11] J.L. Steyn, Master's Thesis, Massachusetts Institute of Technology, 2002.
- [12] F.M. White, *Fluid Mechanics*, 2nd ed. McGraw-Hill Inc, 1986.
- [13] H.D. Young, *University Physics*, 8th ed. Addison Wesley, 1992.

Chapter 7

Sub-Component Study: Piezoelectric Drive Element

7.1 Objectives

The purpose of this sub-component study was to evaluate the fabrication and assembly process flow of the piezoelectric drive element structure, shown in Figure 7.1, and to obtain quasi-static and high-frequency experimental data on completed devices. Specifically, the three primary objectives of this study were:

1. To determine whether both single-layer and double-layer piston structures could be fabricated and assembled in drive element devices. As compared to single-layer pistons, the double-layer design enhances the structural stiffness of the micro-actuator device.
2. To determine whether standard polycrystalline PZT-5H and higher-performing single-crystal PZN-PT materials [4] could be processed and integrated within tethered-piston drive element structures. Although the final active valve devices (detailed in Chapter 9) incorporated solely PZN-PT material, the high cost of this material forced initial studies to work with less costly PZT-5H material.
3. To determine whether both single and multiple piezoelectric elements could be successfully integrated beneath the drive element piston. Multiple elements spread out beneath the piston serve to stiffen the micro-actuator structure. However, tolerancing and bonding of multiple elements within the device is more challenging.

Successful integration of these types of piezoelectric materials with properly etched and bonded tethered piston structures demonstrates the potential for high-frequency, high-stiffness actuation within full active valve devices.

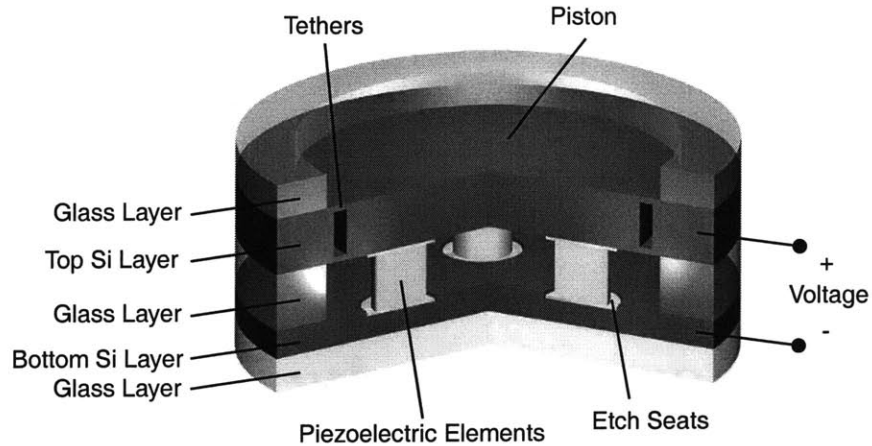


Figure 7.1: 3-D schematic of a piezoelectric drive element device. Three piezoelectric cylinders are sandwiched between a lower support silicon layer and an upper double silicon layer tethered-piston structure. Voltage is carried along the upper and lower silicon layers.

7.2 Device Test-Plan

The overall piezoelectric drive element sub-component study was divided into two parts. In the first part, “1st-generation” drive element devices were fabricated and tested. In the second part, “2nd-generation” drive element devices, slightly different in geometry than the “1st-generation” devices, were fabricated and tested. Ideally, a consistent geometry would have been preferred throughout the full study. Unfortunately, due to research program scheduling and resource limitations, the use of different geometries was unavoidable. The experimental results of the two sub-studies combined together, however, do provide overwhelming evidence that integration of piezoelectric elements within micromachined silicon thin-tethered piston structures is achievable. The overall device test plan is illustrated in Figure 7.2. The three major design variations contained within this sub-component study were: (1) use of a single-layer silicon drive piston structure versus use of a double-layer piston structure, (2) integration of PZT-5H material versus integration of PZN-PT material, and (3) incorporation of a single piezoelectric element beneath the piston versus integration of three elements spread out beneath the piston.

7.2.1 1st Generation Devices

As shown in Figure 7.2, the 1st-generation study included the fabrication and testing of three unique drive element devices, all incorporating a single-layer silicon drive piston. Device 1 incorporates a single PZT-5H cylindrical piezoelectric element centrally located beneath the tethered piston. Device 2 incorporates a single PZN-PT cylindrical piezoelectric element also

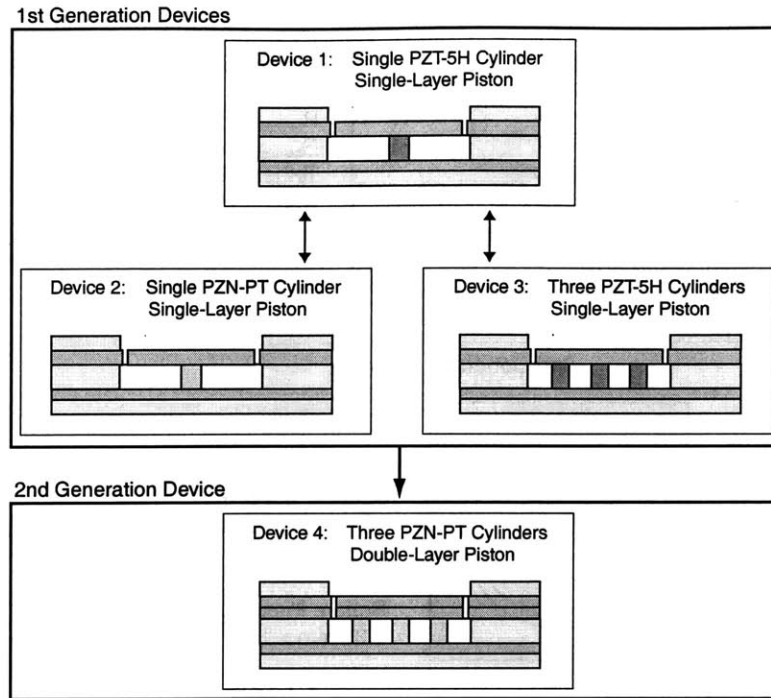


Figure 7.2: Overview of the drive element sub-component test plan. Within the 1st generation study, devices incorporating single and three piezoelectric cylinders (both PZT-5H and PZN-PT) beneath single-layer drive pistons were fabricated and tested. Within the 2nd generation study, devices with three PZN-PT square piezoelectric elements beneath double-layer drive pistons were fabricated and tested.

centrally located beneath the piston structure. Device 3 incorporates three PZT-5H cylindrical elements spread out uniformly beneath the piston. In all three devices, the piezoelectric cylinder thicknesses are $\sim 1\text{mm}$, while the drive piston has a thickness of $390\mu\text{m}$ and the tether has a thickness of $9\mu\text{m}$. Figures 7.3(a) and (b) illustrate the top-view layout and dimensions of these single-cylinder and three-cylinder 1st-generation drive element devices, respectively. Experimental comparison of Device 2 with Device 1 demonstrates the benefits and drawbacks of incorporating the higher-strain capability, yet lower stiffness PZN-PT material versus PZT-5H material. Experimental comparison of Device 3 with Device 1 demonstrates the enhanced stiffening effects of incorporating multiple piezoelectric elements rather than a single centrally-located one within the drive element structure. Additionally, this comparison uncovers any potential difficulties involved in obtaining adequate eutectic bonding between all three cylinders and the adjacent silicon surfaces.

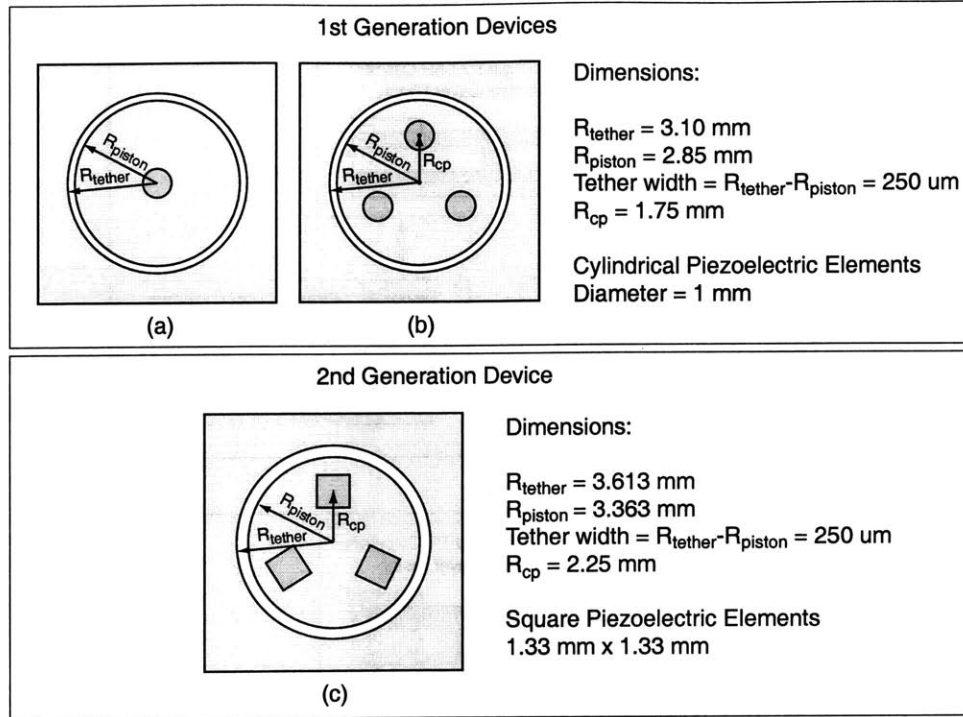


Figure 7.3: Drive element geometries and piezoelectric material layout for 1st and 2nd-generation devices: (a) 1st-generation device with a single piezoelectric cylinder, (b) 1st-generation device with three piezoelectric cylinders, and (c) 2nd-generation device with three piezoelectric square elements.

7.2.2 2nd Generation Device

As shown in Figure 7.2, the 2nd-generation study focused on the integration of three PZN-PT material elements beneath a double-layer drive element piston structure. This double-layer structure, as contained in the final design of the microvalve presented in Chapter 9, is critical for reducing compliance effects within the active valve during piezoelectric actuation. As for the 1st-generation devices, the piezoelectric element thicknesses are $\sim 1 \text{ mm}$. Since the piston is comprised of two layers, its total thickness is $780 \mu\text{m}$ with each tether having a thickness of $8 \mu\text{m}$. Figure 7.3(c) illustrates the top-view layout and dimensions of this 2nd-generation drive element device, Device 4. In order to maximize use of PZN-PT material, square elements rather than cylindrical elements were incorporated in this structure (significantly more piezoelectric elements can be created by dicing a given size plate into squares rather than core-drilling cylinders from this plate). Successful fabrication and experimental evaluation of this final drive element device proves that such a micro-actuator structure can be implemented in the full active valve.

7.3 Device Assembly

As shown in Figure 7.4, the drive element structures consist of five primary layers, two of which are silicon and three of which are glass. The bottom silicon layer contains etched seats for thickness compensation of the piezoelectric elements with respect to the surrounding glass and also contains gold pads for electrical contact. The top silicon layer contains the etched tethered-piston structure. For 1st-generation devices, this layer is formed from a single silicon wafer, whereas for 2nd-generation devices, this layer is formed through wafer-level bonding of two etched silicon wafers. The top and bottom glass layers provide support for clamping during device testing.

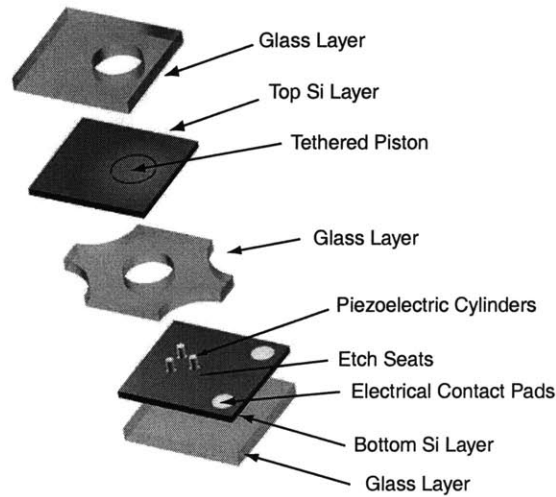


Figure 7.4: Exploded view of a 1st-generation piezoelectric drive element structure. One or more piezoelectric cylinders are arranged within a circular glass chamber, supported beneath by a silicon layer with etched seats and bonded above to a micromachined piston.

As shown in Figure 7.5 and detailed in Chapter 6, a series of wafer-level/die-level anodic bonding steps and a final simultaneous anodic-eutectic bonding step were carried out to complete each of the drive element devices. Following this assembly, wires were soldered to the contact pads on the top and bottom silicon layers to provide electrical contact to the piezoelectric material. Poling of the device was performed by heating the device to approximately half the piezoelectric material Curie temperature ($T_{curie} = 190^{\circ}C$ for PZT-5H and $T_{curie} = 150^{\circ}C$ for PZN-PT) and applying a voltage of 1000V. Photographs of a 1st-generation drive element device prior to and following electrical lead attachment are shown in Figure 7.6(a) and (b) respectively. Photographs of a 2nd-generation drive element are shown in Figure 7.7.

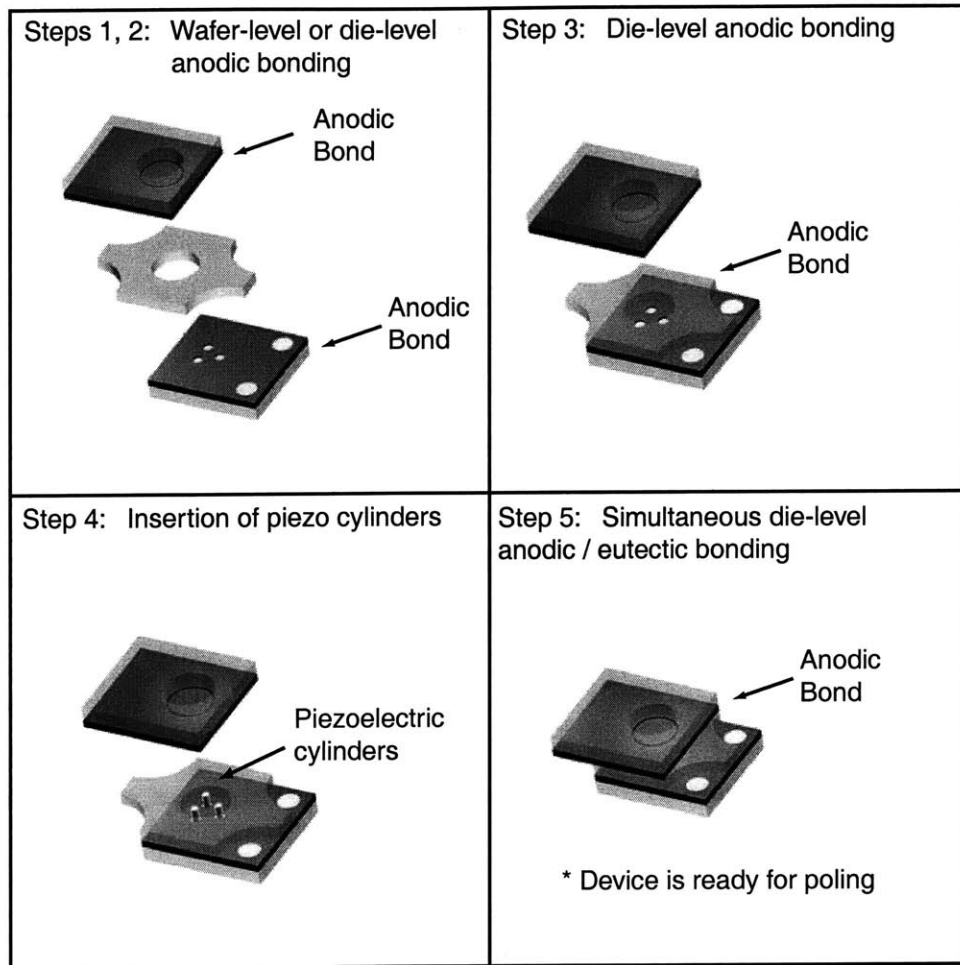


Figure 7.5: Assembly of a piezoelectric drive element device. Die-level anodic bonding procedures at $T=300^{\circ}$ and 1000V were carried out to bond five layers together. The final anodic bonding step also serves to melt the eutectic alloy, forming the bond between the piezoelectric cylinders and the top and bottom silicon layers.

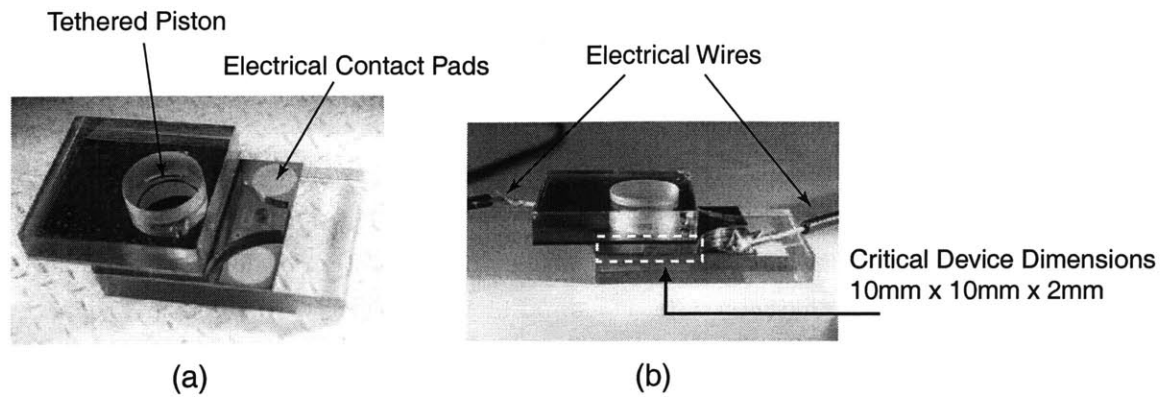


Figure 7.6: Photographs of an assembled 1st-generation piezoelectric drive element device: (a) a packaged device ready for attachment of electrical wires, prior to device poling, (b) a device ready for experimental testing. The critical device dimensions are 10mm x 10mm x 2mm. Thick glass packaging layers were used for clamping purposes during testing.

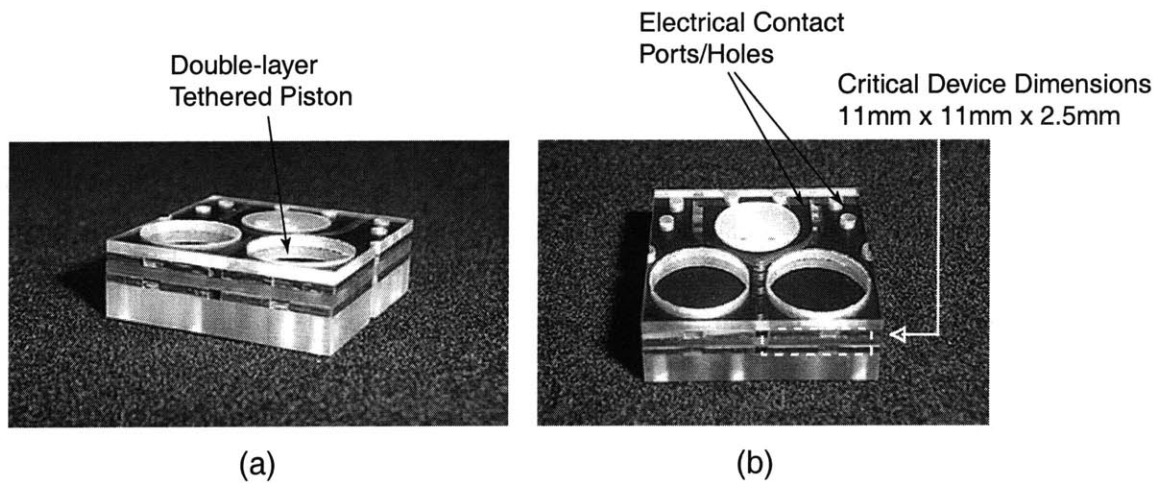


Figure 7.7: Photograph of an assembled 2nd-generation piezoelectric drive element device: thick glass packaging layers were used for clamping purposes during testing.

7.4 Testing Procedure

The process of experimentally testing a given drive element device consisted of three major steps. The first step involved careful microscopic inspection of the device to evaluate the fillet radius profile along the etched drive element tether. For 1st-generation devices, where single-layer pistons were used, measurements were taken following device assembly. However, for 2nd-generation devices, where a bonded double-layer piston prevented viewing of the piston etch, measurements were taken on each of the drive element tethers prior to wafer-level bonding. Knowledge of the fillet radius sizes was important for later evaluation of device performance.

The second step involved characterization of stand-alone piezoelectric material elements that came from the same batch (plate) of material that yielded the elements that were integrated within the device. This was a critical procedure so that comparison of drive element device voltage-deflection behavior could be compared to that of representative piezoelectric material elements.

The third step involved rigorous experimental testing of the device. Each device was rigidly clamped to a test-jig surface and experimentally evaluated using a scanning laser vibrometer system. As shown in Figure 7.8, scan points were defined over the top surface of the tethered piston and along the circumferential boundary supporting the piston. Three measurement procedures were used to characterize device performance. In the first procedure, a low-voltage ($0V \pm 25V$) sweep signal was applied to each device over a frequency range of 10kHz to 200kHz to determine the onset of dynamic modal characteristics. A transfer function of velocity (averaged over all scan points) versus frequency was recorded. Close-up frequency sweeps around dominant modal frequencies were then carried out to obtain high-resolution mode shape behavior. In the second procedure, a sinusoidal voltage of $500V \pm 500V$ was applied to each device at selected frequencies of 15kHz and 7kHz to evaluate device behavior below the modal frequencies. At each of these low-frequencies, displacement time histories at the piston center and at an outer edge of the piston were recorded. In the third procedure, voltage-deflection curves (of the piston center) for varying levels of applied voltage were obtained at a frequency of 100Hz to determine the true quasi-static voltage dependent performance of the device.

7.5 Experimental Results

7.5.1 1st Generation Devices

Measurement of Fillet Radius Profiles

Following assembly of each 1st-generation drive element device, careful inspection of the drive element piston tether was performed to characterize the uniformity of the fillet radii along the tether circumference. As shown in Figure 7.9(a), measurements were taken at eight equally

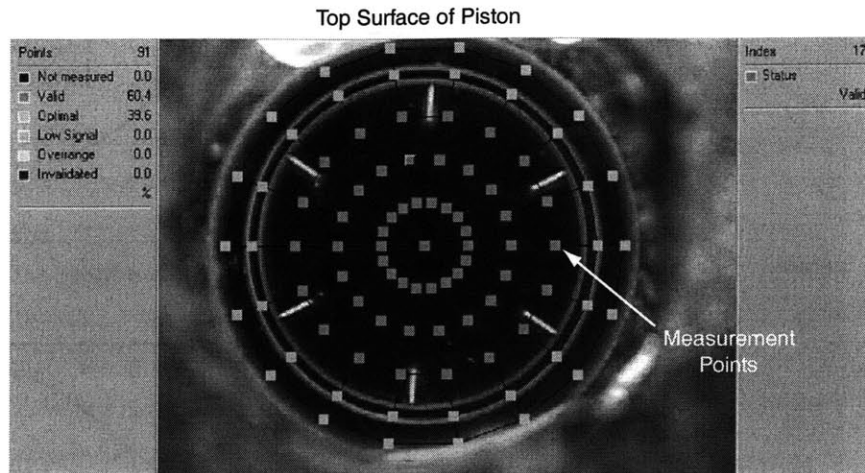


Figure 7.8: A scanning laser vibrometer system was used to characterize modal and quasi-static performance of each device. Measurement points are defined on the top surface of the piston.

spaced locations along the circumference. The first measurement point is located at 12 o'clock and numbering proceeds in the clockwise direction. The measurement terminology is illustrated in Figure 7.9(b). Using a microscope eyepiece with calibrated graduations, the tether width from the base of one fillet radius to the base of the opposite fillet radius was recorded. Additionally, the total trench width was measured. From these measurements, an average value for the fillet radius on each side of the trench was determined. Figure 7.9(c), (d), and (e) present the tether width and fillet radius measurements as a function of location along the tether circumference for Devices 1, 2, and 3, respectively. For Device 1, the tether width varies between $138\mu\text{m}$ and $163\mu\text{m}$ in a single sinusoidal cycle along the circumference (ie: the fillet radii vary from $43\mu\text{m}$ to $56\mu\text{m}$). Likewise, the tether width of Device 2 also varies sinusodially, but with slightly larger variation, between $165\mu\text{m}$ and $200\mu\text{m}$. For these two devices, due to this tether variation, the overall piston/tether stiffness is non-uniform around the circumference. For Device 3, tether width variation is also observed, however, in a more random fashion between $178\mu\text{m}$ and $195\mu\text{m}$.

Characterization of Piezoelectric Material

In order provide a basis for voltage-deflection comparison when testing completed drive element devices, representative PZT-5H and PZN-PT material cylinders were individually characterized (sufficiently long after poling, four days, to ensure adequate relaxation of the material). Figure 7.10 plots the results for three cylinders of each material at 10Hz for a driving voltage of $500V \pm 500V$. A very low frequency was chosen to guarantee true quasi-static behavior. The three PZT-5H cylinders exhibited peak deflections at 1000V between $0.75\mu\text{m}$ and $0.82\mu\text{m}$. The three PZN-PT cylinders exhibited peak deflections at 1000V between $1.35\mu\text{m}$ and $1.55\mu\text{m}$.

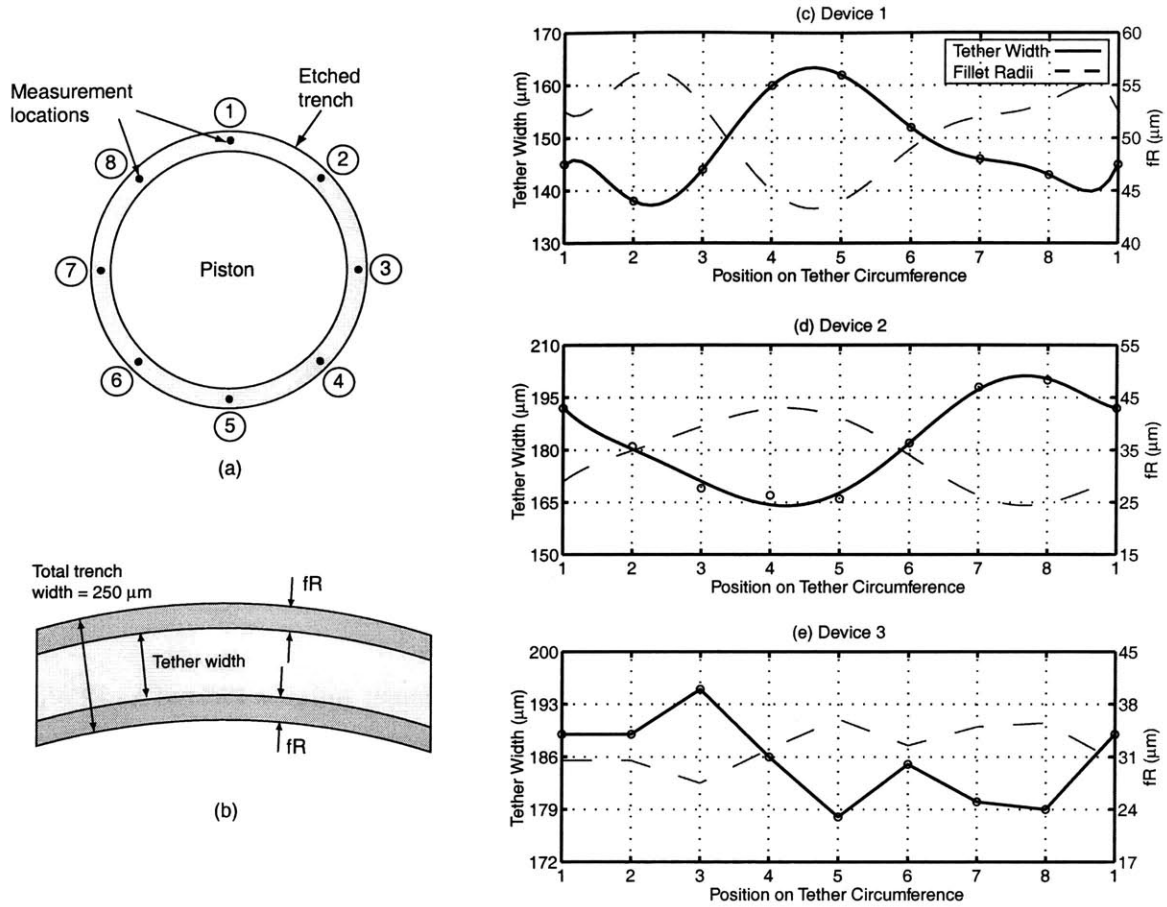


Figure 7.9: Inspection of tether width and fillet radii on Device 1, 2, and 3 tethered pistons: (a) definition of measurement locations around trench circumference, (b) average $fR = \frac{1}{2}(\text{total trench width} - \text{measured tether width})$, (c) Device 1 measurements, (d) Device 2 measurements, and (e) Device 3 measurements.

Finite-element models of drive element devices have indicated that the stiffness of the tether is insignificant compared to that of the piezoelectric materials, and therefore it does little to restrict the free-strain deflection of the piezoelectric material. As a result, these stand-alone piezoelectric element results provide an accurate expectation for quasi-static drive element device voltage-deflection performance.

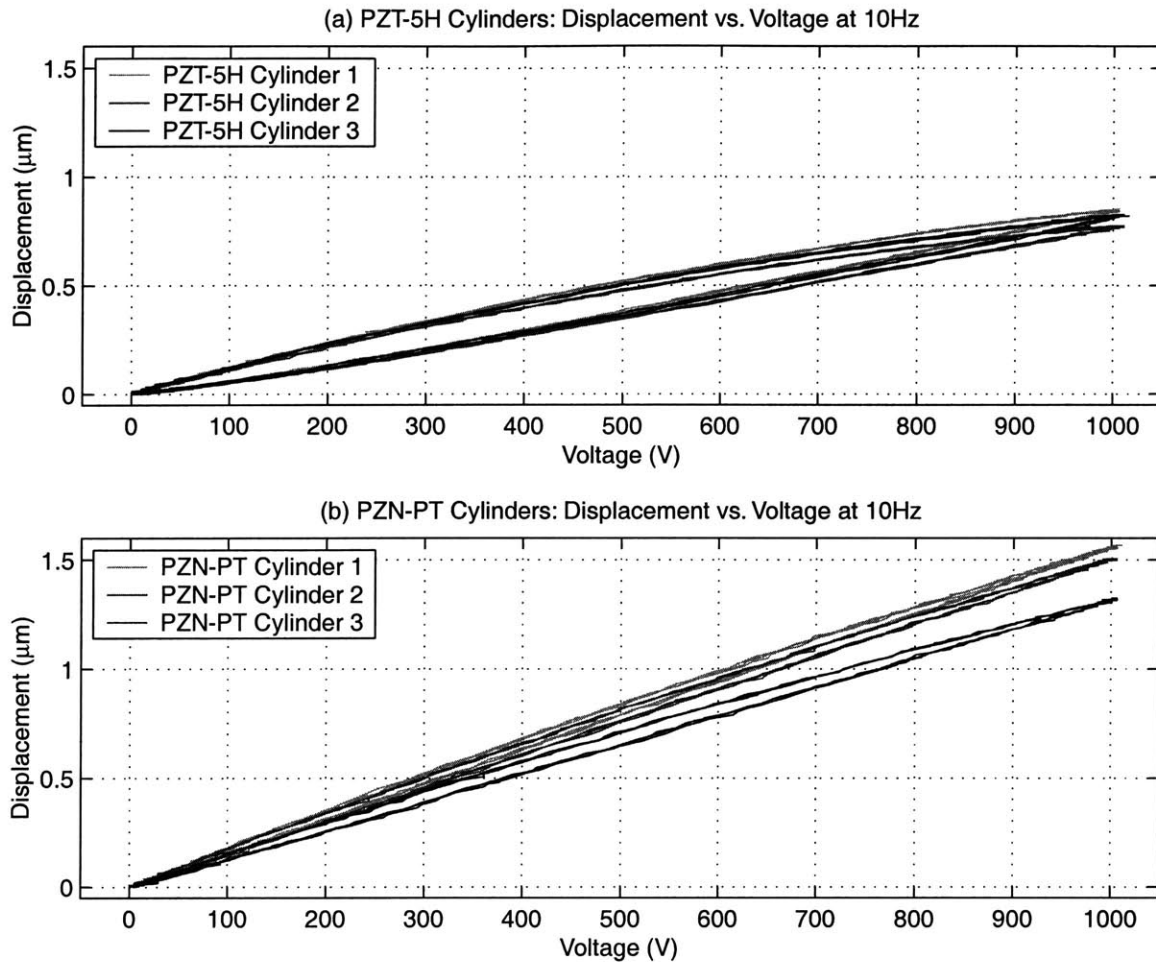


Figure 7.10: Piezoelectric material characterization on representative stand-alone PZT-5H and PZN-PT cylinders: (a) voltage-deflection responses at 10Hz for three different PZT-5H cylinders for $V = 500V \pm 500V$ (these cylinders were taken from the identical PZT-5H material plate that yielded the cylinders used in Devices 1 and 3), (b) voltage-deflection responses at 10Hz for three different PZN-PT cylinders for $V = 500V \pm 500V$ (these cylinders were taken from the identical PZN-PT material plate that yielded the cylinder used in Device 2).

Experimental Testing of Device 1

Figure 7.11(a) plots the transfer function of averaged velocity over the scanned piston surface versus frequency for Device 1. Figure 7.11(b) plots these transfer functions for specific locations on the piston surface, at the center and at an outer edge. Figure 7.12(a) presents experimental mode shapes of the device at selected modal frequencies. The device experiences a “1 – Θ ” tilt mode at $f = 31kHz$, followed by a “plunge” mode at $f = 80kHz$, and a “2 – Θ ” mode at $f = 131kHz$. As shown in Figure 7.12, these modal frequencies correlate well with finite-element models of the device. The frequency difference in the “1 – Θ ” mode between finite-element model and experiment could be attributed to imperfect placement of the cylinder beneath the piston or non-uniform fillet radii around the piston tether. In looking at Figure 7.11(b), notice that the velocity amplitudes are significantly more pronounced at the piston edge compared to the piston center. This is especially true for the “1 – Θ ” tilt mode and the “plunge” mode.

Figure 7.13 illustrates the displacement profile of the device at 15kHz with an applied sinusoidal voltage of $500V \pm 500V$. Slight tilting of the piston surface is observed, and is again likely influenced by imperfect piezoelectric cylinder placement or non-uniformity in fillet radius etching. Figure 7.14 displays the corresponding displacement profiles at the piston center and piston edge. Higher-order dynamic oscillations of $f = 80kHz$ are observed within the lower 15kHz drive frequency. These higher-order oscillations are more pronounced at the piston edge than at the piston center, which could be attributed to non-linearities inherent in the piezoelectric material or in the tether structure. The overall measured peak-peak deflection at the piston center, $\delta_{p-p} = 0.69\mu m$, is slightly lower than the expected range of $\delta_{p-p} = 0.75 - 0.82\mu m$. Most likely, this is a result of material inconsistency among the piezoelectric cylinders.

Figure 7.15 displays the displacement profiles at the piston center and piston edge at a driving frequency of 7kHz. Higher-order dynamic oscillations of $f = 80kHz$ are again observed in the piston edge displacement signal, but with a lower magnitude. As for the piston center response at 15kHz, the overall measured peak-peak deflection at the piston center at 7kHz, $\delta_{p-p} = 0.70\mu m$, is slightly lower than the expected range of $\delta_{p-p} = 0.75 - 0.82\mu m$. Figure 7.16 plots the voltage-deflection curves for the piston center at 100Hz as a function of varying applied voltage levels, from $100V \pm 100V$ to $500V \pm 500V$. Hysteresis in the PZT-5H material is clearly evident from the wide sweeping shapes of the curves. Overall, however, the peak displacement is close to linear with applied voltage.

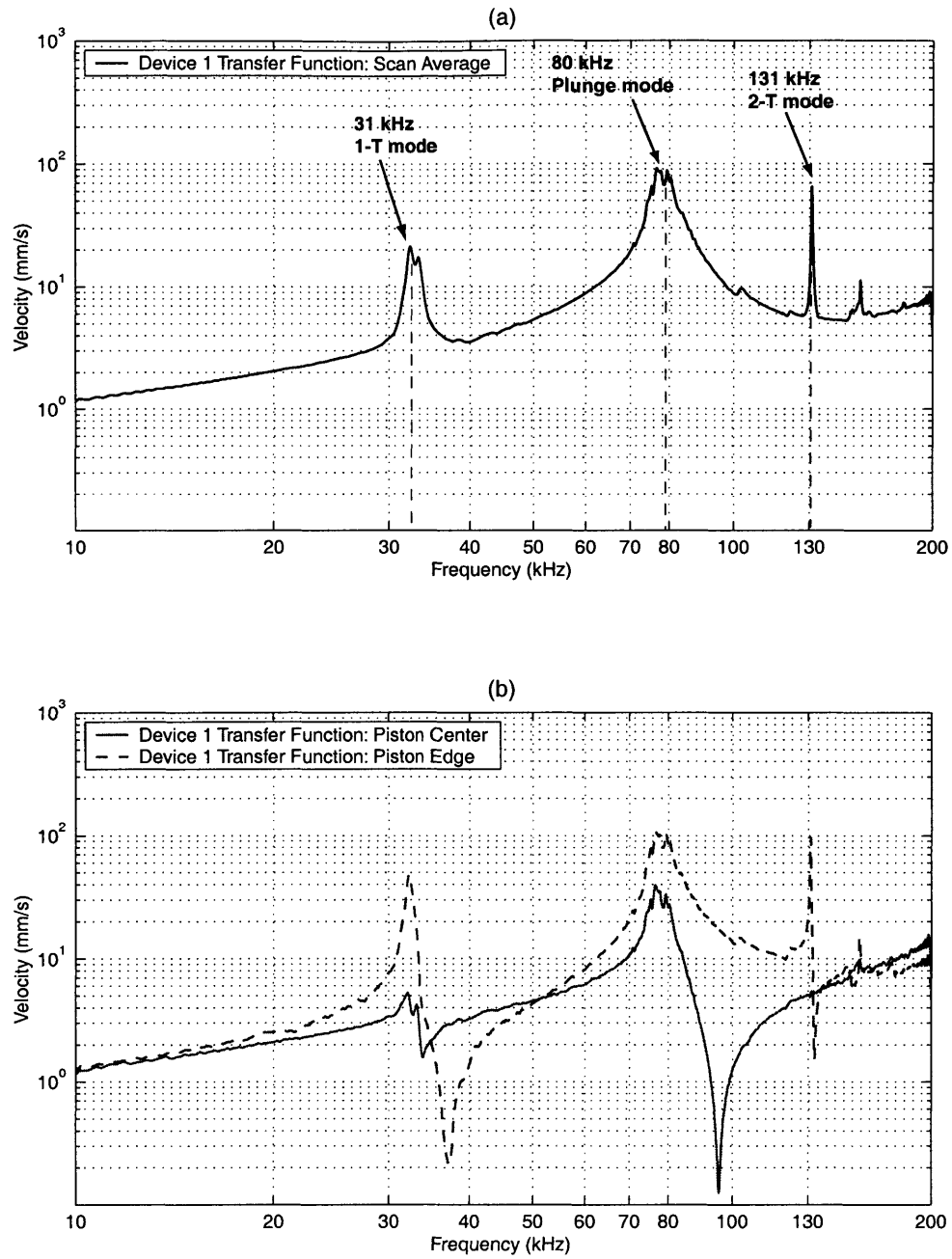


Figure 7.11: Device 1 transfer functions of piston velocity versus frequency for a sweep input from 10kHz to 200kHz and small signal drive voltage $0V \pm 25V$: (a) averaged velocity over piston surface, and (b) velocity at center and edge locations on piston surface. Modal behavior is present at 31kHz, 80kHz, and 131kHz. Phase information was not recorded for this device.

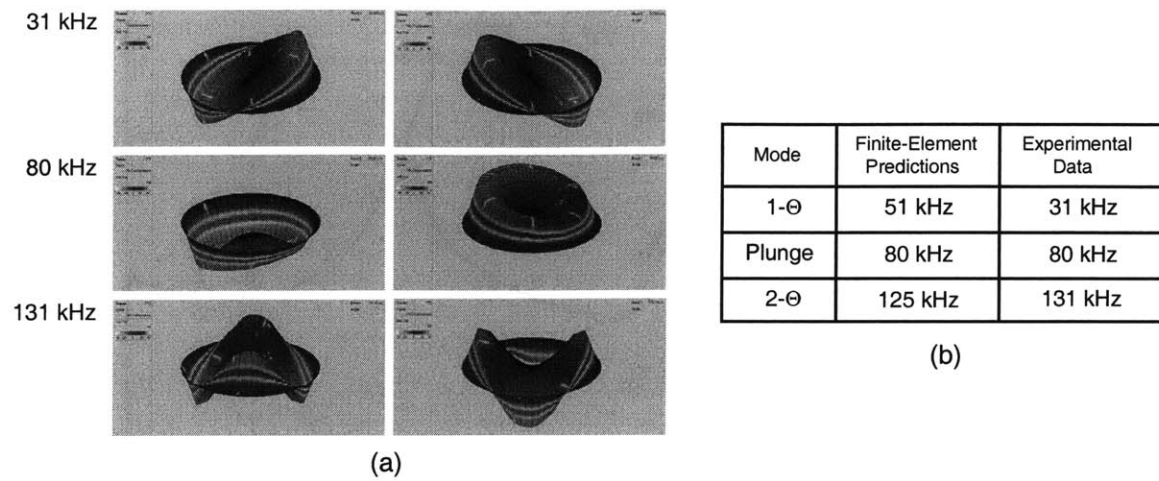


Figure 7.12: Device 1 modal behavior: (a) vibrometer scans of device: “1 – Θ ” tilt mode at $f = 31kHz$, “plunge” mode at $f = 80kHz$, and “2 – Θ ” mode at $f = 131kHz$, (b) comparison to results from the ANSYS finite-element model.

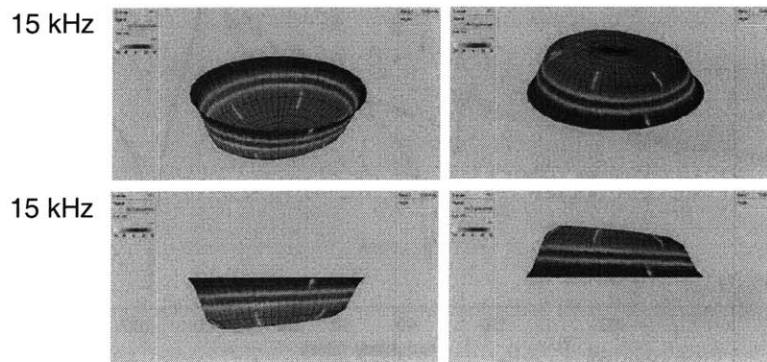


Figure 7.13: Vibrometer scan images of Device 1 low-frequency 15kHz displacement profile. The tilting of the piston surface is likely due to an uncentered piezoelectric cylinder or a non-uniform fillet radius in etched piston trench.

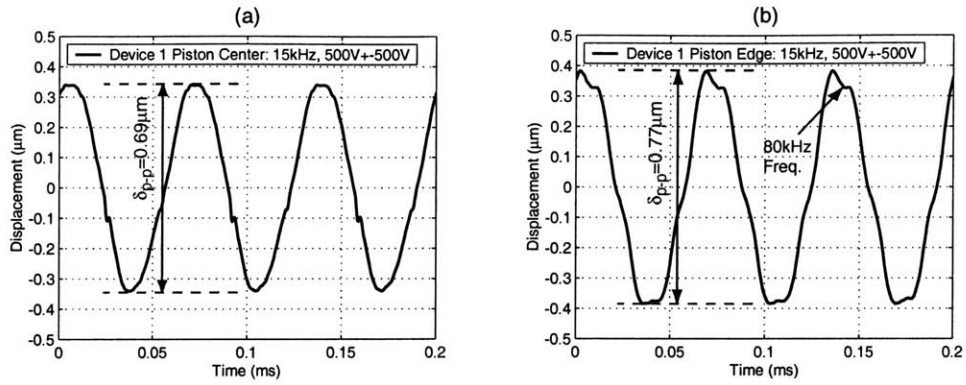


Figure 7.14: Device 1 displacement time histories for a sinusoidal drive voltage of $500V \pm 500V$ at $f = 15kHz$: (a) piston center displacement and (b) piston edge displacement. Note the presence of 80kHz oscillations in the edge displacement time history.

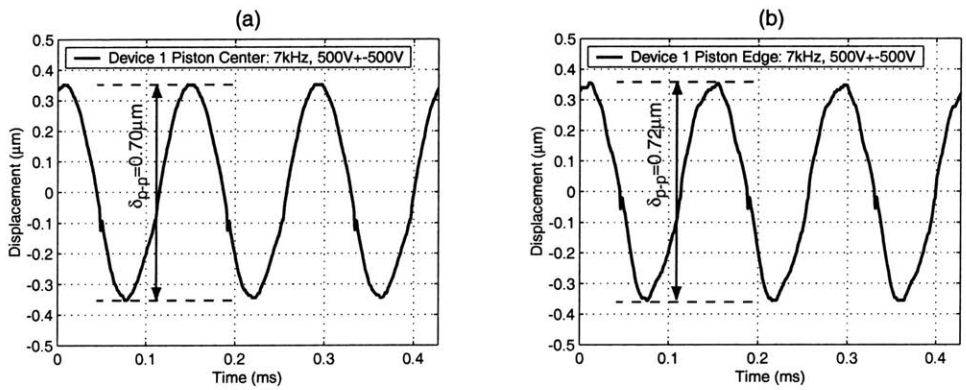


Figure 7.15: Device 1 displacement time histories for a sinusoidal drive voltage of $500V \pm 500V$ at $f = 7kHz$: (a) piston center displacement and (b) piston edge displacement.

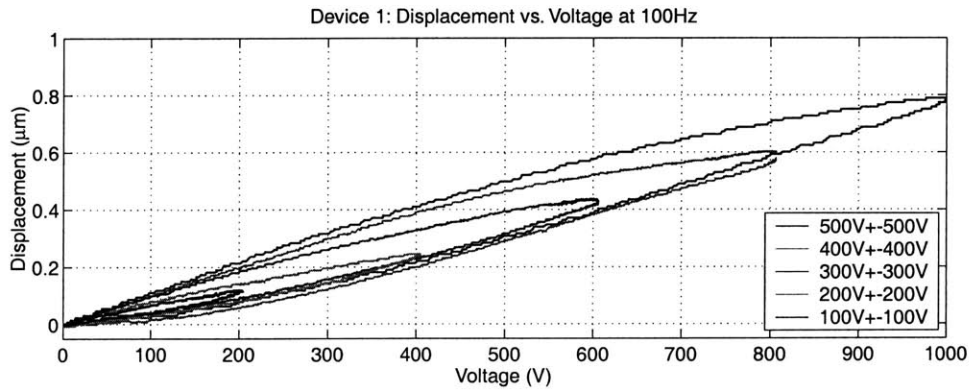


Figure 7.16: Device 1 piston center displacement behavior versus applied voltage at 100Hz.

Experimental Testing of Device 2

Figure 7.17(a) plots the transfer function of averaged velocity over the scanned piston surface versus frequency for Device 2. Figure 7.17(b) plots these transfer functions for specific locations on the piston surface, at the center and at an outer edge. Figure 7.18(a) presents experimental mode shapes of the device at selected modal frequencies. In comparing this dynamic response to that of Device 1, the overall modal shapes are similar, however, the frequencies at which they occur are shifted downward. The “1 – Θ ” tilt mode occurs at $f = 30kHz$, the “plunge” mode at $f = 61kHz$, and the “2 – Θ ” mode at $f = 112kHz$. This frequency shift is expected since PZN-PT is a softer material than PZT-5H. As shown in Figure 7.18(b), these modal frequencies correlate well with finite-element models of the device. In looking at Figure 7.17(b), notice that the velocity amplitudes are significantly more pronounced at the piston edge compared to the piston center. This is especially true for the “1 – Θ ” tilt mode and the “plunge” mode.

The displacement profile of Device 2 at 15kHz with an applied sinusoidal voltage of $500V \pm 500V$ exhibits a non-uniform tilt (see Figure 7.19) in much the same manner as Device 1. The displacement time history at the piston edge exhibits components of the device “plunge” mode (see Figure 7.20). However, in comparison with Device 1 the magnitude of the piston center displacement in Device 2 is significantly increased to $\delta_{p-p} = 1.42\mu m$. This value correlates well with the expected peak-peak displacement range of $\delta_{p-p} = 1.35 - 1.55\mu m$.

Figure 7.21 displays the displacement profiles at the piston center and piston edge at a driving frequency of 7kHz. Dynamic oscillations of $f = 61kHz$ are again observed in the piston edge displacement signal, and this signal has a decreased overall amplitude from the 15kHz response. As for the piston center response at 15kHz, the overall measured peak-peak deflection of the piston center at 7kHz, $\delta_{p-p} = 1.39\mu m$, correlates well to the expected range of $\delta_{p-p} = 1.35 - 1.55\mu m$. Figure 7.22 plots the voltage-deflection curves for the piston center at 100Hz as a function of varying applied voltage levels, from $100V \pm 100V$ to $500V \pm 500V$. Comparing these curves to those of Device 1, it is clear that the PZN-PT material exhibits significantly reduced hysteretic behavior than the PZT-5H material. Additionally, the peak displacement is seen to be linear with applied voltage.

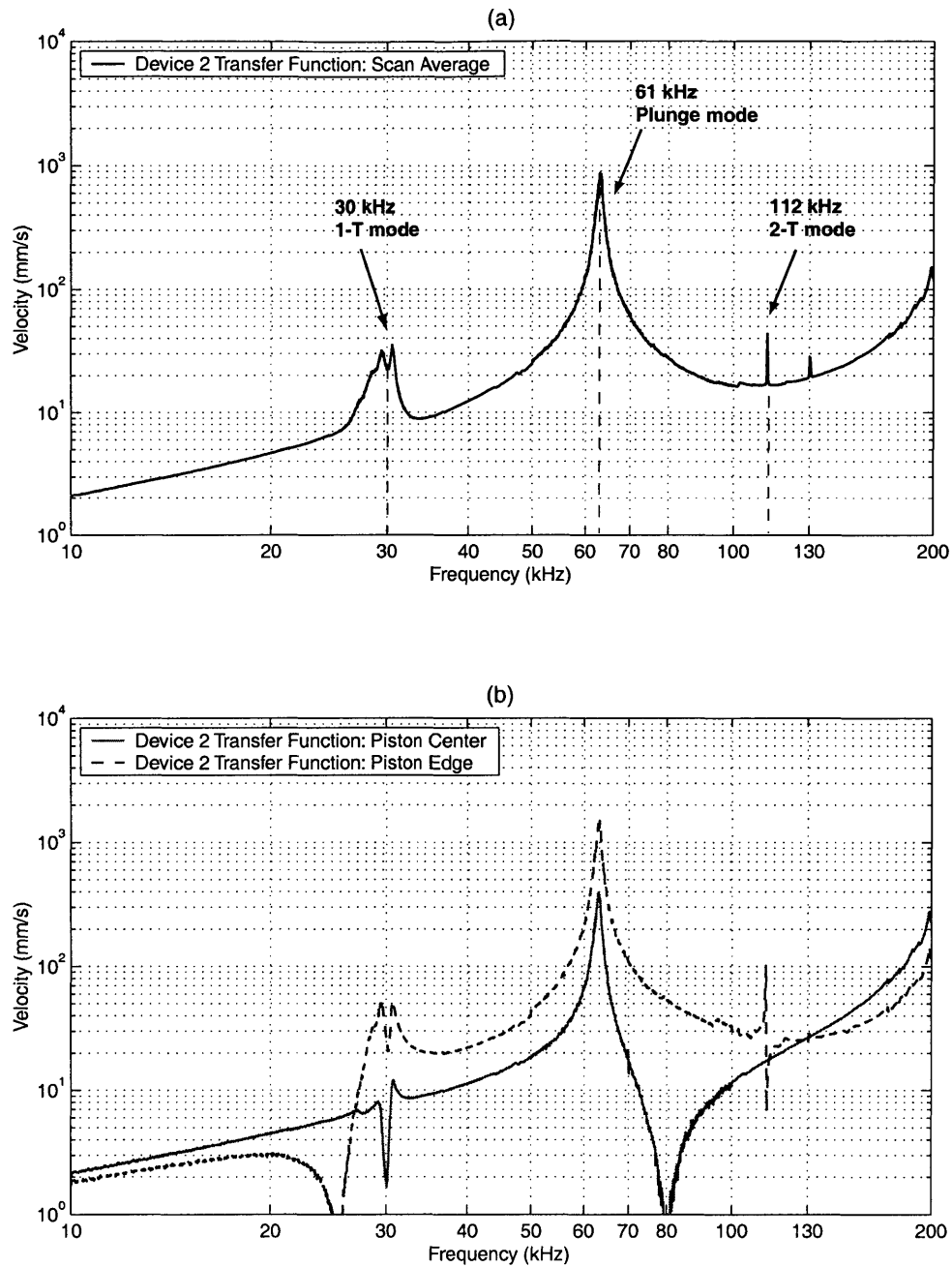


Figure 7.17: Device 2 transfer functions of piston velocity versus frequency for a sweep input from 10kHz to 200kHz and small signal drive voltage $0V \pm 25V$: (a) averaged velocity over piston surface, and (b) velocity at center and edge locations on piston surface. Modal behavior is present at 30kHz, 61kHz, and 112kHz. Phase information was not recorded for this device.

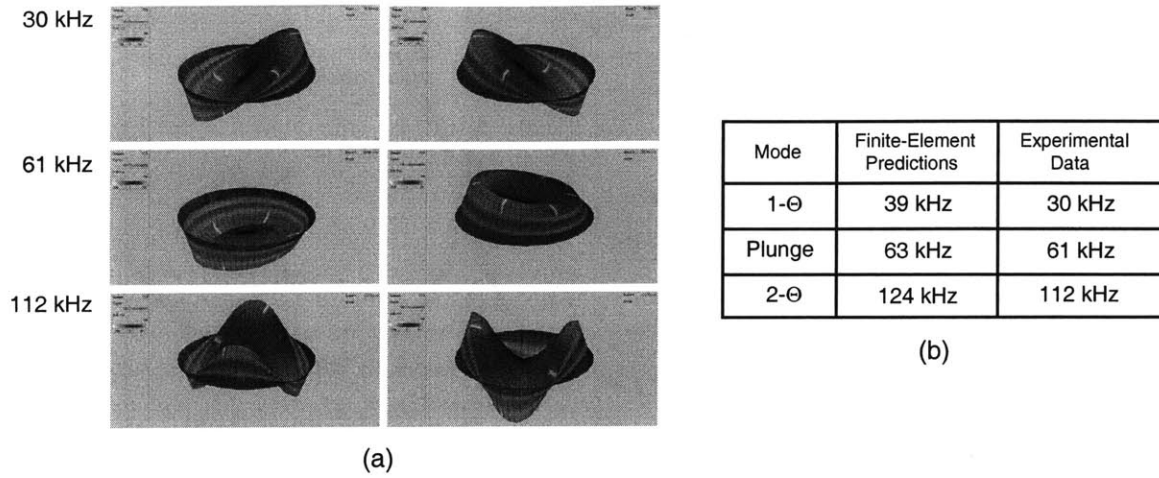


Figure 7.18: Device 2 modal behavior: (a) vibrometer scan images of device behavior: “1 – Θ ” tilt mode at $f = 30kHz$, “plunge” mode at $f = 61kHz$, and “2 – Θ ” mode at $f = 112kHz$, (b) comparison to results from the ANSYS finite-element model.

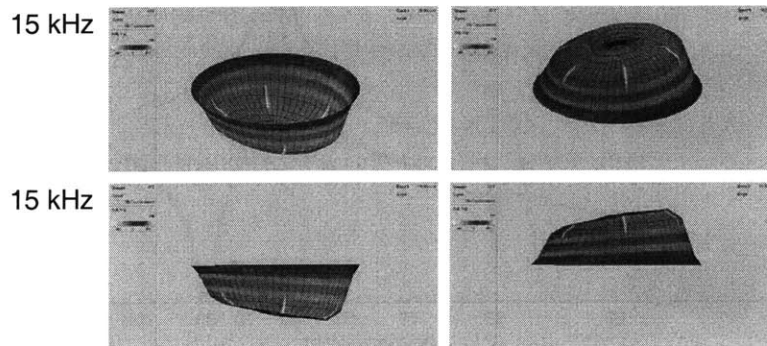


Figure 7.19: Vibrometer scan images of Device 2 low-frequency 15kHz displacement profile. The tilting of the piston surface is likely due to an uncentered piezoelectric cylinder or non-uniform fillet radius in etch piston trench.

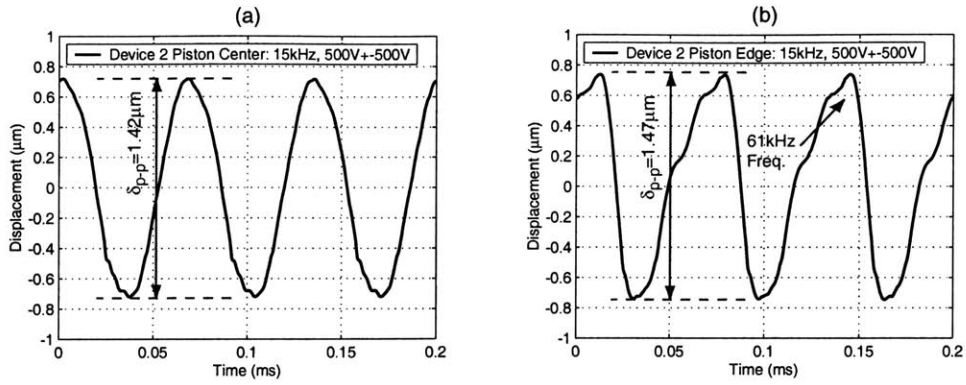


Figure 7.20: Device 2 displacement time histories for a sinusoidal drive voltage of $500\text{V} \pm 500\text{V}$ at $f = 15\text{kHz}$: (a) piston center displacement and (b) piston edge displacement. Note the presence of 61kHz oscillations in the edge displacement time history.

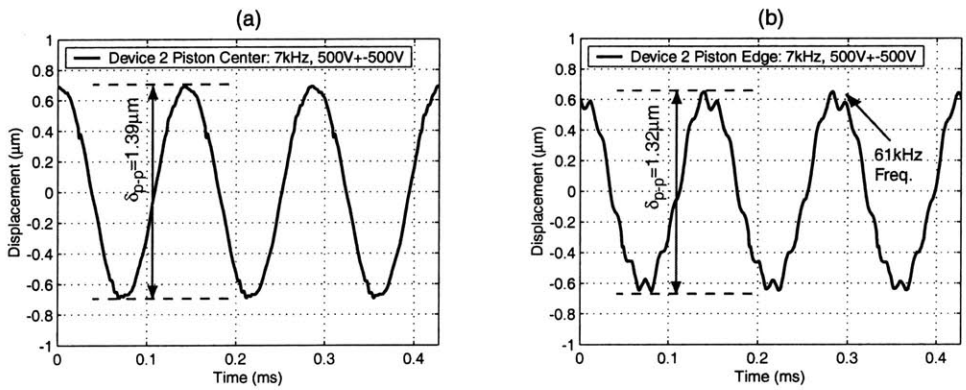


Figure 7.21: Device 2 displacement time histories for a sinusoidal drive voltage of $500\text{V} \pm 500\text{V}$ at $f = 7\text{kHz}$: (a) piston center displacement and (b) piston edge displacement.

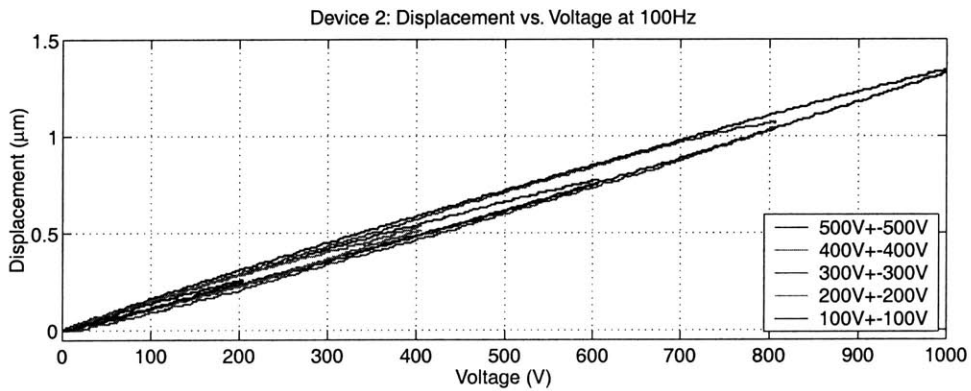


Figure 7.22: Device 2 piston center displacement versus applied voltage at 100Hz.

Experimental Testing of Device 3

Figure 7.23(a) plots the transfer function of averaged velocity over the scanned piston surface versus frequency for Device 3. Figure 7.23(b) plots these transfer functions for specific locations on the piston surface, at the center and at an outer edge. In comparing this dynamic response to that of Device 1, modal behavior is not observed until frequencies near $f = 80kHz$. The placement of multiple cylinders beneath the piston eliminates tilting behavior at frequencies in the 30kHz to 80kHz range. As shown in Figure 7.24, initial modal behavior is characterized by non-symmetric motion of the piston surface, most likely due to unsymmetric placement of the piezoelectric elements beneath the piston, differences in material properties among the elements, or a non-uniform fillet radius profile along the tether circumference. A perfectly symmetric finite-element model of this device predicts 1st modal behavior at 225kHz (see Figure 7.25).

For low-frequency actuation, the multiple piezoelectric cylinder stiffening effect is observed in Figure 7.26 as the displacement profile at 15kHz experiences minimal tilting during actuation. In addition, as shown in Figure 7.27, the displacement time histories at the piston center and piston edge are relatively free from higher order oscillations. A small contribution with frequency $f \sim 90kHz$ is evident in the piston edge displacement time history. As for Device 1, the magnitude of the piston center displacement in Device 3, $\delta_{p-p} = 0.72\mu m$, is slightly lower than the expected range of $\delta_{p-p} = 0.75 - 0.82\mu m$.

Figure 7.28 displays the displacement profiles at the piston center and piston edge at a driving frequency of 7kHz. Again, almost perfect displacement behavior free from higher-order oscillations is observed. The overall measured peak-peak deflection at the piston center at 7kHz, $\delta_{p-p} = 0.76\mu m$, is within the expected range of $\delta_{p-p} = 0.75 - 0.82\mu m$. As was the case for Device 1, the deflection behavior under quasi-static driving conditions (see Figure 7.29) is linear with the applied voltage. Overall, these results indicate that the incorporation of multiple piezoelectric cylinders spread out beneath the tethered piston is achievable.

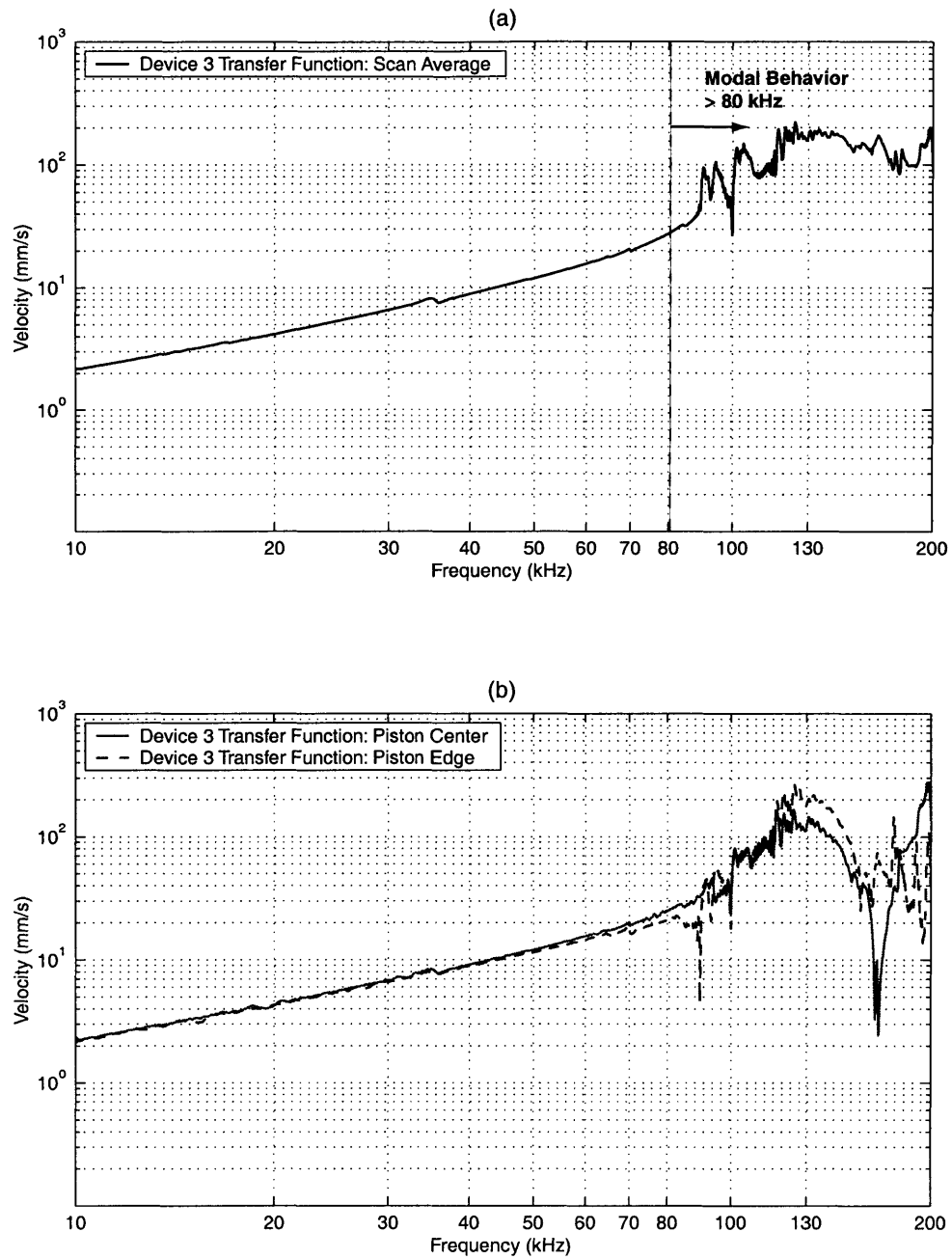


Figure 7.23: Device 3 transfer functions of piston velocity versus frequency for a sweep input from 10kHz to 200kHz and small signal drive voltage $0V \pm 25V$: (a) averaged velocity over piston surface, and (b) velocity at center and edge locations on piston surface. Modal behavior is not present below 80kHz. Phase information was not recorded for this device.

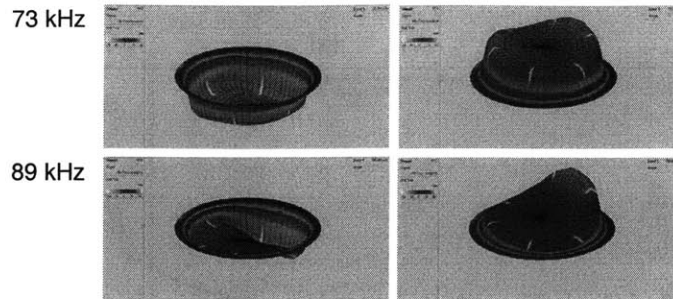


Figure 7.24: Vibrometer scan images of selected Device 3 modal behavior above 70kHz: behavior at 73kHz and 89kHz.

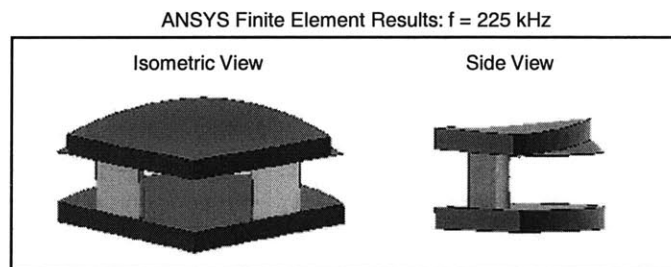


Figure 7.25: Device 3 ANSYS finite-element model prediction for 1st mode shape at 225 kHz.

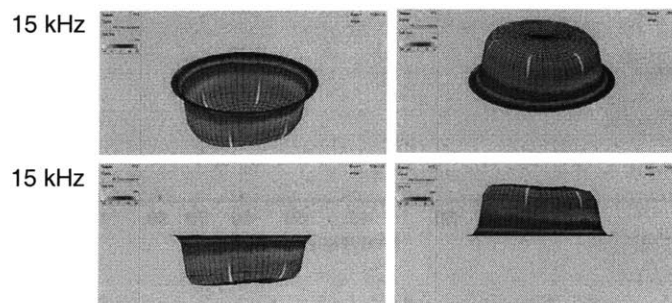


Figure 7.26: Vibrometer scan images of Device 3 low-frequency 15kHz displacement profile. Presence of multiple piezoelectric cylinders beneath piston serves to stiffen actuator structure and reduce tilting behavior.

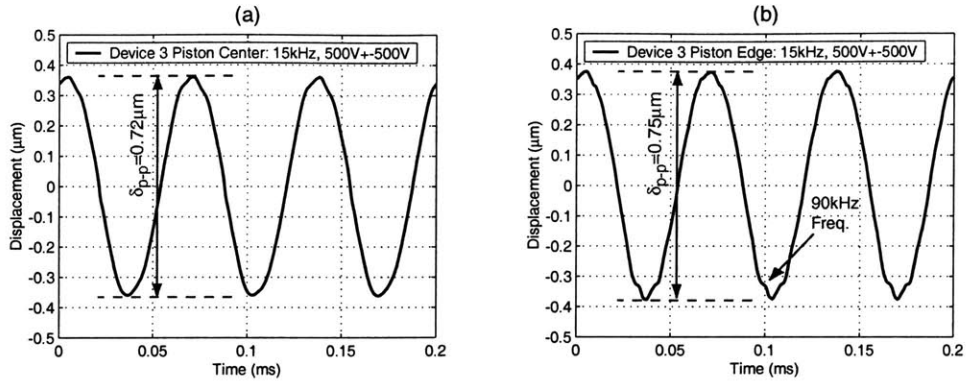


Figure 7.27: Device 3 displacement time histories for a sinusoidal drive voltage of $500V \pm 500V$ at $f = 15kHz$: (a) piston center displacement and (b) piston edge displacement. Note the slight presence of a 90kHz oscillation in the edge displacement time history.

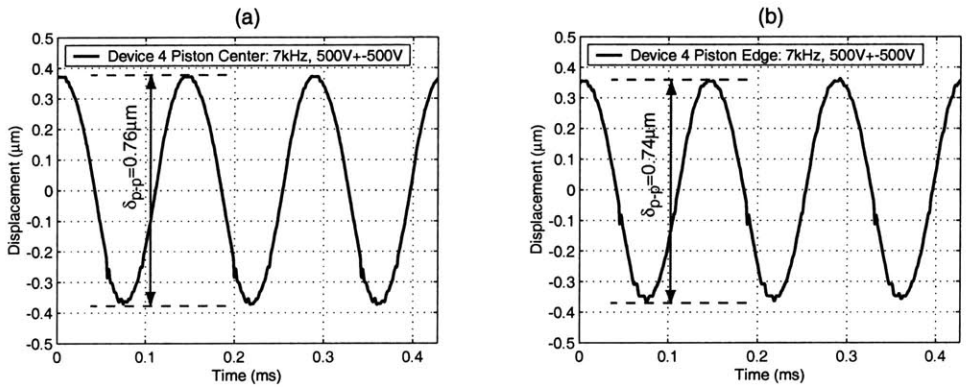


Figure 7.28: Device 3 displacement time histories for a sinusoidal drive voltage of $500V \pm 500V$ at $f = 7kHz$: (a) piston center displacement and (b) piston edge displacement.

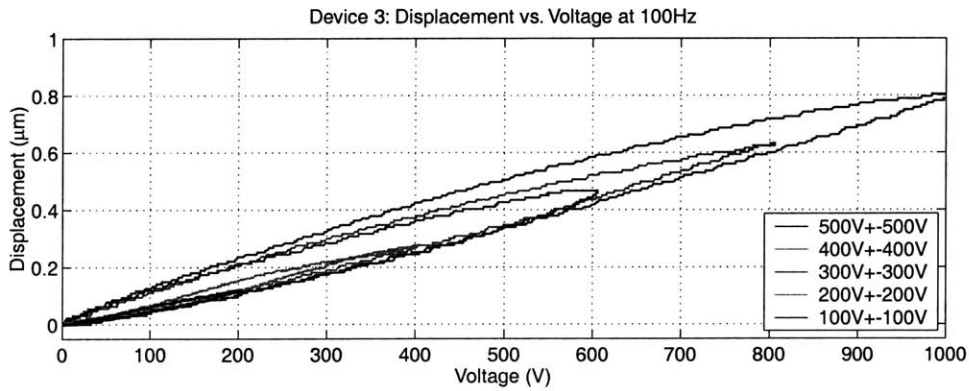


Figure 7.29: Device 3 piston center displacement versus applied voltage at 100Hz.

7.5.2 2nd Generation Device

Measurement of Fillet Radius Profiles

As was performed for the 1st-generation drive element devices, careful inspection of the drive element tethers in Device 4 was also carried out. Since this device incorporates a double-layer piston structure, these inspections were performed prior to wafer-level Si-Si fusion bonding of the piston structure. For the lower piston tethers and upper piston tethers, fillet radii between 25-35 μm (ie: tether widths between 180-200 μm) were measured with no observable defects along the tethers, indicating excellent uniformity during the previous DRIE etching procedures.

Characterization of Piezoelectric Material

PZN-PT material similar to that in the 1st-generation drive element devices was used in Device 4. As a result, the PZN-PT material squares were expected to produce voltage-deflection behavior in the same range as shown in Figure 7.10 (ie: peak deflections at 1000V between 1.35 μm and 1.55 μm).

Experimental Testing of Device 4

Figure 7.30(a) plots the transfer function of averaged velocity over the scanned piston surface versus frequency for Device 4. Figure 7.30(b) plots these transfer functions for specific locations on the piston surface, at the center and at an outer edge. As shown in Figure 7.31, modal behavior begins near 50kHz and is characterized by non-symmetric tilting motion of the piston surface, most likely due to unsymmetric placement of the piezoelectric elements beneath the piston or differences in material properties among the elements. A perfectly symmetric finite-element model of this device predicts 1st modal behavior (piston plunge) at 155kHz and 2nd modal behavior (1- Θ piston tilting) at 288kHz.

For low-frequency actuation at 15kHz and at a voltage of 1000V peak-peak, the drive element piston experiences minimal tilting (as shown in Figure 7.32), indicating a well-built and toleranced drive element device. The degree of piston tilting is illustrated more clearly in Figure 7.33. The displacement time history at the piston center (Figure 7.33(a)) is very smooth with no higher order oscillations. Likewise, the displacement time histories at the piston edge locations with maximum peak-peak motions (Figure 7.33(b)) are also completely free from higher order oscillations. In comparing the peak-peak deflections of these opposite piston edges, the magnitude of tilt is estimated to be $\sim 4\%$ of the piston center deflection. The piston center displacement ($\delta_{p-p} = 1.41\mu m$) correlates well with the expected range of $\delta_{p-p} = 1.35 - 1.55\mu m$. As was the case for the first generation drive element devices, the deflection behavior under quasi-static driving conditions is linear with the applied voltage. Figure 7.34 illustrates this voltage dependent behavior at 100Hz.

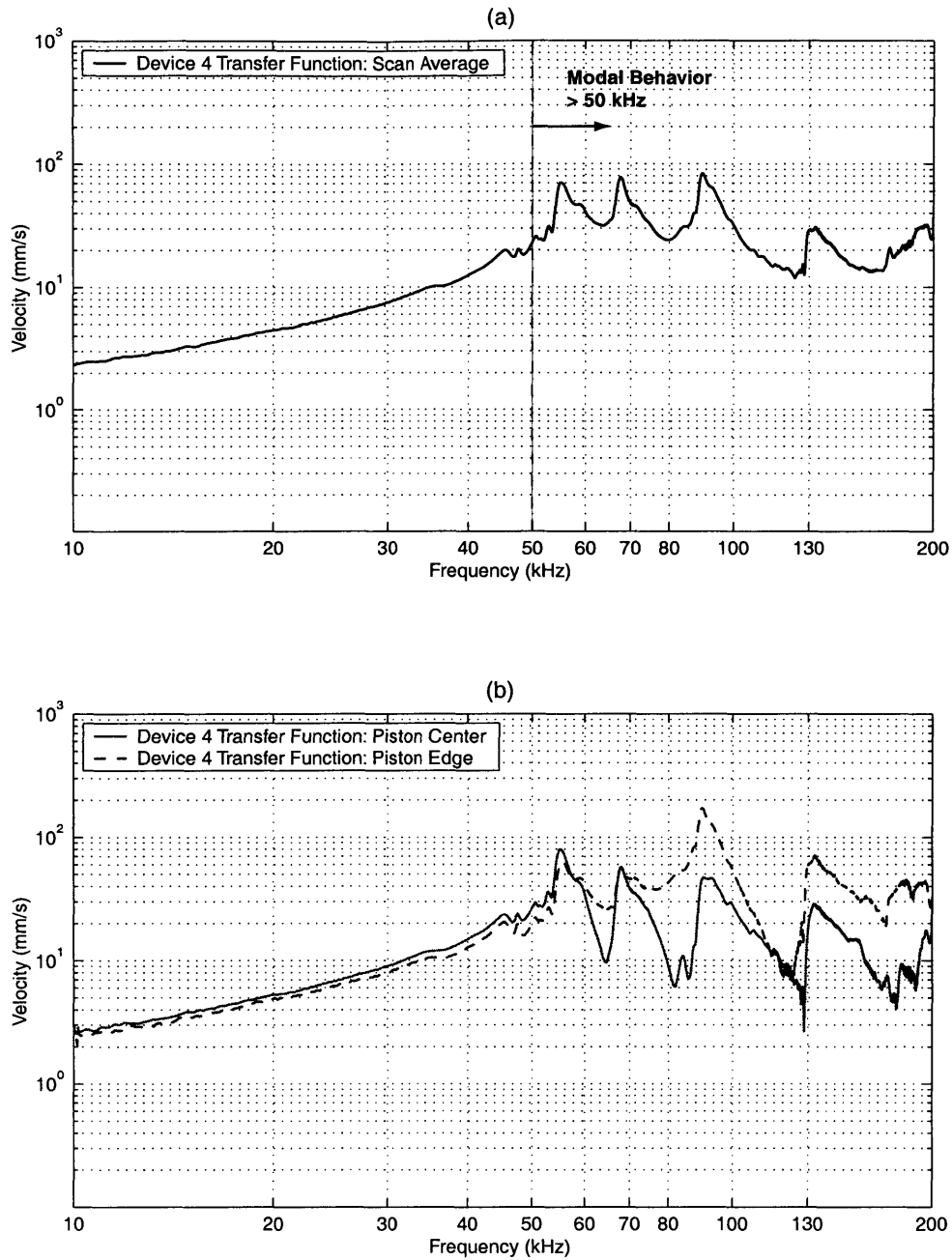


Figure 7.30: Device 4 transfer functions of piston velocity versus frequency for a sweep input from 10kHz to 200kHz and small signal drive voltage $0V \pm 25V$: (a) averaged velocity over piston surface, and (b) velocity at center and edge locations on piston surface. Modal behavior is present near 50kHz. Phase information was not recorded for this device.

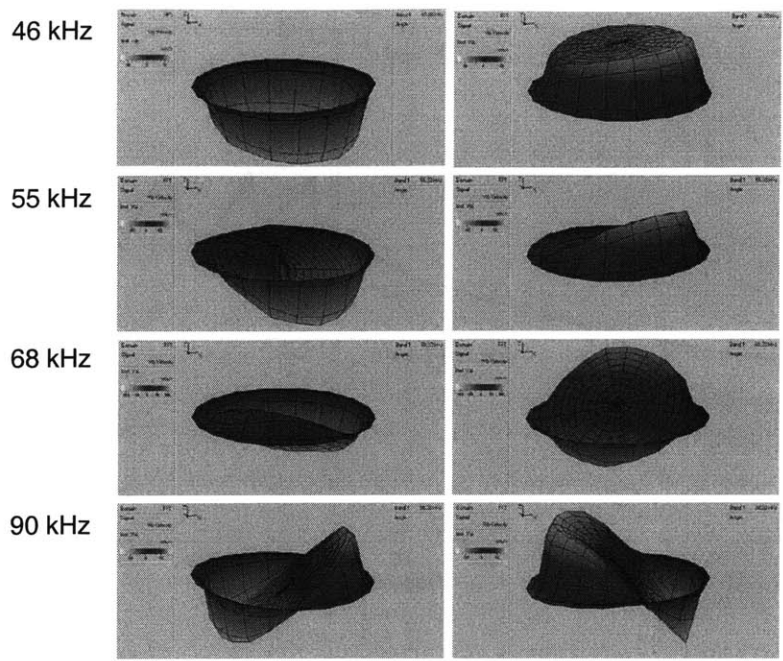


Figure 7.31: Vibrometer scan images of selected Device 4 modal behavior between 45kHz and 90kHz.

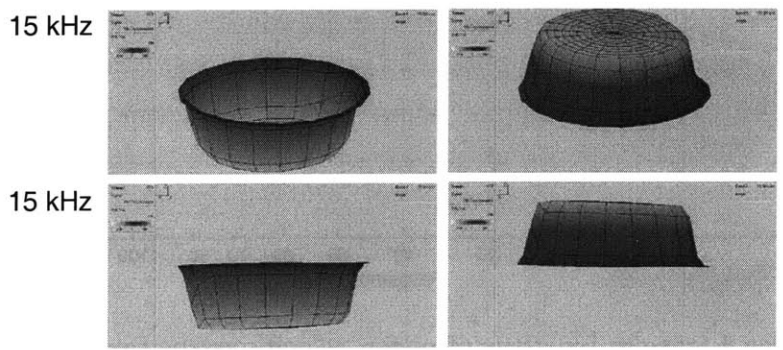


Figure 7.32: Vibrometer scan images of Device 4 low-frequency 15kHz displacement profile. This multiple piezoelectric cylinder device exhibits minimal tilting behavior at 15kHz.

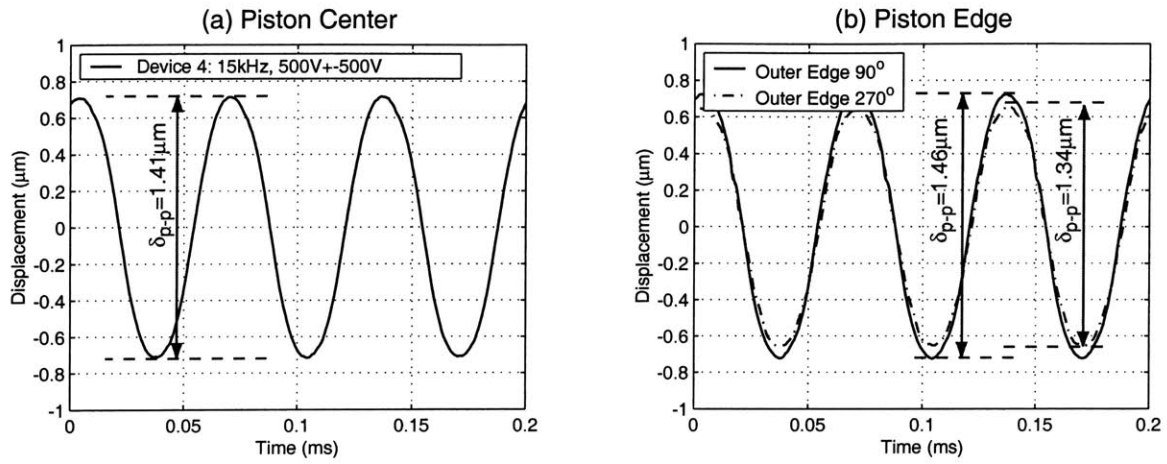


Figure 7.33: Device 4 displacement time histories for sinusoidal drive voltage of $500\text{V} \pm 500\text{V}$ at $f = 15\text{kHz}$: (a) piston center displacement and (b) piston edge displacements. These results indicate a rigid well-toleranced device.

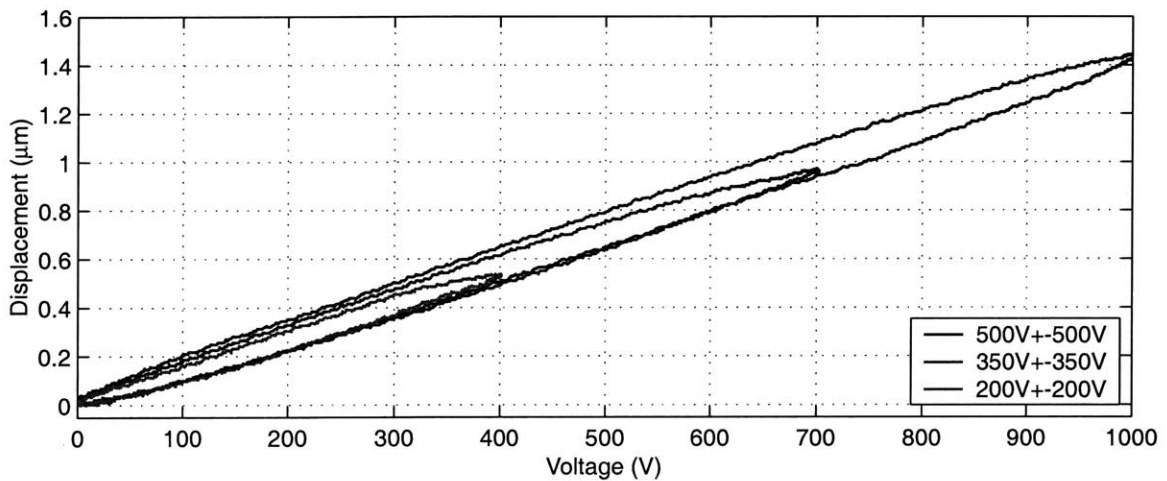


Figure 7.34: Device 4 piston center displacement versus applied voltage at 100Hz.

7.6 Conclusions

This chapter has presented the development and testing of a variety of piezoelectric drive element devices. The results indicate that the incorporation of a single centrally-located piezoelectric element and the incorporation of multiple elements spread out symmetrically beneath single-layer and double-layer tethered piston structures can be performed in a repeatable and predictable fashion. Additionally, processing, tolerancing, and drilling/dicing procedures of high performing PZN-PT elements, in addition to standard polycrystalline PZT-5H elements, have been proven. This drive element manufacturing capability serves now as a foundation for the development and assembly of the full active valve devices presented in the following chapters.

Bibliography

- [1] S.E. Park and T.R. ShROUT, "Characteristics of Relaxor-Based Piezoelectric Single Crystals for Ultrasonic Transducers," *IEEE Trans. Ultrasonics, Ferroelectrics, and Frequency Control*, Vol.44, No.5, Sept. 1997, pp. 1140-1147.
- [2] D.C. Roberts, J.L. Steyn, H.Q. Li, K.T. Turner, R. Mlcak, L. Saggere, S.M. Spearing, M.A. Schmidt, and N.W. Hagood, "A High-Frequency, High-Stiffness Piezoelectric Micro-Actuator For Hydraulic Applications," *Proceedings of the 11th International Conference on Solid-State Sensors and Actuators, Munich, Germany, June 10-14, 2001*.

Chapter 8

Sub-Component Study: Valve Cap and Membrane

8.1 Objectives

The purpose of this study was to evaluate the fabrication process flow of the valve cap and membrane sub-component structure, shown in Figure 8.1, and to experimentally characterize the deflection behavior of a series of these membrane structures to differential pressure loadings. Specifically, the three primary objectives of this study were:

1. To demonstrate the capability to etch valve cap and membrane structures from silicon-on-insulator wafers, with accurate control over the fillet radii at the base of the etch.
2. To experimentally characterize the pressure-deflection behavior of the valve cap and membrane structures, and correlate these results to predictions from the structural models presented in Chapter 3 of this thesis. These structures are pressurized to significant levels at which non-linear large deformation behavior is expected.
3. To provide sensitivity analyses on key geometric parameters such as membrane thickness and fillet radius size to provide an understanding of fabrication process variability on structural pressure-deflection behavior.

Successful fabrication and experimental evaluation of these valve cap and membrane structures enables the further assembly and testing of full active valve devices.

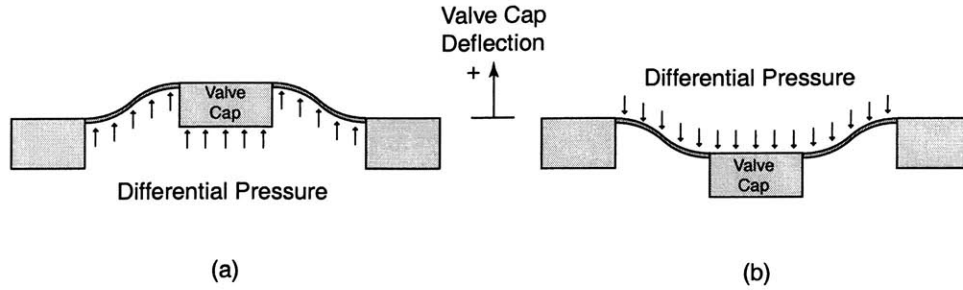


Figure 8.1: 2-D schematic of a valve cap and membrane structure: (a) deformation in response to a positive differential pressure, and (b) deformation in response to negative differential pressure.

8.2 Device Test-Plan

8.2.1 Geometry

The valve cap and membrane structures fabricated for this study had the dimensions illustrated in Figure 8.2. No valve stop exists above the valve cap in the positive direction (unlike in the full active valve device where the fluid orifice is present) in order to facilitate measurement of the valve cap and membrane deflections from above. However, a valve stop in the negative direction, situated $15\mu m$ below the underside of the valve cap, does exist. In response to positive differential pressures across the structure (creating positive valve cap deflections), the membrane is therefore unrestrained. In response to negative differential pressures, however, the valve cap deflection is limited to $-15\mu m$.

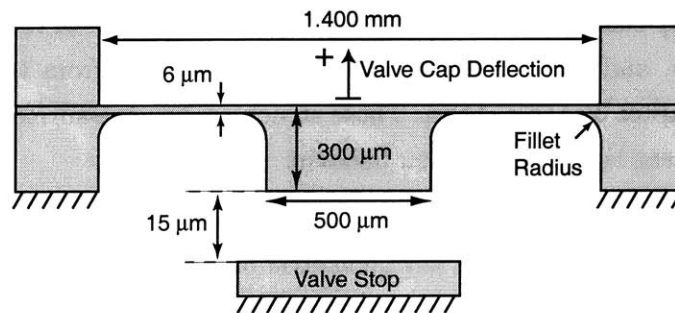


Figure 8.2: Dimensions of the fabricated valve cap and membrane structures: valve cap thickness = $300\mu m$, membrane thickness = $6\mu m$, valve cap diameter = $500\mu m$, and valve membrane outer diameter = 1.4 mm . Fillet radii are shown in schematic.

8.2.2 Device Assembly

As presented in Chapter 7, testing of the valve cap and membrane structure is enabled through fabrication and assembly of the test device illustrated in Figure 8.3. This device consists of Layers N1, N2, N3, 4, 5, 6, N7, N8, and N9. Layers 4, 5, and 6 are identical to those layers used in a full active valve device, however the remaining layers are substituted for the final active valve layers to provide measurement access to the various components. Valve membrane deflection measurements are performed for applied gas pressure to the inside of the HAC chamber and to the top surface of the valve cap and membrane.

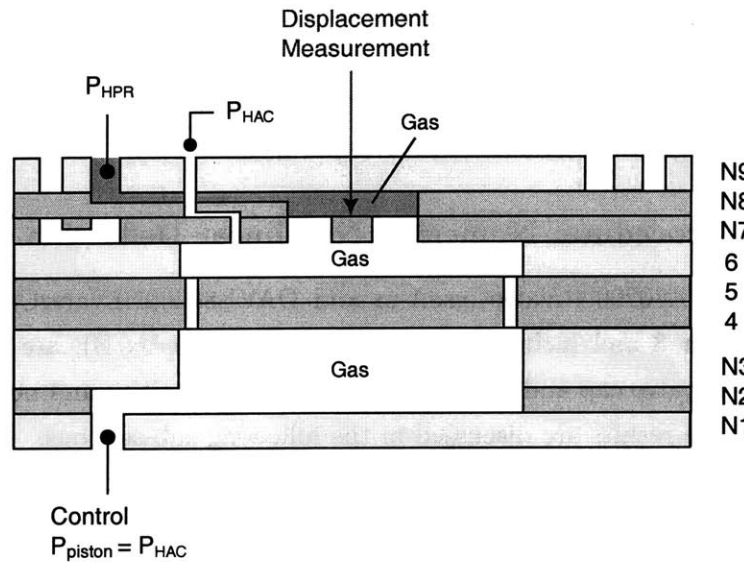


Figure 8.3: Valve cap and membrane sub-component structure. Gas pressure is used above and below the valve structure to obtain pressure-deflection measurements.

8.2.3 Testing Procedure

The valve membrane sub-component device was inserted into the fluids test-rig discussed in Chapter 7 for experimental testing. Gas pressure was independently regulated inside of the hydraulic amplification chamber (P_{HAC}) and above the valve cap and membrane surface (P_{HPR}) so as to provide either a positive or negative differential pressure across the valve cap and membrane structure. The pressure below the unrestrained drive element piston (P_{piston}) was maintained at the same value as P_{HAC} to ensure zero deflection of this structure, thereby minimizing its potential for breaking. Through glass Layer 9, the deflection of the valve cap was monitored using a laser vibrometer system. Differential pressures from -0.40 MPa to 0.40 MPa were imposed on the valve cap and membrane structures and resulting deflection measurements were obtained.

8.3 Theoretical Predictions

In order to accurately predict the response of these valve membrane test structures to various pressure loadings, detailed modeling of the non-linear deflection behavior is required. In addition, sensitivity analyses on the membrane thickness and the fillet radius size are necessary to understand potential differences between predicted and experimental behavior. To accomplish these objectives, two parallel modeling procedures were implemented. The first procedure uses the numerical non-linear deflection code presented in Chapter 3 of this thesis to understand the effects of varying membrane thickness on the deflection behavior of the structure. Because this code is based on simplified plate theory, it does not include fillet radii geometries. As a result, a second procedure is implemented to develop finite-element models of the valve cap and membrane structures, which incorporate fillet radius features. Through the use of both modeling procedures, thorough understanding of the experimental results can be obtained.

8.3.1 1st Modeling Procedure: Numerical Non-linear Deflection Code

The MatlabTM codes, DAVE80200NLValveCaseA.m and DAVE80200NLValveCaseC.m (previously discussed in Chapter 3 and included for reference in Appendix B), are combined to capture the behavior of the valve cap and membrane structure for positive and negative differential pressure loadings. The results are discussed in the following sub-sections.

Baseline Design Pressure-Deflection Behavior

Figure 8.4 plots the valve cap deflection and maximum membrane tensile stress as a function of applied differential pressure from -0.40 MPa to 0.40 MPa. Results for linear and non-linear theory are shown. In comparing these curves, it is clear that non-linear deformation theory is required for accurate prediction of the valve membrane structural behavior. For the peak positive differential pressure of 0.40 MPa, a valve cap deflection of 22.6 μm and corresponding maximum membrane stress of 1.06 GPa are predicted. Due to the presence of a valve stop in the negative direction, a valve cap deflection of -15 μm and a corresponding maximum membrane stress of 1.00 GPa are predicted for an applied differential pressure of -0.40 MPa.

Sensitivity to Valve Membrane Thickness

Although the valve cap and membrane structures tested in this study have measured membrane thicknesses between 6 μm and 7 μm , these measurements are only accurate to within $\pm 1 \mu m$. As a result, it is important to predict the structural behavior over a range of membrane thickness. Figure 8.5 plots the valve cap deflection and maximum membrane tensile stress as a function of applied differential pressure from -0.40 MPa to 0.40 MPa for membrane thicknesses of 6 μm , 7 μm , and 8 μm . In comparison to predictions for the 6 μm membrane (valve cap deflection=22.6

μm), the 7 μm membrane is predicted to deflect 20.8 μm (8 % difference), and the 8 μm membrane is predicted to deflect 19.6 μm (13 % difference) for an applied differential pressure of 0.40 MPa. The corresponding stresses also differ by similar percentages. Based on these predictions, variations in membrane thickness should not drastically effect structural behavior, although it is an important fabrication uncertainty to keep in mind.

Sensitivity to Membrane In-Plane Prestress

During fabrication procedures of the valve cap and membrane structures, the oxide above the membrane is stripped. Ideally, this procedure should eliminate any residual stress contained within the membrane structure. However, other procedures, such as anodic bonding of device layers, could potentially create residual stresses along the valve membrane due to thermal expansion mismatch between the silicon and pyrex layers. Calculations have indicated that these valve membrane structures will experience at most a residual tensile stress of 5 MPa for an anodic bonding temperature of up to 330C (50C above the ideal matched anodic bonding temperature of 280C) [1], a stress which has negligible effect on the stiffness of the valve membranes structures in response to pressure loading. As a result, since the anodic bonding procedures in this thesis are always carried out at 300C, these valve membranes should be free of residual tensile stress.

8.3.2 2nd Modeling Procedure: Finite-element Code

Finite-element models have been developed that incorporate fillet radius features along the inner and outer circumference of the valve membrane. Figure 8.6 displays a mesh of the valve cap and membrane geometry, with detailed focus on the meshing grid around the fillet radius features. In this figure, the fillet radius has size 30 μm . Figure 8.7 shows a representative stress contour plot of the structure when subjected to a positive differential pressure of 0.30MPa.

Sensitivity to Fillet Radius Size

Using these finite-element models, valve cap deflection and maximum membrane stress plots as a function of varying fillet radius are acquired, as shown in Figure 8.8. The fillet radius at the inner and outer valve membrane circumference is varied to be 15 μm , 30 μm , 45 μm , and 60 μm . As evidenced in the plots, an increase in the fillet size serves to stiffen the overall membrane structure, resulting in reduced valve cap deflections. For example, for an applied differential pressure of 0.40 MPa, the valve cap with fR=15 μm experiences a deflection of almost 23 μm whereas the valve cap with fR=60 μm experiences a deflection of approximately 20 μm . The maximum membrane stress curves follow a similar pattern. In the valve cap and membrane

experiments discussed later in this chapter, careful inspection of the membrane fillet radii is performed prior to testing to enable understanding of the structural behavior.

Note on Theoretical Predictions

The presence of a fillet radius along the valve membrane inner and outer membrane surfaces clearly has an effect on the structural stiffness, as evidenced in comparing Figures 8.5 and 8.8. For very small fillet radius sizes, these features act as stress concentrations. As such, the finite-element models with small fillet radii predict stresses significantly larger than those predicted by the numerical code (which includes no effect of fillet radii). Conversely, the finite-element models with large fillet radii predict smaller stresses than those predicted by the numerical code, mainly because the fillet structure actually results in a stiffening of the membrane and a subsequent reduction in the deflection magnitude of the valve cap. The fillet radii features present on the fabricated valve membrane structures discussed in the following experimental section were able to be controlled to within $35 - 50\mu m$, a range which is characterized by reasonably good correlation between finite-element and numerical pressure-deflection predictions. As such, when comparing experimental pressure-deflection behavior with theory in the following section of this chapter, the numerical predictions will be used.

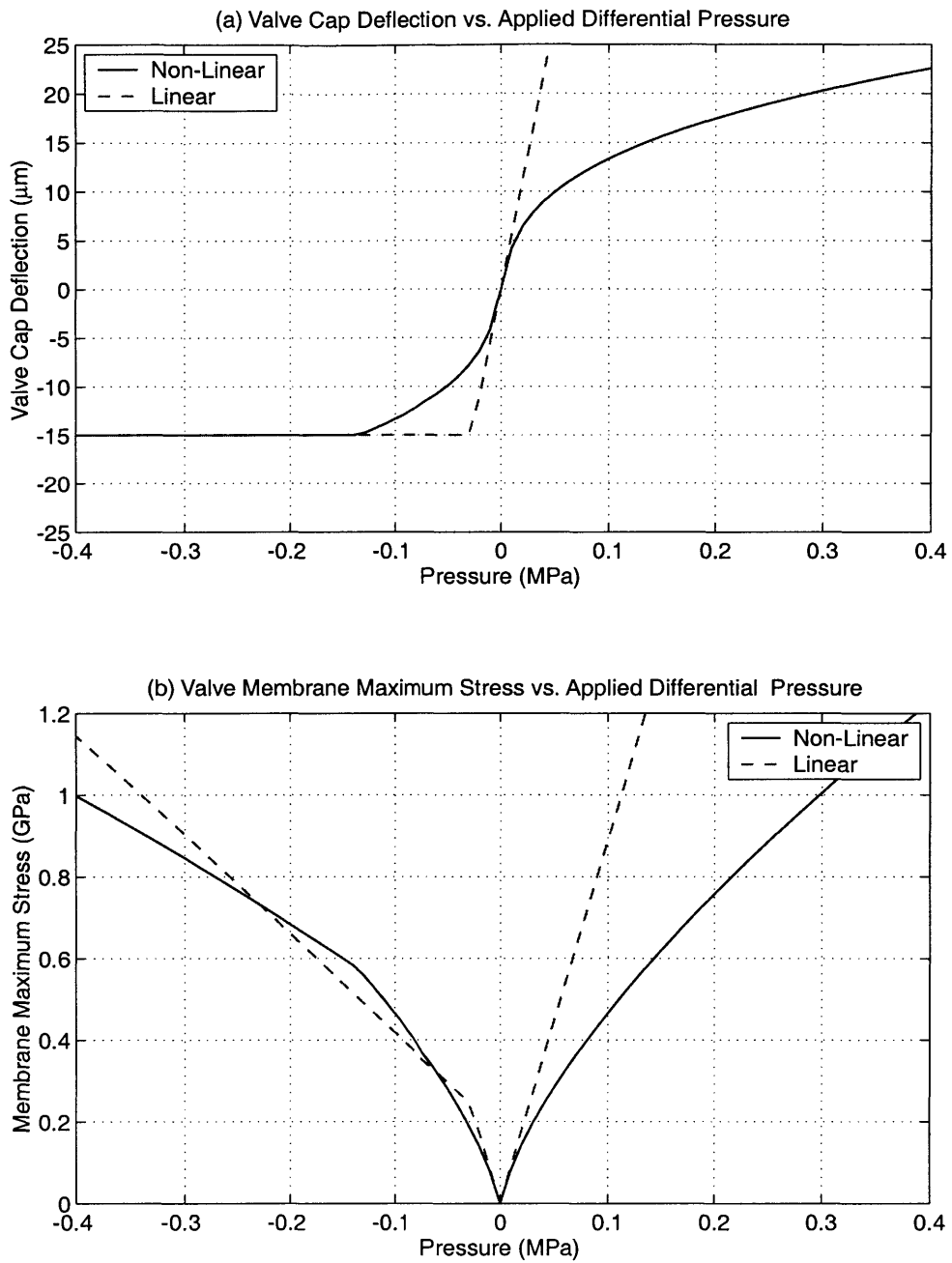


Figure 8.4: Baseline valve cap and membrane design $\rightarrow r_{vc} = 250\mu m, r_{vm} = 700\mu m, t_{vm} = 6\mu m$: (a) valve cap deflection vs. applied differential pressure, and (b) maximum stress in valve membrane vs. applied differential pressure. Note: valve stop present at $-15\mu m$.

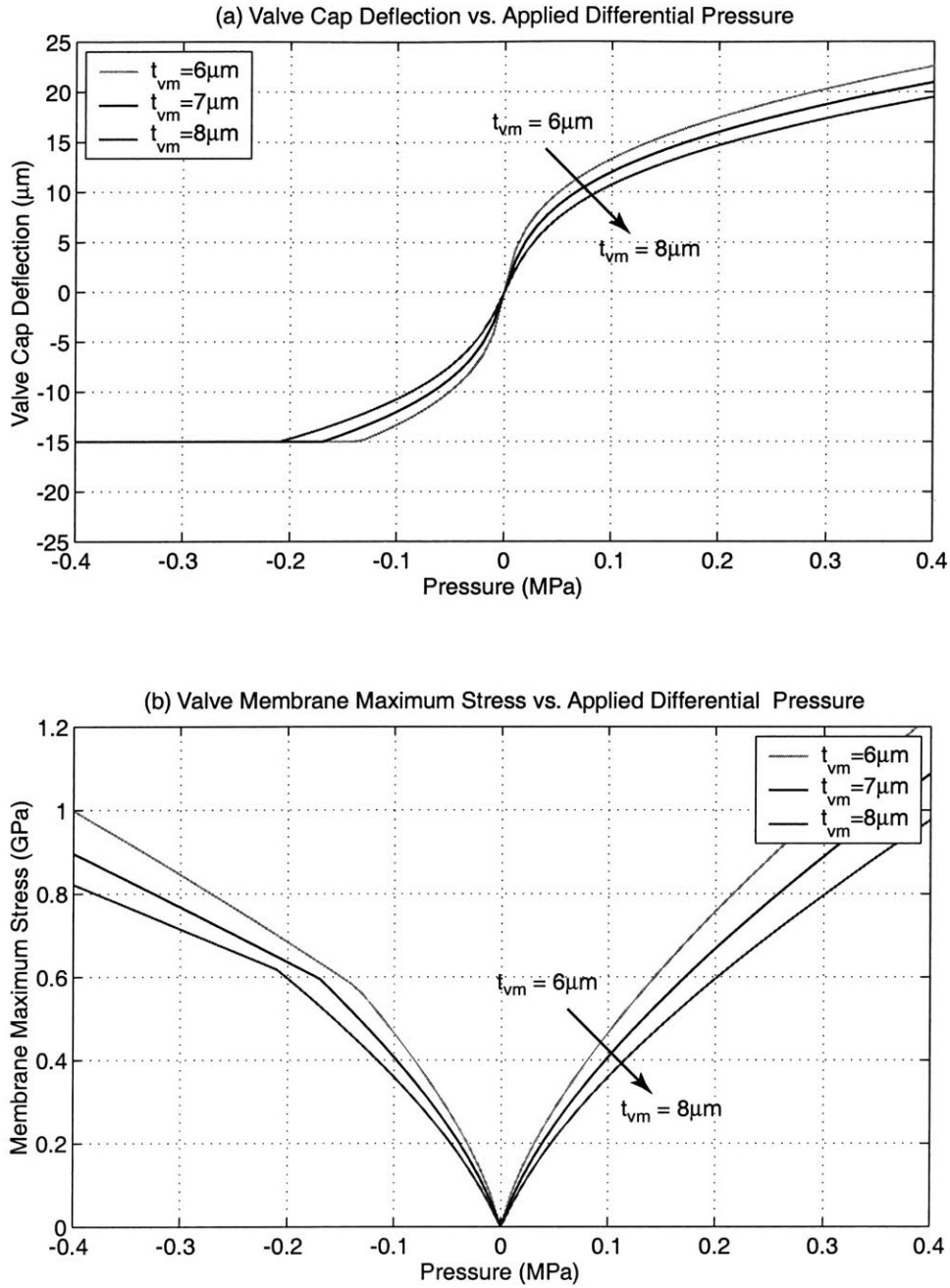


Figure 8.5: Sensitivity of baseline valve cap and membrane design to variations in valve membrane thickness $\rightarrow r_{vc} = 250\mu m, r_{vm} = 700\mu m, t_{vm} = [6\mu m, 7\mu m, 8\mu m]$: (a) valve cap deflection vs. applied differential pressure, and (b) maximum stress in valve membrane vs. applied differential pressure. Note: valve stop present at $-15\mu m$.

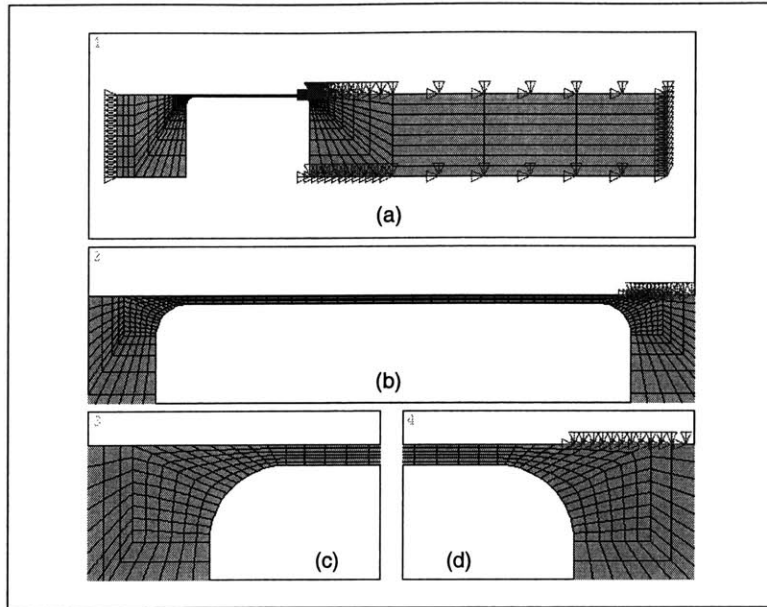


Figure 8.6: Finite-element mesh (ANSYSTM) of valve cap and membrane structure: (a) full view of 2-D axisymmetric model, (b) close-up view of membrane, (c) close-up view of inner fillet radius, and (d) close-up view of outer fillet radius.

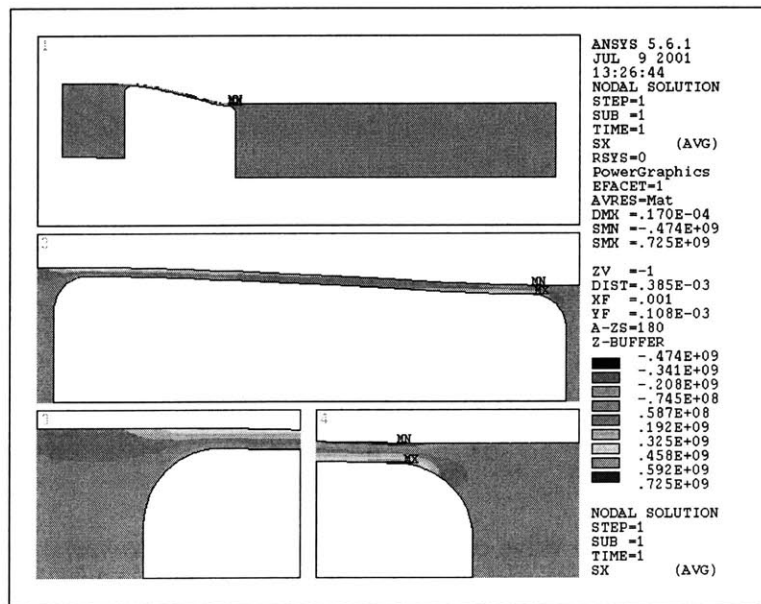


Figure 8.7: Finite-element stress contours resulting from applied differential pressure loading of 0.30MPa . Fillet radii in model are $fR = 30\mu\text{m}$. Peak tensile stress (0.868MPa) occurs at base of fillet radius along outer membrane circumference.

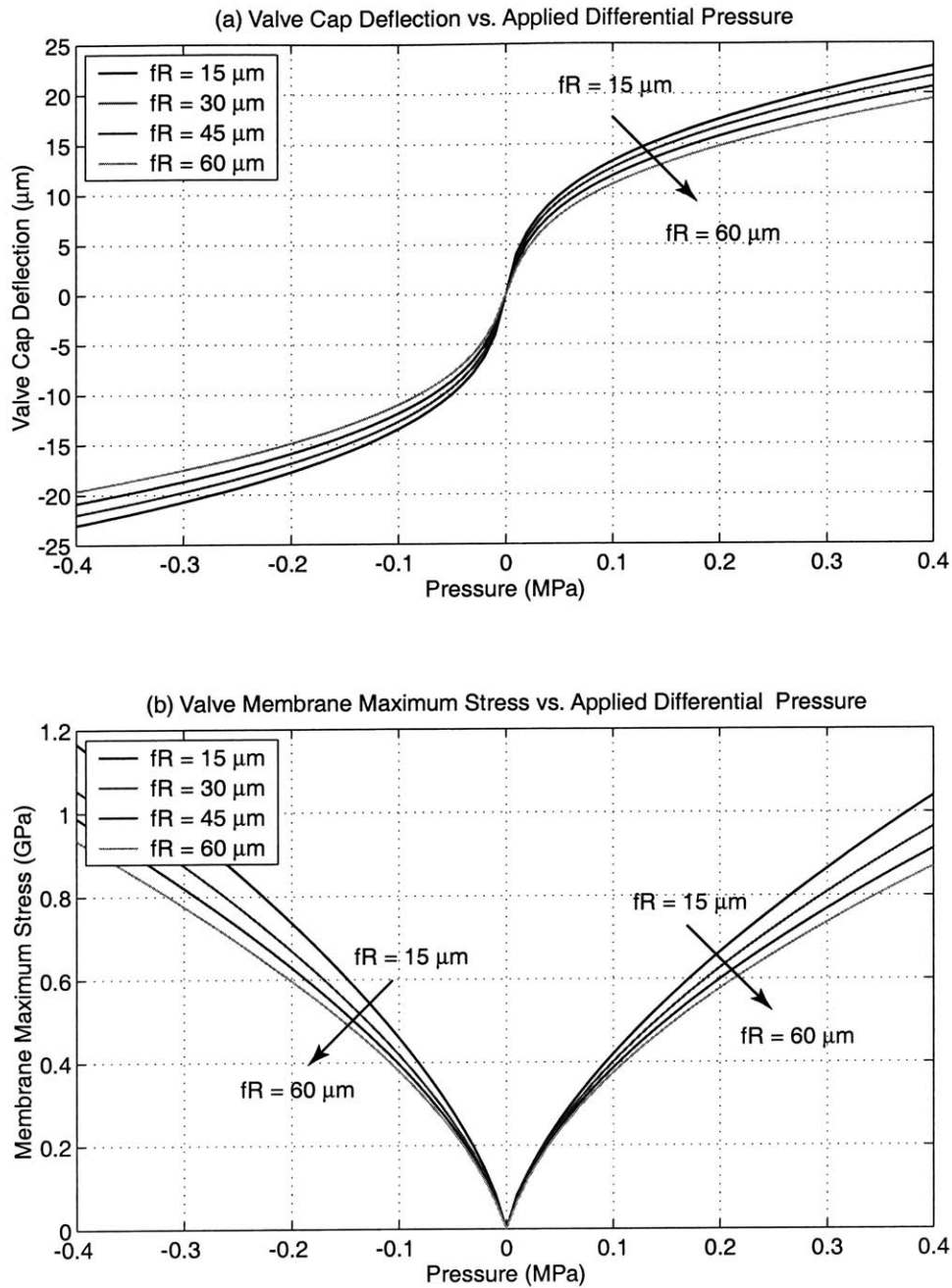


Figure 8.8: Sensitivity of baseline valve cap and membrane design to variations in fillet radius size $\rightarrow r_{vc} = 250\mu m, r_{vm} = 700\mu m, t_{vm} = 6\mu m, fR = [15\mu m, 30\mu m, 45\mu m, 60\mu m]$: (a) valve cap deflection vs. applied differential pressure, and (b) maximum stress in valve membrane vs. applied differential pressure. Note: valve stop at $-15\mu m$ not implemented in this finite-element model.

8.4 Experimental Results

Three representative valve cap and membrane sub-component structures (referred to as Valve Membrane 1, Valve Membrane 2, and Valve Membrane 3 in subsequent discussions) were experimentally tested to validate structural behavior. Prior to testing and before die-level bonding of Stack 4-5-6 to Stack N7-N8-N9, inspection of the valve membrane fillet radii in Layer N7 was performed. This section details these inspections, as well as the experimental pressure-deflection results for each of these membrane structures.

8.4.1 Fillet Radius Inspection

Each of the three representative valve membrane structures was inspected for the presence of defects along the etched membrane and for consistency in fillet radius size. Valve Membrane 1 possessed a consistent fillet radius size of 45-50 μm and no defects along the membrane. Valve Membrane 2 possessed a consistent fillet radius size of 40-50 μm and no defects along the membrane. And similarly, Valve Membrane 3 possessed a fillet radius size of 35-40 μm and no defects along the membrane. Overall, these three valve membrane structures well represent the majority of etched valve membrane structures in their fillet radius consistency and lack of defects.

8.4.2 Pressure-Deflection Results

In order to determine the pressure-deflection behavior of these valve membrane structures, a pressure time history was imposed on the structure using a valve and pressure sensor set-up and the valve cap deflection was measured using a laser vibrometer system. Figure ?? overlays the pressure-deflection results for Valve Membranes 1, 2, and 3 with the structural predictions for $t_{vm} = 6\mu m$ and $t_{vm} = 7\mu m$ presented previously. Overall, all three membrane structures correlate well with each other and with predictions. Note that the valve membrane stops vary between -15 and -16 μm due to non-uniform etch depths during fabrication.

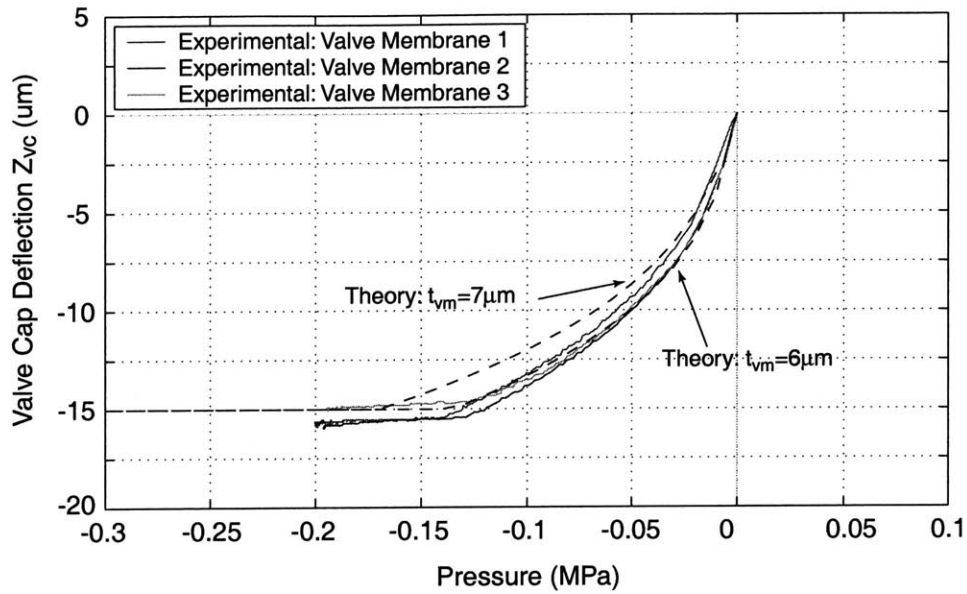


Figure 8.9: Valve cap and membrane experimental pressure-deflection results compared to theoretical expectations. The three representative valve cap and membrane structures correlate well with each other and with predicted behavior. Note that valve stops vary between -15 and $-16 \mu m$ due to non-uniformity in etching these features.

8.5 Conclusions

This chapter has presented successful correlation between valve membrane structural behavior and modeling predictions. Representative valve membranes that possessed consistent fillet radius profiles around the membrane and the absence of any significant etch defects were experimentally characterized. Pressure-deflection results correlate extremely well with predicted behavior obtained using finite-element models and the non-linear deformation code presented in Chapter 3. Overall, this chapter has verified that these valve membrane structures can be consistently fabricated for use in full active valve devices, and that these structures exhibit expected pressure-deflection behavior.

Bibliography

- [1] Corning web information on the thermal expansion behavior of Pyrex 7740 and its use with Silicon for anodic bonding. (<http://www.corning.com/lightingmaterials/waferglass.html>)

Chapter 9

Active Valve Testing

9.1 Objectives

The purpose of this testing study was to evaluate the quasi-static and dynamic structural performance of the complete active valve device and to determine its limitations in regulating the flow of fluid against imposed differential pressures. Specifically, the four primary objectives of this study are:

1. To understand the dynamic behavior of the active valve device and to determine the range of driving frequency for which the valve behaves in a quasi-static manner. In essence, this goal focuses on locating the resonant frequencies of the structure. The effect of having or not having fluid present in the flow channel above the valve cap and membrane on the onset of valve resonant behavior is determined.
2. To evaluate the amplification ratio of the active valve structure under a variety of voltage levels and internal and external bias pressures for a driving frequency below resonance to ensure quasi-static operation. This is accomplished by measuring the drive piston and valve cap deflections under conditions that force the valve cap through its full stroke of operation, including interaction with the valve stops above and below the valve cap.
3. To characterize the differential pressure-flow rate curves for the valve cap and orifice geometry of the active valve device. This is accomplished by measuring an average fluid flow rate through the valve orifice as a function of valve cap opening downward from the upper valve stop. Motion of the valve cap through its stroke is controlled at a very slow rate to achieve quasi-static measurements of flow rate at given valve openings.
4. To characterize the dynamic capability of the active valve structure in regulating fluid flow against a preset differential pressure across the valve at a driving frequency below resonance to ensure quasi-static operation. Successful operation of the valve structure in

this manner proves its capabilities as a flow regulation device. A further goal is to identify the limiting differential pressures against which the active valve can function.

9.2 Device Test-Plan

9.2.1 Geometry

A schematic of the fabricated active valve device is illustrated in Figure 9.1. The device incorporates three PZN-PT piezoelectric square elements (each with cross-sectional area 1.06mm x 1.06mm) beneath a double-layer tethered piston structure. The top and bottom tethers of the piston are each $250\mu m$ in width and each have a thickness of $8\mu m$. A valve cap and membrane structure is positioned above the hydraulic amplification chamber, with a structural stop (formed by the glass Layer 6 within the HAC chamber) $\sim 16.5\mu m$ below the equilibrium position of the valve cap. Glass Layer 6 contains a series of “HAC through-holes” and “HAC radial channels” to carry the fluid from the lower to upper portion of the HAC chamber. The valve cap has a diameter of $500\mu m$ and the valve membrane has an outer diameter of $1400\mu m$. A valve orifice is located $\sim 16.5\mu m$ above the valve cap equilibrium position. The orifice has an inner diameter of $450\mu m$. The drive element piston structure is consistent with the 2nd-generation drive element devices (except for the use of slightly reduced-area square piezoelectric elements) fabricated and tested as part of the drive element sub-component study detailed in Chapter 7. In addition, the valve cap and membrane structure is consistent with the valve structures fabricated and tested as part of the valve cap and membrane sub-component study detailed in Chapter 8.

9.2.2 Plan of Study

As detailed in the introduction to this chapter, the characterization of each active valve device was carried out through a series of four experimental testing studies. The first two studies focus on the dynamic and quasi-static behavior of the active valve structure, while the second two studies focus on the fluid flow regulation capability of the structure. In evaluating these objectives, numerous active valve devices were built. Two of these devices are covered in detail in this chapter (and thesis). The first active valve device (subsequently referred to as device AV1) successfully made it through the majority of all four testing studies. It failed during an experiment to determine its limitations in regulating high pressure flows. The second device (subsequently referred to as device AV2) broke during completion of the first two studies, and as a result, no flow regulation data was taken for this device. A discussion of this failure is described in the chapter. This chapter is organized into two primary sections, in accordance with these experimental testing studies. The first section details the results of the dynamic and

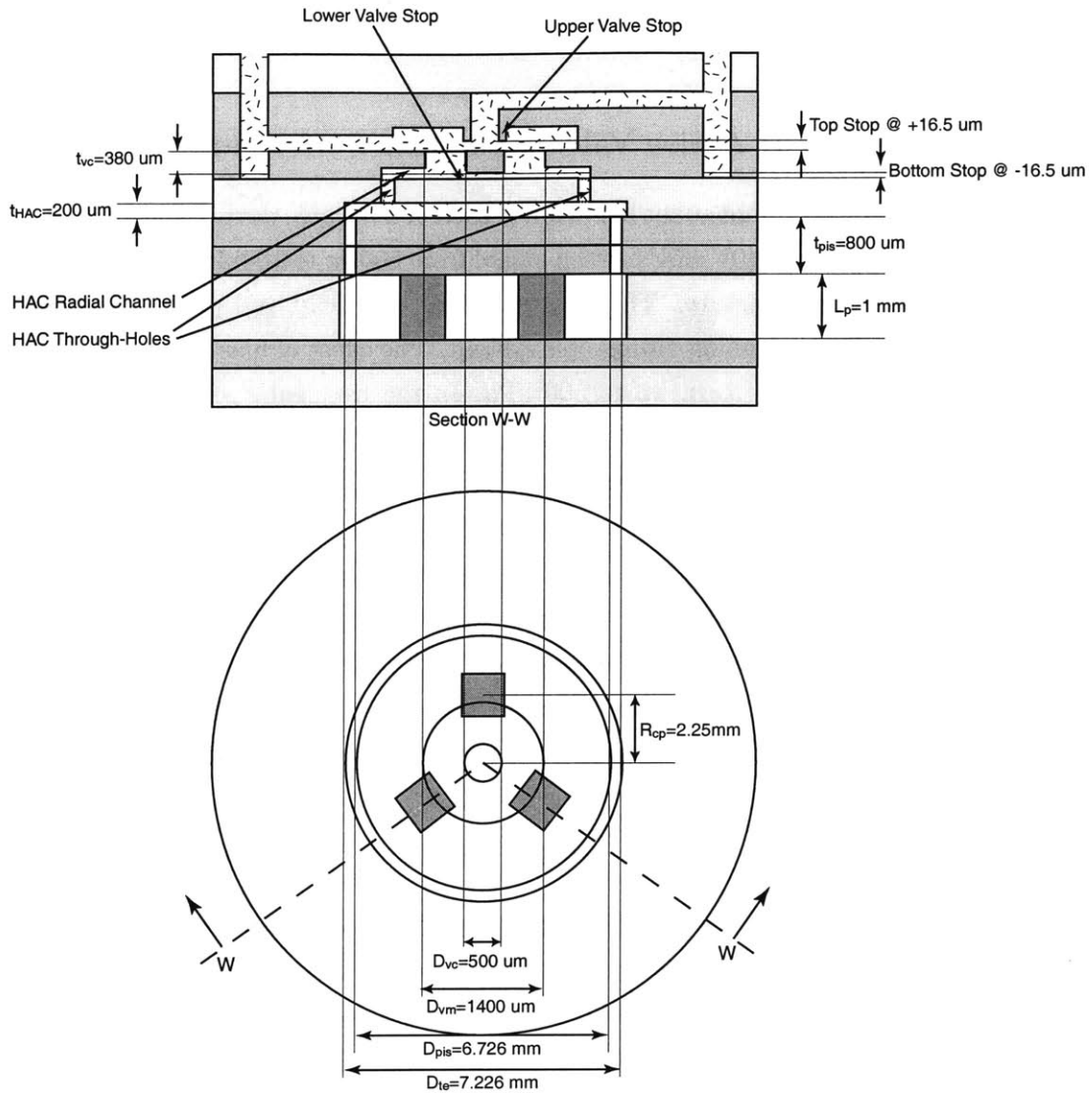


Figure 9.1: Dimensions of active valve devices AV1 and AV2. Three square PZN-PT elements are incorporated beneath a double-layer tethered piston. A valve cap and membrane structure interacts with the fluid orifice structure at $Z_{vc} = +16.5\mu m$ and with the glass Layer 6 structure within the HAC chamber at $Z_{vc} = -16.5\mu m$. In the lower figure, only geometries beneath the valve cap structure (ie: beneath Layer 7) are detailed.

quasi-static active valve testing studies (for both device AV1 and device AV2), and the second section covers the valve flow regulation studies (for device AV1).

9.3 Experimental Testing Section 1: Active Valve Structural Performance

9.3.1 Testing Section 1: Active Valve Structural Performance

To characterize the frequency dependant behavior of each active valve device, the following tests were performed. A low-voltage ($0V \pm 5V$) sweep signal from 500Hz to 100kHz was applied to the piezoelectric drive element structure. The corresponding valve cap and piston displacements were measured using a laser scanning vibrometer system. The effect of bias pressure (ie: $P_{bias} = P_{HAC} = P_1 = P_2$, where $P_{bias} \geq 0$), up to 500 kPa, on the frequency response of the active valve device was evaluated. Additionally, higher-voltage (up to $600V_{pp}$) sweep signals were applied over a lower range of frequency from 500Hz to 3kHz to evaluate the valve cap and piston behavior in a range of quasi-static frequencies below resonance.

To characterize the quasi-static behavior of each active valve device, a series of tests was run at a chosen frequency of operation (ie: 1kHz for these tests) sufficiently below the resonant frequency to ensure quasi-static structural behavior. The effects of increasing voltage and increasing bias pressure on the device amplification ratio were determined. Additionally, the capability of the device to open and close the valve cap against the fluid orifice was evaluated.

Active Valve Device AV1

Figures 9.2 through 9.7 display the structural testing results for active valve device AV1. Figure 9.2 plots the valve cap frequency response from 500Hz to 100kHz for an applied low-voltage sweep signal of $0V \pm 5V$ under the condition that silicon oil is not present above the valve cap and membrane structure and under the condition that silicon oil is present above the valve cap and membrane structure. These tests were performed with $P_{bias} = 500kPa$ to ensure that cavitation of the fluid within the HAC did not occur. Without oil, the resonant frequency of the structure is 10kHz. With oil, this frequency drops to slightly less than 5kHz. This reduction is due to the added mass of the fluid on the top surface of the valve cap and membrane. It is interesting to notice the presence of numerous resonant peaks (at 6.5kHz and 8kHz), in addition to the primary resonant peak at 5kHz, for the response with oil. Without oil, no additional resonant behavior is observed beyond the primary 10kHz resonance until approximately 40kHz. The additional peaks in the response with oil present are most likely a result of fluid-structure interactions between the oil and the experimental test-jig flow tubes external to the device or between the oil and the flow channels internal to the device. Pressure waves could be interacting within these channels and affecting the valve behavior. Additionally, the primary resonant peak of the response (at 5kHz) with oil above the structure is not as sharp as that without oil, due to the increased damping introduced by the fluid within the system. Based on the experimental

resonant peak amplitude, in comparison to expected behavior determined from the active valve model described in Chapter 5, the damping ratio of this structure is estimated to be 0.16.

Figure 9.3 overlays the frequency response of the drive element piston with that of the valve cap, for the case in which oil is present above the valve structure at the same operating conditions as previously described. The piston response exhibits the same resonant peak behavior as the valve cap response. The increase in piston displacement amplitude at frequencies below 1kHz is due to measurement limitations in the vibrometer system (essentially the magnitude of the measured velocities and displacements are of the same order as the noise floor of the system). The results indicate that the amplification ratio of the valve device is steady (between 40x-50x) over the range of frequencies below resonance.

Figure 9.4 plots the low-voltage valve cap frequency response from 500Hz to 100kHz for a varying bias pressure from $P_{bias} = 100kPa$ to $P_{bias} = 500kPa$. For the PZN-PT material integrated within these valve devices, material testing results by Lin [1] indicate that the piezoelectric material strain capability degrades near a compressive stress of 10MPa. For the geometry of these active valve devices tested, a bias pressure of $P_{bias} = 500kPa$ correlates to a compressive stress on the piezoelectric square elements beneath the piston of approximately 6.1MPa. These bias pressure tests therefore evaluate whether degradation occurs up to 6.1MPa. Higher bias pressure tests were to be performed following the completion of all four major testing sections. Clearly from the results, a variation in P_{bias} from 100kPa to 500kPa has no noticeable effect on the frequency response of the structure. Again, the upper limit to P_{bias} was not evaluated until all other experimental tests on the active valve device were completed, for safety reasons, to minimize potential breakage of the device.

Each of the previous frequency sweeps was carried out with the valve cap and membrane structure at its equilibrium position (zero deflection upward or downward) by ensuring that the pressures above the valve cap and membrane structure (P_1 and P_2) were identical to the pressure within the hydraulic amplification chamber (P_{HAC}). Under these conditions, in order to close the valve cap against the valve orifice ($+16.5\mu m$ above this equilibrium position) during quasi-static sinusoidal operation, a large voltage on the piezoelectric drive element could be required. Another potential way of operating the active valve device to ensure that the valve cap can close against the valve orifice for lower operating voltages is to impose a differential pressure (referred to as $\Delta P_{vc,vm} = P_{HAC} - P_1$, where $P_1 = P_2$ for example) across the valve cap and membrane structure to create a positive offset deflection of the valve cap about which oscillation can then occur. This method reduces the overall stroke of the valve cap (due to the non-linearity of the valve membrane - see next paragraph), but ensures valve closure against the orifice. To evaluate this alternative operation concept on the resonant behavior of active valve device, additional low-voltage frequency sweeps were carried out with $\Delta P_{vc,vm} = 20kPa$ and $\Delta P_{vc,vm} = 50kPa$, which produce offset valve cap displacements of $Z_{vc} \sim +6\mu m$ and $Z_{vc} \sim +10\mu m$ respectively.

Figure 9.5 compares the results.

With increasing offset displacement of the valve cap above its equilibrium position, the effective stiffness of the valve membrane structure for low-voltage (and therefore low amplitude) oscillations should increase since the membrane moves into its large-deflection regime. As a result, one would expect the resonant peak to shift to a increased frequency (due to the higher stiffness) and the magnitude of this peak to be reduced (also due to the higher stiffness). As shown in Figure 9.5(a), both of these results are clearly observed. As $\Delta P_{vc,vm}$ is increased from 0kPa to 20kPa to 50kPa, the resonant peak increases from $\sim 5kHz$ to $\sim 6kHz$ to $\sim 6.5kHz$, respectively. Additionally, the valve cap oscillation amplitude decreases from $\sim 4\mu m$ to $\sim 1.6\mu m$ to $\sim 0.8\mu m$ for this increase in $\Delta P_{vc,vm}$. This amplitude reduction is most clearly seen in Figure 9.5(b), which plots the amplitude on a linear scale. High-voltage quasi-static active valve operation under these differential pressure conditions is discussed further in the later half of Testing Section 1.

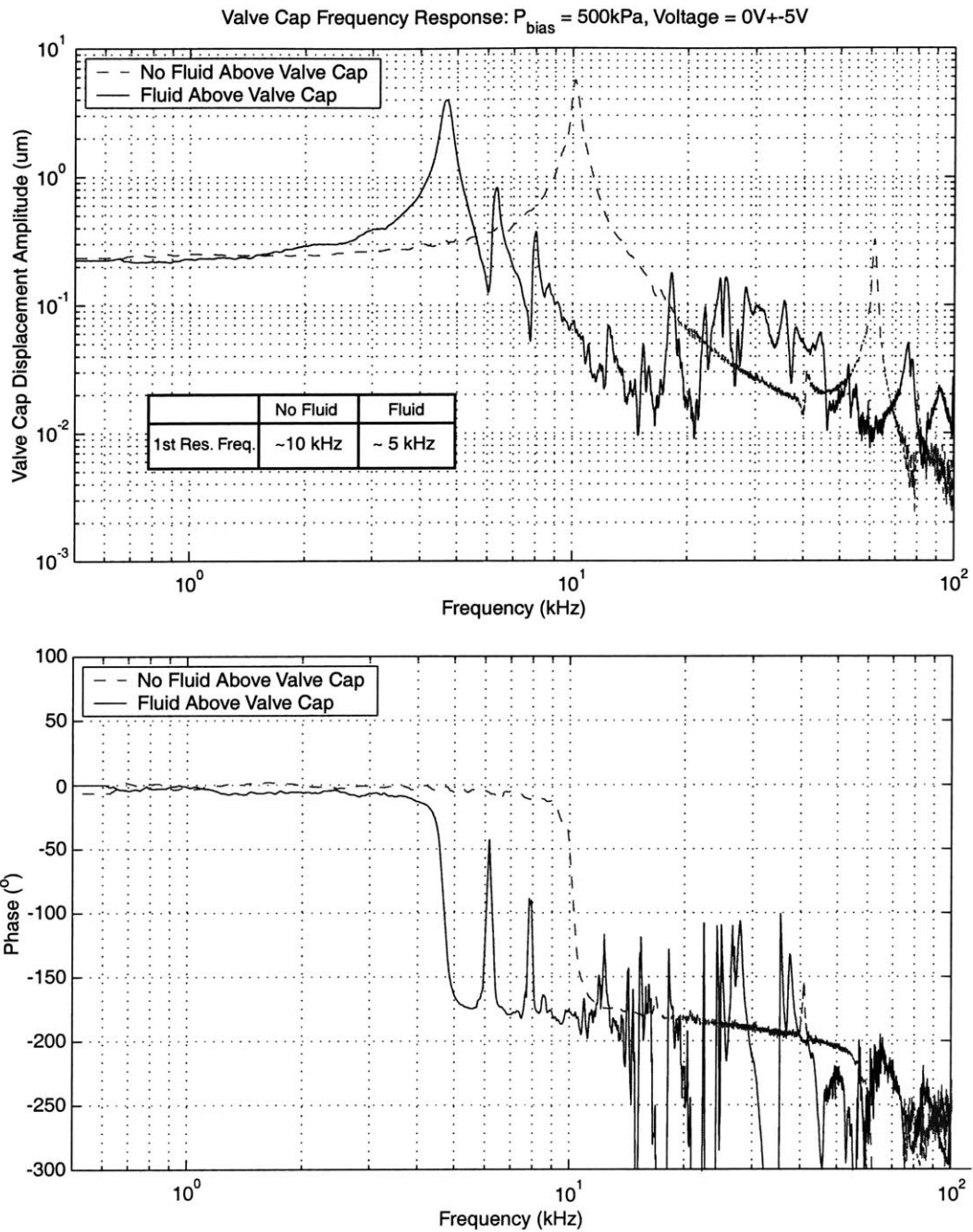


Figure 9.2: Device AV1 low-voltage ($0V \pm 5V$) valve cap frequency response from 500Hz to 100kHz, with and without oil present above the valve structure. The bias pressure in these tests was maintained at $P_{bias} = 500kPa$. The presence of oil in the flow channel above the valve cap creates an added mass that reduces the resonant frequency from 10kHz to 5kHz.

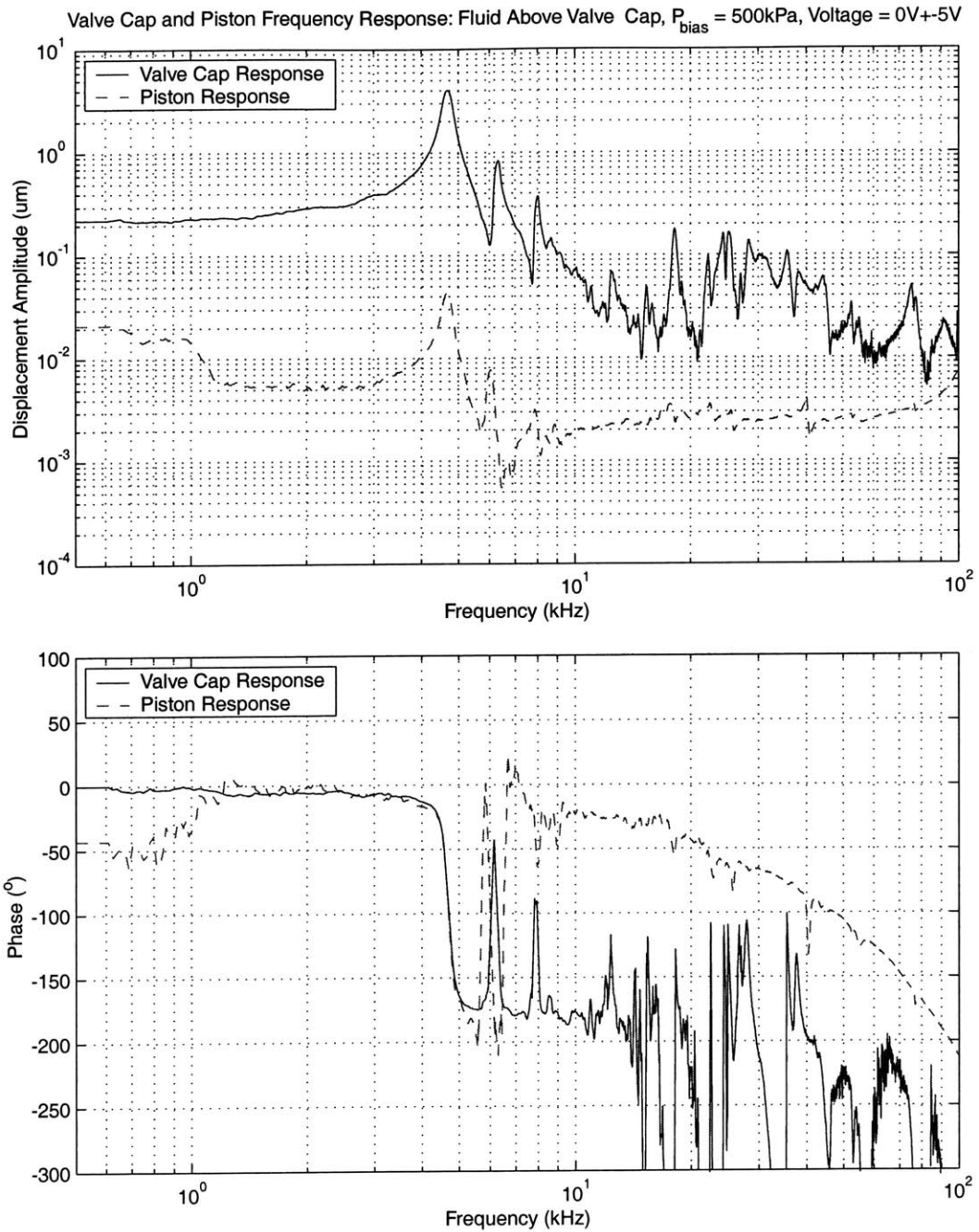


Figure 9.3: Device AV1 low-voltage ($0V \pm 5V$) piston and valve cap frequency responses from 500Hz to 100kHz, with oil present above the valve structure. The bias pressure in these tests was maintained at $P_{bias} = 500kPa$. An amplification ratio between 40x-50x is observed for frequencies below resonance.

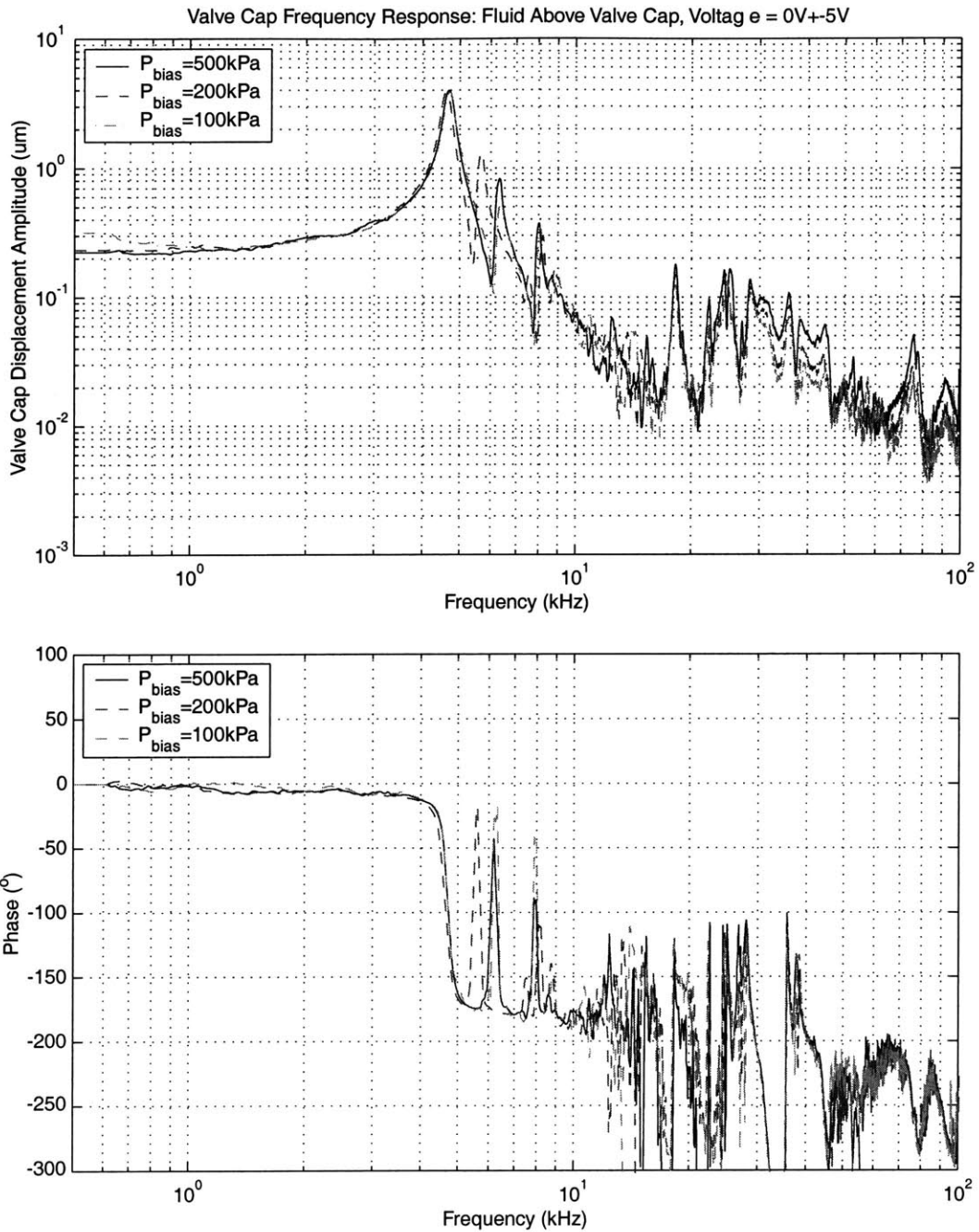


Figure 9.4: Device AV1 low-voltage valve cap frequency responses from 500Hz to 100kHz, for varying P_{bias} . Results indicate that frequency behavior is not affected by an increase in bias pressure from $P_{bias} = 100\text{kPa}$ to $P_{bias} = 500\text{kPa}$.

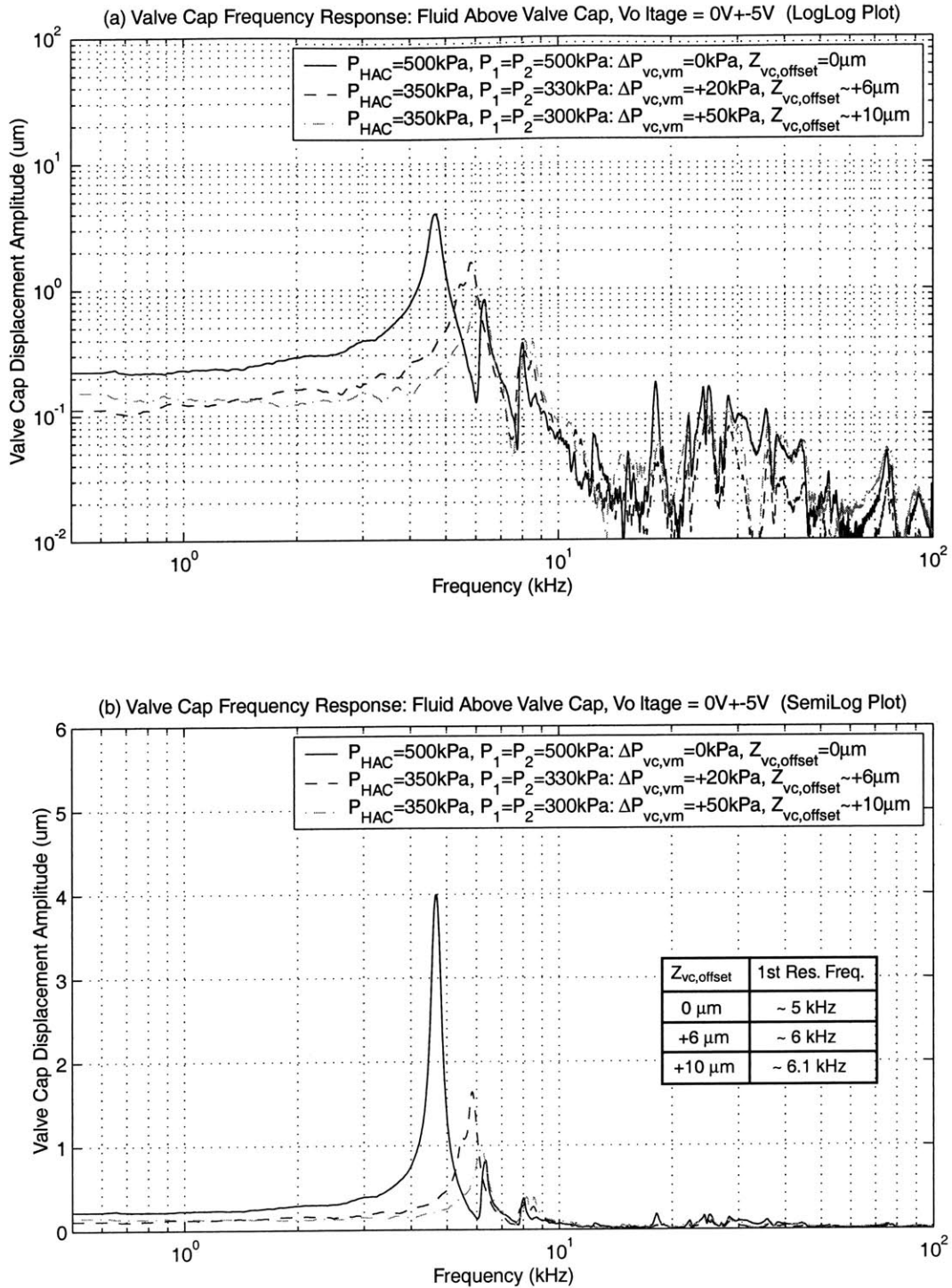


Figure 9.5: Device AV1 low-voltage valve cap frequency responses from 500Hz to 100kHz, for varying differential pressure applied to valve cap and membrane structure. For increasing differential pressure $\Delta P_{vc,vm}$ across valve cap and membrane, the resonant peak shifts upward and the valve cap vibration amplitude decrease. These phenomena are due to the membrane stiffening as it is forced higher into its large-deflection regime.

A series of tests was also run on active valve device AV1 to characterize the high-voltage frequency response of the structure for a range of frequencies below resonance. Since the resonant peak of this device is present at 5kHz, a range was chosen to include 500Hz to 3kHz. Figure 9.6 plots the valve cap frequency response from 500Hz to 3kHz for a series of increasing drive voltage levels from 50Vpp to 600Vpp, all with $P_{bias} = 500kPa$. At the lower voltage drive levels, the valve cap deflection amplitude is essentially constant over these frequencies. As the voltage is increased, regions of increased valve cap deflection appear near 1.7-1.9kHz. This frequency value is approximately $\frac{1}{3}$ of the low-voltage resonant frequency of the active valve device. This region, therefore, is a result of sub-harmonic excitation of the device. Figure 9.7 plots the valve cap versus piston deflection amplitude over this frequency range for an applied voltage of 600Vpp. In comparing these frequency responses, the amplification capabilities of the active valve device is evident. Figure 9.7(a) plots these curves on a logarithmic amplitude scale, and Figure 9.7(b) plots the curves on a linear amplitude scale. Over this range of frequencies, the amplification ratio is between 40x-50x.

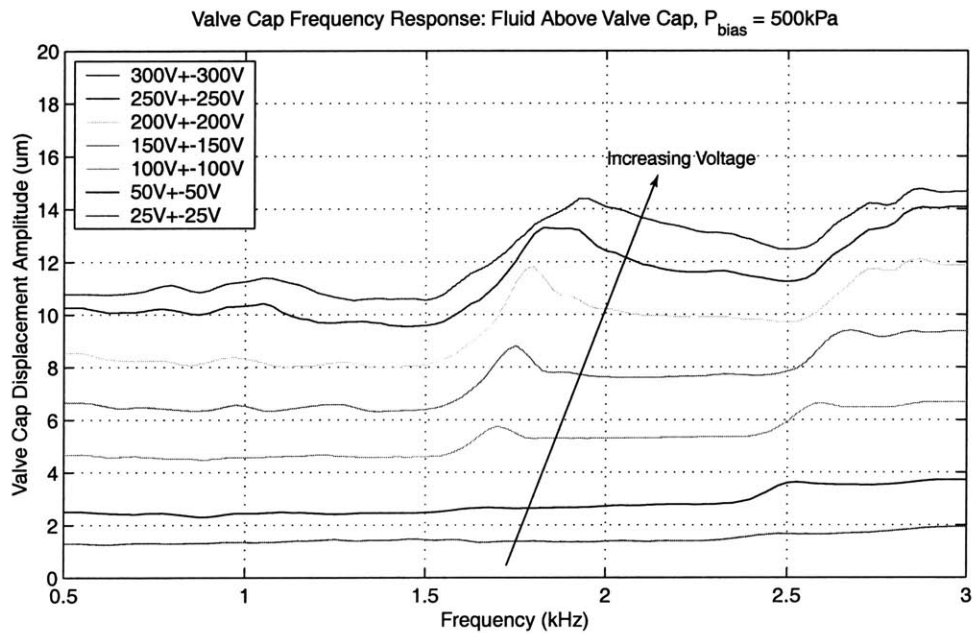


Figure 9.6: Device AV1 valve cap frequency responses from 500Hz to 3kHz, for $P_{bias} = 500kPa$ and increasing high voltage drive levels. Harmonic excitation behavior near $\sim 1.7 - 1.9kHz$ becomes evident as voltage levels are increased (ie: as valve membrane structure moves further into its non-linear large-deflection regime).

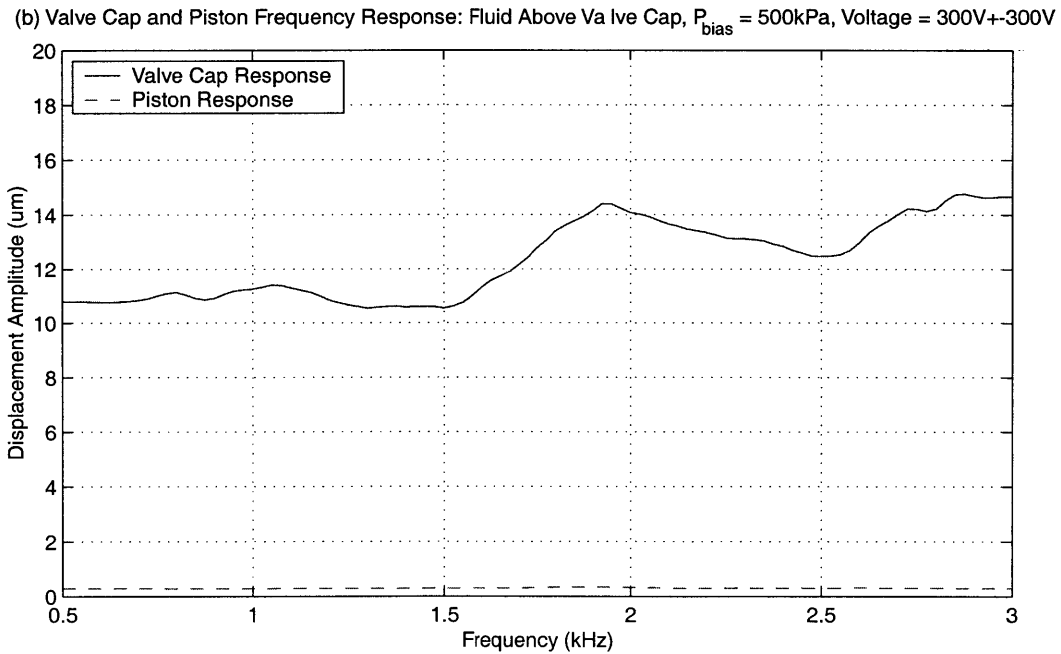
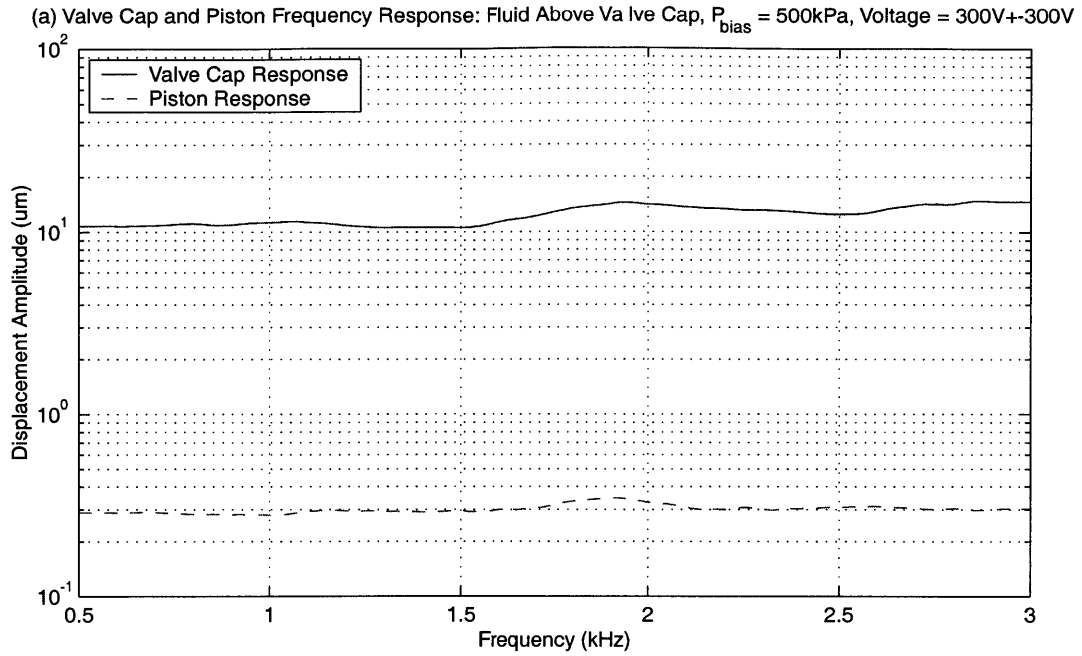


Figure 9.7: Device AV1 high-voltage piston and valve cap frequency responses from 500Hz to 3kHz, for $P_{bias} = 500kPa$. Amplification of active valve device is consistent between 40x-50x over this range of frequency.

The previous frequency sweep experimental tests found the resonant frequency of device AV1 to be $\sim 5kHz$. In order to evaluate the quasi-static performance of the structure under the larger drive voltage levels at which the valve was designed to operate, a frequency of operation of 1kHz was chosen. All subsequent structural testing was performed at this frequency. Figure 9.8 plots the valve cap and piston displacement time histories, respectively, over a range of applied voltages from 50Vpp to 600Vpp. In Figure 9.8(a), the dotted lines at $+16.5\mu m$ and $-16.5\mu m$ indicate the position of the upper and lower valve stops, respectively. For an applied voltage of 50Vpp, the response of the valve cap is purely sinusoidal. As the voltage is increased to 600Vpp, the resulting valve cap displacement time history contains small amplitude higher frequency ($\sim 5kHz$) oscillations due to the non-linear nature of the valve membrane structure. These oscillations become more pronounced as the voltage is increased. In Figure 9.8(b), the drive element deflection time histories are somewhat rough in nature due to the noise level of the measurement system. As the deflections increase in amplitude, the effect of this noise floor diminishes.

Figure 9.9 takes these deflection time histories (at $P_{bias} = 500kPa$), and plots the valve cap peak-peak displacement, piston peak-peak displacement, and corresponding device amplification ratio as a function of applied voltage to the piezoelectric drive element. The amplification ratio is observed to decrease from 49 to 41 with increasing voltage. This decrease is a result of increased pressurization within the HAC chamber due to the increase in the valve membrane stiffness, and therefore increased deformation of the structure and fluid within the chamber, for increased voltage. In essence, as the voltage is increased, a smaller percentage of the drive element swept volume is transferred to the valve membrane since more volume is lost in chamber compliances. Overall, as will be detailed in the model correlation part of Testing Section 1, this range of amplification ratio correlates extremely well with the expected range based on the models developed in the first half of this thesis. These tests were also performed under decreased bias pressures, and these results are additionally presented in Figure 9.9. For decreased P_{bias} , the valve cap and piston deflections slightly increase, most likely due to better performance of the piezoelectric material under lower loading. As expected, however, the amplification ratio is not affected by the reduced bias pressure.

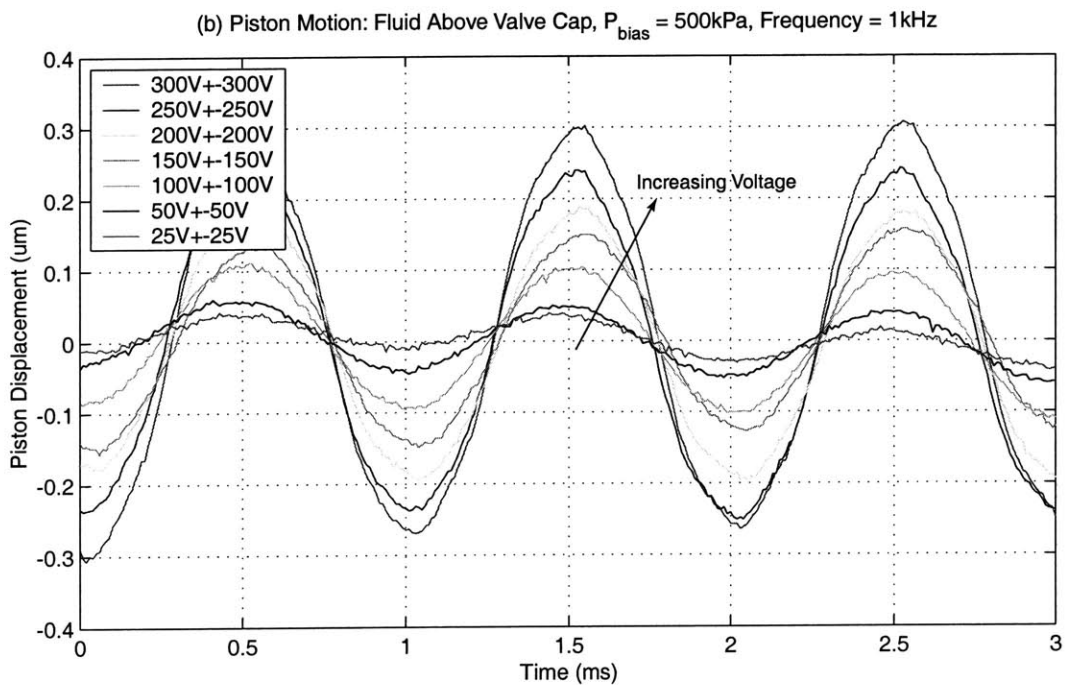
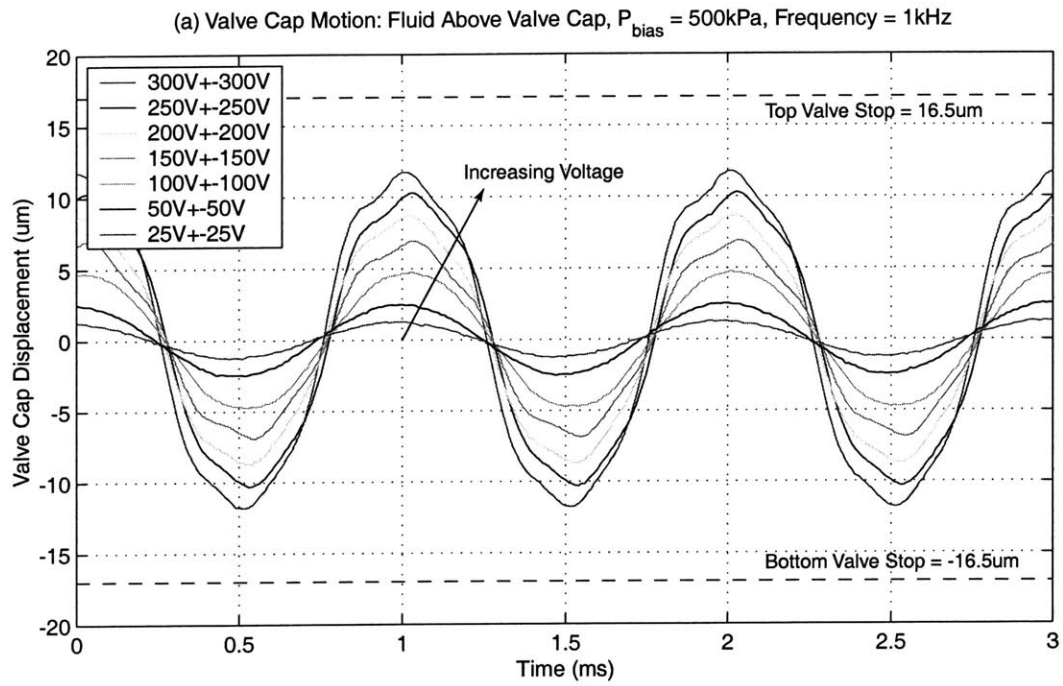


Figure 9.8: Device AV1 valve cap and piston deflection time histories for 1kHz sinusoidal drive voltage levels. As voltage is increased, small amplitude 5kHz oscillations appear in deflection responses. A voltage of 600Vpp is not sufficient to close valve cap against the valve orifice.

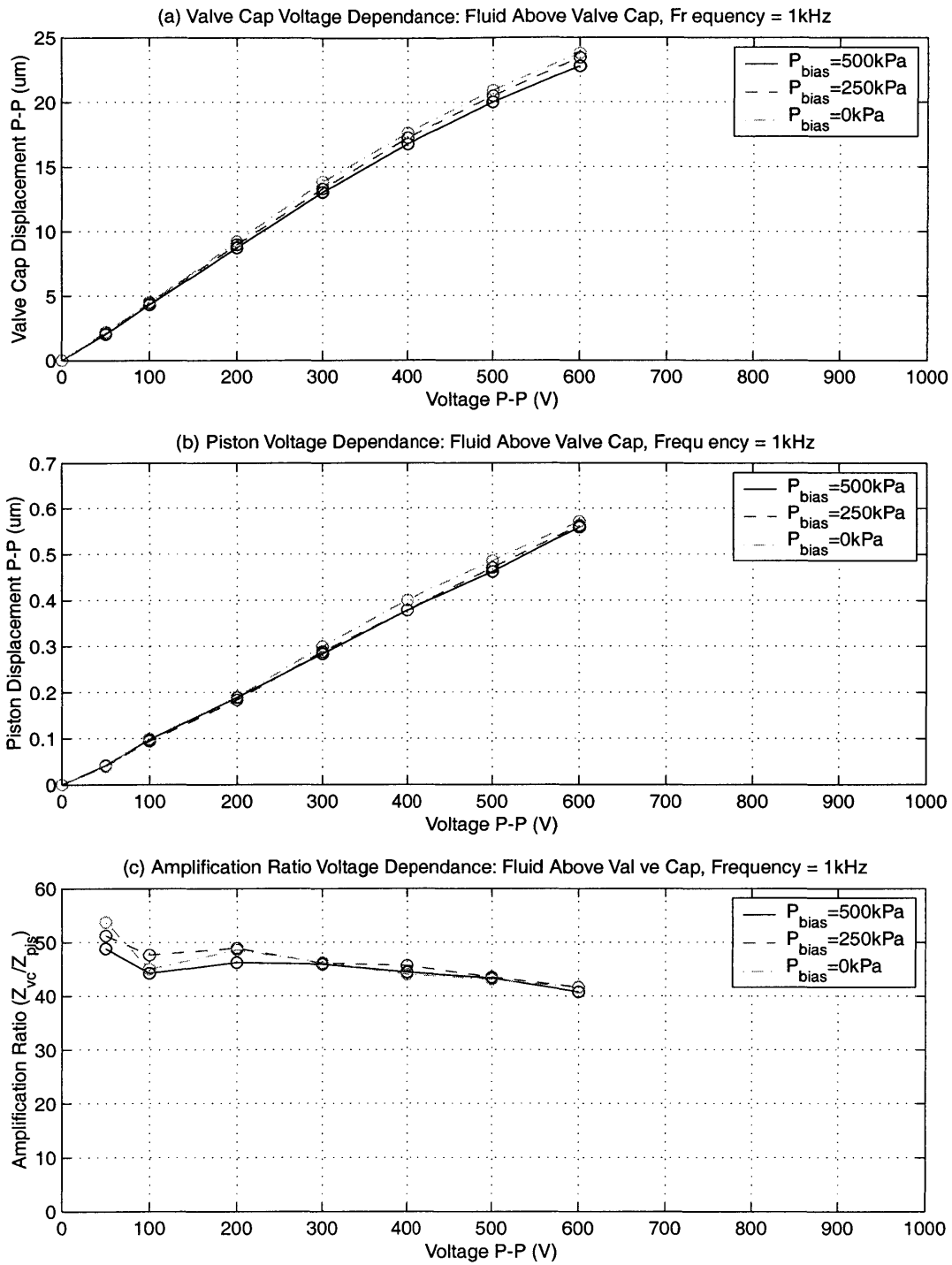


Figure 9.9: Device AV1 valve cap peak-peak motion, piston peak-peak motion, and device amplification ratio as a function of 1kHz sinusoidal drive voltage levels. Due to non-linear stiffness of the valve membrane structure, the amplification ratio decreases from $\sim 50x$ to $\sim 40x$ as the drive voltage is increased to 600Vpp.

In the previous tests at 1kHz, applied voltages were limited to 600Vpp to minimize the potential for device failure (due to stresses in drive element tethers - see the AV2 testing part of Testing Section 1 for an explanation). As a result, the valve cap never was able to close against the valve orifice. In order to observe valve closing and verify that the valve membrane is able to withstand these deflection magnitudes during dynamic operation, a series of tests was performed whereby a differential pressure of $P_{vc,vm} = 50kPa$ was applied across the valve cap and membrane to deflect it to an offset position of $\sim +10\mu m$. Voltages from 50Vpp to 600Vpp were then applied to evaluate closing behavior. Figure 9.10 plots the resulting valve cap deflection time histories. Notice that applied voltages of 500Vpp and 600Vpp successfully force the valve cap closed. Since the valve membrane is offset into its large deflection regime, the higher voltage deflection time histories become non-symmetric about this offset deflection. Additionally, the rounded nature of these curves as the cap hits the upper valve stop (valve orifice) indicates that squeeze-film damping may be playing a positive role in damping out potential vibrations due to high velocity impact of the valve cap on the valve stop.

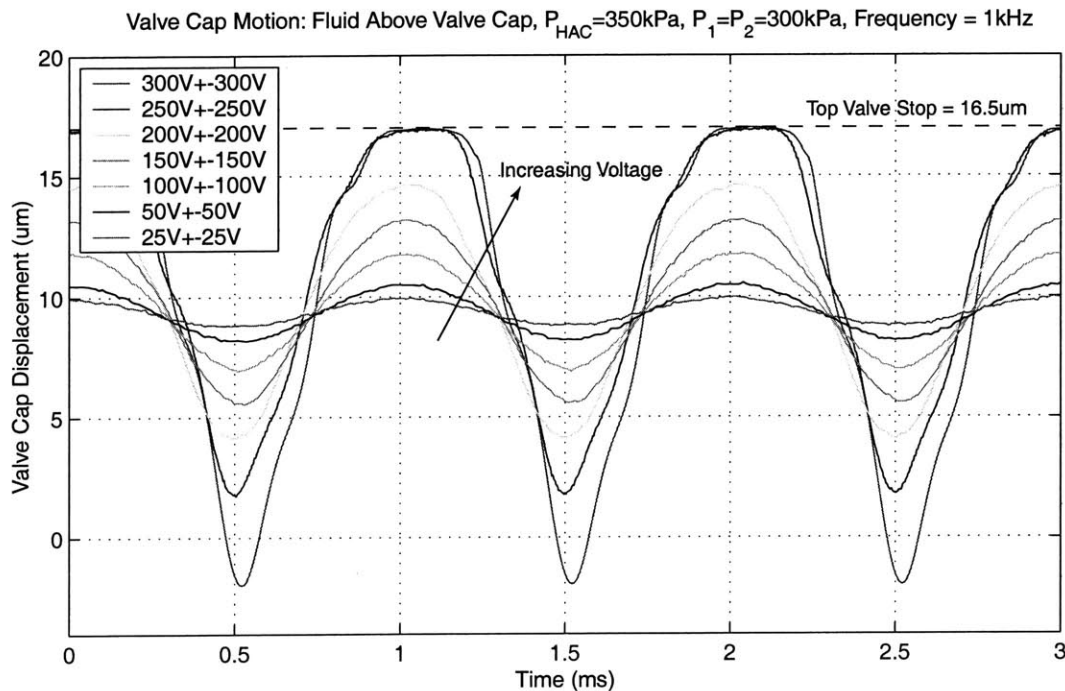


Figure 9.10: Device AV1 valve cap peak-peak motion, piston peak-peak motion, and device amplification ratio as a function of 1kHz sinusoidal drive voltage levels, with $P_{vc,vm} = 50kPa$. As the valve cap impacts the orifice stop, squeeze film damping may be aiding to damp undesired structural vibrations.

Overall, these series of low-voltage frequency sweep tests and higher-voltage quasi-static 1kHz tests have proven that active valve device AV1 successfully operates as a piezoelectrically-

driven hydraulic amplification microactuator structure. The series of tests detailed in Testing Section 2 will evaluate its capability to regulate fluid flow at high-frequency.

Evaluation of Device AV1 High-Frequency Channel The experimental data for device AV1 described in the previous sections was taken using the micromachined high-frequency channel (detailed in Chapter 6) as a means to control the static pressure P_{HAC} within the hydraulic amplification chamber, yet also to allow dynamic pressure fluctuations within the chamber created by piezoelectric actuation of the drive element. This channel, located between the HAC chamber and the external pressure port in the device, was designed to have a length of 1mm, a width of $10\mu m$, and a height of $10\mu m$. Although the previous set of data clearly indicates that this high-frequency channel must be satisfying its objective, the specific limitations of the channel are not clear. In an effort to evaluate the lower-limit frequency at which fluid begins to leak out of this channel during the positive stroke of the drive element actuation cycle, a series of tests for varying applied voltage to the piezoelectric elements were carried out.

In each test, the valve cap displacement amplitude was measured for an applied piezoelectric sinusoidal voltage (100Vpp, 200Vpp, and 400Vpp) over a frequency range from 1kHz to 0.1Hz. Figure 9.11 plots the valve cap displacement amplitude as function of frequency for these different applied voltage levels. Overall, the results indicate that this high-frequency channel behaves as a low pass filter with $\sim 1\%$ reduction in performance at a frequency of $\sim 1 - 2Hz$. These experimental results correlate quite well to the conservative channel design procedure (detailed in Chapter 6) in which a 1% reduction in performance was estimated to occur at a frequency of 48Hz. As a result, during actuation of the active valve at the desired frequencies in excess of 500Hz, the channel allows negligible fluid volume to move into and out of the hydraulic amplification chamber.

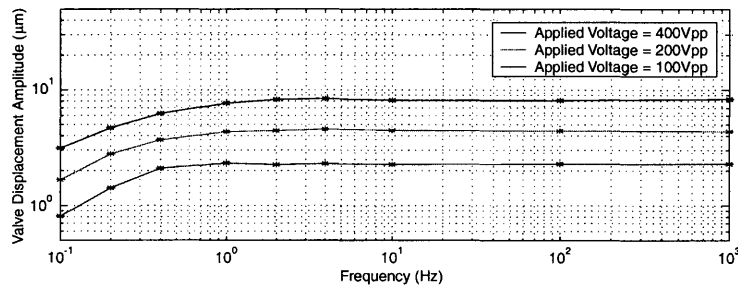


Figure 9.11: Experimental verification of the high-frequency channel in device AV1. The channel, with a length of 1mm, a width of $10\mu m$, and a height of $10\mu m$, successfully restricts fluid flow from the chamber during cyclic actuation down to a cutoff frequency near 1Hz.

Active Valve Device AV2

This section documents the frequency response characteristics and quasi-static operational capabilities of active valve device AV2. The tests performed were identical to those carried out for device AV1. As such, only selected plots are included in this section. The overall objective of this section is to demonstrate that both devices behave in the same manner. As a result, a conclusion can be made that repeatability in fabricating and assembling these devices is excellent.

Figure 9.12 plots the valve cap frequency response from 500Hz to 100kHz for an applied low-voltage sweep signal of $0V \pm 5V$ under the condition that silicon oil is not present above the valve cap and membrane structure and under the condition that silicon oil is present above the valve cap and membrane structure. As for device AV1, these tests were performed with $P_{bias} = 500kPa$ to ensure that cavitation of the fluid within the HAC did not occur. Without oil, the resonant frequency of the structure is evident at 10.5kHz. With oil, this frequency drops to slightly less than 5kHz. These results are essentially the same as those found for device AV1.

Figure 9.13 plots the valve cap frequency responses under these voltage sweep signal inputs for a varying bias pressure. Clearly from the results, a variation in P_{bias} from 100kPa to 500kPa has no noticeable effect on the frequency response of the structure.

Figure 9.14 plots a series of valve cap frequency responses from 500Hz to 3kHz for increasing drive voltage levels from 50Vpp to 500Vpp, all with $P_{bias} = 500kPa$. As was observed for device AV1, as the voltage is increased, regions of increased valve cap deflection appear near 1.7-1.9kHz. This frequency value is approximately $\frac{1}{3}$ of the low-voltage resonant frequency of the active valve device. This region, therefore, is a result of sub-harmonic oscillations of the device. Figure 9.15 plots the valve cap versus piston deflection amplitude over this frequency range for an applied voltage of 500Vpp. In comparing these frequency responses, the amplification capability of the active valve device is evident. Figure 9.15(a) plots these curves on a logarithmic amplitude scale, and Figure 9.15(b) plots them on a linear amplitude scale. Over this range of frequencies, the amplification ratio is in the range of 40x-50x, an identical result as for the amplification ratio found for device AV1.

In order to evaluate the quasi-static performance of device AV2, a frequency of operation of 1kHz was chosen. Figure 9.16(a) and (b) plot the valve cap and piston displacement time histories, respectively, over a range of applied voltages from 50Vpp to 900Vpp. In Figure 9.16(a), the dotted lines at $+16.5\mu m$ and $-16.5\mu m$ indicate the position of the upper and lower valve stops, respectively. For an applied voltage of 50Vpp, the response of the valve cap is purely sinusoidal. As the voltage is increased to 900Vpp, the resulting valve cap displacement time history contains significant higher frequency ($\sim 5kHz$) oscillations due to the non-linear nature of the valve membrane structure. These oscillations become more pronounced as the voltage is increased. In the chronology of the testing procedure for devices AV1 and AV2,

device AV2 was tested before device AV1 was tested. During testing of device AV2, voltage was increased to 1000Vpp. At this voltage level, the drive element piston tethers broke and silicon oil leaked out of the HAC chamber. Data was therefore only able to be taken on the valve cap behavior up to 900Vpp and on the piston behavior up to 800Vpp. This is the reason that device AV1 was tested only up to 600Vpp (see previous section).

Figure 9.17 takes these deflection time histories (at $P_{bias} = 500kPa$), and plots the valve cap peak-peak displacement, piston peak-peak displacement, and corresponding device amplification ratio as a function of applied voltage to the piezoelectric drive element. The amplification ratio is observed to vary from 40x to 50x, mainly decreasing with increasing voltage. As for device AV1, this decrease is a result of increased pressurization within the HAC chamber, and therefore increased deformation of the structure and fluid within the chamber, for increased voltage. In essence, as the voltage is increased, a smaller percentage of the drive element swept volume is transferred to the valve membrane since more volume is lost in chamber compliances. Overall, however, this range of amplification ratio correlates well with the expected range based on the models developed in the first half of this thesis (see Model Correlation part of Testing Section 1).

Piston failure in device AV2 is attributed to the fact that, although the drive element tethers were designed to have a thickness of $8\mu m$, their measured thickness was closer to $6\mu m$. As a result, under the calculated pressure loading of $\sim 700kPa$ (corresponding to drive voltage of 1000V and $P_{bias} = 500kPa$), the drive element tethers were expected to experience a stress approaching 1GPa, a value which is taken as a limit for the structural integrity of the silicon membrane structures [2]. Future drive element piston structures incorporate tethers which have a thickness of $8\mu m$. Although the complete series of tests that were performed on device AV1 were not able to be carried out on device AV2, the test results documented in this section indicate that this valve device also successfully operated as a piezoelectrically-driven hydraulic amplification microactuator structure.

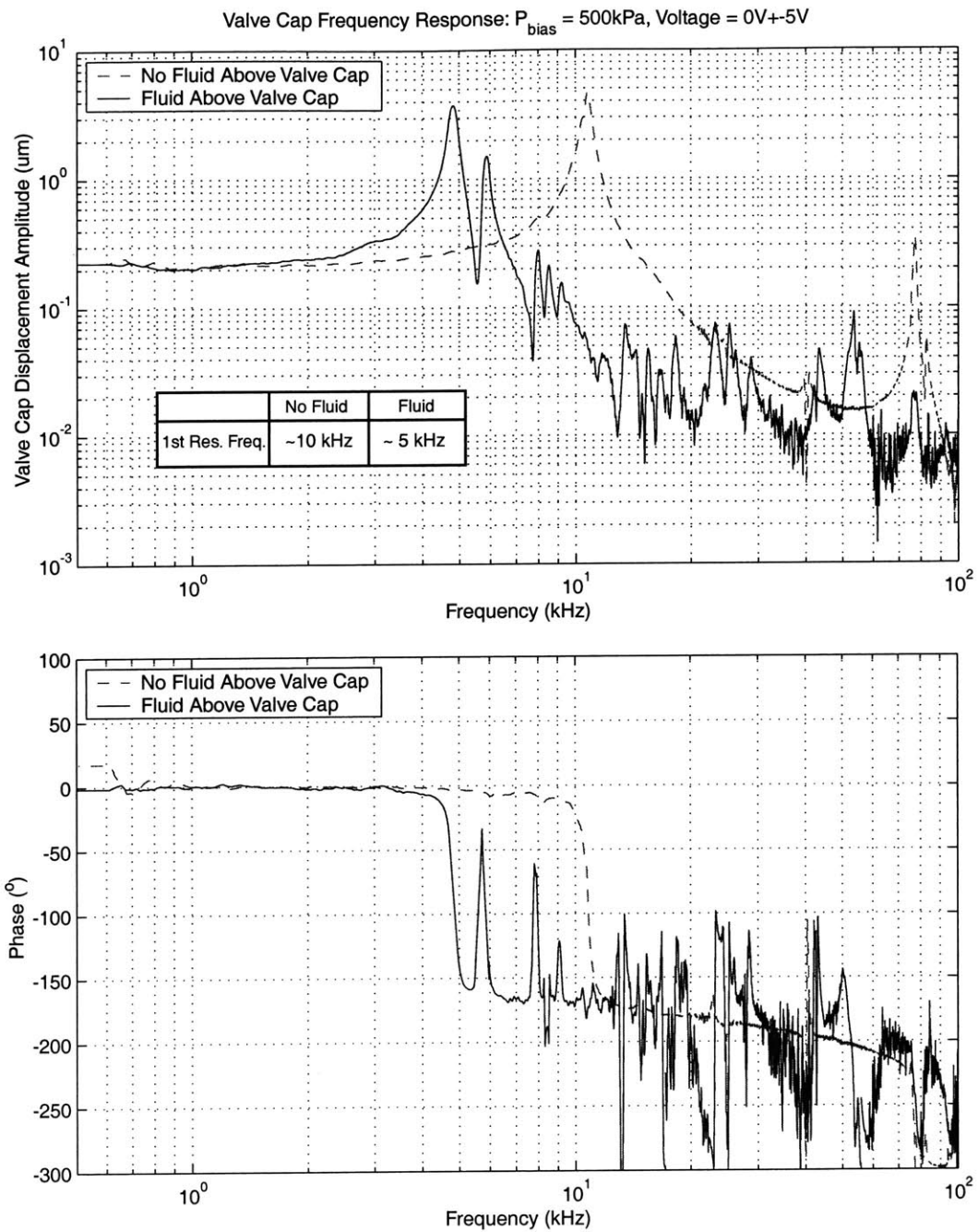


Figure 9.12: Device AV2 low-voltage ($0V \pm 5V$) valve cap frequency response from 500Hz to 100kHz, with and without oil present above the valve structure. The bias pressure in these tests was maintained at $P_{bias} = 500kPa$. The presence of oil in the flow channel above the valve cap creates an added mass that reduces the resonant frequency from 10.5kHz to 5kHz.

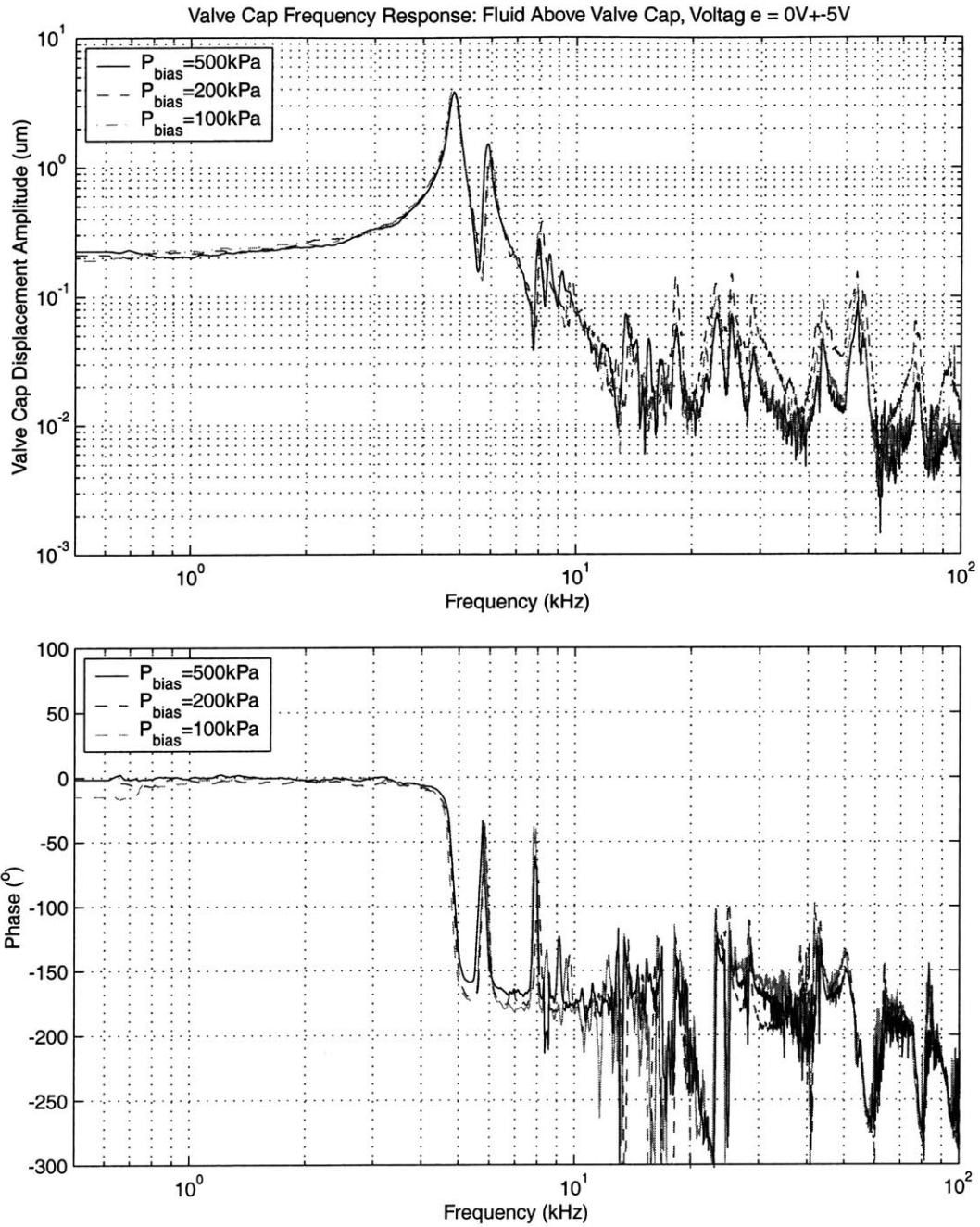


Figure 9.13: Device AV2 low-voltage valve cap frequency responses from 500Hz to 100kHz, for varying P_{bias} . Results indicate that frequency behavior is not affected by an increase in bias pressure from $P_{bias} = 100\text{kPa}$ to $P_{bias} = 500\text{kPa}$.

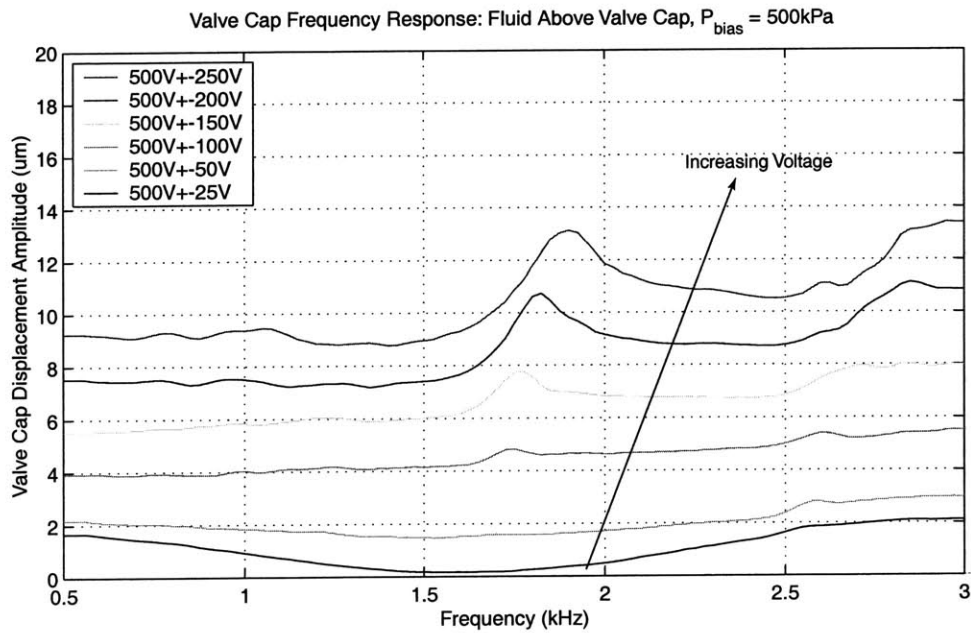


Figure 9.14: Device AV2 valve cap frequency responses from 500Hz to 3kHz, for $P_{bias} = 500kPa$ and increasing high voltage drive levels. Harmonic excitation behavior near $\sim 1.7 - 1.9kHz$ becomes evident as voltage levels are increased (ie: as valve membrane structure moves further into its non-linear large-deflection regime). It is unknown why the valve cap displacement dips downward between 500Hz and 2.5kHz for the voltage drive levels of 50Vpp and 100Vpp.

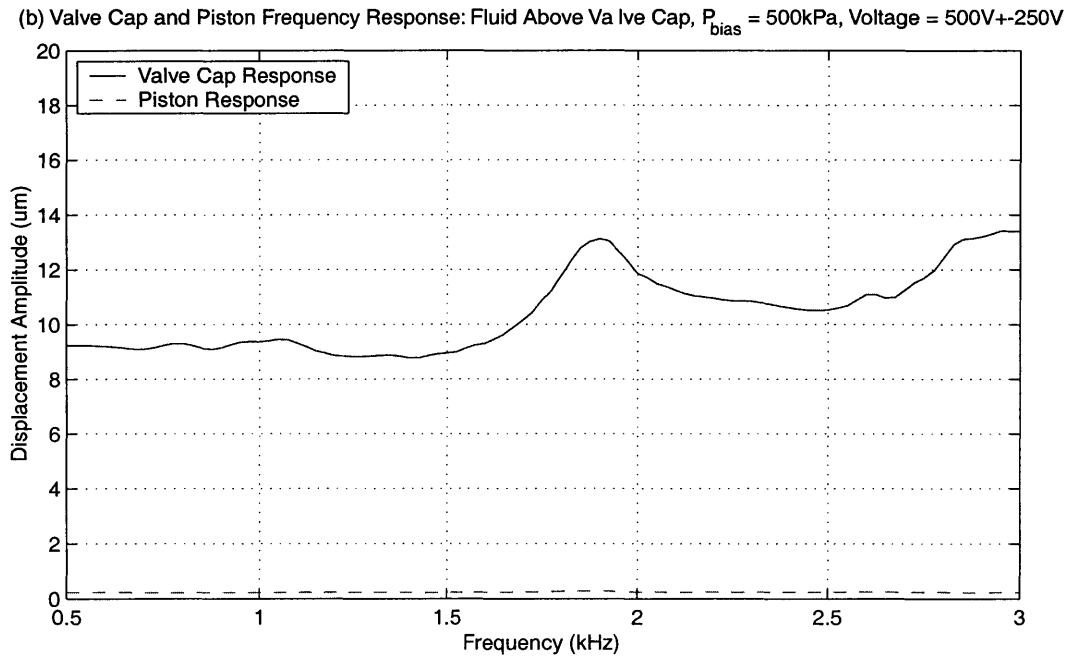
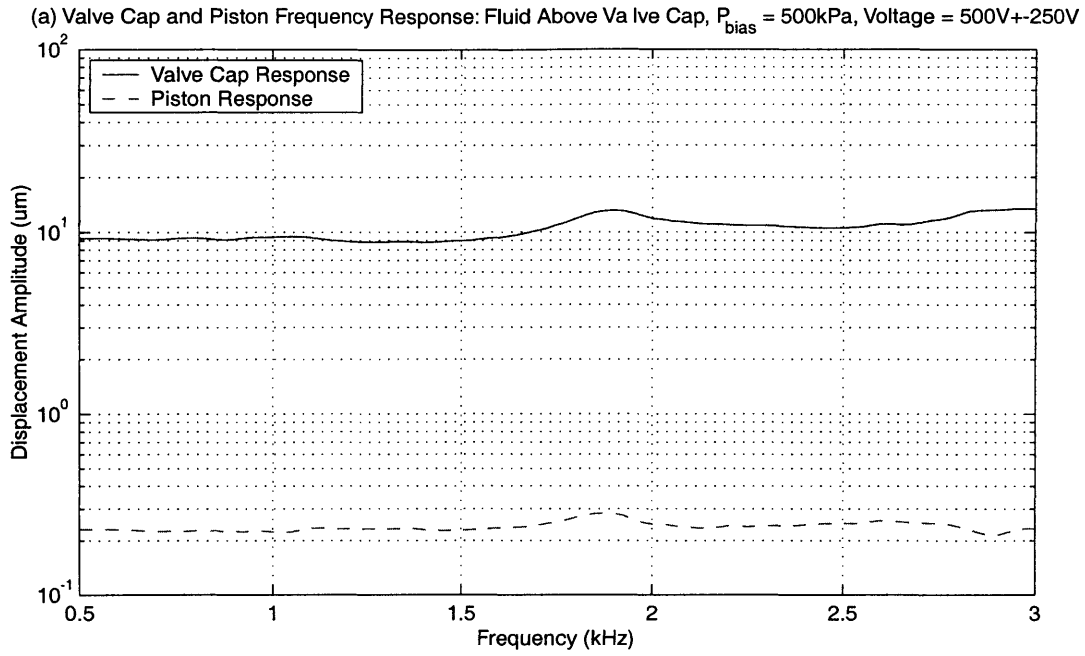


Figure 9.15: Device AV2 high-voltage piston and valve cap frequency responses from 500Hz to 3kHz, for $P_{bias} = 500kPa$. Amplification of active valve device is consistent between 40x-50x over this range of frequency.

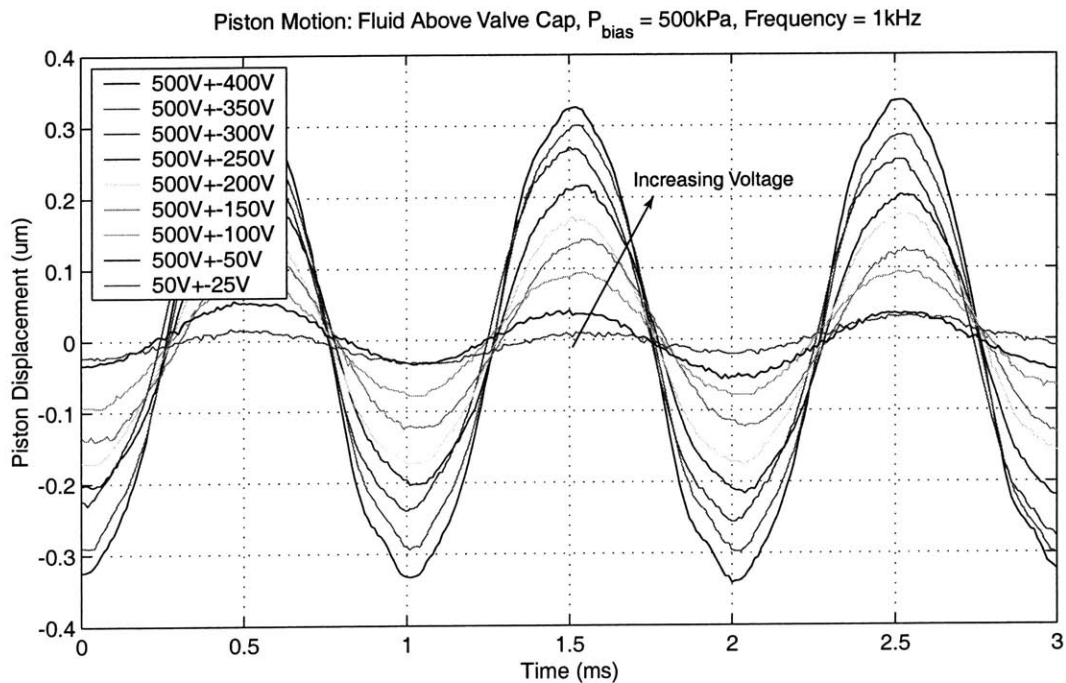
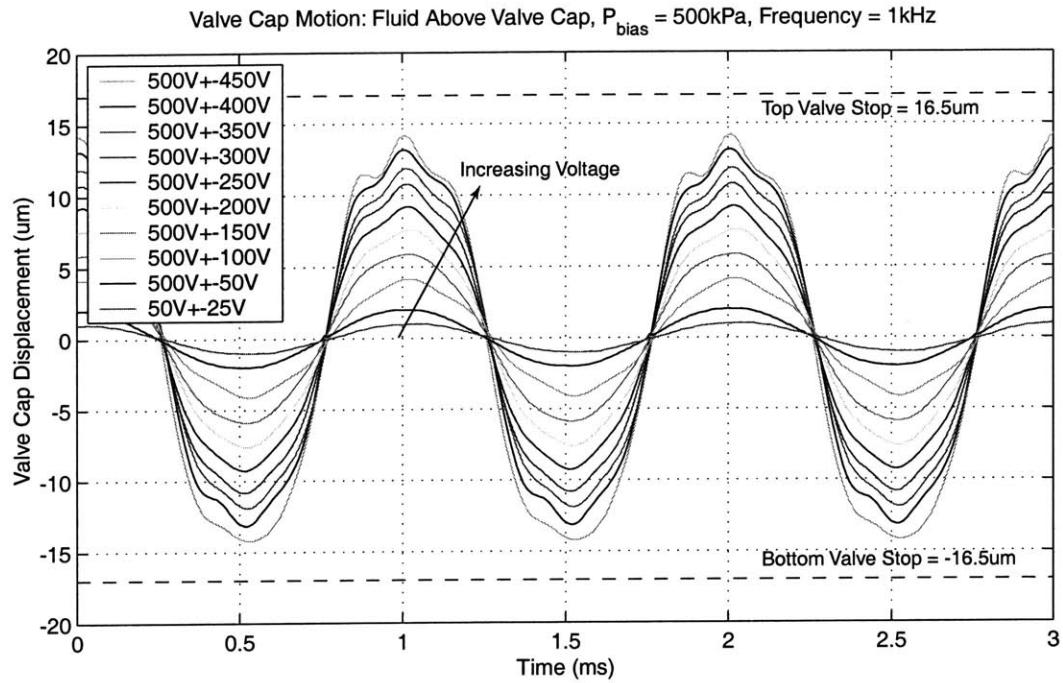


Figure 9.16: Device AV2 valve cap and piston deflection time histories for 1kHz sinusoidal drive voltage levels. As voltage is increased, small amplitude 5kHz oscillations appear in deflection responses. A voltage of 900Vpp is not sufficient to close the valve cap against the valve orifice.

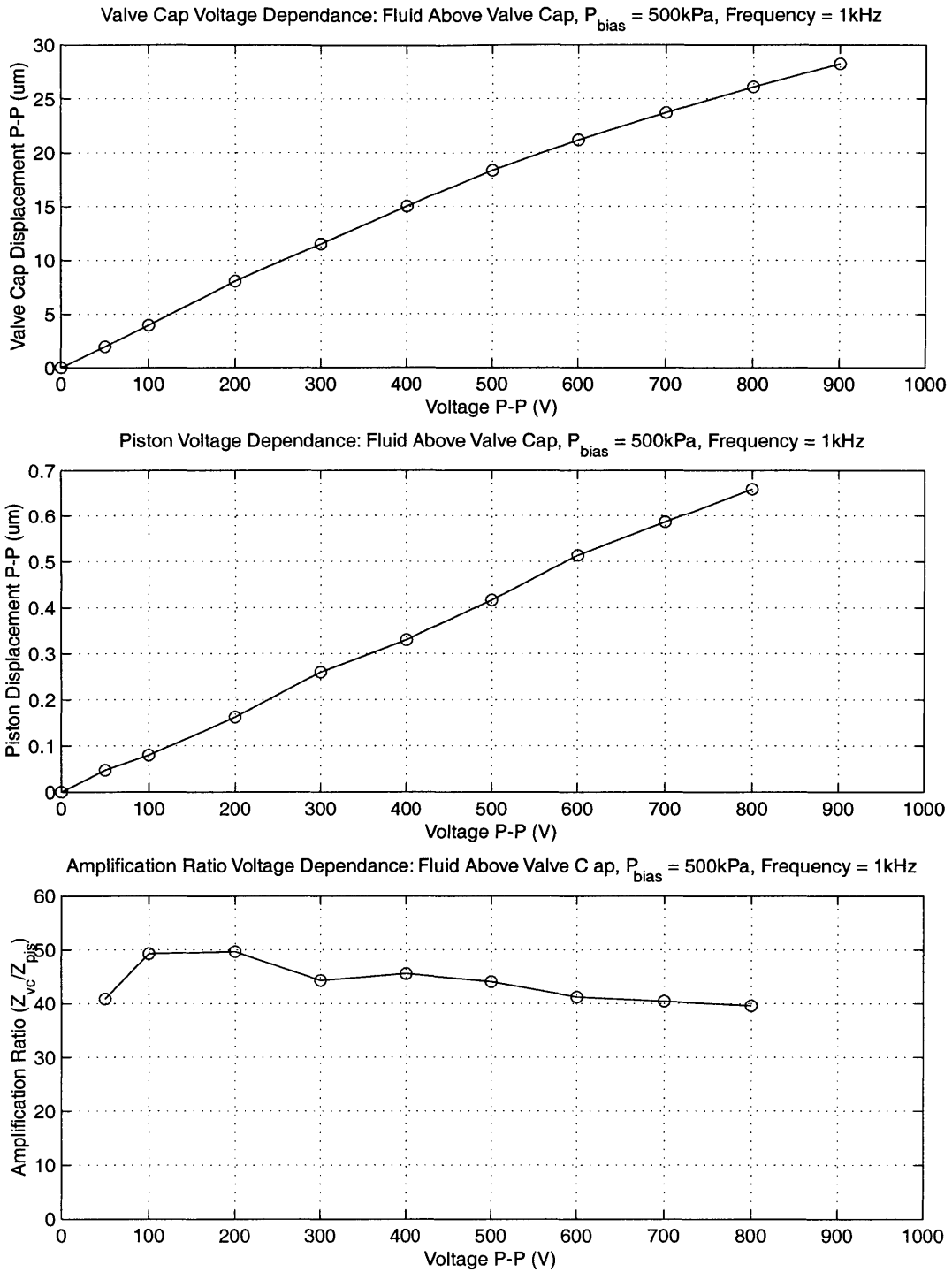


Figure 9.17: Device AV2 valve cap peak-peak motion, piston peak-peak motion, and device amplification ratio as a function of 1kHz sinusoidal drive voltage levels. Due to the non-linear stiffness of the valve membrane structure, the amplification ratio decreases from $\sim 50x$ to $\sim 40x$ as the drive voltage is increased to 900Vpp.

Model Correlation

With the data presented in the previous section, model correlation efforts were pursued to compare these results to the expected results from the analytical and finite-element models documented in the first series of chapters in this thesis. In this section, the high-voltage quasi-static performance at 1kHz is correlated to model expectation using the full non-linear analytical active valve model presented in Chapter 4. Following this, the low-voltage frequency response performance is correlated to the predictions from the active valve finite-element model presented in Chapter 4, as well.

1kHz Quasi-Static Correlation Prior to comparing results for the 1kHz operating conditions, a static pressurization test was performed on the drive element structure within device AV1 to determine the mechanical stiffness of the piezoelectric material elements. In this test, the pressure within the hydraulic amplification chamber was increased from $P_{HAC} = 0kPa$ to $P_{HAC} = 500kPa$ over a time span of 90 seconds, and the displacement of the drive element piston was measured in real-time using the laser vibrometer system. In response to this 500kPa pressurization, the piston moved through a displacement of $0.90\mu m$. With this result and with the geometry of the structure presented in Figure 9.1, the Young's Modulus of the PZN-PT material was determined to be $E_p = 6.76GPa$. This value is 74% of the nominal modulus ($E_p = 9.01GPa$) given by the manufacturer [3] and assumed for active valve design optimization throughout the earlier chapters of this thesis. It should be stated that the manufacturer's material data sheet [3] quoted the modulus within only $\pm 20\%$, and as a result, this experimentally determined reduced modulus from nominal was not completely unexpected. In the model correlation studies that follow, the effect of piezoelectric material Young's Modulus variation is evaluated. Additionally, as presented in Chapter 1, the piezoelectric coefficient assumed in the active valve design procedures was $d_{33} = 2000pC/N$. As shown in Chapter 7, in evaluating performance of the drive element devices, the actual coefficient for high-voltage behavior of this material was found to be in the range of $d_{33} = 1300 - 1500pC/N$. In the model correlation studies that follow, the effect of piezoelectric d_{33} variation is also evaluated.

Figure 9.18 plots the experimental 1kHz sinusoidal voltage drive data for devices AV1 and AV2 against theoretical plots obtained from the full valve analytical model. The operational conditions for these tests and simulations are: a bias pressure $P_{bias} = 500kPa$, a frequency 1kHz, and a varying applied voltage to the piezoelectric material. Shown on this plot are a series of model curves that span the range of d_{33} and E_p coefficients. For example, Model Case 1 assumes an ideal $d_{33} = 2000pC/N$ and an $E_p = 9.01GPa$. At a peak-peak voltage of $V_{p,PP} = 600V$, for example, the model deflection is $Z_{vc,PP} = 32.7\mu m$, as compared to the experimental deflection for device AV1 of $Z_{vc,PP} = 23.1$ and for device AV2 of $Z_{vc,PP} = 21.6$. Reducing the piezoelectric coefficient to $d_{33} = 1500pC/N$ and maintaining $E_p = 9.01GPa$

produces the curve for Model Case 2. A sharp reduction in valve cap deflection is observed. At $V_{p,PP} = 600V$, the model deflection is $Z_{vc,PP} = 27.5\mu m$. Now, reducing the modulus to $E_p = 6.76GPa$ for the expected range of piezoelectric coefficient $d_{33} = 1300 - 1500pC/N$ produces Model Case 3 and Model Case 4, respectively. These are the curves within which the experimental data should lie, since the d_{33} and E_p coefficients are taken from previous experimental studies. For Model Case 3, the model deflection is $Z_{vc,PP} = 25.9\mu m$, and for Model Case 4 the model deflection is $Z_{vc,PP} = 23.7\mu m$.

In observing 9.18(b), the piston deflection experimental data points do fall within these bounds. The experimental valve cap deflection data points, however, lie slightly below the lower bound. These two observations indicate that the drive element structure is well characterized by the values of $d_{33} = 1300 - 1500pC/N$ and $E_p = 6.76GPa$. The lower than expected valve cap deflection experimental data, in comparison to the models, must therefore be a result of additional compliance within the hydraulic coupler mechanism itself. Since Chapter 7 validated that the valve membrane structures correlate extremely well with the non-linear model code, this compliance must be associated with either the fluid itself or a structural compliance of the hydraulic amplification chamber walls. This theory is supported by the amplification ratio data shown in Figure 9.18(c), where the amplification ratio as a function of applied voltage is slightly less than model predictions. However, all amplification ratio data indicate very good correlation within 5 – 10% of model predictions.

In order to further evaluate the issue of a lower than modeled fluid bulk modulus, two further model correlation cases were carried out. In all design chapters of this thesis, the fluid bulk modulus of the silicon oil was assumed to be $K_f = 2.0GPa$ [4]. The previous plots just discussed assumed this value. Depending on how well the fluid is degassed and free of bubbles, this value could be substantially lower. To evaluate the effect of a reduced fluid bulk modulus, Model Case 4 was repeated (with $d_{33} = 1300pC/N$ and $E_p = 6.76GPa$) for $K_f = 1.0GPa$ and $K_f = 0.5GPa$. These cases are label Model Case 5 and Model Case 6, respectively. As shown in Figure 9.19, a change in fluid bulk modulus does indeed result in expectations closer to the experimental data. Even for a reduction in fluid stiffness of 4 times, however, the amplification mechanism still performs well. This is a result of the fact that, in general, the fluid is stiff enough that its volume reduction during pressurization is significantly smaller than the actuation volume change produced by the drive element during operation.

These model correlation studies indicate that for the experimentally determined piezoelectric material properties $d_{33} = 1300 - 1500pC/N$ and $E_p = 6.76GPa$, active devices AV1 and AV2 perform very close to model predictions for quasi-static operation at 1kHz. Slight discrepancies in performance can most likely be attributed to a smaller than expected fluid bulk modulus or equivalent structural compliance within the hydraulic amplification chamber.

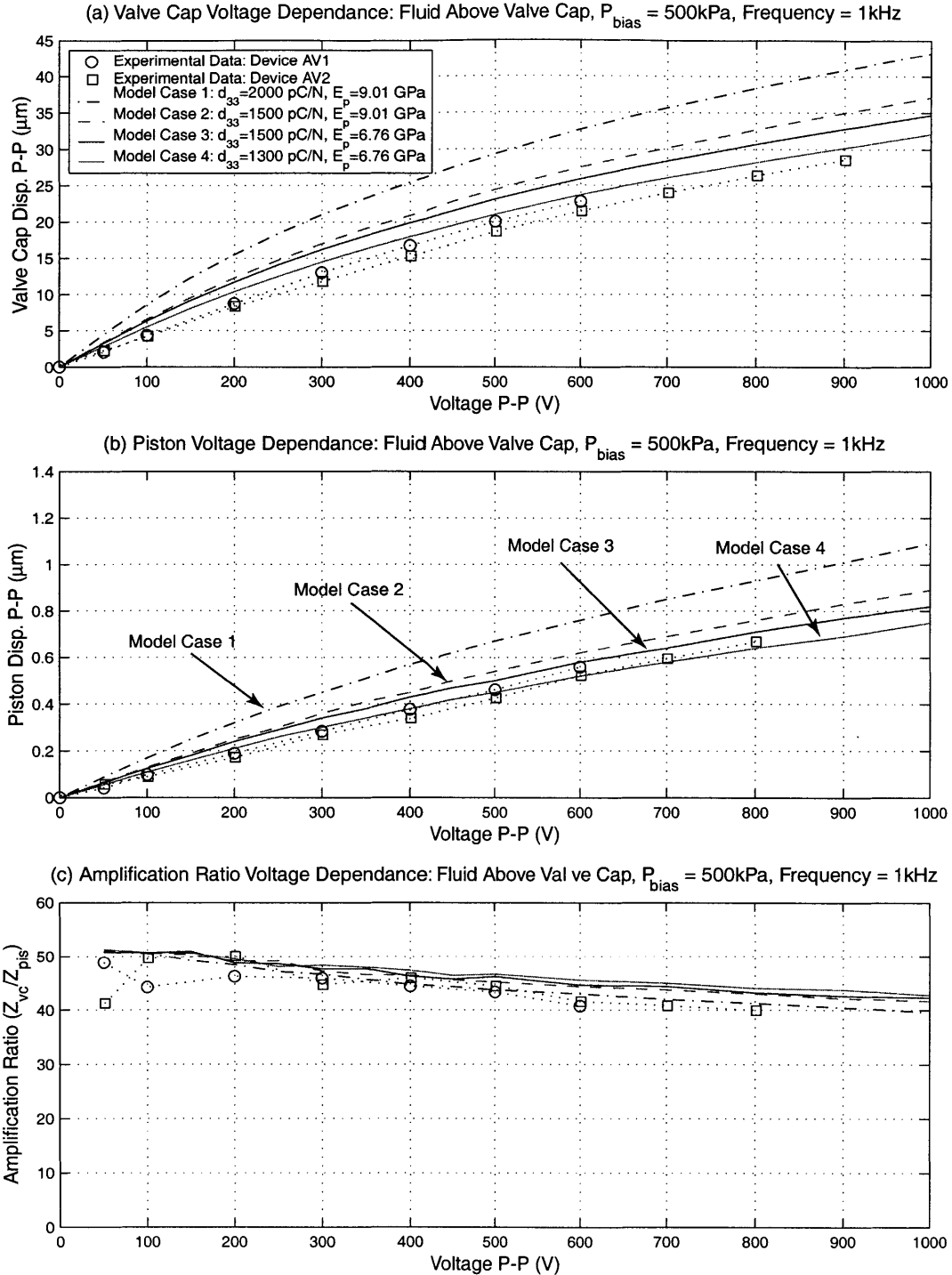


Figure 9.18: Device AV1 and device AV2 quasi-static 1kHz model correlation for fluid bulk modulus $K_f = 2.0\text{GPa}$. Results indicate the piston deflection is very close to the expected theoretical bounds for $d_{33} = 1300 - 1500\text{pC/N}$ and $E_p = 6.76\text{GPa}$. Due to the fact that the valve cap deflection is further from the theoretical bounds, it is believed that fluid compliance or HAC structural compliance is creating a loss mechanism.

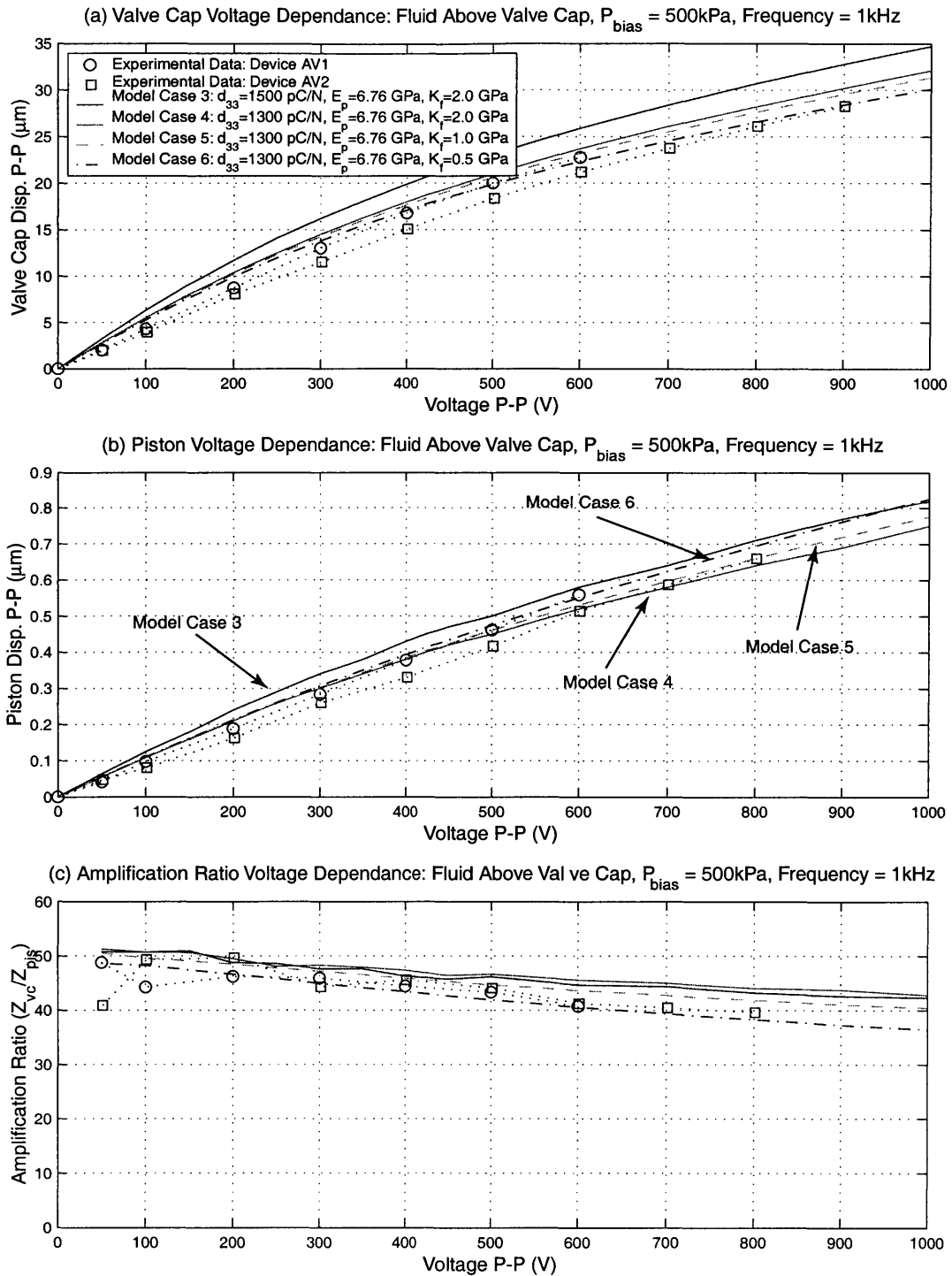


Figure 9.19: Device AV1 and device AV2 quasi-static 1kHz model correlation for varying fluid bulk modulus K_f . Results indicate a 75% reduction in the fluid bulk modulus would enable good correlation between experimental and theoretical results.

Low-Voltage Frequency Response Having correlated the quasi-static 1kHz high-voltage structural behavior of the microvalve to expected results based on the analytic models presented in this thesis, an effort is now made to understand the resonant frequency behavior at low-voltage. The 1st set of tests on device AV1 and device AV2 determined the onset of resonance for a low-voltage ($0V \pm 5V$) sweep signal over a frequency range from 500Hz to 100kHz. These voltage levels were used to ensure that non-linear stretching of the valve membrane structure did not occur. Non-linearities in the structure would create a stiffer operational regime and, therefore, a corresponding increase in the frequency at which “resonance” occurs. As a result, low-voltage excitation produces a conservative estimate for resonant behavior, which can then be used to determine a desirable quasi-static frequency of operation for the valve. Without fluid above the valve cap and membrane structure, devices AV1 and AV2 were found to exhibit resonance at $\sim 10kHz$. With fluid present above the valve cap and membrane structure, resonance was observed at $\sim 5kHz$. In this model correlation section, an effort is made to correlate the active valve resonant behavior without the presence of external fluid to theoretical expectations based on the finite-element model described in Chapter 4. Furthermore, an effort is made to estimate the effect of the external fluid added mass on the active valve resonant frequency and to correlate this effect to the experimental downward shift in resonant frequency from $\sim 10kHz$ to $\sim 5kHz$.

Without Fluid Above Valve Cap and Membrane An axisymmetric 2-D finite-element model was built for this correlation study with no fluid present above the valve cap and membrane. This model incorporates four-node plane elements for the silicon and glass structural parts of the valve and 4-node acoustic fluid elements for the liquid contained within the hydraulic amplification chamber. These acoustic elements enable fluid-structure interaction between the fluid and the surrounding structure of the HAC chamber. Sensitivity analyses were carried out to evaluate the first resonant frequencies of the coupled system, as a function of variations in important structural parameters and material properties. The parameters investigated were (1) the HAC fluid bulk modulus K_f , (2) the valve membrane thickness t_{vm} , (3) the piezoelectric material stiffness E_p , (4) the HAC fluid chamber height t_{HAC} , (5) the bottom support plate thickness t_{bot} , and (6) the top structural plate thickness t_{top} . The results of these sensitivity analyses are shown in Figure 9.20. In each analysis, the experimental baseline design for the active valve is specified. This baseline design includes the following values for the parameters under investigation: $K_f = 2GPa$, $t_{vm} = 6\mu m$, $E_p = 6.76GPa$, $t_{bot} = 1000\mu m$, $t_{top} = 1000\mu m$, and $t_{HAC} = 200\mu m$. With these baseline parameter values, a first modal frequency of 14.1kHz was determined. This theoretical value is significantly larger than the experimentally determined 1st modal frequency of 10kHz, and as a result, the sensitivity analyses that follow are meant to determine why this is.

Figure 9.20(a) shows the effect of reduced bulk modulus on the valve first modal frequency. The active valve was designed assuming a fluid bulk modulus value of $K_f = 2GPa$. The previous quasi-static model correlation section concluded that a reduction in bulk modulus down to $K_f = 0.5GPa$ could explain the voltage-valve cap deflection performance reduction seen experimentally at 1kHz. From this modal analysis, however, it is clear that this reduction in modulus to $K_f = 0.5GPa$ has minimal effect on the 1st modal frequency, dropping it only to 13.7kHz. In fact, a reduction to $K_f = 0.02GPa$ is required to bring the 1st modal frequency down to 10kHz. It is therefore concluded that the expected fluid bulk modulus value of $K_f = 0.5GPa$ is not the prime reason for the lower-than expected 1st modal frequency.

Figure 9.20(b) shows the effect of valve membrane thickness on the valve first modal frequency. Based on the valve membrane pressure-deflection results detailed in Chapter 8 (for which there was excellent correlation between theoretical and experimental results for $t_{vm} = 6\mu m$), it is quite certain that the valve membrane thickness is very near to $t_{vm} = 6\mu m$. Figure 9.20(b) (solid line) shows that even if the thickness were to deviate anywhere within $t_{vm} = 5 - 7\mu m$, the effect on the first modal frequency would be quite small. It is therefore concluded that a slight deviation in valve membrane thickness from the experimentally verified value of $t_{vm} = 6\mu m$ would not be sufficient to reduce the first modal frequency from 14.1kHz to 10kHz. Additionally, the dotted line in this plot illustrates the first modal frequency of the stand-alone valve cap and membrane structure (with no fluid in contact with its bottom surface) as a function of valve membrane thickness. One observes, in this case, that the modal frequency is very sensitive to valve membrane thickness. The important observation here is that the presence of the fluid in the HAC chamber serves to reduce the modal frequency (from 32.9kHz for the stand-alone valve membrane to 19.6kHz for the active valve coupled system) for a large thickness valve membrane (added mass effect to be discussed shortly) whereas for a small thickness valve membrane the presence of fluid in the HAC serves to increase the modal frequency (from 8.7kHz for the stand-alone valve membrane to 12.6kHz for the active valve coupled system). This illustrates the importance of performing full fluid-structural interaction analyses to predict the full valve modal frequency rather than estimating this modal frequency based on just one of the stand-alone structural components of the full valve.

Figure 9.20(c) shows the effect of piezoelectric material modulus E_p on the the valve first modal frequency. In Chapter 9, this E_p value was experimentally determined to be 6.76GPa. It is clear from this plot that the valve modal frequency is insensitive to slight variations (between $E_p = 6 - 8GPa$) in this value. It is therefore concluded that the reduction in the first modal frequency from 14.1kHz to 10kHz can not be attributed to an unexpected value of E_p .

Figures 9.20(d) and 9.20(e) illustrate the effect of the top and bottom structural plate thicknesses on the valve first modal frequency. It makes sense that if the bottom structural plate were to be significantly reduced in thickness, then the drive element portion of the valve

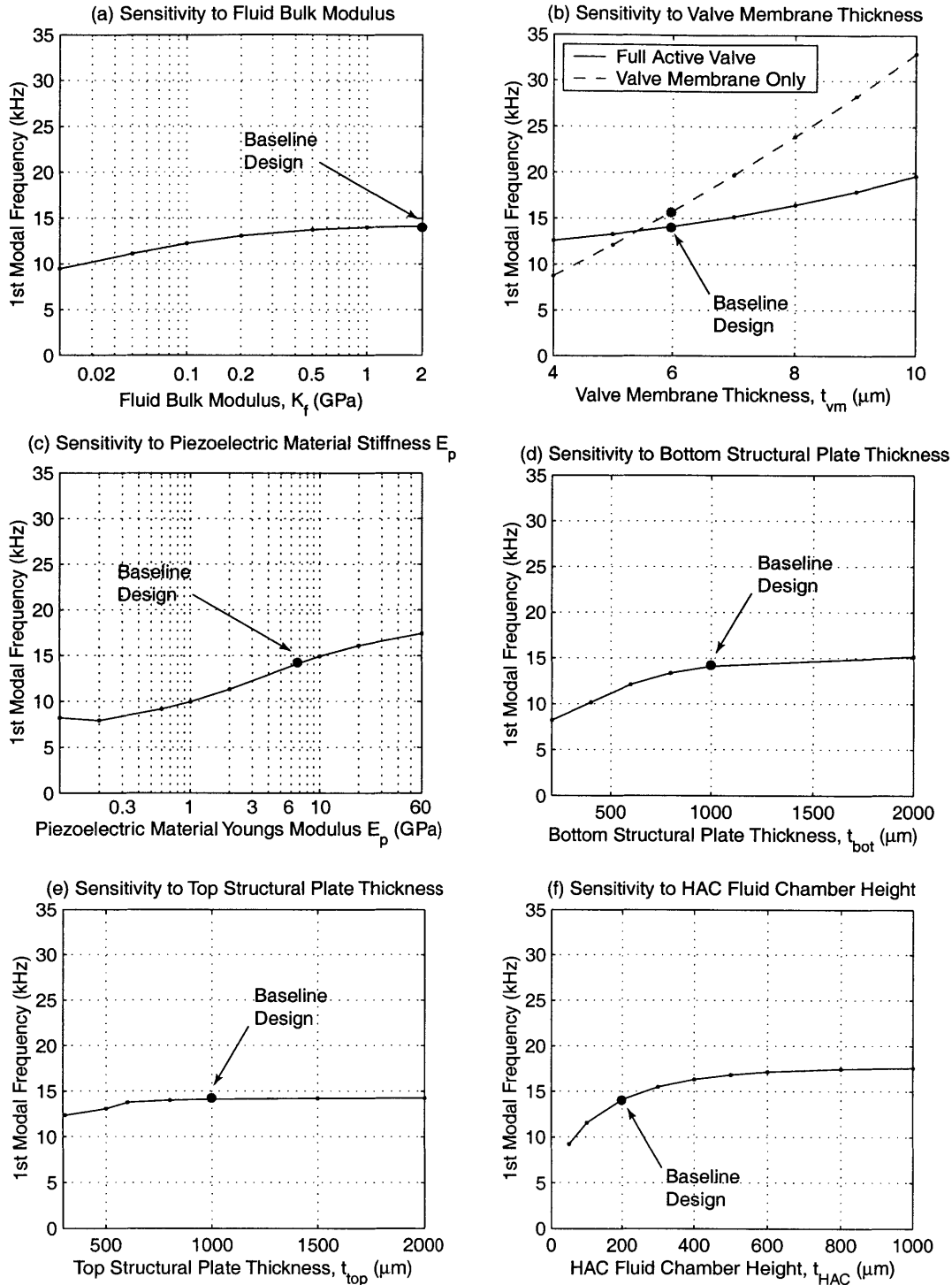


Figure 9.20: Finite-element active valve modal frequency sensitivity studies for (a) the HAC fluid bulk modulus K_f , (b) the valve membrane thickness t_{vm} , (c) the piezoelectric material stiffness E_p , (d) the HAC fluid chamber height t_{HAC} , (e) the bottom support plate thickness t_{bot} , and (f) the top structural plate thickness t_{top} .

would become much softer than in the baseline design, and the full valve modal frequency could be expected to drop. This phenomenon is observed in Figure 9.20(d). Likewise, if the top structural plate were to be significantly reduced in thickness, the HAC structural chamber would become much softer than in the baseline design, and the full valve modal frequency could be expected to drop. This phenomenon is observed in Figure 9.20(e). In the active valve devices experimentally tested in this thesis, however, the thicknesses of these two plates are well-characterized to each have a thickness of at least $1000\mu m$. Therefore, it is concluded that the top and bottom plate thicknesses do not contribute to the reduction in the active valve first modal frequency from 14.1kHz to 10kHz.

Figure 9.20(f) shows the effect of the HAC fluid chamber height t_{HAC} on the the valve first modal frequency. The plot illustrates that the modal frequency is extremely sensitive to a reduction in this chamber height from the baseline design value of $t_{HAC} = 200\mu m$ (where the first modal frequency is 14.1kHz) to a smaller value of $t_{HAC} = 50\mu m$ (where the 1st modal frequency is 9.2kHz). The reason for this significant frequency reduction as the chamber height is reduced is the presence of inertial coupling between the moving drive element piston and the adjacent glass surfaces that form the top of the HAC chamber. A comprehensive discussion of inertia coupling is found in Blevins [5]. The following excerpt is taken from [5]:

As a cross section accelerates in a fluid, pressure gradients will be generated in the surrounding fluid. These pressure gradients can exert fluid forces on adjacent structures. If the adjacent structures are not rigid, they will in turn deflect and generate forces on the accelerating cross section. This interaction between adjacent elastic structures is called inertial coupling. Inertial coupling increases as the distance between structures decreases. Inertial coupling can significantly affect the natural frequencies and mode shapes of [closely-packed structures] if the density of the surrounding fluid is comparable to or larger than the average density of the [structures]. *Blevins, p.403*

Prior to assembly of devices AV1 and AV2, the chamber height t_{HAC} of these devices was measured to be $\sim 200\mu m$. However, the geometry of the glass layer that forms this chamber is significantly more complex (see valve structure shown in Figure 9.1) than just having a volume of fluid $200\mu m$ in height above the drive element piston and beneath the valve cap and membrane. In reality, a series of fluid channels exists (termed “HAC Through Holes” and “HAC Radial Channels” in Figure 9.1) through this glass layer to allow fluid to couple the piston motion to the valve membrane motion. During the design stages of the active valve device, a bottom structural stop beneath the valve cap (at $Z_{vc} = -16.5\mu m$) was set as a requirement. These channels were therefore implemented to satisfy this requirement. The heights of the “HAC Radial Channel” features in Layer 7 are no more than $100\mu m$, and as a

result, acceleration of fluid in these channels could be a significant inertial coupling effect. Based on these arguments, it is concluded that the small-size fluid pathways through the complex glass Layer 6 HAC chamber are the most probable reason for the reduction in active valve modal frequency from the baseline design FEM expectation of $14.1kHz$ to the experimentally-determined frequency of $10kHz$. Future valve design iterations should include larger t_{HAC} chamber heights (ie: $t_{HAC} = 500\mu m$) with no complex fluid routing pathways. Eliminating the presence of the valve cap bottom structural stop might be a necessary consequence.

With Fluid Above Valve Cap and Membrane The previous model correlation section determined that inertial coupling effects between the accelerating fluid and the piston structure within the HAC chamber were the most likely reason for the lower-than expected active valve first modal frequency, when no fluid was present above the valve cap and membrane structure of the valve. Experimentally, without this fluid above the valve cap and membrane, the first modal frequency was found to be $\sim 10kHz$. With this fluid above the valve cap and membrane, the modal frequency was found to be $\sim 5kHz$. The following section attempts to explain this downward shift in valve modal frequency.

The conclusion of this section will be that the presence of fluid above the valve cap and membrane structure serves to increase the effective mass of the valve cap and membrane, thereby reducing the overall modal frequency. This statement is consistent with a discussion found in Blevins [5] concerning the effect of surrounding fluid on a circular plate in vibration. The following excerpt is taken from [5]:

As an elastic plate vibrates in a fluid, the fluid immediately surrounding the plate is set into motion and the plate will radiate sound waves into the far field... In general, the fluid will impose both added mass and damping forces on the plate. The added mass will lower the natural frequency of the plate from that which would be measured in a vacuum, and the damping of the plate will be increased. *Blevins, p.413*

Taking as an example a circular disk with radius r_a exposed on one side to an inviscid compressible fluid of density ρ_{fluid} (Blevins, p.414), the added mass of the disk for acceleration perpendicular to the plane of the disk can be estimated as $M_{added} = \frac{8}{3}\rho_{fluid}r_a^3$. For a back-of-the-envelope calculation on the valve cap and membrane in the active valve, let $r_a = R_{vm}$. The corresponding added mass is therefore $M_{added} = \frac{8}{3}(777\frac{kg}{m^3})(700\mu m)^3 = 7.11e^{-7}kg$. The baseline mass of the valve cap structure is $M_{vc} = \rho_{Si}\pi R_{vc}^2 t_{vc} = (2200\frac{kg}{m^3})\pi(250\mu m)^2(300\mu m) = 1.30e^{-7}kg$.

To therefore estimate the reduction in active valve first modal frequency due to the presence of fluid above the valve cap and membrane, the finite-element model from the previous section

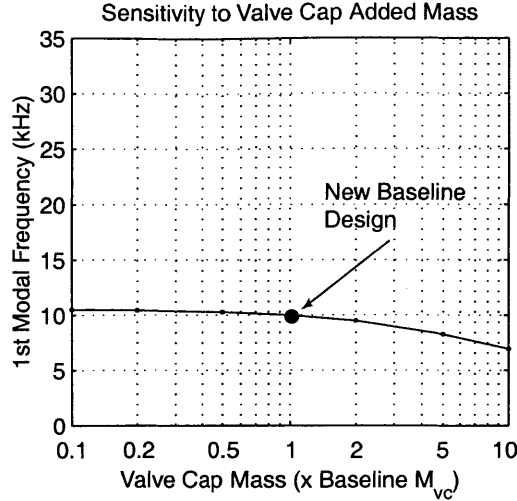


Figure 9.21: Finite-element modal frequency sensitivity to valve cap added mass. The presence of fluid above the valve cap and membrane structure creates an effective added mass to the coupled structure which serves to reduce the first modal frequency of the active valve device.

was run with a modified density of the valve cap material such that its mass was equal to $M_{vc,modified} = M_{vc} + M_{added} = 8.42e^{-7}kg$ (an increase from the original valve cap mass of 6.5 times). In this comparison study, a new baseline valve design was chosen to include a fluid bulk modulus value of $K_f = 0.5GPa$ and an HAC chamber height of $t_{HAC} = 66\mu m$ so that the first modal frequency of the valve without the added mass was exactly 10.0kHz. This baseline FEM model therefore matched the experimental result without fluid above the valve cap and membrane. Now, with the addition of the added mass (x6.5), the first modal frequency of the valve was determined to be 7.8kHz (a 22% decrease from the new baseline design modal frequency of 10.0kHz). Figure 9.21 illustrates the theoretical effect of added mass (from x0.1 to x10) on the first modal frequency of the active valve structure. Over this range of added mass, the first modal frequency is affected, but not substantially.

For the active valve devices tested experimentally, there is a 50% reduction in the first modal frequency (from $\sim 10kHz$ to $\sim 5kHz$) due to the presence of fluid above the valve cap and membrane. The above study on the new baseline design (in which a 22% reduction was calculated) provides for an added mass argument that also applies to the experimental results, however, this value of added mass only partially reduces the first modal frequency to correlate with the experimental results. Since this added mass calculation was for a circular plate in an infinite fluid medium, and since in the real active valve structure, there exist structural surfaces within 50-100 μm of the top surface of the valve cap and membrane, it is likely that the same sort of inertial coupling effects as discussed in the previous section are coming into play. These unmodeled effects could potentially cause a further reduction in first modal frequency.

It is therefore concluded that the fluid mass (acceleration and inertia effects) above the valve cap and membrane and the presence of the flow channel structure near to this valve cap and membrane provide an additional mass seen by the active valve structure as it vibrates, thereby reducing the valve first modal frequency from the case when no fluid exists above the valve cap and membrane. Future active valve design iterations should more thoroughly evaluate this added mass effect on valve dynamic performance. The recommendation section of Chapter 10 further discusses these recommended future analyses.

9.3.2 Testing Section 2: Active Valve Fluid Flow Regulation

To characterize the flow regulation capability of the active valve devices documented in this thesis, a series of tests was performed. The first test focused on experimentally determining the quasi-static flow rate versus valve cap opening curves for varying applied differential pressures $P_1 - P_2$ across the valve orifice. These results were then compared to predictions based on the flow models developed in Chapter 5 of this thesis and based on [2]. The second test evaluated the flow regulation capability of the active valve by varying the duty cycle of valve opening at a prescribed differential pressure $P_1 - P_2$ and measuring the average flow rate through the valve orifice. The third test evaluated the flow regulation capability of the active valve at a prescribed operating frequency of 1kHz for increasing differential pressures across the valve orifice. Limitations in valve performance could therefore be determined as this differential pressure was increased. For each of these tests, an estimate of the measurement error is included in the experimental results plots detailed in this section.

Static Flow Tests

To determine the quasi-static flow rate versus valve opening curves for a series of imposed differential pressures across the valve orifice, the fluids test-rig (described in Chapter 6) was used. In these tests, no voltage was applied to the piezoelectric material. Rather, the valve cap position was controlled by regulating the pressure P_{HAC} to the hydraulic amplification chamber. For a given test run at a desired differential pressure $P_1 - P_2$, P_{HAC} was first increased to move the valve cap upward against the fluid orifice (with $P_1 = P_2 = 0$). P_1 and P_2 were then independently increased to set the desired differential pressure across the orifice. In order to maintain the valve cap against the orifice, P_{HAC} was varied real-time in conjunction with the increases in P_1 and P_2 . With the proper differential pressure set, a data acquisition system was started, into which the valve cap displacement, pressure measurement of P_{HAC} , pressure measurement of P_1 , pressure measurement of P_2 , and flow sensor measurement Q_{avg} were input. As detailed in Chapter 6, the flow rate measurements were taken using a calibrated flow orifice system.

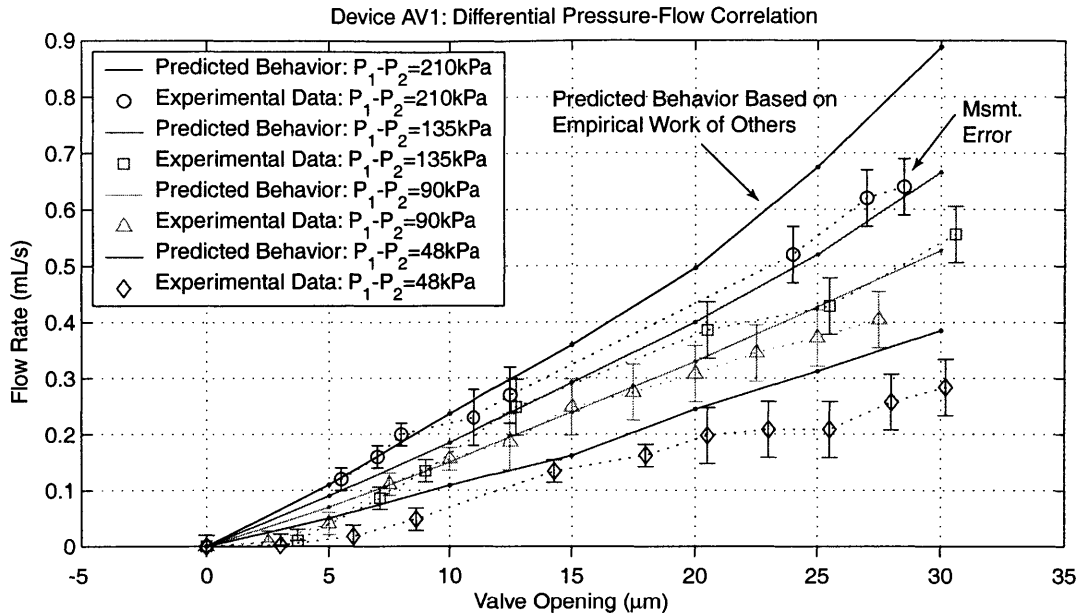


Figure 9.22: Model correlation to device AV1 quasi-static fluid flow rate versus valve opening behavior for differing imposed differential pressures. The experimental flow rates fall approximately 10 – 30% short of predictions based on the empirical work of others. Error bars on the data indicate estimates of measurement error. Two flow sensors of different ranges were used in these experiments, resulting in different levels of measurement error for lower and higher flow rates. These measurement errors were estimated based on the flow sensor calibration errors, the accuracy of the applied differential pressure, and human error associated with controlling the quasi-static nature of the experiments.

In order to obtain quasi-static flow measurements for a given valve cap opening, P_{HAC} was decreased slowly over a period of approximately 10 minutes. The valve cap was allowed to move through its full stroke of 30–33 μm . The time constant of the flow orifice sensor was on the order of a few seconds, and therefore this measurement procedure enabled quasi-static measurements. Tests were performed for differential pressures of $P_1 - P_2 = 48\text{kPa}$, 90kPa, 135kPa, and 210kPa. For each test run, selected points were chosen to plot. Figure 9.22 overlays these experimental results with the predicted behavior based on the flow models used in Chapter 5 of this thesis. Since the Chapter 5 flow models are based on a compilation of empirical work from other researchers, the line of predicted behavior in Figure 9.22 is understood to be of only “limited accuracy”, in other words, it is not based on exact theory. In general, this comparison shows that the predicted behavior based on the empirical work of others overpredicts the flow rate behavior by approximately 10 – 30%. This is most likely due to differing geometric features between the orifice structures contained within the empirical results and the valve orifice structure in this thesis. Specifically, since the empirical results are based on macroscale orifice structures

with rounded and filleted features, one would expect better flow rate capabilities for given applied differential pressure and valve opening than in the microscale valve orifice structure detailed in this thesis, which possesses comparatively sharp corners. Furthermore, at small valve openings, the flow rate appears to be choked. Only when the valve cap reaches an opening of $\sim 4\mu m$ does the fluid really begin to flow. Based on this data, active valve device AV1 can be characterized as a flow control device. These differential-pressure flow experiments were performed for differential pressures up to $P_1 - P_2 = 210kPa$. When tested to differential pressures greater than this value, interesting oscillatory behavior of the valve cap structure occurred. These observations and the corresponding efforts to determine the cause of these phenomena are detailed in the following section.

Self-Oscillatory Behavior of Valve Cap During Static Flow Tests

The original objective of the static flow tests described above was to evaluate the differential pressure-flow behavior through the valve orifice for $P_1 - P_2$ up to 800kPa, since this was the designed-for maximum differential pressure to be experienced in a complete MHT micropumping system. However, in testing the valve beyond $P_1 - P_2 = 210kPa$, self-oscillatory behavior of the valve cap at its resonant frequency of $5kHz$ was observed and measured (remember, in these tests, there is no actuation of the piezoelectric drive elements – all pressures are controlled via external regulators). It is believed that this oscillatory behavior may be induced by vortices and unsteady flow phenomena as the flow transitions from the laminar to the turbulent flow regime. In an effort to evaluate this hypothesis, the following experiments were carried out.

For each of a series of differential pressures ($P_1 - P_2 = 80kPa, 130kPa, 160kPa, 200kPa, 230kPa, 240kPa, 305kPa, \text{ and } 360kPa$), the valve cap was controlled to slowly open from its closed position using the same procedure as for the static flow tests. During this process, the valve opening $Z_{vc,opening}$, the quasi-static flow rate Q_{avg} , and the imposed differential pressure $P_1 - P_2$ were measured real-time. The valve orifice geometry is shown in Figure 9.23. Numerous data points were selected and post-processing operations were performed to calculate the Reynolds number of the flow through the valve orifice, according to the relation $RE_{Dorifice} = \frac{Q_{avg}}{D_{orifice}v}$. Additionally, an “Instability Value” was determined for each data point corresponding to the behavior of the valve cap as it opened. The three types of valve cap behaviors observed (using the laser vibrometer system) during these tests were (1) smooth steady motion of the valve cap, (2) slightly rough motion of the valve cap (but always with negligible amplitude), and (3) oscillatory motion of the valve cap at a frequency of $5kHz$ and with peak-peak displacement of $3 - 4\mu m$. Figure 9.24 displays typical displacement signals over a time period of 10 ms for each of these types of behaviors. At each data point, an Instability Value of 1, 2, or 3 was assigned for each of the respective measured behaviors. Since the valve cap structure essentially reacts as a sensor to any pressure fluctuations in the flow channel above

it, these assigned Instability Values can provide some insight into the behavior of the fluid as it flows through the orifice.

Figure 9.25 displays an example test run for the case of $P_1 - P_2 = 80kPa$. Plots of the Instability Value versus $Z_{vc,opening}$, $P_1 - P_2$ versus $Z_{vc,opening}$, Q_{avg} versus $Z_{vc,opening}$, and $RE_{Dorifice}$ versus $Z_{vc,opening}$ are included. Notice that since the Reynolds number is proportional to the average flow rate, the Q_{avg} and $RE_{Dorifice}$ curves in Figure 9.25(c) are identical, only the axes are scaled differently. Additionally, notice that $P_1 - P_2$ is not constant over the length of the run. During the testing, it was very difficult to maintain the differential pressure at a constant value. For this test case of $P_1 - P_2 = 80kPa$, the valve cap smoothly moves through an opening trajectory, up to approximately $Z_{vc,opening} = 19\mu m$. At these conditions, the valve cap displacement begins to exhibit a slight roughness in its measured displacement (with roughness amplitude less than $0.4\mu m$), but continues to open with no effect on valve cap position. At $Z_{vc,opening} = 28\mu m$, the valve cap displacement returns to smooth behavior. The corresponding Reynolds numbers for these transition points are $RE_{Dorifice} = 788$ and $RE_{Dorifice} = 928$, respectively. In Figure 9.25(a), an Instability Value of 1 represents the smooth motion of the valve cap. An Instability Value of 2 represents slightly rough motion.

In order to obtain some understanding of the relationship between the valve cap behavior and the corresponding $RE_{Dorifice}$, test runs were carried out for the 8 differential pressure settings detailed above. Figure 9.26 plots the Instability Value versus $Z_{vc,opening}$ curve for $P_1 - P_2 = 80kPa$, $P_1 - P_2 = 130kPa$, and $P_1 - P_2 = 160kPa$ respectively. Figure 9.27 plots the Instability Value versus $Z_{vc,opening}$ curve for $P_1 - P_2 = 200kPa$, $P_1 - P_2 = 2300kPa$, and $P_1 - P_2 = 240kPa$ respectively. Figure 9.28 plots the Instability Value versus $Z_{vc,opening}$ curve for $P_1 - P_2 = 305kPa$ and $P_1 - P_2 = 360kPa$ respectively. In observing these plots, it is clear that oscillatory behavior does not occur until the case of $P_1 - P_2 = 200kPa$. Under this differential pressure, at a value of $Z_{vc,opening} = 8\mu m$, the valve cap experiences a transition from smooth motion to oscillatory behavior with a frequency of 5kHz and a peak-peak displacement of $6 - 8\mu m$. The corresponding Reynolds number for this transition is $RE_{Dorifice} = 615$. At a deflection of $Z_{vc,opening} = 19\mu m$, the valve cap stops oscillating and exhibits only slightly rough behavior. The corresponding Reynolds number for this transition is $RE_{Dorifice} = 969$. And finally, when the valve cap approaches the lower valve stop, its motion once again becomes smooth, most likely caused by interaction with the solid surface below it. The corresponding Reynolds number for this transition is $RE_{Dorifice} = 2000$. Similar behavior is observed for larger imposed differential pressures as well. For the case of $P_1 - P_2 = 360kPa$, multiple transitions between smooth, oscillatory, and rough are observed. It appears as though upon separation from the upper valve orifice stop, the valve cap immediately begins to oscillate. It then transitions back to smooth behavior at $Z_{vc,opening} = 4.5\mu m$, back to oscillatory motion at $Z_{vc,opening} = 7.5\mu m$, back to smooth motion at $Z_{vc,opening} = 13\mu m$, and then to rough behavior

at $Z_{vc,opening} = 20\mu m$.

To better understand the relationship between these transition behaviors and the Reynolds number at which they occur, all 8 plots are combined in Figure 9.29. Regions of smooth, rough, and oscillatory behavior are clearly evident. Figure 9.30 is produced by estimating the boundaries between these regions and labeling the corresponding $RE_{Dorifice}$ values at these boundary data points. In this plot, the distinct regions are detailed. Notice that a transition to rough valve cap motion occurs for Reynolds numbers between $RE_{Dorifice} = 800 - 1100$. Additionally, for large differential pressures, oscillatory valve cap behavior begins typically at $RE_{Dorifice} = 500 - 600$. Since rough valve cap behavior is characterized by only a tiny roughness in the displacement response (typically peak-peak displacement of less than $0.4\mu m$), the valve cap itself remains in a stable operating condition. It is only when large amplitude oscillatory response occurs that the valve cap becomes unstable. Figure 9.31 plots this stable versus unstable representation. In essence, smooth and rough valve cap behavior have been grouped together to form the stable regions. Figure 9.32 plots experimental lines of constant Reynolds number over the data points for all 8 test cases and Figure 9.33 compares these lines of constant Reynolds number to the expected lines obtained from model simulations presented in Chapter 4. Notice that all of the experimentally determined lines of constant $RE_{Dorifice}$ are very close to the theoretical predictions for low to moderate values of imposed differential pressure (ie: up to $P_1 - P_2 = 150kPa$). Once the differential pressure is increased further, experimental correlation to theory is still good for low valve openings (lines of constant $RE_{Dorifice} = 400, 500, 800$), however the experimental lines of larger constant $RE_{Dorifice} = 1000, 1500, 2200$ begin to bend more sharply upward from the theoretical predictions. This bending is directly in relation to the region of oscillatory behavior, which is bounded by a value of $RE_{Dorifice} \sim 1000 - 1100$ for the larger differential pressures. If one were to conclude that the measurements of smooth valve cap motion correspond to a laminar flow regime and that the slightly rough valve cap motion corresponds to a turbulent flow regime, it could therefore be argued that the oscillatory behavior of the valve cap structure occurs in a transition regime (characterized by $RE_{Dorifice}$ between ~ 500 and ~ 1100).

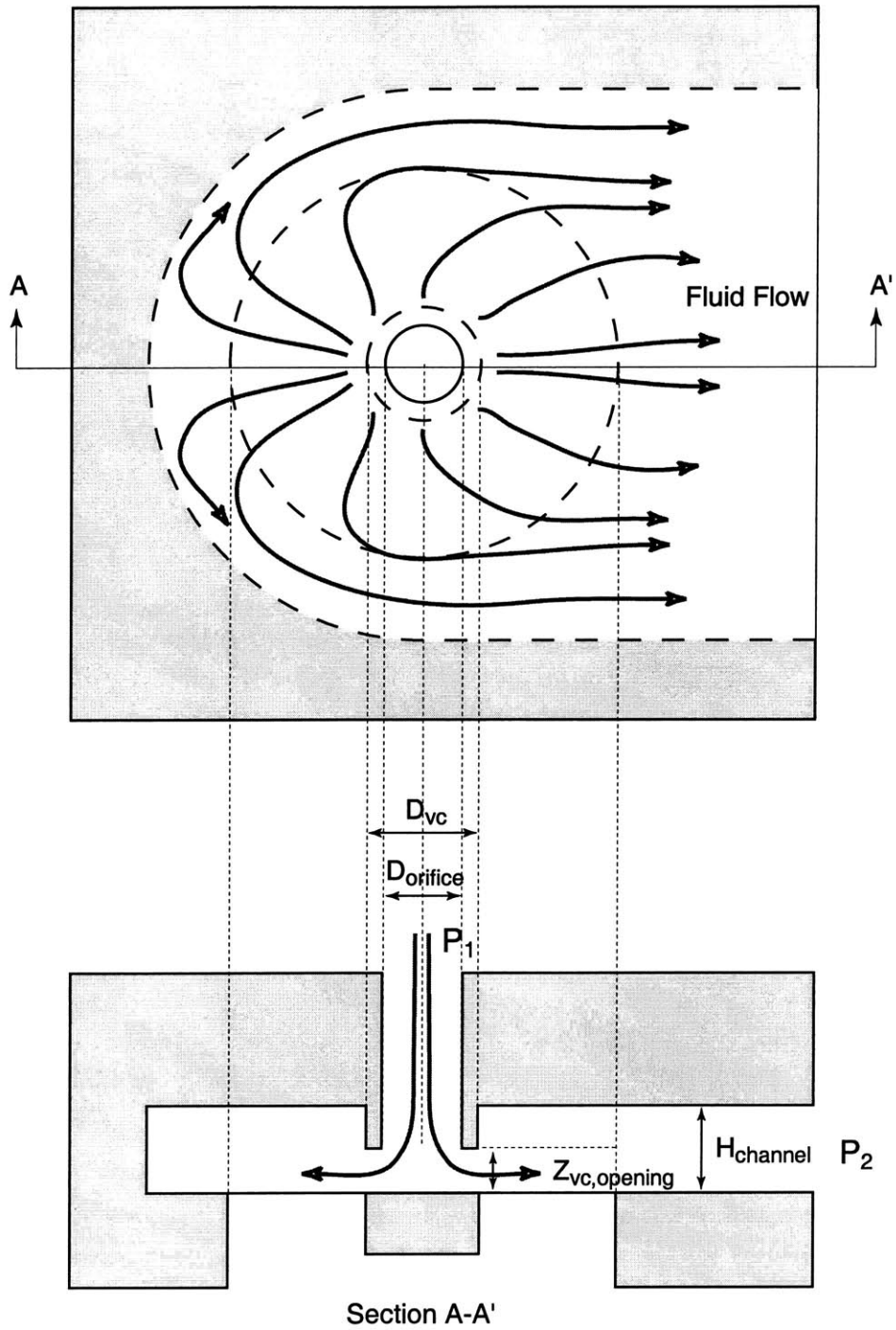


Figure 9.23: Schematic of valve cap and membrane orifice structure. For the active valve geometry tested in this thesis, $D_{orifice} = 500\mu m$, $Z_{vc,opening} = 0-30\mu m$, and $H_{channel} \sim 100\mu m$. Notice that the fluid flows radially outward over valve membrane, primarily to one side of the structure. The other side is blocked.

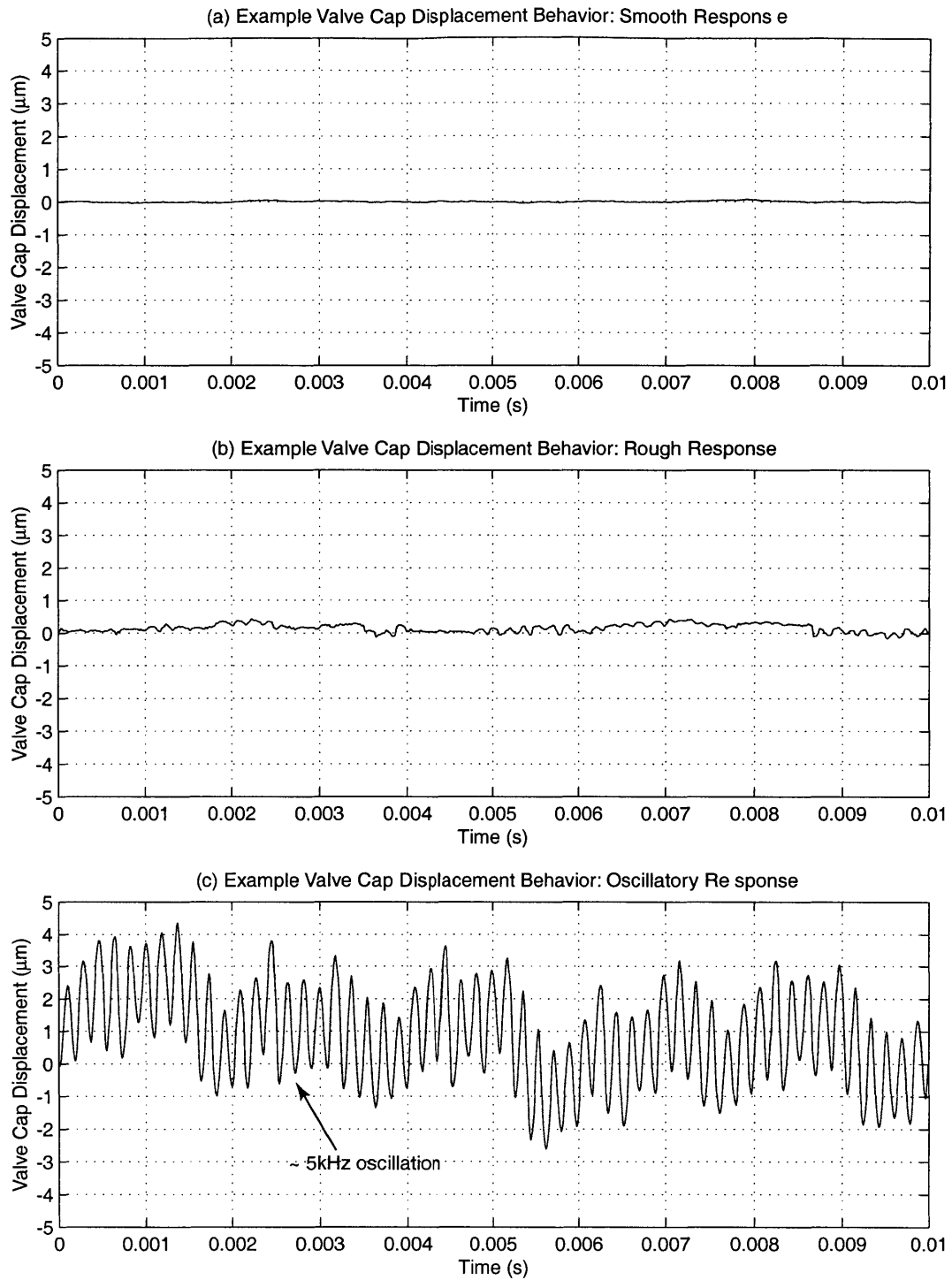


Figure 9.24: Representative displacement signals corresponding to stable and unstable valve cap behavior during quasi-static opening: (a) smooth displacement response (Instability Value=1), (b) slightly rough displacement response (Instability Value=2), characterized by random peak-peak motion less than $0.4\mu\text{m}$, and (c) oscillatory response characterized by $3 - 4\mu\text{m}$ peak-peak oscillations at 5kHz (Instability Value=3).

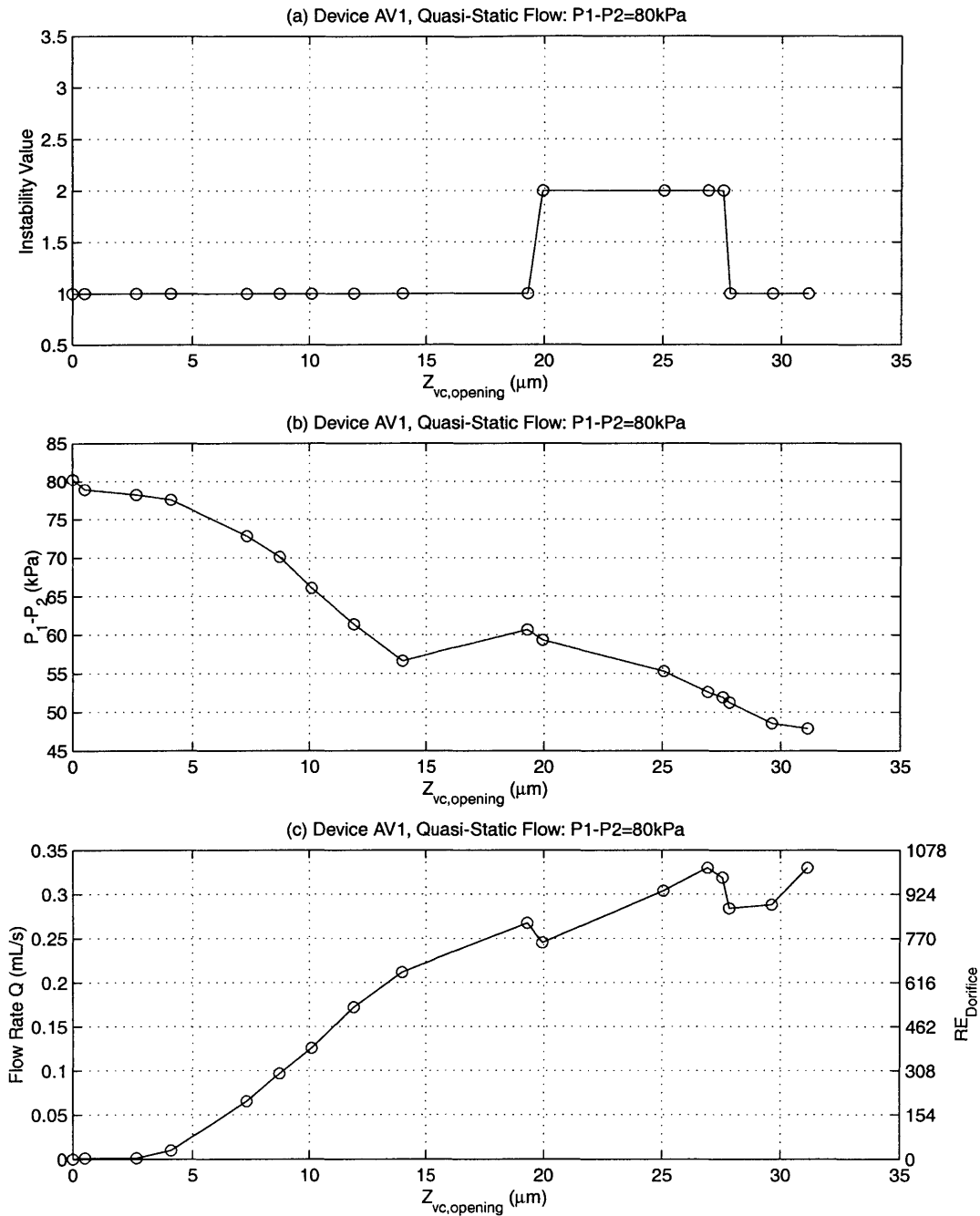


Figure 9.25: Representative plots for valve cap behavior, differential pressure, and flow rate during quasi-static opening for $P_1 - P_2 = 80 \text{ kPa}$. The valve cap opening motion transitions from smooth behavior to rough behavior at a deflection of $Z_{vc,opening} = 19 \mu\text{m}$ and transitions back to smooth behavior at a deflection of $Z_{vc,opening} = 28 \mu\text{m}$.

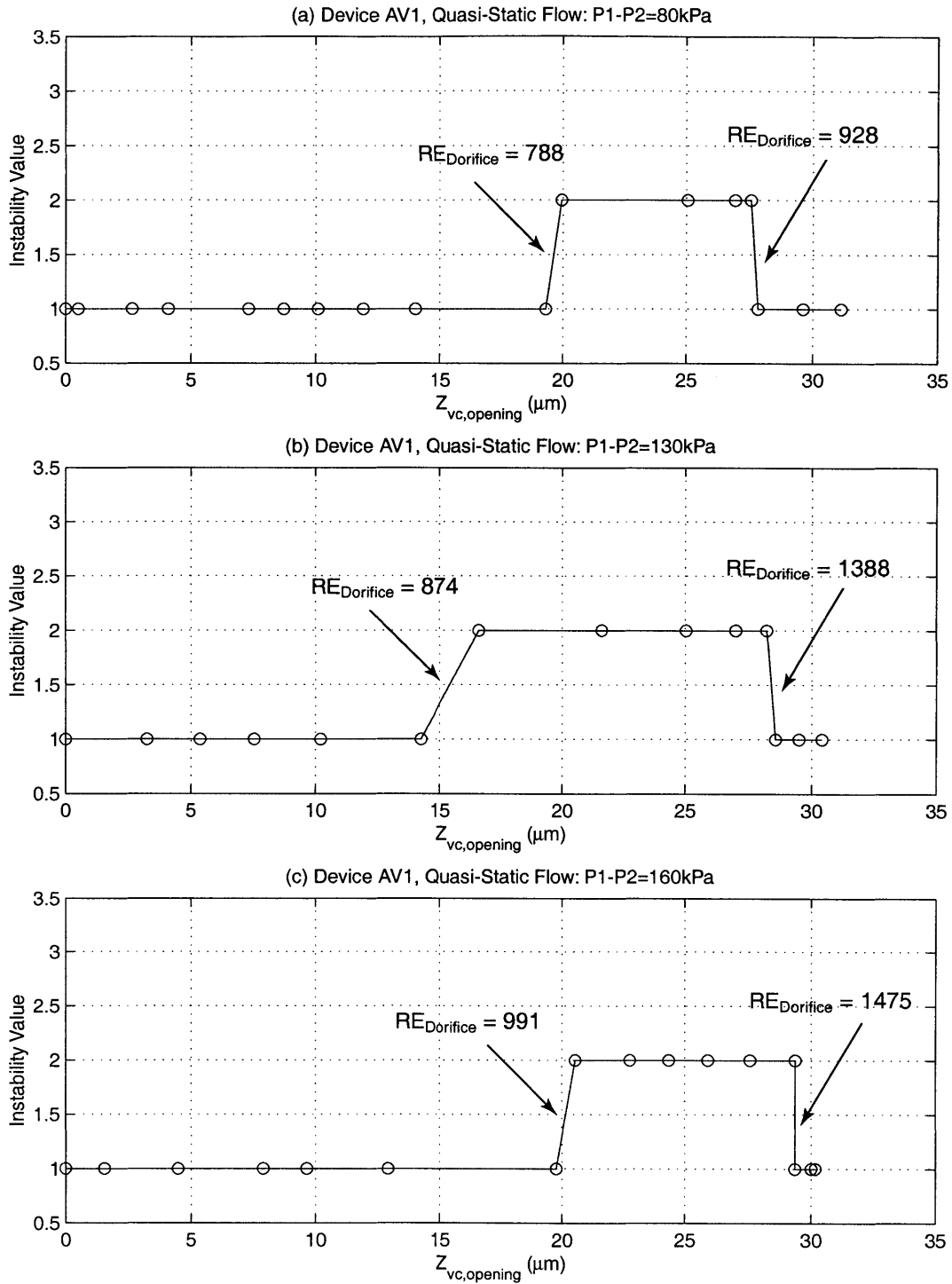


Figure 9.26: Valve cap Instability Values during quasi-static opening for $P_1 - P_2 = 80 \text{ kPa}$, $P_1 - P_2 = 130 \text{ kPa}$, and $P_1 - P_2 = 160 \text{ kPa}$. Corresponding Reynolds numbers are labeled at the transition locations.

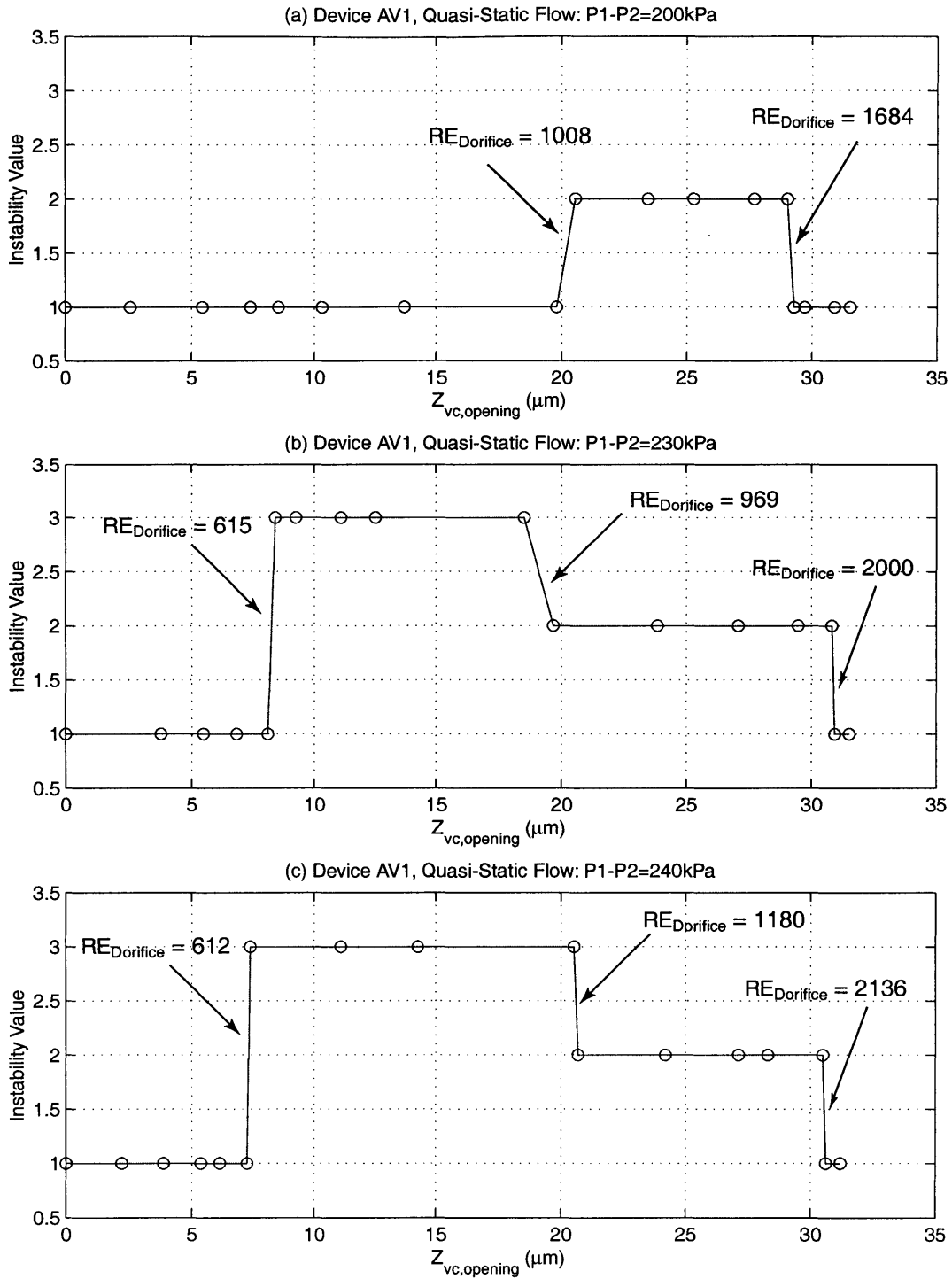


Figure 9.27: Valve cap Instability Values during quasi-static opening for $P_1 - P_2 = 200 \text{ kPa}$, $P_1 - P_2 = 230 \text{ kPa}$, and $P_1 - P_2 = 240 \text{ kPa}$. Corresponding Reynolds numbers are labeled at the transition locations.

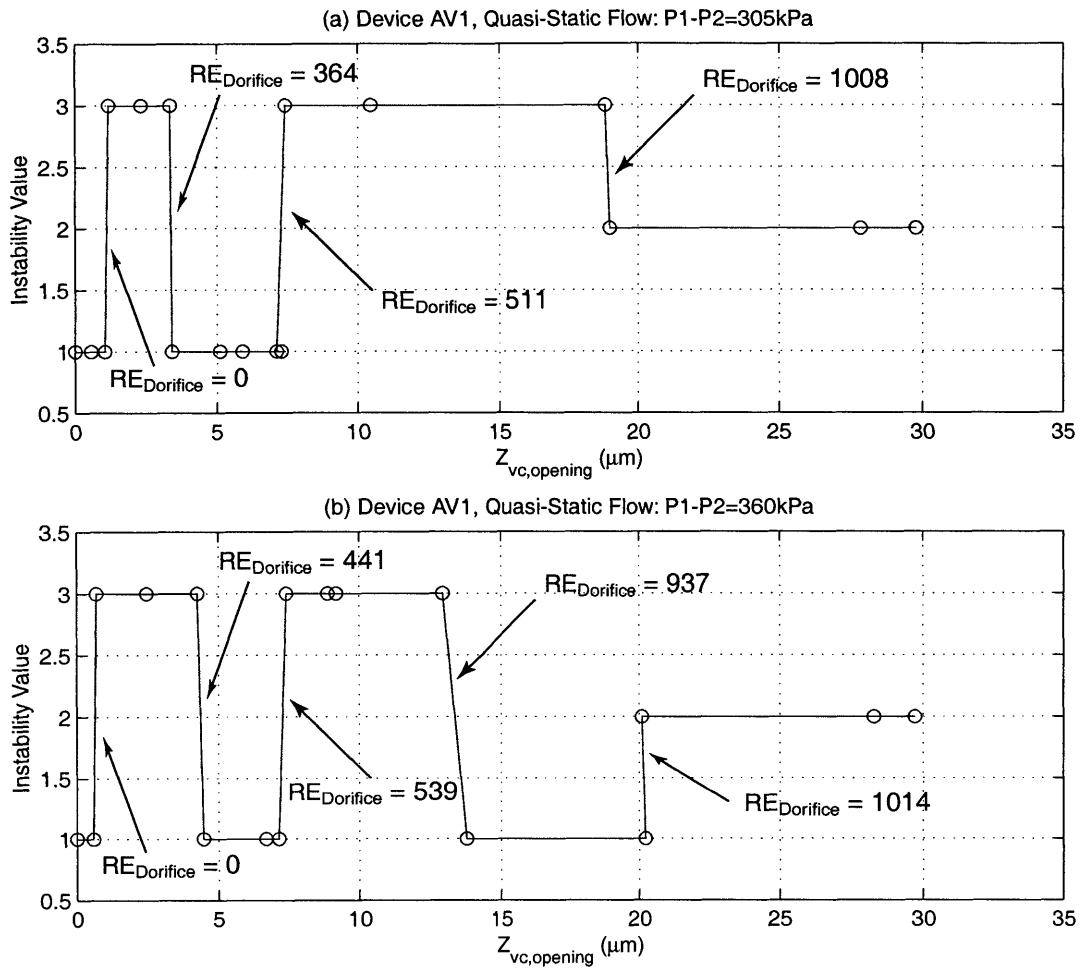


Figure 9.28: Valve cap Instability Values during quasi-static opening for $P_1 - P_2 = 305 \text{ kPa}$ and $P_1 - P_2 = 360 \text{ kPa}$. Corresponding Reynolds numbers are labeled at the transition locations.

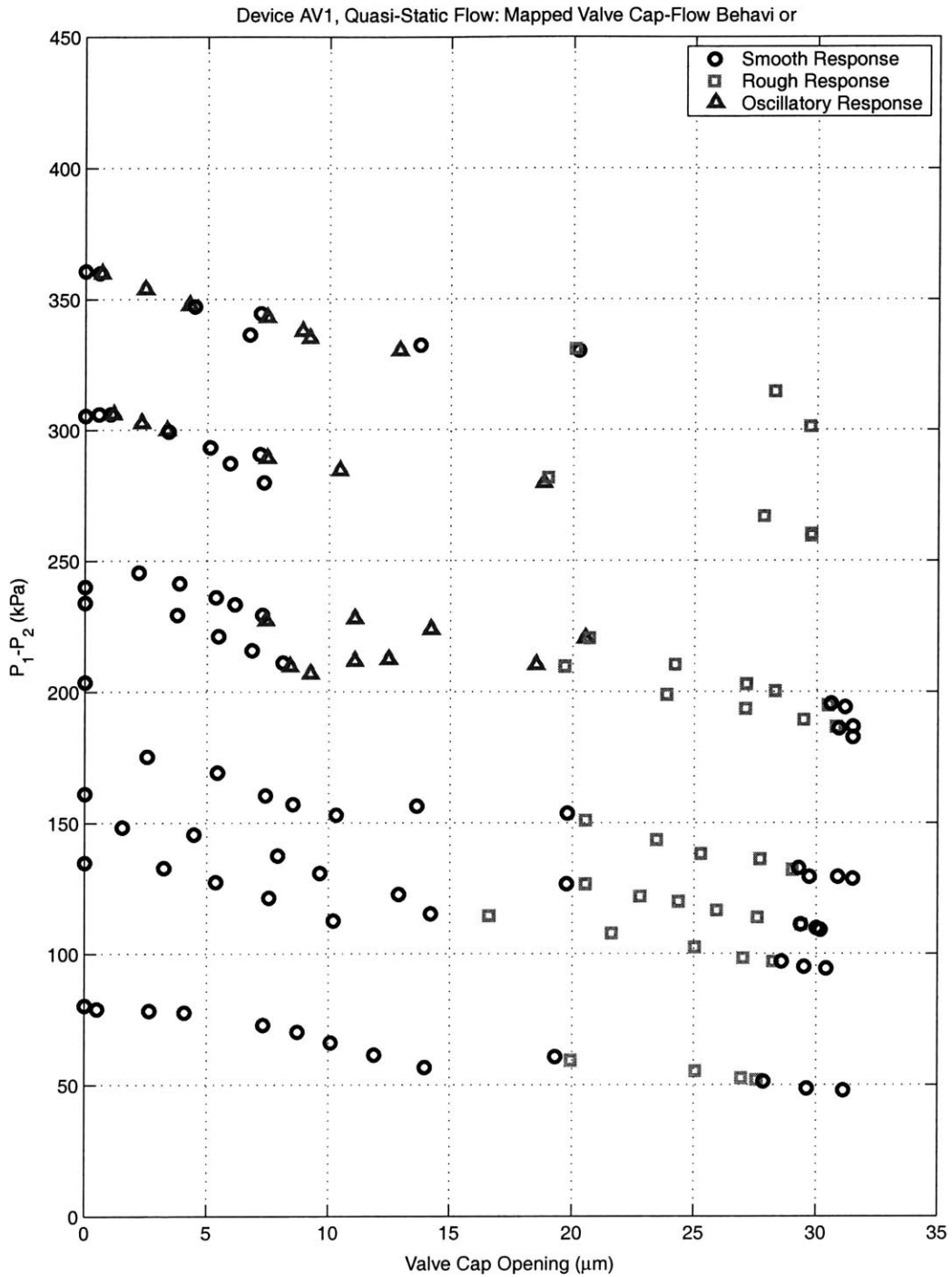


Figure 9.29: Complete grouping of all valve cap Instability Values plotted as $P_1 - P_2$ vs. $Z_{vc,opening}$. Region of valve cap oscillation defined by triangular data points.

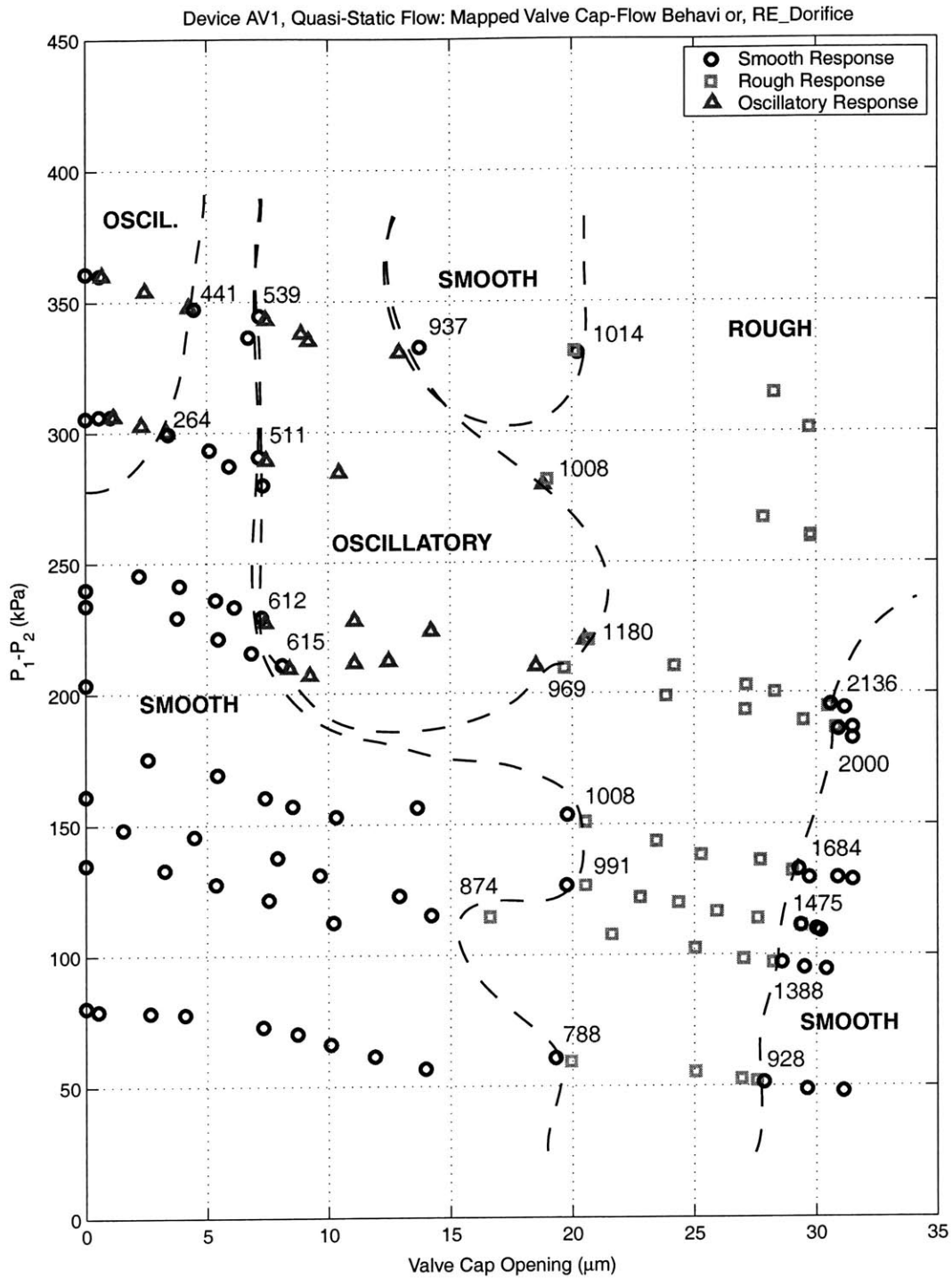


Figure 9.30: Estimated boundaries for smooth, rough, and oscillatory regions plotted as $P_1 - P_2$ vs. $Z_{vc, opening}$. Corresponding transition Reynolds numbers are displayed along these boundary lines.

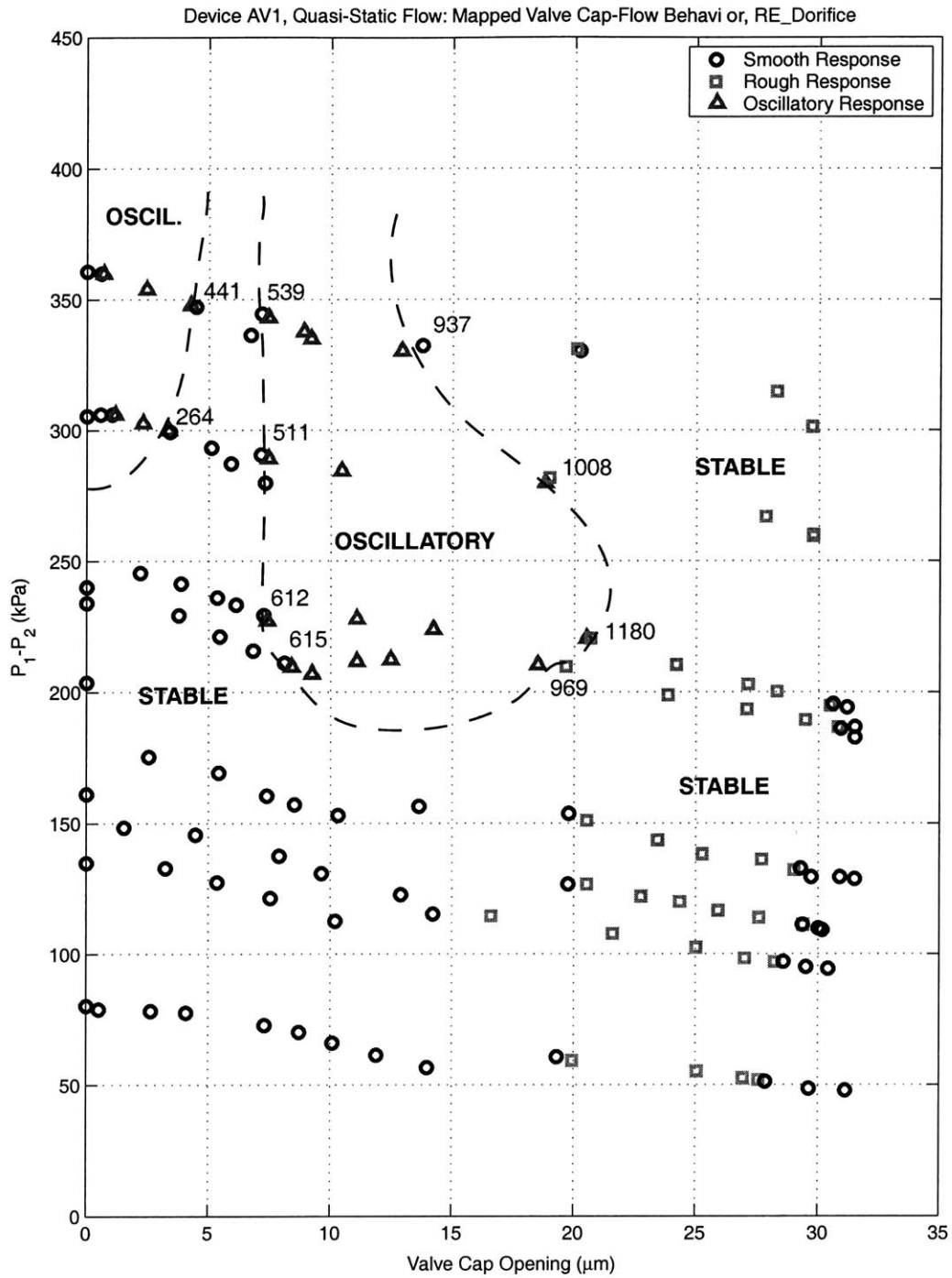


Figure 9.31: Estimated boundaries for unstable and stable regions plotted as $P_1 - P_2$ vs. $Z_{vc,opening}$. Corresponding transition Reynolds numbers are displayed along these boundary lines.

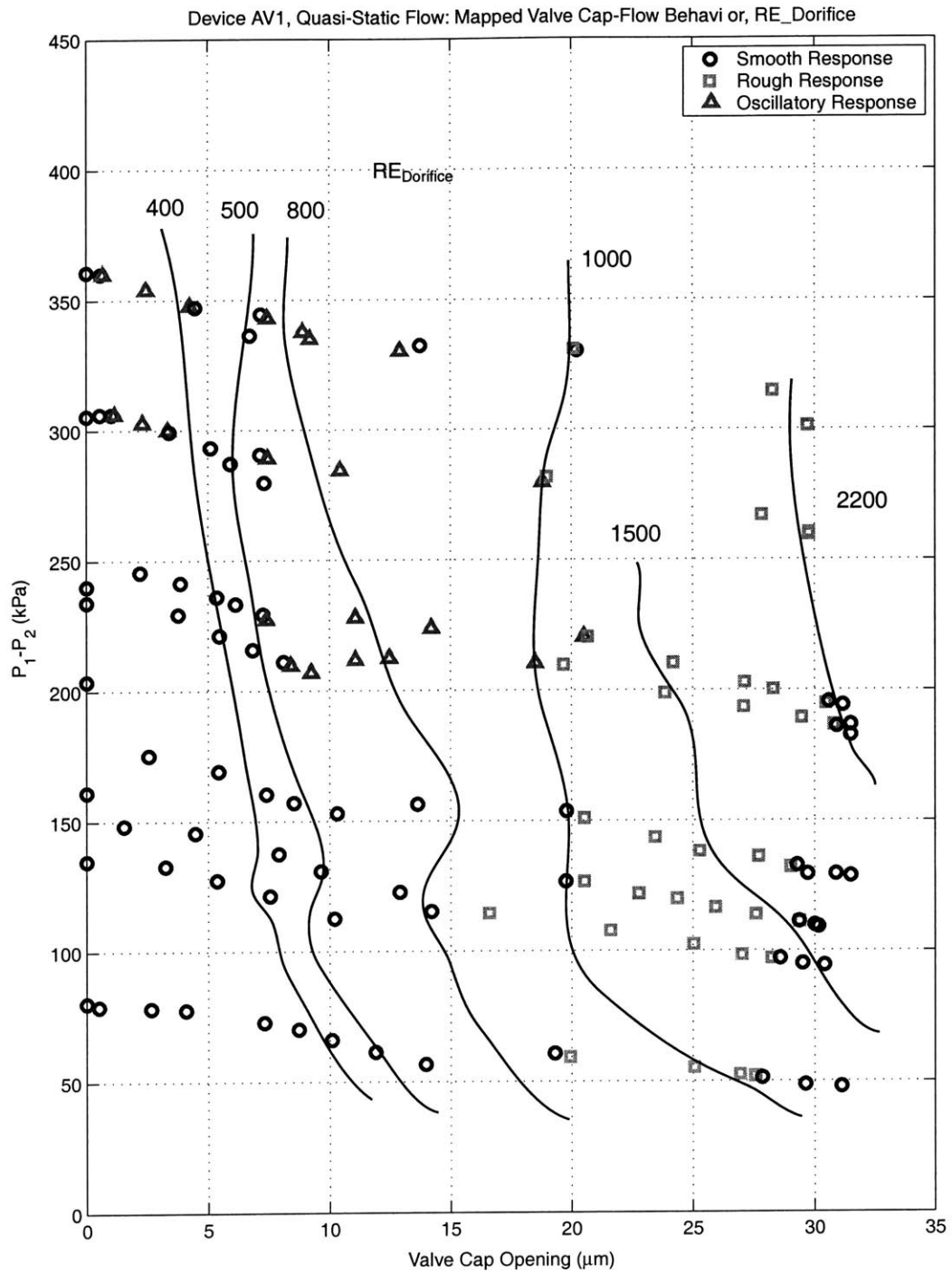


Figure 9.32: Estimated constant Reynolds number curves plotted as $P_1 - P_2$ vs. $Z_{vc,opening}$. Lines are estimated by interpolating between adjacent data points.

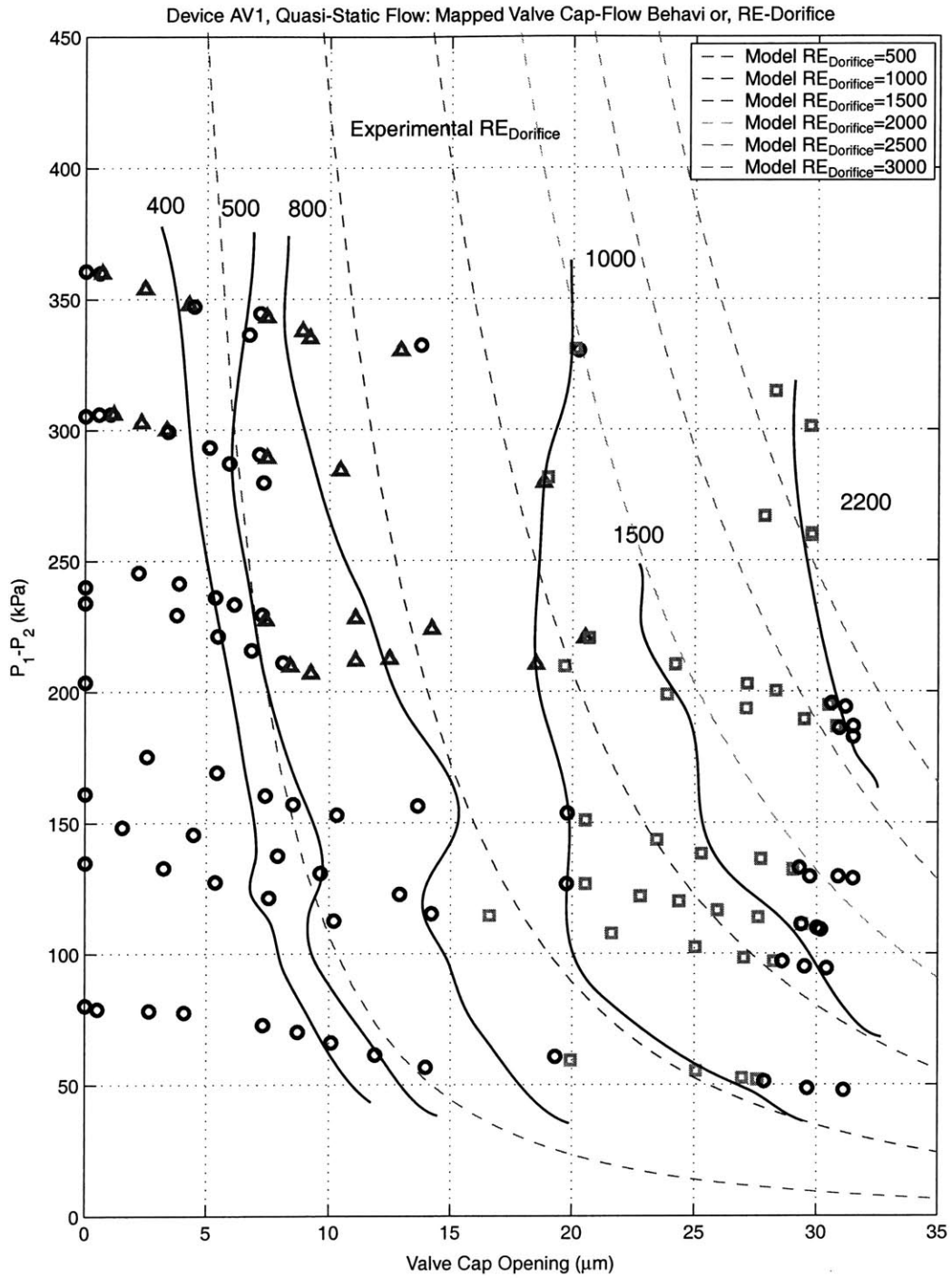


Figure 9.33: Constant Reynolds number curves (experimental vs. model predictions) plotted as $P_1 - P_2$ vs. $Z_{vc,opening}$. Experimental lines are estimated by interpolating between adjacent data points.

The presence of a transition regime between laminar and turbulent flow for the experimental data can be further illustrated by plotting the data in a different way. Typically, in characterizing the physical sections of a fluid system (ie: a constant area pipe, a bend, an orifice, etc), a fluid resistance coefficient for each of the sections can be defined. This resistant coefficient ζ is defined as the total pressure lost through the flow section divided by the dynamic pressure within the flow section [7], written in equation form as

$$\zeta = \frac{\Delta P}{\frac{1}{2}\rho_{fluid}u_{local}^2}, \quad (9.1)$$

where ΔP is the pressure drop through the flow section (in the case of the valve orifice $\Delta P = P_1 - P_2$) and u_{local} is the fluid velocity through the section (in the case of the valve orifice $u_{local} = \frac{Q_{avg}}{A_{orifice}} = \frac{4Q_{avg}}{\pi D_{orifice}^2}$). A universal method for observing the transition between laminar and turbulent flow in a physical section of a flow system is to plot this flow resistance coefficient ζ versus the Reynolds number in that section (in the case of the valve orifice $RE_{D_{orifice}}$). Figure 9.34, taken from [7], shows an example of this type of plot for a generic fluid orifice contraction section of a fluid system, where the quantity $\frac{F_o}{F_1}$ defines the geometric contraction ratio. Notice that for low Reynolds number, ζ is inversely proportional to RE (laminar flow regime) whereas for large RE, ζ is independent of RE (turbulent flow regime). In between these two regions is defined the transition regime where the flow transitions from laminar to turbulent.

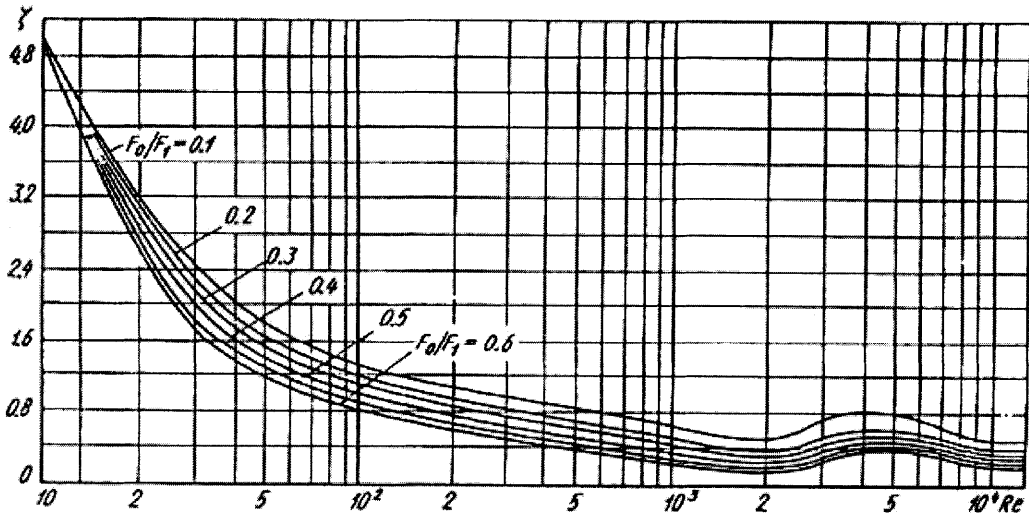


Figure 9.34: Plot of flow resistance coefficient ζ versus Reynolds number for a generic flow orifice contraction structure [7]. The laminar flow regime is characterized by an inversely proportional relationship between ζ and Reynolds number whereas the turbulent flow regime is characterized by no relation between ζ and RE. Transition occurs between these two regimes.

For laminar fluid flow through an orifice, the flow rate is proportional to the applied differential pressure ($Q_{avg} \propto \Delta P$) [2] [7], whereas for turbulent flow the flow rate is quadratically related to the differential pressure ($Q_{avg} \propto \sqrt{\Delta P}$) [2] [7]. Substituting these pressure-flow relations into 9.1, it can be determined that in the laminar flow regime ζ is inversely proportional to the Reynolds number, and that in the turbulent flow regime ζ is independent of the Reynolds number. This is consistent with Figure 9.34. Therefore, for the experimental data in this thesis, a plot similar to Figure 9.34 should be able to be created, where the slope of the ζ curve transitions from a negative value to a value of zero as $RE_{Dorifice}$ increases. In doing this, a determination as to whether the oscillatory valve cap behavior correlates to the transition between the laminar and turbulent flow regimes can be obtained. To evaluate this hypothesis, the experimental data is replotted as $\zeta_{orifice}$ versus $RE_{Dorifice}$ in Figure 9.35.

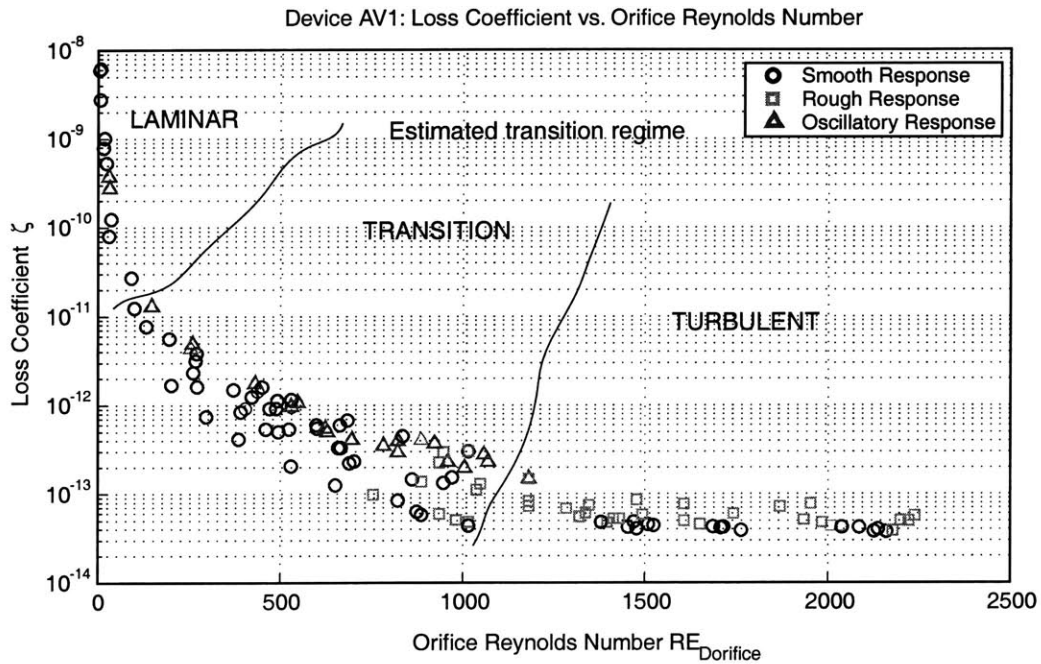


Figure 9.35: Device AV1 estimated laminar, transition, and turbulent flow regimes as a function of $RE_{Dorifice}$ based on experimental data. Laminar regime is characterized by $\zeta \propto \frac{1}{RE_{Dorifice}}$ and turbulent regime is characterized by ζ being independent of $RE_{Dorifice}$. The majority of oscillatory data points occur within estimated boundaries of this transition regime.

Notice that, indeed, for increasing $RE_{Dorifice}$ from 0 to 500, ζ monotonically decreases, and for increasing $RE_{Dorifice}$ from 1100 to 2500, ζ remains constant. One may notice that the points above $RE_{Dorifice} = 1100$ contain both smooth and rough valve cap behavior. Due to the fact that the differentiation between smooth and rough was a difficult task, it could be that in reality the smooth data points were mistaken for rough behavior. However, the important data

points of oscillatory behavior were clearly differentiable from both smooth and rough behavior and therefore there is no question as to their validity. These observations indicate the presence of reasonably well-defined laminar and turbulent flow regimes within the experimental results. Furthermore, the vast majority of the oscillatory data points lie within the region between $RE_{Dorifice} = 500$ and $RE_{Dorifice} = 1100$. Based on these results, it can be argued that the oscillatory behavior of the valve cap is directly related to the presence of transition between laminar and turbulent flow in the valve orifice.

The following question must now be addressed: Does this conclusion that valve cap oscillatory behavior is related to the transition between laminar and turbulent fluid flow make sense? This question is answered through a discussion of laminar, turbulent, and transitional flow regimes based on literature contained within the fluids mechanics community.

As detailed in the fluid modeling portion of Chapter 5, the valve cap and orifice structure consists of two physical flow sections in series: a contraction section followed by an expansion section. Both of these types of flow sections result in the formation of vortices, the severity of which increases as the Reynolds number grows larger. Figure 9.36 (a) and (b) illustrate schematics of a typical fluid expansion section and a fluid contraction section, respectively, and the corresponding regions where vortices are present [7]. In general as fluid passes through these sections, the fluid boundary layers present upstream of the section are not able to remain intact in passing through the section. Shear layers form where the boundary layers separate from the original structural surfaces, and these shear layers tend to roll up in swirling vortices, which create unsteady forces on any surrounding structure [5] (such as the valve cap and membrane in the active valve).

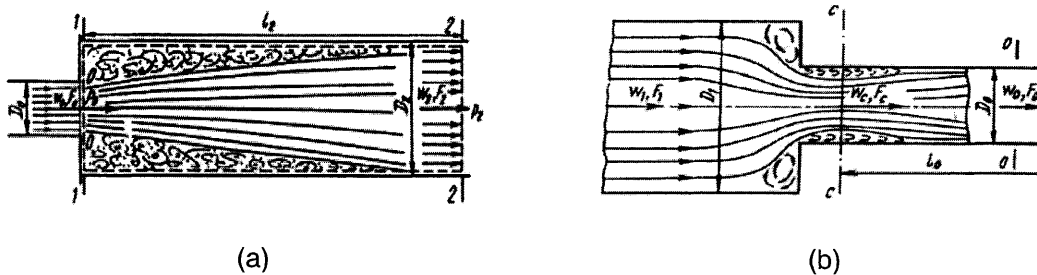


Figure 9.36: Schematic of vorticity formation in contraction and expansion fluid flow sections [7]: (a) expansion section, (b) contraction section.

This unsteady forcing is further enhanced if the flow is experiencing transition between laminar and turbulent behavior. In general, laminar viscous flow is characterized by smooth and steady fluid motion, whereas turbulent flow is characterized by continuous and almost random fluctuation in the velocities of the fluid particles. Both regimes have been studied for

a wide variety of flow geometries. Laminar flow theory is mathematically understood for many of these geometries. Turbulent flow behavior, however, is primarily an experimentally observed fact, which can be analyzed only through statistical understanding [8]. The transition between these two regimes is understood hardly at all. The transition regime is defined as the change (over space, time, and a certain Reynolds number range) of a laminar flow into a turbulent flow. Figure 9.37 illustrates a time history comparison of these three flow regime behaviors.

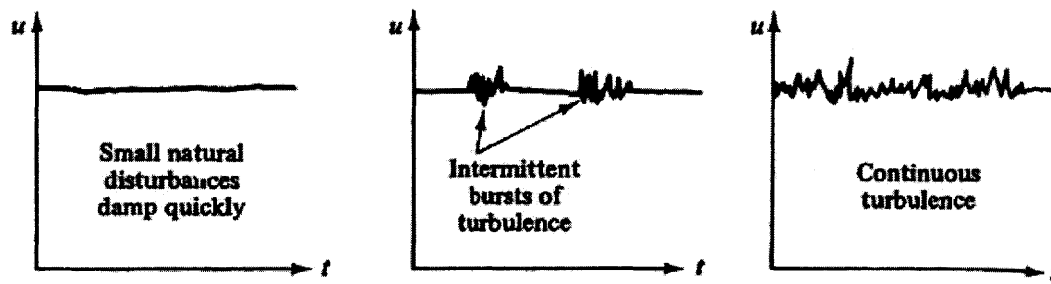


Figure 9.37: Laminar, transition, and turbulent representative flow behavior [8]: (a) laminar flow, (b) transition flow characterized by intermittent bursts of turbulent flow, and (c) turbulent flow.

In laminar flow, there may be occasional natural disturbances in the flow, however, they damp out very quickly. In fully turbulent flow, continuous rapid and random fluctuations are present. In transition, there exist sharp bursts of turbulent fluctuation as the increasing Reynolds number causes a breakdown or instability of laminar motion. Transition through the valve orifice in this thesis, therefore, could very well be characterized by intermittent increases and decreases in the intensity level of the vorticity formation through the orifice, thereby resulting in a significant oscillation of the forcing on the valve cap and the compliant valve membrane structure. It is this vortex-induced structural interaction between the fluid flow and the elastic valve structure that could be setting the valve cap oscillations into motion.

The experimental results presented in this section have provided insight into the approximate value of Reynolds number for which the valve cap structure begins to experience unstable oscillatory behavior. In the valve flow regulation experiments that follow, results will first be obtained for relatively low differential pressure situations to avoid the potential for valve failure due to these oscillations. Once flow regulation has been proved at low differential pressures, tests will then be performed at higher differential pressures to tests the limits of the active valve device under these unknown flow regime conditions.

Duty Cycle Flow Regulation Tests

To evaluate the capability of the active valve to regulate flow for applied voltage to the piezoelectric elements, a series of varying duty cycle test runs were carried out for an imposed differential pressure across the valve orifice of $P_1 - P_2 = 35kPa$. This low differential pressure was chosen to ensure flow regimes that do not excite valve cap oscillatory behavior. For each duty cycle run, the valve cap motion was controlled between a minimum valve cap absolute displacement (from its equilibrium position) of $Z_{vc} = 4.0\mu m$ to a maximum valve cap absolute displacement of $Z_{vc} = 11.5\mu m$. Since the valve orifice is located a distance of $16.5\mu m$ above the equilibrium position of the valve cap, it can be stated equivalently that the valve cap opening was controlled between a minimum opening of $Z_{vc,opening} = 5\mu m$ to a maximum opening of $Z_{vc,opening} = 12.5\mu m$. Duty cycle voltage waveforms from zero to 100 were applied to the active valve such that the resulting valve cap motions shown in Figure 9.38 were obtained. A duty cycle of zero means that the valve cap was maintained constantly at its minimum opening of $Z_{vc,opening} = 5\mu m$ and a duty cycle of 100 means that the valve cap was maintained constantly at its maximum opening of $Z_{vc,opening} = 12.5\mu m$. A duty cycle of 30, for example, means that the valve cap was effectively held at its minimum opening for 70% of the cycle and at its maximum opening for 30% of the cycle.

The results of these tests are shown in Figure 9.39. As the duty cycle is increased from zero to 100, the average flow rate through the valve orifice increases monotonically, thereby proving that the valve device is capable of regulating flow. Using the simulation tools detailed in Chapter 5 of this thesis, predicted results for the flow rates were calculated. These are overlaid with the experimental results in Figure 9.39. The comparison indicates that for reasonable valve openings, the measured flow rate correlates quite well with the model predictions. However, for small valve openings near $Z_{vc,opening} = 5\mu m$, the measured flow rate is significantly less than predicted. In essence, the flow appears to be choked more than expected at small valve openings. This observation agrees with the results at small valve openings of the quasi-static flow rate versus valve opening curves discussed previously. As discussed in the previous static flow test section, since the Chapter 5 flow models are based on a compilation of empirical work from other researchers, the lines of predicted behavior in Figure 9.39 are understood to be of only “limited accuracy”, in other words, they are not based on exact theory. In addition to modeling the case of a controlled valve opening of $Z_{vc,opening} = 5 - 12.5\mu m$, model predictions for a controlled valve opening of $Z_{vc,opening} = 7 - 14.5\mu m$ and a controlled valve opening of $Z_{vc,opening} = 8.5 - 16.5\mu m$ were also determined. These results are also shown in Figure 9.39 to convey the sensitivity of the offset valve opening on flow rate through the orifice. Shifts of a just a few μm s in the opening direction within the flow models result in significantly increased flow rate values.

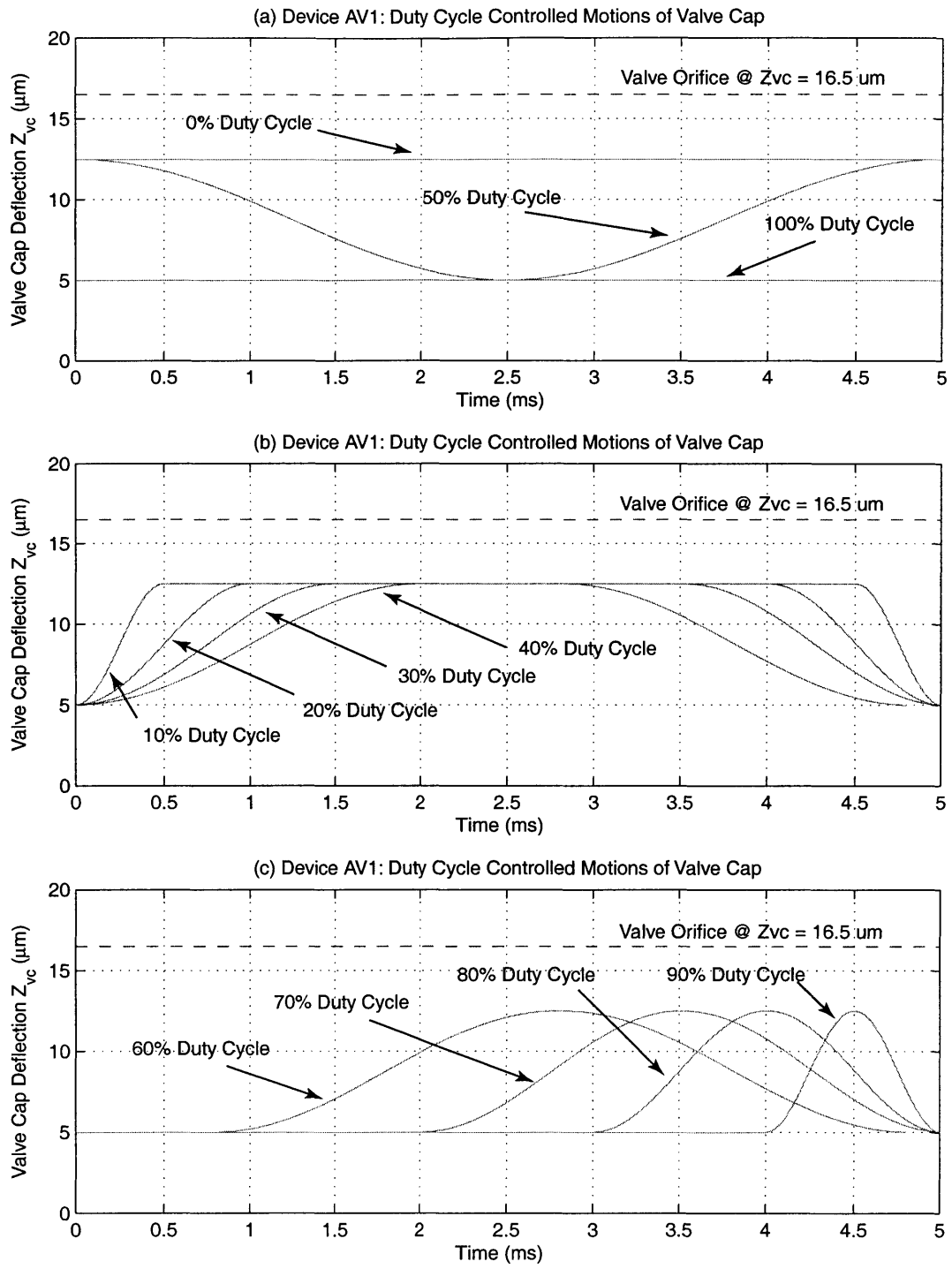


Figure 9.38: Device AV1 valve cap time histories under different duty cycle voltage waveforms to piezoelectric drive element. The valve cap is controlled to reach a maximum valve cap displacement of $Z_{vc} = 12.5\mu m$ and to reach a minimum valve cap displacement of $Z_{vc} = 4\mu m$.

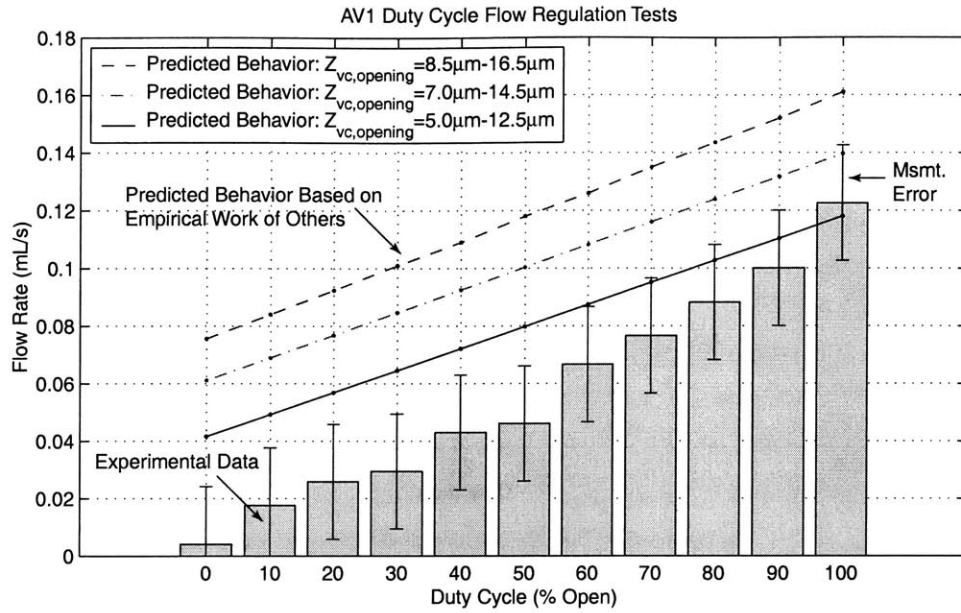


Figure 9.39: Device AV1 model correlation to experimental flow rate results for varying duty cycle inputs. Comparison illustrates good correlation for larger valve openings. For small opening, the flow appears choked. Error bars on the data indicate the measurement error, which was estimated based on the flow sensor calibration error and the accuracy of the applied differential pressure.

1kHz Flow Regulation Tests at Increasing Differential Pressure

To evaluate the capability of the active valve device to regulate flow at 1kHz, a series of tests was carried out for increasing differential pressures across the valve orifice. In addition to proving flow regulation at 1kHz, a further purpose of this study was to determine the maximum differential pressure across which the valve could operate. Since the magnitude of the unstable oscillatory behavior observed for the static flow tests at differential pressures greater than $P_1 - P_2 = 210kPa$ was no more than $3 - 4\mu m$ peak-peak, it was hoped that by operating the active valve device dynamically at 1kHz with total valve cap stroke of $15 - 20\mu m$, the effect of the 5kHz oscillations might not affect the overall flow regulation capability of the valve. As such, tests were performed for differential pressures in excess of $P_1 - P_2 = 210kPa$.

Flow regulation tests at 1kHz were performed for differential pressures $P_1 - P_2 = 24kPa$, $95kPa$, $145kPa$, $200kPa$, $260kPa$, and $340kPa$. By controlling P_{HAC} with respect to the magnitude of P_1 and P_2 , the valve cap was displaced statically upward to a deflection of $Z_{vc} = 11\mu m$. A sinusoidal voltage of $500V_{pp}$ was then applied to the piezoelectric drive element at 1kHz to actuate the valve cap upward against the valve orifice and downward toward the original equilibrium position of the valve cap. In all test runs, it was desired to just barely close the valve cap against the orifice at its maximum displacement, and to maintain $Z_{vc} = 0$ at its

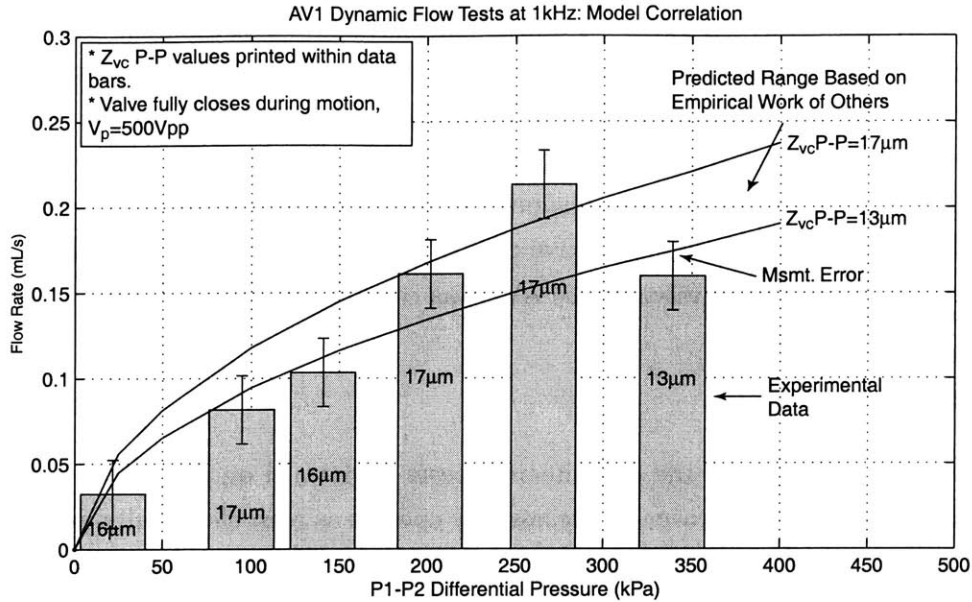


Figure 9.40: Device AV1 dynamic flow regulation model correlation at 1kHz for varying differential pressures. Correlation is good over range of differential pressures. Error bars on the data indicate the measurement error, which was estimated based on the flow sensor calibration error and the accuracy of the applied differential pressure.

minimum displacement. In others words, it was desired to always ensure a valve opening stroke of $16.5\mu m$. Figure 9.40 plots the experimentally measured flow rates for each of the differential pressure test cases. Because of the difficulty in achieving a valve cap stroke during actuation of $Z_{vc,opening} = 16.5\mu m$, the actual measured stroke of the valve cap during actuation is printed inside of each data bar. An applied voltage of $500V_{pp}$ was held constant for all of these test runs. It was noticed that for the differential pressure case of $P_1 - P_2 = 340kPa$, a valve cap stroke of $13\mu m$ resulted, rather than the typical $16 - 17\mu m$ of the previous test cases. It was believed in this case that the piezoelectric material capability may have been affected by the high pressure excursions (estimated maximum to be $P_{HAC} \sim 600kPa$) within the HAC chamber.

Figure 9.40 also plots the experimental results versus the model expectations obtained using the active valve simulation tools developed in Chapter 5. Model predictions for the limiting cases of $Z_{vc,opening} = 13\mu m$ and $Z_{vc,opening} = 17\mu m$ are shown. The model correlation indicates that the active valve regulates flow in excellent correlation with the model predictions. As discussed in the previous flow testing sections, since the Chapter 5 flow models are based on a compilation of empirical work from other researchers, the line of predicted behavior in Figure 9.40 is understood to be of only “limited accuracy”, in other words, it is not based on exact theory. Upon carrying out a subsequent test run at $P_1 - P_2 = 450kPa$, as the differential pressure was being set across the valve orifice, the valve cap was observed to begin oscillating (with no

applied piezoelectric drive element voltage at this point). Very quickly afterward (fractions of a second, the valve cap lodged itself permanently against the bottom orifice. Subsequent efforts to move the valve cap upward by pressurizing and depressurizing the HAC chamber resulted in a $1\mu\text{m}$ amplitude tilting of the valve cap. Based on this response, it is believed that the valve membrane fractured in response to the oscillatory valve cap motion caused by unstable transitional flow through the valve orifice. Because this device failed in this manner, experimental testing of active valve device AV1 was concluded.

9.4 Conclusions

This chapter has summarized the experimental tests performed on active valve devices AV1 and AV2. Both devices were proven to successfully operate as piezoelectrically-driven hydraulic amplification micro-actuator structures. For applied piezoelectric voltages up to 600V_{pp} at 1kHz , these devices demonstrated amplification ratios of drive element deflection to valve cap deflection of 40x - 50x . These amplification ratios correlate within $5 - 10\%$ of the model expectations. Although valve cap peak-peak deflections for the applied voltage levels were measured to be $20 - 30\%$ lower than model expectations for the idealized E_p and d_{33} piezoelectric material coefficients used in the design optimization chapters of this thesis, correlation to model results that incorporate modified piezoelectric material properties based on proper experimental characterization of the material is within $5 - 10\%$.

Flow regulation experiments on active valve device AV1 proved that this valve structure can successfully regulate fluid flow at a frequency of 1kHz for valve cap peak-peak displacements of $17\mu\text{m}$ up to differential pressures of 260kPa . For this condition, a peak average flow rate through the device of 0.21mL/s was obtained under a sinusoidal drive voltage of 500V_{pp} . Additionally, quasi-static differential pressure-flow rate curves were measured up to a differential pressure of 210kPa for the full range of valve cap stroke up to $33\mu\text{m}$. The measured flow rates were $10 - 30\%$ lower than the expected flow rates based on the models presented in Chapter 4. Self-oscillatory motion of the valve membrane was observed for various combinations of valve cap opening and differential pressures in excess of 210kPa . The nature of the flow behavior (based on Reynolds number) was studied for a variety of valve opening situations. The results indicate that these self-excited valve cap oscillations were most probably a result of transitional flow (between laminar and turbulence) through the valve orifice structure, a regime which limited the valve operation to relatively low differential pressures below 350kPa . Overall, this piezoelectrically-driven hydraulic amplification microvalve was successfully proven to regulate fluid flow through microscale channels at high frequency.

Bibliography

- [1] C.Y. Lin, Ph.D. Thesis. MIT. 2002.
- [2] K.T. Turner, An Evaluation of Critical Issues for Microhydraulic Transducers: Silicon Wafer Bonding, Strength of Silicon on Insulator Membranes and Gold-Tin Solder Bonding. MIT Master's Thesis. June 2001.
- [3] TRS Ceramics Data Sheet for PZN-PT.
- [4] Dow-Corning data sheet on silicon oil.
- [5] R.D. Blevins, Formulas for Natural Frequency and Mode Shape, R.E. Krieger, Malabar, FL, 1984.
- [6] J. Carretero and K.S. Breuer, "Measurement and Modeling of the Flow Characteristics of Micro Disk Valves," Proceedings of the 1994 International Mechanical Engineering Conference and Exposition: Microfluidics Symposium, Orlando, FL, Nov. 2000.
- [7] I.E. Idelchik, "Handbook of Fluid Resistance," CRC Press, Boca Raton, FL, 1994.
- [8] F.M. White, "Viscous Fluid Flow," McGraw-Hill, New York, NY, 1991.

Chapter 10

Conclusions and Recommendations

This chapter summarizes the modeling, design, fabrication, and testing research presented in this thesis. The thesis objectives and the thesis contributions are reviewed. Conclusions are drawn based on the results presented and recommendations for future work are detailed. Additionally, it is the purpose of this chapter to evaluate the impact of these thesis results on the performance capabilities and overall future of Micro-Hydraulic Transducer systems.

10.1 Summary and Conclusions

10.1.1 Thesis Summary

The primary objective of this thesis was to develop, from the initial concept stage to the experimental testing of a fabricated device, a piezoelectrically driven hydraulic amplification microvalve for high frequency control of high pressure fluid flow. This research was carried out through a series of modeling, design, fabrication, assembly, and experimental testing tasks. This work demonstrated the valve concept and evaluated the valve performance in comparison to behavior predicted by the models developed in the thesis.

A secondary goal of this thesis was to provide a framework of linear and non-linear structural modeling tools and design procedures that can be implemented in the development of high frequency piezoelectric micropumping and microvalving systems. Additionally, a further goal of this thesis was to present a method for small-scale bulk piezoelectric material integration within silicon micromachined thin-tethered structures, a procedure which can enable the realization of compact high-frequency high-stiffness hydraulic actuator structures.

These objectives were divided into two major sections of the thesis. The first section, consisting of Chapters 1 through 5, focused on the conceptual design of the active valve structure, the development of structural modeling tools to predict the important linear and non-linear structural behaviors of the device component structures, the implementation of these modeling

tools within an active valve simulation architecture, and the development of a systematic design procedure that can be used to generate an active valve geometry based on external hydraulic system performance requirements. The second section, consisting of Chapters 6 through 9, highlighted the fabrication challenges inherent in building this active valve device and defined the fabrication process flow for the assembly of the device, including piezoelectric material integration. Additionally, comprehensive experiments were carried out to experimentally evaluate the piezoelectric drive element sub-component structure, the valve cap and membrane sub-component structure, and the full piezoelectrically-driven hydraulic amplification microvalve device. Each of the chapters is summarized below.

Chapter 1 introduced the concept of the piezoelectrically-driven hydraulic amplification microvalve for use in high specific power hydraulic pumping applications. High frequency, high force actuation capability in the valve is enabled through the incorporation of solid-state bulk piezoelectric material elements beneath a compact and stiff structural piston mechanism. High stroke valve motion is achieved through the incorporation of a hydraulic amplification chamber between the moveable piston structure and a micromachined valve membrane. This enclosed fluid chamber, connecting the large cross-sectional area piston structure to a smaller cross-sectional area valve membrane structure, enables an amplification ($40 - 50x$) of the limited piezoelectric material stroke into a significantly increased valve membrane and valve cap deflection. These design features enable the valve device to simultaneously meet a set of high frequency, high pressure, and large stroke requirements that have not previously been satisfied by other microvalves presented in the literature.

Chapter 2 introduced the geometry of the active valve device and detailed the important structural elements within the device that needed to be accurately modeled. The structural deformations of the piezoelectric material elements, the drive element piston, the bottom support structure, the hydraulic amplification chamber, the top support structure, and the valve cap and membrane structure were modeled using linear plate theory, with bending and shearing deformation effects included. Additionally, theoretical studies were performed to demonstrate the benefits, by stiffening the drive element piston actuation structure, of integrating multiple piezoelectric material elements spread out beneath the drive element piston rather than integrating just a single centrally-located material element beneath the piston. These studies provided the optimal dimensional spacing of the three piezoelectric elements beneath the drive element piston in the fabricated and experimentally characterized active valve devices presented in Chapter 9.

Chapter 3 presented the development of a numerical code to model the large deflection behavior of a thin annular plate structure with rigid central cap under pressure loading. The work presented in this chapter was based on a finite-difference scheme developed by Su [1]. This numerical code served as a modeling tool for use in the full active valve non-linear model and

system simulation presented in Chapter 4. The theory was specifically developed to capture the non-linear stiffening effects present in the valve membrane structure of the active valve. The linear plate theory representation that was presented in Chapter 2 is not able to capture these stiffening effects. A series of valve cap and membrane geometries and pressure loading scenarios, characteristic of those found and experienced in the final active valve device, was presented to demonstrate the capabilities of this modeling tool to capture the large deflection behavior of the structure.

Chapter 4 presented a complete quasi-static structural model of the active valve. This model was comprised of the linear and non-linear modeling tools presented in Chapters 2 and 3, respectively. An evaluation of the assumptions within the structural model was performed through a series of comparison studies to a finite-element model of the active valve structure for a variety of loading scenarios. In addition, the chapter introduced a dynamic simulation architecture for the valve, which included inertia and damping associated with the drive element piston and valve cap structural elements. Calculation of the coupled fluid-structure resonant valve frequency, based on finite-element analyses, was also presented. The predicted resonance was based on a finite-element model that did not include the added mass of the fluid above the valve cap and membrane structure. As a result, this model overpredicted the valve resonant frequency in comparison to experimental results on the fabricated valve devices detailed in Chapter 9.

Chapter 5 formulated a systematic quasi-static design procedure that can be used to generate an active valve geometry based on external hydraulic system performance requirements. This design procedure was based on the modeling tools and simulations developed in Chapters 2, 3, and 4 of the thesis. Additionally, the procedure incorporated the governing fluid flow relations linking the valve cap motion to the external hydraulic system pressures and enabled variation of key parameters within the active valve geometry (such as valve membrane thickness and the number of valve membranes used in parallel) to satisfy predetermined valve membrane stress limitations. A powerful characteristic of the systematic design procedure is the ability to monitor the stress at all positions along the valve membrane for any and all potential pressure loading scenarios experienced by the structure. This enables the designer to very accurately predict the maximum stress that the valve membrane will experience during its full actuation cycle as it opens and closes against the fluid orifice. As a check, full system dynamic simulations were run to validate the goodness of the valve geometry created using the quasi-static design procedure.

Chapter 6 presented an overview of the fabrication challenges encountered and the solutions implemented in the development of the active valve device. These challenges included the wafer-level etching of the drive element and valve membrane structures, the wafer-level silicon-to-silicon and silicon-to-glass bonding operations, preparation and integration of the piezoelec-

tric material elements with the device, die-level assembly and bonding procedures, and the filling of degassed fluid within the hydraulic amplification chamber following device assembly. Additionally, the modeling and design of a micromachined high-resistance fluid channel was documented that enabled a static bias pressure to be imposed on the hydraulic amplification chamber without affecting the high-frequency actuation behavior of the active valve device.

Chapter 6 also presented a detailed sub-component testing plan for the active valve structure. This systematic plan separated the complete active valve structure into manageable sub-component devices according to the primary challenges previously detailed. The piezoelectric drive element sub-component study, whose purpose it was to prove the ability to micromachine the tethered piston structure and integrate bulk piezoelectric material beneath the piston, and the valve cap and membrane sub-component study, whose objective it was to validate the non-linear large deflection behavior of the valve membrane structures, were outlined. Additionally, the full active valve testing plan was outlined.

Chapter 7 presented the experimental results for the piezoelectric drive element sub-component study. A series of drive element devices was fabricated in an effort to demonstrate that both standard polycrystalline PZT-5H piezoelectric material as well as higher-strain single-crystal PZN-PT piezoelectric material could be incorporated beneath micromachined piston structures. An additional goal was to demonstrate that devices with three piezoelectric elements spread out beneath the drive piston could be manufactured in a reliable manner. Quasi-static high-voltage experimental tests were performed on these devices at a frequency of 15kHz and dynamic low-voltage frequency tests were carried out between frequencies of 10kHz and 200kHz to identify modal characteristics.

The results indicated that the procedure formulated in Chapter 6 for integrating piezoelectric material elements, both PZT-5H and PZN-PT, within these micromachined structures is repeatable. All devices fabricated experienced a tolerance match between the piezoelectric elements and the surrounding supporting structures within $\sim 1\mu m$, thereby ensuring predictable “push-up” of the piston structure during assembly. Drive element devices incorporating a single piezoelectric material beneath the piston experienced modal “1- Θ ” tilting behavior at frequencies as low as 30kHz. Additionally, quasi-static actuation of the devices at 15kHz and 1000Vpp resulted in a slight tilting of the piston structures as they moved up and down through their actuation cycles. These tilting effects were attributed to imperfect placement of the piezoelectric element beneath the center of the piston and to non-uniform fillet radius etch profiles, characterized through microscope measurements, around the etched tether of the piston. Drive element devices incorporating three piezoelectric material elements experienced negligible tilting behavior during actuation at 15kHz and 1000Vpp due to the enhanced support of the piston from below. For these devices, modal behavior was not observed until frequencies in excess of 50kHz. This sub-component study successfully demonstrated the capability to fabricate and

assemble these component structures for use in full active valve devices.

Chapter 8 presented the experimental results for the valve cap and membrane sub-component study. A series of valve membrane structures was fabricated and inspected to ensure adequate fillet radius control at the base of the etched features. Pressure-deflection experiments were carried out for differential pressures across the structure of up to 200kPa in an effort to characterize its non-linear large deflection behavior. Theoretical studies, using the non-linear numerical tools presented in Chapter 3, were carried out to determine deformation and membrane stress sensitivities to valve membrane thickness and fillet radius size. The experimental valve cap deflections, in response to pressure loading, were found to correlate within $\sim 5\%$ of theoretical expectations. The valve membranes were deflected sufficiently to impact the valve stop in glass Layer 6, a condition which results in a predicted membrane stress of 0.65GPa. In these tests, no membranes fractured. This sub-component study successfully demonstrated the capability to fabricate the valve cap and membrane structure required in the full active valve device and verified that this structure behaves as predicted in its non-linear large deflection regime.

Chapter 9 presented the experimental results of the full active valve testing study. The goals of these experiments were to evaluate the quasi-static and dynamic structural performance of the active valve device and determine some initial limitations in its ability to regulate fluid flow against imposed differential pressures. For the purposes of this study, two active valve devices were built and experimentally characterized. Both devices were proven to successfully operate as piezoelectrically-driven hydraulic amplification microactuator structures. For applied piezoelectric voltages up to 600Vpp at 1kHz, these devices demonstrated amplification ratios of drive element deflection to valve cap deflection of 40x-50x. These amplification ratios correlate within 5 – 10% of the model expectations. Although valve cap peak-peak deflections for the applied voltage levels were measured to be 20 – 30% lower than model expectations for the idealized E_p and d_{33} piezoelectric material coefficients used in the design optimization chapters of this thesis, correlation to model results that incorporate modified piezoelectric material properties based on proper experimental characterization of the material is within 5 – 10%.

Flow regulation experiments proved that this valve structure can successfully regulate fluid flow at a frequency of 1kHz for valve cap peak-peak displacements of $17\mu m$ up to differential pressures of 260kPa. For this condition, a peak average flow rate through the device of 0.21mL/s was obtained under a sinusoidal drive voltage of 500Vpp. Additionally, quasi-static differential pressure-flow rate curves were measured up to a differential pressure of 210kPa for the full range of valve cap stroke up to $33\mu m$. The measured flow rates are 10 – 30% lower than those expected based on the models presented in Chapter 4. The onset of transition and turbulent flow regimes, which depending on the valve cap opening and the differential pressure could set the valve cap into self-excited oscillatory motion, was identified for differential pressures in excess of 210kPa. The nature of the flow behavior (based on Reynolds number) was studied

for a variety of valve opening situations. The results indicate that these self-excited valve cap oscillations were most likely a result of a transition flow regime between laminar and turbulence through the valve orifice structure, a regime which limits the valve operation to relatively low differential pressures below 350kPa. Overall, though, this piezoelectrically-driven hydraulic amplification microvalve has been successfully proven to regulate fluid flow through microscale channels at high frequency.

10.1.2 Thesis Contributions

The results presented in this thesis support the following conclusions, which address the primary objectives of this research:

1. A piezoelectrically-driven hydraulic amplification microvalve is a viable concept for the regulation of high differential pressure ($> 300kPa$) fluid flows at high frequency ($\geq 1kHz$), resulting in significant fluid flow capability.
2. Integration of miniaturized bulk piezoelectric materials (with dimensions less than 1mm x 1mm x 1mm) within micromachined thin-tethered piston structures is a viable method for achieving compact high frequency, high force actuation capability in microhydraulic systems.
3. Linear and non-linear modeling tools for the design of active valve devices, such as this one which incorporate thin-membrane valve structures, have been developed. These modeling tools enable accurate monitoring of real-time membrane stress levels at all locations along the membrane for all potential pressure loading scenarios experienced by the structure.

Although performing short of the original frequency and differential pressure design specifications set forth at the beginning of this thesis, the demonstrated valve capabilities place this device superior to any other microvalve presented in the literature (see Chapter 1) for simultaneously meeting a set of high frequency (1-10kHz), high pressure(0.1-1MPa), and large stroke (15-40 μm) requirements for regulating liquid fluid flows in micro hydraulic systems. It is the belief of this author that future design iterations could be successful in creating a microvalve structure that could operate at a frequency of 10-15kHz against differential pressures approaching 1MPa. The following section details further work that could enable this design goal and addresses the question “What do the results of this thesis mean to the overall future of high-specific power Micro-Hydraulic Transducer systems?”.

10.2 Recommended Further Work and the Future of MHTs

The results presented in this thesis have identified a number of issues and areas which require further development and investigation. In this section, these issues will first be organized into those that are deemed fundamentally critical for the development of the next generation piezoelectrically-driven hydraulic amplification active valve to meet the high frequency ($>10\text{kHz}$) and large differential pressure ($\sim 1\text{MPa}$) requirements set forth at the beginning of this thesis, and those that are worth investigating as a means to make modest improvements in device performance and to ease manufacturability concerns. Once this overall list has been defined, each of the issues will then be discussed in detail.

Based on the results of this thesis, it is clear that a piezoelectrically-driven hydraulic amplification microvalve can be designed, built, and successfully operated to regulate liquid fluid flows. The valve design experimentally characterized in this thesis, however, fell short of its operational goals in two primary ways. The first of these shortcomings was the valve's low 1st modal structural frequency (5kHz), which limited valve quasi-static operation frequency to 1-2kHz. Since the original design goal was to operate this valve within an MHT system at a frequency of at least 10kHz, it can be stated that the valve severely underperformed. This is a shortcoming that this author believes can be overcome in future design iterations with more attention given to the important fluid-structural coupling and added mass phenomena that directly affect the valve's dynamic behavior. The second of these shortcomings was the unexpected interaction between the valve structure and the fluid flow at differential pressures in excess of 210kPa. Chapter 9 included a thorough analysis of the related experimental data, resulting in the conclusion that the unstable self-oscillatory valve cap behavior was most probably caused by instabilities within the flow regime (such as vortices) as a transition from laminar to turbulence occurs. Whereas the first shortcoming can be overcome fairly easily within a redesign effort, this flow-induced instability issue is likely to require significantly more effort in the future (both in modeling and in detailed experimentation) to better characterize the fluid flow regimes that occur through these sorts of microvalve orifices and to more accurately capture interactions between these flow phenomena and adjacent compliant structures (such as the valve cap and membrane in this active valve design).

The two issues previously discussed are the critical ones which have most severely limited this active valve to lower than desired performance levels. On the positive side, however, it can be confidently stated that all of the structural models developed in this thesis for predicting quasi-static valve performance (Chapters 1-5) were in extremely good correlation with the 1 kHz experimental data presented in Chapter 9. The experimentally characterized valve cap deflections and valve amplification ratios for the full range of operating voltages were within 5-10% of model expectations, a result which confirms these documented models as important

tools within future valve design iterations. The additional areas of recommended future work (in addition to the two major issues discussed above), therefore, fall not within the realm of active valve structural modeling, but rather within the area of material characterization and microfabrication. Under the heading of material characterization is, first, the need for better understanding of single-crystal PZN-PT piezoelectric materials and, second, the need for better understanding of the stress limitations within etched single-crystal silicon material (especially SOI wafers). Under the heading of microfabrication are a variety of issues relating to the manufacturability of this highly-complex, multilayer valve structure.

In summary, the recommended future work is divided into the following sections: (1) a valve structural redesign phase to enable quasi-static operational frequencies at or above 10kHz, (2) a major program to characterize the flow regimes through microvalve orifices and to understand the potential impact that this flow behavior has in interacting with adjacent compliant structures (flow induced structural instabilities), (3) further characterization of the actuation capabilities of single-crystal piezoelectric materials and the stress limitations of SOI etched structures, and (4) the re-evaluation of user-intensive microfabrication steps and the development of a less complex active valve structure. These sections of recommended future work are discussed in detail in the following sections.

10.2.1 Redesign for Enhanced Operational Frequency

The modal frequency model correlation studies performed in Chapter 9 identified the hydraulic amplification chamber geometry as a key contributor to the reduction in frequency of the valve 1st modal frequency. Additionally, it was determined that the added mass of the external fluid above the valve cap and membrane structure had an important effect in limiting this frequency as well. A redesign effort should be performed on this active valve to increase its first modal frequency to within the range of 10-15kHz. The active valve geometry tested in this thesis incorporated a Layer 6 HAC chamber geometry characterized by a chamber height of $t_{HAC} = 200\mu m$ and a series of small dimensioned through-holes and flow channels (with dimensions as small as $100\mu m$) connecting the lower half of the HAC chamber to the upper half of the chamber. This intricate geometry was required in order to guarantee the presence of a rigid motion stop $\sim 16.5\mu m$ below the underside of the valve cap. In such closely-packed structures, inertial coupling between the structural elements and the accelerating fluid can significantly reduce modal frequencies of the system, as discussed in Chapter 9. The next generation active valve should incorporate an HAC chamber with reasonable height (ie: $t_{HAC} = 500\mu m$) and without any complex arrangement of holes and channels. The chamber should be a single simple cylindrical volume defined on its bottom surface by the tethered piston and on its top surface by the valve cap membrane and top support structure. In this re-design, no bottom stop would be present, a necessary consequence. Based on experimental

testing in this thesis, the valve should still operate successfully without this stop present. The simplification of this chamber geometry will, therefore, minimize the effect of inertia coupling and allow for a higher 1st modal frequency. One may argue that a larger volume fluid chamber will increase the compliance of this coupling mechanism between the piston and the valve membrane, an argument which is true. However, the degree to which performance would be reduced is negligible compared to the benefit of a higher operating frequency. Additionally, by incorporating the external fluid above the valve cap and membrane within future finite-element models, the influence if this added mass can be taken into account in designing a valve to meet a quasi-static frequency greater than 10kHz.

The modal frequency model correlation study performed in Chapter 9 also presented the effect of valve membrane thickness on the overall 1st valve modal frequency. It was shown that an increase in valve membrane thickness from $t_{vm} = 6\mu m$ to $t_{vm} = 10\mu m$ would increase the 1st modal frequency of the active valve from 14kHz to 20kHz (without fluid above valve cap and membrane). This is based on the fact that, in general, the stiffness of a plate scales with the cube of its thickness. This stiffening would help to increase the modal frequency, however, it would require more actuation authority from the drive element portion of the valve. Based on the tradeoffs documented in Chapter 5 of this thesis, such a tradeoff in frequency for a slightly larger piezoelectric material volume beneath the piston is worthy of investigation in the next generation design. Careful attention to the potential deflections and predicted stress levels seen in this larger thickness membrane during actuation would be required to maintain structural integrity. In essence, this redesign effort should use the exact modeling tools documented in Chapter 5 of this thesis, but include a more rigorous modal frequency evaluation during the process. An additional benefit of a thicker valve membrane would be the potential for reducing the magnitude of the flow-induced instability (to be discussed in the following section) caused by the interaction of the fluid flow through the orifice with the adjacent compliant valve membrane. A significantly stiffer membrane structure might eliminate the severity of this interaction all together.

10.2.2 Understanding of Flow Induced Structural Instabilities

For the active valve devices experimentally characterized in this thesis, flow-induced structural vibrations of the valve cap and membrane limited the differential pressure across which the active valve could regulate flow. Although significant analysis work was performed on the experimental data containing this instability behavior and although a plausible explanation for the said behavior was put forth in the conclusions of this thesis, it is believed by the author that a vast number of fluid flow issues and questions must be further investigated and answered before the observed phenomena can be understood fully and before the impact on full MHT systems can be estimated. These issues focus on two major tasks: (1) the characterization

of the flow behavior through microvalve orifices and (2) the understanding of the interaction between this flow through microvalve orifices and any adjacent compliant structures. These tasks are detailed in the following sections.

Flow Characterization Through Microvalve Orifices

The majority of experimental testing on valves for use within microsystems has been done on macroscale valves. The fluid models used throughout this thesis, in fact, were based on this method of testing, with the results being accepted at the microscale [2]. In order to fully understand the flow behavior as the Reynolds number passes from zero to in excess of 10,000 during valve opening and closing, and in particular, to understand the critical nature of the transition regime between laminar and turbulent flow, microscale valve experiments must be carried out. These experiments must utilize rigid valve cap structures that are in no way affected by the fluid flow, and conversely, that do not themselves influence the flow behavior. In this way, an understanding of vortex formation and flow instabilities can be obtained independent of adjacent compliant structures. Tests could be performed using many of the microfabricated layers used for the active valve in this thesis. However, one would need to incorporate a precisely controlled solenoid or long piezoelectric stack actuator bonded to a rigid valve cap (without an adjacent compliant membrane) which could be moved upward and downward against the fluid orifice. It is critical that no compliant structures exist in the region of the orifice flow so that the resulting flow behavior is solely a function of the orifice geometry and applied operating conditions. The following experimental tests could be carried out:

1. Slow static valve opening tests, identical to those performed in the instability section of Chapter 9, whereby the valve cap is lowered from its fully closed position against the valve orifice over a sufficiently long period of time (~ 10 minutes) to ensure flow behavior for a static valve opening. The valve cap deflection, flow rate, and dynamic pressure directly upstream and downstream of the valve cap should be measured and recorded real-time. Without a compliant structure (ie: the valve membrane) present during this test, an understanding of the relationships between differential pressure, flow rate, and dynamic pressure can be obtained and an estimation of the laminar, transition, and turbulent flow regimes could be carried out.
2. In conjunction with the test described above, flow velocimetry measurement techniques should be implemented to visualize the flow as it passes through the microvalve orifice. Vortex shedding and unsteady flow phenomena could be identified in an effort to evaluate the regions of laminar, transition, and turbulent flow as a function of Reynolds number. These velocimetry techniques are designed to illuminate and measure particle and surface motions using infrared wavelengths, taking advantage of the fact that silicon is largely

transmissive to light with wavelengths greater than $1\mu m$. Such a system could allow observation of particles within the flow stream inside of the silicon-based valve orifice microdevice [3]. By analyzing images using both time-of-flight and phase-locked techniques, quantitative measurements about the motion of the fluid could be taken.

3. Using both of the above testing methods, valve orifices with varying types of orifice “sharpness” could be evaluated. The creation of vortices in these microstructures is most likely enhanced by the sharp expansion that occurs as fluid flows radially outward across the membrane. Current MEMS fabrication processes limit the degree of “chamfering” that can be done on corners. It is possible, though, that future microfabrication processes will be developed to enable smoothing of these types of orifice structures.

With the experiments described above, a thorough characterization of the flow behavior through microvalve orifices could be obtained, independent from its interaction with adjacent compliant structures.

Flow-Induced Instabilities of Adjacent Valve Membrane Structure

With a detailed understanding of the flow regimes through microvalve orifice geometries, experiments could be run to evaluate the impact of these flow regimes on the stability of adjacent compliant valve cap membrane structures. The structures tested could be similar to the full valves tested in this thesis. The following experimental tests could be carried out:

1. During the slow valve opening tests discussed previously, it would be very useful to capture instantaneous snapshots (with period $\sim 10ms$) repeatedly during the full 10 minute long experimental test. This would require a more sophisticated A/D measurement system than was used in this thesis, in which low data sampling rates (ie: 10 data points per second) could be used for the extended period test and much higher sampling rates (ie: 1,000,000 data points per second) could be used for the snapshots. In this manner, during valve opening, as the valve cap transitions from stable to unstable oscillatory behavior, these snapshots could capture the nature of this transition behavior.
2. Additionally, during these tests, rather than measuring just the center point of the valve cap using the laser vibrometer system, it would be informative to scan over the entire surface of the valve cap. In this manner, tilting motion of the valve cap could be analyzed as a cause of any unstable flow behavior. Since the valve cap stiffness is minimal for tilting motions (no net volume change beneath the valve cap occurs), these motions could easily be caused by unstable flow regions around the valve cap or, conversely, unstable flow behavior (vortices) could be a result of valve cap tilting. Therefore, measurement of the valve cap tilting could be informative. The spot size of the laser vibrometer system

used in this thesis, however, is too large for such a spatial measurement procedure. Micro laser vibrometer systems could be attempted, however, these systems are typically housed within microscope stage set-ups, which would limit the ability to incorporate the active valve test-rig and jig under the lens. Further brainstorming ideas are needed for outfitting such a small spot size measurement technique.

3. In addition to measuring the whole valve cap motion during this testing, it would also be beneficial to spatially measure the deformation of the valve cap membrane. In this manner, the onset of structural oscillations could be matched with estimated flow regime phenomena. Unfortunately, in the current system, the valve membrane is not in the line of sight of the vibrometer laser beam, due to the presence of silicon layers above and below. Velocimetry (to measure the motion of a moving surface) could be a potential solution, as discussed earlier. Or other sensing methods could be used to measure the dynamic behavior of the membrane, such as incorporation of piezoresistive material in the membrane. This method, however, would require significant fabrication complexity and the need for electrical lead-ins and lead-outs to the membrane, which would only further increase the complexity of the device assembly and bonding procedures.
4. A further interesting experiment which could be performed on the existing active valve design would be to reverse the flow direction through the valve orifice and determine if the same flow-induced vibrations occur. Since in either flow direction the orifice is comprised of a contraction and an expansion of similar magnitude area ratio, the flow is expected to behave consistently. The one main difference, however, is that over the compliant membrane itself, the flow will be experiencing a contraction rather than an expansion, a difference which might result in less severe formation of vortices. The instability discussion in Chapter 9, however, did include schematics from the fluid mechanics literature that indicated similar vorticity fields for both expansion and contraction flow geometries.

A further recommended task would be to develop a theoretical model for the fluid-structural interaction between this flow behavior and the compliant valve structure, using FEM and CFD analyses. The major problem with this, however, is that these modeling procedures require user input for governing flow relations. Since transition regimes between laminar and turbulent flow are not understood theoretically, there would be no way to instruct these programs on how to behave. As a result, the models would be only as accurate as the user's understanding of the flow behavior, which unfortunately is severely limited.

10.2.3 Materials Characterization

In the development of this active valve device, single-crystal ferroelectric material was the desired material for use due to its enhanced strain capabilities in comparison to the polycrys-

talline PZT-5H material. The published [4] PZN-PT material properties ($d_{33} = 2000pC/N$ and $E_p = 9.01GPa$) used in the design and optimization chapters of this thesis were found to overpredict the actual capability of the material based on the experiments detailed in Chapters 7 and 9. As a result, overall valve deflection versus voltage was lower than designed for. More detailed characterization studies should be performed on this PZN-PT material to better understand its actuation capabilities under the high voltage and relatively high stress conditions experienced in these active valve devices. Additionally, further development efforts by the manufacturers of this material to improve its performance characteristics (and maintain consistency across different batches of material) would enable more reliable design iterations to take place. In general, this valve design desires a piezoelectric material with as large a d_{33} and as large a Young's modulus E_p as possible.

Additionally from a materials standpoint, the reliability of the active valve device and its capabilities for operating against large pressures and with significant valve cap stroke are directly affected by the yield stress levels of the etched silicon membranes that form the valve and the drive piston tethers. Given a value for yield stress (ie: in the design and optimization section of this thesis a value of 1 GPa was used [5]), the systematic design procedure presented in Chapter 5 is able to generate an active valve geometry that guarantees a maximum stress during theoretical operation below this value of yield stress. This assumed limit, therefore, directly influences the resulting size and dimensions of the active valve device. Further work to better characterize this yield stress limit (based on defects in the etched structures) or further work to enhance the strength of these filleted features with possible post DRIE smoothing procedures would enable more compact valve designs that work at higher stress levels.

10.2.4 Microfabrication Issues

From a fabrication and assembly standpoint, this active valve device is far from a cost-effective manufacturable entity, primarily due to the extremely intensive Silicon-on-Insulator wafer DRIE etching steps for Layers 4, 5, and 7. Currently these etch procedures require tight control of fillet radii dimensions at the base of $300 - 400\mu m$ deep etches, a requirement which necessitates numerous human inspection and handling steps. If etch procedures could be developed that minimize the depth of this etch so as to improve fillet radius uniformity across a given valve membrane structure or piston tether, the processing time and human intervention requirements could be drastically reduced. Additionally, the reliabilities of wafer-level silicon-to-silicon fusion bonding and silicon-glass anodic bonding are far from optimal at present. Although improvements in yields on a given wafer have occurred over the course of this MHT program at MIT, further optimization and processing studies could only help to improve wafer yields.

Finally, this active valve device is a 9-layer silicon and glass structure with integrated piezoelectric material elements. A general philosophy is "the fewer number of layers, the better", as

long as each of the reduced layers is not substantially increased in complexity. Efforts should be pursued to redesign this active valve structure to still maintain the required structural elements, yet do so in such a way that eliminates as many layers as possible. A further improvement to the device would be to find a way to create a micro-seal between the hydraulic amplification chamber and the piezoelectric material chamber without the need for solid annular tethered structures. Limitations exist now in the ability to create very deep, thin and smooth gap etches in silicon. If such a thin trench could be micromachined and if a relatively compliant polymer material of some sort could be made to fill that thin gap, then the drive element piston would be capable of moving up and down in response to the piezoelectric material voltage without the need for these micromachined annular tethers. Of course, new problems such as electrical contact to the top surface of the piezoelectric materials and the release of a free-standing piston structure present themselves. Fabrication brainstorming ideas such as these should be continued in an effort to progress to next-generation valve devices.

10.2.5 Future of MHTs

This chapter has reviewed the performance of the active valve and has outlined a series of future activities that could be pursued in an effort to improve its performance. In general, the piezoelectrically-driven hydraulic amplification microvalve documented in this thesis successfully outperforms all liquid-regulation active valves previously presented in the literature (see Chapter 1), in terms of simultaneously satisfying a set of high frequency ($\sim 1kHz$), high pressure ($\sim 300kPa$), and large stroke ($\sim 40\mu m$) requirements. In this sense, the development of the device has been a success. However, the performance limitations observed through device experimentation indicate that, in order for this valve technology to be successful in the designed-for high specific power ($\sim 1000\frac{W}{kg}$) micropumping applications (MHTs) introduced in Chapter 1, significant further research and redesign is required. Even with the current limited active valve capabilities observed in this thesis, however, full MHT micropumping systems incorporating these valves are estimated to operate with specific powers between $25\text{-}30\frac{W}{kg}$, at least an order of magnitude larger than the best micropumping systems ($2.5\frac{W}{kg}$) presented in the literature and detailed in Chapter 1. With this future work, it may be possible to realize an active valve device capable of operating at the desired quasi-static operational frequency ($> 10kHz$) and high differential pressure ($> 1MPa$), enabling it to successfully regulate liquid flow within the higher specific power MHT systems.

As detailed in this chapter, a structural redesign effort should be pursued, incorporating updated finite-element models with inertia coupling and external fluid added mass effects, to achieve a valve design with quasi-static frequency in excess of 10kHz. It is the belief of this author that, by simplifying the hydraulic amplification chamber geometry, increasing the valve membrane thickness, and increasing the piezoelectric material volume beneath the drive element

piston, this frequency enhancement could be readily achieved while maintaining similar stroke capability. However, this guarantees only that the structure can successfully operate as a high-frequency microactuator against a constant external loading. It is the differential pressure applied to the device, and the resulting fluid flow through the valve orifice structure that will most likely limit the flow regulation capability of the structure, as observed in this thesis. The future work to more comprehensively understand the fluid flow regimes through these small scale orifice structures and, more importantly, the interaction of this flow with the adjacent compliant valve membrane structure is, therefore, of vital importance to the success of higher-performing valve devices for use in MHT systems. It is quite possible that by increasing the valve membrane thickness, as discussed in this chapter, the valve flow-induced structural oscillations could be significantly reduced. However, this hypothesis can only be proven through the detailed fluid-structural coupling models and experimental procedures recommended in this chapter. It is, therefore, the belief of this author that this microvalve device can be successfully redesigned to meet the structural high frequency requirements for use in high specific power MHT systems. What is unknown in this stage of the research, however, is the expected nature of fluid-structural interaction and corresponding flow-induced vibrations of the valve cap and membrane at these higher drive frequency levels and higher differential pressures. Future research must address these issues.

Bibliography

- [1] Y.H. Su, K.S. Chen, D.C. Roberts, and S.M. Spearing, "Large Deflection Analysis of a Pre-Stressed Annular Plate With a Rigid Boss Under Axisymmetric Loading," *Journal of Micromech. Microeng.* 11 (2001) pp. 645-653.
- [2] J. Carretero and K.S. Breuer, "Measurement and Modeling of the Flow Characteristics of Micro Disk Valves," Proceedings of the 1994 International Mechanical Engineering Conference and Exposition: Microfluidics Symposium, Orlando, FL, Nov. 2000.
- [3] K.S. Breuer, J.C. Bird, G. Han, and K.J.A. Westin, "Infrared Diagnostics for the measurement of fluid and solid motion in micromachined Devices," Proceedings, ASME IMECE, New York, NY. November 2001.
- [4] S.E. Park and T.R. Shrout, "Characteristics of Relaxor-Based Piezoelectric Single Crystals for Ultrasonic Transducers," *IEEE Trans. Ultrasonics, Ferroelectrics, and Frequency Control*, Vol.44, No.5, Sept. 1997, pp. 1140-1147.
- [5] K.T. Turner, An Evaluation of Critical Issues for Microhydraulic Transducers: Silicon Wafer Bonding, Strength of Silicon on Insulator Membranes and Gold-Tin Solder Bonding. MIT Master's Thesis. June 2001.

Appendix A

Support Documentation for Active Valve Linear Model

A.1 ChapterExample.mws

```

File: ChapterExample.mws
David C. Roberts
This file calculates the linear deflection and swept volume of an annular plate with outer
radius a and inner radius b. There is an applied pressure P from inner radius b to
outer radius a. The plate is guided at r=b and clamped at r=a. This problem is included
in the modeling chapter as a demonstration example of how this linear theory is carried
out. The pressure P serves to deflect the plate in the positive direction. These calculations
include deflections due to bending and shearing effects, since the plate thickness is not
necessarily << than the plate outer radius.
[ > restart;
  > Digits:=40;

```

Digits := 40

Calculate Deflection, Swept Volume Due to BENDING

Define Governing Plate Bending Equation and Shear Force

```

[ > eqn:='diff(1/x*diff(r*diff(w(x),x),x),x)=Q(x)/D';

```

$$eqn := \frac{\partial}{\partial r} r \left(\frac{\partial w(r)}{\partial r} \right) = \frac{Q(r)}{D}$$

```

[ Shear force in terms of P:
  > Q(x) := P*Pi*(x^2-b^2)/(2*Pi*x);

```

$$Q(r) := \frac{1}{2} \frac{P(r^2 - b^2)}{r}$$

Integrate the Governing Plate Bending Equation

```

[ Calculate the deflection, w_bending(r), due to bending:
  > Q1(x) := (int(Q(x)/D,x)+C1)*x;
  > Q2(x) := (int(Q1(x),x)+C2)/x;
  > w_bending(x) := int(Q2(x),x)+C3;

```

$$Q1(r) := \left(\frac{1}{4} \frac{P r^2}{D} - \frac{1}{2} \frac{P b^2 \ln(r)}{D} + C1 \right) r$$

$$Q2(r) := \frac{\frac{1}{16} \frac{P r^4}{D} - \frac{1}{4} \frac{P b^2 r^2 \ln(r)}{D} + \frac{1}{8} \frac{P b^2 r^2}{D} + \frac{1}{2} C1 r^2 + C2}{r}$$

$$w_bending(r) := \frac{1}{64} \frac{P r^4}{D} - \frac{1}{8} \frac{P b^2 r^2 \ln(r)}{D} + \frac{1}{8} \frac{P b^2 r^2}{D} + \frac{1}{4} C1 r^2 + C2 \ln(r) + C3$$

Apply BCs and Solve for W_bending(r)

```

[ > BC1:=subs({r=a},w_bending(x))=0;

```

$$BC1 := \frac{1}{64} \frac{P a^4}{D} - \frac{1}{8} \frac{P b^2 a^2 \ln(a)}{D} + \frac{1}{8} \frac{P b^2 a^2}{D} + \frac{1}{4} C1 a^2 + C2 \ln(a) + C3 = 0$$

```

[ > BC2:=subs({r=a},diff(w_bending(x),x))=0;

```

$$BC2 := \frac{1}{16} \frac{P a^3}{D} - \frac{1}{4} \frac{P b^2 a \ln(a)}{D} + \frac{1}{8} \frac{P b^2 a}{D} + \frac{1}{2} C1 a + \frac{C2}{a} = 0$$

```

[ > BC3:=subs({r=b},diff(w_bending(x),x))=0;

```

$$BC3 := \frac{3}{16} \frac{P b^3}{D} - \frac{1}{4} \frac{P b^3 \ln(b)}{D} + \frac{1}{2} C1 b + \frac{C2}{b} = 0$$

```

[ > Set1:=solve({BC1,BC2,BC3},{C1,C2,C3});
[ Determine the general expression for plate deflection, W_bending(r):
[ > W_bending(x) := collect(subs(Set1,w_bending(x)),{D,P});

```

Page 1

$$W_bending(r) := \left(\left(\frac{1}{64} r^4 - \frac{1}{8} b^2 r^2 \ln(r) + \frac{1}{8} b^2 r^2 - \frac{1}{32} \frac{(-a^4 + 4 b^2 a^2 \ln(a) - 2 b^2 a^2 + 3 b^4 - 4 b^4 \ln(b)) r^2}{-a^2 + b^2} \right. \right. \\ \left. \left. - \frac{1}{16} \frac{b^2 a^2 \left(a^2 - b^2 + 4 b^2 \ln\left(\frac{b}{a}\right) \right) \ln(r)}{-a^2 + b^2} \right. \right. \\ \left. \left. - \frac{1}{64} \frac{a^2 (a^4 - 4 b^2 a^2 \ln(a) - 3 b^2 a^2 + 2 b^4 + 8 b^4 \ln(b) + 16 b^4 \ln(a)^2 - 4 b^4 \ln(a) - 16 b^4 \ln(a) \ln(b))}{-a^2 + b^2} \right) \right) P / D$$

[Determine the plate deflection at r=b. This is denoted Wb_bending.

> Wb_bending:=collect(simplify(subs({r=b},W_bending(r))),{D,P});

$$Wb_bending := -\frac{1}{64} \left(\left(7 b^4 a^2 - 3 b^6 - 4 b^4 \ln(b) a^2 - 5 b^2 a^4 + 4 b^4 a^2 \ln(a) + 4 b^2 a^4 \ln(b) + 16 b^4 a^2 \ln(b) \ln\left(\frac{b}{a}\right) + a^6 \right. \right. \\ \left. \left. - 4 a^4 b^2 \ln(a) + 16 a^2 b^4 \ln(a)^2 - 16 a^2 b^4 \ln(a) \ln(b) \right) \right) P / (D (-a^2 + b^2))$$

Calculate Swept Volume, dV_bending, Due to Bending

[This is the swept volume under only the plate. The swept volume from r=0 to r=b must also be considered.

> dV_bending:=collect(simplify(int(2*Pi*r*W_bending(x),x=b..a)),{Pi,D,P});

$$dV_bending := \frac{1}{192} P \pi \left(-a^8 + 10 a^6 b^2 - 24 a^4 b^4 - 48 a^4 b^4 \ln\left(\frac{b}{a}\right) \ln(a) + 24 a^4 b^4 \ln\left(\frac{b}{a}\right) - 48 a^4 b^4 \ln(a)^2 \right. \\ \left. + 48 a^4 b^4 \ln(a) \ln(b) + 22 b^6 a^2 - 7 b^8 + 48 b^6 a^2 \ln(b) \ln\left(\frac{b}{a}\right) - 24 b^6 a^2 \ln\left(\frac{b}{a}\right) + 48 b^6 a^2 \ln(a)^2 - 48 b^6 a^2 \ln(a) \ln(b) \right) \\ / (D (-a^2 + b^2))$$

Calculate Deflection, Swept Volume Due to SHEARING

Define Governing Plate Shearing Equation and Integrate

> eqn2 := 'diff(w(x),x)=-alpha*Q(x)/G/h';

$$eqn2 := \frac{\partial}{\partial r} w(r) = -\frac{\alpha Q(r)}{G h}$$

[Calculate the deflection, W_shearing, due to shear effects (shear coefficient, alpha=1.5):

> w_shearing(x) := int(-alpha*Q(x)/G/h,x)+C4;

$$w_shearing(r) := -\frac{1}{4} \frac{\alpha P r^2}{G h} + \frac{1}{2} \frac{\alpha P b^2 \ln(r)}{G h} + C4$$

Apply BC and Solve for W_shearing(r)

> BC4:=subs({r=a},w_shearing(x))=0;

$$BC4 := -\frac{1}{4} \frac{\alpha P a^2}{G h} + \frac{1}{2} \frac{\alpha P b^2 \ln(a)}{G h} + C4 = 0$$

> Set2:=solve({BC4},{C4});

> W_shearing(x) :=subs(Set2,w_shearing(x));

$$W_shearing(r) := -\frac{1}{4} \frac{\alpha P r^2}{G h} + \frac{1}{2} \frac{\alpha P b^2 \ln(r)}{G h} - \frac{1}{4} \frac{\alpha P (-a^2 + 2 b^2 \ln(a))}{G h}$$

[Determine the plate deflection at r=b. This is denoted Wb_shearing.

> Wb_shearing:=collect(simplify(subs({r=b},W_shearing(x))),{P});

$$Wb_shearing := -\frac{1}{4} \frac{\alpha P (b^2 - 2 b^2 \ln(b) - a^2 + 2 b^2 \ln(a))}{G h}$$

Calculate Swept Volume Due to Shearing, dV_shearing

```
> dV_shearing:=collect(simplify(int(2*Pi*r*W_shearing(r),r=b..a)),{P});
dV_shearing:=
$$\frac{1}{8} \frac{\pi \alpha P (a^4 - 4 b^2 a^2 + 3 b^4 - 4 b^4 \ln(b) + 4 b^4 \ln(a))}{G h}$$

```

Total Deflection and Swept Volume

```
Sum the deflections due to bending and shear into the total plate deflection at r=b, Wb:
> Wb:=collect(Wb_bending + Wb_shearing, {P});
Wb:=
$$\left( -\frac{1}{64} \left( 7 b^4 a^2 - 3 b^6 - 4 b^4 \ln(b) a^2 - 5 b^2 a^4 + 4 b^4 a^2 \ln(a) + 4 b^2 a^4 \ln(b) + 16 b^4 a^2 \ln(b) \ln\left(\frac{b}{a}\right) + a^6 \right. \right. \\ \left. \left. - 4 a^4 b^2 \ln(a) + 16 a^2 b^4 \ln(a)^2 - 16 a^2 b^4 \ln(a) \ln(b) \right) / (D (-a^2 + b^2)) - \frac{1}{4} \frac{\alpha (b^2 - 2 b^2 \ln(b) - a^2 + 2 b^2 \ln(a))}{G h} \right) P$$

Sum the displaced volumes due to bending and shear into the total displaced volume, dV:
> dV:=collect(dV_bending+dV_shearing, {P});
dV:=
$$\left( \frac{1}{192} \pi \left( -a^8 + 10 a^6 b^2 - 24 a^4 b^4 - 48 a^4 b^4 \ln\left(\frac{b}{a}\right) \ln(a) + 24 a^4 b^4 \ln\left(\frac{b}{a}\right) - 48 a^4 b^4 \ln(a)^2 + 48 a^4 b^4 \ln(a) \ln(b) \right. \right. \\ \left. \left. + 22 b^6 a^2 - 7 b^8 + 48 b^6 a^2 \ln(b) \ln\left(\frac{b}{a}\right) - 24 b^6 a^2 \ln\left(\frac{b}{a}\right) + 48 b^6 a^2 \ln(a)^2 - 48 b^6 a^2 \ln(a) \ln(b) \right) / (D (-a^2 + b^2)) \right. \\ \left. + \frac{1}{8} \frac{\pi \alpha (a^4 - 4 b^2 a^2 + 3 b^4 - 4 b^4 \ln(b) + 4 b^4 \ln(a))}{G h} \right) P$$

```

Substitution of Example Values

```
> Wb_EXAMPLE:=evalf(subs({alpha=1.5, a=3.15e-3, b=0.80e-3, E=165e9, nu=0.22, h=1000e-6}, subs(
P=1e6, D=E*h^3/(12*(1-nu^2)), G=E/2/(1+nu), Wb)));
Wb_EXAMPLE := .986574732573098211629339004226204575890 10-7
> dV_EXAMPLE:=evalf(subs({alpha=1.5, a=3.15e-3, b=0.80e-3, E=165e9, nu=0.22, h=1000e-6}, subs(
P=1e6, D=E*h^3/(12*(1-nu^2)), G=E/2/(1+nu), dV)));
dV_EXAMPLE := .1320442285992528857571432424955844654522 10-11
```

A.2 FullActiveValve(LINEAR).mws [see Section 2.4]

```

File: FullActiveValve(LINEAR).mws
David C. Roberts
This file solves the linear valve analytical model described in Chapter 2 of thesis. The inputs are P1, P2, and Vp.
The valve behavior is calculated.
> restart;
> digits:=40;

```

Digits := 40

Step 1: Define Linear Quasi-Static Relations

Piezoelectric Material

[This relation assumes perfect d33 actuation (no effect of transverse clamping).
> EQN1 := Z[p] = d{33}*V[p] - (L[p]/E[p])*T[p];

$$EQN1 := Z_p = d_{33} V_p - \frac{L_p T_p}{E_p}$$

[This relation determines the piezo charge.
> EQN2 := Q[p] = (eT{33}*A[p]/L[p])*V[p] + (d{33}*A[p])*T[p];

$$EQN2 := Q_p = \frac{eT_{33} A_p V_p}{L_p} + d_{33} A_p T_p$$

Bottom Structural Compliance

[Circular plate with stress imposed over central region.
> EQN3 := Z[bot] = (Xi[Zbot,T]) * T[p];

$$EQN3 := Z_{bot} = \Xi_{Zbot, T} T_p$$

Drive Element Tethers

> EQN4 := Z[te] =
(Xi[Zttop,F]*Xi[Ztbot,F]) / (Xi[Zttop,F]+Xi[Ztbot,F]) * (A[p]*T[p]-A[piis]*P[HAC]) -
(Xi[Zttop,P]*Xi[Ztbot,P]) / (Xi[Zttop,P]+Xi[Ztbot,P]) * P[HAC];

$$EQN4 := Z_{te} = \frac{\Xi_{Zttop, F} \Xi_{Ztbot, F} (A_p T_p - A_{pis} P_{HAC})}{\Xi_{Zttop, F} + \Xi_{Ztbot, F}} - \frac{\Xi_{Zttop, P} \Xi_{Ztbot, P} P_{HAC}}{\Xi_{Zttop, P} + \Xi_{Ztbot, P}}$$

> EQN5 := dV[te] =
(Xi[dVttop,F]*Xi[Ztbot,F]) / (Xi[Zttop,F]+Xi[Ztbot,F]) * (A[p]*T[p]-A[piis]*P[HAC]) -
(Xi[dVttop,P]*Xi[dVtbot,P]) / (Xi[dVttop,P]+Xi[dVtbot,P]) * P[HAC] + A[piis]*Z[te];

$$EQN5 := dV_{te} = \frac{\Xi_{dVttop, F} \Xi_{Ztbot, F} (A_p T_p - A_{pis} P_{HAC})}{\Xi_{Zttop, F} + \Xi_{Ztbot, F}} - \frac{\Xi_{dVttop, P} \Xi_{dVtbot, P} P_{HAC}}{\Xi_{dVttop, P} + \Xi_{dVtbot, P}} + A_{pis} Z_{te}$$

Drive Element Piston

> EQN6 := Z[piis] = Xi[Zpis,T]*T[p] - Xi[Zpis,P]*P[HAC];

$$EQN6 := Z_{pis} = \Xi_{Zpis, T} T_p - \Xi_{Zpis, P} P_{HAC}$$

> EQN7 := dV[piis] = Xi[dVpis,T]*T[p] - Xi[dVpis,P]*P[HAC];

$$EQN7 := dV_{pis} = \Xi_{dVpis, T} T_p - \Xi_{dVpis, P} P_{HAC}$$

Fluid Compressibility

> EQN8 := dV[fluid] = -(V[HAC]/K[l])*P[HAC];

Page 1

$$EQN8 := dV_{fluid} = -\frac{V_{HAC} P_{HAC}}{K_f}$$

Top Structural Compliance

```

> EQN9 := Z[top] = Xi[Ztop,P]*P[HAC] + Xi[Ztop,F]*F[vm];
EQN9 := Z_top = Xi_top,P * P_HAC + Xi_top,F * F_vm
> EQN10 := dV[top] = Xi[dVtop,P]*P[HAC] + Xi[dVtop,F]*F[vm] + A[vm]*Z[top];
EQN10 := dV_top = Xi_top,P * P_HAC + Xi_top,F * F_vm + A_vm * Z_top
> EQN11 := F[vm] = (A[vm]-A[vc])*(P[HAC]-P[2]) + A[vc]*(P[HAC]-P[1]);
EQN11 := F_vm = (A_vm - A_vc) * (P_HAC - P_2) + A_vc * (P_HAC - P_1)

```

Valve Cap/Membrane

[Note: I have included the contribution to valve cap deflection due to top chamber deflection. The corresponding volume contribution is already included in the Top Structural Compliance section.

```

> EQN12 := Z[vc] = Xi[Zvc,P]*(P[HAC]-P[2]) + Xi[Zvc,F]*F[vc] + Z[top];
EQN12 := Z_vc = Xi_vc,P * (P_HAC - P_2) + Xi_vc,F * F_vc + Z_top
> EQN13 := dV[vm] = Xi[dVvm,P]*(P[HAC]-P[2]) + Xi[dVvm,F]*F[vc] + A[vc]*Z[vc];
EQN13 := dV_vm = Xi_top,P * (P_HAC - P_2) + Xi_top,F * F_vc + A_vc * Z_vc
> EQN14 := F[vc] = (P[HAC]-P[1])*A[vc];
EQN14 := F_vc = A_vc * (P_HAC - P_1)

```

Deflection, Swept Volume Conservation

[All structural deflections and swept volumes are defined to be positive in the upward direction.

```

> EQN15 := Z[p] + Z[bot] = Z[te] + Z[pis];
EQN15 := Z_p + Z_bot = Z_te + Z_pis
> EQN16 := 0 = dV[te] + dV[pis] + dV[fluid] - dV[top] - dV[vm];
EQN16 := 0 = dV_te + dV_pis + dV_fluid - dV_top - dV_vm

```

Other Relations

[Variables as functions of other variables.

```

> EQN17 := Z[de] = Z[te] + Z[pis];
EQN17 := Z_de = Z_te + Z_pis

```

Step 2: Define Geometric/Material Parameters

```

[ Geometric Parameters:
> R[vc]:=0.31e-3; R[vm]:=0.80e-3; t[vm]:=10e-6; A[vc]:=Pi*R[vc]^2; A[vm]:=Pi*R[vm]^2;
t[vc]:=400e-6;
> L[p]:=1e-3; R[p]:=1e-3; A[p]:=Pi*R[p]^2;
> R[pis]:=3e-3; R[ch]:=3.225e-3; t[pis]:=800e-6; t[topte]:=10e-6; t[botte]:=10e-6;
A[pis]:=Pi*R[pis]^2;
> t[bot]:=1000e-6;
> H[HAC]:=400e-6; V[HAC]:=Pi*R[ch]^2*B[HAC] + Pi*(R[vm]^2-R[vc]^2)*t[vc];
> t[top]:=1000e-6;
[ Material Parameters:

```

```
[ > d[33]:=2000e-12: sD[33]:=16.4e-12: sE[33]:=111e-12: E[p]:=1/sE[33]:
eT[33]:=d[33]^2/(sE[33]-sD[33]): E[s1]:=165e9: nu[s1]:=0.22: K[f]:=2e9: alpha[s1]:=1.25:
```

Step 3: Calculate Linear Plate Coefficients

Bottom Structural Compliance

```
[ Circular plate clamped at outer radius (r=a) with stress imposed over central region (r=0 to r=b).
Positive deflection is upward, whereas positive stress acts downward. This relation includes
bending and shearing effects, see BottomChamberPlate(WORST).mws.
[ > eqn:='diff(1/r*diff(r*diff(Z(x),r),r),r)=Q(x)/D':
[ > Q_0b(x):=-Tp*Pi*x^2/(2*Pi*x):
[ > Q1(x):=(int(Q_0b(x)/D,x)+C1)*x:
Q2(x):=(int(Q1(x),x))/x:
Zbot_0b_bending(x):=int(Q2(x),x)+C3:
[ > BC1:=subs({r=b},Zbot_0b_bending(x))=Zb_bending:
[ > BC2:=subs({r=b},diff(Zbot_0b_bending(x),r))=dZb_bending:
[ > BC3:=subs({r=b},diff(diff(Zbot_0b_bending(x),r),r) +
nu/r*diff(Zbot_0b_bending(x),r))=d2Zb_bending:
[ > eqn:='diff(1/r*diff(r*diff(Z(x),r),r),r)=Q(x)/D':
[ > Q_ba(x):=-Tp*Pi*b^2/(2*Pi*x):
[ > Q1(x):=(int(Q_ba(x)/D,x)+C4)*x:
Q2(x):=(int(Q1(x),x)+C5)/x:
Zbot_ba_bending(x):=int(Q2(x),x)+C6:
[ > BC4:=subs({r=a},Zbot_ba_bending(x))=0:
[ > BC5:=subs({r=a},diff(Zbot_ba_bending(x),r))=0:
[ > BC6:=subs({r=b},Zbot_ba_bending(x))=Zb_bending:
[ > BC7:=subs({r=b},diff(Zbot_ba_bending(x),r))=dZb_bending:
[ > BC8:=subs({r=b},diff(diff(Zbot_ba_bending(x),r),r) +
nu/r*diff(Zbot_ba_bending(x),r))=d2Zb_bending:
[ > Set1:=solve({BC1,BC2,BC3,BC4,BC5,BC6,BC7,BC8},{C1,C3,C4,C5,C6,Zb_bending,dZb_bending,d
2Zb_bending}):
[ > Zbot_0b_BENDING(x):=collect(subs(Set1,Zbot_0b_bending(x)),{D,Tp}):
[ > Zbot_ba_BENDING(x):=collect(subs(Set1,Zbot_ba_bending(x)),{D,P}):
[ > dVbot_0b_BENDING:=collect(simplify(int(2*Pi*r*Zbot_0b_BENDING(x),r=0..b)),{Tp}):
[ > dVbot_ba_BENDING:=collect(simplify(int(2*Pi*r*Zbot_ba_BENDING(x),r=b..a)),{Tp}):
[ > eqn4:='diff(Z(x),r)=-alpha*Q(x)/G/h':
[ > Zbot_0b_shearing(x):=int(-alpha*Q_0b(x)/G/h,x)+C7:
[ > BC9:=subs({r=b},Zbot_0b_shearing(x))=Zb_shearing:
[ > eqn4:='diff(Z(x),r)=-alpha*Q(x)/G/h':
[ > Zbot_ba_shearing(x):=int(-alpha*Q_ba(x)/G/h,x)+C8:
[ > BC10:=subs({r=a},Zbot_ba_shearing(x))=0:
[ > BC11:=subs({r=b},Zbot_ba_shearing(x))=Zb_shearing:
[ > Set2:=solve({BC9,BC10,BC11},{C7,C8,Zb_shearing}):
[ > Zbot_0b_SHEARING(x):=collect(subs(Set2,Zbot_0b_shearing(x)),{D,Tp}):
[ > Zbot_ba_SHEARING(x):=collect(subs(Set2,Zbot_ba_shearing(x)),{D,Tp}):
```

Page 3

```

[ > dVbot_0b_SHEARING:=collect(simplify(int(2*Pi*r*Zbot_0b_SHEARING(x),x=0..b)),{Tp}):
[ > dVbot_ba_SHEARING:=collect(simplify(int(2*Pi*r*Zbot_ba_SHEARING(x),x=b..a)),{Tp}):
[ > Zbot_0b(x):=collect(Zbot_0b_BENDING(x) + Zbot_0b_SHEARING(x),{Tp}):
[ > Zbot_ba(x):=collect(Zbot_ba_BENDING(x) + Zbot_ba_SHEARING(x),{Tp}):
[ > dVbot:=collect(dVbot_0b_BENDING + dVbot_ba_BENDING + dVbot_0b_SHEARING +
dVbot_ba_SHEARING,{Tp}):
[ > Xi[Zbot,T]:=subs({r=0,Tp=1},Zbot_0b(x));
Xi[Zbot,T]:=evalf(subs({a=R[ch],b=R[p],alpha=alpha[si],h=t[bot],D=E[si]*t[bot]^3/(12*(
1-nu[si]^2)),G=E[si]/(2*(1+nu[si]))},Xi[Zbot,T]));

```

$$\Xi_{Zbot,T} := -\frac{1}{64} \frac{b^2 \left(-3b^2 + 4a^2 + 4b^2 \ln\left(\frac{b}{a}\right) \right)}{D} - \frac{1}{4} \frac{\alpha b^2 (1 - 2 \ln(b) + 2 \ln(a))}{G h}$$

$$\Xi_{Zbot,T} := -.5212199372749083675326231687472284135238 \cdot 10^{-13}$$

Drive Element Tethers

```

TOP TETHER
Annular plate clamped at outer radius (r=a) and guided at inner radius (r=b) with pressure applied
downward over tether and concentrated force applied upward at inner radius (r=b). These relations
include bending effects only, see TetherTop2.mws.
[ > eqn:=diff(1/r*diff(r*diff(Z(x),x),x),x)=Q(x)/D':
[ > Q(x):=F[topte]/(2*Pi*r) - PHAC*Pi*(r^2-b^2)/(2*Pi*r):
[ > Q1(x):=(int(Q(x)/D,x)+C1)*r:
Q2(x):=(int(Q1(x),x)+C2)/x:
Ztether1_bending(x):=expand(int(Q2(x),x)+C3):
[ > BC1:=subs({r=a},Ztether1_bending(x))=0:
[ > BC2:=subs({r=a},diff(Ztether1_bending(x),x))=0:
[ > BC3:=subs({r=b},diff(Ztether1_bending(x),x))=0:
[ > Set1:=solve({BC1,BC2,BC3},{C1,C2,C3}):
[ > Ztether1_BENDING(x):=collect(subs(Set1,Ztether1_bending(x)),{F[topte],D,PHAC}):
[ > Ztether1:=collect(simplify(subs({r=b},Ztether1_BENDING(x)),{F[topte],D,PHAC}):
[ > dVtether1_BENDING:=collect(simplify(int(2*Pi*r*Ztether1_BENDING(x),x=b..a)),{Pi,F[topt
e],D,PHAC}):
[ > Xi[Ztetop,F]:=subs({PHAC=0,F[topte]=1},Ztether1):
Xi[Ztetop,F]:=evalf(subs({a=R[ch],b=R[pi],h=t[topte],D=E[si]*t[topte]^3/(12*(1-nu[si]
^2)),Xi[Ztetop,F]));

```

$$\Xi_{Ztetop,F} := -\frac{1}{64} \frac{8b^2a^2 - 4b^4 + 16b^2a^2 \ln\left(\frac{b}{a}\right) \ln(b) - 4a^4 + 16a^2 \ln(a)^2 b^2 - 16a^2 \ln(a) b^2 \ln(b)}{\pi(a^2 - b^2) D}$$

$$\Xi_{Ztetop,F} := .3358560090822692575226480248142747504821 \cdot 10^{-5}$$

```

[ > Xi[Ztetop,P]:=-subs({PHAC=1,F[topte]=0},Ztether1);
Xi[Ztetop,P]:=evalf(subs({a=R[ch],b=R[pi],h=t[topte],D=E[si]*t[topte]^3/(12*(1-nu[si]
^2)),Xi[Ztetop,P]));

```

$$\Xi_{Ztetop,P} := \frac{1}{64} \left(7\pi b^4 a^2 - 3\pi b^6 - 5\pi a^4 b^2 + 4\pi b^4 a^2 \ln(a) - 4\pi b^4 \ln(b) a^2 + 4\pi b^2 a^4 \ln(b) + 16\pi b^4 a^2 \ln(b) \ln\left(\frac{b}{a}\right) \right)$$

```

+ pi*a^4 - 4*pi*a^2*b^2*ln(a) + 16*pi*a^2*ln(a)^2*b^4 - 16*pi*a^2*ln(a)*b^4*ln(b) ) / (pi*(a^2 - b^2)*D)
Xi[dVttop,F] := .7246716855091782654098385470407258607940 10^11
Xi[dVttop,F] := subs({PHAC=0,F[topote]=1,dVtether1_BENDING);
Xi[dVttop,F] := evalf(subs({a=R[ch],b=R[pi],h=t[topote],D=E[si]*t[topote]^3/(12*(1-nu[si]^2))},Xi[dVttop,F]));
Xi[dVttop,F] := -1/192*(-12*b^4*ln(b)^2 + 24*b^4*a^2*ln(b/a) - 3*a^6 + 12*a^4*b^2*ln(b) - 12*a^4*b^2*ln(a) - 24*a^4*b^2*ln(b/a)
+ 48*a^4*ln(a)^2*b^2 + 48*a^4*b^2*ln(b/a)*ln(a) - 48*a^4*ln(a)*b^2*ln(b) + 15*a^4*b^2 + 48*a^2*ln(a)*b^4*ln(b) - 48*b^4*a^2*ln(b/a)*ln(b)
- 48*a^2*ln(a)^2*b^4 - 21*b^4*a^2 + 12*b^4*a^2*ln(a) + 9*b^6) / ((a^2 - b^2)*D)
Xi[dVttop,F] := .7246716855091782654098385470406784 10^11
Xi[dVttop,F] := -subs({PHAC=1,F[topote]=0,dVtether1_BENDING);
Xi[dVttop,F] := evalf(subs({a=R[ch],b=R[pi],h=t[topote],D=E[si]*t[topote]^3/(12*(1-nu[si]^2))},Xi[dVttop,F]));
Xi[dVttop,F] := 1/192*((24*b^6*a^2*ln(b/a) + a^8 - 48*a^4*ln(a)*b^4*ln(b) + 48*a^4*b^4*ln(b/a)*ln(a) + 48*a^4*ln(a)^2*b^4 - 24*a^4*b^4*ln(b/a)
+ 24*a^4*b^4 - 10*a^6*b^2 - 48*b^6*a^2*ln(b/a)*ln(b) - 48*a^2*ln(a)^2*b^6 + 48*a^2*ln(a)*b^6*ln(b) + 7*b^6 - 22*b^6*a^2)*pi) / (
(a^2 - b^2)*D)
Xi[dVttop,F] := .1672014327695025501669898411677512555127 10^16
BOTTOM TETHER
Annular plate clamped at outer radius (r=a) and guided at inner radius (r=b) with concentrated
force applied upward at inner radius (r=b) and pressure over annulus. These relations include
bending effects only, see TetherBottom3.mws.
[ > eqn:=diff(1/r*diff(x*diff(Z(x),x),x),x)=Q(x)/D':
[ > Q(x):=F[botte]/(2*pi*x) - PHAC*pi*(x^2-b^2)/(2*pi*x):
[ > Q1(x):=(int(Q(x)/D,x)+C1)*x:
[ > Q2(x):=(int(Q1(x),x)+C2)/x:
[ > Ztether2_bending(x):=expand(int(Q2(x),x)+C3):
[ > BC1:=subs({r=a},Ztether2_bending(x))=0:
[ > BC2:=subs({r=a},diff(Ztether2_bending(x),x))=0:
[ > BC3:=subs({r=b},diff(Ztether2_bending(x),x))=0:
[ > Set1:=solve({BC1,BC2,BC3},{C1,C2,C3}):
[ > Ztether2_BENDING(x):=collect(subs(Set1,Ztether2_bending(x)),{F[botte],D,PHAC}):
[ > Ztether2:=collect(simplify(subs({r=b},Ztether2_BENDING(x)),{F[botte],D,PHAC}):
[ > dVtether2_BENDING:=collect(simplify(int(2*pi*x*Ztether2_BENDING(x),x=b..a)),{pi,F[botte],D,PHAC}):
[ > Xi[Ztbot,F] := subs({PHAC=0,F[botte]=1,Ztether2):
Xi[Ztbot,F] := evalf(subs({a=R[ch],b=R[pi],h=t[botte],D=E[si]*t[botte]^3/(12*(1-nu[si]^2))},Xi[Ztbot,F]));

```

```

Xi [Ztebot, P] := -1/64 * (8*b^2*a^2 - 4*b^4 + 16*b^2*a^2*ln(b/a) * ln(b) - 4*a^4 + 16*a^2*ln(a)^2*b^2 - 16*a^2*ln(a)*b^2*ln(b)) / (pi*(a^2 - b^2)*D)
Xi [Ztebot, P] := .3358560090822692575226480248142747504821 10^5
> Xi [Ztebot, P] := -subs ({PHAC=1, F[botte]=0, Ztether2});
Xi [Ztebot, P] := evalf (subs ({a=R[ch], b=R[pi], h=t[botte], D=E[si]*t[botte]^3/(12*(1-nu[si]^2))}, Xi [Ztebot, P]));
Xi [dVtebot, P] := 1/64 * (7*pi*b^4*a^2 - 3*pi*b^6 - 5*pi*a^4*b^2 + 4*pi*b^4*a^2*ln(a) - 4*pi*b^4*ln(b)*a^2 + 4*pi*b^2*a^4*ln(b) + 16*pi*b^4*a^2*ln(b)*ln(b/a) + pi*a^6 - 4*pi*a^4*b^2*ln(a) + 16*pi*a^2*ln(a)^2*b^4 - 16*pi*a^2*ln(a)*b^4*ln(b)) / (pi*(a^2 - b^2)*D)
Xi [dVtebot, P] := .7246716855091782654098385470407258607940 10^11
> Xi [dVtebot, P] := subs ({PHAC=0, F[botte]=1, dVtether2_BENDING});
Xi [dVtebot, P] := evalf (subs ({a=R[ch], b=R[pi], h=t[botte], D=E[si]*t[botte]^3/(12*(1-nu[si]^2))}, Xi [dVtebot, P]));
Xi [dVtebot, P] := -1/192 * (-12*b^4*ln(b)*a^2 + 24*b^4*a^2*ln(b/a) - 3*a^6 + 12*a^4*b^2*ln(b) - 12*a^4*b^2*ln(a) - 24*a^4*b^2*ln(b/a) + 48*a^4*ln(a)^2*b^2 + 48*a^4*b^2*ln(b/a)*ln(a) - 48*a^4*ln(a)*b^2*ln(b) + 15*a^4*b^2 + 48*a^2*ln(a)*b^4*ln(b) - 48*b^4*a^2*ln(b/a)*ln(b) - 48*a^2*ln(a)^2*b^4 - 21*b^4*a^2 + 12*b^4*a^2*ln(a) + 9*b^6) / ((a^2 - b^2)*D)
Xi [dVtebot, P] := .7246716855091782654098385470406784 10^11
> Xi [dVtebot, P] := -subs ({PHAC=1, F[botte]=0, dVtether2_BENDING});
Xi [dVtebot, P] := evalf (subs ({a=R[ch], b=R[pi], h=t[botte], D=E[si]*t[botte]^3/(12*(1-nu[si]^2))}, Xi [dVtebot, P]));
Xi [dVtebot, P] := 1/192 * (24*b^6*a^2*ln(b/a) + a^8 - 48*a^4*ln(a)*b^4*ln(b) + 48*a^4*b^4*ln(b/a)*ln(a) + 48*a^4*ln(a)^2*b^4 - 24*a^4*b^4*ln(b/a) + 24*a^4*b^4 - 10*a^6*b^2 - 48*b^6*a^2*ln(b/a)*ln(b) - 48*a^2*ln(a)^2*b^6 + 48*a^2*ln(a)*b^6*ln(b) + 7*b^8 - 22*b^6*a^2) / ((a^2 - b^2)*D)
Xi [dVtebot, P] := .1672014327695025501669898411677512555127 10^16

```

Drive Element Piston (More Compliant: Hinged Outer Circumference)

Circular plate hinged at outer radius (r=a) with pressure acting downward over entire plate (from r=0 to r=a) and stress acting upward in central region (from r=0 to r=b). Positive plate deflection is defined in the upward direction. These relations include bending and shearing effects, see Piston(WORST).mws.

```

> eqn := 'diff(1/x*diff(x*diff(Z(x), x), x), x) = Q(x)/D':
> Q_0b(x) := (Tp-PHAC)*Pi*r^2/(2*Pi*r):
> Q1(x) := (int(Q_0b(x)/D, x) + C1)*r:
Q2(x) := (int(Q1(x), x)):
Zpis_0b_bending(x) := int(Q2(x), x) + C3:
> BC1 := subs ({x=b}, Zpis_0b_bending(x)) = Zb_bending:
> BC2 := subs ({x=b}, diff(Zpis_0b_bending(x), x)) = dZb_bending:
> BC3 := subs ({x=b}, diff(diff(Zpis_0b_bending(x), x), x) +

```



```

[ nu/x*diff(Zpis_0b_bending(x),x)=d2Zb_bending:
[ > eqn:=diff(1/x*diff(x*diff(Z(x),x),x),x)=Q(x)/D':
[ > Q_ba(x):=Tp*Pi*b^2/(2*Pi*x) - PHAC*Pi*x^2/(2*Pi*x):
[ > Q1(x):=(int(Q_ba(x)/D,x)+C4)*x:
[ > Q2(x):=(int(Q1(x),x)+C5)/x:
[ > Zpis_ba_bending(x):=int(Q2(x),x)+C6:
[ > BC4:=subs({x=a},Zpis_ba_bending(x))=0:
[ > BC5:=subs({x=a},diff(diff(Zpis_ba_bending(x),x),x) +
nu/x*diff(Zpis_ba_bending(x),x))=0:
[ > BC6:=subs({x=b},Zpis_ba_bending(x))=Eb_bending:
[ > BC7:=subs({x=b},diff(Zpis_ba_bending(x),x))=dZb_bending:
[ > BC8:=subs({x=b},diff(diff(Zpis_ba_bending(x),x),x) +
nu/x*diff(Zpis_ba_bending(x),x))=d2Zb_bending:
[ > Set1:=solve({BC1,BC2,BC3,BC4,BC5,BC6,BC7,BC8},{C1,C3,C4,C5,C6,Zb_bending,dZb_bending,
d2Zb_bending}):
[ > Zpis_0b_BENDING(x):=collect(subs(Set1,Zpis_0b_bending(x)},{D,Tp,PHAC}):
[ > Zpis_ba_BENDING(x):=collect(subs(Set1,Zpis_ba_bending(x)},{D,Tp,PHAC}):
[ > dVpis_0b_BENDING:=collect(simplify(int(2*Pi*x*Zpis_0b_BENDING(x),x=0..b)},{Tp,PHAC}):
[ > dVpis_ba_BENDING:=collect(simplify(int(2*Pi*x*Zpis_ba_BENDING(x),x=b..a)},{Tp,PHAC}):
[ > eqn4:=diff(Z(x),x)=-alpha*Q(x)/G/h':
[ > Zpis_0b_shearing(x):=int(-alpha*Q_0b(x)/G/h,x)+C7:
[ > BC9:=subs({x=b},Zpis_0b_shearing(x))=Zb_shearing:
[ > eqn4:=diff(Z(x),x)=-alpha*Q(x)/G/h':
[ > Zpis_ba_shearing(x):=int(-alpha*Q_ba(x)/G/h,x)+C8:
[ > BC10:=subs({x=a},Zpis_ba_shearing(x))=0:
[ > BC11:=subs({x=b},Zpis_ba_shearing(x))=Zb_shearing:
[ > Set2:=solve({BC9,BC10,BC11},{C7,C8,Zb_shearing}):
[ > Zpis_0b_SHEARING(x):=collect(subs(Set2,Zpis_0b_shearing(x)},{D,Tp,PHAC}):
[ > Zpis_ba_SHEARING(x):=collect(subs(Set2,Zpis_ba_shearing(x)},{D,Tp,PHAC}):
[ > dVpis_0b_SHEARING:=collect(simplify(int(2*Pi*x*Zpis_0b_SHEARING(x),x=0..b)},{Tp,PHAC}):
[ > dVpis_ba_SHEARING:=collect(simplify(int(2*Pi*x*Zpis_ba_SHEARING(x),x=b..a)},{Tp,PHAC}):
[ > Zpis_0b(x):=collect(Zpis_0b_BENDING(x) + Zpis_0b_SHEARING(x)},{Tp,PHAC}):
[ > Zpis_ba(x):=collect(Zpis_ba_BENDING(x) + Zpis_ba_SHEARING(x)},{Tp,PHAC}):
[ > Zpis_0:=subs({x=0},collect(Zpis_0b_BENDING(x) + Zpis_0b_SHEARING(x)},{Tp,PHAC})):
[ > dVpist:=collect(simplify(dVpis_0b_BENDING + dVpis_ba_BENDING + dVpis_0b_SHEARING +
dVpis_ba_SHEARING)},{Tp,PHAC}):
[ > Xil[Zpis,T] := subs({PHAC=0,Tp=1},Zpis_0);
Xil[Zpis,T]:=evalf(subs({a=R[pi],b=R[p],nu=nu[si],alpha=alpha[si],h=t[pi],D=E[si]*t[
pi]^3/(12*(1-nu[si]^2)),G=E[si]/(2*(1+nu[si]))},Xil[Zpis,T]));
Xi1_Zpis_T:=1/64 * (-7*b^4 + 12*b^2*a^2 + 4*v*b^2*a^2 - 3*v*b^4 + 4*ln(b/a)*b^4 + 4*ln(b/a)*v*b^4) / ((1+v)*D) - 1/4 * alpha*(-b^2 + 2*b^2*ln(b) - 2*ln(a)*b^2) / G*h

```



```

[ > BC5:=subs({r=a},diff(Zpis_ba_bending(x),x))=0:
[ > BC6:=subs({r=b},Zpis_ba_bending(x))=Zb_bending:
[ > BC7:=subs({r=b},diff(Zpis_ba_bending(x),x))=dZb_bending:
[ > BC8:=subs({r=b},diff(diff(Zpis_ba_bending(x),x),x) +
nu/x*diff(Zpis_ba_bending(x),x))=d2Zb_bending:
[ > Set1:=solve({BC1,BC2,BC3,BC4,BC5,BC6,BC7,BC8},{C1,C3,C4,C5,C6,Zb_bending,dZb_bending,d
2Zb_bending}):
[ > Zpis_0b_BENDING(x):=collect(subs(Set1,Zpis_0b_bending(x)),{D,Tp,PHAC}):
[ > Zpis_ba_BENDING(x):=collect(subs(Set1,Zpis_ba_bending(x)),{D,Tp,PHAC}):
[ > dVpis_0b_BENDING:=collect(simplify(int(2*Pi*x*Zpis_0b_BENDING(x),r=0..b)),{Tp,PHAC}):
[ > dVpis_ba_BENDING:=collect(simplify(int(2*Pi*x*Zpis_ba_BENDING(x),r=b..a)),{Tp,PHAC}):
[ > eqn4:='diff(Z(x),x)=-alpha*Q(x)/G/h':
[ > Zpis_0b_shearing(x):=int(-alpha*Q_0b(x)/G/h,x)+C7:
[ > BC9:=subs({r=b},Zpis_0b_shearing(x))=Zb_shearing:
[ > eqn4:='diff(Z(x),x)=-alpha*Q(x)/G/h':
[ > Zpis_ba_shearing(x):=int(-alpha*Q_ba(x)/G/h,x)+C8:
[ > BC10:=subs({r=a},Zpis_ba_shearing(x))=0:
[ > BC11:=subs({r=b},Zpis_ba_shearing(x))=Zb_shearing:
[ > Set2:=solve({BC9,BC10,BC11},{C7,C8,Zb_shearing}):
[ > Zpis_0b_SHEARING(x):=collect(subs(Set2,Zpis_0b_shearing(x)),{D,Tp,PHAC}):
[ > Zpis_ba_SHEARING(x):=collect(subs(Set2,Zpis_ba_shearing(x)),{D,Tp,PHAC}):
[ > dVpis_0b_SHEARING:=collect(simplify(int(2*Pi*r*Zpis_0b_SHEARING(x),r=0..b)),{Tp,PHAC}):
:
[ > dVpis_ba_SHEARING:=collect(simplify(int(2*Pi*r*Zpis_ba_SHEARING(x),r=b..a)),{Tp,PHAC}):
:
[ > Zpis_0b(r):=collect(Zpis_0b_BENDING(x) + Zpis_0b_SHEARING(x),{Tp,PHAC}):
[ > Zpis_ba(r):=collect(Zpis_ba_BENDING(x) + Zpis_ba_SHEARING(x),{Tp,PHAC}):
[ > Zpis_0:=subs({r=0},collect(Zpis_0b_BENDING(x) + Zpis_0b_SHEARING(x),{Tp,PHAC})):
[ > dVpist:=collect(simplify(dVpis_0b_BENDING + dVpis_ba_BENDING + dVpis_0b_SHEARING +
dVpis_ba_SHEARING),{Tp,PHAC}):
[ > Xi2[Zpis,T] := subs({PHAC=0,Tp=1},Zpis_0);
Xi2[Zpis,T]:=evalf(subs({a=R[pi],b=R[p],nu=nu[si],alpha=alpha[si],h=t[pi],D=E[si]*t[
pi]^3/(12*(1-nu[si]^2)),G=E[si]/(2*(1+nu[si]))},Xi2[Zpis,T]));

$$\Xi_{2_{Zpis,T}} := \frac{-\frac{3}{64}b^4 + \frac{1}{16}b^3a^2 + \frac{1}{16}\ln\left(\frac{b}{a}\right)b^4}{D} - \frac{1}{4} \frac{\alpha(-b^2 + 2b^2\ln(b) - 2\ln(a)b^2)}{Gh}$$


$$\Xi_{2_{Zpis,T}} := .7888483668699864076767250030356035147167 10^{-13}$$

[ > Xi2[Zpis,P] := -subs({PHAC=1,Tp=0},Zpis_0);
Xi2[Zpis,P]:=evalf(subs({a=R[pi],b=R[p],nu=nu[si],alpha=alpha[si],h=t[pi],D=E[si]*t[
pi]^3/(12*(1-nu[si]^2)),G=E[si]/(2*(1+nu[si]))},Xi2[Zpis,P]));

$$\Xi_{2_{Zpis,P}} := \frac{1}{64} \frac{a^4}{D} + \frac{1}{4} \frac{\alpha a^2}{Gh}$$


$$\Xi_{2_{Zpis,P}} := .223063742897727272727272727272727272727273 10^{-12}$$

[ > Xi2[dVpis,T] := subs({PHAC=0,Tp=1},dVpist);

```

```
Xi2[dVpis,T] := evalf (subs ({a=R[piis], b=R[p], nu=nu[si], alpha=alpha[si], h=t[piis], D=E[si]*t
[piis]^3/(12*(1-nu[si]^2)), G=E[si]/(2*(1+nu[si]))}, Xi2[dVpis,T]));
```

$$\Xi_{dVpis,T} := \frac{1}{192}$$

$$\pi \left(48 \alpha b^2 a^2 D - 24 \alpha b^4 D - 3 b^4 G h a^2 + 24 b^6 G h \ln \left(\frac{h}{a} \right) + 3 b^2 G h a^2 - 24 b^6 G h \ln(b) + 24 b^6 G h \ln(a) + b^6 G h \right) / (D G h)$$

$$\Xi_{dVpis,T} := .6341969310342016231443513844306627385162 \cdot 10^{-18}$$

```
> Xi2[dVpis,P] := -subs ({PHAC=1, Tp=0}, dVpiis);
```

```
Xi2[dVpis,P] := evalf (subs ({a=R[piis], b=R[p], nu=nu[si], alpha=alpha[si], h=t[piis], D=E[si]*t
[piis]^3/(12*(1-nu[si]^2)), G=E[si]/(2*(1+nu[si]))}, Xi2[dVpis,P]));
```

$$\Xi_{dVpis,P} := -\frac{1}{192} \frac{\pi(-a^6 G h - 24 \alpha a^4 D)}{D G h}$$

$$\Xi_{dVpis,P} := .2347316925014454026966632223282621962794 \cdot 10^{-17}$$

Drive Element Piston (Averaged Compliance)

This section averages the compliances effects from the previous two sections on the piston. In reality, the tethers are compliant enough that they don't provide a rigid boundary condition at r=a, however they are not soft enough to provide a hinge there either. Therefore, the compliance is assumed as the average of the two. This effect has been shown with FEM.

```
> DERatio:=0.5;
```

$$DERatio := .5$$

```
> Xi[Zpis,T] := (1-DEratio)*Xi1[Zpis,T] + (DEratio)*Xi2[Zpis,T];
```

$$\Xi_{Zpis,T} := .1377449219142713680403997730308330787445 \cdot 10^{-12}$$

```
> Xi[Zpis,P] := (1-DEratio)*Xi1[Zpis,P] + (DEratio)*Xi2[Zpis,P];
```

$$\Xi_{Zpis,P} := .5035147372159090909090909090909090909090909090909092 \cdot 10^{-12}$$

```
> Xi[dVpis,T] := (1-DEratio)*Xi1[dVpis,T] + (DEratio)*Xi2[dVpis,T];
```

$$\Xi_{dVpis,T} := .1466311782062712642937790352294156777490 \cdot 10^{-17}$$

```
> Xi[dVpis,P] := (1-DEratio)*Xi1[dVpis,P] + (DEratio)*Xi2[dVpis,P];
```

$$\Xi_{dVpis,P} := .6312099450503241827158900246632211207317 \cdot 10^{-17}$$

Top Structural Compliance

Annular plate clamped at outer radius (r=a) and free at inner radius (r=b) with a pressure applied underneath plate from r=b to r=a and a concentrated force applied upward at r=b. Positive plate deflection is defined in the upward direction. These relations include bending and shearing effects, see TopChamberPlate.mws.

```
> eqn := diff(1/r*diff(x*diff(Z(x),r),r),r) = Q(r)/D' :
```

```
> Q(x) := Fvm/(2*Pi*x) + PHAC*Pi*(x^2-b^2)/(2*Pi*x) :
```

```
> Q1(x) := (int(Q(x)/D,x)+C1)*x :
```

```

Q2(x):=(int(Q1(x),x)+C2)/x:
Ztop_bending(x):=int(Q2(x),x)+C3:
[ > BC1:=subs({r=a},Ztop_bending(x))=0:
[ > BC2:=subs({r=a},diff(Ztop_bending(x),x))=0:
[ > BC3:=subs({r=b},diff(diff(Ztop_bending(x),x),x)+nu/x*diff(Ztop_bending(x),x))=0:
[ > Set1:=solve({BC1,BC2,BC3},{C1,C2,C3}):
[ > Ztop_BENDING(x):=collect(subs(Set1,Ztop_bending(x)),{Fvm,D,PHAC}):
[ > Ztop_bend:=collect(simplify(subs({r=b},Ztop_BENDING(x))),{Fvm,D,PHAC}):
[ > dVtop_BENDING:=collect(simplify(int(2*Pi*r*Ztop_BENDING(x),r=b..a)),{Pi,Fvm,D,PHAC}):
[ > eqn2:='diff(Z(x),x)=-alpha*Q(x)/G/h':
[ > Ztop_shearing(x):=int(-alpha*Q(x)/G/h,x)+C4:
[ > BC4:=subs({r=a},Ztop_shearing(x))=0:
[ > Set2:=solve({BC4},{C4}):
[ > Ztop_SHEARING(x):=subs(Set2,Ztop_shearing(x)):
[ > Ztop_shear:=collect(simplify(subs({r=b},Ztop_SHEARING(x))),{Fvm,PHAC}):
[ > dVtop_SHEARING:=collect(simplify(int(2*Pi*r*Ztop_SHEARING(x),r=b..a)),{Fvm,PHAC}):
[ > Ztop1:=collect(Ztop_bend+Ztop_shear,{Fvm,PHAC}):
[ > dVtop1:=collect(dVtop_BENDING+dVtop_SHEARING,{Fvm,PHAC}):
[ > Xi[Ztop,F]:=subs({PHAC=1,Fvm=0},Ztop1):
Xi[Ztop,F]:=evalf(subs({a=R[ch],b=R[vm],nu=nu[si],alpha=alpha[si],h=t[top],D=E[si]*t[
op]^3/(12*(1-nu[si]^2)),G=E[si]/(2*(1+nu[si]))},Xi[Ztop,F]));
Xi[Ztop,F]:=-1/64*(3*pi*b^5*v-pi*b^4*a^2-16*pi*b^4*a^2*ln(b)*ln(b/a)-16*pi*b^4*a^2*ln(b)*ln(b/a)+4*pi*a^4*v*b^2*ln(a)
+16*pi*a^2*ln(a)*b^4*ln(b)-16*pi*a^2*ln(a)^2*b^4*v-4*pi*b^4*a^2*v*ln(a)+7*pi*b^6+4*pi*b^4*ln(b)*a^2*v-pi*a^6*v-4*pi*b^2*a^4*ln(b)v
+16*pi*a^2*ln(a)v*b^4*ln(b)+pi*a^6-7*pi*a^4*b^2-16*pi*a^2*ln(a)^2*b^4+4*pi*a^4*b^2*ln(a)-7*pi*b^4*a^2*v+5*pi*b^2*v*a^4
+20*pi*b^4*a^2*ln(a)-4*pi*b^2*a^4*ln(b)-20*pi*b^4*ln(b)*a^2)/(pi*(-a^2+a^2*v-b^2-v*b^2)*D)
+1/4*(alpha*(-b^2*pi+2*b^2*ln(b)*pi+a^2*pi-2*b^2*ln(a)*pi)/G*h*pi)
Xi[Ztop,F]:=.1442510763604847433456380046056248573029 10^-12
[ > Xi[Ztop,F]:=subs({PHAC=0,Fvm=1},Ztop1):
Xi[Ztop,F]:=evalf(subs({a=R[ch],b=R[vm],nu=nu[si],alpha=alpha[si],h=t[top],D=E[si]*t[
op]^3/(12*(1-nu[si]^2)),G=E[si]/(2*(1+nu[si]))},Xi[Ztop,F]));
Xi[Ztop,F]:=-1/64*(8*v*b^5*a^2+16*a^2*ln(a)^2*b^2+32*b^2*ln(b)*a^2-32*a^2*ln(a)*b^2-4*v*a^4-4*v*b^4+4*a^4
+16*b^2*a^2*ln(b)*ln(b/a)+16*b^2*a^2*ln(b/a)*ln(b)-16*a^2*ln(a)v*b^2*ln(b)-16*a^2*ln(a)*b^2*ln(b)+16*a^2*ln(a)^2*v*b^2
+8*b^2*a^2-12*b^4)/(pi*(-a^2+a^2*v-b^2-v*b^2)*D)+1/4*(alpha*(-2*ln(b)+2*ln(a))/G*h*pi)
Xi[Ztop,F]:=.1775479105428133086725272014729944768799 10^-7
[ > Xi[dVtop,F]:=subs({PHAC=1,Fvm=0},dVtop1):
Xi[dVtop,F]:=evalf(subs({a=R[ch],b=R[vm],nu=nu[si],alpha=alpha[si],h=t[top],D=E[si]*t[
op]^3/(12*(1-nu[si]^2)),G=E[si]/(2*(1+nu[si]))},Xi[dVtop,F]));

```

```

Xi [dVtop,F] := -1/192 * ( (-2*a^6*b^2 - 13*b^8 + a^8 + 12*a^4*b^4 + 2*b^6*a^2 - 48*a^2*ln(a)*v*b^6*ln(b) + 22*a^2*v*b^6 + 10*a^6*v*b^2
- 24*a^4*v*b^4 - a^8*v - 7*v*b^8 - 48*a^4*b^4*ln(b/a)*v*ln(a) + 48*a^2*b^6*ln(b/a)*v*ln(b) + 48*a^4*ln(a)*v*b^4*ln(b) - 24*b^6*a^2*ln(b/a)
- 48*a^4*ln(a)^2*b^4 + 24*a^4*b^4*ln(b/a) + 48*a^2*ln(a)^2*b^6 + 48*a^2*ln(a)^2*b^6*v + 48*a^4*ln(a)*b^4*ln(b) - 48*a^4*b^4*ln(b/a)*ln(a)
+ 48*b^6*a^2*ln(b/a)*ln(b) - 48*a^2*ln(a)*b^6*ln(b) - 48*a^4*ln(a)^2*b^4*v - 24*a^2*b^6*ln(b/a)*v + 24*a^4*b^4*ln(b/a)*v - 48*b^6*ln(a)*a^2
+ 48*b^6*ln(b)*a^2 ) / ((-a^2 + a^2*v - b^2 - v*b^2)*D) - 1/8 * (4*b^2*a^2*pi - a^4*pi - 3*b^4*pi + 4*b^4*ln(b)*pi - 4*b^4*ln(a)*pi) / (G*h)
Xi [dVtop,F] := .1638097346275169420654979054561191650143 10^-17
> Xi [dVtop,F] := subs({FHAC=0,Fvm=1,dVtop1});
Xi [dVtop,F] := evalf(subs({a=R[ch],b=R[vm],nu=nu[si],alpha=alpha[si],h=t[top],D=E[si]*t[
top]^3/(12*(1-nu[si]^2)),G=E[si]/(2*(1+nu[si]))},Xi [dVtop,F]));
Xi [dVtop,F] := -1/192 * ( -21*a^4*b^2 - 84*b^4*ln(b)*a^2 + 84*b^4*a^2*ln(a) - 3*b^4*a^2 + 3*a^6 + 9*v*b^6 + 21*b^6 - 48*a^2*ln(a)^2*v*b^4
- 24*a^4*b^2*ln(b/a)*v + 48*a^4*ln(a)^2*v*b^2 + 48*a^4*b^2*ln(b/a)*v*ln(a) + 12*a^2*v*ln(a)*b^4 - 12*a^2*v*b^4*ln(b)
+ 48*a^2*v*ln(a)*b^4*ln(b) - 48*b^4*a^2*ln(b/a)*v*ln(b) - 48*a^4*ln(a)*v*b^2*ln(b) - 3*a^6*v + 24*b^4*a^2*ln(b/a)*v + 15*a^4*v*b^2
- 12*a^4*ln(a)*v*b^2 + 12*a^4*v*b^2*ln(b) - 21*a^2*v*b^4 + 48*a^4*b^2*ln(b/a)*ln(a) - 48*a^4*ln(a)*b^2*ln(b) + 48*a^2*ln(a)*b^4*ln(b)
- 48*b^4*a^2*ln(b/a)*ln(b) + 24*b^4*a^2*ln(b/a) + 12*a^4*b^2*ln(b) - 12*a^4*b^2*ln(a) - 24*a^4*b^2*ln(b/a) + 48*a^4*ln(a)^2*b^2
- 48*a^2*ln(a)^2*b^4 ) / ((-a^2 + a^2*v - b^2 - v*b^2)*D) - 1/8 * (-2*a^2 + 2*b^2 - 4*b^2*ln(b) + 4*ln(a)*b^2) / (G*h)
Xi [dVtop,F] := .1442510763604847433456380046056248573035 10^-12

```

Valve Cap/Membrane

```

[ Annular plate clamped at outer radius (r=a) and guided at inner radius (r=b) with differentia;
  pressure applied underneath plate from r=b to r=a and concentrated force applied upward at
  r=b. Positive plate deflection is defined in the upward direction. These relations only include
  bending effects, see ValveCapMembrane.mws.
[ > eqn:=diff(1/r*diff(r*diff(w(x),x),x),x)=Q(x)/D':
[ > Q(x):=Fvc/(2*Pi*x) + Fvm*Pi*(x^2-b^2)/(2*Pi*x):
[ > Q1(x):=(int(Q(x)/D,x)+C1)*r:
  Q2(x):=(int(Q1(x),x)+C2)/x:
  Zvm_bending(x):=expand(int(Q2(x),x)+C3):
[ > BC1:=subs({r=a},Zvm_bending(x))=0:
[ > BC2:=subs({r=a},diff(Zvm_bending(x),x))=0:
[ > BC3:=subs({r=b},diff(Zvm_bending(x),x))=0:
[ > Set1:=solve({BC1,BC2,BC3},{C1,C2,C3}):
[ > Zvm_BENDING(x):=collect(subs(Set1,Zvm_bending(x)),{Fvc,D,Fvm}):
[ > Zvc1:=collect(simplify(subs({r=b},Zvm_BENDING(x))),{Fvc,D,Fvm}):
[ > dVvm_BENDING:=collect(simplify(int(2*Pi*r*Zvm_BENDING(x),r=b..a)),{Pi,Fvc,D,Fvm}):

```

```

> Xi[Zvc,P] := subs({Fvc=0,Pvm=1},Zvc1);
Xi[Zvc,P] := evalf(subs({a=R[vm],b=R[vc],h=t[vm],D=E[si]*t[vm]^3/(12*(1-nu[si]^2))},Xi[Zvc,P]));
Xi_Zvc_P := 1/64 * (7*pi*b^4*a^2 - 3*pi*b^6 - 5*pi*a^4*b^2 + 4*pi*b^4*a^2*ln(a) - 4*pi*b^4*ln(b)*a^2 + 4*pi*b^2*a^4*ln(b) + 16*pi*b^4*a^2*ln(b)*ln(b/a) + pi*a^6 - 4*pi*a^4*b^2*ln(a) + 16*pi*a^2*ln(a)^2*b^4 - 16*pi*a^2*ln(a)*b^4*ln(b)) / (pi*(a^2-b^2)*D)
Xi_Zvc_P := .1236306944873668358747037186342053319349 10^9

> Xi[Zvc,F] := subs({Fvc=1,Pvm=0},Zvc1);
Xi[Zvc,F] := evalf(subs({a=R[vm],b=R[vc],h=t[vm],D=E[si]*t[vm]^3/(12*(1-nu[si]^2))},Xi[Zvc,F]));
Xi_Zvc_F := 1/64 * (4*a^4 - 16*a^2*ln(a)^2*b^2 + 4*b^4 - 8*b^2*a^2 - 16*b^2*a^2*ln(b/a)*ln(b) + 16*a^2*ln(a)*b^2*ln(b)) / (pi*(a^2-b^2)*D)
Xi_Zvc_F := .0001891300225883061570524241081849325118186

> Xi[dVvm,P] := subs({Fvc=0,Pvm=1},dVvm_BENDING);
Xi[dVvm,P] := evalf(subs({a=R[vm],b=R[vc],h=t[vm],D=E[si]*t[vm]^3/(12*(1-nu[si]^2))},Xi[dVvm,P]));
Xi_dVvm_P := 1/192 * ((24*b^6*a^2*ln(b/a) + a^8 - 48*a^4*ln(a)*b^4*ln(b) + 48*a^4*b^4*ln(b/a)*ln(a) + 48*a^4*ln(a)^2*b^4 - 24*a^4*b^4*ln(b/a) + 24*a^4*b^4 - 10*a^6*b^2 - 48*b^6*a^2*ln(b/a)*ln(b) - 48*a^2*ln(a)^2*b^6 + 48*a^2*ln(a)*b^6*ln(b) + 7*b^8 - 22*b^6*a^2)*pi) / ((a^2-b^2)*D)
Xi_dVvm_P := .9031509650514488184176314920963760635496 10^-16

> Xi[dVvm,F] := subs({Fvc=1,Pvm=0},dVvm_BENDING);
Xi[dVvm,F] := evalf(subs({a=R[vm],b=R[vc],h=t[vm],D=E[si]*t[vm]^3/(12*(1-nu[si]^2))},Xi[dVvm,F]));
Xi_dVvm_F := 1/192 * (-15*a^4*b^2 - 9*b^6 - 48*a^2*ln(a)*b^4*ln(b) + 48*b^4*a^2*ln(b/a)*ln(b) + 21*b^4*a^2 + 48*a^2*ln(a)^2*b^4 + 12*b^4*ln(b)*a^2 - 12*b^4*a^2*ln(a) - 24*b^4*a^2*ln(b/a) + 3*a^6 - 48*a^4*b^2*ln(b/a)*ln(a) + 48*a^4*ln(a)*b^2*ln(b) - 48*a^4*ln(a)^2*b^2 - 12*a^4*b^2*ln(b) + 24*a^4*b^2*ln(b/a) + 12*a^4*b^2*ln(a)) / ((a^2-b^2)*D)
Xi_dVvm_F := .123630694487366835874703718634205331944 10^9

```

Step 4: Solve Equations

```

> Solutions:=solve({EQN1,EQN2,EQN3,EQN4,EQN5,EQN6,EQN7,EQN8,EQN9,EQN10,EQN11,EQN12,EQN13,EQN14,EQN15,EQN16,EQN17},{Z[p],T[p],Z[bot],Z[te],P[HAC],dV[te],Z[pis],dV[pis],dV[fluid],Z[top],dV[top],F[vm],Z[vc],dV[vm],F[vc],Q[p],Z[de]});
> SolutionsValues:=evalf(subs({P[1]=0.5e6,P[2]=0e6,V[p]=500},Solutions));
SolutionsValues := { T_p = 2231936350709793062278122870357821015647 10^7,
Z_bot = -.1163329724718546223813989792182145983230 10^6, Z_p = .7522550650712129700871283613902818672634 10^6,
dV_pa = .1872711788601659056212980592568417325255 10^-11, F_vm = .2949951827261501434908943661858065648750,

```

$Q_p = .8044211902127622847866619042834808352349 \cdot 10^{-7}$, $dV_{fuel} = -.1525217750740688068517105409610629628775 \cdot 10^{-11}$,
 $P_{HAC} = 221796.6922473865376986184401155057549960$, $dV_n = .1327480701927576751967670781787336404598 \cdot 10^{-10}$,
 $Z_{pis} = .1957599951338435463759510228801996409326 \cdot 10^{-6}$, $Z_{vcc} = .00001157278902917103407170790367469559248067$,
 $dV_{isp} = .4807373020567373342830674851203196699054 \cdot 10^{-12}$, $F_{vc} = -.08399154105942311823880775989422955139809$,
 $Z_{dr} = .6359220925993583477057293821720672689401 \cdot 10^{-6}$, $Z_n = .4401620974655148013297783592918676280078 \cdot 10^{-6}$,
 $dV_{vm} = .1314156375508000117308951551571083207255 \cdot 10^{-10}$, $Z_{top} = .3723198942120302708075553839325050285056 \cdot 10^{-7}$

[>

Appendix B

Support Documentation for Non-Linear Valve Cap/Membrane

B.1 NLValveCapMembrane-CaseA.m [see Section 3.5]

```

function [y,r,Vtotal,psi,W,theta,xi,thetaND,psiND,sigma_r_top,sigma_r_bot,yvc,maxstress] =
NLValveCapMembrane_CaseA(Pvm,Fvc,rb,ra,tvm,E,nu,flagNL,No)

%NLValveCapMembrane_CaseA.m

%David C. Roberts
%This Matlab code solves for the non-linear deflection behavior of the valve cap
%/membrane under loading Pvm and Fvc. The deflection, slope,
%curvature, swept volume, and membrane stress are calculated. Case A refers to the
%fact that we are applying both loading inputs Pvm and Fvc and determining the
%structural response. Prior to calling of this code, the user must define Pvm and
%Fvc as functions of P1, P2, and PHAC. The loadings are used as follows:
% Pvm = pressure differential across valve membrane = PHAC-P2
% Fvc = force seen by valve cap = Avc*(PHAC-P1)
%The plate/membrane is characterized by inner radius rb, outer radius ra, thickness
%tvm, and material properties E and nu. If flagNL=0, only linear theory will be
%considered. If flagNL=1, non-linear theory will be considered. No is the value of
%the in-plane pretension. In this file yvc is the valve cap deflection (Zvc).

format long;

%%%%%%%%%%%%%%%%%%%%%%%%%%%%%%%%%%%%%%%%%%%%%%%%%%%%%%%%%%%%%%%%%%%%%%%%
%Convert Inputs to Dimensionless Quantities
P = (Pvm*ra^4)/(E*tvm^4); %Dimensionless loading of pressure difference across
cap/membrane
F = (Fvc*ra^2)/(pi*E*tvm^4); %Dimensionless loading due to additional force on cap

%%%%%%%%%%%%%%%%%%%%%%%%%%%%%%%%%%%%%%%%%%%%%%%%%%%%%%%%%%%%%%%%%%%%%%%%

beta = sqrt((1-nu)/(1+nu))*(rb/ra);
k = (ra/tvm)*sqrt((12*(1-nu^2)*No)/(E*tvm*(1-beta^2)));
s = beta*k;

%%%%%%%%%%%%%%%%%%%%%%%%%%%%%%%%%%%%%%%%%%%%%%%%%%%%%%%%%%%%%%%%%%%%%%%%
%%Section 2: Define grid spacing and coordinate transformation parameters
%%for finite-difference method
%%%%%%%%%%%%%%%%%%%%%%%%%%%%%%%%%%%%%%%%%%%%%%%%%%%%%%%%%%%%%%%%%%%%%%%%
Npoints=200; %The total # of grid points to use (MUST KEEP IT EVEN)
alpha=1.01; %Grid density parameter
phi=(alpha+1)/(alpha-1); %Grid density ratio
hr = 1/(Npoints-1); %Size of grid spacing
eta = 0:hr:1; %Vector of evenly spaced points between 0 and 1

xi_b = rb/ra; %Non-dimensional position of inner radius
xi_c = (rb+ra)/(2*ra); %Non-dimensional position of midpoint along membrane
xi_a = ra/ra; %Non-dimensional position of outer radius

%For the grid points from xi_b to xi_c, define the derivatives of eta with respect to xi
for i=1:Npoints/2,
xi(i) = xi_b + (alpha-1)*(xi_c-xi_b)*(phi-phi^(1-2*eta(i)))/(1+phi^(1-2*eta(i)));
m = (alpha-1)*(xi_c-xi_b);
m2 = m*phi - m + 2*xi_b;
deta(i) = (0.5/log(phi))*(m*(1+phi))/((m*phi-(xi(i)-xi_b))*(m+(xi(i)-xi_b)));
d2eta(i) = -(0.5/log(phi))*(m*(1+phi)*(m2-2*xi(i)))/((m*phi-(xi(i)-xi_b))*(m+(xi(i)-
xi_b)))^2;
end

%For the grid points from xi_c to xi_a
for i=Npoints/2+1:Npoints,
xi(i) = xi_b + (alpha-1)*(xi_c-xi_b)*(phi-phi^(1-2*eta(i)))/(1+phi^(1-2*eta(i)));
m = (alpha-1)*(xi_c-xi_b);
m2 = m*phi - m + 2*xi_b;
deta(i) = (0.5/log(phi))*(m*(1+phi))/((m*phi-(xi(i)-xi_b))*(m+(xi(i)-xi_b)));
d2eta(i) = -(0.5/log(phi))*(m*(1+phi)*(m2-2*xi(i)))/((m*phi-(xi(i)-xi_b))*(m+(xi(i)-
xi_b)))^2;
end

```

```

%%%%%%%%%%%%%%%%%%%%%%%%%%%%%%%%%%%%%%%%%%%%%%%%%%%%%%%%%%%%%%%%%%%%%%%%
%%Section 3: Finite-Difference Implementation
%%%%%%%%%%%%%%%%%%%%%%%%%%%%%%%%%%%%%%%%%%%%%%%%%%%%%%%%%%%%%%%%%%%%%%%%

%Governing equations at internal points (from 2 to Npoints-1)
for i=2:Npoints-1,
    A(i,i-1) = (xi(i)^2*deta(i)^2)/(hr^2) - (xi(i)^2*d2deta(i) + xi(i)*deta(i))/(2*hr);
    A(i,i) = -( 2*xi(i)^2*deta(i)^2)/(hr^2) + (s^2+1) + xi(i)^2*k^2 );
    A(i,i+1) = (xi(i)^2*deta(i)^2)/(hr^2) + (xi(i)^2*d2deta(i) + xi(i)*deta(i))/(2*hr);

    B(i,i-1) = (xi(i)^2*deta(i)^2)/(hr^2) - (xi(i)^2*d2deta(i) + 3*xi(i)*deta(i))/(2*hr);
    B(i,i) = -(2*xi(i)^2*deta(i)^2)/(hr^2);
    B(i,i+1) = (xi(i)^2*deta(i)^2)/(hr^2) + (xi(i)^2*d2deta(i) + 3*xi(i)*deta(i))/(2*hr);

    C(i) = 6*(1-nu^2)*P*(xi(i)^3 - xi(i)*(rb/ra)^2) + 6*(1-nu^2)*F*xi(i);
end

%Boundary condition equations at xi_b (grid point #1)
A(1,1) = 1;
B(1,1) = -3*xi(1)*deta(1)/(2*hr) + (1-nu);
B(1,2) = 4*xi(1)*deta(1)/(2*hr);
B(1,3) = -xi(1)*deta(1)/(2*hr);
C(1) = 0;

%Boundary condition equations at xi_a (grid point #Npoints)
A(Npoints,Npoints) = 1;
B(Npoints,Npoints-2) = xi(Npoints)*deta(Npoints)/(2*hr);
B(Npoints,Npoints-1) = -4*xi(Npoints)*deta(Npoints)/(2*hr);
B(Npoints,Npoints) = 3*xi(Npoints)*deta(Npoints)/(2*hr) + (1-nu);
C(Npoints) = 0;

%%%%%%%%%%%%%%%%%%%%%%%%%%%%%%%%%%%%%%%%%%%%%%%%%%%%%%%%%%%%%%%%%%%%%%%%
%%Section 4: Provide an initial guess for the theta vector (plate slope), to be
%%used in the finite-difference iteration procedure.
%%%%%%%%%%%%%%%%%%%%%%%%%%%%%%%%%%%%%%%%%%%%%%%%%%%%%%%%%%%%%%%%%%%%%%%%

if k==0,
    %theta = (-0.75*(1-nu^2)*P*xi.*(1-xi.^2))'; %Linear result
    theta=xi';
else
    theta=xi';
end

%%%%%%%%%%%%%%%%%%%%%%%%%%%%%%%%%%%%%%%%%%%%%%%%%%%%%%%%%%%%%%%%%%%%%%%%
%%Section 5: Matrix Manipulation Procedure
%%%%%%%%%%%%%%%%%%%%%%%%%%%%%%%%%%%%%%%%%%%%%%%%%%%%%%%%%%%%%%%%%%%%%%%%

Niterations=500; %Perform up to 500 iterations
tolerance1=1e-8;
tolerance2=1e-8;
omega=0.45; %Under-relaxation parameter
if flagNL=1 %This variable is passed into file.
    NLoption=1; %0 = Linear solution; 1 = NonLinear solution
else
    NLoption=0;
end

for i=1:Niterations,
    i;
    for j=2:Npoints-1 %Define D vector for each iteration
        D(j) = -0.5*theta(j).^2;
    end
    D(1)=0;
    D(Npoints)=0;

    Sr = inv(B)*D'*NLoption; %Solve for Sr
end

```

```

v_Sr = 12*(1-nu^2)*xi'.^2.*Sr;          %Calculate non-linear correction term v_Sr
A2 = A - diag(v_Sr,0);                 %Subtract non-linear correction term from A
theta_new = inv(A2)*C';                 %Calculate new theta vector

inner_product = (theta_new'*theta)/sqrt(theta_new'*theta_new)/sqrt(theta'*theta);
length_ratio = sqrt(theta_new'*theta_new)/sqrt(theta'*theta);

if (1-inner_product) >= tolerance1 | (1-length_ratio) >= tolerance2
    theta = (1-omega)*theta + omega*theta_new;
else
    break;
end
end

%%%%%%%%%%%%%%%%%%%%%%%%%%%%%%%%%%%%%%%%%%%%%%%%%%%%%%%%%%%%%%%%%%%%%%%%%%%%%%
%%Section 6: Calculate Deflection, Curvature, Stress, and Swept Volume in this
%%post-processing section.
%%%%%%%%%%%%%%%%%%%%%%%%%%%%%%%%%%%%%%%%%%%%%%%%%%%%%%%%%%%%%%%%%%%%%%%%%%%%%%

%PLATE DEFLECTION: Calculate plate deflection vector from the final theta vector,
%using 2nd-order forward, backward, and central difference methods to express
%theta in terms of W. Then, using matrix inversion to obtain the vector W.
i=1; %BC at rb
Wmatrix(i,i) = deta(i)*(-3/(2*hr));
Wmatrix(i,i+1) = deta(i)*(2/hr);
Wmatrix(i,i+2) = deta(i)*(-1/(2*hr));

for i=2:Npoints-1 %Inner grid points
    Wmatrix(i,i-1) = deta(i)*(-1/(2*hr));
    Wmatrix(i,i+1) = deta(i)*(1/(2*hr));
end

%BC at ra --> Do not do for the outer boundary condition. We already know that
%the deflection at ra is equal to zero.

W = inv(Wmatrix(1:Npoints-1,1:Npoints-1))*theta(1:Npoints-1);
W=[W;0];
%Done

%PLATE CURVATURE: Calculate plate curvature vector from the final theta vector,
%using 2nd-order forward, backward, and central difference methods.
i=1; %BC at rb
psi(i) = deta(i)*(1/(2*hr))*(-3*theta(i) + 4*theta(i+1) - theta(i+2));

for i=2:Npoints-1 %Inner grid points
    psi(i) = deta(i)*(1/(2*hr))*(theta(i+1) - theta(i-1));
end

i=Npoints; %BC at ra
psi(i) = deta(i)*(1/(2*hr))*(3*theta(i) - 4*theta(i-1) + theta(i-2));
%Done

%PLATE STRESS: Calculate the stress vectors in the plate.

for i=1:Npoints
    Sro(i) = (k^2/(12*(1-nu^2)))*(1 + beta^2/(xi(i)^2));
    sigma_r_top(i) = (E*tvm^2/ra^2)*(Sro(i) + Sr(i) - (1/(2*(1-nu^2)))*(psi(i) +
(nu*theta(i))./xi(i)));
    sigma_r_bot(i) = (E*tvm^2/ra^2)*(Sro(i) + Sr(i) + (1/(2*(1-nu^2)))*(psi(i) +
(nu*theta(i))./xi(i)));
end
if max(sigma_r_top) > max(sigma_r_bot)
    maxstress = abs(max(sigma_r_top));
else
    maxstress = abs(max(sigma_r_bot));
end

```

```

end
%Done

%CONVERSION TO NON_DIMENSIONAL PARAMETERS
r=xi*ra;
y=W*tvm;
thetaND=theta*tvm/ra; %This non-dimensional theta is dw/dr
psiND=psi*tvm/(ra^2); %This non-dimensional psi is d2w/dr2

%PLATE SWEEP VOLUME: Calculate total swept volume under cap and membrane.
V=0;
for i=1:Npoints-1
    dV(i) = pi*(r(i+1)^2-r(i)^2)*0.5*(y(i+1)+y(i));
    V = V + dV(i);
end
yvc = y(1);
Vcap = yvc*pi*rb^2;
Vtotal = Vcap + V;
%Done

```

B.2 NLValveCapMembrane-CaseB.m [see Section 3.5]

```

function
[y,r,Vtotal,psi,W,theta,xi,thetaND,psiND,sigma_r_top,sigma_r_bot,yvc,Pvm,maxstress] =
NLValveCapMembrane_CaseB(Fvcstar,yvc_imposed,rb,ra,tv,E,nu,flagNL,No)

%NLValveCapMembrane_CaseB.m

%David C. Roberts
%This Matlab code solves for the non-linear deflection behavior of the valve cap/
%membrane under loading Fvcstar and a desired valve cap deflection at r=rb. The
%required Pvm to produce this deflection and the resulting deflection, slope,
%curvature, swept volume, and membrane stress are calculated. Case B refers to the
%fact that we are applying a known cap force (in addition to that due to Pvm) and
%imposing a cap deflection, and then solving for the required Pvm and the resulting
%structural response. Prior to calling of this code, the user must define Fvcstar
%as a function of P1 and P2. This Fvcstar loading is defined as follows:
% Fvcstar = Avc*(P2-P1)
%After running this code, the user can then back out PHAC using the following relation:
% PHAC = Pvm+P2
%The plate/membrane is characterized by inner radius rb, outer radius ra, thickness
%tvm, and material properties E and nu. If flagNL=0, only linear theory will be
%considered. If flagNL=1, non-linear theory will be considered. No is the value of
%the in-plane pretension. In this file, yvc is the valve cap deflection (Zvc).

format long;

%%%%%%%%%%%%%%%%%%%%%%%%%%%%%%%%%%%%%%%%%%%%%%%%%%%%%%%%%%%%%%%%%%%%%%%%
%Convert Inputs to Dimensionless Quantities
Wb=yvc_imposed/tvm;
F = (Fvcstar*ra^2)/(pi*E*tvm^4); %Dimensionless loading due to additional force on cap

%%%%%%%%%%%%%%%%%%%%%%%%%%%%%%%%%%%%%%%%%%%%%%%%%%%%%%%%%%%%%%%%%%%%%%%%

beta = sqrt((1-nu)/(1+nu))*(rb/ra);
k = (ra/tvm)*sqrt((12*(1-nu^2)*No)/(E*tvm*(1-beta^2)));
s = beta*k;

%%%%%%%%%%%%%%%%%%%%%%%%%%%%%%%%%%%%%%%%%%%%%%%%%%%%%%%%%%%%%%%%%%%%%%%%
%%Section 2: Define grid spacing and coordinate transformation parameters
%%for finite-difference method
%%%%%%%%%%%%%%%%%%%%%%%%%%%%%%%%%%%%%%%%%%%%%%%%%%%%%%%%%%%%%%%%%%%%%%%%
Npoints=200; %The total # of grid points to use (MUST KEEP IT EVEN)
alpha=1.01; %Grid density parameter
phi=(alpha+1)/(alpha-1); %Grid density ratio
hr = 1/(Npoints-1); %Size of grid spacing
eta = 0:hr:1; %Vector of evenly spaced points between 0 and 1

xi_b = rb/ra; %Non-dimensional position of inner radius
xi_c = (rb+ra)/(2*ra); %Non-dimensional position of midpoint along membrane
xi_a = ra/ra; %Non-dimensional position of outer radius

%For the grid points from xi_b to xi_c, define the derivatives of eta with respect to xi
for i=1:Npoints/2,
xi(i) = xi_b + (alpha-1)*(xi_c-xi_b)*(phi-phi^(1-2*eta(i)))/(1+phi^(1-2*eta(i)));
m = (alpha-1)*(xi_c-xi_b);
m2 = m*phi - m + 2*xi_b;
deta(i) = (0.5/log(phi))*(m*(1+phi))/((m*phi-(xi(i)-xi_b))*(m+(xi(i)-xi_b)));
d2eta(i) = -(0.5/log(phi))*(m*(1+phi)*(m2-2*xi(i)))/((m*phi-(xi(i)-xi_b))*(m+(xi(i)-xi_b)))^2;
end

%For the grid points from xi_c to xi_a
for i=Npoints/2+1:Npoints,
xi(i) = xi_b + (alpha-1)*(xi_c-xi_b)*(phi-phi^(1-2*eta(i)))/(1+phi^(1-2*eta(i)));
m = (alpha-1)*(xi_c-xi_b);
m2 = m*phi - m + 2*xi_b;
deta(i) = (0.5/log(phi))*(m*(1+phi))/((m*phi-(xi(i)-xi_b))*(m+(xi(i)-xi_b)));
d2eta(i) = -(0.5/log(phi))*(m*(1+phi)*(m2-2*xi(i)))/((m*phi-(xi(i)-xi_b))*(m+(xi(i)-xi_b)))^2;
end

```

```

end

%%%%%%%%%%%%%%%%%%%%%%%%%%%%%%%%%%%%%%%%%%%%%%%%%%%%%%%%%%%%%%%%%%%%%%%%
%%Section 3: Finite-Difference Implementation
%%%%%%%%%%%%%%%%%%%%%%%%%%%%%%%%%%%%%%%%%%%%%%%%%%%%%%%%%%%%%%%%%%%%%%%%

%Governing equations at internal points (from 2 to Npoints-1)
for i=2:Npoints-1,
    A(i,i-1) = (xi(i)^2*deta(i)^2)/(hr^2) - (xi(i)^2*d2eta(i) + xi(i)*deta(i))/(2*hr);
    A(i,i) = -( 2*xi(i)^2*deta(i)^2)/(hr^2) + (s^2+1) + xi(i)^2*k^2 );
    A(i,i+1) = (xi(i)^2*deta(i)^2)/(hr^2) + (xi(i)^2*d2eta(i) + xi(i)*deta(i))/(2*hr);

    B(i,i-1) = (xi(i)^2*deta(i)^2)/(hr^2) - (xi(i)^2*d2eta(i) + 3*xi(i)*deta(i))/(2*hr);
    B(i,i) = -(2*xi(i)^2*deta(i)^2)/(hr^2);
    B(i,i+1) = (xi(i)^2*deta(i)^2)/(hr^2) + (xi(i)^2*d2eta(i) + 3*xi(i)*deta(i))/(2*hr);

    C(i) = 6*(1-nu^2)*F*xi(i);
end

%Boundary condition equations at xi_b (grid point #1)
A(1,1) = 1;
B(1,1) = -3*xi(1)*deta(1)/(2*hr) + (1-nu);
B(1,2) = 4*xi(1)*deta(1)/(2*hr);
B(1,3) = -xi(1)*deta(1)/(2*hr);
C(1) = 0;

%Boundary condition equations at xi_a (grid point #Npoints)
A(Npoints,Npoints) = 1;
B(Npoints,Npoints-2) = xi(Npoints)*deta(Npoints)/(2*hr);
B(Npoints,Npoints-1) = -4*xi(Npoints)*deta(Npoints)/(2*hr);
B(Npoints,Npoints) = 3*xi(Npoints)*deta(Npoints)/(2*hr) + (1-nu);
C(Npoints) = 0;

%IMPORTANT: Since P is an unknown, an extra column and row are added to A to solve for P
%and therefore the added entry to C is the non-dimensional deflection Wb.

%Define entries in additional column of A
A(1,Npoints+1) = 0; %BC at r=rb
for i=2:Npoints-1
    A(i,Npoints+1) = -6*(1-nu^2)*(xi(i)^3); %central points
end
A(Npoints,Npoints+1) = 0; %BC at r=ra
A(Npoints+1,Npoints+1) = 0; %This is a meaningless entry so it must be zero.

%Define entries in additional row of A
A(Npoints+1,1) = -(hr/2)/deta(1);
for i=2:Npoints-1
    A(Npoints+1,i) = -(hr)/deta(i);
end
A(Npoints+1,Npoints) = -(hr/2)/deta(Npoints);

%Define additional entry in C
C(Npoints+1) = Wb;

%%%%%%%%%%%%%%%%%%%%%%%%%%%%%%%%%%%%%%%%%%%%%%%%%%%%%%%%%%%%%%%%%%%%%%%%
%%Section 4: Provide an initial guess for the theta vector (plate slope), to be
%%used in the finite-difference iteration procedure.
%%%%%%%%%%%%%%%%%%%%%%%%%%%%%%%%%%%%%%%%%%%%%%%%%%%%%%%%%%%%%%%%%%%%%%%%

if k==0,
    %theta = (-0.75*(1-nu^2)*P*xi.*(1-xi.^2))'; %Linear result
    theta=xi';
else
    theta=whoops;
end

```

```

%%%%%%%%%%%%%%%%%%%%%%%%%%%%%%%%%%%%%%%%%%%%%%%%%%%%%%%%%%%%%%%%%%%%%%%%
%%Section 5: Matrix Manipulation Procedure
%%%%%%%%%%%%%%%%%%%%%%%%%%%%%%%%%%%%%%%%%%%%%%%%%%%%%%%%%%%%%%%%%%%%%%%%
Niterations=500;          %Perform up to 500 iterations
tolerance1=1e-8;
tolerance2=1e-8;
omega=0.45;              %Under-relaxation parameter
if flagNL==1             %This variable is passed into file.
    NLoption=1;          %0 = Linear solution; 1 = NonLinear solution
else
    NLoption=0;
end

for i=1:Niterations,
    i;
    for j=2:Npoints-1     %Define D vector for each iteration
        D(j) = -0.5*theta(j).^2;
    end
    D(1)=0;
    D(Npoints)=0;

    Sr = inv(B)*D'*NLoption; %Solve for Sr
    v_Sr = 12*(1-nu^2)*xi'.^2.*Sr; %Calculate non-linear correction term v_Sr
    v_Sr(Npoints+1) = 0; %Make v_Sr the proper length
    A2 = A - diag(v_Sr,0); %Subtract non-linear correction term from A
    theta_new = inv(A2)*C'; %Calculate new theta vector
    P_result = theta_new(Npoints+1); %Record the calculated value of P
    theta_new = theta_new(1:Npoints); %Remove the P entry from the theta vector

    inner_product = (theta_new'*theta)/sqrt(theta_new'*theta_new)/sqrt(theta'*theta);
    length_ratio = sqrt(theta_new'*theta_new)/sqrt(theta'*theta);

    if (1-inner_product) >= tolerance1 | (1-length_ratio) >= tolerance2
        theta = (1-omega)*theta + omega*theta_new;
    else
        break;
    end
end

%%%%%%%%%%%%%%%%%%%%%%%%%%%%%%%%%%%%%%%%%%%%%%%%%%%%%%%%%%%%%%%%%%%%%%%%
%%Section 6: Calculate Deflection, Curvature, Stress, and Swept Volume in this
%%post-processing section.
%%%%%%%%%%%%%%%%%%%%%%%%%%%%%%%%%%%%%%%%%%%%%%%%%%%%%%%%%%%%%%%%%%%%%%%%

%PRESSURE Pvm: Calculate the differential pressure across the membrane.
Pvm = P_result*E*tvm^4/ra^4;
%Done

%PLATE DEFLECTION: Calculate plate deflection vector from the final theta vector,
%using 2nd-order forward, backward, and central difference methods to express
%theta in terms of W. Then, using matrix inversion to obtain the vector W.
i=1; %BC at rb
Wmatrix(i,i) = deta(i)*(-3/(2*hr));
Wmatrix(i,i+1) = deta(i)*(2/hr);
Wmatrix(i,i+2) = deta(i)*(-1/(2*hr));

for i=2:Npoints-1 %Inner grid points
    Wmatrix(i,i-1) = deta(i)*(-1/(2*hr));
    Wmatrix(i,i+1) = deta(i)*(1/(2*hr));
end

%BC at ra --> Do not do for the outer boundary condition. We already know that
%the deflection at ra is equal to zero.

W = inv(Wmatrix(1:Npoints-1,1:Npoints-1))*theta(1:Npoints-1);

```



```

W=[W;0];
%Done

%PLATE CURVATURE: Calculate plate curvature vector from the final theta vector,
%using 2nd-order forward, backward, and central difference methods.
i=1; %BC at rb
psi(i) = deta(i)*(1/(2*hr))*(-3*theta(i) + 4*theta(i+1) - theta(i+2));

for i=2:Npoints-1 %Inner grid points
    psi(i) = deta(i)*(1/(2*hr))*(theta(i+1) - theta(i-1));
end

i=Npoints; %BC at ra
psi(i) = deta(i)*(1/(2*hr))*(3*theta(i) - 4*theta(i-1) + theta(i-2));
%Done

%PLATE STRESS: Calculate the stress vectors in the plate.

for i=1:Npoints
    Sro(i) = (k^2/(12*(1-nu^2)))*(1 + beta^2/(xi(i)^2));
    sigma_r_top(i) = (E*tvm^2/ra^2)*(Sro(i) + Sr(i) - (1/(2*(1-nu^2)))*(psi(i) +
(nu*theta(i))./xi(i)));
    sigma_r_bot(i) = (E*tvm^2/ra^2)*(Sro(i) + Sr(i) + (1/(2*(1-nu^2)))*(psi(i) +
(nu*theta(i))./xi(i)));
end
if max(sigma_r_top) > max(sigma_r_bot)
    maxstress = abs(max(sigma_r_top));
else
    maxstress = abs(max(sigma_r_bot));
end
%Done

%CONVERSION TO NON_DIMENSIONAL PARAMETERS
r=xi*ra;
y=W*tvm;
thetaND=theta*tvm/ra; %This non-dimensional theta is dw/dr
psiND=psi*tvm/(ra^2); %This non-dimensional psi is d2w/dr2

%PLATE SWEEP VOLUME: Calculate total swept volume under cap and membrane.
V=0;
for i=1:Npoints-1
    dV(i) = pi*(r(i+1)^2-r(i)^2)*0.5*(y(i+1)+y(i));
    V = V + dV(i);
end
yvc = y(1);
Vcap = yvc*pi*rb^2;
Vtotal = Vcap + V;
%Done

```

B.3 NLValveCapMembrane-CaseC.m [see Section 3.5]

```

function
[y,r,Vtotal,psi,W,theta,xi,thetaND,psiND,sigma_r_top,sigma_r_bot,yvc,Fvc,maxstress] =
NLValveCapMembrane_CaseC(Pvm,yvc_imposed,rb,ra,tvm,E,nu,flagNL,No)

%NLValveCapMembrane_CaseC.m

%David C. Roberts
%This Matlab code solves for the non-linear deflection behavior of the valve cap/
%membrane under loading Pvm and a desired valve cap deflection at r=rb. The required
%Fvc to produce this deflection and the resulting deflection, slope, curvature,
%swept volume, and membrane stress are calculated. Case C refers to the fact that
%we are applying Pvm and imposing a cap deflection, and then solving for the Fvc
%and the resulting structural response. Prior to calling this code, the user must
%define Pvm as a function of PHAC and P2. This Pvm loading is defined as follows:
% Pvm = PHAC-P2
%
%
%
%The plate/membrane is characterized by inner radius rb, outer radius ra, thickness
%tvm, and material properties E and nu. If flagNL=0, only linear theory will be
%considered. If flagNL=1, non-linear theory will be considered. No is the value of
%the in-plane pretension. In this file, yvc is the valve cap deflection (Zvc).

format long;

%%%%%%%%%%%%%%%%%%%%%%%%%%%%%%%%%%%%%%%%%%%%%%%%%%%%%%%%%%%%%%%%%%%%%%%%
%Convert Inputs to Dimensionless Quantities
Wb=yvc_imposed/tvm;
P = (Pvm*ra^4)/(E*tvm^4); %Dimensionless loading of pressure across cap/membrane

%%%%%%%%%%%%%%%%%%%%%%%%%%%%%%%%%%%%%%%%%%%%%%%%%%%%%%%%%%%%%%%%%%%%%%%%

beta = sqrt((1-nu)/(1+nu))*(rb/ra);
k = (ra/tvm)*sqrt((12*(1-nu^2)*No)/(E*tvm*(1-beta^2)));
s = beta*k;

%%%%%%%%%%%%%%%%%%%%%%%%%%%%%%%%%%%%%%%%%%%%%%%%%%%%%%%%%%%%%%%%%%%%%%%%
%%Section 2: Define grid spacing and coordinate transformation parameters
%%for finite-difference method
%%%%%%%%%%%%%%%%%%%%%%%%%%%%%%%%%%%%%%%%%%%%%%%%%%%%%%%%%%%%%%%%%%%%%%%%
Npoints=200; %The total # of grid points to use (MUST KEEP IT EVEN)
alpha=1.01; %Grid density parameter
phi=(alpha+1)/(alpha-1); %Grid density ratio
hr = 1/(Npoints-1); %Size of grid spacing
eta = 0:hr:1; %Vector of evenly spaced points between 0 and 1

xi_b = rb/ra; %Non-dimensional position of inner radius
xi_c = (rb+ra)/(2*ra); %Non-dimensional position of midpoint along membrane
xi_a = ra/ra; %Non-dimensional position of outer radius

%For the grid points from xi_b to xi_c, define the derivatives of eta with respect to xi
for i=1:Npoints/2,
xi(i) = xi_b + (alpha-1)*(xi_c-xi_b)*(phi-phi^(1-2*eta(i)))/(1+phi^(1-2*eta(i)));
m = (alpha-1)*(xi_c-xi_b);
m2 = m*phi - m + 2*xi_b;
deta(i) = (0.5/log(phi))*(m*(1+phi))/((m*phi-(xi(i)-xi_b))*(m+(xi(i)-xi_b)));
d2eta(i) = -(0.5/log(phi))*(m*(1+phi)*(m2-2*xi(i)))/((m*phi-(xi(i)-xi_b))*(m+(xi(i)-xi_b)))^2;
end

%For the grid points from xi_c to xi_a
for i=Npoints/2+1:Npoints,
xi(i) = xi_b + (alpha-1)*(xi_c-xi_b)*(phi-phi^(1-2*eta(i)))/(1+phi^(1-2*eta(i)));
m = (alpha-1)*(xi_c-xi_b);
m2 = m*phi - m + 2*xi_b;
deta(i) = (0.5/log(phi))*(m*(1+phi))/((m*phi-(xi(i)-xi_b))*(m+(xi(i)-xi_b)));
d2eta(i) = -(0.5/log(phi))*(m*(1+phi)*(m2-2*xi(i)))/((m*phi-(xi(i)-xi_b))*(m+(xi(i)-xi_b)))^2;
end

```

```

end

%%%%%%%%%%%%%%%%%%%%%%%%%%%%%%%%%%%%%%%%%%%%%%%%%%%%%%%%%%%%%%%%%%%%%%%%%%%%%%
%%Section 3: Finite-Difference Implementation
%%%%%%%%%%%%%%%%%%%%%%%%%%%%%%%%%%%%%%%%%%%%%%%%%%%%%%%%%%%%%%%%%%%%%%%%%%%%%%

%Governing equations at internal points (from 2 to Npoints-1)
for i=2:Npoints-1,
    A(i,i-1) = (xi(i)^2*deta(i)^2)/(hr^2) - (xi(i)^2*d2deta(i) + xi(i)*deta(i))/(2*hr);
    A(i,i) = -( 2*xi(i)^2*deta(i)^2)/(hr^2) + (s^2+1) + xi(i)^2*k^2 );
    A(i,i+1) = (xi(i)^2*deta(i)^2)/(hr^2) + (xi(i)^2*d2deta(i) + xi(i)*deta(i))/(2*hr);

    B(i,i-1) = (xi(i)^2*deta(i)^2)/(hr^2) - (xi(i)^2*d2deta(i) + 3*xi(i)*deta(i))/(2*hr);
    B(i,i) = -(2*xi(i)^2*deta(i)^2)/(hr^2);
    B(i,i+1) = (xi(i)^2*deta(i)^2)/(hr^2) + (xi(i)^2*d2deta(i) + 3*xi(i)*deta(i))/(2*hr);

    C(i) = 6*(1-nu^2)*P*(xi(i)^3 - xi(i)*(rb/ra)^2);
end

%Boundary condition equations at xi_b (grid point #1)
A(1,1) = 1;
B(1,1) = -3*xi(1)*deta(1)/(2*hr) + (1-nu);
B(1,2) = 4*xi(1)*deta(1)/(2*hr);
B(1,3) = -xi(1)*deta(1)/(2*hr);
C(1) = 0;

%Boundary condition equations at xi_a (grid point #Npoints)
A(Npoints,Npoints) = 1;
B(Npoints,Npoints-2) = xi(Npoints)*deta(Npoints)/(2*hr);
B(Npoints,Npoints-1) = -4*xi(Npoints)*deta(Npoints)/(2*hr);
B(Npoints,Npoints) = 3*xi(Npoints)*deta(Npoints)/(2*hr) + (1-nu);
C(Npoints) = 0;

%IMPORTANT: Since F is an unknown, an extra column and row are added to A to solve for F
%and therefore the added entry to C is the non-dimensional deflection Wb.

%Define entries in additional column of A
A(1,Npoints+1) = 0; %BC at r=rb
for i=2:Npoints-1 %central points
    A(i,Npoints+1) = -6*(1-nu^2)*xi(i);
end
A(Npoints,Npoints+1) = 0; %BC at r=ra
A(Npoints+1,Npoints+1) = 0; %This is a meaningless entry so it must be zero.

%Define entries in additional row of A
A(Npoints+1,1) = -(hr/2)/deta(1);
for i=2:Npoints-1
    A(Npoints+1,i) = -(hr)/deta(i);
end
A(Npoints+1,Npoints) = -(hr/2)/deta(Npoints);

%Define additional entry in C
C(Npoints+1) = Wb;

%%%%%%%%%%%%%%%%%%%%%%%%%%%%%%%%%%%%%%%%%%%%%%%%%%%%%%%%%%%%%%%%%%%%%%%%%%%%%%
%%Section 4: Provide an initial guess for the theta vector (plate slope), to be
%%used in the finite-difference iteration procedure.
%%%%%%%%%%%%%%%%%%%%%%%%%%%%%%%%%%%%%%%%%%%%%%%%%%%%%%%%%%%%%%%%%%%%%%%%%%%%%%

if k==0,
    %theta = (-0.75*(1-nu^2)*P*xi.*(1-xi.^2))'; %Linear result
    theta=xi';
else
    theta=xi';
end

```

```

%%%%%%%%%%%%%%%%%%%%%%%%%%%%%%%%%%%%%%%%%%%%%%%%%%%%%%%%%%%%%%%%%%%%%%%%
%%Section 5: Matrix Manipulation Procedure
%%%%%%%%%%%%%%%%%%%%%%%%%%%%%%%%%%%%%%%%%%%%%%%%%%%%%%%%%%%%%%%%%%%%%%%%

Niterations=500;           %Perform up to 500 iterations
tolerance1=1e-8;
tolerance2=1e-8;
omega=0.45;               %Under-relaxation parameter
if flagNL==1              %This variable is passed into file.
    NLoption=1;           %0 = Linear solution; 1 = NonLinear solution
else
    NLoption=0;
end

for i=1:Niterations,
    i;
    for j=2:Npoints-1      %Define D vector for each iteration
        D(j) = -0.5*theta(j).^2;
    end
    D(1)=0;
    D(Npoints)=0;

    Sr = inv(B)*D'*NLoption; %Solve for Sr
    v_Sr = 12*(1-nu^2)*xi'.^2.*Sr; %Calculate non-linear correction term v_Sr
    v_Sr(Npoints+1) = 0; %Make v_Sr the proper length
    A2 = A - diag(v_Sr,0); %Subtract non-linear correction term from A
    theta_new = inv(A2)*C'; %Calculate new theta vector
    F_result = theta_new(Npoints+1); %Record the calculated value of F
    theta_new = theta_new(1:Npoints); %Remove the F entry from the theta vector

    inner_product = (theta_new'*theta)/sqrt(theta_new'*theta_new)/sqrt(theta'*theta);
    length_ratio = sqrt(theta_new'*theta_new)/sqrt(theta'*theta);

    if (1-inner_product) >= tolerance1 | (1-length_ratio) >= tolerance2
        theta = (1-omega)*theta + omega*theta_new;
    else
        break;
    end
end

%%%%%%%%%%%%%%%%%%%%%%%%%%%%%%%%%%%%%%%%%%%%%%%%%%%%%%%%%%%%%%%%%%%%%%%%
%%Section 6: Calculate Deflection, Curvature, Stress, and Swept Volume in this
%%post-processing section.
%%%%%%%%%%%%%%%%%%%%%%%%%%%%%%%%%%%%%%%%%%%%%%%%%%%%%%%%%%%%%%%%%%%%%%%%

%CALCULATE Fvcstar
Fvc = F_result*(pi*E*tvm^4)/(ra^2); %Dimensionalize the additional cap force
%Done

%PLATE DEFLECTION: Calculate plate deflection vector from the final theta vector,
%using 2nd-order forward, backward, and central difference methods to express
%theta in terms of W. Then, using matrix inversion to obtain the vector W.
i=1; %BC at rb
Wmatrix(i,i) = deta(i)*(-3/(2*hr));
Wmatrix(i,i+1) = deta(i)*(2/hr);
Wmatrix(i,i+2) = deta(i)*(-1/(2*hr));

for i=2:Npoints-1 %Inner grid points
    Wmatrix(i,i-1) = deta(i)*(-1/(2*hr));
    Wmatrix(i,i+1) = deta(i)*(1/(2*hr));
end

%BC at ra --> Do not do for the outer boundary condition. We already know that
%the deflection at ra is equal to zero.

W = inv(Wmatrix(1:Npoints-1,1:Npoints-1))*theta(1:Npoints-1);
W=[W;0];

```

```

%Done

%PLATE CURVATURE: Calculate plate curvature vector from the final theta vector,
%using 2nd-order forward, backward, and central difference methods.
i=1; %BC at rb
psi(i) = deta(i)*(1/(2*hr))*(-3*theta(i) + 4*theta(i+1) - theta(i+2));

for i=2:Npoints-1 %Inner grid points
    psi(i) = deta(i)*(1/(2*hr))*(theta(i+1) - theta(i-1));
end

i=Npoints; %BC at ra
psi(i) = deta(i)*(1/(2*hr))*(3*theta(i) - 4*theta(i-1) + theta(i-2));
%Done

%PLATE STRESS: Calculate the stress vectors in the plate.

for i=1:Npoints
    Sro(i) = (k^2/(12*(1-nu^2)))*(1 + beta^2/(xi(i)^2));
    sigma_r_top(i) = (E*tvm^2/ra^2)*(Sro(i) + Sr(i) - (1/(2*(1-nu^2)))*(psi(i) +
(nu*theta(i))./xi(i)));
    sigma_r_bot(i) = (E*tvm^2/ra^2)*(Sro(i) + Sr(i) + (1/(2*(1-nu^2)))*(psi(i) +
(nu*theta(i))./xi(i)));
end
if max(sigma_r_top) > max(sigma_r_bot)
    maxstress = abs(max(sigma_r_top));
else
    maxstress = abs(max(sigma_r_bot));
end
%Done

%CONVERSION TO NON_DIMENSIONAL PARAMETERS
r=xi*ra;
y=W*tvm;
thetaND=theta*tvm/ra; %This non-dimensional theta is dw/dr
psiND=psi*tvm/(ra^2); %This non-dimensional psi is d2w/dr2

%PLATE SWEEP VOLUME: Calculate total swept volume under cap and membrane.
V=0;
for i=1:Npoints-1
    dV(i) = pi*(r(i+1)^2-r(i)^2)*0.5*(y(i+1)+y(i));
    V = V + dV(i);
end
yvc = y(1);
Vcap = yvc*pi*rb^2;
Vtotal = Vcap + V;
%Done

```


Appendix C

Support Documentation for Full Non-Linear Active Valve Model

C.1 FullActiveValve(Non-Linear).mws [Section 4.1]

```

File: FullActiveValve(NON-LINEAR).mws
David C. Roberts
This file creates the active valve matrix used in the full non-linear active valve Matlab model developed by Dave Roberts.
This file defines all the active valve relations (except for the non-linear membrane relations which are solved for in the
Matlab code:NLActiveValveMatlab.m) and solves for the coefficients of the valve matrix A.
> restart;
> Digits:=40;

Digits := 40

Step 1: Define Linear Quasi-Static Relations

Piezoelectric Material
[ This relation assumes perfect d33 actuation (no effect of transverse clamping).
> EQN1 := Z[p] = d[33]*V[p] - (L[p]/E[p])*T[p];

EQN1 := Z_p = d_33 V_p - \frac{L_p T_p}{E_p}

[ This relation determines the piezo charge.
> EQN2 := Q[p] = (eT[33]*A[p]/L[p])*V[p] + (d[33]*A[p])*T[p];

EQN2 := Q_p = \frac{eT_{33} A_p V_p}{L_p} + d_{33} A_p T_p

Bottom Structural Compliance
[ Circular plate with stress imposed over central region.
> EQN3 := Z[bot] = (Xi[Zbot,T]) * T[p];

EQN3 := Z_bot = \Xi_{Zbot, T} T_p

Drive Element Tethers
> EQN4 := Z[te] =
(Xi[Ztetop,F]*Xi[Ztbot,F]) / (Xi[Ztetop,F]+Xi[Ztbot,F]) * (A[p]*T[p]-A[pi]*P[HAC]) -
(Xi[Ztetop,P]*Xi[Ztbot,P]) / (Xi[Ztetop,P]+Xi[Ztbot,P]) * P[HAC];

EQN4 := Z_te = \frac{\Xi_{Ztetop, F} \Xi_{Ztbot, F} (A_p T_p - A_{pis} P_{HAC})}{\Xi_{Ztetop, F} + \Xi_{Ztbot, F}} - \frac{\Xi_{Ztetop, P} \Xi_{Ztbot, P} P_{HAC}}{\Xi_{Ztetop, P} + \Xi_{Ztbot, P}}

> EQN5 := dV[te] =
(Xi[dVtetop,F]*Xi[Ztbot,F]) / (Xi[Ztetop,F]+Xi[Ztbot,F]) * (A[p]*T[p]-A[pi]*P[HAC]) -
(Xi[dVtetop,P]*Xi[dVtbot,P]) / (Xi[dVtetop,P]+Xi[dVtbot,P]) * P[HAC] + A[pi]*Z[te];

EQN5 := dV_te = \frac{\Xi_{dVtetop, F} \Xi_{Ztbot, F} (A_p T_p - A_{pis} P_{HAC})}{\Xi_{Ztetop, F} + \Xi_{Ztbot, F}} - \frac{\Xi_{dVtetop, P} \Xi_{dVtbot, P} P_{HAC}}{\Xi_{dVtetop, P} + \Xi_{dVtbot, P}} + A_{pis} Z_{te}

Drive Element Piston
> EQN6 := Z[pi] = Xi[Zpis,T]*T[p] - Xi[Zpis,P]*P[HAC];

EQN6 := Z_pis = \Xi_{Zpis, T} T_p - \Xi_{Zpis, P} P_{HAC}

> EQN7 := dV[pi] = Xi[dVpis,T]*T[p] - Xi[dVpis,P]*P[HAC];

EQN7 := dV_pis = \Xi_{dVpis, T} T_p - \Xi_{dVpis, P} P_{HAC}

Fluid Compressibility
> EQN8 := dV[fluid] = -(V[HAC]/K[z])*P[HAC];

```


$$EQN8 := dV_{pud} = -\frac{V_{HAC} P_{HAC}}{K_f}$$

Top Structural Compliance

```
[ > EQN9 := Z[top] = Xi[Ztop,P]*P[HAC] + Xi[Ztop,F]*F[vm];
EQN9 := Z_top = Xi_Ztop,P*P_HAC + Xi_Ztop,F*F_vm
[ > EQN10 := dV[top] = Xi[dVtop,P]*P[HAC] + Xi[dVtop,F]*F[vm] + lambda[vm]*Z[top];
EQN10 := dV_top = Xi_dVtop,P*P_HAC + Xi_dVtop,F*F_vm + lambda_vm*Z_top
[ > EQN11 := F[vm] = (A[vm]-lambda[vc])*(P[HAC]-P[2]) + A[vc]*(P[HAC]-P[1]);
EQN11 := F_vm = (A_vm - lambda_vc)*(P_HAC - P_2) + A_vc*(P_HAC - P_1)
```

Valve Cap/Membrane

[The only valve/cap membrane relation defined here is the sum of the forces on the valve cap.

```
[ > EQN12 := F[vc] = (P[HAC]-P[1])*A[vc];
EQN12 := F_vc = (P_HAC - P_1)*A_vc
```

Deflection, Swept Volume Conservation

[All structural deflections and swept volumes are defined to be positive in the upward direction.

```
[ > EQN13 := Z[p] + Z[bot] = Z[te] + Z[pi];
EQN13 := Z_p + Z_bot = Z_te + Z_pi
```

Other Relations

[Variables as functions of other variables.

```
[ > EQN14 := Z[de] = Z[te] + Z[pi];
EQN14 := Z_de = Z_te + Z_pi
```


Step 2: Define Geometric/Material Parameters

```
[ Geometric Parameters:
[ > R[vc]:=0.31e-3: R[vm]:=0.80e-3: t[vm]:=10e-6: A[vc]:=Pi*R[vc]^2: A[vm]:=Pi*R[vm]^2:
t[vc]:=400e-6:
[ > L[p]:=1e-3: R[p]:=1e-3: A[p]:=Pi*R[p]^2:
[ > R[pi]:=3e-3: R[ch]:=3.225e-3: t[pi]:=800e-6: t[topte]:=10e-6: t[botte]:=10e-6:
A[pi]:=Pi*R[pi]^2:
[ > t[bot]:=1000e-6:
[ > H[HAC]:=400e-6: V[HAC]:=Pi*R[ch]^2*H[HAC] + Pi*(R[vm]^2-R[vc]^2)*t[vc]:
[ > t[top]:=1000e-6:
[ Material Parameters:
[ > d[33]:=2000e-12: sD[33]:=16.4e-12: sE[33]:=111e-12: E[p]:=1/sE[33]:
eT[33]:=d[33]^2/(sE[33]-sD[33]): E[si]:=165e9: nu[si]:=0.22: K[f]:=2e9: alpha[si]:=1.25:
```

Step 3: Calculate Linear Plate Coefficients

- Bottom Structural Compliance [identical to FullActiveValve(LINEAR).mws]
- Drive Element Tethers [identical to FullActiveValve(LINEAR).mws]
- Drive Element Piston (More Compliant: Hinged Outer Circumference) [identical to

FullActiveValve(LINEAR).mws]

 Drive Element Piston (Less Compliant: Rigid Outer Circumference) [identical to FullActiveValve(LINEAR).mws]

 Drive Element Piston (Averaged Compliance) [identical to FullActiveValve(LINEAR).mws]

 Top Structural Compliance [identical to FullActiveValve(LINEAR).mws]

Step 4: Solve Equations

The variables [Zp, Tp, Qp, Zbot, Ztc, dVtc, Zpis, dVpis, dVfluid, Ztop, dVtop, Fvm, Fvc, and Zde] are solved for in terms of the other variables [Vp, P1, P2, and PHAC]. Once solved for, each of the coefficients is assigned to the proper location in matrix A, which are then passed to NLAActiveValveMatlab.m.

```
> Solutions:=solve({EQN1,EQN2,EQN3,EQN4,EQN5,EQN6,EQN7,EQN8,EQN9,EQN10,EQN11,EQN12,EQN13,EQN14},{Z[p],T[p],Q[p],Z[bot],Z[tc],dV[tc],Z[pis],dV[pis],dV[fluid],Z[top],dV[top],F[vm],F[vc],Z[de]}):  
[>  
A11:=evalf(subs({V[p]=1,P[1]=0,P[2]=0,P[HAC]=0},subs(Solutions,Z[p]))):  
[> A12:=evalf(subs({V[p]=0,P[1]=1,P[2]=0,P[HAC]=0},subs(Solutions,Z[p]))):  
[> A13:=evalf(subs({V[p]=0,P[1]=0,P[2]=1,P[HAC]=0},subs(Solutions,Z[p]))):  
[> A14:=evalf(subs({V[p]=0,P[1]=0,P[2]=0,P[HAC]=1},subs(Solutions,Z[p]))):  
[>  
A21:=evalf(subs({V[p]=1,P[1]=0,P[2]=0,P[HAC]=0},subs(Solutions,T[p]))):  
[> A22:=evalf(subs({V[p]=0,P[1]=1,P[2]=0,P[HAC]=0},subs(Solutions,T[p]))):  
[> A23:=evalf(subs({V[p]=0,P[1]=0,P[2]=1,P[HAC]=0},subs(Solutions,T[p]))):  
[> A24:=evalf(subs({V[p]=0,P[1]=0,P[2]=0,P[HAC]=1},subs(Solutions,T[p]))):  
[>  
A31:=evalf(subs({V[p]=1,P[1]=0,P[2]=0,P[HAC]=0},subs(Solutions,Q[p]))):  
[> A32:=evalf(subs({V[p]=0,P[1]=1,P[2]=0,P[HAC]=0},subs(Solutions,Q[p]))):  
[> A33:=evalf(subs({V[p]=0,P[1]=0,P[2]=1,P[HAC]=0},subs(Solutions,Q[p]))):  
[> A34:=evalf(subs({V[p]=0,P[1]=0,P[2]=0,P[HAC]=1},subs(Solutions,Q[p]))):  
[>  
A41:=evalf(subs({V[p]=1,P[1]=0,P[2]=0,P[HAC]=0},subs(Solutions,Z[bot]))):  
[> A42:=evalf(subs({V[p]=0,P[1]=1,P[2]=0,P[HAC]=0},subs(Solutions,Z[bot]))):  
[> A43:=evalf(subs({V[p]=0,P[1]=0,P[2]=1,P[HAC]=0},subs(Solutions,Z[bot]))):  
[> A44:=evalf(subs({V[p]=0,P[1]=0,P[2]=0,P[HAC]=1},subs(Solutions,Z[bot]))):  
[>  
A51:=evalf(subs({V[p]=1,P[1]=0,P[2]=0,P[HAC]=0},subs(Solutions,Z[tc]))):  
[> A52:=evalf(subs({V[p]=0,P[1]=1,P[2]=0,P[HAC]=0},subs(Solutions,Z[tc]))):  
[> A53:=evalf(subs({V[p]=0,P[1]=0,P[2]=1,P[HAC]=0},subs(Solutions,Z[tc]))):  
[> A54:=evalf(subs({V[p]=0,P[1]=0,P[2]=0,P[HAC]=1},subs(Solutions,Z[tc]))):  
[>  
A61:=evalf(subs({V[p]=1,P[1]=0,P[2]=0,P[HAC]=0},subs(Solutions,dV[tc]))):  
[> A62:=evalf(subs({V[p]=0,P[1]=1,P[2]=0,P[HAC]=0},subs(Solutions,dV[tc]))):  
[> A63:=evalf(subs({V[p]=0,P[1]=0,P[2]=1,P[HAC]=0},subs(Solutions,dV[tc]))):
```

```

[ > A64:=evalf(subs({V[p]=0,P[1]=0,P[2]=0,P[HAC]=1},subs(Solutions,dV[te]))):
[ >
[ > A71:=evalf(subs({V[p]=1,P[1]=0,P[2]=0,P[HAC]=0},subs(Solutions,Z[piis]))):
[ > A72:=evalf(subs({V[p]=0,P[1]=1,P[2]=0,P[HAC]=0},subs(Solutions,Z[piis]))):
[ > A73:=evalf(subs({V[p]=0,P[1]=0,P[2]=1,P[HAC]=0},subs(Solutions,Z[piis]))):
[ > A74:=evalf(subs({V[p]=0,P[1]=0,P[2]=0,P[HAC]=1},subs(Solutions,Z[piis]))):
[ >
[ > A81:=evalf(subs({V[p]=1,P[1]=0,P[2]=0,P[HAC]=0},subs(Solutions,dV[piis]))):
[ > A82:=evalf(subs({V[p]=0,P[1]=1,P[2]=0,P[HAC]=0},subs(Solutions,dV[piis]))):
[ > A83:=evalf(subs({V[p]=0,P[1]=0,P[2]=1,P[HAC]=0},subs(Solutions,dV[piis]))):
[ > A84:=evalf(subs({V[p]=0,P[1]=0,P[2]=0,P[HAC]=1},subs(Solutions,dV[piis]))):
[ >
[ > A91:=evalf(subs({V[p]=1,P[1]=0,P[2]=0,P[HAC]=0},subs(Solutions,dV[fluid]))):
[ > A92:=evalf(subs({V[p]=0,P[1]=1,P[2]=0,P[HAC]=0},subs(Solutions,dV[fluid]))):
[ > A93:=evalf(subs({V[p]=0,P[1]=0,P[2]=1,P[HAC]=0},subs(Solutions,dV[fluid]))):
[ > A94:=evalf(subs({V[p]=0,P[1]=0,P[2]=0,P[HAC]=1},subs(Solutions,dV[fluid]))):
[ >
[ > A101:=evalf(subs({V[p]=1,P[1]=0,P[2]=0,P[HAC]=0},subs(Solutions,Z[top]))):
[ > A102:=evalf(subs({V[p]=0,P[1]=1,P[2]=0,P[HAC]=0},subs(Solutions,Z[top]))):
[ > A103:=evalf(subs({V[p]=0,P[1]=0,P[2]=1,P[HAC]=0},subs(Solutions,Z[top]))):
[ > A104:=evalf(subs({V[p]=0,P[1]=0,P[2]=0,P[HAC]=1},subs(Solutions,Z[top]))):
[ >
[ > A111:=evalf(subs({V[p]=1,P[1]=0,P[2]=0,P[HAC]=0},subs(Solutions,dV[top]))):
[ > A112:=evalf(subs({V[p]=0,P[1]=1,P[2]=0,P[HAC]=0},subs(Solutions,dV[top]))):
[ > A113:=evalf(subs({V[p]=0,P[1]=0,P[2]=1,P[HAC]=0},subs(Solutions,dV[top]))):
[ > A114:=evalf(subs({V[p]=0,P[1]=0,P[2]=0,P[HAC]=1},subs(Solutions,dV[top]))):
[ >
[ > A121:=evalf(subs({V[p]=1,P[1]=0,P[2]=0,P[HAC]=0},subs(Solutions,F[vm]))):
[ > A122:=evalf(subs({V[p]=0,P[1]=1,P[2]=0,P[HAC]=0},subs(Solutions,F[vm]))):
[ > A123:=evalf(subs({V[p]=0,P[1]=0,P[2]=1,P[HAC]=0},subs(Solutions,F[vm]))):
[ > A124:=evalf(subs({V[p]=0,P[1]=0,P[2]=0,P[HAC]=1},subs(Solutions,F[vm]))):
[ >
[ > A131:=evalf(subs({V[p]=1,P[1]=0,P[2]=0,P[HAC]=0},subs(Solutions,F[vc]))):
[ > A132:=evalf(subs({V[p]=0,P[1]=1,P[2]=0,P[HAC]=0},subs(Solutions,F[vc]))):
[ > A133:=evalf(subs({V[p]=0,P[1]=0,P[2]=1,P[HAC]=0},subs(Solutions,F[vc]))):
[ > A134:=evalf(subs({V[p]=0,P[1]=0,P[2]=0,P[HAC]=1},subs(Solutions,F[vc]))):
[ >
[ > A141:=evalf(subs({V[p]=1,P[1]=0,P[2]=0,P[HAC]=0},subs(Solutions,Z[de]))):
[ > A142:=evalf(subs({V[p]=0,P[1]=1,P[2]=0,P[HAC]=0},subs(Solutions,Z[de]))):
[ > A143:=evalf(subs({V[p]=0,P[1]=0,P[2]=1,P[HAC]=0},subs(Solutions,Z[de]))):
[ > A144:=evalf(subs({V[p]=0,P[1]=0,P[2]=0,P[HAC]=1},subs(Solutions,Z[de]))):
[ >

```

 Step 5: Output Matrix to Matlab File

Now that all the matrix coefficients have been solved for, it is necessary to output these values to a file which Matlab can read.

Also,

output the important valve geometry parameters (rb, ra, tvn, E, nu) for use in the non-linear Matlab code.

```
> interface(echo=0);
> writeto('NLActiveValveMatrix.m');
> printf('A(1,1) = %+2.08e;',A11);
> printf('A(1,2) = %+2.08e;',A12);
> printf('A(1,3) = %+2.08e;',A13);
> printf('A(1,4) = %+2.08e;',A14);
> printf('A(2,1) = %+2.08e;',A21);
> printf('A(2,2) = %+2.08e;',A22);
> printf('A(2,3) = %+2.08e;',A23);
> printf('A(2,4) = %+2.08e;',A24);
> printf('A(3,1) = %+2.08e;',A31);
> printf('A(3,2) = %+2.08e;',A32);
> printf('A(3,3) = %+2.08e;',A33);
> printf('A(3,4) = %+2.08e;',A34);
> printf('A(4,1) = %+2.08e;',A41);
> printf('A(4,2) = %+2.08e;',A42);
> printf('A(4,3) = %+2.08e;',A43);
> printf('A(4,4) = %+2.08e;',A44);
> printf('A(5,1) = %+2.08e;',A51);
> printf('A(5,2) = %+2.08e;',A52);
> printf('A(5,3) = %+2.08e;',A53);
> printf('A(5,4) = %+2.08e;',A54);
> printf('A(6,1) = %+2.08e;',A61);
> printf('A(6,2) = %+2.08e;',A62);
> printf('A(6,3) = %+2.08e;',A63);
> printf('A(6,4) = %+2.08e;',A64);
> printf('A(7,1) = %+2.08e;',A71);
> printf('A(7,2) = %+2.08e;',A72);
> printf('A(7,3) = %+2.08e;',A73);
> printf('A(7,4) = %+2.08e;',A74);
> printf('A(8,1) = %+2.08e;',A81);
> printf('A(8,2) = %+2.08e;',A82);
> printf('A(8,3) = %+2.08e;',A83);
> printf('A(8,4) = %+2.08e;',A84);
> printf('A(9,1) = %+2.08e;',A91);
> printf('A(9,2) = %+2.08e;',A92);
> printf('A(9,3) = %+2.08e;',A93);
> printf('A(9,4) = %+2.08e;',A94);
> printf('A(10,1) = %+2.08e;',A101);
> printf('A(10,2) = %+2.08e;',A102);
> printf('A(10,3) = %+2.08e;',A103);
```

Page 5

```
[ > printf('A(10,4) = %+2.08e;',A104);
[ > printf('A(11,1) = %+2.08e;',A111);
[ > printf('A(11,2) = %+2.08e;',A112);
[ > printf('A(11,3) = %+2.08e;',A113);
[ > printf('A(11,4) = %+2.08e;',A114);
[ > printf('A(12,1) = %+2.08e;',A121);
[ > printf('A(12,2) = %+2.08e;',A122);
[ > printf('A(12,3) = %+2.08e;',A123);
[ > printf('A(12,4) = %+2.08e;',A124);
[ > printf('A(13,1) = %+2.08e;',A131);
[ > printf('A(13,2) = %+2.08e;',A132);
[ > printf('A(13,3) = %+2.08e;',A133);
[ > printf('A(13,4) = %+2.08e;',A134);
[ > printf('A(14,1) = %+2.08e;',A141);
[ > printf('A(14,2) = %+2.08e;',A142);
[ > printf('A(14,3) = %+2.08e;',A143);
[ > printf('A(14,4) = %+2.08e;',A144);
[ > printf('rvc = %+2.08e;',R[vc]);
[ > printf('rvm = %+2.08e;',R[vm]);
[ > printf('tvm = %+2.08e;',t[vm]);
[ > printf('Esi = %+2.08e;',E[si]);
[ > printf('nusi = %+2.08e;',nu[si]);
[ > writeto('terminal');
[ >
```

C.2 NActiveValveMatlab.m [Section 4.1]

```

%[NActiveValveMatlab.m]    DAVID C. ROBERTS
%
% This file calculates the behavior of the active valve, with non-linear valve/cap
%membrane deformation included. First, the Maple file FullActiveValve(Non-Linear).mws
%is run in order to generate the matrix of linear valve relation coefficients. That matrix
%is then used in this file.

clear;
close all;
format long;
NActiveValveMatrix;          %Read in the linear matrix coefficients and the valve geometry
                             %from this file, which was generated by running
                             %NActiveValveMaple.mws. The matrix values go from A11,A12,A13,
                             %A14, A21, ..., A141,A142,A143,A144 and the valve geometry
                             %variables read in are rvc, rvm, tvn, Esi, nusi.

#####DEFINE INPUT PARAMETERS#####
Vp=500;                       %Piezo Voltage
P1=0.5e6;                     %Pressure on top of valve cap
P2=0e6;                       %Pressure on top of valve membrane
flagNL=1;                     %Include non-linearity if flagNL=1
No=0;                         %Initial in-plane prestress

#####PROVIDE INITIAL GUESS FOR PHAC#####
PHACguess=0.0013e6;
PHAC1=PHACguess;
PHAC2=PHACguess;
check0=1;
check1=1;
i=0
j=0

%Determine Volume discrepancy for initial PHAC guess
U=[Vp P1 P2 PHAC1];          %Vector of input parameters to compliance matrix
S=A*U';                      %S is the vector of all linear responses
Fvc=S(13); Pvm=PHAC1-P2;     %Define these loadings for use in NActiveValve_MembraneCaseA.m
[y,r,Vtotal,psi,W,theta,xi,thetaND,psiND,sigma_r_top,sigma_r_bot,yvc,maxstress] =
NActiveValve_MembraneCaseA(Pvm,Fvc,rvc,rvm,tvm,Esi,nusi,flagNL,No);
dVvm=Vtotal; dVte=S(6); dVpis=S(8); dVfluid=S(9); dVtop=S(11);
check1 = (dVvm + dVtop - dVte - dVpis - dVfluid);
check0=check1;
%Done

%Determine range of PHAC (between PHAC0 and PHAC1) within which the real PHAC lies
while check0*check1/(abs(check0*check1))> 0
    i=0
    j=j+1

    PHAC0 = PHAC1;
    PHAC1 = PHAC2
    check0 = check1

    U=[Vp P1 P2 PHAC1];      %Vector of input parameters to compliance matrix
    S=A*U';                  %S is the vector of all linear responses
    Fvc=S(13); Pvm=PHAC1-P2; %Define these loadings for use in
NActiveValve_MembraneCaseA.m
    [y,r,Vtotal,psi,W,theta,xi,thetaND,psiND,sigma_r_top,sigma_r_bot,yvc,maxstress] =
NActiveValve_MembraneCaseA(Pvm,Fvc,rvc,rvm,tvm,Esi,nusi,flagNL,No);
    dVvm=Vtotal; dVte=S(6); dVpis=S(8); dVfluid=S(9); dVtop=S(11);
    check1 = (dVvm + dVtop - dVte - dVpis - dVfluid);

    if check1 < 0
        PHAC2 = 10*PHAC1;

```

```

elseif check1 > 0
    PHAC2 = 0.1*PHAC1;
else
    break;
end
end
end

if PHAC1<PHAC0          %rearrange PHAC0 to be less than PHAC1
    PHACmax=PHAC0;
    PHACmin=PHAC1;
    PHAC1=PHACmax
    PHAC0=PHACmin
else
end
%DONE,it has been determined that PHAC lies between PHAC0 and PHAC1

j=0;

%Determine solution for Pvc
PHACm=0.5*(PHAC0+PHAC1);
firsthalf=0;

while abs((PHAC1-PHAC0)/PHAC0) > 0.0001

    i=1
    j=j+1

    if firsthalf==1

        U=[Vp P1 P2 PHACm];          %Vector of input parameters to compliance matrix
        S=A*U';                      %S is the vector of all linear responses
        Fvc=S(13); Pvm=PHACm-P2;     %Define these loadings for use in
NLActiveValve_MembraneCaseA.m
        [y,r,VtTotal,psi,W,theta,xi,thetaND,psiND,sigma_r_top,sigma_r_bot,yvc,maxstress] =
NLActiveValve_MembraneCaseA(Pvm,Fvc,rvc,rvm,tvm,Esi,nusi,flagNL,No);
        dVvm=VtTotal; dVte=S(6); dVpis=S(8); dVfluid=S(9); dVtop=S(11);
        checkm = (dVvm + dVtop - dVte - dVpis - dVfluid);

    else

        U=[Vp P1 P2 PHAC0];          %Vector of input parameters to compliance matrix
        S=A*U';                      %S is the vector of all linear responses
        Fvc=S(13); Pvm=PHAC0-P2;     %Define these loadings for use in
NLActiveValve_MembraneCaseA.m
        [y,r,VtTotal,psi,W,theta,xi,thetaND,psiND,sigma_r_top,sigma_r_bot,yvc,maxstress] =
NLActiveValve_MembraneCaseA(Pvm,Fvc,rvc,rvm,tvm,Esi,nusi,flagNL,No);
        dVvm=VtTotal; dVte=S(6); dVpis=S(8); dVfluid=S(9); dVtop=S(11);
        check0 = (dVvm + dVtop - dVte - dVpis - dVfluid);

        U=[Vp P1 P2 PHACm];          %Vector of input parameters to compliance matrix
        S=A*U';                      %S is the vector of all linear responses
        Fvc=S(13); Pvm=PHACm-P2;     %Define these loadings for use in
NLActiveValve_MembraneCaseA.m
        [y,r,VtTotal,psi,W,theta,xi,thetaND,psiND,sigma_r_top,sigma_r_bot,yvc,maxstress] =
NLActiveValve_MembraneCaseA(Pvm,Fvc,rvc,rvm,tvm,Esi,nusi,flagNL,No);
        dVvm=VtTotal; dVte=S(6); dVpis=S(8); dVfluid=S(9); dVtop=S(11);
        checkm = (dVvm + dVtop - dVte - dVpis - dVfluid);

    end

    if check0*checkm <= 0
        PHAC1=PHACm;
        firsthalf=1;
    else
        PHAC0=PHACm;
        firsthalf=0;
    end
end

```

```

    PHACm=0.5*(PHAC0+PHAC1)
end
PHAC=PHACm;
%DONE, PHAC solution has been determined

%Evaluate all parameters for last value of PHACm

U=[Vp P1 P2 PHACm];      %Vector of input parameters to compliance matrix
S=A*U';                  %S is the vector of all linear responses
Fvc=S(13); Pvm=PHACm-P2; %Define these loadings for use in NActiveValve_MembraneCaseA.m
[y,r,Vtotal,psi,W,theta,xi,thetaND,psiND,sigma_r_top,sigma_r_bot,yvc,maxstress] =
NActiveValve_MembraneCaseA(Pvm,Fvc,rvc,rvm,tvm,Esi,nusi,flagNL,No);

Zp=S(1)                  %Print to screen all results
Tp=S(2)
Qp=S(3)
Zbot=S(4)
Zte=S(5)
dVte=S(6)
Zpis=S(7)
dVpis=S(8)
dVfluid=S(9)
Ztop=S(10)
dVtop=S(11)
Fvm=S(12)
Fvc=S(13)
Zde=S(14)
Zvc=yvc+Ztop
dVvm=Vtotal
maxstress
%DONE

```

5216-26